

**MATERIALS RESEARCH SOCIETY  
SYMPOSIUM PROCEEDINGS VOLUME 455**

# **Structure and Dynamics of Glasses and Glass Formers**

Symposium held December 2-6, 1996, Boston, Massachusetts, U.S.A.

## **EDITORS:**

**C.A. Angell**

*Arizona State University  
Tempe, Arizona, U.S.A.*

**K.L. Ngai**

*Naval Research Laboratory  
Washington, D.C., U.S.A.*

**J. Kieffer**

*University of Illinois, Urbana  
Urbana, Illinois, U.S.A.*

**T. Egami**

*University of Pennsylvania  
Philadelphia, Pennsylvania, U.S.A.*

**G.U. Nienhaus**

*University of Ulm  
Ulm, Germany*

**DTIC QUALITY INSPECTED 2**



**PITTSBURGH, PENNSYLVANIA**

19971001 061

## **Structure and Dynamics of Glasses and Glass Formers**

**MATERIALS RESEARCH SOCIETY  
SYMPOSIUM PROCEEDINGS VOLUME 455**

# **Structure and Dynamics of Glasses and Glass Formers**

Symposium held December 2-6, 1996, Boston, Massachusetts, U.S.A.

## **EDITORS:**

**C.A. Angell**

*Arizona State University  
Tempe, Arizona, U.S.A.*

**K.L. Ngai**

*Naval Research Laboratory  
Washington, D.C., U.S.A.*

**J. Kieffer**

*University of Illinois, Urbana  
Urbana, Illinois, U.S.A.*

**T. Egami**

*University of Pennsylvania  
Philadelphia, Pennsylvania, U.S.A.*

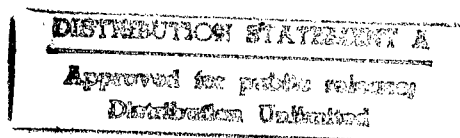
**G.U. Nienhaus**

*University of Ulm  
Ulm, Germany*



**PITTSBURGH, PENNSYLVANIA**

**DTIC QUALITY INSPECTED 2**



19971001 061

This work was supported in part by the Army Research Office under Grant Number DAAG55-97-1-0005. The views, opinions, and/or findings contained in this report are those of the author(s) and should not be construed as an official Department of the Army position, policy, or decision, unless so designated by other documentation.

This material is based upon work supported by the National Science Foundation under Grant No. DMR-9619352. Any opinions, findings, and conclusions or recommendations expressed in this materials are those of the author (s) and do not necessarily reflect the views of the National Science Foundation.

This work was supported in part by the Office of Naval Research under Grant Number N00014-97-1-0104. The United States Government has a royalty-free license throughout the world in all copyrightable material contained herein.

Single article reprints from this publication are available through University Microfilms Inc., 300 North Zeeb Road, Ann Arbor, Michigan 48106

CODEN: MRSPDH

Copyright 1997 by Materials Research Society.  
All rights reserved.

This book has been registered with Copyright Clearance Center, Inc. For further information, please contact the Copyright Clearance Center, Salem, Massachusetts.

Published by:

Materials Research Society  
9800 McKnight Road  
Pittsburgh, Pennsylvania 15237  
Telephone (412) 367-3003  
Fax (412) 367-4373  
Website: <http://www.mrs.org/>

Library of Congress Cataloging in Publication Data

Structure and dynamics of glasses and glass formers : symposium held December 2-6, 1996, Boston, Massachusetts, U.S.A. / editors, C.A. Angell, K.L. Ngai, J. Kieffer, T. Egami, G.U. Nienhaus  
p. cm—(Materials Research Society symposium proceedings ; v. 455)  
Includes bibliographical references and index.  
ISBN 1-55899-359-2

I. Glass—Congresses. I. Angell, C.A. II. Ngai, K.L. III. Kieffer, J. IV. Egami, T. V. Nienhaus, G.U. VI. Series: Materials Research Society symposium proceedings ; v. 455.

TP845.S77 1997  
666'.1—dc21

97-20773  
CIP

Manufactured in the United States of America



## CONTENTS

Preface .....	xi
Materials Research Society Symposium Proceedings .....	xii

### PART I: SHORT-TIME DYNAMICS

*Dynamics at the Glass Transition in Polymers: Results From Neutron Spectroscopy .....	3
<i>D. Richter, A. Arbe, and J. Colmenero</i>	
*Fast Dynamics in Glass-Forming Polymers Revisited .....	17
<i>J. Colmenero, A. Arbe, C. Mijangos, and H. Reinecke</i>	
*Anomalies of the Fast Relaxation Dynamics at $T_g$ in Strong Glass Formers .....	35
<i>A. Brodin and L.M. Torell</i>	
*Dielectric Spectroscopy at High Frequencies on Glass- Forming Liquids .....	47
<i>P. Lunkenheimer, A. Pimenov, M. Dressel, B. Gorshunov, U. Schneider, B. Schiener, R. Böhmer, and A. Loidl</i>	
*Dynamics of a Supercooled Lennard-Jones System: Qualitative and Quantitative Tests of Mode-Coupling Theory .....	59
<i>Walter Kob and Markus Nauroth</i>	
*Fast Dynamics in Glass-Forming Systems: Vibrations Versus Relaxation .....	69
<i>A.P. Sokolov</i>	
*Fast Dynamics in Glass Formers: Relation to Fragility and the Kohlrausch Exponent .....	81
<i>K.L. Ngai and C.M. Roland</i>	
*Relaxation Processes and the Mixed Alkali Effect in Alkali Metasilicate Glasses .....	91
<i>J. Habasaki, I. Okada, and Y. Hiwatari</i>	

### PART II: RELAXATION DYNAMICS OF GLASSES AND GLASS FORMERS

*Dynamical Heterogeneities in Glass-Forming Materials .....	105
<i>A. Heuer, S.C. Kuebler, U. Tracht, H.W. Spiess, and K. Okun</i>	

\*Invited Paper

<b>*Slow Dielectric Relaxation of Supercooled Liquids Investigated by Nonresonant Spectral Hole Burning</b> .....	117
<i>R.V. Chamberlin, B. Schiener, and R. Böhmer</i>	
<b>Dynamic Heterogeneity by Higher Moments of a Relaxing Quantity</b> .....	127
<i>R. Richert</i>	
<b>Fluctuation Model for Structural Relaxation and the Glass Transition</b> .....	133
<i>C.T. Moynihan and J-H. Whang</i>	
<b>Cooperative Length Scale of Aroclor Near Its Dynamic Glass Transition</b> .....	141
<i>A.K. Rizos and K.L. Ngai</i>	
<b>Possible Causes of the Change of Dynamics in Glass-Forming Materials Subjected to Reduced Dimension</b> .....	147
<i>K.L. Ngai and A.K. Rizos</i>	
<b>Dynamics in a Nonfragile Glass-Forming Liquid</b> .....	151
<i>B. Rufflé, S. Beaufils, J. Etrillard, J. Gallier, B. Toudic, C. Ecolivet, G. Coddens, J.P. Ambroise, E. Guéguen, and R. Marchand</i>	
<b>Rotational Dynamics of a Molecular Probe in Tri-Cresyl Phosphate: From "Stick" to "Slip" Boundary Conditions</b> .....	157
<i>M.G. Bagliesi, F. Cianflone, and D. Leporini</i>	
<b>*A Unified Theory for the Glass Transition Dynamics and Its Singularities</b> .....	163
<i>T. Odagaki, J. Matsui, M. Fujisaki, and M. Higuchi</i>	
<b>Fragility of Polymeric Liquids: Correlations Between Thermodynamic and Dynamic Properties</b> .....	171
<i>Dina M. Colucci and Gregory B. McKenna</i>	
<b>Modeling DSC Annealing Peaks for Polyetherimide: Incorporation of Temperature Gradients</b> .....	177
<i>Sindee L. Simon</i>	
<b>Glass Transition and Ultrasonic Relaxation in Polystyrene</b> .....	183
<i>A. Sahnoune and L. Piché</i>	
<b>Time and Ensemble Averaged Dynamic Light Scattering in Ortho Terphenyl Above and Below the Glass Transition</b> .....	189
<i>D.L. Sidebottom and C.M. Sorensen</i>	
<b>Reorientational Dynamics and Intermolecular Cooperativity of Reactive Systems</b> .....	195
<i>Jovan Mijovic</i>	

\*Invited Paper

### PART III: GLASSLIKE SYSTEMS, SIMULATIONS, AND MODELS

<b>*From Spin Glasses to Glasses</b> .....	203
<i>J.P. Bouchaud and M. Mezard</i>	
<b>*A Model for Relaxation in Supercooled Liquids and Polymer Melts</b> .....	211
<i>T. Pakula and J. Teichmann</i>	
<b>Temperature Dependence of Spatial and Dynamic Heterogeneities Above the Ising Spin Glass Transition</b> .....	223
<i>S.C. Glotzer, P.H. Poole, A. Coniglio, and N. Jan</i>	
<b>Glassy and Crystalline States in a Model Without Disorder: Spin Analog of a Structural Glass</b> .....	229
<i>Lei Gu and Bulbul Chakraborty</i>	
<b>Slow Dynamics in Supercooled Water</b> .....	235
<i>Francesco Sciortino, Piero Tartaglia, Paola Gallo, and Sow-Hsin Chen</i>	
<b>Local Structure of MD Simulated Soda-Lime-Silicate Glass</b> .....	241
<i>Xianglong Yuan and Alastair N. Cormack</i>	
<b>The Coupling Model of Relaxation: An Alternative for the Study of an Interacting System of Small Particles</b> .....	247
<i>J. Castro</i>	
<b>1/f Dielectric Fluctuations at the Glass Transition</b> .....	253
<i>N.E. Israeloff and W. Wang</i>	
<b>Molecular-Dynamics Simulation of Alkali Borate Glass Using Coordination Dependent Potential</b> .....	259
<i>Byeongwon Park and Alastair N. Cormack</i>	
<b>Molecular-Dynamics Simulations of Fracture in Amorphous Silica</b> .....	267
<i>Jinghan Wang, Andrey Omeltchenko, Rajiv K. Kalia, and Priya Vashishta</i>	
<b>Slow Dynamics and Glasslike Behavior of Liquid Crystals Dispersed in Nanoporous Media</b> .....	273
<i>F.M. Aliev and G.P. Sinha</i>	
<b>Simulation of Pressure Effects on Glasses</b> .....	279
<i>Y. Kogure and M. Doyama</i>	
<b>Separation of Diffusive Jump Motion and Trapped Motion of Atoms in a Glass-Forming Process Via Molecular-Dynamics Simulation</b> .....	285
<i>J. Matsui, M. Fujisaki, and T. Odagaki</i>	

\*Invited Paper

#### PART IV: CONTRASTING METALLIC, IONIC, BIO, AND POLYMER SYSTEMS

<b>Crystallization Pathway in the Bulk Metallic Glass</b> <b>Zr<sub>41.2</sub>Ti<sub>13.8</sub>Cu<sub>12.5</sub>Ni<sub>10</sub>Be<sub>22.5</sub> .....</b>	<b>295</b>
<i>S. Schneider, P. Thiyagarajan, U. Geyer, and W.L. Johnson</i>	
<b>Small Atom Diffusion and Breakdown of Stokes-Einstein Relation in the Supercooled Liquid State of Zr-Ti-Cu-Ni-Be Alloys .....</b>	<b>301</b>
<i>U. Geyer, S. Schneider, Y. Qiu, M-P. Macht, T.A. Tombrello, and W.L. Johnson</i>	
<b>*Metastability and Properties of Metallic Bulk Glass Forming Alloys .....</b>	<b>307</b>
<i>H-J. Fecht</i>	
<b>*Crystalline, Glassy, and Molten Electrolytes: Conductivity Spectra and Model Considerations .....</b>	<b>319</b>
<i>K. Funke</i>	
<b>Space-Time-Correlations for Cation Motion in Alkali Silicates .....</b>	<b>331</b>
<i>John Kieffer</i>	
<b>Protein Dynamics From Intramolecular Electron Transfer .....</b>	<b>337</b>
<i>G.U. Nienhaus, B.H. McMahon, J.D. Müller, and C.A. Wraight</i>	
<b>*Proteins and Glasses .....</b>	<b>343</b>
<i>Hans Frauenfelder</i>	
<b>Electron Speckle and Higher-Order Correlation Functions From Amorphous Thin Films .....</b>	<b>349</b>
<i>J. Murray Gibson, M.M.J. Treacy, and D. Loretto</i>	
<b>*Network Structure of Oxide Glasses Containing Alkali and Other Ions by Diffraction and MD Simulations .....</b>	<b>357</b>
<i>Itaru Yasui, H. Nagasawa, H. Matsumoto, and T. Mabuchi</i>	
<b>Strong Liquid Behavior of Zr-Ti-Cu-Ni-Be Bulk Metallic Glass-Forming Alloys .....</b>	<b>369</b>
<i>Ralf Busch, Andreas Masuhr, Eric Bakke, and William L. Johnson</i>	

#### PART V: STRUCTURE, ENERGETICS, AND POLYAMORPHISM

<b>Liquid and Glassy State Polyamorphism in the System Y<sub>2</sub>O<sub>3</sub>-Al<sub>2</sub>O<sub>3</sub> .....</b>	<b>377</b>
<i>Paul F. McMillan, Chung Ho, Siv Aasland, Amir Yeganeh-Haeri, and Richard Weber</i>	
<b>*A Crystallographic Guide to The Structure of Borate Glasses .....</b>	<b>381</b>
<i>Adrian C. Wright, Natalia M. Vedishcheva, and Boris A. Shakhmatkin</i>	

\*Invited Paper

<b>Glass Formation and Local Topological Instability of Atomic Structure</b> .....	397
<i>T. Egami</i>	
<b>Intermediate Range Order in Sodium Tellurite Glasses</b> .....	405
<i>J.W. Zwanziger, J.C. McLaughlin, and S.L. Tagg</i>	
<b>*Two Species/Nonideal Solution Model for Amorphous/Amorphous Phase Transitions</b> .....	411
<i>Cornelius T. Moynihan</i>	

#### **PART VI: STRUCTURE AND DYNAMICS OF GLASSES AND GLASS FORMERS**

<b>Development of the Glassy State of Benzophenone and Effect of Heating Rate From the Glassy State on Solidification</b> .....	429
<i>Paul E. Thoma and John J. Boehm</i>	
<b>Structural Studies of Rare-Earth Doped Phosphate Glasses</b> .....	435
<i>A. Matic, L. Börjesson, A. Wannberg, and R.L. McGreevy</i>	
<b>2D Lattices on Substrates With Randomly Distributed Pinning Centers: A Possible Scaling Law for Domain Sizes</b> .....	441
<i>Surajit Sen, Zhi-Xiong Cai, and David J. Schummer</i>	
<b>Effect of Size Dispersity on the Melting Transition</b> .....	447
<i>M.R. Sadr-Lahijany, P. Ray, S.T. Harrington, and H.E. Stanley</i>	
<b>Atomic Force Probe of Mesoscopic Dielectric and Viscoelastic Fluctuations Near the Glass Transition</b> .....	453
<i>L.E. Walther and N.E. Israeloff</i>	
<b>Liquid-Liquid Phase Separation of Melts and Glasses in Ferric Ferrous Oxide-Silica System</b> .....	459
<i>A. Yasumori, A. Koike, Y. Kameshima, K. Okada, T. Yano, M. Yamane, and S. Inoue</i>	
<b>The Effect of Iron and Oxygen Additions on the Properties of Zr-Al-Cu-Ni Bulk Metallic Glass-Forming Alloys</b> .....	465
<i>J. Eckert, N. Mattern, M. Seidel, and L. Schultz</i>	
<b>Spectral Characterization and Excited-State Interactions Between Rare-Earth Ions Doped in Borosilicate and Sol-Gel Glasses: Energy Transfer Up-Conversion in the Pr-Sm System</b> .....	471
<i>Z. Assefa, R.G. Haire, and N.A. Stump</i>	
<b>Spectroscopic Investigations of the Network Structure in Borovanadate Glasses</b> .....	477
<i>O. Attos, M. Massot, H.S. Mavi, and C. Julien</i>	

\*Invited Paper

<b>Optical Spectroscopy of Pentavalent Chromium Ions in Glass .....</b>	<b>483</b>
<i>Huabiao Yuan, Weiyi Jia, D. Cohen, W.M. Yen, and B.G. Aitken</i>	
<b>New Fe-Ni-Based Metal-Metalloid Glassy Alloys Prepared by Mechanical Alloying and Rapid Solidification .....</b>	<b>489</b>
<i>J.J. Suñol, M.T. Clavaguera-Mora, N. Clavaguera, and T. Pradell</i>	
<b>Synthesis and Properties of Bulk Metallic Glasses in Pd-Ni-P and Pd-Cu-P Alloys .....</b>	<b>495</b>
<i>Y. He and R.B. Schwarz</i>	
<b>Nitridation of Bioresorbable Phosphate Glass .....</b>	<b>501</b>
<i>H. Jiang and W.C. LaCourse</i>	
<b>Formation and Properties of Amorphous and Nanocrystalline Phases in Mechanically Alloyed Fe-Based Multicomponent Alloys .....</b>	<b>507</b>
<i>N. Schlorke, J. Eckert, and L. Schultz</i>	
<b>Author Index .....</b>	<b>513</b>
<b>Subject Index .....</b>	<b>515</b>

## PREFACE

The initiative for a symposium on this subject was taken by John Kieffer and, in response to his proposal to MRS, Austen Angell was asked by Karl Zeradski to play some part in its organization. He agreed to do so on the assurance that John, as well as several other experts in different areas such as Kai Ngai on polymers and liquids in general, Takashi Egami on metallic glasses and Uli Nienhaus on biophysical systems, would help. The brunt of the organization was borne by John Kieffer and we all owe him a strong vote of thanks for its ultimate success. A somewhat uncontrolled system of invitations, in judicious mixture with a selection of good contributed talks, seems by most accounts to have resulted in a satisfying, indeed exciting, scientific program.

This is a field in which the participants have failed to resolve the main questions despite an effort enduring over some 150 years, with 30-year recurrences of high activity. The latest of these cycles is in process and may not yet have peaked. It is, of course, unknown at this point whether the problems will be resolved in this cycle, though history is against it. Nevertheless, the presentations at this symposium, almost all of which are recorded in this volume, represent an excellent cross section of the attacks on the problem and will serve as essential reading to those who carry the torch to final success, or into the next cycle, as the case may be.

That we were able to cover the conference fees of all participants, and also give significant additional financial assistance in many cases where it was warranted, is thanks to the generous financial support of the Army Research Office, National Institute of Standards and Technology, National Science Foundation/Solid State Chemistry Program, and Office of Naval Research. We are indebted to Ms. Karen Nicholson of the Naval Research Laboratory for her valuable help over a period of three months in getting the manuscripts ready for publication.

C.A. Angell  
K.L. Ngai  
J. Kieffer  
T. Egami  
G.U. Nienhaus

March 1997

## MATERIALS RESEARCH SOCIETY SYMPOSIUM PROCEEDINGS

- Volume 420— Amorphous Silicon Technology—1996, M. Hack, E.A. Schiff, S. Wagner, R. Schropp, A. Matsuda 1996, ISBN: 1-55899-323-1
- Volume 421— Compound Semiconductor Electronics and Photonics, R.J. Shul, S.J. Pearton, F. Ren, C-S. Wu, 1996, ISBN: 1-55899-324-X
- Volume 422— Rare-Earth Doped Semiconductors II, S. Coffa, A. Polman, R.N. Schwartz, 1996, ISBN: 1-55899-325-8
- Volume 423— III-Nitride, SiC, and Diamond Materials for Electronic Devices, D.K. Gaskill, C.D. Brandt, R.J. Nemanich, 1996, ISBN: 1-55899-326-6
- Volume 424— Flat Panel Display Materials II, M. Hatalis, J. Kanicki, C.J. Summers, F. Funada, 1997, ISBN: 1-55899-327-4
- Volume 425— Liquid Crystals for Advanced Technologies, T.J. Bunning, S.H. Chen, W. Hawthorne, T. Kajiyama, N. Koide, 1996, ISBN: 1-55899-328-2
- Volume 426— Thin Films for Photovoltaic and Related Device Applications, D. Ginley, A. Catalano, H.W. Schock, C. Eberspacher, T.M. Peterson, T. Wada, 1996, ISBN: 1-55899-329-0
- Volume 427— Advanced Metallization for Future ULSI, K.N. Tu, J.W. Mayer, J.M. Poate, L.J. Chen, 1996, ISBN: 1-55899-330-4
- Volume 428— Materials Reliability in Microelectronics VI, W.F. Filter, J.J. Clement, A.S. Oates, R. Rosenberg, P.M. Lenahan, 1996, ISBN: 1-55899-331-2
- Volume 429— Rapid Thermal and Integrated Processing V, J.C. Gelpey, M.C. Öztürk, R.P.S. Thakur, A.T. Fiory, F. Roozeboom, 1996, ISBN: 1-55899-332-0
- Volume 430— Microwave Processing of Materials V, M.F. Iskander, J.O. Kiggans, Jr., J.Ch. Bolomey, 1996, ISBN: 1-55899-333-9
- Volume 431— Microporous and Macroporous Materials, R.F. Lobo, J.S. Beck, S.L. Suib, D.R. Corbin, M.E. Davis, L.E. Iton, S.I. Zones, 1996, ISBN: 1-55899-334-7
- Volume 432— Aqueous Chemistry and Geochemistry of Oxides, Oxyhydroxides, and Related Materials, J.A. Voight, T.E. Wood, B.C. Bunker, W.H. Casey, L.J. Crossey, 1997, ISBN: 1-55899-335-5
- Volume 433— Ferroelectric Thin Films V, S.B. Desu, R. Ramesh, B.A. Tuttle, R.E. Jones, I.K. Yoo, 1996, ISBN: 1-55899-336-3
- Volume 434— Layered Materials for Structural Applications, J.J. Lewandowski, C.H. Ward, M.R. Jackson, W.H. Hunt, Jr., 1996, ISBN: 1-55899-337-1
- Volume 435— Better Ceramics Through Chemistry VII—Organic/Inorganic Hybrid Materials, B.K. Coltrain, C. Sanchez, D.W. Schaefer, G.L. Wilkes, 1996, ISBN: 1-55899-338-X
- Volume 436— Thin Films: Stresses and Mechanical Properties VI, W.W. Gerberich, H. Gao, J-E. Sundgren, S.P. Baker 1997, ISBN: 1-55899-339-8
- Volume 437— Applications of Synchrotron Radiation to Materials Science III, L. Terminello, S. Mini, H. Ade, D.L. Perry, 1996, ISBN: 1-55899-340-1
- Volume 438— Materials Modification and Synthesis by Ion Beam Processing, D.E. Alexander, N.W. Cheung, B. Park, W. Skorupa, 1997, ISBN: 1-55899-342-8
- Volume 439— Microstructure Evolution During Irradiation, I.M. Robertson, G.S. Was, L.W. Hobbs, T. Diaz de la Rubia, 1997, ISBN: 1-55899-343-6
- Volume 440— Structure and Evolution of Surfaces, R.C. Cammarata, E.H. Chason, T.L. Einstein, E.D. Williams, 1997, ISBN: 1-55899-344-4
- Volume 441— Thin Films—Structure and Morphology, R.C. Cammarata, E.H. Chason, S.C. Moss, D. Ila, 1997, ISBN: 1-55899-345-2
- Volume 442— Defects in Electronic Materials II, J. Michel, T.A. Kennedy, K. Wada, K. Thonke, 1997, ISBN: 1-55899-346-0
- Volume 443— Low-Dielectric Constant Materials II, K. Uram, H. Treichel, A.C. Jones, A. Lagendijk, 1997, ISBN: 1-55899-347-9



## MATERIALS RESEARCH SOCIETY SYMPOSIUM PROCEEDINGS

- Volume 444— Materials for Mechanical and Optical Microsystems, M.L. Reed, M. Elwenspoek, S. Johansson, E. Obermeier, H. Fujita, Y. Uenishi, 1997, ISBN: 1-55899-348-7
- Volume 445— Electronic Packaging Materials Science IX, P.S. Ho, S.K. Groothuis, K. Ishida, T. Wu, 1997, ISBN: 1-55899-349-5
- Volume 446— Amorphous and Crystalline Insulating Thin Films—1996, W.L. Warren, J. Kanicki, R.A.B. Devine, M. Matsumura, S. Cristoloveanu, Y. Homma, 1997, ISBN: 1-55899-350-9
- Volume 447— Environmental, Safety, and Health Issues in IC Production, R. Reif, A. Bowling, A. Tonti, M. Heyns, 1997, ISBN: 1-55899-351-7
- Volume 448— Control of Semiconductor Surfaces and Interfaces, S.M. Prokes, O.J. Glembocki, S.K. Brierley, J.M. Woodall, J.M. Gibson, 1997, ISBN: 1-55899-352-5
- Volume 449— III-V Nitrides, F.A. Ponce, T.D. Moustakas, I. Akasaki, B.A. Monemar, 1997, ISBN: 1-55899-353-3
- Volume 450— Infrared Applications of Semiconductors—Materials, Processing and Devices, M.O. Manasreh, T.H. Myers, F.H. Julien, 1997, ISBN: 1-55899-354-1
- Volume 451— Electrochemical Synthesis and Modification of Materials, S.G. Corcoran, P.C. Searson, T.P. Moffat, P.C. Andricacos, J.L. Deplancke, 1997, ISBN: 1-55899-355-X
- Volume 452— Advances in Microcrystalline and Nanocrystalline Semiconductors—1996, R.W. Collins, P.M. Fauchet, I. Shimizu, J.-C. Vial, T. Shimada, A.P. Alvisatos, 1997, ISBN: 1-55899-356-8
- Volume 453— Solid-State Chemistry of Inorganic Materials, A. Jacobson, P. Davies, T. Vanderah, C. Torardi, 1997, ISBN: 1-55899-357-6
- Volume 454— Advanced Catalytic Materials—1996, M.J. Ledoux, P.W. Lednor, D.A. Nagaki, L.T. Thompson, 1997, ISBN: 1-55899-358-4
- Volume 455— Structure and Dynamics of Glasses and Glass Formers, C.A. Angell, T. Egami, J. Kieffer, U. Nienhaus, K.L. Ngai, 1997, ISBN: 1-55899-359-2
- Volume 456— Recent Advances in Biomaterials and Biologically-Inspired Materials: Surfaces, Thin Films and Bulk, D.F. Williams, M. Spector, A. Bellare, 1997, ISBN: 1-55899-360-6
- Volume 457— Nanophase and Nanocomposite Materials II, S. Komarneni, J.C. Parker, H.J. Wollenberger, 1997, ISBN: 1-55899-361-4
- Volume 458— Interfacial Engineering for Optimized Properties, C.L. Briant, C.B. Carter, E.L. Hall, 1997, ISBN: 1-55899-362-2
- Volume 459— Materials for Smart Systems II, E.P. George, R. Gotthardt, K. Otsuka, S. Troler-McKinstry, M. Wun-Fogle, 1997, ISBN: 1-55899-363-0
- Volume 460— High-Temperature Ordered Intermetallic Alloys VII, C.C. Koch, N.S. Stoloff, C.T. Liu, A. Wanner, 1997, ISBN: 1-55899-364-9
- Volume 461— Morphological Control in Multiphase Polymer Mixtures, R.M. Briber, D.G. Peiffer, C.C. Han, 1997, ISBN: 1-55899-365-7
- Volume 462— Materials Issues in Art and Archaeology V, P.B. Vandiver, J.R. Druzik, J. Merkel, J. Stewart, 1997, ISBN: 1-55899-366-5
- Volume 463— Statistical Mechanics in Physics and Biology, D. Wirtz, T.C. Halsey, J. van Zanten, 1997, ISBN: 1-55899-367-3
- Volume 464— Dynamics in Small Confining Systems III, J.M. Drake, J. Klafter, R. Kopelman, 1997, ISBN: 1-55899-368-1
- Volume 465— Scientific Basis for Nuclear Waste Management XX, W.J. Gray, I.R. Triay, 1997, ISBN: 1-55899-369-X
- Volume 466— Atomic Resolution Microscopy of Surfaces and Interfaces, D.J. Smith, R.J. Hamers, 1997, ISBN: 1-55899-370-3

*Prior Materials Research Society Symposium Proceedings available by contacting Materials Research Society*

**Part I**

**Short-Time Dynamics**

## DYNAMICS AT THE GLASS TRANSITION IN POLYMERS: RESULTS FROM NEUTRON SPECTROSCOPY

D. RICHTER\*, A. Arbe\*\*, J. Colmenero\*\*

\*Institut für Festkörperforschung, Forschungszentrum Jülich GmbH, Jülich, Germany

\*\*Departamento de Física de Materiales, Universidad del País Vasco, San Sebastian, Spain

### ABSTRACT

This short review presents quasielastic neutron scattering and dielectric experiments on the  $\alpha$  and  $\beta_{\text{slow}}$  relaxation in polybutadiene and polyvinylchloride. Exploiting the momentum transfer dependent dynamic structure factor, spatial information about the underlying molecular motions is obtained. While the  $\beta_{\text{slow}}$  process reveals itself as a local jump with average jump distances of about 1.5 Å, the  $\alpha$  relaxation is diffusive and occurs statistically independently from the  $\beta_{\text{slow}}$  process. With this result a consistent interpretation of dielectric spectra on the same polymer is achieved. Finally some new results on the  $\alpha$  process in PVC are presented.

### INTRODUCTION

Glass forming polymers exhibit relaxation processes covering a huge dynamic range [1-3]. As an example Fig.1 displays the relaxation map for 1,4 polybutadiene [4-8]. The displayed data have been obtained by dielectric and mechanical spectroscopy as well as by dynamic light scattering and neutron spectroscopy. We observe a number of different relaxation processes. The structural  $\alpha$  relaxation which supports the flow of the material slows down dramatically in the neighborhood of the glass transition temperature  $T_g$ . At a temperature about 20% above  $T_g$  a secondary relaxation ( $\beta_{\text{slow}}$ ) splits from the primary  $\alpha$  relaxation. This process exhibits an Arrhenius-like temperature dependence and persists into the glassy state. At very high frequencies in the picosecond regime anomalous vibrations, the so-called Boson peak, and associated with it a fast relaxation process termed  $\beta_{\text{fast}}$  is found. Both, the Boson peak as well as the  $\beta_{\text{fast}}$  process exhibit only very little temperature dependence. Though the relaxation processes, in particular the  $\alpha_{\text{slow}}$  and  $\beta_{\text{slow}}$  relaxations, have been investigated by spectroscopic methods like dielectric and mechanical measurements since at least 50 years, still not very much is known about the molecular mechanism behind these relaxations. This deficiency relates to the fact that these spectroscopic methods although providing a very large dynamic range and high sensitivity in the time or frequency domain they do not reveal spatial information.

Such space-time sensitivity can be provided by inelastic and quasielastic neutron scattering because cold and thermal neutrons possess wavelengths corresponding to the interatomic distances and at the same time thermal energies. Other than X-rays providing structural information neutrons reveal knowledge where an atom is situated and in which direction it moves at what speed. In this way space-time observation of individual molecules is facilitated. In particular, the neutron spin echo (NSE) method reveals information about the time-dependent dynamic structure factor  $S(Q,t)$  which reflects the time-dependent density-density correlations

$$\frac{S(Q,t)}{S(Q)} = \langle \delta\rho(Q,t) \delta\rho(Q,0) \rangle \quad (1)$$

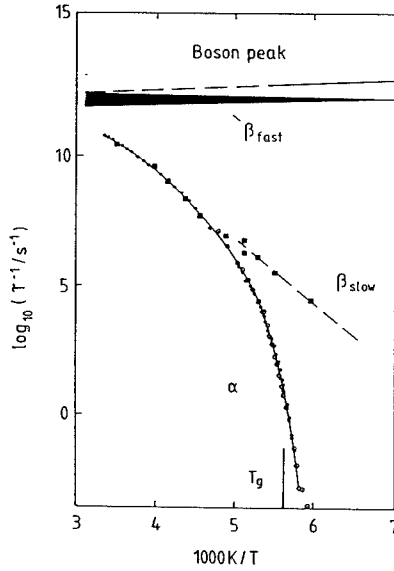


Fig.1: Relaxation map for (1,4) polybutadiene covering the prevailing dynamical features around the glass transition. The frequency range for the Boson peak and the associated fast relaxation like dynamics ( $\beta_{fast}$ ) are indicated schematically [15]. The full and open circle along the  $\alpha$  relaxation trace represent dielectric [7] and mechanical [8] results respectively. The full squares display characteristic rates obtained from neutron spin echo spectroscopy [5,6]. The time scale of the  $\alpha$  process has been shifted to match that of the microscopic data. The dashed line represents the temperature dependence of the  $\beta_{slow}$  process observed by dielectric spectroscopy [9].

$\delta\rho(Q,t)$  is the Fourier component of a density fluctuation to the wave vector  $Q$  at a time  $t$ .  $S(Q)$  denotes the static structure factor and  $Q=4\pi/\lambda \sin(\Theta/2)$  is the scattering vector, where  $\lambda$  is the neutron wave length and  $\Theta$  the scattering angle.

In this work we present neutron spin echo results on the  $Q$ -dependent dynamic structure factor of polybutadiene [9,10] and some new results on PVC [11]. First, these data are analyzed in the  $\beta$  relaxation regime revealing spatial information about this relaxation process. Thereafter, we consider the merging regime of the  $\alpha$  and  $\beta$  relaxation and show the statistical independence of both relaxation processes. We revisit dielectric results on polybutadiene and interpret them consistently on the basis of the insight gained from the NSE investigations. Finally, we present some new results on PVC which are interpreted in the same spirit resolving an old puzzle on the seemingly very strongly stretched relaxation function of the  $\alpha$  process.

## EXPERIMENTAL RESULTS: POLYBUTADIENE

The experiments were performed on deuterated 1,4 polybutadiene (PB) which was synthesized anionically yielding a random microstructure of 52% cis, 41% trans, and 7% vinyl groups. The glass transition occurs in this sample at 178 K. The neutron spin echo experiments have been performed at the spectrometer IN11 of the ILL Grenoble. In order to access a wide  $Q$  range, different neutron wave lengths have been employed.

Fig.2 displays the static structure factor of 1,4 PB. In the low  $Q$  regime,  $Q \leq 3.5 \text{ \AA}^{-1}$   $S(Q)$  exhibits two maxima. The first maximum at around  $Q=1.5 \text{ \AA}^{-1}$  shifts strongly with temperature and relates to interchain correlations depending on the soft van der Waals interactions. On the other

hand the second peak at  $Q \approx 3 \text{ \AA}^{-1}$  is not affected by temperature - it originates mainly from interchain correlations characterized by covalent bonds between the different atoms. The lower part of Fig.2 displays NSE spectra taken on the first and second peak of  $S(Q)$ . In both cases the experimental time scale was scaled with that set by the viscosity relaxation.

As can be seen, the NSE relaxation curves taken at the first interchain peak under this scaling collapse to a common master curve following a Kohlrausch-William-Watts (KWW) stretched exponential relaxation. Obviously, the microscopic relaxation taking place at a characteristic interchain distance, follows the same temperature behavior as the macroscopic relaxation relating to the flow. At the second peak, on the other hand, the NSE relaxation spectra behave very differently. As can be seen immediately, the microscopic time scale does not scale with the viscosity relaxation - the different relaxation curves do not collapse on a single master curve.

As already indicated by the master curve in Fig.2, the characteristic times at the first structure factor peak follow the Vogel-Fulcher temperature dependence of the  $\alpha$  relaxation, those observed at the second peak display an Arrhenius temperature dependence with an activation energy agreeing perfectly well with the dielectric  $\beta$  relaxation observed at the same sample. Thus, at the first and the second peak of the static structure factor, qualitatively different dynamics takes place. At the interchain peak, the temperature dependence of the  $\alpha$  relaxation is found while at the intrachain maximum, a temperature dependence characteristic for the secondary  $\beta_{\text{slow}}$  process reveals itself in the spin echo data.

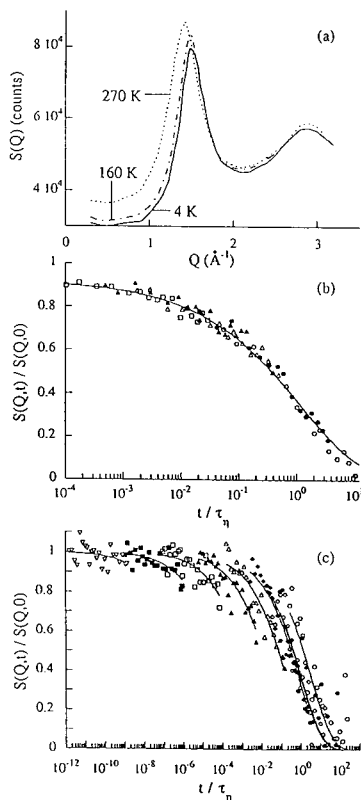


Fig.2: (a) Static structure factor obtained by D1B (ILL) for deuterated PB at different temperatures (extracted from [15]. (b) Scaling representation of the NSE data at  $1.48 \text{ \AA}^{-1}$  ( $\circ$  280 K;  $\bullet$  260 K;  $\Delta$  240 K;  $\blacktriangle$  230 K;  $\square$  220 K); (c) The same kind of representation for  $2.71 \text{ \AA}^{-1}$  ( $\circ$  300 K;  $\bullet$  280 K;  $\diamond$  260 K;  $\blacklozenge$  240 K;  $\Delta$  220 K;  $\blacktriangle$  205 K;  $\square$  190 K;  $\blacksquare$  180 K;  $\nabla$  170 K). Solid lines correspond to KWW functions (see text).

## EVALUATION OF THE $\beta_{\text{slow}}$ PROCESS

At temperatures below the merging temperature  $T_m \approx 220$  K where the secondary and the primary relaxation merge, the  $\alpha$  process rapidly becomes very slow and within the time window of the NSE spectrometer mainly the secondary  $\beta_{\text{slow}}$  process is observed. This secondary relaxation has been investigated in detail by dielectric spectroscopy and is normally interpreted in terms of a distribution of local elemental jumps where each jumper follows an activated behavior [12]

$$\tau = \tau_0^D \exp\left(\frac{E}{kT}\right) \quad (2)$$

where  $\tau_0^D$  is a prefactor and  $E$  the activation energy. Each of these local jumpers relaxes with a single exponential decay:  $\phi(t) \propto \tau_0 \exp[-t/\tau(E)]$ . The activation energies are distributed according to a Gaussian distribution function  $g(E)$  [9]

$$g(E) \approx \exp\left(-\left(\frac{E - E_0}{\sigma}\right)^2\right) \quad (3)$$

For the  $\beta_{\text{slow}}$  process in PB, the different parameters assume the following values:  $(\sigma[\text{eV}] = 0.145 - 2.55 \cdot 10^{-4} \text{ T[K]}; \tau_0^D = 3.5 \cdot 10^{-17} \text{ s}; E_0 = 0.41 \text{ eV})$

How does such a picture now translate into a dynamic structure factor? As elemental jumps we consider jumps between two energy minima which are separated by a distance  $d$ . This distance may depend on the activation energy  $E$ . For such an elemental jumper jumping with a relaxation rate  $1/\tau$  the self-correlation function which is observed by incoherent scattering is readily written down

$$\begin{aligned} S_s(Q, t) &= \frac{1}{2} \left[ 1 + \frac{\sin Qd}{Qd} \right] + \frac{1}{2} \left[ 1 - \frac{\sin Qd}{Qd} \right] \exp\left[-\frac{2t}{\tau(E)}\right] \\ &= S_{el} + S_{inel} \exp\left(-\frac{2t}{\tau(E)}\right) \end{aligned} \quad (4)$$

It contains two contributions, an elastic part staying constant with time revealing the spatial information about the jump distance  $d$ . The second term decays with the characteristic relaxation rate and informs about the dynamics

In a neutron spin echo experiment we deal with the pair correlation function, sensitive not only to the self part but to all interference effects between different moving atoms. The total scattering under these circumstances is given by the static structure factor  $S(Q)$ . If we now consider that the different jumpers are not correlated, then all the interference terms between different jumping units drop and the time dependent part in the scattering function has the same  $Q$  dependence as for the self-correlation function (strictly speaking this is only true if the spatial extension of a single jumper is small enough in order not to modulate the intensity within the observed  $Q$  range) [10]. With this approximation the dynamic structure factor for the pair correlation function becomes

$$\frac{S^\beta(Q, t)}{S(Q)} = 1 - \frac{S_{inel}}{S(Q)} + \frac{S_{inel}}{S(Q)} \exp\left[-\frac{2t}{\tau(E)}\right] \quad (5)$$

In order to describe the  $\beta_{\text{slow}}$  relaxation in addition  $S^b(Q, t)$  has to be averaged over the distribution function for the activation energies  $g(E)$ . For the energy dependence of the jump distance, thereby, the result of the soft potential model  $d \propto E^{1/4}$  has been taken.

Fig.3 displays the inelastic scattering contribution to the NSE spectra following this model. As a solid line also the static structure factor is displayed. Due to the renormalization of the inelastic contribution by the static structure factor  $S(Q)$  the form factor of the  $\beta_{\text{slow}}$  process is strongly reduced in the regime of the first structure factor peak (Fig.3 displays the form factors for a jump distance of  $d=1.5 \text{ \AA}$  which is obtained from a fit to the data.). Thus, the above simple model immediately explains why at the positions of the first and second peak of the static structure factor, a different dynamic may be observed. The simple jump model has been fitted to the NSE spectra at temperatures  $T \leq 205 \text{ K}$ . Thereby, the distribution function for the activation energies was taken from dielectric spectroscopy. With a joint fit under common variation of parameters all NSE spectra can be accounted for. For the relevant activation energies a jump distance  $d=1.5 \text{ \AA}$  has been found. Quite unexpectedly, the evaluation reveals also that the density fluctuations which are observed by NSE spectroscopy relax about 250 times faster than the corresponding dipoles seen in dielectric spectroscopy. This result is not yet understood.

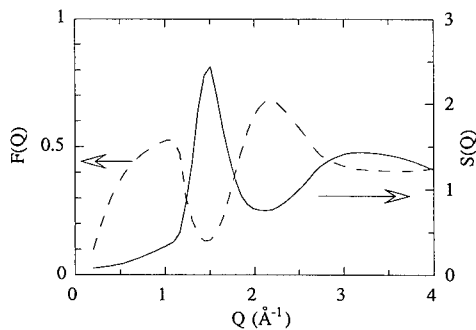


Fig.3: Quasielastic contribution to the coherent scattering function of the  $\beta_{\text{slow}}$  process  $F(Q) \equiv S_{\text{inel}}/S(Q)$  and static structure factor  $S(Q)$  as a function of  $Q$ .

#### THE MERGING REGION OF $\alpha$ AND $\beta_{\text{slow}}$ PROCESSES

As explained above, the  $\beta_{\text{slow}}$  process can be well understood in terms of a localized jump process where the local jumpers move by about  $1.5 \text{ \AA}$ . On the other hand, the flow supporting  $\alpha$  process is diffusive - neutron spectroscopy on the  $\alpha$  relaxation commonly reveals a strong dispersion in  $Q$ :  $\tau \propto Q^{-2/\gamma}$  where  $\gamma$  is the stretching exponent in the KWW function [13,14].

How do these two processes combine? In the evaluation of dielectric data, normally a superposition of the  $\alpha$  and  $\beta$  spectra is assumed. This implies that one assumes an inhomogeneous system, where in some areas of the sample molecules perform  $\beta$  relaxation, while in others  $\alpha$  relaxation occurs. Here we will take a different point of view. We assume that the  $\alpha$  and the  $\beta$  relaxation are statistically independent processes. Thus, a given molecule takes part in both processes independently. Under these circumstances, the self correlation function in real space is a spatial convolution of the self correlation functions of both processes. In  $Q$  space after Fourier transformation such a convolution becomes a product and the self part of the dynamic structure

factor can be written as a product of the  $\alpha$  and the  $\beta$  relaxation function. In order to describe the pair correlation function, we take the so-called Vinyard approximation and write

$$S^{\alpha\beta}(Q, t) = \varphi^\alpha(Q, t) S^\beta(Q, t) \quad (6)$$

Thereby, the coherent structure factor of the  $\beta$  relaxation takes the part of  $S(Q)$  in the Vinyard approximation and  $\varphi^\alpha$  is the self correlation function for the  $\alpha$  relaxation

$$\varphi^\alpha(Q, t) = \exp \left[ - \left( \frac{t}{\tau^\alpha(Q)} \right)^\gamma \right] \quad (7)$$

where  $\tau^\alpha(Q)$  is the  $Q$  dependent characteristic relaxation time of the  $\alpha$  relaxation. Inserting the expression  $S^\beta(Q, t)$  (Equ.(5)) into Equ.(6) we have

$$\frac{S^{\alpha\beta}(Q, t)}{S(Q)} = \left\langle \left[ 1 - \frac{S_{inel}}{S(Q)} \right] \varphi^\alpha(Q, t) + \frac{S_{inel}}{S(Q)} \exp \left[ - \frac{2t}{\tau(E)} \right] \varphi^\alpha(Q, t) \right\rangle_{g(E)} \quad (8)$$

We have two contributions to the relaxation function. The first relaxes with the relaxation function of the  $\alpha$  relaxation and has a form factor given by the complement to the inelastic form factor of the  $\beta$  relaxation. The second part relaxes by a relaxation function which is a product of the  $\alpha$  and the  $\beta$  relaxation function. The corresponding  $Q$  dependent form factor is that of the inelastic part of  $S^\beta$ .

With this ansatz the NSE spectra in the merging regime have been evaluated. In order to keep the number of parameters small, the dynamic structure factor for the  $\beta_{slow}$  relaxation was extrapolated from the low temperature results and only the  $Q$  dependent characteristic time of the  $\alpha$  process was fitted. With this approach we obtain results as displayed in Fig.4. In the upper part, characteristic spectra at three different  $Q$  values are shown for four different temperatures each. In the lower part, NSE spectra at eight different  $Q$  values taken at 260 K are displayed. In each case the solid lines display the model predictions. As we may see, a very good overall agreement is achieved.

Fig.5 presents the resulting  $Q$  and  $T$  dependencies of the characteristic relaxation time for the  $\alpha$  relaxation. For the  $Q$  dependence a simple power law is found with little indications for a de Gennes narrowing which would be expected close to the first structure factor peak. The temperature dependence for the such evaluated characteristic times agrees well with what would be expected from the viscosity relaxation (solid lines).

Thus, using the picture of elemental jumps for the  $\beta$  process taking the distribution function for the activation energies from dielectric spectroscopy and assuming statistically independent  $\alpha$  and  $\beta$  relaxations a very good description of the dynamic structure factor in the  $Q$  regime up to  $3 \text{ \AA}^{-1}$  is obtained. In particular, using the temperature range below the merging temperature, spatial information about the  $\beta$  relaxation is obtained, which then is used in order to disentangle the complex relaxation behavior above the merging temperature. Thereby, it turns out that with the assumption of statistically independent  $\alpha$  and  $\beta$  processes, which is contrary to the common approach taken in dielectric spectroscopy, a very consistent description is achieved. We further would like to comment on the power law behavior of the characteristic time  $\tau^\alpha(Q)$  of the  $\alpha$  process. Such a strongly dispersive  $Q$  dependence means that the  $\alpha$  process in the  $\alpha\beta$  range relates to



a diffusive process with very small step length  $\ell \leq 0.5 \text{ \AA}$  at least. The power law dependence with an exponent  $n=3.6$  indicates anomalous diffusion, where the diffusion constant depends on the spatial range covered.

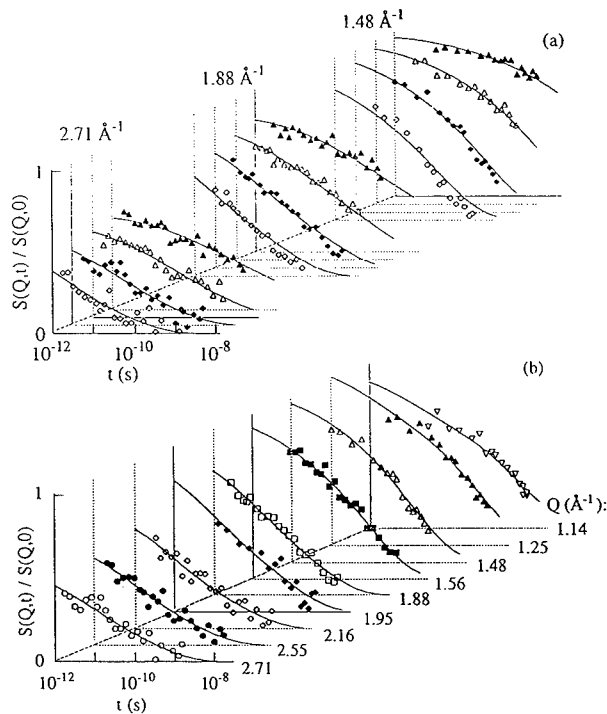


Fig.4: (a) NSE spectra for the  $Q$  values indicated at 220 K ( $\blacktriangle$ ), 240 K ( $\triangle$ ), 260 K ( $\blacklozenge$ ), and 280 K ( $\diamond$ ). (b) at 260 K for the  $Q$  values indicated; solid lines are fitting curves (see text).

## REVISITING DIELECTRIC RESULTS

Evaluating dielectric spectra in terms of a superposition of  $\alpha$  and  $\beta_{\text{slow}}$  contributions, for the two characteristic relaxation times, a temperature dependence is found as shown in Fig.6. The  $\beta_{\text{slow}}$  process exhibits the characteristic Arrhenius law while the  $\alpha$  process displays a strong non-Arrhenius temperature dependence which disagrees considerably with that of the viscosity relaxation indicated by a solid line. We also note that at  $T_m$  both processes seem to cross.

We will now reevaluate these dielectric spectra using the convolution approach suggested by the NSE results. Fig.7 displays a fit of such a constructed dielectric response functions to the PB data. As can be seen a very good description over the full temperature range can be achieved. Fig.8 presents the outcome for the characteristic relaxation time of the  $\alpha$  relaxation including also (solid line) the prediction from the viscosity relaxation. Apparently now all the discrepancies visible in Fig.6 are resolved: Using the convolution approach the characteristic time for the  $\alpha$  relaxation as measured by dielectric spectroscopy agrees well with the viscosity relaxation time. The small deviations at low temperatures occur below the glass transition temperature, where the system falls out of equilibrium. Obviously, using the approach of statistically independent motions in the  $\alpha$  and  $\beta$  process both, the  $Q$  dependent spin echo spectra as well as the broad band dielectric results can be consistently interpreted.

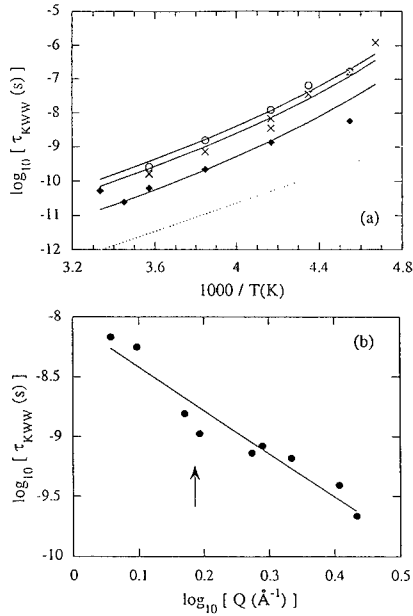


Fig.5: (a) Temperature dependence of the characteristic times of the  $\alpha$  relaxation,  $\tau_{KWW}$ , for  $Q=1.48 \text{ \AA}^{-1}$  (O);  $1.88 \text{ \AA}^{-1}$  (x); and  $2.71 \text{ \AA}^{-1}$  (◆); solid lines show the temperature dependence of the viscosity; the timescale (maximum of the distribution) of the  $\beta_{\text{slow}}$  relaxation is also shown for comparison (dashed line); (b)  $Q$  dependence of  $\tau_{KWW}$  at 260 K.

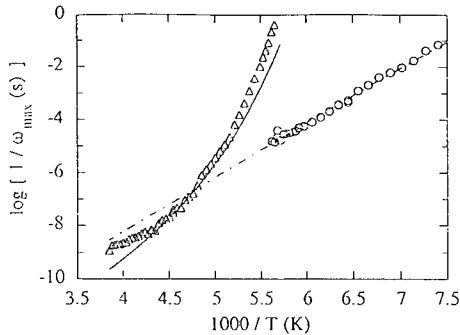


Fig.6: Temperature dependence of the characteristic timescale defined as the inverse of the frequencies of the dielectric loss maxima for the main relaxation process ( $\Delta$ ) and the  $\beta_{\text{slow}}$  relaxation (O); the solid line shows the temperature behavior of the viscosity and the dashed dotted line the Arrhenius-like dependence of the  $\beta_{\text{slow}}$  relaxation.

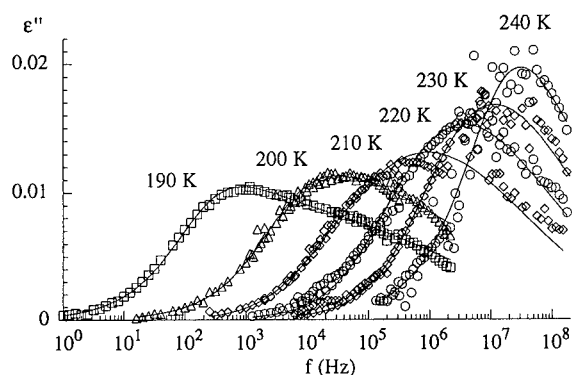


Fig.7: Dielectric loss curves obtained for PB at 190 K ( $\square$ ), 200 K ( $\Delta$ ), 210 K ( $\diamond$ ), 220 K ( $\circ$ ), 230 K ( $\diamond$ ), and 240 K ( $\circ$ ); solid lines through the points are the corresponding fitting curves.

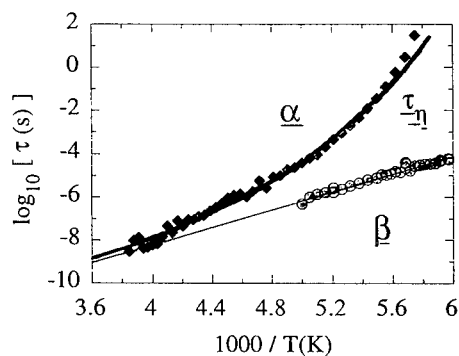


Fig.8: Temperature dependence for the dielectric characteristic times  $\tau_\alpha$  and  $\tau_\beta$  as obtained by the convolution approach; solid lines: (upper) viscosity relaxation  $\tau_\eta$ ; (lower) Arrhenius behavior of the  $\beta_{\text{slow}}$  process.

## EXPERIMENTAL RESULTS ON PVC

Other than most glassforming polymers PVC appears to exhibit a very broad  $\alpha$  process. Stretching exponents in the order of  $\gamma=0.2$  have been reported which are distinctly different to the usual values of  $0.4 \leq \gamma \leq 0.5$  found for other polymers. In addition PVC exhibits a strong  $\beta$  relaxation. Fig.9 presents the results of neutron spin echo experiments on the position of the first structure factor peak at  $Q=1.2 \text{ \AA}^{-1}$ . The data are shown in a scaled form where the time has been rescaled by the characteristic time of the dielectric  $\alpha$  process. Obviously all data collapse beautifully on a master curve showing that the dipole relaxations observed in dielectric spectroscopy and the interchain density fluctuations seen by neutron spin echo spectroscopy at the first structure factor peak follow the same temperature behavior. On the other hand the shape of the relaxation functions differ strongly. The neutron spectra are well described by a stretching expo-

ment of  $\gamma=0.5$  in strong contradiction to the dielectric shape parameter. For illustration a relaxation function with  $\gamma=0.23$  corresponding to the dielectric result is included in the figure.

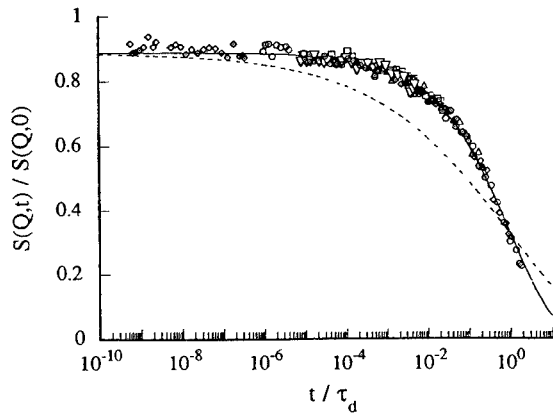


Fig.9: Dynamic structure factor of PVC measured at the first peak of the static structure factor ( $Q=1.2$ ). The data are scaled with the temperature dependent characteristic time of the dielectric  $\alpha$  process; solid line KWW function with  $\gamma=0.5$ ; dashed line  $\gamma=0.23$ .

How can we understand these results? We take the same approach as for polybutadiene and include additional measurements at  $Q=2.1 \text{ \AA}^{-1}$  and  $Q=2.9 \text{ \AA}^{-1}$ . We assume that the  $\alpha$  and  $\beta$  process are independent of each other. We take the  $\beta$  process from the distribution of jump rates found from dielectric spectroscopy. We describe the  $\alpha$  process by a stretched exponential (Equ.(7)) where the temperature shift factor is taken from dielectric measurements.

The question now is what is the right shape parameter? Can the neutron results be understood using the dielectric value of 0.23 or are we forced to the larger value of 0.5 resulting from a scaling of the data at  $Q=1.2 \text{ \AA}^{-1}$ . An analysis following the lines of Equ.(8) can be done for both stretching parameters keeping them fixed in each case. Using the dielectric value of 0.23 it turns out that consistent description of the neutron spectra cannot be achieved. On the other hand with the larger stretching parameter of 0.5 an overall successful description of all the spectra at different temperatures and  $Q$  values is obtained. Fig.10 gives an example of the general agreement we can obtain following an analysis according to Equ.(8). For all  $Q$  values and temperatures the theoretical scattering function describes the experimental data extremely well. This is true for the first structure factor maximum, for the first minimum as well as for the second maximum of the static structure factor. If we now consider the quasielastic contribution to the scattering function in a similar way as in Fig.3 we get the following result. At the first peak of the static structure factor there is basically no contribution from the local jump processes. This relates to the very sharp peak of  $S(Q)$  which is characteristic for this material and secondly we observe that above  $Q=1.5 \text{ \AA}^{-1}$  the local process which in this case has a jump distance of  $d=1.3 \text{ \AA}$  has a strong weight in the dynamic structure factor.

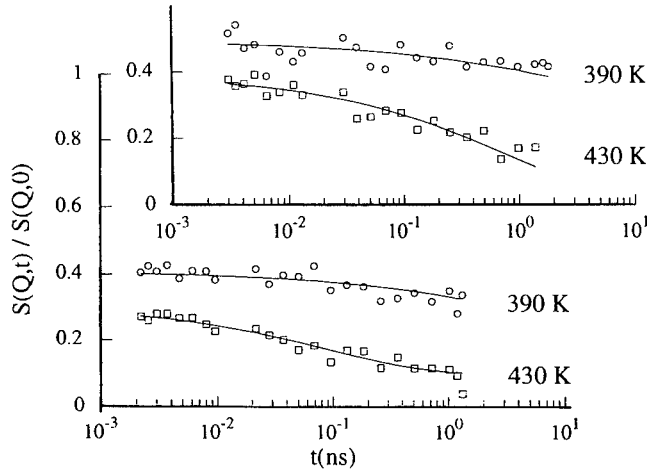


Fig.10: NSE spectra at  $Q=2.1 \text{ \AA}^{-1}$  upper figure, and  $Q=2.9 \text{ \AA}^{-1}$  lower figure; the solid lines represent the joint fit (see text).

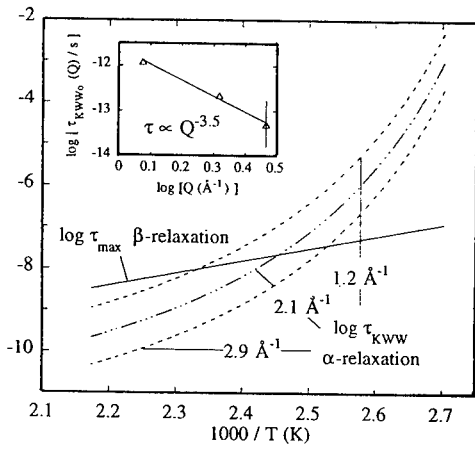


Fig.11: Characteristic relaxation times of the  $\alpha$  relaxation observed at different  $Q$  values; dashed lines:  $\tau_{\max}$  for the dielectric  $\beta$  relaxation in PVC; solid line: insert  $Q$  dependence of the characteristic time for the  $\alpha$  relaxation as obtained from a joint fit of the PVC NSE data.

Fig.11 displays the characteristic relaxation times for the  $\beta$  relaxation (solid line) and the  $\alpha$  relaxation at different  $Q$  values. We observe that the  $\beta$  relaxation cuts fully through the  $\alpha$  region and severe mixing of both processes takes place. Only because the renormalization of the dynamic structure factor with  $S(Q)$  (see Equ.(8)) provides the selectivity for the different relaxation

processes, NSE spectroscopy is able to distinguish the different processes. Again as can be seen in the insert of Fig.11 the characteristic relaxation time of the  $\alpha$  process follows a power law to high  $Q$  signifying a more or less continuous diffusion process. Other than the case of polybutadiene here the characteristic time of the density fluctuations present in the  $\beta$  process agrees within a half an order of magnitude with that of the dipole relaxation seen in dielectric spectroscopy.

Finally with these neutron results at hand new dielectric experiments were performed in the high frequency regime in order to see whether a more narrow  $\alpha$  process can be observed. Indeed at  $T=435$  K the dielectric susceptibility can be fitted with the Kohlrausch-William-Watts function with a stretching exponent of 0.51 very close to the neutron result [11]. Thus, in a temperature regime where the dielectric loss is not affected by other processes, PVC behaves very normal exhibiting a stretching exponent which is even on the less fragile side for polymers.

## CONCLUSIONS

Quasielastic neutron scattering operates on lengths and times scales corresponding to the microscopic relaxation processes in glass forming polymers. From the  $Q$  dependent dynamic structure factor information about the space-time development of these relaxation processes can be obtained. The experiments which have been presented here show that in 1,4 polybutadiene the  $\beta_{\text{slow}}$  process consists of local jumps with a jump distance of about 1.5 Å. Furthermore, from an evaluation of the data in the merging regime it becomes clear that  $\alpha$  and  $\beta_{\text{slow}}$  relaxation are statistically independent processes which a given molecule may undergo at the same time. While the  $\beta$  process may be understood as a local jump, the  $\alpha$  relaxation shows strong dispersion in  $Q$  signifying a diffusive process. NSE studies on PVC can be understood in the same frame. Again local jump distances of  $d \approx 1.3$  Å evolve. In particular the  $Q$  selectivity of neutron scattering leads to an unambiguous identification of the  $\alpha$  lineshape demonstrating that other than believed up to now, the  $\alpha$  process in PVC does not exhibit any anomalous width. Future development should take place in the evaluation of coherent dynamic structure factors taking into account the real geometry of the moving units. The interpretation of the coherent dynamic structure factors will also greatly benefit from computer simulations on realistic chains.

## ACKNOWLEDGEMENT

The author acknowledges the very fruitful collaboration with A. Allegria, (San Sebastian) and B. Farago (Grenoble) on this subject.

## REFERENCES

1. Dynamics of disordered materials, ed. by D. Richter, A.J. Dianoux, W. Petry and J. Teixeira, Springer Proceedings in Physics 37 (Springer Verlag, Berlin, 1989)
2. Dynamics of disordered Materials II, ed. by A.J. Dianoux, W. Petry and D. Richter (North Holland, Amsterdam, 1993)

3. W. Goetze in *Liquids, Freezing and the Glass Transition*, ed. by J.P. Hansen, D. Levesque and J. Zinn-Justin (North-Holland, Amsterdam, 1991)
4. B. Frick, D. Richter, W. Petry and U. Buchenau, *Z. Phys.*, **B70**, 73 (1988)
5. D. Richter, B. Frick, and B. Farago, *Phys. Rev. Lett.* **61**, 2465 (1988)
6. D. Richter, R. Zorn, B. Farago, B. Frick, and L.J. Fetters, *Phys. Rev. Lett.* **68**, 71 (1992)
7. R. Zorn, F. Mopsik, G.B. McKenna, L. Willner, unpublished
8. R. Zorn, G.B. McKenna, L. Willner, and D. Richter, *Macromolecules* **28**, 8552 (1995)
9. A. Arbe, U. Buchenau, L. Willner, D. Richter, B. Farago, and J. Colmenero, *Phys. Rev. Lett.* **76**, 1872 (1996)
10. A. Arbe, D. Richter, J. Colmenero, and B. Farago, *Phys. Rev. E* **54**, 3853 (1996)
11. A. Arbe, J. Colmenero, A. Alegria, B. Farago, and D. Richter, unpublished
12. see e.g. N.G. Crum, B.E. Read, and G. Williams in '*Anelastic and Dielectric Effects in Polymer Solids*' (Wiley, London 1967)
13. J. Colmenero, A. Alegria, J.M. Alberdi, F. Alvarez, and B. Frick, *Phys. Rev.* **B44**, 7321 (1991)
14. J. Colmenero, A. Arbe, and A. Alegria, *Phys. Rev. Lett.* **71**, 2603 (1993)
15. R. Zorn, A. Arbe, J. Colmenero, B. Frick, and U. Buchenau, *Phys. Rev.* **E52**, 782 (1995)

## FAST DYNAMICS IN GLASS-FORMING POLYMERS REVISITED

J. COLMENERO\*, A. ARBE\*, C. MIJANGOS\*\*, H. REINECKE\*\*

\* Departamento de Física de Materiales, Facultad de Química, Apdo. 1072, 20080 San Sebastián, Spain, wapcolej@sq.ehu.es

\*\* CSIC, Instituto de Ciencia y Tecnología de Polímeros, Juan de la Cierva 3, 28006 Madrid, Spain

### ABSTRACT

The so called “fast-dynamics” of glass-forming systems as observed by time of flight (TOF) neutron scattering techniques is revisited. TOF-results corresponding to several glass-forming polymers with different chemical microstructure and glass-transition temperature are presented together with the theoretical framework proposed by us to interpret these results. The main conclusion is that the TOF-data can be explained in terms of quasiharmonic vibrations and the particular short time behavior of the segmental dynamics. The segmental dynamics display in the very short time range ( $t \approx 2$  ps) a crossover from a simple exponential behavior towards a non-exponential regime. The first exponential decay, which is controlled by C-C rotational barriers, can be understood as a trace of the behavior of the system in absence of the effects (correlations, cooperativity, memory effects...) which characterize the dense supercooled liquid like state against the normal liquid state. The non-exponential regime at  $t > 2$  ps corresponds to what is usually understood as  $\alpha$  and  $\beta$  relaxations. Some implications of these results are also discussed.

### INTRODUCTION

“Fast-dynamics” is in principle an ill-defined term. In the framework of polymer science, a fast process usually means a process with a characteristic time scale faster than the corresponding one to the segmental dynamics. This kind of processes are usually localized rotations or librations of side groups attached to the main chain. A typical example is the methyl group rotation which shows a characteristic time scale in the order of  $10^{-11}$  s or  $10^{-12}$  s and which depends on temperature following an Arrhenius law. In the world of neutron scattering practitioners “fast dynamics” usually means a dynamical process which can be observed as a quasielastic broadening by means of time of flight (TOF) techniques, which cover a time scale roughly speaking from  $10^{-13}$  s to  $10^{-11}$  s. However, the observation of a quasielastic broadening by TOF does not necessarily imply that the value of the corresponding characteristic timescale (relaxation time) is within the TOF window.

In the framework of the glass-forming dynamics, the question of the so called “fast-dynamics” emerges in the middle of the 80’s directly linked to the development of the mode



coupling theory (MCT) [1]. This theory predicts an intermediate regime for the time dependence of the density-density correlation connecting the first microscopic decay with the mesoscopic dynamics known as the  $\alpha$ -relaxation. It is worthy of remark that in the framework of the MCT this intermediate regime is not an actual process, i. e., a process with a well defined characteristic time scale (relaxation time). The intermediate regime of the MCT was unfortunately called  $\beta$ -process producing a big confusion due to the fact that the same term was associated for a long time to another universal process in glass-forming systems, the  $\beta$  (Johari-Goldstein) relaxation [2]. This  $\beta$  (Johari-Goldstein) relaxation is, in contrast to the MCT- $\beta$ -process, an actual process (i. e., with a well defined time scale) which can be observed separated from the  $\alpha$ -process at temperatures around and below the calorimetric glass transition temperature,  $T_g$ , by means of relaxation techniques [3]. Very recently this process has also been observed by neutron spin echo (NSE) techniques in a glass-forming polymer (1,4-polybutadiene) [4].

From an experimental point of view, the first observations associated to the MCT-fast dynamics correspond to neutron scattering experiments also carried out in the last years of the 80's. There were two kinds of different experiments. One set corresponds to NSE techniques (see as representative examples [5,6]). These techniques directly measure the time dependence of the normalized density-density correlation function  $S(Q,t)$  at different values of the momentum transfer  $Q$ . The time scale covered by NSE ranges roughly between  $5 \times 10^{-12}$  s and  $10^{-9}$  s, and the first experiments were made at the  $Q$ -value corresponding to the first maximum of the static structure factor  $S(Q)$ . The values obtained for  $S(Q,t)$  at the shortest time available ( $\approx 5$  ps) were always less than one ( $\approx 0.85$ ). This was considered as an indirect proof of the existence of the MCT- $\beta$ -regime, without taking into account the possible decay of  $S(Q,t)$  due to vibrations or, even in the framework of the MCT, to the microscopic regime whatever it may be. The other set of experiments corresponds to TOF-measurements techniques (see as a representative example [7]). Several investigations by TOF found a quasielastic broadening in different glass-forming systems setting up around and above  $T_g$ . However, in the case of TOF measurements the presence of vibrational contributions including the additional excitations, which are known as the Boson peak, was clear. The first papers tried to separate the effect of vibrations subtracting from the high temperature spectra the low ( $T \ll T_g$ ) ones where only the vibrational contribution is present [7]. A Lorentzian fit of the resulting curves gives a relaxation time with a value of about 1 ps and hardly depending on temperature. It is clear that this result is model-dependent (not only due to the way of separating vibrational contributions but also because of the assumption of a Lorentzian shape) although sometimes it is believed that "simple manipulations" of the data are "by definition" model-independent. These model-dependent analysis of the first TOF results produced the myth of considering as a typical feature of the fast dynamics that their time scale is essentially temperature independent, contrarily to the expectation for a thermally activated process. This myth still persists in the introductory part of some very recent publications. At that

time the fast dynamics measured by TOF was also associated with the  $\beta$ -process of the MCT. Several papers tried, without quantitative success, to check MCT predictions transforming TOF data in susceptibility plots. During the last years different interpretations, other than the MCT one, have been proposed [8-10] for understanding what we would like to define here as “fast-dynamics”: the particular TOF behavior in glass-forming systems around and above  $T_g$ . Unfortunately the situation still is not clear and different ideas are open to controversy. Over last years, we have investigated this topic in glass forming polymers by means of TOF techniques [11-14]. The goal of this paper is to present a summary of the work done, including new results recently obtained, as well as to outline and discuss our theoretical approach for understanding the results obtained.

## EXPERIMENTAL BACKGROUND

The results reported in this paper correspond to TOF neutron scattering techniques. By means of these techniques we measure the scattering function  $S(Q, \omega)$ , which represents the material specific part of the cross section of scattering a neutron with a certain momentum transfer  $\hbar Q$  and energy transfer  $\hbar \omega$ . It can be decomposed into an incoherent and a coherent contribution,  $S_{inc}(Q, \omega)$  and  $S_{coh}(Q, \omega)$  respectively. The former is determined by the self-correlation function of the nuclei, the latter by the two-particle correlation function - both Fourier transformed in space and time. Because the self-correlation function does not contain information about the arrangement of the nuclei in the space,  $S_{inc}(Q, \omega)$  does not include any structural information in its  $Q$  dependence; its  $Q$  dependence is only determined by the spatial extent of the single-particle motion. In contrast,  $S_{coh}(Q, \omega)$  usually reflects the spatial order as the static structure factor  $S(Q)$  from a diffraction experiment does. The intensities of both kinds of scattering depend strongly on the nuclei observed. Especially, protons cause an exceptionally strong incoherent scattering ( $\sigma_{inc} = 80.27$  barns/nucleus,  $\sigma_{coh} = 1.76$  barns/nucleus) while deuterons give rise to more coherent scattering ( $\sigma_{inc} = 2.05$  barns/nucleus,  $\sigma_{coh} = 5.59$  barns/nucleus). Therefore, protonated polymers are nearly completely incoherent scatters while fully deuterated polymers are predominantly coherent scatters.

Fig. 1 (A) shows as an example representative TOF spectra corresponding to fully deuterated poly(vinyl chloride) (PVC-d3). The actual data have been interpolated to constant  $Q = 2.2 \text{ \AA}^{-1}$  and scaled by Bose and Debye Waller factors. For the temperature and the energy range shown here this scaling is essentially only a multiplication by a constant factor so that the shape of  $S(Q, \omega)$  remains unaffected. This representation displays some kind of universal features of the short time dynamics of glass forming fragile (in the well known Angell's meaning [15]) systems and in particular of glass forming polymers. First of all the scaled spectra fall in a master curve up to a certain temperature  $T_f$  ( $T_f \approx 200 \text{ K}$  in this case) indicating that the scattering is dominated by harmonic contributions in this temperature range (at least within the standard

experimental accuracy in this kind of experiments: estimated error bar  $\approx \pm 5\%$ ). At higher temperatures additional scattering starts to accumulate in the quasielastic region of the spectra ( $\hbar\omega < 3$  meV). This quasielastic component clearly dominates the spectra in the high temperature range well above the glass transition temperature  $T_g$  ( $T_g \approx 358$  K in this sample). Another universal feature is that the low temperature harmonic spectra always show additional excitations, concerning the Debye density of states, which are usually known as the Boson-peak (it follows the Bose statistics). These excitations, which are more prominent in the case of strong glasses (Angell's terminology [15]), appear to be related with the anomalies in the thermal properties of glasses in the low temperature region about 10 - 20 K. Another kind of universal behavior of the short time dynamics emerges when the  $S(Q,\omega)$  data are Fourier transformed to the time domain. The function so obtained  $S(Q,t)$  is usually known as intermediate scattering function. Fig. 1 (B) shows as a representative example  $S(Q,t)$  corresponding to PVC-d3 which has been obtained from the corresponding  $S(Q,\omega)$  data by Fourier transformation and deconvolution with the instrumental resolution function. In the high temperature region above  $T_g$ ,  $S(Q,t)$  so obtained always shows a change in the time dependence at a crossover time,  $t_c$ , of about 2 ps for polymer systems. The same figure also shows the  $S(Q,t)$  corresponding to the low temperature region well below  $T_g$  where the harmonic contributions dominate the dynamics. In this case  $S(Q,t)$  shows the typical time dependence of vibrations: a fast decay to a constant value which defines the mean squared displacement. The time value  $t_{ph}$  at which  $S(Q,t)$  reaches its constant value is in the case shown in the figure about 0.5 ps. These results show that in the energy (time) regime covered by TOF techniques, both, vibrations and relaxations coexist. Thereby, in order to analyze the data, we have to consider models or at least analysis procedures based on certain approximations which allow to separate (or to consider) the two contributions to the spectra. Different approaches have been proposed over last years. Almost all these models can be classified in two different categories: models based on classical solid state ideas stressing the importance of the role played by phonons in general and liquid like models which consider the "normal liquid" state as a starting point of view. A representative model of the former category is the vibration-relaxation model [8,12], while we can consider the well known mode coupling theory (MCT) [1] as a clear example of the liquid like group. In principle one can expect that solid like models are more suitable for the glassy state, i. e., the low temperature range until  $T_g$ , and liquid like models for the high temperature region well above  $T_g$ . However, one should also expect some kind of smooth transition from a correct solid like model to a correct liquid like model in some intermediate temperature regime. The approach followed by us for analyzing TOF data of glass forming polymers can be classified as a liquid like model. Therefore, the range of applicability of this model should be in principle the high temperature range ( $T > T_g + 50$  K) where the quasielastic scattering clearly dominates the scattering curves. However, we will show that the application of this approach to the low temperature range close

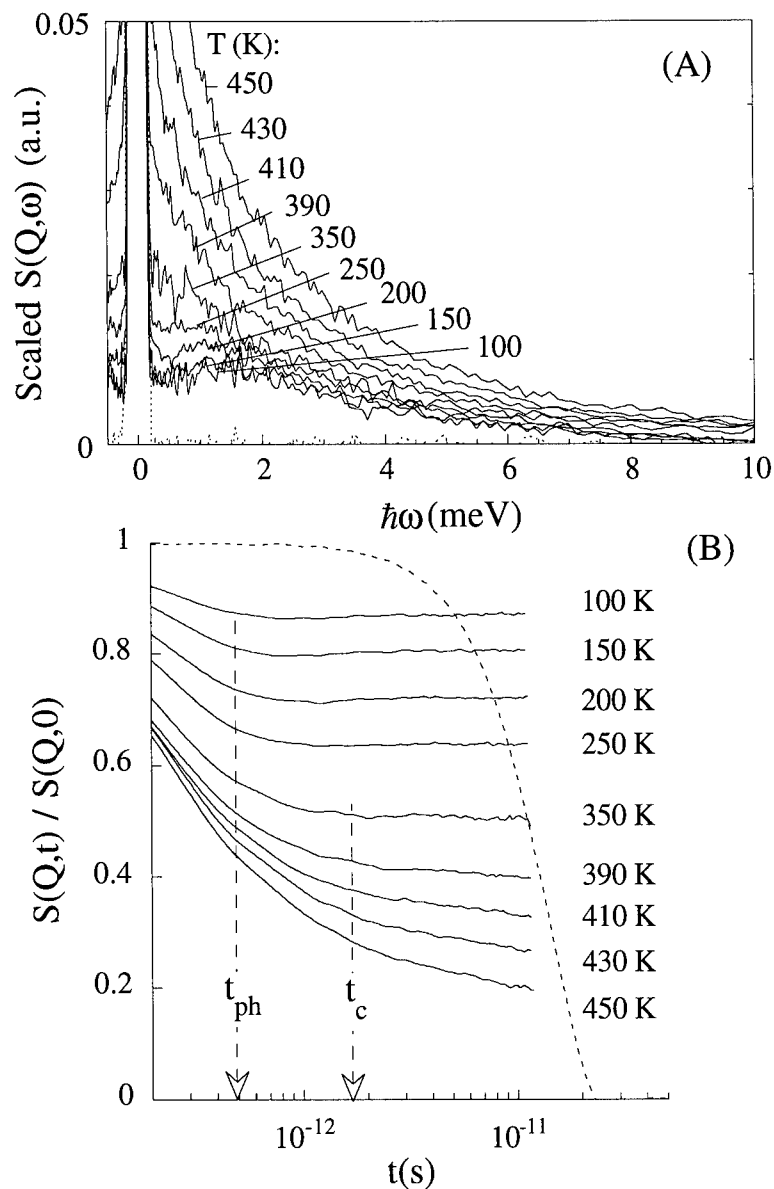


Fig. 1. Deuterated PVC spectra at  $Q = 2.2 \text{ \AA}^{-1}$  and the temperatures indicated. (A): In the frequency domain, scaled by the Debye Waller- and Bose-factors to a reference temperature of 350 K. (B): Fourier transformed into the time domain. The dashed lines show the instrumental resolution function.

to  $T_g$  also gives consistent results.

## DATA ANALYSIS PROCEDURE

Our approach is based on the idea that in the short time regime, before the crossover time  $t_c$ , above introduced, the dynamics of a glass forming liquid in general should be similar to the dynamics of a normal liquid. This idea is in fact a basic idea also involved in the MCT, where  $t_c$  is called  $t_0$  and the normal liquid behavior is usually called “microscopic” dynamics. In this theory, deviations from the normal liquid behavior set up at  $t_0$  due to the well known feed-back mechanism which is the core of the theory. On the other hand, the idea of a crossover from a microscopic like dynamics towards a correlated complex dynamics is a universal feature of several models and theories dealing with the dynamics of chain like objects and other complex systems [16-20] and without taking into account vibrational contributions. In all of these models the crossover at  $t_c$  takes place due to the correlations among the different units (spins, bonds, segments, ...) implying some kind of cooperative dynamics in the sense that configurational rearrangements occur by correlated motions rather than by independent movements of units (it is noteworthy that the feed-back mechanism involved in the memory function formalism of the MCT can also be understood in this way). Thereby, the short time regime is like a trace of the dynamics of the system in absence of correlations among their units. In this regime, a given relaxation function usually displays a simple exponential decay. In fact it has been recently suggested [21] that almost any model based on a master equation formulation leads to initial exponential relaxation crossing over to a non exponential relaxation in the short time regime. The spirit of this crossover is captured by the so called coupling model proposed a long time ago by Ngai [22,10]. However, while in most of the models described in references [16-21] the crossover time appears to depend in some way on the control variables, the coupling model involves an approximately constant crossover time, which can be understood in terms of classical chaos models, as it has been recently reported [23]. A real example of this kind of crossover is displayed by the dynamics of colloidal suspensions [24] which can also be formulated in terms of a memory function formalism based on a Smoluchowski equation, giving rise to a simple collective diffusion (exponential decay) in the short time expansion solution. However, in the case of glass forming systems, the question is how to describe the dynamics of a normal liquid which should also include some vibrational contribution. It is noteworthy that, as we are dealing with neutron scattering TOF data, the Q-range covered (roughly between 1 and 2  $\text{\AA}^{-1}$ ) is just the range where the static structure factor  $S(Q)$  of polymers displays the first maximum, which mainly corresponds to inter-chain correlations. In this particular Q-range the dynamics of simple liquids show diffusive like behavior [25], at least at times higher than  $10^{-13}$  s.

Thus, with this ideas in mind, our approach considers that the dynamics of a glass forming liquid at times shorter than  $t_c$  can be described in terms of simple heuristic oscillatory-

diffusive models which were proposed for simple liquids, at the Q-range above mentioned, a long time ago (see ref. [25] and references therein). In the framework of these models, it is considered that a particle is diffusing with a quasiharmonic vibration superimposed being both processes statistically independent. In this framework, we can write a model scattering function as a convolution product

$$S(Q, \omega) \equiv S^{\text{rela}}(Q, \omega) \otimes S^{\text{harm}}(Q, \omega) \quad (1)$$

where we have adopted the term “rela” (relaxation) for the nonharmonic scattering. To compare this model function to the experimental curves we have to convolute the expression in Eq. (1) with the measured instrumental resolution function  $R(Q, \omega)$ . Therefore the experimental spectra should be given in this framework by

$$S^{\text{expt}}(Q, \omega) = S^{\text{rela}}(Q, \omega) \otimes S^{\text{harm}}(Q, \omega) \otimes R(Q, \omega) \quad (2)$$

We can rewrite Eq. (2) as

$$S^{\text{expt}}(Q, \omega) = S^{\text{rela}}(Q, \omega) \otimes R^{\text{effect}}(Q, \omega) \quad (3)$$

where  $R^{\text{effect}}(Q, \omega)$  plays the role of an effective resolution for the so-called relaxation process given by

$$R^{\text{effect}}(Q, \omega) = S^{\text{harm}}(Q, \omega) \otimes R(Q, \omega) \quad (4)$$

Therefore  $R^{\text{effect}}(Q, \omega)$  is the experimental scattering curve corresponding to harmonic vibrations at the temperature considered. It can be obtained from the harmonic spectra at low temperature ( $T \leq T_f$ ) properly scaled by the Bose and Debye-Waller factors. Fourier transforming Eq. (3) into the time domain,

$$S^{\text{expt}}(Q, t) = S^{\text{rela}}(Q, t) R^{\text{effect}}(Q, t) \quad (5)$$

Then we calculate  $S^{\text{rela}}(Q, t)$  by dividing the Fourier transformation of the experimental spectra by the Fourier transformation of the effective resolution spectra obtained as described above.  $S^{\text{rela}}(Q, t)$  obtained by this procedure is a normalized function [ $S^{\text{rela}}(Q, t=0) = 1$ ] because the Fourier transformation procedure above described involves division by the integral of  $S^{\text{expt}}(Q, \omega)$ . This integral is in the coherent case the static structure factor  $S(Q)$ . In the following, in order to simplify our notation we will call  $S(Q, t)$  to  $S^{\text{rela}}(Q, t)$ . The rest of the paper deals only with this function. If our starting ideas are correct, the behavior of the  $S(Q, t)$  obtained from the experimental data by following the above described procedure should correspond to a diffusive

like behavior in the time scale until the crossover at  $t_c$ .

## SUMMARY OF THE RESULTS OBTAINED

The results reported here correspond to the following samples investigated by us: protonated poly(vinyl chloride) (PVC), fully deuterated poly(vinyl chloride) (PVC-d3), protonated 1,4-polybutadiene (1,4-PB), fully deuterated 1,4-polybutadiene (1,4-PB-d6), and polyisoprene with the methyl group deuterated (PI-d3). The samples are mainly main-chain polymers without side groups (in the case of PI-d3, the methyl groups were deuterated in order to suppress incoherent scattering from its rapid motion). The molecular weight,  $M_W$ , polydispersity,  $M_W / M_N$  and glass transition temperature,  $T_g$ , of these samples are: PVC ( $M_W \approx 70 \times 10^3$ ;  $M_W / M_N \approx 2$ ;  $T_g \approx 358$  K); 1,4-PB ( $M_W \approx 80 \times 10^3$ ;  $M_W / M_N \approx 1$ ;  $T_g \approx 181$  K) and PI ( $M_W \approx 70 \times 10^3$ ;  $M_W / M_N \approx 1$ ;  $T_g \approx 205$  K). The TOF measurements here reported were carried out by means of the spectrometers IN6 and G62 of the Institut Laue Langevin (Grenoble, France) and Léon Brillouin (C. E. Saclay, France) respectively. More details about sample preparation and characterization, as well as TOF measurements, can be found in previous papers [11,12]. It is noteworthy that similar results than the reported ones here below have also been obtained in other polybutadiene samples with different microstructures ranging from 1,2-PB [poly(vinyl ethylene)] to 1,4-PB [26].

Fig. 2 shows an example of the results obtained for  $S(Q,t)$ . As can be seen,  $S(Q,t)$  also displays a change in the time dependence at  $t_c \approx 2$  ps. This  $t_c$  value is almost universal for all the polymers investigated. Moreover it turns out that  $t_c$  hardly depends on  $Q$  and temperature. The short time region until about  $t_c$  can now be well described by a simple exponential decay as it is shown in the figure.

At  $t_c$ ,  $S(Q,t)$  deviates towards a non exponential decay although the exact shape of this decay cannot be obtained only from TOF data. We will focus our attention here in the short time exponential decay. The data of the different polymers investigated were fitted in this region to an equation like  $S(Q,t) = \exp(-t/\tau_D)$  where the relaxation time  $\tau_D$  is  $Q$ - and temperature dependent. We will summarize the results obtained for  $\tau_D(Q,T)$  in the case of incoherent scattering (self correlation function) and coherent scattering (pair correlation function).

In the case of incoherent scattering the  $Q$ - and temperature dependence obtained for  $\tau_D(Q,T)$  can be factorized as

$$\tau_D(Q,T) = Q^{-b} D_0^{-1} \exp\left(\frac{E}{K_B T}\right) \quad (6)$$

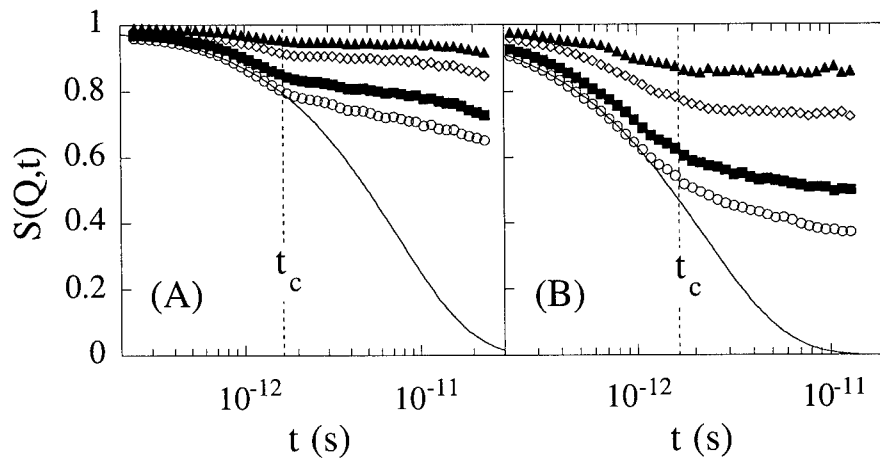


Fig. 2. Intermediate scattering function corresponding to segmental relaxation of PVC at 350, 390, 430 and 450 K (from top to bottom). (A): Incoherent case at  $Q = 1.5 \text{ \AA}^{-1}$ ; (B) coherent case at  $2.2 \text{ \AA}^{-1}$ . Solid lines are exponential fitting curves.

with  $b \leq 2$  and  $D_0^{-1}$  a preexponential factor. The activation energy  $E$  corresponds to the barrier for conformational transitions in isolated chains, which in fact is similar to the C-C rotational barrier in the corresponding polymers (4.5 Kcal/mol for PVC, 2 Kcal/mol for PB and 3 Kcal/mol in the case of PIP, see ref. [12] and references therein). An example of this temperature dependence is shown in Fig. 3 for PVC.

In the case of coherent scattering the obtained  $\tau_D(Q,T)$  follows the well known de Gennes narrowing [27]

$$\tau_D^{\text{coh}}(Q,T) = S(Q) \tau_D^{\text{incoh}}(Q,T) \quad (7)$$

which is a signature of collective diffusion in normal liquids. Fig. 4 shows this behavior in the case of PVC and 1.4-PB.

On the other hand, in the case of coherent scattering we can compare the  $S(Q,t)$  values deduced from TOF by this procedure with the obtained ones by means of NSE technique. This technique directly measures the normalized  $S(Q,t)$  in a time scale roughly between 1 ps to 1 ns, i. e., overlapping in almost one decade with the time scale covered by TOF. Fig. 5 shows the comparison between the normalized coherent  $S(Q,t)$  corresponding to PVC at two different  $Q$ -values. As can be seen in the overlapping region both set of data match perfectly. The intermediate scattering function measured by NSE has been interpreted in terms of the segmental



dynamics which, depending on the polymer and the  $Q$ -range explored, is dominated by the so called  $\alpha$ -relaxation or by a combination of the  $\alpha$  and  $\beta$  (Johari-Goldstein) relaxations (see refs. [4, 28] and D. Richter paper in this issue). Fitting curves corresponding to this regime are included in Fig. 5 as well as the exponential decay corresponding to  $t < t_c$ .

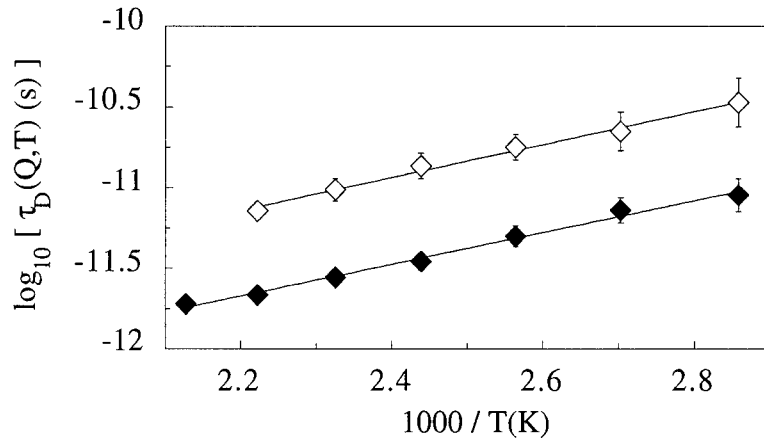


Fig. 3. Arrhenius plot of the characteristic times of the exponential regime in PVC in the incoherent at  $Q = 1.5 \text{ \AA}^{-1}$  ( $\diamond$ ) and in the coherent case at  $2.2 \text{ \AA}^{-1}$  ( $\blacklozenge$ ).

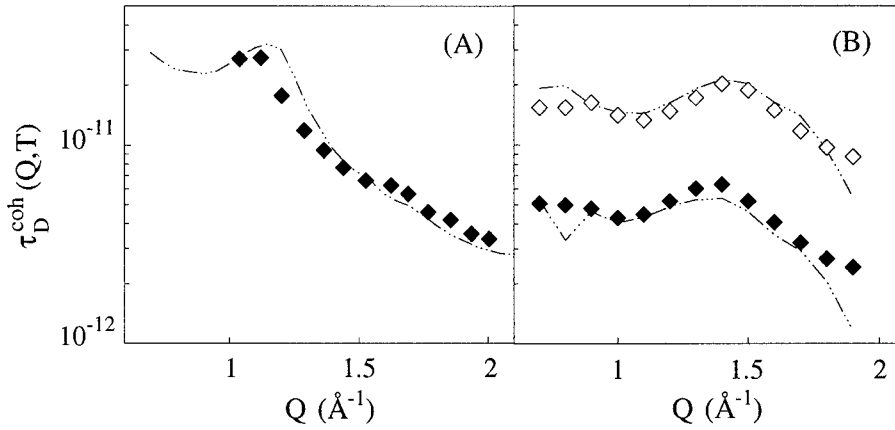


Fig. 4.  $Q$ -dependence of  $\tau_D^{\text{coh}}(Q,T)$ : (A) in PVC-d3 at 445 K; (B) in 1,4-PB-d6 at 200 K ( $\diamond$ ) and 280 K ( $\blacklozenge$ ). Dashed-dotted lines correspond to  $S(Q) \tau_D^{\text{incoh}}(Q,T)$ .

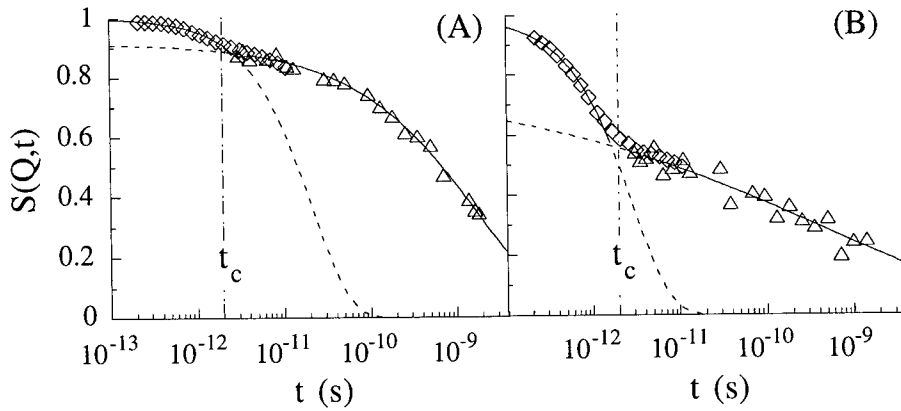


Fig. 5. Normalized coherent intermediate scattering function of PVC-d3: (A) at  $1.2 \text{ \AA}^{-1}$  and 450 K; (B) at  $2.1 \text{ \AA}^{-1}$  and 430 K. Data obtained from TOF ( $\diamond$ ) and NSE ( $\Delta$ ) measurements. Lines through the points are fitting curves.

## DISCUSSION

The results obtained in the short time regime until  $t_c$ , summarized in Eqs. (6)-(7), correspond to the diffusive behavior we can expect for a simple liquid at the  $Q$ -values close to the first maximum of the static structure factor. These results are thereby completely consistent with the starting point of our analysis procedure. Moreover, taking into account both, TOF and NSE data, we can describe the time dependence of the intermediate scattering function  $S(Q,t)$  associated to the segmental relaxation in glass forming polymers as:

$$S(Q,t) = \begin{cases} \exp \left[ - \frac{t}{\tau_D(Q,T)} \right] & t < t_c \\ S^{\alpha\beta}(Q,t) & t > t_c \end{cases} \quad (8)$$

where  $S^{\alpha\beta}(Q,t)$  means the normalized scattering function corresponding to the  $\alpha\beta$ -relaxation which in the coherent case is measured by NSE. However, it is worthy of remark that this description should be only taken as a parametrization of a general solution for  $S(Q,t)$  valid in all the time range. For instance, the time  $\tau_D$  involved in the short time part of Eq. (8) does not represent any actual characteristic time scale of the glass forming state of the system. It only informs us about the behavior of the system in absence of the effects (correlations, cooperativity, memory effects...) which characterize the dynamics of the glass forming state in contrast to the dynamics of the simple liquid state. However, the behavior at longer times  $t > t_c$  is not

independent of the short time behavior characterized by  $\tau_D$ . If  $t_c$  approximately depends neither on temperature nor on  $Q$ , the continuity of the  $S(Q,t)$  function at  $t = t_c$  defines a close relationship between the short and long time behavior. This can formally be expressed as:

$$\exp \left[ - \frac{t_c}{\tau_D(Q,T)} \right] = S^{\alpha\beta}(Q,t_c) \quad (9)$$

If  $S^{\alpha\beta}(Q,t)$  is approximated by a stretched exponential,  $S^{\alpha\beta}(Q,t) = \exp \{ - [t / \tau_w(Q,T)]^\beta \}$ , with a constant value of the shape parameter  $\beta$ , Eq. (9) transforms into

$$\tau_w(Q,T) = [t_c^{\beta-1} \tau_D(Q,T)]^{1/\beta} \quad (10)$$

which is the so called "second universality" proposed a long time ago by Ngai [23] in the framework of the coupling model (in this framework  $n = 1 - \beta$  is the "coupling parameter"). However, it has been demonstrated [4,28] that in the  $Q$ -range around the minimum and the second maximum of the static structure factor  $S(Q)$ , the contribution of the localized motions involved in the  $\beta$  (Johari-Goldstein) relaxation or other secondary processes affects very much the time dependence of  $S^{\alpha\beta}(Q,t)$ . In this  $Q$ -range, we cannot approximate  $S^{\alpha\beta}(Q,t)$  by a "simple" stretched exponential function with a more or less constant  $\beta$ -value as in the case of the pure  $\alpha$ -relaxation. This poses some doubts about the applicability of the above mentioned "second universality" to this  $Q$ -range. Only at  $Q$ -values around the first maximum of  $S(Q)$ , where the pure  $\alpha$ -process dominates  $S^{\alpha\beta}(Q,t)$ , this relationship should be properly applied. In any case, the idea behind the "second universality" proposed by Ngai, i. e., to relate the slow dynamics at  $t > t_c$  with the microscopic behavior, still remains valid even in such a  $Q$ -range, provided that a generalized second universality, as defined by Eq. (9), is used instead of the simplified Eq. (10). On the other hand, it is worthy of remark that in the usual applications of the MCT it is almost always considered that the behavior at  $t > t_c$  ( $t_0$  in this theory) can be taken as independent of the microscopic dynamics. Such a procedure is based on the idea that when the microscopic part of the memory kernel of such a theory is dropped out, the resulting MCT-equations display scale invariance. Thereby  $t_0$  can be considered as an uncritical fit parameter, which only depends smoothly on the control parameters [1]. However, it is clear that the connection between the dynamics for short times and that for long times is switched on when the complete kernel, including the microscopic part, is taken into account. Therefore, even in the framework of the MCT a generalized second universality, like Eq. (9), could be written once a particular model for the microscopic dynamics is chosen.

On the other hand, the diffusive like character of the short time segmental dynamics

(Eqs. (6)-(8) for  $t < t_c$ ) suggests the possibility of writing a general equation for the intermediate scattering function based on a Smoluchowski memory function formalism [24]. This can be written for the coherent case (pair correlation) as:

$$\frac{\partial S(Q,t)}{\partial t} + \frac{D Q^2}{S(Q)} \left\{ S(Q,t) - \int_0^t H(Q,t-t') S(Q,t') dt' \right\} = 0 \quad (11)$$

where  $H(Q,t-t')$  is a memory function and  $D$  a diffusion coefficient defined in terms of Eq. (6) as  $D = D_0 \exp(-E / K_B T)$ . The equation for the self part of the intermediate scattering function (incoherent case) would be similar but without taking into account  $S(Q)$ . In this formalism (which can be considered as a "colloid analogue" for the segmental dynamics), at times  $t < t_c$  the memory function term does not contribute and Eq. (11) can be approximated by

$$\frac{\partial S(Q,t)}{\partial t} + \frac{D Q^2}{S(Q)} S(Q,t) = 0 \quad (12)$$

which gives an exponential solution for the normalized  $S(Q,t)$ :

$$S(Q,t) = \exp \left[ - \frac{D Q^2}{S(Q)} t \right] \quad (13)$$

At times of the order of  $t_c$ , the memory term starts to play an important role changing the time dependence of  $S(Q,t)$  as compared to the exponential form. It is clear that Eq. (11) is only a formalism and in order to get the  $S(Q,t)$  solution valid for all the time we need a theory for the memory function. Moreover, we have to point out that, according to our starting point of view, the solution of Eq. (11) only deals with the relaxational contribution to the segmental dynamics. The complete intermediate scattering function would be in our approach the product of this solution and the harmonic vibrational contribution  $S^{\text{harm}}(Q,t)$  discussed in the section of data analysis.

Finally we can comment about the two main approximations involved in the oscillatory-diffusive model for the normal liquid behavior at the  $Q$ -range of the first maximum of  $S(Q)$ , which is the base of our analysis procedure of the TOF-data. As it was previously described the approximations made are: i) vibrations and relaxations are considered as statistically independent processes and ii) quasi-harmonic approximation for vibrations. Concerning the first point, it is generally assumed that this approach should be a good approximation when the time scale of vibrations and the time scale of relaxations are well separated. In our case, the time scale of vibrations is a phonon time scale of the order of  $5 \times 10^{-13}$  s. Now, what is the characteristic time scale of our segmental relaxation? One can say that it is the time scale characteristic of the first

Debye decay. This depends on  $Q$  and temperature but in the usual range investigated is of the order of  $10^{-11}$  s, i. e., about two orders of magnitude larger than the corresponding to vibrations. Therefore, the statistical independence would be a good approximation. The situation still becomes more clear if we consider that the relaxation behavior is described by a function  $S(Q,t)$  with a complex time dependence which we parametrize [Eq. (8)] in terms of the behavior at times shorter and larger than the crossover one. The actual time scale of such a function can only be defined by the average relaxation time:

$$\bar{\tau}(Q,T) = \int_0^{\infty} S(Q,t) dt \quad (14)$$

This time is always larger than the Debye time and of course larger than the phonon time scale. This implies that the statistical independence is even better fulfilled.

Concerning the point ii), our approach means that we are extrapolating to the high temperature range above  $T_g$  the harmonic behavior of the low energy vibrations found at temperatures well below  $T_g$ , where  $S(Q,\omega)$  does not show any evidence of relaxational contributions (no quasielastic broadening). The main problem for checking this approximation is that it is not possible to know whether the low frequency part of the density of vibrational states is changing through  $T_g$ , because at  $T > T_g$  this part of the spectrum is usually masked by the huge quasielastic broadening. Therefore, it is not easy to imagine any model independent evaluation of possible anharmonic effects due, for example, to a softening of the Boson peak. It is noteworthy that in a different kind of glass-forming system (some multicomponent metallic glasses) the vibrational density of states can be studied through  $T_g$  without the overlapping of relaxational contributions [29]. This can be explained in terms of the particular temperature dependence of the viscosity. In this case, it has been recently reported that the density of vibrational states does not change through  $T_g$  and that the Boson peak does not show any dispersion [29]. Of course we do not know whether these results can be translated to other different glass-forming systems. These results however are at least one example showing up that the density of vibrational states in glass-forming systems has not necessarily to change through the glass-transition.

In our case, up to now we can only give indirect arguments supporting our approximation. First of all, we think that possible deviations from the harmonic behavior due to any softening of the Boson peak above  $T_g$  should not affect the results obtained in this temperature range in a significant manner, because the Boson peak in the fragile polymers investigated is quite weak. Thus the effect of a possible softening should be negligible in comparison with the huge quasielastic broadening. On the other hand the consistency of the results obtained by comparing coherent and incoherent scattering (in particular the de Gennes

narrowing) is hardly compatible with a big mistake in the evaluation of the relaxational / vibrational counterparts of  $S(Q,t)$ .

## CONCLUSIONS

The main conclusion of this work is that the intermediate scattering function  $S(Q,t)$  associated to local segmental relaxation in glass-forming polymers, always displays a short time exponential decay crossing over to a non-exponential regime at a time  $t_c$ . The crossover time  $t_c$  is of the order of 2 ps and hardly depends on the momentum transfer and temperature. The first exponential decay, which is controlled by C-C rotational barriers, can be understood, in the framework of several models, as a trace of the behavior of the system in absence of the effects (correlations, cooperativity, memory effects...) which characterize the dense supercooled liquid like state. The non-exponential regime at  $t > 2$  ps corresponds to what is usually understood as  $\alpha$ - and  $\beta$ -relaxations.

In this framework, the so-called fast-dynamics of glass-forming systems (at least in the case of glass-forming polymers) can be explained in terms of quasiharmonic vibrations and the particular short time behavior of the segmental dynamics, i. e., it does not imply a different dynamical fast process.

## ACKNOWLEDGMENTS

We acknowledge financial support from MEC PB94-0468 and Basque Government PI95/005 projects, Gipuzkoako Foru Aldundia and Iberdrola. A. Arbe acknowledges the grant of the Basque Government.

## REFERENCES

1. See for example W. Götze in Liquids, Freezing and the Glass Transition, edited by J. P. Hansen, D. Levesque, and J. Zinn-Justin (North-Holland, Amsterdam 1991), p. 287.
2. G. P. Johari and M. Goldstein, J. Chem. Phys. **53**, 2372 (1970).
3. See, as an example, N. G. McCrum, B. E. Read and G. Williams in Anelastic and Dielectric Effects in Polymer Solids, (Wiley, London, 1967).
4. A. Arbe, U. Buchenau, L. Willner, D. Richter, B. Farago and J. Colmenero, Phys. Rev. Lett. **76**, 1872 (1996).
5. F. Mezei, W. Knaak and B. Farago, Phys. Rev. Lett. **58**, 571 (1987).
6. D. Richter, B. Frick and B. Farago, Phys. Rev. Lett. **61**, 2465 (1988).
7. F. Fujara and W. Petry, Europhys. Lett. **4**, 921 (1987).

8. U. Buchenau, C. Schönfeld, D. Richter, T. Kanaya, K. Kaji and R. Wehrman, Phys. Rev. Lett. **73**, 17 (1994).
9. A. P. Sokolov, A. Kisliuk, D. Quitmann, A. Kudlik and E. Rössler, J. Non-Cryst. Solids **172-174**, 138 (1994).
10. K. L. Ngai, C. M. Roland and G. N. Greaves, J. Non-Cryst. Solids **182**, 172 (1995).
11. J. Colmenero, A. Arbe and A. Alegría, Phys. Rev. Lett. **71**, 2603 (1993).
12. R. Zorn, A. Arbe, J. Colmenero, B. Frick, D. Richter and U. Buchenau, Phys. Rev. E **52**, 781 (1995).
13. J. Colmenero, A. Arbe, G. Coddens, B. Frick, C. Mijangos and H. Reinecke, Phys. Rev. Lett. **78**, 1928 (1997)
14. J. Colmenero and A. Arbe, Macromol. Symp. (accepted for publication).
15. The fragility  $D$  is defined by Angell [see for example, C. A. Angell, J. Non-Cryst. Solids **131-133**, 13 (1991)] as an exponent in the Vogel-Fulcher expression for the viscosity  $\eta = \eta_0 \exp [DT_0 / (T - T_0)]$ , where  $T_0$  represents the Vogel temperature. A glass former is called fragile if the viscosity diverges rapidly as  $T$  varies from  $T_0$  in contrast to strong systems, which show simple activation behavior.
16. R. J. Glauber, J. Math. Phys. **4**, 294 (1963).
17. See, e. g., J. Jäkle in Disordered Effects in Relaxation Processes, edited by R. Richert and A. Blumen (Springer-Verlag, Berlin 1994), p. 233, and references therein.
18. J. E. Shore and R. Zwanzig, J. Chem. Phys. **63**, 5445 (1975).
19. See as an updated review, Y. Bahar, B. Erman and L. Monnerie in Advances in Polymer Science **116**, edited by L. Monnerie and U. W. Suter (Springer-Verlag, Berlin 1994), p. 143.
20. N. Lemke and Y. A. Campbell, Physica A **230**, 554 (1996).
21. J. Javier Brey and A. Prados, Phys. Rev. E **53**, 458 (1996).
22. K. L. Ngai, Comments Solid State Phys. **9**, 128 (1979); for a recent application of this model see, e. g., K. L. Ngai and A. K. Rizos, Phys. Rev. Lett. **76**, 1296 (1996).
23. Kwork Yeung Tsang and K. L. Ngai, Phys. Rev. E **54**, R3067 (1996).
24. See as a recent review: P. N. Pusey in Liquids, Freezing and the Glass Transition, edited by J. P. Hansen, D. Levesque and J. Zinn-Justin (North-Holland, Amsterdam 1991), p. 762.
25. See for example: T. Springer in Quasielastic Neutron Scattering for the Investigation of

Diffusive Motions in Solids and Liquids (Springer-Verlag, Berlin 1972).

- 26. J. Hendricks et al., to be published.
- 27. P. G. deGennes, *Physica* **25**, 128 (1959).
- 28. A. Arbe, D. Richter, J. Colmenero and B. Farago, *Phys. Rev. E* **54**, 3853 (1996).
- 29. A. Meyer, J. Wuttke, W. Petry, A. Peker, R. Bormann, G. Coddens, L. Kranich, O. G. Randl and H. Schober, *Phys. Rev. B* **53**, 12107 (1996).



## ANOMALIES OF THE FAST RELAXATION DYNAMICS AT $T_g$ IN STRONG GLASS FORMERS

A. BRODIN and L.M. TORELL

Department of Physics, Chalmers University of Technology, S-412 96 Göteborg, Sweden

### ABSTRACT

Structural dynamics of two network forming glasses,  $B_2O_3$  and  $GeO_2$ , has been investigated by Raman scattering over a wide temperature range from  $\sim 10$  K to above the respective glass transition temperatures ( $T_g \approx 526$  K for  $B_2O_3$  and 800 K for  $GeO_2$ ). The spectra are analyzed in terms of two distinct contributions, related to vibrational and fast relaxational dynamics, respectively, and conventionally referred to as the boson peak (BP) and quasielastic scattering (QS). A quantity proportional to the fast relaxation strength may be deduced from the integral intensity of QS relative to BP of the spectra. It turns out, that for  $T < T_g$  the so-obtained QS intensity of the two glasses is similar and smoothly temperature dependent, and can qualitatively be described by e.g. the defect model or the soft potential model. As  $T_g$  is passed, there is a pronounced change in behavior and dramatic differences between the two systems are observed. Thus, the fast relaxational dynamics is obviously affected by  $T_g$ , a finding which is in contrast to the predictions of the mode coupling theory (MCT) of a single crossover temperature  $T_c > T_g$ . Moreover, the experimentally obtained value of the MCT exponent  $a$ , describing the shape of the fast dynamics, is by far exceeding the limiting value ( $a = 0.395$ ) of the theory, the deviation increasing with the strength of the system ( $a \approx 0.7$  for  $B_2O_3$  and  $\approx 0.9$  for  $GeO_2$ ). The observed difference between the two glasses is discussed in terms of the fragility of the system manifested in jumps in the specific heat temperature dependences.

### INTRODUCTION

#### Glass Transition

Supercooling a liquid at a rate that exceeds the rate of structural rearrangement produce a metastable state which, if cooling proceeds to a sufficiently low temperature, is called a glass. A glass is commonly regarded as a liquid which has lost its ability to flow, the disordered system being locked in one of its infinitely many potential minima by quickly reducing the thermal energy. Structurally a glass is hardly distinguishable from its corresponding melt, yet the enormous (by many orders of magnitude) slowing down of the transport properties in the glass transition range, leads to quite abrupt changes in many other physical parameters (for reviews of the glass transition phenomena see e.g. Refs. 1-3). In particular, the specific heat exhibits an almost step-wise behavior, changing typically by 10 to 100% between liquid- and solid-like values at the transition temperature (Fig.1). This is commonly associated with the "ergodicity breaking" during cooling, such that certain liquid degrees of freedom become "frozen" and kinetically inaccessible. The calorimetrically determined glass transition temperature  $T_g$  is conventionally defined as the temperature of onset of the heat capacity increase  $\Delta C_p$  when heating the system from below  $T_g$  at some constant rate (usually 10 K/min). This definition is to some extent arbitrary as the so-obtained  $T_g$  slightly depends on the heating rate. This observation merely illustrates the fact that the *experimentally* determined glass transition is of kinetic origin, being obtained when the average structural relaxation time exceeds the time of observation.

Glass forming liquids represent a wide variety of systems with different molecular interactions from strong covalent bondings, weaker hydrogen bondings to the weak van-der-Waals and ionic bonds. The different systems may be classified according to the temperature dependence in the transition range of the shear viscosity ( $\eta$ ) or, equivalently, the average structural relaxation time ( $\langle\tau\rangle \propto \eta$ ). It turns out that for most systems the temperature dependence may be approximated by the Vogel-Tamman-Fulcher (VTF) equation

$$\langle\tau\rangle = \tau_0 \exp [D T_0 / (T - T_0)] \quad (1)$$

with  $\tau_0$ ,  $D$  and  $T_0$  as parameters. The Arrhenius law, reflecting temperature activated processes, is then obtained in the limit  $T_0 \rightarrow 0$ ,  $D \rightarrow \infty$  and reads:

$$\langle\tau\rangle = \tau_A \exp (E_A / T) \quad (2)$$

To be able to compare different glass formers in the same plot irrespective of large differences in  $T_g$ , one usually presents  $\log \langle\tau\rangle$  versus inverse temperature scaled by  $T_g$ , see Fig.2. The laboratory glass transition temperature is then identified as the temperature at which the relaxation time equals a characteristic value, usually taken to be  $\langle\tau(T_g)\rangle = 100$  s. The  $D$ -parameter of Eq.1 is in such a plot directly related to the slope at  $T_g$  ("steepness index"), and it reflects the resistance of the substance towards temperature induced changes. Taking the  $D$ -value as a reference, Angell has suggested the much quoted strong-fragile classification scheme of glass forming liquids.<sup>3</sup> It turns out that liquids with strong covalent or hydrogen bonds exhibit a nearly Arrhenius temperature behavior (large  $D$ -values) and are accordingly classified as "strong", while at the other extreme, molecular and ionic systems with extremely small  $D$ -values ( $\sim 3$ ) are called "fragile". Strong extremes are, for example, those with open-network tetrahedrally bonded structures like  $\text{SiO}_2$  and  $\text{GeO}_2$  ( $D \approx 100$ ).  $\text{B}_2\text{O}_3$  is another example of a covalently bonded network, in this case formed by randomly connected

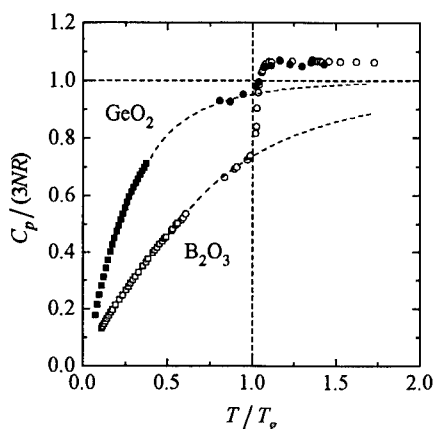


**Figure 1.** Specific heat of  $\text{B}_2\text{O}_3$  and  $\text{GeO}_2$  versus temperature scaled by  $T_g$  (taken from Ref. 29).  $N$  is the number of atoms per formula unit and  $R$  is the gas constant.

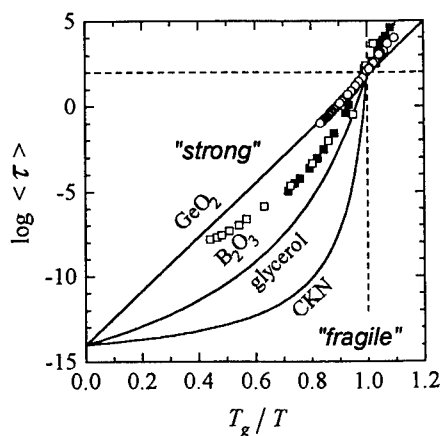


**Figure 2.** Temperature dependence of the average structural relaxation time  $\langle\tau\rangle$  for various glassformers in an Arrhenius plot scaled with the respective glass transition temperatures (taken from Ref. 29).

two-dimensional  $\text{BO}_3$  units. It is also regarded as a "strong" system, despite a significantly smaller  $D$ -value ( $D \approx 35$ ). There is generally a correlation between the fragility of a system and the change of the heat capacity around  $T_g$ : the  $\Delta C_p$  jump is commonly small for strong liquids and increases as the fragility increases. Thus the glass transition is from various aspects more "abrupt" for the fragile systems.

While the glass transition appears to be quite abrupt, the relevant temperature range of an undercooled liquid extends well into the "liquid" state, as the true thermodynamic equilibrium is only reached at the melting temperature  $T_m$ . Two different dynamic regimes can then be considered for  $T > T_g$ . A low-viscosity regime  $T > T_c$  ( $T_c$  is some characteristic temperature in the transition range,  $T_g < T_c < T_m$ ) with a behavior similar to that of a normal liquid, and here the microscopic motion can be associated with a continuous flow process. A high-viscosity regime ( $T_g < T < T_c$ ) is characterized by the diffusing particles staying relatively long in "cages" formed by the surrounding particles, and discrete hops over such barriers appears to be a more adequate description of the microscopic dynamics. The phenomenology just presented has been quantitatively described in the mode coupling theory (MCT),<sup>2,4,5</sup> by which traditional liquid theories were extended to address the supercooled regime. A diverging solution (ergodic to non-ergodic transition) was demonstrated in MCT on a purely kinetic basis. In a mathematically idealised case, where the presence of hopping processes is neglected, the "ideal glass transition" is expected to occur at the critical temperature  $T_c$ . It has been shown that many experimental systems, such as colloidal suspensions<sup>6,7</sup> and certain fragile liquids,<sup>8-12</sup> may indeed be described by MCT. Comparing real systems with the MCT predictions it turns out that  $T_c$  is to be found considerably above  $T_g$ . Recent attempts to test the applicability of the theory to "stronger" systems<sup>13-15</sup> show a transition scenario qualitatively similar to what MCT predicts, although there are severe quantitative disagreements between the experimental data and the theory. Moreover, the observed discrepancies seem to increase with the "strength" of the system. However, none of the systems tested so far belongs to the "strong extreme".

Since experimental liquids behave differently on supercooling, according to their structure and strong-fragility character, the strong-fragile properties are likely to have implications for the dynamical behavior in the corresponding glassy state. The question of correlations between the low- and high-temperature properties of glass formers has been addressed in a number of studies,<sup>16-18</sup> and, for instance, the anomalous low-temperature specific heat and quasielastic light scattering observed in the glassy state have been related to the strong-fragility properties.<sup>17</sup> Still, from the limited experimental data available, it is far from clear whether such correlations are universal features of glasses.

In the present paper we will examine the fast relaxation spectrum for moderately strong  $\text{B}_2\text{O}_3$  and for extremely strong  $\text{GeO}_2$  to see whether deviations from MCT is a general finding for non-fragile systems and whether they depend on the strength of the system. We will also analyse the low temperature data according to the soft potential model (SPM), see below, in order to see whether the strong-fragile properties also have implications on the dynamical behavior in the corresponding glassy state.

#### Inelastic Light Scattering as a Probe of Glassy and Liquid Dynamics

Inelastic light scattering from condensed matter is due to fluctuations of the dielectric susceptibility, which in turn are related to the spectrum of dynamic excitations of the system. The lowest-frequency excitations supported by a glass - and likewise by crystals and liquids - are hydrodynamic modes (sound waves), and these give rise to coherent momentum-allowed scattering (Brillouin lines). In the case of a disordered system one also has to consider the incoherent, disorder-induced scattering at zero momentum transfer.<sup>19</sup> Hence, in contrast to the

first order scattering from crystals, the whole spectrum of dynamic excitations becomes "visible" in the scattering spectra from glasses. In the glassy state most of the excitations may be considered as (quasi)harmonic vibrations and we may treat them as a system of harmonic oscillators (harmonic approximation). Raman susceptibility of a single oscillator of eigenfrequency  $\omega_i$  may then be written as

$$I_i^{Ram}(\omega, \omega_i) / [n(\omega, T) + 1] = \text{Im } \chi(\omega, \omega_i) = C(\omega_i) \delta(\omega - \omega_i) / \omega_i \quad (3)$$

where

$$\chi(\omega, \omega_i) = C(\omega_i) / (\omega^2 - \omega_i^2 - i\varepsilon), \quad \varepsilon \rightarrow +0 \quad (4)$$

is the complex susceptibility of a harmonic oscillator,  $n(\omega, T)$  is the Bose occupation number, and  $C(\omega_i)$  is the light-to-vibration coupling coefficient for the  $\omega_i$  mode. Performing summation of Eq.3 over all eigenmodes  $\omega_i$ , one gets the familiar result of Shuker and Gammon:<sup>20</sup>

$$I^{Ram}(\omega) / [n(\omega, T) + 1] = C(\omega) g(\omega) \quad (5)$$

where  $g(\omega)$  is the density of vibrational states. It is well known that for many glasses at low temperatures Raman spectra presented in the temperature reduced form of Eq.5, exhibit a frequency dependence which is usually close to  $\omega^4$  at low frequencies and then develops into a broad peak at 20-100  $\text{cm}^{-1}$  - the boson peak (BP).<sup>19,21,22</sup> Without going into detail, we note, that BP reflects low-frequency vibrational excitations of the system, which are observable below the glass transition temperature and, in some cases, even above. Apart from BP the Raman spectra of glasses demonstrate another characteristic feature, usually denoted "quasielastic scattering" (QS), which is observable at elevated temperatures ( $T > 20-50$  K) as an excess over the vibrational spectrum in the low frequency range  $< 20-30 \text{ cm}^{-1}$ . QS exhibits a stronger temperature variation than that of the Bose factor and is usually attributed to some relaxational processes which in disordered systems can proceed even though the system is macroscopically "frozen". Although the origin of the phenomenon is still a matter of debate, a formal framework for describing the effect was presented long ago. It was suggested,<sup>19,23</sup> that the deviations of the glass network from strictly harmonic behavior can be described by replacing in the susceptibility function of Eq.4 the square  $\omega_i^2$  of the harmonic eigenfrequency by  $\omega_i^2 + M(\omega, \omega_i)$ .  $M(\omega, \omega_i)$  may be regarded as a "memory function". A possible mechanism is that relaxation processes supported by the disordered structure (e.g. two-level systems performing thermally activated jumps over barriers) act as a random force upon the harmonic modes, and the latter perceive it as a viscous-like damping. The phenomenon is then similar to the true viscous damping of hydrodynamic modes in liquids, which leads to broadening of the Brillouin lines and the appearance of the quasielastic Rayleigh component. A quantity similar to the Landau-Placzek ratio may then be evaluated to describe the damping strength, being the ratio of the integral QS intensity over that of BP. The phenomenology just presented implies that QS and BP are intimately related. This is supported by the experimental fact that the depolarization ratio of QS is the same as that of BP (at least in the low frequency range).<sup>19</sup> In the following we will therefore consider only depolarized scattering, since then the contribution of the elastic (polarized) line is suppressed. Moreover, there are firm indications that it is the depolarized spectrum which reflects more closely the density of states of the system.<sup>24</sup>

The general spectral behavior discussed above is schematically demonstrated in Fig.3, on a log-log scale using the Raman susceptibility representation. The fast relaxational spectrum (QS)

is in Fig.3 seen to grow in strength all the way up to  $T_g$  (without appreciably changing its spectral shape<sup>22</sup>), while BP remains nearly unchanged below  $T_g$ . This is the solid state regime, where any relaxations due to viscous flow are kinetically arrested. The liquid degrees of freedom become released as the temperature is raised above  $T_g$ , and the corresponding viscous relaxation peak shows up on the low frequency side when the inverse relaxation time becomes comparable to the low frequency limit of the accessible spectral window. Following conventional notation, we shall denote the two relaxational contributions as due to "fast"  $\beta$ -processes and "slow"  $\alpha$ -processes, respectively.

The two-step relaxation spectrum, illustrated in Fig.3 for  $T > T_g$ , is the scenario predicted in MCT and it seems to be the universal behavior of glass forming liquids, at least for the fragile liquids.<sup>8-12</sup> MCT predicts that the two relaxational processes ( $\alpha$  and  $\beta$ ) are closely related. This leads to that the frequency behavior of the fast relaxation spectrum, which is at focus in the present work, can be approximated by  $\omega^a$  with the exponent  $a$  being constrained by scaling laws to the frequency behavior ( $\propto \omega^{-b}$ ) of the slow relaxation spectrum. In particular, MCT predicts that the  $a$ -value is restricted such  $a \leq 0.395$ , a condition that can easily be checked experimentally. Experimental data show that MCT describes the fast process for fragile systems surprisingly well, even quantitatively, such that the proposed scaling laws between the two exponents ( $a$  and  $b$ ) are obeyed. However, for non-fragile systems the  $a$ -value is reported to be considerably larger than that obtained from the scaling laws, and the deviation seems to increase as the fragility of the system decreases.<sup>25</sup>

## EXPERIMENT

Vitreous  $B_2O_3$  samples were prepared from powder containing about 3% water. Samples for measurements above  $T_g$  were made by melting the powder directly in a light scattering silica cell placed in an optical furnace. In order to obtain water free samples the liquid was kept at  $\sim 1000^\circ C$  under vacuum for  $\sim 15$  hours.  $B_2O_3$  samples for low temperature measurements were cut out of a bar. The latter was made by melting the powder in a platinum crucible in a high-temperature vacuum oven and thereafter keeping at  $1180^\circ C$  for several hours followed by slow cooling for  $\sim 10$  hours. Special care was taken to grind/polish the surfaces of the bulk sample and protect it from air humidity.  $GeO_2$  samples were made of a bar, prepared from  $GeO_2$  powder (99.99%) in a platinum crucible in vacuum (kept at  $1300^\circ C$  overnight, and thereafter slowly cooled within the oven for  $\sim 10$  hours).

Raman scattering measurements were performed over a temperature range of  $\sim 10 - 1300 K$ ; a helium cryostat was used for measurements at temperatures below RT and an optical furnace for measurements performed above RT. Depolarized and polarized Raman spectra were obtained at right angle scattering geometry using a double grating monochromator (Spex model 1403) with the spectral slit widths typically set to  $1 cm^{-1}$ . As an excitation source an  $Ar^+$  laser was used operating at 488 nm and 200-500 mW. To avoid undue sample heating, the laser excitation

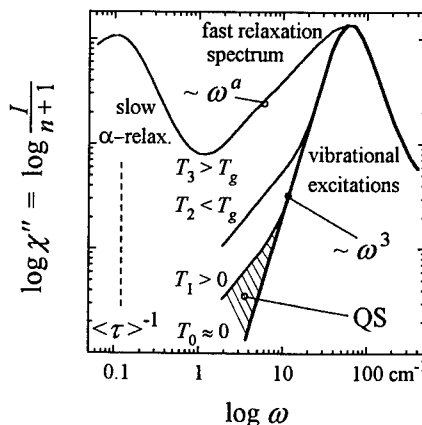


**Figure 3.** Typical Raman susceptibility spectra of a glass-former at various temperatures using a log-log scale.

power was kept below  $\sim 70$  mW during the low-temperature scans. The proper temperature of the sample was determined from the ratio of the Stokes and anti-Stokes scattering. The spectra exhibit a depolarization ratio in the low frequency range of  $\sim 0.45$  for  $\text{GeO}_2$  and  $\sim 0.61$  for  $\text{B}_2\text{O}_3$ , the values being approximately independent of temperature and frequency up to  $\sim 30 \text{ cm}^{-1}$  for both systems. The depolarized spectra are used for the analyses discussed below.

## RESULTS AND DISCUSSION

### Raman Spectra of $\text{B}_2\text{O}_3$ and $\text{GeO}_2$

Fig. 4 shows the depolarised Raman scattering spectra of  $\text{GeO}_2$  and  $\text{B}_2\text{O}_3$  for some selected temperatures. The data are presented in Raman spectral density (temperature normalised) form  $S(\omega) = I(\omega)/(\omega(n+1))$  (which is equivalent to dividing by  $k_B T/\hbar$  in the range where  $\hbar\omega \ll k_B T$ ), such that the trivial temperature dependence for the first order scattering is removed. The spectra exhibit the typical behavior of glasses discussed in the preceding section: a vibrational contribution demonstrated by the behavior of BP at low temperatures  $T \sim 10$  K, and a temperature dependent "quasielastic excess" at elevated temperatures. The BP contribution (or at least its high frequency part, which is clearly distinguished from QS at all temperatures) remains nearly unchanged as the temperature is raised up to  $T_g$ .

Certain further conclusions can immediately be made by comparing the spectra of  $\text{GeO}_2$  and  $\text{B}_2\text{O}_3$  in Fig. 4. If the temperature is raised above  $T_g$ , then in the case of  $\text{B}_2\text{O}_3$  (and in contrast to  $\text{GeO}_2$ ) the quasielastic intensity exhibits a pronounced rise being significantly stronger than a gradual increase at temperatures below  $T_g$ . This is accompanied by softening of BP at  $T > T_g$ , (Fig.4). This behavior is observed for temperatures up to  $\sim 850$  K, while above this temperature the spectra of  $\text{B}_2\text{O}_3$  stay more or less unchanged (the traces at  $T=823$ , 1023 and 1223 K nearly coincide). Hence,  $\text{B}_2\text{O}_3$  exhibits a qualitatively different temperature behavior, in comparison to  $\text{GeO}_2$ . Besides, there exists some characteristic temperature  $T_c > T_g$  in the case of  $\text{B}_2\text{O}_3$ , which separates two temperature regions of qualitatively different dynamics. In order to further compare the observed behavior with that predicted from MCT, we now present the measured spectra in

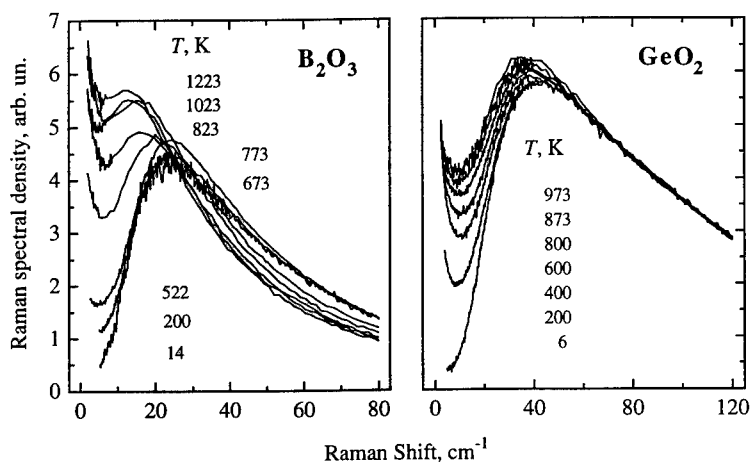
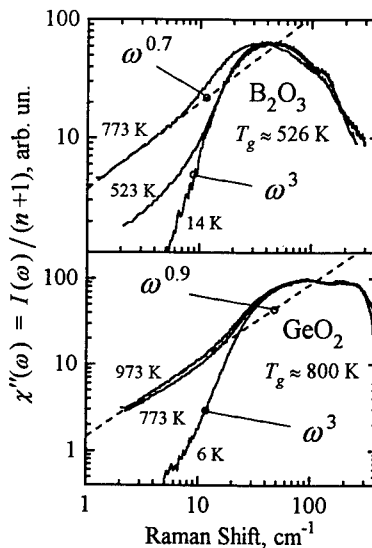


Figure 4. Raman spectral densities of  $\text{B}_2\text{O}_3$  ( $T_g \approx 526$  K) and  $\text{GeO}_2$  ( $T_g \approx 800$  K) at selected temperatures, as indicated.

the Raman susceptibility form  $\chi''(\omega) = I^{Ram}(\omega) / [n(\omega, T) + 1]$ , see Fig. 5. It may be anticipated from Fig. 5, that above  $T_g$  the fast relaxation spectrum exhibits a nearly temperature independent shape, which may be approximated by a power function  $\propto \omega^a$ , as suggested for the  $\beta$ -process of MCT. The exponent  $a$  is found to be  $\sim 0.7$  for  $B_2O_3$  and  $\sim 0.9$  for  $GeO_2$ . It is seen that both values exceed the limiting value  $a = 0.395$  of the theory. We also note that for the strong extreme,  $GeO_2$ , the deviation is larger. This is in accordance with previous observations,<sup>25</sup> obtained for less strong (though still non-fragile) systems, for which too large  $a$ -values compared to those predicted in MCT were reported, and with a deviation which increased as the fragility decreased.

#### Data Treatment

The previously mentioned qualitative differences observed in the temperature dependences of quasielastic intensities of  $B_2O_3$  and  $GeO_2$  (Fig. 4) shall now be quantified to facilitate a comparison of the two systems. We first present some of the spectra from Fig. 4 for different glasses in the same plot, Fig. 6. In Fig. 6 spectra for two chosen temperatures are shown, namely the lowest temperature of observation, where only the vibrational contribution is present, and a temperature close to  $T_g$ . It can be seen in Fig. 6 that as the temperature increases, the contribution from QS increases and a minimum at about  $\sim 5-10 \text{ cm}^{-1}$  appears between the quasielastic peak and BP. It has been proposed that the ratio of the intensity at the minimum to the intensity at the boson peak maximum, taken at  $T_g$ , can be used to characterize the relaxational and vibrational contributions of the spectrum.<sup>17</sup> Based on such estimates, there seems to be some correlation between this value and the fragility of the system such that the ratio increases with increasing fragility. A weakness of such an approach is that the intensity of the BP maximum is at  $T_g$  likely to be affected by not only vibrational but also relaxational contributions (see Fig. 6), an effect which is even more pronounced for fragile systems. For the extremely fragile ionic system CKN ( $Ca-K-NO_3$ ), for instance, BP cannot be distinguished at  $T_g$ , since it is completely smeared out by the quasielastic spectrum.<sup>17</sup> Another weakness



**Figure 5.** Raman susceptibility spectra of  $B_2O_3$  (upper part) and  $GeO_2$  (lower part) at three selected temperatures (lowest measured  $T$ ,  $T = T_g$  and  $T > T_g$ ). Dashed lines show approximated shape of the fast relaxational part of the spectra.

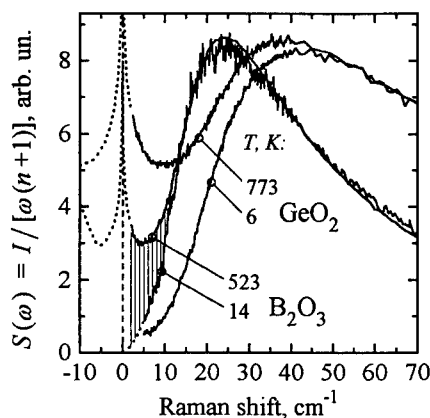


**Figure 6.** Temperature normalized Raman spectral densities of  $B_2O_3$  and  $GeO_2$  at the lowest measured temperatures and at  $T_g$ . Dotted curves are extrapolations, following given curvatures in Fig. 5. Shaded area is proportional to the quasielastic contribution as discussed in the text.

is that using neutron scattering data for the same purpose, different values are obtained from those based on light scattering, because of the different coupling coefficients (Eq.5) of the two techniques. A more adequate measure of the QS intensity can be obtained by subtracting the vibrational contribution  $S_{vib}(\omega, T)$ , which may be estimated from the low temperature ( $T_0$ ) spectrum, and calculating the integral intensity of the "excess" scattering due to relaxations, see the shaded area in Fig.6 for  $B_2O_3$ . The relaxational to vibrational contribution can then be estimated from the ratio of the integrated excess scattering to the integral intensity of the vibrational contribution (proportional to the area of BP). We denote this ratio as  $g(T)$  and define it as follows:

$$g(T) = \frac{\int_0^{\infty} d\omega (S(\omega, T) - S_{vib}(\omega, T))}{\int_0^{\infty} d\omega S_{vib}(\omega, T)} \quad (6)$$

In the case QS is related to the damping of the vibrational part, as discussed in the preceding section, then  $g(T)$  acquires the same meaning as the corresponding parameter introduced in the pioneering work by Winterling.<sup>23</sup> It is then independent of peculiarities of the coupling coefficient  $\tilde{C}(\omega)$  (Eq.5) and similar behavior is expected from a measure of  $g(T)$  using either light or incoherent neutron scattering data.

Certain assumptions are needed in order to apply Eq.6 on the experimental spectra in Fig.4. First we assume that the vibrational contribution in the temperature reduced representation of Fig.4 is independent of temperature, as discussed above, and put  $S_{vib}(\omega, T) = S(\omega, T_0)$ . Here  $T_0$  is the lowest measured temperature, where all relaxations are suppressed. To account for different measuring conditions at different temperatures, the spectra in Fig.4 can then for  $T > T_0$  be scaled to some common integral intensity in the high frequency range  $> 60 \text{ cm}^{-1}$ , where apparently only vibrational contributions are present. Such assumptions become however questionable for  $T > T_g$ , where the vibrational contribution exhibits certain softening. Hence, it is preferable to use Eq.6 only for  $T \leq T_g$ , while we also need a procedure applicable to the spectra at all temperatures. We note however that the *spectral shape of QS* is nearly independent of temperature, which may be anticipated from Fig.5 by comparing the two spectra obtained close to, respective far above, the glass transition temperature. This finding also holds for lower temperatures, as we note both from an analysis of the shape of the "excess" scattering  $S(\omega, T) - S(\omega, T_0)$  and from similar observations previously reported for  $GeO_2$  as well as for some other network glasses.<sup>22</sup> This means that the temperature behavior of the integrated QS intensity is identical to that taken over any restricted frequency interval, and a quantity *proportional* to  $g(T)$  may then be defined:

$$g_1(T) = \frac{\int_{\omega_1}^{\omega_2} d\omega (S(\omega, T) - S(\omega, T_0))}{\int_{\omega_1}^{\omega_2} d\omega S(\omega, T_0)} \propto g(T) \quad (7)$$

Using Eq.7 we may now choose a range of integration  $[\omega_1, \omega_2]$  such that the changes of  $S_{vib}(\omega, T)$  at high temperatures do not introduce any significant error into the result, for instance given by the low frequency limit of the spectra ( $\omega_1 \approx 2 \text{ cm}^{-1}$ ) and some frequency  $\omega_2$  below the maximum of BP, where the QS contribution still dominates. The so-obtained  $g_1(T)$  may then be



scaled to obtain  $g(T)$  by evaluating the "true" value of Eq.6 at selected temperatures  $T \leq T_g$ , for which the scaling procedure of the high frequency part is relevant. In Fig.7 we present the so-obtained values of  $g(T)$  for the two glasses. The spectra for  $T \leq T_g$  were reduced to the same integral intensity in the high frequency range  $> 60 \text{ cm}^{-1}$ , while those for  $T > T_g$  were used as measured, as any scaling would become questionable due to the mentioned softening of the vibrational part. The range of integration was chosen  $5\text{--}10 \text{ cm}^{-1}$  for  $\text{B}_2\text{O}_3$  and  $5\text{--}15 \text{ cm}^{-1}$  for  $\text{GeO}_2$ . It is clear from Figs. 4, 5 and 6 that in these spectral ranges and at high temperatures the spectral intensities are dominated by QS, i.e. the uncertainty of subtracting the temperature dependent vibrational contribution (if Eq. 6 was directly applied) is effectively eliminated. To obtain the "true"  $g(T)$ , needed to scale  $g_1(T)$ , the spectra at RT and  $T_g$  were used and Eq.6 was applied. The range of integration was then extended to  $2\text{--}250 \text{ cm}^{-1}$  for  $\text{B}_2\text{O}_3$  and  $2\text{--}350 \text{ cm}^{-1}$  for  $\text{GeO}_2$ , such that the essential part of the whole spectral density was covered. The effect of neglecting the experimentally inaccessible range  $0\text{--}2 \text{ cm}^{-1}$  was estimated, according to Figs. 5 and 6, to be less than 15% for both systems.

#### Dynamics Below $T_g$

An immediate observation from Fig.7 is the surprisingly similar values and behavior of  $g(T)$  of the two systems in the glassy state. This is expected from the suggested correlation between the fragility, on one hand, and the quasielastic intensity at  $T_g$ , on the other,<sup>17</sup> since both  $\text{B}_2\text{O}_3$  and  $\text{GeO}_2$  are regarded as "strong" systems. They are both represented by a strong covalently bonded network, though the local structure is clearly different, being composed of planar  $\text{BO}_3$  triangles in  $\text{B}_2\text{O}_3$  versus three-dimensional  $\text{GeO}_4$  tetrahedra in  $\text{GeO}_2$ . Relaxations in the glassy state are generally referred to structural "defects" on the molecular level, and one therefore expects the relaxation strength of the corresponding quasielastic intensity to be structure-dependent. A defect should then be understood as an atom, or rather a group of atoms, possessing intrinsic instability, which can be described by e.g. a two-level system (TLS). The so-called defect model has been suggested<sup>19</sup> to explain the QS phenomenon in terms of thermally activated relaxations of TLS's at sufficiently high temperatures ( $>10\text{--}20 \text{ K}$ ), i.e. beyond the TLS tunneling regime. The model of tunneling systems, on the other hand, successfully describes the anomalous properties of glasses observed at low ( $<10\text{--}15 \text{ K}$ ) temperatures, usually referred to as "universal".<sup>26</sup> However no simple correlation was found between the low temperature acoustic properties due to TLS's and properties like fragility or glass transition temperature.<sup>16</sup> Thus, we cannot deduce whether the observed similarity of  $g(T)$  in the solid state of the two oxide glasses of the present study is a consequence of their "strong" character in the strong-fragility plot, or it is caused by similar number of "defects" which has no significant structure dependence.

In the soft potential model (SPM) one considers, in addition to TLS's, soft quasiharmonic oscillators that provide a relaxational contribution to the dynamics at elevated temperatures.<sup>27</sup>

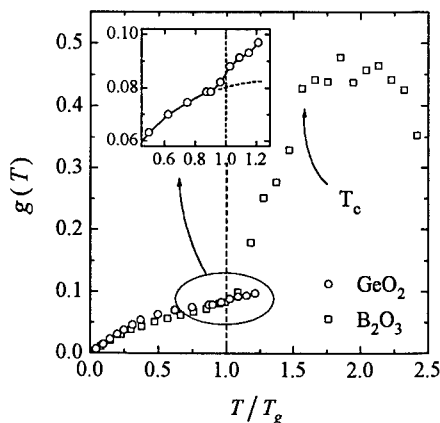


**Figure 7.** Relative quasielastic intensity (see Eqs. 6, 7 and text for definition) versus temperature scaled by  $T_g$  for  $\text{B}_2\text{O}_3$  and  $\text{GeO}_2$ . Insert: temperature range around  $T_g$  for  $\text{GeO}_2$  shown in more detail.

The model predicts that the scattered intensity is proportional to the inverse mean free path of acoustical phonons  $l^{-1}$ . The latter is affected by different processes such as relaxations of TLS's, relaxations in single well potentials (SW), and resonant quasi-harmonic excitations in single wells, which give contributions according to

$$l^{-1} = l^{-1}_{\text{TLS}} + l^{-1}_{\text{rel, SW}} + l^{-1}_{\text{res, SW}}$$

At low enough temperatures the relaxation processes are frozen and only resonant excitations contribute. The Raman susceptibility spectra at low temperatures are then expected to follow a  $\omega^3$  dependence at low frequencies. This is indeed observed both for  $\text{B}_2\text{O}_3$  and  $\text{GeO}_2$ , see Fig.5. Next we discuss the temperature evolution of the quasielastic intensity as presented in Fig.7. According to SPM relaxations in single wells will result in a spectral contribution which is linear in temperature, while TLS's contribution corresponds to  $T^{0.75}$  dependence (although using a slightly different distribution function of TLS's than that used in SPM, a linear in  $T$  contribution from TLS's can be obtained<sup>28</sup>). We now present the data from Fig.7 on a log-log scale in order to facilitate comparisons with these power dependences, Figure 8. We note in Fig.8 for both glasses a linear behavior at low temperatures which gradually changes into a  $T^{0.7}$  dependence as  $T_g$  is approached. Thus both the frequency and temperature dependences of the spectra follow closely the SPM predictions.

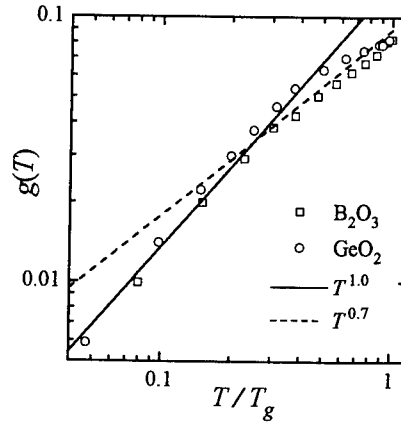


**Figure 8.** Log-log plot of the temperature dependence of the quasielastic intensity (from Fig. 7) below  $T_g$ .

#### Dynamics Around and Above $T_g$

Next we focus the attention on the behavior of  $g(T)$  at  $T_g$  and in the temperature range above the glass transition temperature, see Fig.7. In contrast to the similar behavior of  $\text{B}_2\text{O}_3$  and  $\text{GeO}_2$  in the glassy state, one finds drastic differences above  $T_g$ . In both cases the quasielastic intensity exhibits a crossover around  $T_g$ , which is demonstrated by a weak rise of  $g(T)$  in the case of  $\text{GeO}_2$  (see insert in Fig.7), whereas for  $\text{B}_2\text{O}_3$  the intensity increases dramatically. The quasielastic scattering can be analysed in terms of MCT, which predicts fast so-called  $\beta$ -processes in this frequency range. According to MCT the strength of the  $\beta$ -processes is constant above some crossover  $T_c > T_g$  whereas it rapidly decreases below  $T_c$ . The temperature dependence of the integrated low frequency (i.e. quasielastic + vibrational) intensity has previously been investigated at high temperatures in  $\text{B}_2\text{O}_3$  and a crossover temperature  $T_c$  was indeed detected.<sup>15</sup> It occurred at some temperature  $T_c \approx 900$  K much above  $T_g$  (526 K), and it is indicated in Fig.7 where the crossover at  $T_c$  for  $\text{B}_2\text{O}_3$  is clearly seen. The detected  $T_c$  was then identified with the critical temperature of MCT. The present data clearly show that there is also another crossover in the behavior of the fast dynamics than that related to  $T_c$  of MCT, namely a crossover at the *conventional* glass transition temperature. This is not discussed in MCT in its present form.

Based on the strong-fragile character of the two glasses, we note that while the structural difference of the two systems seems to have no effect on the fast relaxation dynamics in their glassy state, this is obviously not so above  $T_g$ , where large differences occur. We assume that

basically the same structural "defects" (i.e. unstable local configurations) are likewise responsible for QS above  $T_g$ . We further assume that the basic structure of such "defects" does not change appreciably across the transition temperature, since the local molecular structure as such does not undergo any transition at  $T_g$ , and there are no indications of any abrupt changes in the medium-range order. Hence, the temperature dependence of the *number* of "defects" must abruptly change at  $T_g$ . In the glassy state the structure is "frozen" in time, as the primary structural relaxation processes are kinetically arrested. Consequently, the concentration of structural "defects" is likely to be constant. Once the transition temperature is passed, the structural rearrangements due to viscous flow may create new locally instable configurations, i.e. "defects", which may explain why we observe a sudden increase of the quasielastic intensity. The rate of such a process obviously depends on the relative resistance of the system against temperature induced structural changes. Hence, we expect a strong dependence of the QS intensity on the fragility in the transition range, as indeed is observed for  $\text{GeO}_2$  and  $\text{B}_2\text{O}_3$  of the present study (Fig.7).

It is instructive to compare the behavior of the QS intensity in Fig.7 with the temperature evolution of other properties, which likewise can be related to new states, or liquid-like degrees of freedom, released on passing  $T_g$ . This is for instance reflected in the abrupt changes of the specific heat at the glass transition, Fig.1, with a magnitude  $\Delta C_p$  which seems to correlate with the fragility of the system, varying from ~10% to ~100% for strong respective fragile extremes of the classification.<sup>3</sup> The value of  $\Delta C_p$  for the strong glass  $\text{GeO}_2$  amounts to about 10%, while moderately strong  $\text{B}_2\text{O}_3$  demonstrates a significantly larger value of ~30%, see Fig.1. This is still a moderate jump as compared to changes observed for fragile extremes, e.g. ~70% in the case of ionic CKN.<sup>3</sup> Above the jump,  $C_p$  reaches liquid-like values for both systems, though they are still in their supercooled states, as the true thermodynamic equilibrium is only reached at the melting temperature  $T_m$ . The similar qualitative behavior of  $\Delta C_p$  and  $g(T)$  at  $T_g$  for the two systems (Figs. 1 and 7) then suggests that the new liquid-like modes, which become available at  $T_g$  and which cause  $\Delta C_p$ , are accompanied by a number of new unstable states, giving rise to the relaxational spectrum. We then expect that the increase of QS above  $T_g$  correlates with the number of new liquid-like modes proportional to  $\Delta C_p$ . Though the difference in the quasielastic scattering intensity observed for  $\text{GeO}_2$  and  $\text{B}_2\text{O}_3$  may qualitatively be explained by the difference in their fragility and by the behavior of  $C_p(T)$ , we find no simple quantitative correlations.

## CONCLUSIONS

Fast relaxational and low frequency vibrational dynamics of strong glass formers have been studied from low frequency Raman scattering of  $\text{GeO}_2$  and  $\text{B}_2\text{O}_3$ . The fast relaxational processes are demonstrated by quasielastic scattering (QS) which dominates the spectra in the low frequency region ( $< 20 \text{ cm}^{-1}$ ). The low frequency vibrational dynamics is manifested by a peak (the so-called boson peak) located around  $\sim 40 \text{ cm}^{-1}$  for  $\text{GeO}_2$  and  $\sim 25 \text{ cm}^{-1}$  for  $\text{B}_2\text{O}_3$ . Below  $T_g$  the two glasses exhibit nearly the same quasielastic intensity, if scaled by their respective vibrational contributions, and with almost identical temperature dependence, which can be described by the soft potential model. Above  $T_g$  there is a clear difference in the QS intensity of the two systems. We find that there are significant quantitative disagreements with MCT from an analysis of the shape of the fast ( $\beta$ ) relaxational spectrum for both glasses, the disagreement being even more evident for the stronger glass former  $\text{GeO}_2$ . Moreover, the temperature behavior of the intensity of the fast relaxational spectrum exhibits another crossover at the *conventional* calorimetric glass transition temperature  $T_g$ , such that the strength of the  $\beta$ -relaxation process rapidly increases above  $T_g$ , an observation which is not addressed in MCT. The effect is more pronounced in the more fragile  $\text{B}_2\text{O}_3$  system. Assuming that QS of the glass is due to thermally

induced relaxations of structural "defects" or local unstable configurations of glassy network, an explanation is suggested in terms of the number of additional defects, created upon the release of liquid degrees of freedom at  $T_g$ . The rise of the QS intensity above  $T_g$  is then related to the corresponding jump  $\Delta C_p$  of the heat capacity and, accordingly, to the fragility. We suggest from the present data that while the quasielastic intensity at and below  $T_g$  exhibits no obvious dependence on the fragility, the strong-fragile characteristics are manifested in the *crossover* of the temperature dependence of QS at  $T_g$  and by the *magnitude* of the QS increase just above  $T_g$ .

#### REFERENCES

1. J. Jägle, Rep. Prog. Phys. **49**, 171 (1986).
2. W. Götze and L. Sjögren, Rep. Prog. Phys. **55**, 241 (1992).
3. C. A. Angell, Science **267**, 1924 (1995).
4. U. Bengtzelius, W. Götze and A. Sjölander, J. Phys. C **17**, 5915 (1984).
5. E. Leutheusser, Phys. Rev. A **29**, 2765 (1984).
6. W. van Meegen, S. M. Underwood and P. N. Pusey, Phys. Rev. Lett. **67**, 1586 (1991).
7. W. van Meegen and S. M. Underwood, Phys. Rev. Lett. **70**, 2766 (1993).
8. W. Knaak, F. Mezei, B. Farago, Europhys. Lett. **7**, 529 (1988).
9. G. Li, W. M. Du, X. K. Chen, H. Z. Cummins, and N. J. Tao, Phys. Rev. A **45**, 3867 (1992).
10. G. Li, W. M. Du, A. Sakai, H. Z. Cummins, Phys. Rev. A **46**, 3343 (1992).
11. W. M. Du, G. Li, H. Z. Cummins, M. Fuchs, J. Toulouse, and L. A. Knauss, Phys. Rev. E **49**, 2192 (1994).
12. W. Steffen, A. Patkowski, H. Gläser, G. Meier, and E. W. Fischer, Phys. Rev. E **49**, 2992 (1994).
13. E. Rössler, A. P. Sokolov, A. Kisliuk, D. Quitmann, Phys. Rev. B **49**, 14967 (1994).
14. J. Wuttke, J. Hernaudez, G. Li, G. Coddens, H. Z. Cummins, F. Fujara, W. Petry, and H. Sillescu, Phys. Rev. Lett. **72**, 3052 (1994).
15. A. Brodin, L. Börjesson, D. Engberg, L.M. Torell, and A.P. Sokolov, Phys. Rev. B **53**, 11511 (1996).
16. J. F. Berret and M. Meissner, Z. Phys. B **70**, 65 (1988).
17. A. P. Sokolov, E. Rössler, A. Kisliuk and D. Quitmann, Phys. Rev. Lett. **71**, 2062 (1993).
18. A. P. Sokolov, A. Kisliuk, D. Quitmann, A. Kudlik, and E. Rössler, J. Non-Cryst.Sol. **172-174**, 138 (1994).
19. J. Jägle, in: *Amorphous Solids: Low-Temperature Properties* (Ref. 26), p.135.
20. R. Shuker and R. W. Gammon, Phys. Rev. Lett. **4**, 222 (1970).
21. A. P. Sokolov, A. Kisliuk, D. Quitmann, and E. Duval, Phys. Rev. B **48**, 7692 (1993).
22. G. Carini, G. D'Angelo, G. Tripodo, A. Fontana, A. Leonardi, G. A. Saunders, and A. Brodin, Phys. Rev. B **52**, 9342 (1995).
23. G. Winterling, Phys. Rev. B **12**, 2432 (1975).
24. R. M. Martin and F. L. Galeener, Phys. Rev. B **23**, 3071 (1981).
25. A. P. Sokolov, W. Steffen and E. Rössler, Phys. Rev. E **52**, 5105 (1995).
26. For a review, see *Amorphous Solids: Low-Temperature Properties*, edited by W. A. Phillips (Springer-Verlag, Berlin, 1981).
27. U. Buchenau, Yu.M. Galperin, V.L. Gurevich, D.A. Parshin, M.A. Ramos, and H.R. Schober, Phys. Rev. B **46**, 2798 (1992).
28. D. Tielbörger, R. Merz, R. Ehrenfels, and S. Hunklinger, Phys. Rev. B **45**, 2750 (1992).
29. A. Brodin and L.M. Torell, J. Ram. Spectrosc. **27**, 723 (1996).

## DIELECTRIC SPECTROSCOPY AT HIGH FREQUENCIES ON GLASS FORMING LIQUIDS

P. LUNKENHEIMER<sup>1</sup>, A. PIMENOV<sup>1</sup>, M. DRESSEL<sup>1</sup>, B. GORSHUNOV<sup>1,\*</sup>, U. SCHNEIDER<sup>1</sup>, B. SCHIENER<sup>2</sup>, R. BÖHMER<sup>2,\*\*</sup>, A. LOIDL<sup>1</sup>

<sup>1</sup>Experimentalphysik V, Universität Augsburg, Universitätsstr. 2, D-86135 Augsburg, Germany

<sup>2</sup>Inst. für Festkörperphysik, TH Darmstadt, Hochschulstr. 6, D-64289 Darmstadt, Germany

### ABSTRACT

Dielectric spectroscopy up to 950 GHz has been performed on various glass formers as glycerol, propylene-carbonate, and Salol. Special attention is given to the dielectric loss,  $\epsilon''$ , in the crossover regime from the  $\alpha$ -relaxation to the far-infrared (FIR) response where it can be directly compared to the dynamic susceptibilities obtained by neutron and light scattering techniques. We observe a minimum in  $\epsilon''(\nu)$  at high frequencies which cannot be explained by a simple transition from  $\alpha$ -relaxation peak to the FIR bands but has to be attributed to additional fast processes. In all materials investigated,  $\epsilon''(\nu)$  increases significantly sublinear above the minimum. The ratio of the intensity of the  $\alpha$ -process and the fast process as determined from our dielectric experiments is significantly higher compared to the results from the scattering experiments.

### INTRODUCTION

Stimulated by recent theoretical approaches, the fast dynamics in glass-forming liquids came into the focus of interest. Various scenarios have been proposed to describe or predict the dynamic susceptibility at high frequencies in the GHz-THz region [1-5]. Maybe the most controversially discussed approach is the mode coupling theory (MCT) of the glass transition [1] which makes distinct predictions for the high-frequency region. The relevant frequency range up to now has been investigated mainly by neutron and light scattering experiments (see, e.g., [6-11]). Only recently, we were able to extend the frequency range of dielectric experiments on glass-forming liquids up to 370 GHz [12] using backward wave oscillators as coherent sources of electromagnetic radiation [13]. These experiments, which have been performed on glycerol, for the first time revealed the existence of a relatively broad minimum in the frequency dependence of the dielectric loss,  $\epsilon''(\nu)$ , at frequencies above GHz. Its functional form and temperature dependence cannot be explained by a simple crossover from the structural ( $\alpha$ -) relaxation to the FIR response but is indicative of additional fast processes prevailing in this glass-forming liquid. In the present paper we will provide results on glycerol in an extended frequency range up to 950 GHz. In addition we will show first results on two other molecular glass-formers: propylene carbonate (PC) and Salol. All results are compared to the susceptibilities as obtained from the scattering experiments, as well as to theoretical predictions.

### EXPERIMENT

Broadband dielectric measurements involve the use of various techniques. At frequencies  $10 \mu\text{Hz} \leq \nu \leq 1 \text{ kHz}$  measurements were performed in the time domain using a spectrometer which is based on a design described by Mopsik [14]. The autobalance bridge HP4284 was used at  $20 \text{ Hz} \leq \nu \leq 1 \text{ MHz}$ . For the radio-frequency and microwave range ( $1 \text{ MHz} \leq \nu \leq 10 \text{ GHz}$ ) a reflectometric technique was employed [15] using the HP4191 impedance analyzer and the

HP8510 network analyzer. In addition, at frequencies  $100 \text{ MHz} \leq \nu \leq 40 \text{ GHz}$  data were taken in transmission with the HP8510 network analyzer using waveguides and coaxial lines filled with the sample material. Various ovens, closed-cycle refrigerators, and He-cryostats have been utilized to cover the various temperature ranges.

In the most relevant frequency range around 100 GHz, quasi-optical measurements were performed by utilizing the submillimeter spectrometer "Epsilon" [13]. The Mach-Zehnder setup of the interferometer allows the determination of both components, the transmission coefficient and the change in phase upon passing of the electromagnetic wave through the sample. Five different backward wave oscillators were employed to cover the frequency range from 60 GHz up to 950 GHz; the signal was detected by a Golay cell and amplified using lock-in technique. The liquids were put in specially designed cells made of polished stainless steel with thin plane-parallel glass windows with a typical diameter of 15 mm; depending on the range of frequency and temperature the thickness of the sample cell was varied between 1 mm and 30 mm. The cell was placed at the end of a cold finger of a continuous flow He<sup>4</sup>-cryostat allowing to perform the experiments down to 10 K. High temperature measurements were carried out in a custom-made oven up to 500 K. The data were analyzed by using optical formulas for multilayer interference [16] with the known thickness and optical parameters of the windows in order to get the real and imaginary part of the dielectric constant of the sample as a function of frequency at various temperatures.

To cover the complete frequency range, a single  $\epsilon''(\nu)$  curve at a given temperature combines results from different experimental setups. For the measurements  $\nu \leq 40 \text{ GHz}$  there are some uncertainties of the absolute values originating from an ill-defined geometry of the samples or parasitic elements. Therefore it often was necessary to shift  $\log \epsilon''$  values of the measurements at the lower frequencies with respect to the high-frequency results in order to construct a smooth  $\epsilon''(\nu)$  curve. It is important to note that  $\epsilon''(\nu, T)$  from each experimental setup is shifted by one gauge factor only, which depends neither on frequency nor on temperature. In addition, the high-frequency results obtained with the quasi-optical spectrometer provide a very precise absolute values of  $\epsilon''$ .

## RESULTS AND DISCUSSION

### Glycerol

Glycerol ( $T_g \approx 190 \text{ K}$ ) is a relatively strong [17] hydrogen-bonded glass former with a fragility parameter [18] of  $m \approx 53$ . From neutron and light scattering experiments [9-11] the imaginary part of the dynamical susceptibility,  $\chi''$ , has been determined. At frequencies of some 100 GHz  $\chi''(\nu)$  exhibits a minimum. These results have been compared to the predictions of the MCT and deviations from the simplest scaling laws of MCT have been found. This finding was attributed to additional vibrational excitations contributing at the high-frequency wing of the minimum and leading to a relatively steep increase of  $\chi''(\nu)$  towards the microscopic excitation bands [9-11]. These vibrational contributions which give rise to a peak, commonly called Boson-peak, seem to be most pronounced in strong glass formers as glycerol [19]. In a recent work [20] it has been shown that using a more sophisticated evaluation within MCT it is possible to describe the scattering data on glycerol, including the Boson peak. In earlier dielectric experiments the relaxation dynamics in glycerol has been studied over almost 16 decades in frequency, up to 40 GHz [3, 21-23]. A minimum could not be detected and clear deviations from the light and neutron scattering results were obtained. However, it has been pointed out very early by Wong and Angell [5] that a minimum dielectric loss must exist in the crossover region between

structural relaxation and the FIR resonances. They predicted that at low temperatures a plateau should develop due to a constant (i.e. frequency independent) loss.

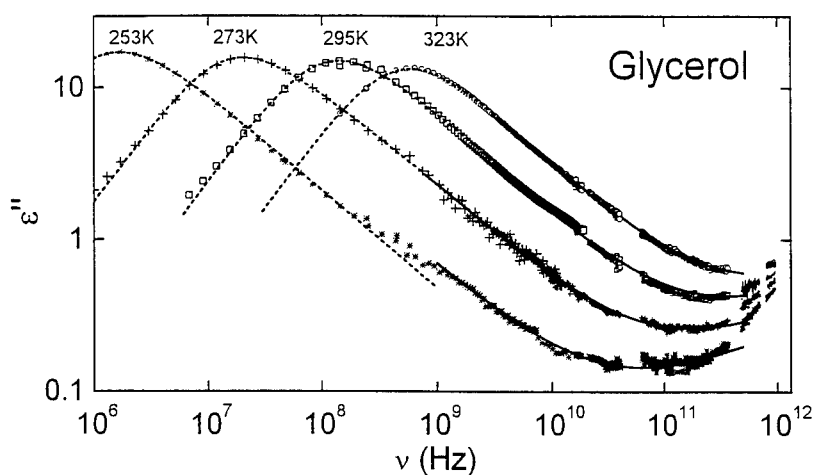


Fig. 1. Frequency dependence of the dielectric loss of glycerol for four temperatures. The dashed lines are fits using the CD ansatz [24] (compare to the fits using the KWW function in Fig. 1 of [12]). The solid lines have been calculated with the MCT expression, Eq. (1), with  $a = 0.325$  and  $b = 0.63$  which corresponds to an exponent parameter  $\lambda = 0.705$ .

Figure 1 shows the dielectric loss,  $\epsilon''(\nu)$ , for frequencies up to 950 GHz. At the highest frequencies investigated a minimum shows up. At lower frequencies, the data reveal a well developed  $\alpha$ -peak which, close to the maximum, can be described by the Fourier transform of the Kohlrausch-Williams-Watts (KWW) function,  $\Phi_0 \exp[-(t/\tau)^\beta]$ , with the stretching exponent  $\beta$  and the relaxation time  $\tau$  [12,23]. The exponent  $\beta$  increases with temperature varying between 0.65 at 180 K and 0.85 at 330 K. The relaxation time  $\tau$  increases significantly stronger than thermally activated and can be parameterized according to a Vogel-Fulcher (VF) law with a VF temperature close to 130 K [3,23]. At temperatures  $T > 260$  K the high-frequency wing of the loss peak reveals only one power-law which smoothly connects to the low-frequency side of the minimum (Fig. 1). In this regime the structural relaxation can be fitted much better using the Cole-Davidson (CD) ansatz [24] (dashed lines in Fig. 1). In contrast to the KWW fits, the resulting shape parameter  $\beta_{CD}$  is almost temperature independent with values varying between 0.62 and 0.69. In this context it is interesting to note that within MCT a temperature independent behavior of the shape of the  $\alpha$ -relaxation process is expected for  $T > T_c$ . At temperatures below 260 K, an additional power law develops at high frequencies with exponents clearly smaller than  $\beta$  which significantly differs from the KWW and, to a lesser degree, also from the CD fit. At these temperatures, the  $\alpha$ -response can be described perfectly well using Nagel's universal scaling ansatz [3].

In Fig. 2 the present dielectric results are compared with the neutron and light scattering data of Wuttke *et al.* [10,11]. As the scattering results give no information of the absolute value of  $\chi''$

the datasets have been scaled. Independent of the scaling procedure the  $\chi''(\nu)$  from the scattering experiments increase significantly stronger towards high frequencies if compared to the dielectric results. It seems that there are additional contributions, most probably of vibrational origin which couple only weakly to the dipolar reorientations determining the dielectric response. This additional density of states, whose contribution to  $\chi''(\nu)$  is usually termed Boson peak, seems to significantly contribute to density correlations specially in strong liquids, as has been worked out in detail by Sokolov *et al.* [19].

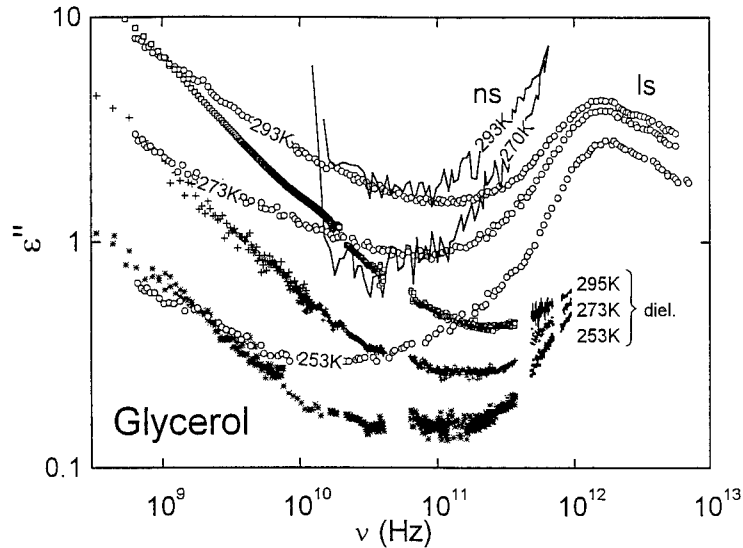


Fig. 2. Frequency dependence of the dielectric loss of glycerol ( $\square, +, *$ ) compared to the imaginary part of the susceptibility as calculated from the light ( $\circ$ ) and neutron scattering results (lines) of Wuttke *et al.* [10, 11]. The scattering data sets have been vertically shifted to give a comparable intensity of the  $\alpha$ -process.

Fig. 2 suggests that these contributions are most pronounced in the neutron scattering results and to a lesser extent in the light scattering results. While in neutron scattering experiments a good coupling to the density fluctuations is achieved, it recently has been found that light scattering experiments are much more influenced by the coupling to orientational fluctuations [25].

In Fig. 3 we analyze the minimum region in terms of a simple crossover from the structural relaxation to the FIR response. Fig. 3a shows the dielectric loss vs. frequency at 273 K, replotted from Fig. 1. The high frequency wing of the  $\alpha$ -response follows a power law with an exponent of -0.63. The increase of  $\epsilon''(\nu)$  towards the FIR bands is assumed to follow a power law with an exponent of 1, a behavior that is common to a variety of glasses [26]. In the region of the minimum, the two contributions are assumed to be superimposed. Depending on the strength and the resonance frequency of the FIR peak, two possible scenarios are obtained (Fig. 3a). In scenario 1 (dashed line) the minimum susceptibility is fixed at the experimentally observed value. However, the frequency of the minimum cannot be described correctly. In scenario 2 (dash-



dotted line) the minimum frequency is fixed at the experimentally observed value. But now the minimum is too deep and additional processes have to be considered in order to describe the experimental curve. If one introduces an additional constant loss contribution [5] it is possible to obtain good fits to the data. However, to take account of the whole data set (Fig. 1), a *temperature dependent* constant loss is necessary, as demonstrated in Fig. 3b. The temperature dependence of the constant loss is shown in the inset. It has to be stated clearly that up to now there is no theoretical foundation of such an assumption. But from these considerations it becomes obvious that an additional process at high frequencies has to be taken into account. Fast processes are considered by the coupling model (CM) [2] and the MCT [1].

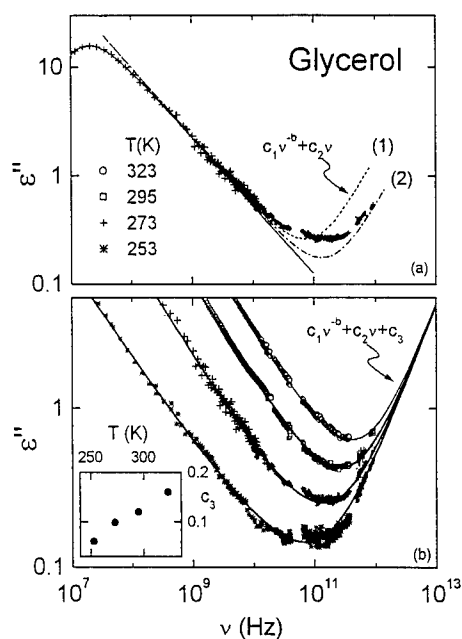


Fig. 3. (a) Frequency dependence of the dielectric loss in glycerol for 273 K. The solid line is a fit using the CD ansatz with  $\beta_{CD} = 0.63$ . The dashed and dash-dotted lines have been calculated using the expression indicated in the figure with  $b = 0.63$ . (b)  $\epsilon''(\nu)$  for various temperatures. The solid lines are fits by the expression indicated in the figure with  $b = 0.63$  and  $c_2 = 4.4 \times 10^{-15}$  for all temperatures except for 253 K where  $b = 0.56$ . The resulting temperature dependence of  $c_3$  is shown in the inset.

Following the predictions of the CM, for large  $\beta$  values the fast process becomes less prominent and a minimum cannot be expected as a consequence of the fast process alone. In order to describe the minimum observed in the neutron and light scattering experiments on glycerol [10,11] and also in the results of a molecular dynamics simulation of *ortho*-terphenyl [27] within the framework of the CM, Roland *et al.* [27,28] took into account additional vibrational contributions. But then again the problem of the temperature dependent constant loss is encountered.

In the following we try to describe our data using the MCT. Both the minimum and the transition region to the  $\alpha$ -process can be described by the MCT using the interpolation [1]:

$$\epsilon''(\nu) = \epsilon_{\min} [a(\nu/\nu_{\min})^{-b} + b(\nu/\nu_{\min})^a]/(a+b) \quad (1)$$

The exponents  $a$  and  $b$  describe the high and low frequency wing of the minimum, respectively, which are identical for all temperatures and constrained by the exponent factor  $\lambda = \Gamma^2(1-a)/\Gamma(1-2a) = \Gamma^2(1+b)/\Gamma(1+2b)$  where  $\Gamma$  denotes the Gamma function. This restricts the exponent  $a$  to values below 0.4, i.e. a significantly sublinear increase of  $\epsilon''(\nu)$  at frequencies above the minimum is predicted.  $\epsilon_{\min}$  and  $\nu_{\min}$  are the height and the position of the minimum, respectively. We want to emphasize that Eq. (1) is only an approximation of  $\epsilon''(\nu)$  near the minimum and valid only above  $T_c$ . In addition, it does not take account of the Boson peak contributions. However, it is useful for a first comparison of model predictions and experimental results. The solid lines in Fig. 1 are obtained by Eq. (1) with  $\lambda = 0.705$  ( $a = 0.325$ ,  $b = 0.63$ ) [12]. While the data are well described up to the minimum frequency, at the highest frequencies investigated clear discrepancies between data and fit become obvious. This may well be due to the remainders of the excess vibrational contributions observed in the neutron- and light-scattering experiments and an analysis including the Boson peak contribution [20] is necessary to describe the data up to the highest frequencies. However, from Fig. 1 it seems reasonable that position and height of the minimum determined from the fits is only weakly influenced by these contributions. An analysis of the critical behavior near  $T_c$  neglecting the Boson peak is performed in [12]. We want to emphasize that the deviations at high frequencies were interpreted as indications for systematic deviations from MCT predictions by Sokolov et al. [19]. This behavior has been documented for many glass forming systems [19] and was ascribed to a coupling of vibrational and fast relaxational excitations [29].

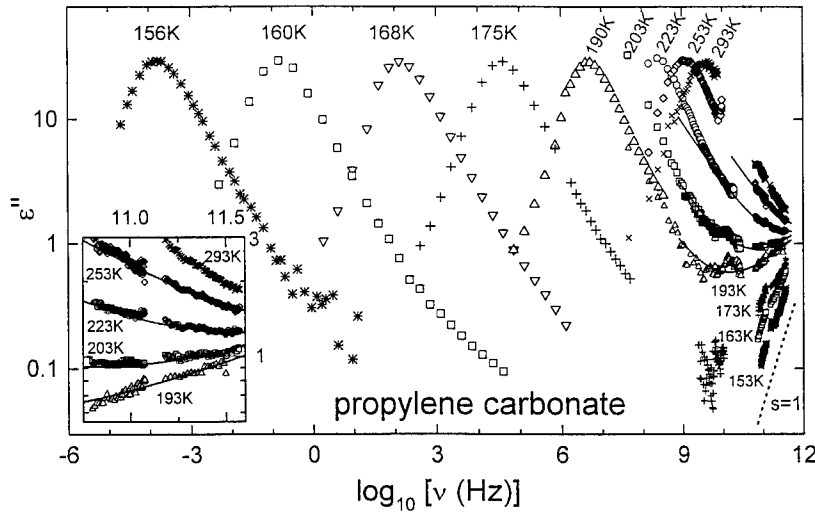


Fig. 4. Frequency dependence of the dielectric loss of PC for various temperatures. The solid lines are fits using Eq. (1) with  $a = 0.29$  and  $b = 0.5$ , i.e.  $\lambda = 0.78$ . The dotted line indicates a linear behavior. The inset gives a magnified view of the high frequency behavior.

#### Propylene Carbonate

In this section we want to show first results on PC. Similar to glycerol, PC ( $T_g \approx 160$  K) is a dipolar system. However, in contrast to the relatively strong, hydrogen-bonded glycerol, PC can

be characterized as a fragile ( $m=104$ ) van der Waals liquid. Figure 4 shows the dielectric loss of PC over more than 17 decades of frequency. The data up to 1 GHz have already been published in [30]. At low frequencies a well developed  $\alpha$ -peak is observed which agrees well with the results from other groups [31]. At high frequencies a minimum shows up. The solid lines are fits using the MCT interpolation formula, Eq. (1) with  $\lambda = 0.78$  ( $a=0.29$  and  $b=0.5$ ). The obtained  $\lambda$  is identical to that obtained from light scattering results [32] and also consistent with a recent analysis of solvation dynamics experiments [33]. The inset gives a magnified view of the high-frequency range. A good agreement of data and fits is obtained.

The MCT predicts a significant change in the behavior of  $\epsilon''(\nu)$  at  $T_c$ : For  $T < T_c$ ,  $\epsilon''(\nu)$  should exhibit a so-called "knee" at a frequency  $\nu_k$ , i.e. a change of power law from  $\epsilon'' \sim \nu^4$  at  $\nu > \nu_k$  to  $\epsilon'' \sim \nu$  at  $\nu < \nu_k$ . As seen in Fig. 4, at temperatures  $T \leq 193$  K the slope of  $\epsilon''(\nu)$  increases significantly and approaches a linear behavior (dotted line). This behavior could be indicative of the "knee" with  $\nu_k$  located above the investigated frequency range. However, we have to stress that these data are taken at the edge of the resolution of the spectrometer and further experiments up to higher frequencies are in progress to corroborate these preliminary low-temperature results.

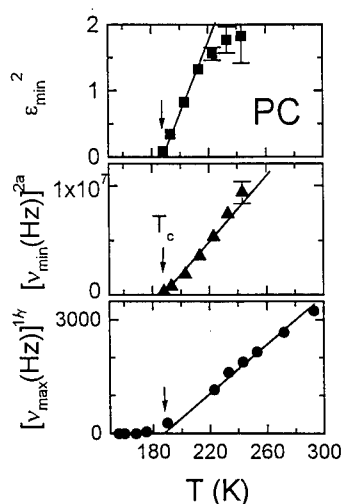


Fig. 5. Temperature dependence of the height and frequency position of the dielectric loss minimum and of the  $\alpha$ -peak position for PC. Representation have been chosen that result in straight lines according to the predictions of the MCT. The solid lines extrapolate to a  $T_c$  of 187 K for all three quantities.

The critical temperature  $T_c$  should manifest itself in the temperature dependence of the  $\epsilon''(\nu)$ -minimum [1]. MCT predicts for  $T > T_c$ :  $\epsilon_{\min} \sim (T-T_c)^{1/2}$  and  $\nu_{\min} \sim (T-T_c)^{1/(2a)}$ . The MCT also predicts a critical temperature dependence of the time scale of the  $\alpha$ -process:  $\nu_{\max} \sim (T-T_c)^\gamma$  with an exponent  $\gamma$  which is determined by the exponents  $a$  and  $b$ :  $\gamma = 1/(2a) + 1/(2b)$ . These critical temperature dependences should be observed above  $T_c$  only as at lower temperatures hopping processes become important which are treated within advanced versions of MCT only [1]. In Fig. 5 the critical behavior is examined.  $\epsilon_{\min}$ ,  $\nu_{\min}$ , and  $\nu_{\max}$  are plotted in a way that according to MCT should result in straight lines extrapolating to  $T_c$ . The three quantities follow this prediction and a  $T_c$  of 187 K is obtained. This lies in the same range as the  $T_c$  obtained from light scattering (179 K) [32], neutron scattering (180-200K) [34] and solvation dynamics experiments (176 K) [33].

In Fig. 6 the dielectric response of PC is compared to the susceptibility obtained by light scattering [32]. Here a scaling with respect to the height of the  $\epsilon''$ -minimum has been chosen. As in glycerol the ratio of the intensity of the  $\alpha$ -process and the fast process is smaller in the scattering results compared to the dielectric results. From Fig. 6 it becomes obvious that both susceptibilities exhibit very similar frequency dependences at temperatures below 193 K but deviate at higher temperatures. As no information about the absolute value of  $\chi''$  can be deduced from the light scattering experiments, it is difficult to decide if the  $\alpha$ -process contributes more strongly (suggested by the scaling chosen for Fig. 6) or the fast process contributes less to the dielectric results if compared to the light scattering data. Some indication in favor of the first case may be obtained from the fact that the  $\alpha$ -relaxation timescales deduced from the peak position differ for both methods. This clearly indicates quite a different coupling to the structural relaxation. In glycerol we ascribed the difference in both responses to the additional Boson peak intensity seen in the scattering experiments but to a much lesser extent in the dielectric experiments. In the more fragile PC the Boson peak contribution is less important as can be deduced from the clearly sublinear increase of  $\chi''(\nu)$  from the light scattering data which can well be described within MCT [32].

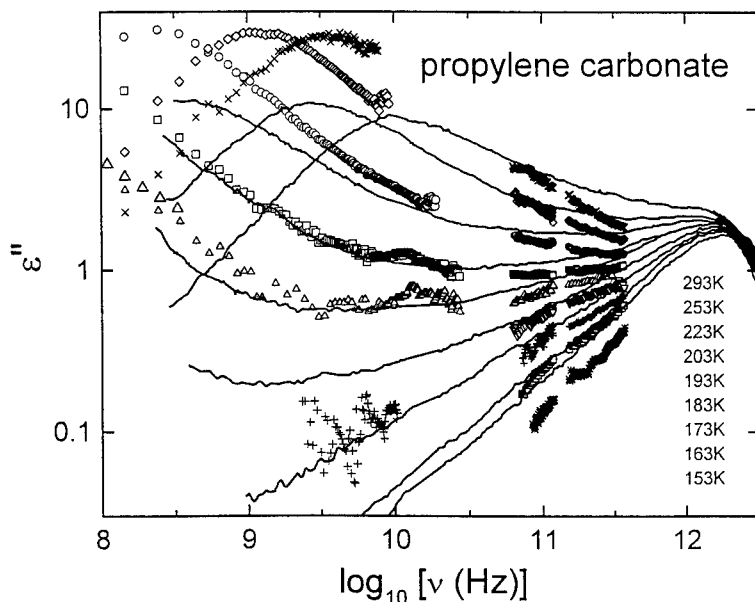


Fig. 6. Frequency dependence of the dielectric loss of PC (symbols) for various temperatures (listed from top to bottom in the figure) compared to the imaginary part of the susceptibility as calculated from the light scattering results of Du *et al.* [32] (lines, temperatures from top to bottom: 295, 250, 220, 200, 190, 180, 170, 160, and 150 K). The scattering data sets have been vertically shifted to match the dielectric data at the minimum region.

## Salol

Salol (phenyl-salicylate,  $T_g \approx 218$  K) can be characterized as a van der Waals liquid with a intermediate fragility of  $m \approx 63$ . Up to now we have performed measurements using one BWO and near room temperature only. However, even this somewhat restricted data set is sufficient to give clear evidence of a minimum in  $\epsilon''(\nu)$  if plotted together with the dielectric data of Hofmann et al. [22], obtained at frequencies below 10 GHz (Fig. 7). In addition, in Fig. 7 the light scattering data of Li et al. [35] are included. A scaling has been chosen that leads to a good agreement of our data and the data of Li et al.. Very similar to PC (Fig. 6) the ratio of  $\alpha$ -peak intensity and intensity of the fast process determining the minimum is smaller for the scattering results. Again the Boson peak seems to play a less important role as can be inferred from the very weak increase of  $\chi''(\nu)$  above the minimum.

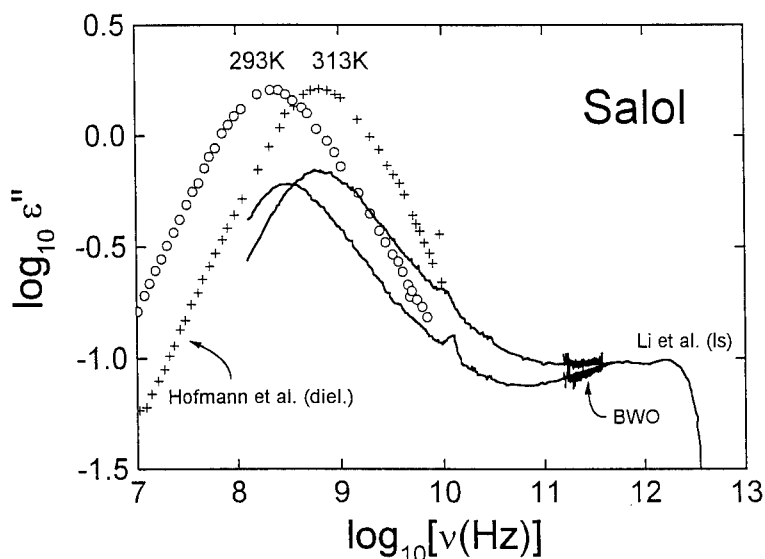


Fig. 7. Frequency dependence of the dielectric loss of Salol (symbols and lines marked "BWO") compared to the imaginary part of the susceptibility from the light scattering results of Li et al. [35] (lines, same temperatures). The dielectric data below 10 GHz have been taken from [22]. The scattering data sets have been vertically shifted to match the dielectric data at the minimum region.

## CONCLUSIONS

In conclusion, we have presented high-frequency dielectric loss spectra of three different glass formers. The  $\epsilon''$ -spectra of all materials investigated reveal a susceptibility minimum at high frequencies. Together with our findings in the two ionic conducting glass formers  $[\text{Ca}(\text{NO}_3)_2]_{0.4}[\text{KNO}_3]_{0.6}$  and  $[\text{Ca}(\text{NO}_3)_2]_{0.4}[\text{RbNO}_3]_{0.6}$  [36] up to now five materials which belong

to very different classes of glass formers have been shown to exhibit a minimum in  $\epsilon''(\nu)$  indicating a quite general behavior. In all cases the observed minimum is relatively broad and cannot be ascribed to a pure crossover from the  $\alpha$ -relaxational process to the far-infrared response. For the investigated molecular glass-formers the ratio of the intensity of the  $\alpha$ -process and the fast process as determined from light and/or neutron scattering experiments is smaller if compared to the dielectric results. In the relatively strong, hydrogen bonded glass former glycerol this difference can be attributed to vibrational excitations contributing mainly to the scattering results and giving rise to the Boson peak. This seems not to be the case for the van der Waals liquids PC and Salol where the Boson peak is less pronounced and a different coupling to the structural relaxations and microscopic processes has to be assumed. For glycerol and PC the frequency and temperature dependences of the measured dielectric responses have been compared to the predictions of the simplest version of MCT. For PC the data are in rather good accord with the model predictions. For glycerol the increase of  $\epsilon''(\nu)$  above the minimum is steeper than expected from the simple model and a more sophisticated evaluation is necessary to test the agreement with the theory. The data show unambiguously that there are non-trivial additional processes contributing to the susceptibility at high frequencies which should be taken into account by any theoretical approach of the glass transition.

#### ACKNOWLEDGEMENTS

We gratefully acknowledge stimulating discussions with C.A. Angell, W. Götze, K.L. Ngai, W. Petry, L. Sjögren, and A.P. Sokolov. We thank Yu.G. Goncharov, R. Kohlhaas, and H. Rall for performing parts of the measurements and A. Maiazza for the preparation of the CKN and CRN samples.

#### REFERENCES

- \*Permanent address: Institute of General Physics, Russian Academy of Sciences, Moscow, Russia.
- \*\*Present address: Institut für Physikalische Chemie, Johannes-Gutenberg Universität Mainz, Mainz, Germany.
- 1. W. Götze and L. Sjögren, Rep. Progr. Phys. **55**, 241 (1992).
- 2. K.L. Ngai, Comments Solid State Phys. **9**, 121 (1979); K.L. Ngai in Disorder Effects on Relaxational Processes, edited by R. Richert and A. Blumen (Springer, Berlin 1994), p.89.
- 3. P.K. Dixon, L. Wu, S.R. Nagel, B.D. Williams, and J.P. Carini, Phys. Rev. Lett. **65**, 1108 (1990).
- 4. N. Menon and S.R. Nagel, Phys. Rev. Lett. **74**, 1230 (1995).
- 5. J. Wong and C.A. Angell in Glass: Structure by Spectroscopy, M. Dekker, New York, 1974, p. 750.
- 6. W. Petry and J. Wuttke, Transp. Theory Statist. Phys. **24**, 1075 (1995)
- 7. W. Knaak, F. Mezei, and B. Farago, Europhys. Lett. **7**, 529 (1988).
- 8. G. Li, W.M. Du, X.K. Chen, H.Z. Cummins, and N.Z. Tao, Phys. Rev. A **45**, 3867 (1992).
- 9. E. Rössler, A.P. Sokolov, A. Kisluk, and D. Quitmann, Phys. Rev. E **49**, 14967 (1994).
- 10. J. Wuttke, J. Hernandez, G. Li, G. Coddens, H.Z. Cummins, F. Fujara, W. Petry, and H. Sillescu, Phys. Rev. Lett. **72**, 3052 (1994).
- 11. J. Wuttke, W. Petry, G. Coddens, and F. Fujara, Phys. Rev. E **52**, 4026 (1995).

12. P. Lunkenheimer, A. Pimenov, M. Dressel, Yu. G. Goncharov, R. Böhmer, and A. Loidl, *Phys. Rev. Lett.* **77**, 318 (1996).
13. A.A. Volkov, Yu.G. Goncharov, G.V. Kozlov, S.P. Lebedev, and A.M. Prokhorov, *Infrared Phys.* **25**, 369 (1985); A.A. Volkov, G.V. Kozlov, and A.M. Prokhorov, *Infrared Phys.* **29**, 747 (1989).
14. F.I. Mopsik, *Rev. Sci. Instrum.* **55**, 79 (1984).
15. R. Böhmer, M. Maglione, P. Lunkenheimer, and A. Loidl, *J. Appl. Phys.* **65**, 901 (1989).
16. M. Born and E. Wolf, *Principles of Optics*, 6th edition, Pergamon Press, Oxford, 1980.
17. C.A. Angell, *J. Chem. Phys. Solids* **49**, 863 (1988).
18. R. Böhmer and C.A. Angell, *Phys. Rev. B* **45**, 10091 (1992).
19. A.P. Sokolov, W. Steffen, and E. Rössler, *Phys. Rev. E* **52**, 5105 (1995).
20. T. Franosch, W. Götze, M. Mayr, and A.P. Singh, preprint
21. A. Schönhals, F. Kremer, A. Hofmann, E.W. Fischer, and E. Schlosser, *Phys. Rev. Lett.* **70**, 3459 (1993).
22. A. Hofmann, F. Kremer, E.W. Fischer, and A. Schönhals, in *Disorder Effects on Relaxational Processes*, edited by R. Richert and A. Blumen (Springer, Berlin 1994), p. 309.
23. P. Lunkenheimer, A. Pimenov, B. Schiener, R. Böhmer, and A. Loidl, *Europhys. Lett.* **33**, 611 (1996).
24. D.W. Davidson and R.H. Cole, *J. Chem. Phys.* **19**, 1485 (1951).
25. H.Z. Cummins, G. Li, W. Du, R.M. Pick, and C. Dreyfus, *Phys. Rev. E* **53**, 896 (1996).
26. U. Strom, J.R. Hendrickson, R.J. Wagner, and P.C. Taylor, *Solid State Commun.* **15**, 1871 (1977); U. Strom and P.C. Taylor, *Phys. Rev. B* **16**, 5512 (1977); C. Liu and C.A. Angell, *J. Chem. Phys.* **93**, 7378 (1990).
27. C.M. Roland, K.L. Ngai, and L.J. Lewis, *J. Chem. Phys.* **103**, 4632 (1995).
28. C.M. Roland and K.L. Ngai, *J. Chem. Phys.* **103**, 1152 (1995).
29. A.P. Sokolov, A. Kisliuk, D. Quitmann, A. Kudlik, and E. Rössler, *J. Non-Cryst. Solids* **172-174**, 138 (1994); A.P. Sokolov, private communication.
30. R. Böhmer, B. Schiener, J. Hemberger, and R.V. Chamberlin, *Z. Phys. B* **99**, 91 (1995).
31. For a compilation of dielectric results on the  $\alpha$ -relaxation in PC see: C.A. Angell, L. Boehm, M. Oguni, and D.L. Smith, *J. Molecular Liquids* **56**, 275 (1993).
32. W.M. Du, G. Li, H.Z. Cummins, M. Fuchs, J. Toulouse, and L.A. Knauss, *Phys. Rev. E* **49**, 14967 (1994).
33. J. Ma, D. Vanden Bout, and M. Berg, *Phys. Rev. E* **54**, 2786 (1996).
34. L. Börjesson, M. Elmroth, and L.M. Torell, *Chem. Phys.* **149**, 209 (1990); L. Börjesson and W.S. Howells, *J. Non-Cryst. Solids* **131-133**, 53 (1991).
35. G. Li, M. Du, A. Sakai, and H.Z. Cummins, *Phys. Rev. A* **46**, 3343 (1992).
36. P. Lunkenheimer, A. Pimenov, and A. Loidl, submitted to *Phys. Rev. Lett.*

## Dynamics of a Supercooled Lennard-Jones System: Qualitative and Quantitative Tests of Mode-Coupling Theory

Walter Kob\* and Markus Nauroth

Institut für Physik, Johannes Gutenberg-Universität, Staudinger Weg 7,  
D-55099 Mainz, Germany

We present the results of a molecular dynamics computer simulation of a supercooled binary Lennard-Jones mixture. By investigating the temperature dependence of the diffusion constant and of the intermediate scattering function, we show that the ideal version of the mode-coupling theory of the glass transition is able to give a good qualitative description of the dynamics of this system. Using the partial structure factors, as determined from the simulation, as input, we solve the mode-coupling equations in the long time limit. From the comparison of the prediction of the theory for the critical temperature, the exponent parameter, the wave-vector dependence of the nonergodicity parameters and the critical amplitudes with the results of the simulation, we conclude that the theory is also able to predict correctly the non-universal properties of the dynamics of a supercooled simple liquid.

## 1 Introduction

In the last few years it has been shown that the mode-coupling theory (MCT) of the glass transition is able to give a quite accurate description of the dynamics of certain supercooled liquids. An introduction to the theory can be found in the review articles of Ref. [1] and a collection of many investigations that have been done in order to test the validity of the theory is compiled in Ref. [2].

Although it has convincingly been shown that there are systems for which MCT gives a good description of the dynamics [2], a few questions remain still open: i) So far it is still not clear for what type of systems the theory is valid. Is it only for glass formers that are basically simple liquids or does MCT also describe more complex liquids? ii) Since so far many of the predictions of the theory are of an asymptotic nature, i.e. are valid only very close to the critical temperature  $T_c$ , it is not clear how important the corrections to these asymptotic results are if one is at a finite distance from  $T_c$ . iii) To what extent are also the non-universal predictions of the theory correct, e.g. is the theory able to predict *quantitatively* the critical temperature or the wave-vector dependence of the nonergodicity parameter?

Partial answers to these questions can be found in the above mentioned articles and in Ref. [3] but it is clear that quite a bit of work is left to be done. The goal of this paper is to address the question whether MCT is able to describe the dynamics of a supercooled binary Lennard-Jones system on a qualitative *and* quantitative basis. In order to study this question we determined the dynamics of such a system by means of a molecular dynamics computer simulation and compared the so obtained dynamics with the (universal) predictions of the theory. From this simulation we also obtained the temperature dependence of the partial structure factors, the crucial input to the theory to make non-universal predictions and then solved the mode-coupling equations in the limit of long times. The so obtained solutions could then be compared with the results from the molecular dynamics simulation.



## 2 Model and Details of the Simulation

The system we consider is a binary mixture of Lennard-Jones particles. Both types of particles (type  $A$  and  $B$ ) have the same mass  $m$  and interact with the potential  $V_{\alpha\beta} = \{(\sigma_{\alpha\beta}/r)^{12} - (\sigma_{\alpha\beta}/r)^6\}$  with  $\alpha, \beta \in \{A, B\}$ . The parameters of the potential are  $\epsilon_{AA} = 1.0$ ,  $\sigma_{AA} = 1.0$ ,  $\epsilon_{AB} = 1.5$ ,  $\sigma_{AB} = 0.8$ ,  $\epsilon_{BB} = 0.5$ , and  $\sigma_{BB} = 0.88$ . In the following we will measure length in units of  $\sigma_{AA}$ , energy in units of  $\epsilon_{AA}$  (setting  $k_B = 1$ ) and time in units of  $(m\sigma_{AA}^2/48\epsilon_{AA})^{1/2}$ . The resulting equations of motion were integrated with the velocity form of the Verlet algorithm with a time step of 0.01 for  $T \geq 1.0$  and 0.02 for  $T < 1.0$ . The length of the runs were chosen such that they always exceeded the typical  $\alpha$ -relaxation time of the system at the corresponding temperature. The temperatures we studied were  $T = 5.0, 4.0, 3.0, 2.0, 1.0, 0.8, 0.6, 0.55, 0.50, 0.475$ , and  $0.466$ . The number of  $A$  and  $B$  particles was 800 and 200, respectively. More details on the simulation can be found in [4, 5].

## 3 Mode-Coupling Equations

For a binary mixture of particles with concentrations  $x_i$  it is convenient to write the mode-coupling equations of motion for the partial intermediate scattering functions  $F_{ij}(\mathbf{q}, t) = \langle \delta\rho_i^*(\mathbf{q}, t) \delta\rho_j(\mathbf{q}, 0) \rangle$ , where  $\delta\rho_i(\mathbf{q}, t)$  is the density fluctuation for wave-vector  $\mathbf{q}$  at time  $t$  for species  $i$ , in matrix form. Thus one obtains [6, 7, 8]

$$\ddot{\mathbf{F}}(\mathbf{q}, t) + \boldsymbol{\Omega}^2(\mathbf{q})\mathbf{F}(\mathbf{q}, t) + \int_0^t d\tau \mathbf{M}(\mathbf{q}, t - \tau) \dot{\mathbf{F}}(\mathbf{q}, \tau) = 0 \quad , \quad (1)$$

where the frequency matrix  $\boldsymbol{\Omega}^2$  is given by  $[\boldsymbol{\Omega}^2(\mathbf{q})]_{ij} = q^2 k_B T (x_i/m_i) \sum_k \delta_{ik} [\mathbf{S}^{-1}(\mathbf{q})]_{kj}$ , with  $m_i$  being the mass of a particle of species  $i$  and  $\mathbf{S}(\mathbf{q})$  stands for the  $2 \times 2$  matrix consisting of the partial structure factors  $S_{ij}(\mathbf{q})$ .

Within the mode-coupling approximation the memory term  $\mathbf{M}$  is given at long times by

$$M_{ij}(\mathbf{q}, t) = \frac{k_B T}{2n m_i x_j} \int \frac{d\mathbf{k}}{(2\pi)^3} \sum_{\alpha\beta} \sum_{\alpha'\beta'} V_{i\alpha\beta}(\mathbf{q}, \mathbf{k}) V_{j\alpha'\beta'}(\mathbf{q}, \mathbf{q} - \mathbf{k}) F_{\alpha\alpha'}(\mathbf{k}, t) F_{\beta\beta'}(\mathbf{q} - \mathbf{k}, t) \quad , \quad (2)$$

where  $n$  is the particle density and the vertex  $V_{i\alpha\beta}(\mathbf{q}, \mathbf{k})$  is given by

$$V_{i\alpha\beta}(\mathbf{q}, \mathbf{k}) = \frac{\mathbf{q} \cdot \mathbf{k}}{q} \delta_{i\beta} c_{i\alpha}(\mathbf{k}) + \frac{\mathbf{q} \cdot (\mathbf{q} - \mathbf{k})}{q} \delta_{i\alpha} c_{i\beta}(\mathbf{q} - \mathbf{k}) \quad , \quad (3)$$

and the matrix of the direct correlation function is defined by

$$c_{ij}(\mathbf{q}) = \frac{\delta_{ij}}{x_i} - [\mathbf{S}^{-1}(\mathbf{q})]_{ij} \quad . \quad (4)$$

A similar expression to Eq. (2) exists for the memory kernel of the incoherent intermediate scattering function [8].

In the following we will assume that the system is isotropic. The nonergodicity parameter for the coherent intermediate scattering function,  $f_{c,ij}(q)$ , can be calculated with the iteration

$$\mathbf{f}^{(l+1)}(q) = \frac{\mathbf{S}(q) \cdot \mathbf{N}[\mathbf{f}^{(l)}, \mathbf{f}^{(l)}](q) \cdot \mathbf{S}(q) + q^{-2} |\mathbf{S}(q)| |\mathbf{N}[\mathbf{f}^{(l)}, \mathbf{f}^{(l)}](q)| \mathbf{S}(q)}{q^2 + \text{Tr}(\mathbf{S}(q) \cdot \mathbf{N}[\mathbf{f}^{(l)}, \mathbf{f}^{(l)}](q)) + q^{-2} |\mathbf{S}(q)| |\mathbf{N}[\mathbf{f}^{(l)}, \mathbf{f}^{(l)}](q)|} \quad , \quad (5)$$

where the matrix  $\mathbf{N}(q)$  is given by  $N_{ij}(q) = m_i M_{ij}(q) / x_i k_B T$ . A similar expression exists for the nonergodicity parameter of the incoherent intermediate scattering function[8].

From the stability matrix of this iteration one can compute  $e(q)$  and  $\hat{e}(q)$ , the right and left eigenvector of this matrix for its largest eigenvalue. The critical amplitudes of MCT,  $h_{ij}(q)$ , are then given by  $e_{c,ij}(q)$ , the right eigenvector at the critical temperature.

A further important quantity of MCT is the exponent parameter  $\lambda$  which can be computed from [6, 7, 8]:

$$\lambda = \int_0^\infty dq \sum_{n=11,12,22} \hat{e}_{c,n}(q) \left( \frac{1}{q^2} (\mathbf{S}(q) - \mathbf{f}_c(q)) \cdot \mathbf{M}[\mathbf{e}_c, \mathbf{e}_c] \cdot (\mathbf{S}(q) - \mathbf{f}_c(q)) \right)_n. \quad (6)$$

In order to compute the integral in Eq. (2) we discretised  $q$ -space by choosing 300 grid point in the interval  $[0, 40]$ . More details on the calculations can be found in Refs. [8].

## 4 Results

One of the most important predictions of MCT is that there exists a critical temperature  $T_c$  at which the diffusion constant  $D$  and the inverse of the  $\alpha$ -relaxation time  $\tau$  vanish with a power-law, i.e.

$$D(T) \propto (T - T_c)^\gamma, \quad \tau^{-1} \propto (T - T_c)^\gamma. \quad (7)$$

Note, that the exponents in the two power-laws are predicted to be the same. This prediction of the theory can be used to locate the critical temperature by fitting the low temperature data for  $D$  or  $\tau^{-1}$  to a power-law. From the mean squared displacement of a tagged particle we have computed the diffusion constant [4, 5] and from the incoherent intermediate scattering function we have determined the  $\alpha$ -relaxation time  $\tau$  of the system [9]. In Fig. 1 we show the so obtained data versus  $T - T_c$ , where  $T_c$  was determined from fitting the low temperature data with the power-laws given in Eq. (7). From the figure we recognize that

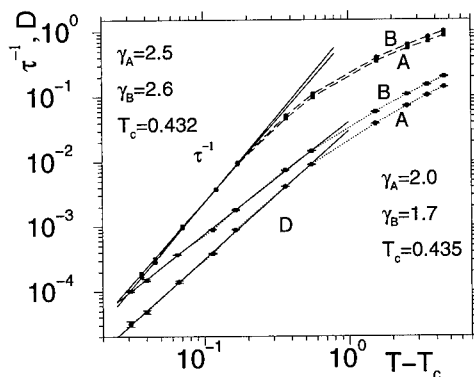


Figure 1: Temperature dependence of the diffusion constant  $D$  and the inverse of the  $\alpha$ -relaxation time  $\tau$  for the two types of particles. The straight lines are fits with power-laws and  $\gamma$  is the exponent of the power-law.

at low temperatures the data can indeed be fitted very well by power-laws, solid lines, in agreement with the prediction of the theory. We also find that the value of the critical temperature is essentially independent of the quantity investigated, as it should be according to the theory. The values of the critical exponents  $\gamma$  are almost identical if one considers the relaxation times for the  $A$  and the  $B$  particles and relatively close to each other for the diffusion constant of the  $A$  and the  $B$  particles. However, the exponents for the two relaxation times and the two diffusion constants differs significantly for each other, in contradiction to the prediction of the theory.

A further important prediction of the theory is that the time correlation functions show a two-step relaxation behavior when plotted versus the logarithm of time. In Fig. 2 we show the incoherent intermediate scattering function of the  $A$  particles for all temperatures investigated. From this figure we see that for high temperatures, curves to the left, the correlation functions decay rapidly to zero. The final part of this relaxation is essentially exponential. If the temperature is lowered, the correlation functions show at intermediate times a small shoulder which, if the temperature is lowered further, develops into a plateau. Thus we find that at low temperatures the correlation functions show indeed the two-step relaxation process predicted by MCT. The physical meaning of the two-step relaxation process is that the first step corresponds to the relaxation of the particles in the cage that is formed by their neighbors. Only for long times this cage breaks up and the time correlation functions show the second relaxation step, the so-called  $\alpha$ -relaxation.

MCT predicts that in the  $\alpha$ -relaxation regime all correlation functions  $\phi(t)$  obey the so-called time temperature superposition principle (TTSP) which means that if one plots the correlation function for different times versus the rescaled time  $t/\tau(T)$ , where  $\tau(T)$  is the  $\alpha$ -relaxation time, all the curves will fall onto a master curve  $\Phi(t)$ , i.e.

$$\phi(t) = \Phi(t/\tau(T)) \quad (8)$$

In Fig. 3 we show the same data as in Fig. 2 versus the rescaled time  $t/\tau(T)$ , where we defined  $\tau(T)$  to be the time it takes the correlation function to decay to  $e^{-1}$  of its initial value. We see that in the  $\alpha$ -relaxation regime the curves for low temperatures fall nicely on

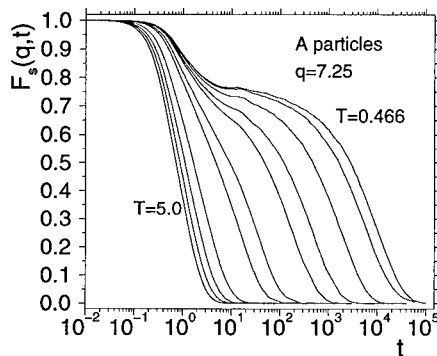


Figure 2: Incoherent intermediate scattering function for the  $A$  particles for all temperatures investigated. The value of  $q$  is at the maximum of the structure factor for the  $AA$  correlation.

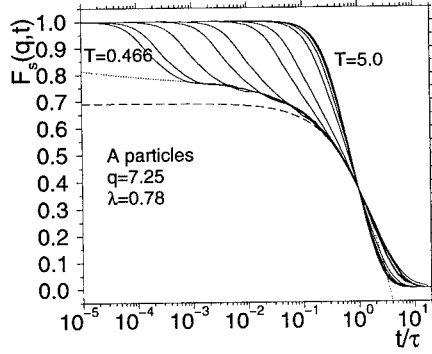


Figure 3: Incoherent intermediate scattering function for the  $A$  particles for all temperatures investigated versus the rescaled time  $t/\tau(T)$ . The dashed line is a fit with a KWW function and the dotted line is a fit with the  $\beta$ -correlator proposed by MCT.

a master curve, thus confirming the prediction of the theory. A further result of MCT is that the *late* part of this master curve is fitted well with a so-called Kohlrausch-Williams-Watts (KWW) law, i.e.  $\Phi(t) = A \exp(-(t/\tau)^\beta)$ . The result of a fit with this functional form is included in the figure as well (dashed line) and from the quality of this fit we conclude that this prediction of MCT holds for our system also. Similar results were found for all other types of correlation functions investigated [9].

MCT also predicts that in the  $\beta$ -relaxation regime, i.e. the time interval in which the correlation functions are close to the plateau, the correlation functions are described by the so-called  $\beta$ -correlator. This function is the solution of an integral equation provided by the theory and can be solved only numerically [1]. This equation, and hence the  $\beta$ -correlator, depends on one parameter, the so-called exponent parameter  $\lambda$ . This parameter is usually treated as a fit parameter in order to fit the correlation functions in the  $\beta$ -relaxation regime with the  $\beta$ -correlator. It can, however, be computed from the time dependence of the structure factor (see below). In Fig. 3 we have also included the result of a fit to the master curve with the  $\beta$ -correlator (dotted curve) and we see that the fit is very good in the late  $\beta$ -relaxation regime. The exponent parameter we determined from this fit is  $\lambda = 0.78$ , which we will compare later with the value computed from the MCT calculation.

From the figure we also see that in the *early*  $\beta$ -relaxation regime, i.e. in the time regime where the correlator is in the vicinity of the plateau but still approaching it, the  $\beta$ -correlator does not give a good fit to the curves. The reason for this is likely the fact that for our system the relaxation dynamics in the early  $\beta$ -relaxation regime is strongly influenced by the dynamics at very short times. Since the mentioned prediction of the theory concerning the early  $\beta$ -relaxation is a result which was derived under the assumption that the short time dynamics can, because of the separation of time scales, be neglected, it is not too surprising to see that this prediction of the theory does not hold for our case. This point of view is also given support by the fact that in a recent computer simulation of the same system considered here, but with the difference that the Newtonian dynamics was substituted by a *stochastic* dynamics, we found that the *early*  $\beta$ -relaxation could be described much better with the  $\beta$ -

correlator than it is the case here [10]. Thus this shows that this prediction of MCT becomes more readily observable if the influence of the short time dynamics is weakened.

We now discuss the results of our investigations in which we tested whether MCT is also able to predict correctly the non-universal properties of the relaxation dynamics of this system. From the just described molecular dynamics simulations we extracted the temperature dependence of the partial structure factors and used those to solve the mode-coupling equations in the long time limit (see Sec. 3). More details on these calculations can be found in Ref. [8].

The first quantity we computed was the critical temperature  $T_c$ , which is obtained as the highest temperature for which the iteration given in Eq. (5) converges to a nontrivial solution. From this calculation we determined  $T_c$  to be 0.92, which is about twice as large as the value of  $T_c$  as determined from our simulation ( $T_c = 0.435$ ). Thus at first view this discrepancy seems to be surprisingly large. That this is, however, not necessarily the case, can be seen as follows. Consider the case of a soft-sphere system, i.e. a system in which the particles interact with the potential  $V(r) = (\sigma/r)^{12}$ . For this potential it is known that the thermodynamically relevant parameter is the coupling constant  $\Gamma = n/T^{1/4}$ , where  $n$  is the particle density[11]. Thus we see that  $\Gamma$  depends only weakly on temperature. It is well known that in dense liquids it is mainly the repulsive hard core which is responsible for their structure [12]. Since the soft-sphere system and the Lennard-Jones system have the same type of hard core we can expect that also in the latter system the dependence of the thermodynamics state on temperature is only weak. If we assume that the dependence of the coupling constant on temperature is of the same form as the one for the soft-sphere system we thus conclude that an error in the critical temperature corresponds to an error in the critical coupling constant of only 20%. This discrepancy is similar to the one that was found for analogous calculations in a soft sphere system [6] or colloidal systems [13, 14], which are described well by a hard sphere model.

The next quantity we consider is the exponent parameter  $\lambda$  which can be computed from Eq. (6). Our calculations gave a value of  $\lambda$  of 0.72, which has to be compared with the value determined from our fit of the  $\beta$ -correlator in the  $\beta$ -relaxation regime,  $\lambda = 0.78$ . Thus we find that the discrepancy between simulation and theory is 10%, which is comparable with the one found in the soft sphere system or in the colloidal systems [6, 13, 14].

We now turn our attention to the nonergodicity parameter  $f_c$ , i.e., the height of the plateau of a time correlation function at  $T_c$ . In Fig. 4 we show the  $q$  dependence of  $f_c$  for the incoherent and coherent intermediate scattering function for the  $A$  particles. The dashed curves are the results from the computer simulation and the solid curves the one from the theoretical calculation. We see that the qualitative agreement between the theory and the simulation is very good in that the overall shape of the two corresponding curves are the same. The theory also correctly predicts that for large wave-vectors the curve for the coherent part oscillates around the one for the incoherent part. For wave-vectors in the vicinity of the first peak in the structure factor ( $q_{max} \approx 7.2$ ) the agreement between theory and simulation is even *quantitatively* very good in that the difference between the corresponding curves is on the order of only a few percent. Taking into account that no fit-parameter is involved this agreement is quite remarkable. For large values of  $q$  the theoretical curve differs more from the one of the simulation. The reason for this is probably the fact that in the derivation of the mode-coupling equations a factorization approximation is made which is likely to be unreliable for large values of  $q$  [1]. A different possibility might be that the way the nonergodicity parameter was determined in the simulation gives rise to

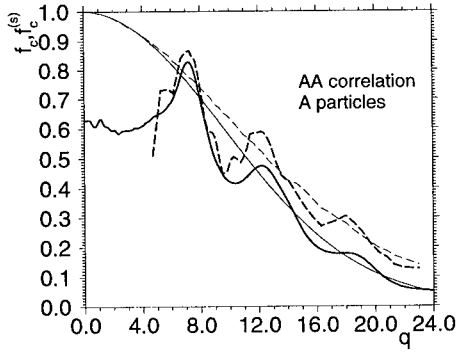


Figure 4: Nonergodicity parameter for the incoherent (thin lines) and coherent (bold lines) intermediate scattering function for the  $A$  particles. Dashed lines: simulation. Solid lines: prediction of MCT.

systematic errors in  $f_c(q)$  [8, 9].

We also mention that the theory is also able to predict with good accuracy the wave vector dependence of the nonergodicity parameter for the  $AB$  correlation and the one for the incoherent and coherent intermediate scattering function for the  $B$  particles [8]. Since the wave-vector dependence of these quantities is significantly different from the one for the  $A$  particles, this is a highly nontrivial result.

A further remarkable prediction of the theory is that in the  $\beta$ -relaxation regime all time correlation functions should obey the so-called factorization property. This means that a time correlation function  $\phi(t)$  can be written as  $\phi(t) = f_c + h g_{\pm}(t)$ , where  $f_c$  is the nonergodicity parameter discussed above, the amplitude  $h$  depends on  $\phi$  but not on time and the function  $g_{\pm}(t)$  is independent of  $\phi$  (the  $\pm$  in  $g_{\pm}(t)$  corresponds to  $T \lesseqgtr T_c$ ). Since the whole time dependence is thus given by the  $\phi$  independent function  $g_{\pm}(t)$  it is, for a given system, “universal”. If we apply this factorization property to a  $q$  dependent correlation function, such as the intermediate scattering function, it means that  $F(q, t)$  can be written as

$$F(q, t) = f_c(q) + h(q)g_{\pm}(t) \quad (9)$$

where  $f_c(q)$  is the nonergodicity parameter we discussed in Fig. 4. Using the space Fourier transform of this equation it is easy to show that

$$\frac{F(r, t) - F(r, t')}{F(r', t) - F(r', t')} = \frac{h(r)}{h(r')} \quad (10)$$

must hold. Here  $t$  and  $t'$  are times in the  $\beta$ -relaxation regime and  $r$  and  $r'$  are arbitrary. Thus the prediction of the theory is that the left hand side of this equation is independent of time, if this time is in the  $\beta$ -relaxation regime. We have found that this is actually the case [5] and proceed now to test whether MCT is able to predict correctly the  $r$  dependence of the right hand side of the equation, i.e. the ratio  $h(r)/h(r')$ .

From the simulation we computed the left hand side of Eq. (10) and the results for the distinct part of the van Hove function for the  $AA$  correlation is shown in Fig. 5a. The

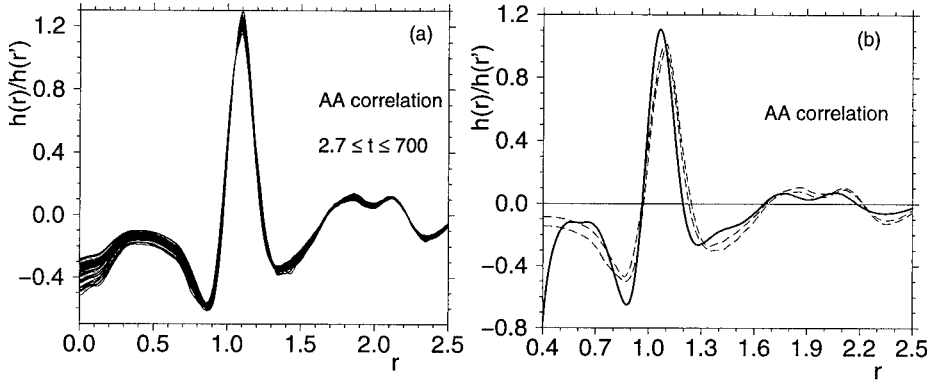


Figure 5: a) Left hand side of Eq. (10) for times in the  $\beta$ -relaxation regime. b)  $r$ -dependence of the critical amplitude  $h(r)$  for the  $AA$  correlation. Thin dashed lines: upper and lower estimate from the simulation. Bold line: prediction of the theory.

curves correspond to different times in the  $\beta$ -relaxation regime and we recognize that they all cluster around a master curve. If one considers times outside the  $\beta$ -relaxation regime, the corresponding curves show strong deviations from this master curve [5]. From the curves shown in Fig. 5a we determined an upper and lower bound for  $h(r)/h(r')$  and we show these curves in Fig. 5b (thin dashed lines). The prediction of the theory for this ratio is shown as a bold line. We thus see that for this quantity the agreement between the theory and the simulation is very good in that also small details, like the small dip in the vicinity of  $r = 1.9$ , are reproduced correctly. For small distances the agreement between simulation and theory is not very good. The reason for this is likely the fact mentioned in the discussion of Fig. 4 that MCT becomes unreliable for very large values of  $q$ , i.e. for small distances.

In Fig 6 we show the critical ratios for the  $AB$  and  $BB$  correlations. For the case of the  $AB$  correlation the agreement between theory and simulation is again very good (except for small distances). For the case of the  $BB$  correlation the agreement is only of a qualitative nature in that the location of the various peaks is reproduced correctly by the theory. However, their height is not predicted accurately.

## 5 Summary

We have presented the results of a molecular dynamics computer simulation of a super-cooled binary Lennard-Jones mixture. By investigating the dynamics of this system, we have demonstrated that, in the temperature range considered, the idealized version of the mode-coupling theory of the glass transition gives a very good description of this dynamics. In particular we find that at low temperatures  $D$ , the diffusion constant of the particles, as well as  $\tau$ , the  $\alpha$ -relaxation times of the intermediate scattering function, shows a power-law behavior. In agreement with MCT, the critical temperature is independent of the quantity considered, but that, in contrast to the prediction of the theory, the critical exponent for  $D$  and  $\tau^{-1}$  are different. In accordance with the theory, the intermediate scattering func-

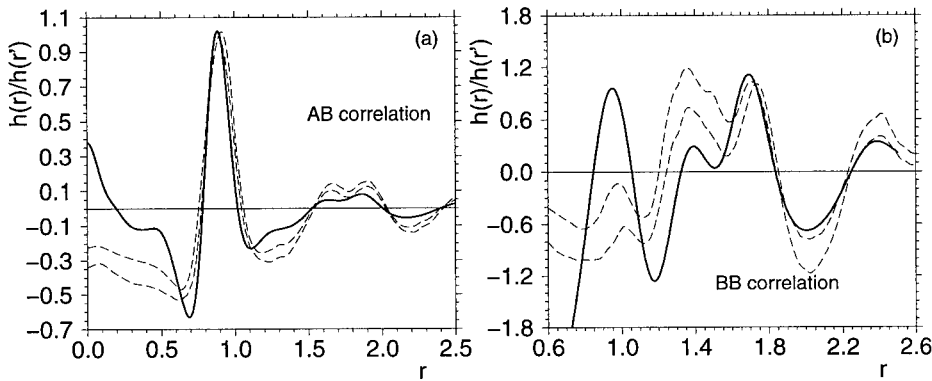


Figure 6:  $r$ -dependence of the critical amplitude  $h(r)$  for the  $AB$  (a) and  $BB$  (b) correlation. Thin dashed lines: upper and lower estimate from the simulation. Bold lines: prediction of the theory.

tion shows a two step relaxation behavior and obeys the time-temperature superposition principle. The *early* part of the  $\beta$ -relaxation regime does not seem to be described well by the  $\beta$ -correlator proposed by MCT, probably due to the strong influence of the microscopic dynamics. In contrast to this, the late  $\beta$ -relaxation regime can be fitted very well by the  $\beta$ -correlator and the exponent parameter determined from this fit is in agreement with the one expected from the critical exponent for the  $\alpha$ -relaxation time  $\tau$ .

Using the partial structure factors, as determined from the simulation, as input, we solved the MCT equation in the limit of long times. From these calculations we find that MCT overestimates the critical temperature by about a factor of 2. We argue, however, that this relatively large discrepancy between the critical temperatures is due to the fact that the thermodynamic state of the system is only a weak function of temperature. The prediction of MCT is significantly better for the exponent parameter and the wave-vector dependence of the nonergodicity parameters. For the latter we find that the prediction of MCT agrees with the results of the simulation to within a few percent for wave-vectors in the vicinity of the main peak in the structure factor. The theory is also able to give very good predictions for the space dependence of the critical amplitudes  $h(r)$ . Thus we conclude that for this Lennard-Jones system MCT is not only able to make *qualitative* correct predictions, but also *quantitative* correct predictions, and thus is a good theory to predict also the non-universal quantities of the dynamics of a supercooled simple liquid.

Acknowledgments: We thank M. Fuchs and W. Götze for many very helpful discussions. Part of this work was supported by the DFG under SFB 262/D1.



## References

- [\*] Electronic mail: kob@moses.physik.uni-mainz.de  
[http://www.cond-mat.physik.uni-mainz.de/~kob/home\\_kob.html](http://www.cond-mat.physik.uni-mainz.de/~kob/home_kob.html)
- [1] W. Götze, in *Liquids, Freezing and the Glass Transition* Eds.: J. P. Hansen, D. Levesque and J. Zinn-Justin, Les Houches. Session LI, 1989, (North-Holland, Amsterdam, 1991)i, p. 287; W. Götze and L. Sjögren, Rep. Prog. Phys. **55**, 241 (1992); R. Schilling, in *Disorder Effects on Relaxational Processes* Eds.: R. Richert and A. Blumen, (Springer, Berlin, 1994), p. 193; H. Z. Cummins, G. Li, W. M. Du, and J. Hernandez, Physica A **204**, 169 (1994); W. Kob, in *Experimental and Theoretical Approches to Supercooled Liquids: Advances and Novel Applications* Eds.: J. Fourkas, D. Kivelson, U. Mohanty and K. Nelson, (ACS, Washington, 1997).
- [2] Theme Issue on Relaxation Kinetics in Supercooled Liquids-Mode Coupling Theory and its Experimental Tests; Ed. S. Yip. Volume **24**, No. 6-8 (1995) of *Transport Theory and Statistical Physics*.
- [3] T. Franosch, M. Fuchs, W. Götze, M. R. Mayr, and A. P. Singh, (preprint 1996).
- [4] W. Kob and H. C. Andersen, Phys. Rev. Lett. **73**, 1376 (1994).
- [5] W. Kob and H. C. Andersen, Phys. Rev. E **51**, 4626 (1995).
- [6] J.-L. Barrat and A. Latz, J. Phys.: Condens. Matter **2**, 4289 (1990).
- [7] M. Fuchs, PhD Thesis, University of Munich, 1993.
- [8] M. Nauroth and W. Kob, Phys. Rev. E (in press); M. Nauroth, Diploma Thesis, University of Mainz 1995.
- [9] W. Kob and H. C. Andersen, Phys. Rev. E **52**, 4134 (1995).
- [10] T. Gleim, W. Kob and K. Binder, (unpublished).
- [11] B. Bernu, J.-P. Hansen, Y. Hiwatari and G. Pastore, Phys. Rev. A **36**, 4891 (1987).
- [12] J.-P. Hansen and I. R. McDonald, *Theory of Simple Liquids* (Academic, London, 1986).
- [13] P. N. Pusey and W. van Megen, Phys. Rev. Lett. **59**, 2083 (1987); W. van Megen, S. M. Underwood and P. N. Pusey, Phys. Rev. Lett. **67**, 1586 (1991); W. van Megen and S. M. Underwood, Phys. Rev. E **47**, 248 (1993); W. van Megen and S. M. Underwood, Phys. Rev. Lett. **70**, 2766 (1993); W. van Megen and S. M. Underwood, Phys. Rev. E **49**, 4206 (1994).
- [14] W. Götze and L. Sjögren, Phys. Rev. A **43**, 5442 (1991).

## FAST DYNAMICS IN GLASS FORMING SYSTEMS: VIBRATIONS VS RELAXATION

A.P.SOKOLOV

Max-Planck Institut für Polymerforschung, Ackermannweg 10, 55021 Mainz, Germany  
on leave from Institute of Automation & Electrometry Russ.Ac.Sci., 630090, Novosibirsk, Russia

### ABSTRACT

Two contributions specific for the spectra of the fast dynamics in glass forming systems, a broad quasielastic scattering and the boson peak, are analyzed. It is shown that the vibrational contribution (the boson peak) decreases strongly in fragile systems. Some speculations about dependence of the degree of fragility (a la Angell) on peculiarity of the spectrum of fast dynamics are presented. The existence of some intrinsic relation between the broad quasielastic contribution and the boson peak is demonstrated from analysis of the recent neutron and Raman scattering data. It is shown that this relation can be explained in framework of the model of damped oscillator. The model ascribes the quasielastic contribution to the scattering of light or neutrons on the vibrations around the boson peak, which are damped by some relaxation channel and have a quasielastic part in their response function. It is demonstrated that the model can explain many peculiar properties of the fast dynamics in the Raman, neutron and far-infrared absorption spectra.

### INTRODUCTION

It is well-known that the main difference between dynamic spectra of crystals and glasses (or other disordered systems) appears in the mesoscopic frequency range ( $\nu \sim 10$ -1000 GHz). Ordered crystals in this frequency range usually have acoustic vibrations with Debye-like density of states  $g(\nu) \propto \nu^2$  only. However, in all glass forming systems a strong deviations from the Debye-like behavior was found [1]: at very low frequencies ( $\nu < 100$  GHz) some anharmonic relaxation-like contribution dominates the spectrum and at higher frequencies an excess harmonic vibrational contribution shows up. The anharmonic contribution gives a linear term in specific heat  $C_p$  at temperatures below 1K and is usually ascribed to a motion in double-well potentials. The excess vibrational contribution appears as a bump in  $C_p/T^3$  at  $T \sim 5$ -10K and is usually ascribed to quasilocal vibrations. These both contributions show up also in neutron and Raman scattering spectra as a broad quasielastic contribution and as the so-called boson peak. The quasielastic contribution exists in glasses even at temperatures much below the glass transition temperature  $T_g$  and usually strongly increases with  $T$ . The vibrational contribution, the boson peak, in contrast has nearly harmonic temperature variations. It is evident that these two contributions are characteristic for disordered materials, however, their nature is still not clear.

A new interest in this problem was stimulated by recent investigations of the glass transition dynamics. The spectrum in the frequency range of interest ( $\sim 10$ -1000 GHz) was called the spectrum of the fast dynamics (because it is fast in comparison with the characteristic time scales of the primary  $\alpha$ -relaxation and of the slow Johari-Goldstein  $\beta$ -relaxation). Several results reveal that the excitations in this mesoscopic frequency range can play a crucial role in the dynamics of the glass transition [2-4]. In particular, it was found that the ratio between TLS and the excess vibrational contributions correlates with the degree of fragility of the system [3]. Fragility, which was first introduced by Angell [5], is a property of glass forming liquids at temperatures around

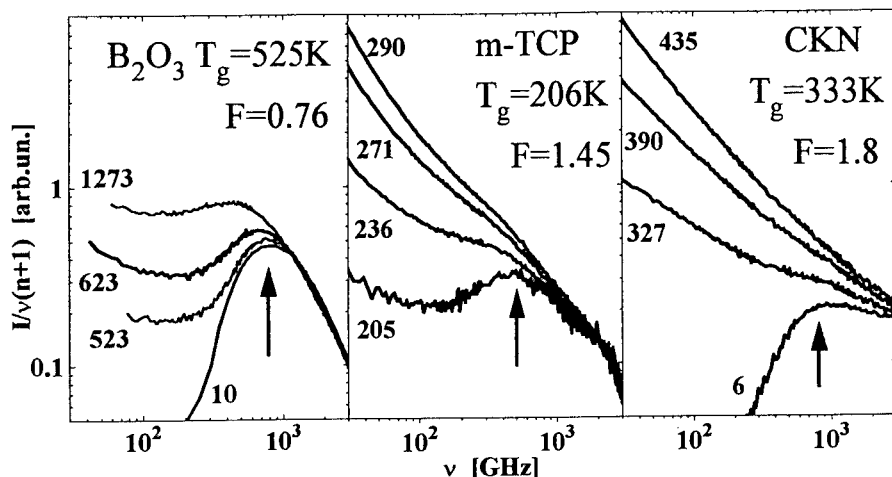


Fig.1 Low-frequency Raman spectra of different glass forming systems. Arrows show the boson peak,  $(n+1)=[1-\exp(-h\nu/kT)]^{-1}$  is a temperature Bose factor.

$T_g$ . Thus some correlation between the low-temperature anomalies and the properties of the supercooled melt was suggested [3].

The main goal of the present contribution is an analysis of the low-energy excitation spectra from the point of view of fragility of different glass forming systems. Also the mechanism of the quasielastic scattering in glasses will be discussed.

#### FAST DYNAMICS AND THE DEGREE OF FRAGILITY

It is known that the quasielastic intensity in neutron or Raman scattering increases strongly with temperature above  $T_g$ . In contrast, the vibrational contribution, the boson peak, varies only slightly with temperature, i.e. it shows nearly harmonic behavior. The ratio of these two contributions was found to be different for different systems. Fig.1 presents the Raman spectra of 3 different glass formers. One can see that the boson peak is well pronounced in the case of a rather strong glass former  $B_2O_3$  even up to extremely high temperature  $\sim 2.5T_g$ ; the boson peak is well pronounced around  $T_g$  and disappears at higher temperatures in the case of intermediate glass former m-tricresyl phosphate (m-TCP); the boson peak is not a distinct peak even at  $T_g$  in the case of extremely fragile system Ca-K- $NO_3$  (CKN). The similar tendency can be found also in the inelastic neutron scattering spectra. So, the ratio of these two contributions to the spectrum of the fast dynamics correlates with the degree of fragility  $F$  of the system ( $F=E_\eta(T_g)/T_g$  is defined as an apparent activation energy of viscous flow  $E_\eta$  at  $T_g$  divided by  $T_g$ ): harmonic vibrational contribution dominates the spectrum of strong systems up to very high temperatures whereas the anharmonic quasielastic contribution dominates the spectrum of fragile systems already at  $T_g$ . To characterize the ratio of these two contributions it was suggested [3] to use the ratio of the intensities at the minimum and at the maximum of the spectrum  $R_1=(I_n)_{\min}/(I_n)_{\max}$  (Fig. 1).

Fig.2a presents  $R_1(T_g)$  vs  $F$  for different glass formers and, indeed, shows a correlation between these two parameters. Analysis of the low-temperature anomalies in the specific heat data showed similar trend [3]: the ratio of the anharmonic TLS contribution (the linear term in

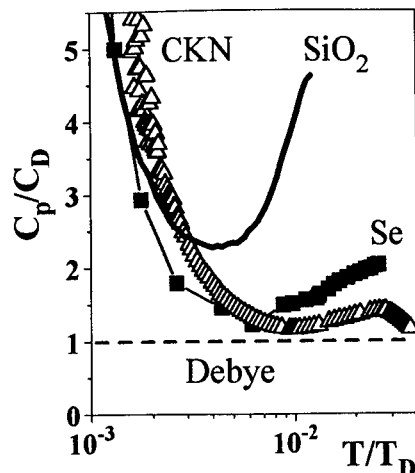
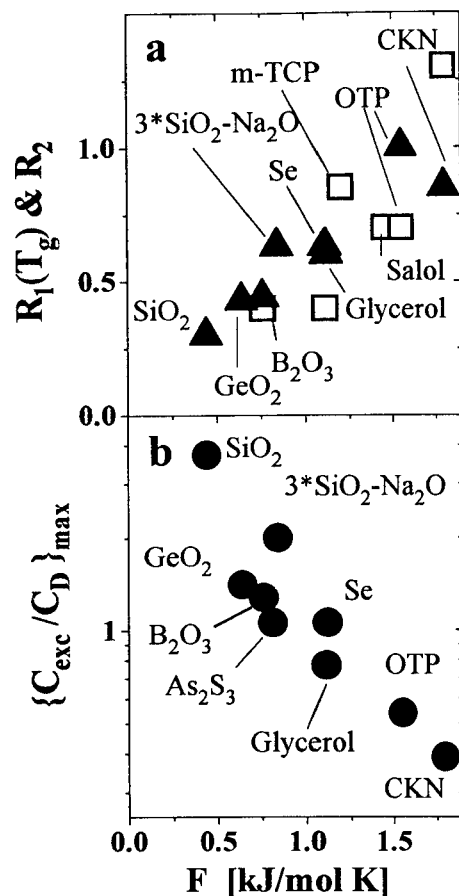


Fig.2 (a) The ratio of the anharmonic to harmonic contributions to the Raman spectra  $R_1$  ( $\square$ ) and to the specific heat  $R_2$  ( $\blacktriangle$ ) (data from [3]) and (b) the excess vibrational contribution for different glass formers vs degree of fragility.

Fig.3 Specific heat at low temperatures for extremely fragile CKN, intermediate Se and extremely strong glass former  $\text{SiO}_2$  (data from [6]). Both axes are scaled with the Debye values.

$C_p$ ) to the excess vibrational contribution (the bump in  $C_p/T^3$ )  $R_2$  (for definition see [3]) increases with the increase of fragility (Fig.2a). Fig.3 presents a comparison of the specific heat data for  $\text{SiO}_2$ , Se and CKN.  $C_p$  and temperature are scaled with the values expected in the Debye model. The linear term in this presentation appears to be rather similar in these systems (slightly higher in CKN), while the excess vibrational contribution differs significantly. Fig.2b presents the ratio of the excess vibrational contribution at the maximum to the Debye value  $C_{\text{exc}}/C_D = (C_p/C_D - 1)_{\text{max}}$  vs degree of fragility and shows a strong correlation between these two quantities.

A similar analysis of the linear term in the specific heat does not show clear correlations. Moreover, analysis of literature data shows that TLS contribution depends strongly on the sample preparation and may vary by more than one order of magnitude for substances having essentially the same chemical composition [6,7]. The excess vibrational contribution, in contrast, depends on the sample preparation only weakly, but varies strongly with chemical composition: it is large for strong glasses, smaller for intermediate systems and very small for the fragile ones (Figs.2,3).

Many authors relate the excess vibrational contribution to strong scattering of vibrations caused by fluctuations of elastic constants and/or density in disordered structures [8-11]. The

scattering leads to a drastic decrease of the mean free path of vibrations  $L(v)$  and, in particular, can increase the vibrational density of states  $g(v)$  in a certain frequency range where  $L(v)$  reaches the Ioffe-Regel criteria for localization [9,11]. According to this approach the amount of the excess vibrational contribution is related to the amplitude of the elastic constants fluctuations in disordered systems [6]: more homogeneous structure will have lower density of the excess vibrations. That suggests an explanation for the difference in  $g(v)$  between strong and fragile systems [6]: structural fluctuations (inhomogeneities) are large in strong systems and smaller in fragile ones. This suggestion seems to be reasonable if one compares microstructure of covalent (usually strong) systems with ionic or van der Waals (usually fragile) glasses: strong inhomogeneities are expected in a rigid 3-dimensional covalent structure while rather weak ones should exist in the structure where movable ions or molecules can easily smoothen any fluctuations. According to this suggestion quenching of the glass forming systems should increase the excess  $g(v)$  due to increase of the amplitude of structural fluctuations. In contrast, the excess  $g(v)$  should decrease under high pressure due to smoothening of structural fluctuations. Analysis of the literature data, indeed, supports these predictions: excess  $g(v)$  increases in quenched samples [12,13] and decreases under high pressure [14].

The results presented in Figs.2,3 show that the degree of anharmonicity of the fast dynamics spectrum (the ratio of the anharmonic contribution to the vibrational one) at very low temperatures and at  $T_g$  correlates with the degree of fragility of the system. This suggests that the behavior of the structural  $\alpha$ -relaxation around  $T_g$  can be related to peculiarities of the fast dynamics spectrum. This relation is astonishing because around  $T_g$  the time scale of the  $\alpha$ -relaxation  $\tau_\alpha$  is separated from the fast dynamics by more than 10 orders of magnitude. However, until now there is no clear explanation how the fast dynamics, its anharmonicity, can influence the dynamics on a macroscopic time scale.

Recently Buchenau and Zorn [2] suggested a relation between viscosity  $\eta$  and a local mean-squared displacement of atoms  $\langle u^2 \rangle_{loc}$ :  $\log(\eta) \propto 1/\langle u^2 \rangle_{loc}$ . Although a ground for the suggested relation is not clear, a reasonable qualitative agreement has been demonstrated for the case of Se [2]. Let us follow this suggestion and analyze a difference of  $\langle u^2 \rangle_{loc}$  between strong and fragile systems. In strong systems  $\langle u^2 \rangle_{loc}$  is dominated by the vibrational contribution. The latter has rather harmonic temperature variation which gives  $\langle u^2 \rangle_{loc} \propto kT$ . As a result the viscosity will show an Arrhenius temperature variations. In fragile systems the anharmonic contribution dominates  $\langle u^2 \rangle_{loc}$  and the latter varies stronger than  $kT$ . As a result the viscosity shows non-Arrhenius temperature variation and deviations from Arrhenius behavior will be large in systems with higher anharmonic contribution. So, in that way one can explain the found correlation between the degree of fragility and anharmonicity of the fast dynamic spectrum.

## QUASIELASTIC SCATTERING AND ITS RELATION WITH THE BOSON PEAK

### Experimental evidences for the relation between the two contributions

The anharmonic contribution which appears in the neutron and light scattering spectra as a broad quasielastic component is usually ascribed to direct scattering by relaxation modes (motion of atoms in double-well potentials, etc.). However, already in 1975 Winterling [15] proposed another mechanism for the quasielastic light scattering in glasses: it can be related to scattering of photons by vibrations around the boson peak which are damped by some relaxation channel, and the damped part of the vibrational response appears as the quasielastic contribution (similar with

the Mountain mode in traditional hydrodynamics [16]). Since that time this mechanism did not receive much attention.

Nevertheless, there are a few experimental evidences in favor of this mechanism. The first one is a depolarization ratio, which is defined as the ratio of the depolarized to polarized light scattering intensities. For the quasielastic scattering it varies from ~0.25 for ZBLAN glass [17] and ~0.3 for SiO<sub>2</sub> up to the maximum value ~0.75 in most of organic and ionic systems. But in all cases it was found to be the same as for the boson peak! The second evidence appears in the dynamic structure factor  $S(q,E)$  obtained in coherent neutron scattering experiments. The detailed analysis of  $S(q,E)$  in the region of the quasielastic scattering which has been done for SiO<sub>2</sub> [18] and recently for polybutadiene (PB) [19] reveals in all cases the same peculiar  $q$ -dependence as for the vibrations around the boson peak.

The third evidence comes from the recent comparison of the Raman and neutron scattering spectra. Fig.4a shows the comparison of the spectra of PB at a few temperatures below and above  $T_g$  (~180K). First of all the Raman spectra show that the quasielastic contribution is significant already at  $T=60K$ . The comparison of the spectra reveals their difference in the frequency range where the vibrational contribution dominates (at frequencies above the boson peak maximum, or at low temperatures). Traditionally the vibrational contribution to the Raman spectra is described using Shuker and Gammon equation [20]:

$$I_{ij}(\nu) = C_{ij}(\nu)g(\nu) [n(\nu)+1] / \nu \quad (1)$$

Here  $C_{ij}(\nu)$  is a light to the vibration coupling coefficient, indexes  $ij$  correspond to different polarizations of the scattered light. Assuming that the same vibrations contribute to the Raman and neutron scattering spectra one concludes that  $C_{ij}(\nu)$  is a frequency dependent function. Detailed analysis for different glass forming systems shows that  $C_{ij}(\nu)$  has rather linear frequency dependence. One can see that from the spectra of  $C_{ij}(\nu)$  at  $T=60K$  presented in Fig.4b. However, in the region where the quasielastic contribution dominates (low frequency and high temperatures) the both neutron and Raman spectra are similar (Fig.4a). One can introduce some kind of effective coupling coefficient for the quasielastic contribution  $C_{qes}(\nu)$  (similar with the definition eq.1) and it appears to be constant (Fig.4b). Especially important finding is that  $C_{qes}(\nu)=const \approx C_{ij}(\nu_{max})$ . Similar result has been found for other glass formers like SiO<sub>2</sub>, and polystyrene [21]. It shows that the broad quasielastic contribution appears in the Raman spectra with the intensity related to that one of the vibrations just around the frequency of the boson peak maximum.

#### The model and its qualitative predictions

All these evidences show that there is some intrinsic relation between the broad quasielastic contribution and the vibrations around the boson peak. This relation can be well explained in the framework of the approach suggested by Winterling [15] and further developed in a few recent papers [22-24]. The main assumption of this approach is that the elastic response function of the vibration with frequency  $\Omega$  can be written as:

$$D(\Omega, \omega) = \{ \omega^2 - \Omega^2 [1 - M(\omega, \Omega)] \}^{-1} \quad (2)$$

here  $M(\omega, \Omega)$  is a memory function which characterizes all damping processes and has real  $M'(\omega, \Omega)$  and imaginary  $M''(\omega, \Omega)$  parts. The eq.2 presents very general expression, which is also used in hydrodynamic and in mode-coupling approaches. It assumes that relaxation processes in

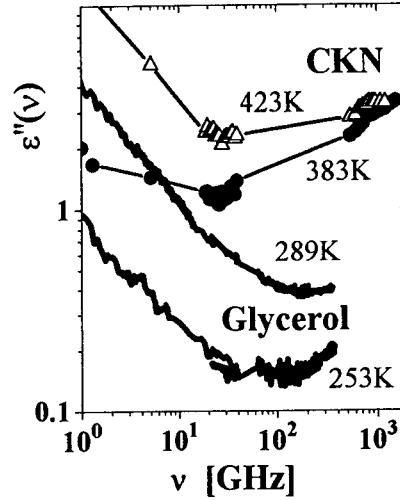
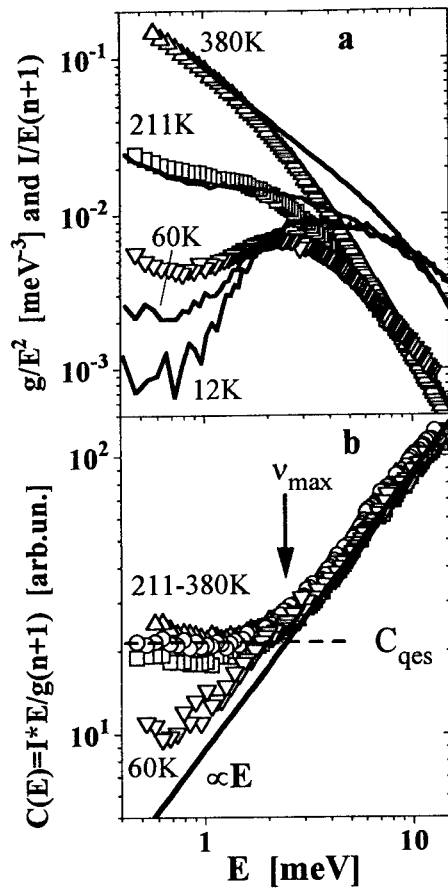


Fig.4 a Comparison of neutron (symbols) and Raman (lines) spectra of PB (data from [21]).

b Effective coupling coefficient estimated from the spectra.

Fig.5 High frequency dielectric data for CKN (from [25]) and for Glycerol (from [26]) around the minimum between the  $\alpha$ -relaxation and the spectrum of the fast dynamics.

the disordered media act as a random force upon the harmonic vibration and the latter perceives it as a viscous-like damping.

An important consequence of the assumption (eq.2) is that the susceptibility function  $\chi''(\omega, \Omega) \propto \text{Im}\{D(\omega, \Omega)\}$  of this vibrations has two parts: (i) inelastic at

$$\omega \sim \Omega [1 - M'(\omega, \Omega)]^{1/2} \quad (3a)$$

with the halfwidth:

$$\Gamma \approx \Omega M''(\Omega, \Omega)/2 \quad (3b)$$

and (ii) a quasielastic "relaxation-like" contribution at lower frequencies. The latter is similar with the Mountain mode in hydrodynamic approach for the Brillouin scattering [16]. In the case of a weak damping  $|M(\Omega, \Omega)| \ll 1$  the "relaxation-like" contribution of the mode at frequencies  $\omega \ll \Omega$  will be presented:

$$\chi_{\text{rel}}''(\omega, \Omega) \propto M''(\omega, \Omega) / \Omega^2 \quad (4)$$

If there are many vibrations then the resulting spectrum will be a sum over all vibrational contributions.

Our main assumption is that the formalism of the model can be applied to the vibrations in the frequency range around the boson peak and that all vibrations at this frequency range are damped in a similar way (eq.2). In this case one can write for the dynamic structure factor  $S(q, \omega)$  in the neutron scattering:

$$S(q, \omega)/n(\omega) = \int d\Omega \chi_p''(\omega, \Omega) g(q, \Omega) \approx \int d\Omega \text{Im}\{D(\omega, \Omega)\} g(q, \Omega) \quad (5a)$$

for the light scattering intensity:

$$I_{ij}(\omega)/(n(\omega)+1) = \int d\Omega \chi_{ij}''(\omega, \Omega) g(\Omega) \approx \int d\Omega C_{ij}(\Omega) \text{Im}\{D(\omega, \Omega)\} g(\Omega) \quad (5b)$$

and for the dielectric  $\epsilon''(\omega)$ :

$$\epsilon''(\omega) = \int d\Omega \chi_{ir}''(\omega, \Omega) g(\Omega) \approx \int d\Omega K_{ir}(\Omega) \text{Im}\{D(\omega, \Omega)\} g(\Omega) \quad (5c)$$

here  $g(q, \Omega)$  is a density of the vibrational states,  $q$  is a wave vector which is skipped for the light scattering and  $\epsilon''(\omega)$ , because in the frequency range of interest they do not show any  $q$ -dependence;  $\chi_p''$ ,  $\chi_{ij}''$  and  $\chi_{ir}''$  are susceptibility functions correspondingly for the density fluctuations, polarisability and  $\epsilon''$  caused by the vibrational mode,  $K_{ir}(\Omega)$  is the infrared photon to the vibration coupling coefficient.

According to this formalism the inelastic vibrational contribution (the boson peak) may have a different shape in the neutron, Raman and far-infrared (FIR) absorption spectra, depending on the coupling coefficients  $C_{ij}(\Omega)$  and  $K_{ir}(\Omega)$ . In particular, at very low temperatures where the damping processes are negligible and  $D(\omega, \Omega)$  is essentially a delta function one will have traditional expressions for the vibrational contribution:

$$\chi_{vp}(q, \omega) = [S(q, \omega)/n(\omega)]_{T \rightarrow 0} \approx g(q, \omega)/\omega \quad (6a)$$

$$\chi_{vij}(\omega) = [I_{ij}(\omega)/(n(\omega)+1)]_{T \rightarrow 0} \approx C_{ij}(\omega) g(\omega)/\omega \quad (6b)$$

$$\epsilon_v''(\omega) = [\epsilon''(\omega)]_{T \rightarrow 0} \approx K_{ir}(\omega) g(\omega)/\omega \quad (6c)$$

So, the comparison of the spectra at low temperatures can reveal the frequency dependence of the coupling coefficients  $C_{ij}(\omega)$  and  $K_{ir}(\omega)$ . As it was shown above (Fig.4) this comparison for the light and neutron scattering spectra shows nearly linear frequency dependence for  $C_{ij}(\omega)$  in many glasses. There are no clear data about  $K_{ir}(\omega)$ , but a similarity of the FIR and the Raman spectra [12] suggests that  $K_{ir}(\omega)$  should have a frequency dependence similar with that one of  $C_{ij}(\omega)$ .

In order to do the next step one should specify the memory function. One of the way is suggested in mode-coupling approach. This way, however, needs a knowledge of the static structure factor, interatomic potential and based on a solution of very complicated equations [27]. Another way, usually used in hydrodynamic approach, is a modeling of the memory function. In our evaluation we will follow this way. An important question is dependence of  $M(\omega, \Omega)$  on  $\Omega$ . In the hydrodynamic approach  $M(\omega, \Omega)$  is essentially independent on  $\Omega$ , i.e.  $M(\omega, \Omega) \equiv M(\omega)$ . It appears in hydrodynamic as a long-wavelength limit  $V/\Omega \gg r_a$ , here  $V$  is a sound velocity and  $r_a$  is an interatomic (intermolecular) distance. In the frequency range around the boson peak the value  $V/\Omega$  is still significantly large than  $r_a$  and we assume that the hydrodynamic approach for  $M(\omega, \Omega)$  still can be applied. There are some experimental results supporting this assumption: the sound-like behavior expected in the hydrodynamic limit,  $\Omega \approx Vq$  and  $\Gamma \propto \Omega^2$ , has been found up to



~400GHz for LA modes in SiO<sub>2</sub> and some other glasses [28]; the recent measurements of inelastic X-ray scattering also demonstrated the same behavior for LA mode in SiO<sub>2</sub>, glycerol and LiCl-water solution even at frequencies above the boson peak [29]. So, this assumption looks reasonable although still needs a theoretical justification.

Now one can make some qualitative predictions. Let's analyze the "relaxation-like" contribution in the case of a weak damping  $|M(\Omega)| \ll 1$ . Then, using eqs.(4,5) one gets:

$$S_{rel}(q, \omega)/n(\omega) \propto M''(\omega) \int d\Omega g(q, \Omega) / \Omega^2 \quad (7a)$$

$$I_{rel}(\omega)/(n(\omega)+1) \propto M''(\omega) \int d\Omega C_{ij}(\Omega) g(\Omega) / \Omega^2 \quad (7b)$$

$$\varepsilon''(\omega) \propto M''(\omega) \int d\Omega K_{ij}(\Omega) g(\Omega) / \Omega^2 \quad (7c)$$

It shows that the quasielastic "relaxation-like" contribution should have the same shape in neutron, light and FIR-absorption spectra, although the vibrational contribution itself can be different due to the frequency dependence of  $C_{ij}(\Omega)$  and  $K_{ij}(\Omega)$ . The similarity of the broad quasielastic component in neutron and light scattering spectra is demonstrated in Fig.4 for PB and has been recently demonstrated for some other glass formers [21]. Eqs.7 give a few other qualitative predictions for the "relaxation-like" contribution:

- (i) The q-dependence of this contribution in the neutron scattering spectra should be related to the q-dependence of the vibrations averaged over  $g(q, \Omega)/\Omega^2$  (eq.7a);
- (ii) The depolarization ratio of the quasielastic contribution in the light scattering spectra should be equal to the depolarization ratio of the vibrational contribution averaged over  $g(\Omega)/\Omega^2$  (eq.7b);
- (iii) The intensity of this contribution should be related to that one of the vibrations weighted with  $g(\Omega)/\Omega^2$ .

$g(\Omega)/\Omega^2$  in all glasses has a maximum, the boson peak. Thus one would expect that the integration over all vibrations will give the averaged value close to the value at the frequency of the boson peak maximum  $\omega \approx \omega_{max}$ . So, the model explains (i) why the q-dependence of the quasielastic neutron scattering has the same peculiarities as the vibrations around the boson peak, (ii) why the quasielastic light scattering has the same depolarization ratio as the vibrations around the boson peak maximum and (iii) why the quasielastic intensity related to that one of the boson peak (Fig.4 and [21,23]). The latter can be expressed using eqs.7:

$$C_{qes}(\omega) = I_{rel}(\omega)/S_{rel}(q, \omega) \approx \int d\Omega C_{ij}(\Omega) g(\Omega)/\Omega^2 / \int d\Omega g(\Omega)/\Omega^2 \approx C_{ij}(\Omega_{max}) \quad (8)$$

So, the qualitative predictions (eqs.7) are in a good agreement with the recent neutron and light scattering results mentioned in a previous section and explain peculiarities of the broad quasielastic scattering spectra and similarity of its properties with the vibrational properties. We would like to stress at that point that the presented discussion is related to the broad quasielastic contribution but not to the  $\alpha$ -relaxation where many other contributions can be significant.

The qualitative predictions (eqs.7) give also an interesting suggestion for explanation of some peculiarities in  $\varepsilon''(\omega)$ . It was found that the spectrum of  $\varepsilon''(\omega)$  differs from the light (and/or neutron) scattering spectra around susceptibility minimum between the  $\alpha$ -relaxation and the fast dynamics contributions. Last decade an interest to analysis of the minimum was strongly stimulated by achievements of the mode-coupling theory of the glass transition [27], which gave certain predictions for the spectral shape of the minimum and its temperature variations. This

minimum was found to be rather similar in the light and neutron scattering spectra of different glass formers. However, in the case of the  $\epsilon''(\omega)$  the minimum was not found at the same frequency range: in the case of glycerol it was found at much higher frequencies [26] (Fig.5) and it was not found until now in salol. The known exceptions are molten salts, in particular, CKN where the minimum was found at the same frequency range as in the light (and/or neutron) scattering spectra [30].

It is evident that the position of the minimum depends on the intensity of the fast dynamics relative to that one of the  $\alpha$ -relaxation: the lower is the intensity of the fast dynamics spectrum the higher will be the frequency of the minimum. According to the suggested model the amplitude of the fast dynamics spectrum is related to the amplitude of the vibrational contribution around the boson peak maximum. For  $\epsilon''(\omega)$  the latter depends on modulation of dipole moment by the vibrations (eq.7c). In the case of neutral molecules like salol or glycerol this modulation is rather weak and the amplitude of the fast dynamics spectrum in  $\epsilon''(\omega)$  should be small. However, in the case of ionic systems like CKN the vibrations of charged particles will modulate strongly the dipole moment and should give a significant contribution to  $\epsilon''(\omega)$ . This suggestion is supported by analysis of FIR absorption data for different glass formers. It was shown in [31] that the infrared photon to the vibration coupling coefficient  $K_{ir}(\Omega)$  varies  $\sim 1000$  times depending on the chemical composition of the glass: it is strongest for ionic and semiconducting glasses and very weak for neutral systems like  $\text{SiO}_2$  and polystyrol. Thus one can assume that in salol and glycerol the boson peak and, as a consequence, the whole spectrum of the fast dynamics appears in  $\epsilon''(\omega)$  with the amplitude much weaker than that one of the  $\alpha$ -relaxation (see the example of glycerol in Fig.5). As a result the minimum shifts to higher frequency. And only in ionic systems like CKN due to the vibrations of charged particles the spectrum of the fast dynamics has relatively high amplitude in  $\epsilon''(\omega)$  (Fig.5) and the minimum appears in the same frequency range as in the light (and/or neutron) scattering spectra.

#### Quantitative analysis of the light and neutron scattering spectra of PB

In that section we will analyze neutron and Raman spectra of PB in framework of the suggested model (in more details it will be described elsewhere [32]). The qualitative analysis presented above has been done in an assumption of a weak damping  $|M(\Omega)| \ll 1$ . For a quantitative analysis, however, one should use full expressions. Using eqs.2,5 and assuming that all vibrations up to some frequency  $\Omega_{lim}$  are damped in a similar way one can write for the dynamic structure factor:

$$\frac{S(q, \omega)}{n(\omega)} = M''(\omega) \cdot \int_0^{\Omega_{lim}} \frac{d\Omega \chi_{vp}(q, \Omega)}{\Omega \{ [\omega^2 / \Omega^2 - 1 + M'(\omega)]^2 + [M''(\omega)]^2 \}} \quad (9a)$$

and for the light scattering intensity:

$$\frac{I_{ij}(\omega)}{n(\omega) + 1} = M''(\omega) \cdot \int_0^{\Omega_{lim}} \frac{d\Omega \chi_{vij}(\Omega)}{\Omega \{ [\omega^2 / \Omega^2 - 1 + M'(\omega)]^2 + [M''(\omega)]^2 \}} \quad (9b)$$

Here,  $\chi_{vp}(q, \omega)$  and  $\chi_{vij}(\omega)$  are the vibrational spectrum at low temperatures as defined in eqs.6. In order to calculate the spectra one should know the frequency dependence of the memory function. For simplicity we will assume a single Debye relaxation, and the memory function will have the form:

$$M(\omega) = \delta^2 / (1 + \omega^2 \tau^2) \quad \text{and} \quad M''(\omega) = \delta^2 \omega \tau / (1 + \omega^2 \tau^2) \quad (10)$$

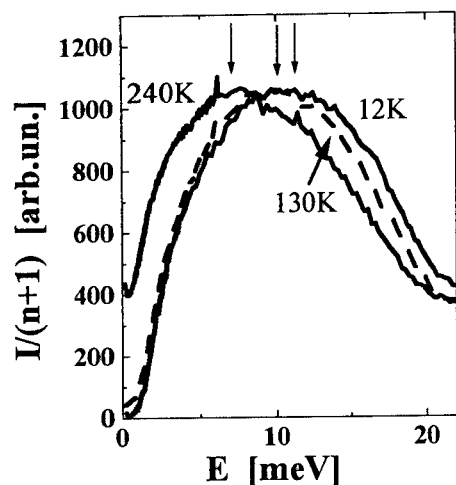


Fig.6 The Raman susceptibility of PB. The arrows show the position of the maximum  $\Omega_{\text{end}}(T)$ .

(Fig.7). Moreover, one can estimate the quasi-harmonic softening  $\Omega(T)$  from the shift of the end of the acoustic branch  $\Omega_{\text{end}}$  with temperature (Fig.6). Analysis shows (Fig.7a) that  $\Omega(T)$  follows well to the temperature variations of  $\Omega_{\text{end}}(T)$  determined from the Raman susceptibility spectrum. One also can compare the full shift of the vibration frequency  $\Omega_{\text{vib}}(T) = \Omega(T) * [1 - \delta^2]^{-0.5}$  (eqs.3a, 10) with the shift of the Brillouin line. The comparison is presented in Fig.8b and shows a good agreement between the results of the fit and the Brillouin data.

In order to analyze now the  $q$ -dependence in the coherent neutron scattering spectra of PB we use in eq.9a the spectrum of the sound-like contribution at  $T=60\text{K}$  as  $\chi_{\text{vp}}(q, \omega)$  and calculate its evolution with temperature using parameters obtained from the fit of the total neutron scattering spectra (Fig.8). The predicted spectral shape of the sound-like contribution for a few temperatures is presented in Fig.7 and shows a good qualitative agreement with the experimental data.

Thus it is demonstrated that the suggested model can describe consistently the data of the Raman, coherent and incoherent neutron scattering data. The results of the fit is found to be in agreement with the Brillouin line shift. More detailed comparison with acoustic attenuation data in framework of the model has been done in [33] for  $\text{SiO}_2$  and polystyrene. In that case, following to the traditional approach used for analysis of the acoustic data, a distribution of the relaxation times has been assumed instead of eq.10. The analysis showed a good agreement with acoustic data for  $\Omega(T)$  and  $\delta^2$  on both qualitative and quantitative levels [33].

## CONCLUSIONS

The presented analysis of the fast dynamics spectra of glasses shows that the density of the excess vibrational contribution (the boson peak) decreases with increase of the fragility of the system. It is suggested to relate the decrease to the decrease of the amplitude of structural fluctuations. Some ideas about possible relation of the anharmonicity of the fast dynamics and the

Here  $\delta^2$  is a vibration-relaxation coupling (or relaxation strength) and  $\tau$  is the relaxation time. Using the eqs.9,10 we did a fit of the experimental neutron and Raman spectra. The Raman spectrum at  $T=12\text{K}$  was used as the vibrational  $\chi_{\text{vj}}(\omega)$  in eq.9b, and the total neutron spectrum at  $T=60\text{K}$  was used as the vibrational  $\chi_{\text{vp}}(q, \omega)$  in eq.9a.  $\Omega_{\text{lim}}=10\text{ meV}$  was chosen as the end of the acoustic branch (Fig.6). Free fit parameters were  $\delta(T)$ ,  $\tau(T)$  and  $\Omega(T)$ . The latter is the quasi-harmonic softening which takes into account changes of the whole vibrational spectrum  $\chi_{\text{v}}\{\Omega(T)/\Omega(0)\}$  with temperature. A reasonable agreement with the experimental spectra have been obtained with  $\tau(T)$  rather temperature independent ( $\sim 0.2\text{ meV}^{-1}$  for both neutron and Raman spectra) and  $\delta(T)$  and  $\Omega(T)$  presented in Fig.7

Important result is that the fit parameters obtained from analysis of neutron and Raman spectra show a good quantitative agreement

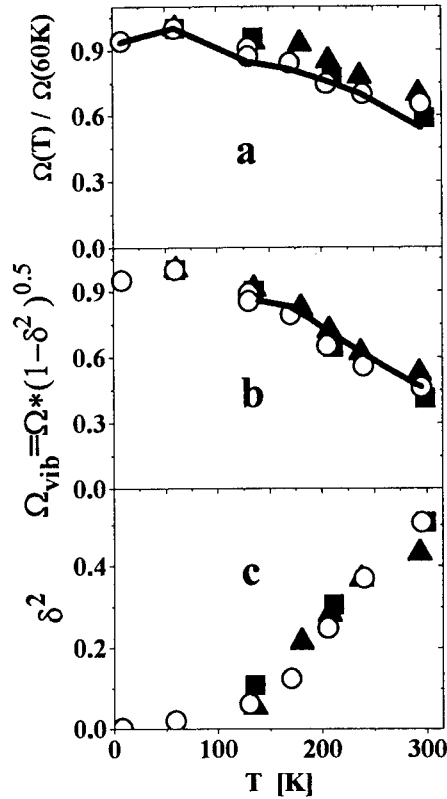


Fig.7 Parameters of the fit for the Raman (o) incoherent (■) and coherent (▲) neutron scattering spectra of PB. Line in (a) shows  $\Omega_{\text{end}}(T)$ ; in (b) the shift of the Brillouin LA mode.

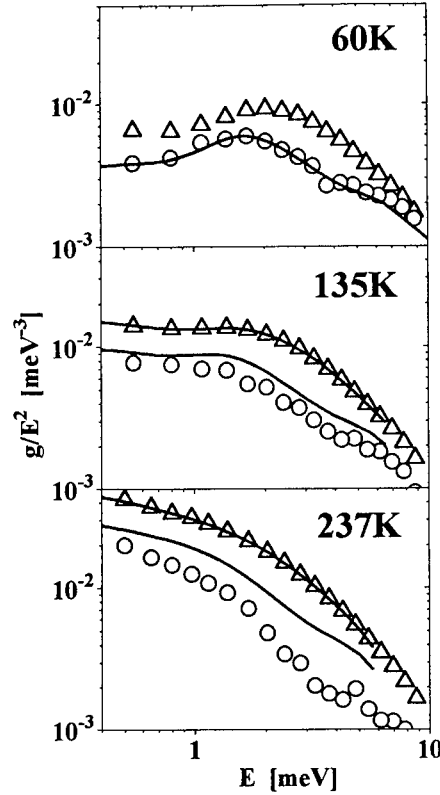


Fig.8 Coherent neutron scattering spectra of PB (▲), (o) shows the sound-like contribution (data from [19]). The lines show the results of the fit for the total spectrum and predictions for the sound-like contribution.

degree of fragility are discussed. It is shown that there is some intrinsic relation between the anharmonic contribution and the boson peak. It can be explained in the framework of the model of damped oscillator. The main suggestion of the model is that the broad quasielastic contribution appears not due to direct scattering of the light or neutrons on relaxators but due to scattering on the vibrations around the boson peak damped by some relaxation channel. It explains the similarity of the properties of the quasielastic contribution with the properties of the boson peak and gives consistent description of the Raman, neutron and Brillouin scattering data.

#### ACKNOWLEDGMENTS

Author is grateful to V.N.Novikov, D.Quitmann and U.Buchenau for many helpful discussions and to Max-Planck Gesellschaft for financial support. Partial financial support by INTAS (No. INTAS-93-2185) and EC HCM-Network (No.CHRX-CT92-0009) is gratefully acknowledged.

## REFERENCES

1. Amorphous Solids: Low-Temperature Properties, Ed. Phillips W.A., Springer-Verlag, Berlin, 1981.
2. U.Buchenau, R.Zorn, Europhys.Lett. **18**, 523(1992).
3. A.P.Sokolov, E.Rössler, A.Kisliuk, D.Quitmann Phys.Rev.Lett. **71**,2062(1993).
4. V.N.Novikov, E.Rössler, V.K.Malinovsky, N.V.Surovtsev, Europhys.Lett. **35**, 289(1996).
5. C.A.Angell in Relaxation in Complex Systems, eds.K.L.Ngai and G.B.Wright, Office Naval Res., Washington 1984, p.3.
6. A.P.Sokolov, R.Calemczuk, B.Salce, et al. Phys.Rev.Lett. (submitted).
7. R.B.Stephens, Phys.Rev.B **8**, 2896(1973) and Phys.Rev.B **13**, 852(1976).
8. S.R.Elliott, Europhys.Lett. **19**, 201(1992).
9. W.Schirmacher, M.Wagener, Sol.St.Comm. **86**, 597(1993).
10. M.Foret, E.Courtens, R.Vacher, J.-B.Suck, Phys.Rev.Lett. **77**, 3831(1996).
11. G.Polatsek, et al. Phys.Rev.B **39**, 9353(1989).
12. N.Ahmad, K.W.Hutt, W.A.Phillips, J.Phys.C:Sol.State **19**, 3765(1986).
13. S.L.Isakov, et al., Sol.St.Comm. **86**, 123(1993).
14. T.Arai, H.Kataura, H.Yasouka, S.Onari, J.Non-Cryst.Sol. **77&78**, 1149(1985).
15. G.Winterling, Phys.Rev.B **12**, 2432(1975).
16. J.P.Boon and S.Yip, Molecular Hydrodynamics (McGraW-Hill, New York, 1980).
17. J.Schroeder, et al., J.Non-Cryst.Sol. **161**, 173(1993).
18. U.Buchenau, et al., Phys.Rev.Lett. **60**, 1318(1988).
19. U.Buchenau, A.Wischnewski, D.Richter, B.Frick Phys.Rev.Lett. **77**, 4035(1996).
20. R.Shuker, R.W.Gammon, Phys.Rev.Lett. **25**, 222(1970).
21. A.P.Sokolov, et al. Phys.Rev.B **52**, R9815(1995).
22. V.Z.Gochiyaev, et al., Phil.Mag.B **63**, 777(1991).
23. A.P.Sokolov Phys.B **219&220**, 251(1996).
24. S.Kojima, V.N.Novikov Phys.Rev.B **54**, 222(1996).
25. K.L.Ngai, et al. in Non-equilibrium phenomena in supercooled fluids, glasses and amorphous materials, ed.M.Giordano, D.Leporini, M.P.Tosi, World Scientific, Singapore, 1996, pp.3-21.
26. P.Lunkenheimer, et al. Phys.Rev.Lett. **77**, 318(1996).
27. W.Götze, L.Sjögren Rep.Progr.Phys. **55**, 241(1992).
28. T.C.Zhu, et al. Phys.Rev.B **44**, 4281(1991) and C.J.Morath, et al. Phys.B **219&220**, (1996).
29. C.Masciovecchio, et al. Phys.Rev.Lett. **76**, 3356(1996) and P.Benassi, et al., ibid., **77**, 3835(1996).
30. A.Pimenov, et al. Phys.Rev.E **54**, 676(1996).
31. U.Strom, et al. Sol.St.Comm. **15**, 1871(1974).
32. A.P.Sokolov, V.N.Novikov, B.Strube (to be submitted).
33. A.P.Sokolov, V.N.Novikov, B.Strube Europhys.Lett. (submitted).

## FAST DYNAMICS IN GLASS-FORMERS: RELATION TO FRAGILITY AND THE KOHLRAUSCH EXPONENT

K.L. NGAI and C.M. ROLAND

Naval Research Laboratory, Washington, DC 20375-5320 USA, ngai@estd.nrl.navy.mil

### ABSTRACT

From the Raman spectra and related inferences from low temperature specific heat data, Sokolov and coworkers have established that the ratio of the quasielastic and vibrational contributions at low temperatures (5–10K) up to  $T_g$  correlates well with the degree of fragility and  $\beta$  of the glass-former. As pointed out by Sokolov (see his contribution in this Volume) such a correlation between the fast dynamics and structural  $\alpha$ -relaxation at  $T_g$  (i.e.,  $m$  and  $\beta$ ) is intriguing, since at and below  $T_g$ , the  $\alpha$ -relaxation time  $\tau_\alpha$  is more than twelve orders of magnitude longer than the quasielastic contribution and the boson peak. We show in this paper how the Coupling Model (CM) may provide an explanation for this correlation.

### INTRODUCTION

In the past, studies of the relaxational properties of glass-forming materials were mainly confined to the macroscopic time regime (ca.  $\gg 1$  nanosecond). Within the past several years, quasielastic neutron scattering (QENS), dynamic light scattering, and high frequency conductivity (dielectric) measurements have increased our knowledge concerning dynamics in the “mesoscopic” frequency range,  $\nu \sim 10$  to 1000 GHz [1-8]. In this frequency range, all glass-forming materials exhibit marked deviations from the acoustic vibrations, with Debye-like density of states (i.e.,  $g(\nu) \propto \nu^2$ ), found in crystalline solids. An excess harmonic vibrational contribution appears at higher frequencies, along with a broad, anharmonic “relaxational” contribution at lower frequencies. The vibrational contribution dominates the spectrum at low temperatures, appearing as a peak, commonly referred to as the boson peak. After scaling the low frequency Raman spectra by the Bose factor, the vibrational contribution is found to vary only slightly with temperature, indicating nearly harmonic vibrations. Although the boson peak is generally ascribed to some quasilocal vibrations, its exact physical origin is unclear. The anharmonic, broad contribution, which we will refer to as the *quasielastic* contribution, appears in glasses even at temperatures well below the glass transition temperature  $T_g$ ; it increases rapidly with temperature above  $T_g$ . The intensity of the quasielastic contribution relative to the boson peak differs for different glass-formers. It was found [1-3] that the relative contribution from quasielastic scattering is weak for “strong” glasses, like  $B_2O_3$ , even up to temperatures as high as 2.5 times  $T_g$ . On the other hand, the relative contribution from quasielastic scattering is strong for “fragile” glasses, such as  $0.40KNO_3-0.60Ca(NO_3)_2$ , even at  $T_g$ . The relative intensity of the quasielastic contribution at  $T_g$  correlates well with the fragility,  $m$ , defined as [1-3,9,10]

$$m \equiv \partial \log \tau_\alpha / \partial (T_g / T), \quad (1)$$

where  $\tau_\alpha$  is the structural  $\alpha$ -relaxation time, and  $T_g$  is defined as the temperature at which  $\tau_\alpha$  attains a value of  $10^2$  s. It has been shown [9] that  $m$  correlates strongly with the magnitude of the stretch exponent  $\beta$  of the Kohlrausch function

$$C(t) = \exp(-t / \tau_\alpha)^\beta, \quad (2)$$

describing the structural relaxation of glass-formers at macroscopic times (i.e. at temperatures near  $T_g$ ). Accordingly, a parallel observation is that the relative intensity of the quasielastic contribution must also correlate with  $\beta$ . The latter correlation was demonstrated explicitly from Raman scattering data of polymers [11]. As an aside, we point out that Sokolov [4] discusses the quasielastic contribution *relative* to the vibration contribution, which should not be confused with the absolute intensity of the boson peak. It is well-known that the latter is weaker for more fragile glasses.

From the Raman spectra and related considerations drawn from low temperature (5~10K) specific heat data, Sokolov and coworkers [1-4] established that the ratio of the quasielastic to vibrational contributions of a glass-former at low temperatures up to  $T_g$  correlates well with the degree of fragility, as well as  $\beta$ . As pointed out by Sokolov [4], this correlation between the fast dynamics spectrum and characteristics of the structural  $\alpha$ -relaxation at  $T_g$  (i.e.,  $m$  and  $\beta$ ) is intriguing, because at and below  $T_g$ , the  $\alpha$ -relaxation time  $\tau_\alpha$  is more than twelve orders of magnitude longer than the quasielastic contribution and the boson peak. The interesting situation of a correlation of the fast dynamics spectrum with macroscopic dynamics occurring at a disparate time scale requires explanation. The objective of this paper is to show the manner in which the CM [12-16] may account for this phenomenon.

#### ANHARMONICITY AND THE COUPLING MODEL OF RELAXATION

The coupling model [12-17] was introduced a long time ago and applied to the diffusion or relaxation dynamics of systems with anharmonic interactions, including glass-forming materials. The first development [12] was based on the Gaussian Orthogonal Ensemble [18-20] level-spacings-distribution, which turns out to be the result of semiclassical quantization of hamiltonian systems with nonlinear (anharmonic) interactions [18-20]. Recently a theoretical basis of the CM has been found in nonlinear dynamics (chaos) of classical Hamiltonians with nonlinear (anharmonic) interactions [21]. Although development of a rigorous theory remains to be done, several simple but solvable models found by our group [14-16] and by others [22] support the basic results of the CM. These results are as follows. There exists a temperature insensitive cross-over time,  $t_c$ , before which units relax independently with a correlation function

$$\phi(t) = \exp(-\frac{t}{\tau_\alpha}) \quad \text{for } t < t_c \quad (3)$$

and after ( $t > t_c$ ) the relaxation is described by a slowed-down nonexponential correlation function,  $\phi_{\text{slow}}$ . The time dependence of  $\phi_{\text{slow}}$  depends on the relaxation process. A particularly convenient function, compatible with simple models [14-16], computer simulations, and experimental data for coupled systems is

$$\phi_{\text{slow}}(t) = \exp[-(t / \tau^*)^{1-n}] \quad \text{for } t > t_c \quad (4)$$

where  $n$  is called the coupling parameter, whose value lies within the range  $0 \leq n < 1$ , increasing with interaction. Actually the crossover is never sharp at a point in time  $t_c$  as stated here. This practice is for the sake of convenience only. Obviously Eq.4 is the same as Eq.1 with the identification  $\beta \equiv 1-n$ . For motion of molecules [23-25] and ions in ionic glasses [26-28], such a cross-over has been deduced by various experimental techniques as occurring at  $t_c \approx O(2 \text{ ps})$ . Colloidal particles with large radii ( $\sim 10^2$

nm) have weaker interaction, and exhibit a broad crossover onset at a much longer  $t_c \approx 10^{-3}$  s [29]. Continuity of the two pieces of the correlation function at  $t=t_c$  leads to the important relation

$$\tau^* = [t_c^{-n} \tau_0]^{1/(1-n)} \quad (5)$$

linking the effective relaxation time,  $\tau^*$ , (i.e. after cooperative dynamical constraints are manifest) with the independent relaxation time,  $\tau_0$  (prior to interaction among the relaxing units).

It has been shown from simple models [14-16] that the coupling parameter  $n$  increases monotonically with the strength of the nonlinear (anharmonic) interaction. In the absence of anharmonic interaction, the relaxation is a simple exponential function of time. When anharmonic interaction is present, the relaxation is still a simple exponential, but only up to a time equal to  $t_c$ , after which it may assume the form of a stretched exponential. The nonexponentiality parameter  $n$ , as well as the effective relaxation time  $\tau^*$ , both increase with increasing anharmonic interaction (Eqs. 2-4). Tsironis and Aubry [22] found similar results in their study of energy relaxation of a lattice. When anharmonicity is introduced through the hard  $\phi^4$  potential,  $V(u_i) = u_i^2/2 + u_i^4/4$ , where  $u_i$  is the displacement at site  $i$ , the relaxation at short times is still exponential [30], but crosses over to slower nonexponential at longer time. The relaxation is increasingly slowed and more nonexponential at higher temperatures because the anharmonicity of the hard  $\phi^4$  potential becomes more important at higher temperatures. These models, though simple, have demonstrated that anharmonic interactions and anharmonic potentials cause an increase of the nonexponentiality and the relaxation time of the structural relaxation.

In real materials, anharmonic (nonlinear) interactions between the basic molecular units are quite common. Examples include: (i) intermolecular interaction between monomer units in polymers and small molecules in a glass-forming van der Waals liquid, as modeled by the Lennard-Jones potential [17,28,29]; (ii) the entanglement interaction between polymer chains [17,28,29]; (iii) Coulomb interaction between ions in glass-forming electrolytes, such as the much studied  $0.4\text{Ca}(\text{NO}_3)_2 \cdot 0.6\text{KNO}_3$  [28]; and (iv) hard-sphere-like interaction between colloidal particles [29]. These materials are all associated with highly anharmonic interactions, giving rise to nonlinear (chaotic) dynamics [14-16,22]. In some real materials, analogues can be found to the results of the simple models exhibiting increases of both the nonexponentiality  $n$  and the relaxation time  $\tau^*$ . Examples include the ionic conductors and colloidal particle suspensions, where respectively an increase of ionic concentration and colloidal particle volume fraction enhances the anharmonic interaction, with corresponding increases of  $n$  and  $\tau^*$  [17,29]. Larger  $n$  will lead to stronger temperature dependence of  $\tau^*$ , (and higher degree of fragility), a consequence of Eq. 5 [9,10,17]. Thus, the degree of both fragility,  $m$ , and nonexponentiality,  $1-\beta$ , are anticipated by the CM. Since the physics of the CM are based on anharmonic interaction or anharmonic potentials, evidently fragility and nonexponentiality of the structural  $\alpha$ -relaxation increase with anharmonicity.

## ANHARMONICITY AND THE COUPLING MODEL FOR FAST DYNAMICS

### At Low Temperatures

As discussed in the previous Section, the CM has principally been applied to relaxational and diffusional processes. However, it can certainly be generalized to consideration of the spectrum of quasi-local vibration, including the boson peak. Currently, the physical origin of the



boson peak is a subject of debate. We believe that the broad quasielastic contribution to scattered light or neutrons, discussed in the Introduction, originates from the boson peak in the presence of anharmonicity. This view concurs with that of Sokolov and coworkers [31], based on earlier work by Winterling [32], that the broad quasielastic contribution arises from damping of the vibrations constituting the boson peak, supported by the similar properties found experimentally for the quasielastic contribution and the boson peak [4]. In Raman scattering, the quasielastic contribution and the boson peak have the same depolarization ratio [33], and the same value of the light-to-vibration coupling coefficient [3,6]. In coherent neutron scattering from silica [34] and polybutadiene [7], the dynamic structure factor  $S(Q, E)$  in the region of the quasielastic contribution has the same peculiar  $Q$ -dependence seen for vibrations in the boson peak. These experimental facts are consistent with the damped oscillator model [31], and a more recent extension [35] that considers damping of vibrations by phonon density fluctuations via third order anharmonicity. These models, which have brought out many interesting features of the fast dynamics, are based on perturbation theory. We point out that the same results are expected from nonlinear Hamiltonian dynamics for anharmonic vibrations, in the spirit of the CM as possibly can be shown for some simple models.

The effect of anharmonicity on vibrations was studied by Tsironis and Aubry [22] for the anharmonic hard  $\phi^4$  potential with a single well, but the results are for energy relaxation, not the vibration spectrum. The latter can be obtained through Fourier transform [36-38] of the displacement-displacement correlation function. Although this has not been done for the hard  $\phi^4$  potential, this is an appropriate model to obtain the quasielastic contribution from anharmonicity of the boson peak. Anharmonicity will become more important at higher temperatures in this model, and is expected to give rise to a quasielastic contribution that has a stronger temperature dependence than the boson peak. The displacement-displacement correlation function was obtained by Flach and coworkers [36-38] for the soft  $\phi^4$  potential, which, however, has a double-well potential, perhaps not appropriate for vibrations in the boson peak. Nevertheless, the molecular dynamics simulations (MDS) of Flach et al. have found a low frequency quasielastic contribution, although its frequency dependence differs from what is observed in glass-forming liquids, suggesting it may be due to the double-well potential of their model. It is plausible that the displacement-displacement correlation function calculated for more appropriate models, such as the hard  $\phi^4$  potential, will reproduce the fast dynamics of glass-forming liquids at temperatures below  $T_g$ . Of course, this is speculative until the calculation has been done.

The motion of the basic structural units in glass forming liquids is best described in terms of its mean square displacement,  $\langle r^2(t) \rangle$  [39-43]. At sufficiently low temperatures, structural  $\alpha$ -relaxation is suppressed in the mesoscopic time scales,  $2 \times 10^{-11} > t > 2 \times 10^{-13}$  s, whereby  $\langle r^2(t) \rangle$  is governed by free flight at very short times and by vibrations at short times. In fact, structural  $\alpha$ -relaxation per se occurs at much longer times, only then making a significant contribution to  $\langle r^2(t) \rangle_{\text{rel}}$ . The other contributions, including the vibrational contribution  $\langle r^2(t) \rangle_{\text{vib}}$ , initially increase in proportion to  $t^2$ , before leveling off at times of the order of a few picoseconds to a constant value, referred to as the Debye-Waller factor (DWF). The DWF has a linear  $T$ -dependence if the vibrations are harmonic; anharmonicity, if present, enhances the linear temperature dependence. At intermediate times  $\langle r^2(t) \rangle_{\text{vib}}$  may rise to a maximum, before leveling off to the constant DWF. This overshoot causes a slight bump in plots of  $\log(\langle r^2(t) \rangle_{\text{vib}})$  versus  $\log t$ . Roe [39] was the first to show that the overshoot in  $\langle r^2(t) \rangle_{\text{vib}}$ , obtained from molecular dynamics simulation (MDS) of a least fragile glass-forming polymer polyethylene [9,10], is the origin of the structure seen in the dynamic structure factor,  $S(Q, \omega)$ , or the susceptibility,

$\chi''(Q, \omega)$ . This structure is commonly referred to as the boson peak, and has also been observed in MDS of other nonfragile glass-forming materials [42,43]. Although the bump in  $\langle r^2(t) \rangle_{\text{vib}}$  does not unequivocally reveal the physical origin of the boson peak, this description of the boson peak in terms of mean squared displacement makes it easier to realize that anharmonic interactions and the anharmonic potential exert the same effect on the structural  $\alpha$ -relaxation and the boson peak.

Thus, large anharmonicity gives rise not only to a higher degree of fragility (larger  $m$ ) and to larger nonexponentiality (smaller  $\beta$ ) for the structural  $\alpha$ -relaxation at macroscopic times [9,10,17], but also to a larger ratio of the quasielastic contribution to the vibrational contribution in the fast dynamics at mesoscopic time scales (viz., preceding discussion). These dual consequences of anharmonicity in the structural  $\alpha$ -relaxation near  $T_g$  and the fast dynamics spectrum below  $T_g$  can account for Sokolov's observation that the two have correlated properties. The principal goal of the present work is to elaborate on this idea., although it should be emphasized that invoking anharmonicity is not sufficient to explain Sokolov's correlation. A theory or model is required as well in order to connect anharmonicity to the fragility ( $m$ ) and nonexponentiality ( $\beta$ ) of the structural  $\alpha$ -relaxation, and to the relative strength of the quasielastic contribution to the fast dynamics spectrum. For the former, we can make recourse to the CM of relaxation; however, for the latter, we can only surmise that nonlinear Hamiltonian dynamics, when applied to suitable models like those with the hard  $\phi^4$  potential, will reproduce the fast dynamics spectrum.

#### At High Temperatures

At high temperatures above  $T_g$ , the structural  $\alpha$ -relaxation accelerates, moving into the mesoscopic time regime, whereby its contribution,  $\langle r^2(t) \rangle_{\text{rel}}$ , to the mean squared displacement can be seen at the longer time side of the mesoscopic time window. Likewise, in dynamic light scattering and neutron scattering, the  $\alpha$ -relaxation can be seen towards the corresponding lower frequency side of the mesoscopic frequency range. In this high temperature regime, another correlation of a property of the fast dynamics spectrum with fragility ( $m$ ) and nonexponentiality ( $\beta$ ) has been established [43-46]. To do this one compares the fast dynamics spectra in the frequency domain, or the intermediate scattering function in the time domain, of different glass-formers, all having the same value of the  $\alpha$ -relaxation frequency or time ( $\tau^*$  in the Kohlrausch function given by Eq.4), for example  $10^{-10.5}$ s. This is an objective way of comparing glass-formers, which may have widely different glass transition temperatures. Under this condition, the following observations can be drawn [44] from experimental and MDS work. Fragile glass-formers (with larger  $m$  and smaller  $\beta$ ) such as polymers [23,24,47], CKN [48] and OTP [25,41,49] exhibit prominent fast relaxation at the sub-picosecond and picosecond time range, which completely overwhelms the vibrational boson peak. In strong and intermediate liquids like  $\text{ZnCl}_2$  [50,51], glycerol [45,52], methanol [46,53], and  $\text{B}_2\text{O}_3$  [5], with smaller  $m$  and larger  $\beta$  nearly equal to unity, the fast relaxation is either weak or absent, leaving the boson peak unobscured. The fast "relaxation" process in this time range is often interpreted as the  $\beta$ -process of mode coupling theory (MCT) [54,55]. The fast relaxation process can alternatively be identified with the independent relaxation process given by Eq.3 of the CM since  $t_c$  is of the order of a picosecond. In the past [28] we have called this independent relaxation process the  $\alpha$ -fast relaxation, and naturally the Kohlrausch part given by Eq.4 the  $\alpha$ -slow relaxation. The two together make up the entire  $\alpha$ -relaxation, with  $\tau^*$  longer than  $\tau_0$ . Using equation 5 of the CM, it can be shown (see Figure 1 of Ref.44), that the prominence or intensity of the  $\alpha$ -fast relaxation increases with the nonexponentiality (larger  $n$  or smaller  $\beta$ ) or fragility of the glass-former. Thus, the CM accounts

for the empirical correlation between the prominence of the fast relaxation process (when identified with the  $\alpha$ -fast relaxation) and the fragility of the glass-former.

Another basis for comparing the fast dynamics of different glass-formers is through their mean squared displacements  $\langle r^2(t) \rangle$ , all measured in the mesoscopic time window at, for example, few picoseconds. At low temperatures, only  $\langle r^2(t) \rangle_{\text{vib}}$  is observed, but in this section we are

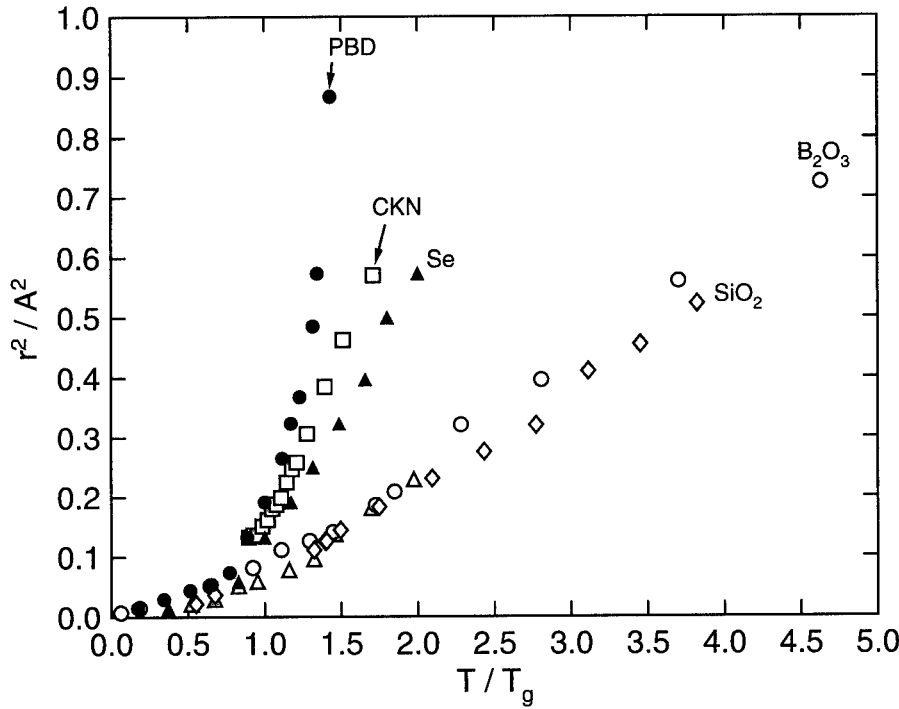


Figure 1. The mean squared displacement of various glass-formers, polybutadiene (PBD), calcium-potassium nitrate (CKN), selenium (Se), boron trioxide ( $B_2O_3$ ) and silica ( $SiO_2$ ), in order of decreasing fragility, plotted against normalized temperature  $T/T_g$ .

interested in high temperatures, where the relaxational contribution  $\langle r^2(t) \rangle_{\text{rel}}$  may show up. Since different glass-formers can have very different glass transition temperatures, an objective comparison is through a plot of  $\langle r^2(t) \rangle$  versus  $T_g$ -normalized temperature, first done by Angell and coworkers [43]. In Fig. 1 we reproduce these results [43], along with data for CKN deduced from the neutron scattering results of Kartini et al. [48]. The steepest rise in Fig.1 corresponds to polybutadiene, which is the most fragile glass-former (smallest  $\beta$  and the largest  $m$  [9,10]). The steepness of the curves for the rest of the materials in Fig. 1 decreases in proportion to their fragility. At high temperatures,  $\langle r^2(t) \rangle_{\text{rel}}$  dominates  $\langle r^2(t) \rangle$ , reaffirming the correlation between the prominence of the fast relaxation process and the fragility of the glass-former. This correlation for  $\langle r^2(t) \rangle$  is anticipated by the CM [44].

### Anharmonicity

A difficulty in describing fast dynamics above  $T_g$  is separating the relaxation dynamics from the vibrational contribution. Some investigators simply avoid the issue, citing the absence of a rigorous solution to this complicated problem [56]. A more ambitious approach is that undertaken by Colmenero and coworkers [23] and Zorn et al.[24], who employ the “harmonic approximation” to extrapolate low temperature results, wherein only the vibrational component is manifest. Although this approximation gives at least qualitatively satisfactory results, it is clear (see, for example Reference 48) that deviation of the DWF from the low temperature behavior can be expected above  $T_g$ . The error inherent to the use of the harmonic approximation may be relatively small; nevertheless, there is uncertainty in any extrapolation of the phonon contribution to very high temperatures. Accordingly, for higher temperatures our practice had been to take the magnitude of the DWF to be a parameter adjusted to yield agreement between calculation and experiment.

To illustrate this approach, displayed in Fig.2 are the values for the DWF used in fitting the density-density correlation function of OTP over a range of temperatures [25]. At low

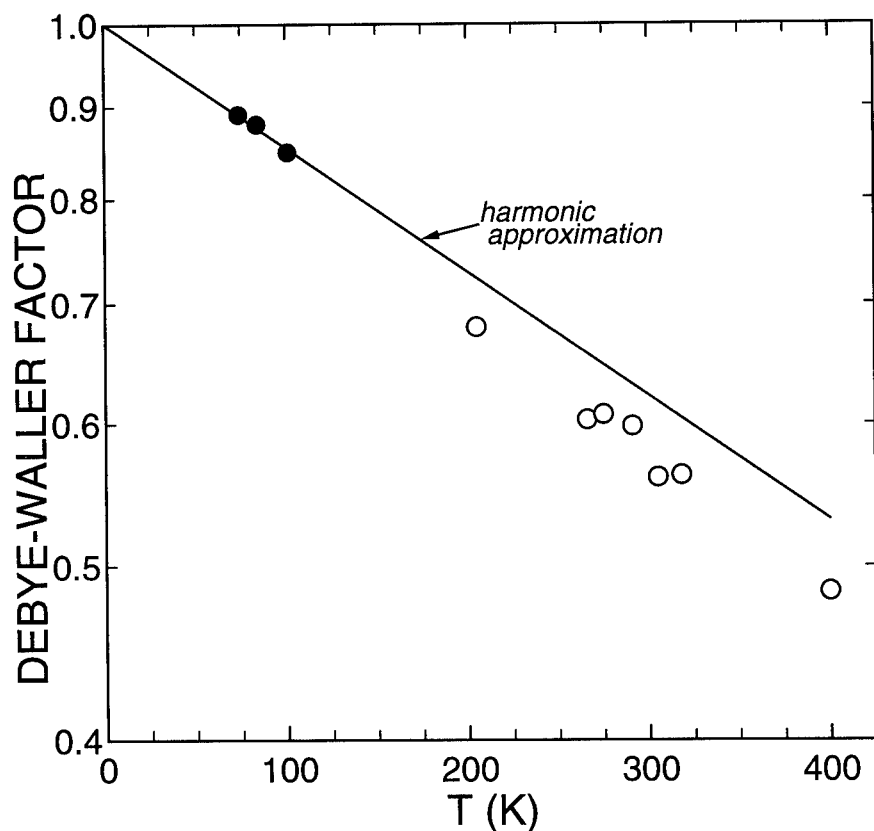


Figure 2. The long time limiting value of the phonon contribution to the self intermediate scattering function determined from fitting low ( $\bullet$ ) and high temperature ( $\circ$ ) MDS data of OTP. The solid line represents extrapolation of the low temperature values for harmonic phonons. The actual values of the DWF at high temperatures obtained from the fit to the data lie below this line, reflecting anharmonicity of the vibrational motions of OTP.

temperature ( $\ll T_g$ ), the vibrational correlation function dominates, and the values of the DWF (solid symbols) can be accurately determined. Note that from zero Kelvin through these data points, the harmonic approximation holds. For the higher temperatures in Fig.2 (hollow symbols), however, there is a systematic decrease in the DWF from the extrapolation of the low temperature "harmonic" data. The lower DWF, reflects the anharmonicity of the vibrations. Nevertheless with inclusion of anharmonicity, meaningful results have been obtained from an analysis of the MDS data [41] using the coupling model [25], indicating that this approach is capable of describing the fast relaxation dynamics of OTP.

## CONCLUSIONS

Anharmonicity, through interaction in the context of nonlinear Hamiltonian dynamics, is the physical basis of the CM [14-16,22]. It is an immediate consequence of the CM that greater anharmonicity (stronger interaction) yields more fragile macroscopic time dynamics; these conditions correspond to larger  $m$  and smaller  $\beta$ .

It is apparent that anharmonicity is the cause of the quasielastic contribution that appears together with the boson peak at low temperatures below  $T_g$ , where structural  $\alpha$ -relaxation makes no contribution in the mesoscopic time region. The CM can be extended to consider the dynamics of vibrations, including the boson peak. We anticipate that higher anharmonicity (stronger interaction) will lead to a larger ratio of the quasielastic contribution to the vibrational contribution under equivalent conditions. Such an accounting for relaxation and vibration behaviors would explain the observation of Sokolov and coworkers that more fragile glass-formers exhibit a larger ratio of quasielastic to vibrational contributions. Similar conclusions can be drawn from other methods [35] by making the assumption that fragile glass-formers are more anharmonic. This approach is useful in elucidating the importance of anharmonicity to the fast dynamics at low temperatures. However, until this method [35] can also provide a description of the structural  $\alpha$ -relaxation dynamics at all time scales, such a treatment is incomplete, lacking any connection to fragility. The CM has been applied primarily to relaxation processes, such as the structural  $\alpha$ -relaxation. In this work we indicate that the CM when applied to vibrations may also lead us from anharmonicity to the observed characteristics of the fast dynamics.

## ACKNOWLEDGMENTS

This work is supported by the Office of Naval Research. We thank Dr. A.P. Sokolov for helpful discussion of his experimental data and Dr. V.N. Novikov for providing a copy of his preprint.

## REFERENCES

1. A.P. Sokolov, E. Rössler, A. Kisliuk, and D. Quitmann, *Phys.Rev.Lett.* **71**, 2002 (1993).
2. A.P. Sokolov et al., *J. Non-Cryst.Solids* **172-174**, 138 (1994).
3. Amorphous Solids: Low-Temperature Properties, edited by W.A. Phillips, (Springer, Berlin 1981).
4. A.P. Sokolov, in this Volume.
5. A. Brodin, D. Engberg, L.M. Torell, L. Börjesson, A.P.Sokolov, *Phys.Rev.B* **53**,11511(1996).
6. A.P. Sokolov, U. Buchenau, W. Steffen, B. Frick and A. Wischnevski, *Phys.Rev.B* **52**, 3. R9815(1995).
7. U. Buchenau, Wischnevskii, D. Richter, and B. Frick, *Phys.Rev.Lett.* **77**, 4035 (1996).
8. E. Duval, A. Boukenter, T. Achibat, *J.Phys.:Cond. Matt.* **2**, 10227 (1990).
9. D.J. Plazek and K.L. Ngai, *Macromolecules* **24**, 1222 (1991); K.L. Ngai and C.M. Roland, *Macromolecules* **26**, 6824 (1993).
10. R. Böhmer, K.L. Ngai, C.A. Angell and D.J. Plazek, *J.Chem.Phys.* **94**, 3018 (1994).
11. K.L. Ngai, W. Steffen and A.P. Sokolov, *J.Chem.Phys.* in press (1997).
12. K.L. Ngai *Comments Solid State Phys.* **9**,127 (1979).
13. K.L. Ngai and C.T. White, *Phys.Rev.B* **20**, 2475 (1979).
14. K.L. Ngai and K.Y. Tsang, *Macromol. Chem. Macromol.Symp.***90**, 95 (1995).
15. R.W. Rendell, *Phys.Rev.E* **48**, R17 (1993).
16. K.Y. Tsang and K.L. Ngai *Physical Review E* **54**, R3067 (1996).
17. For various applications of the coupling model see K.L. Ngai in Relaxational Properties in Disordered Systems, edited by R. Richert and A. Blumen, Springer, p.89 (1995).
18. C.E. Porter, Statistical Theories of Spectra: Fluctuations, Academic, New York (1965).
19. M.V. Berry, *Proc.Roy.Soc.London A***423**, 219 (1989).
20. M.C. Gutzwiller, Chaos in Classical and Quantum Mechanics, Springer, Berlin (1990).
21. R.S. McKay and J.D. Meiss eds, Hamiltonian Dynamic Systems, Adam Hilger, Bristol (1987).
22. G.P.Tsironis and Aubry S. *Phys.Rev.Lett.***77**, 5225 (1996).
23. J. Colmenero, A.Arbe and A. Alegria, *Phys.Rev.Lett.* **71**, 2603 (1993).
24. R. Zorn, A. Arbe, J. Colmenero, B. Frick, D. Richter, and U. Buchenau, *Phys.Rev.E* **52**, 781 (1995).
25. C.M. Roland, K.L. Ngai and L.J. Lewis, *J.Chem.Phys.* **103**, 4632 (1995).
26. C. Cramer, K. Funke and T. Saatkamp, *Phil.Mag.* **B71**, 701 (1995).
27. C. Cramer, K. Funke, M. Buscher, A. Happe, T. Saatkamp, and D. Wilmer, *Phil.Mag.* **B71**, 713 (1995).
28. K.L. Ngai, C. Cramer, T. Saatkamp, and K. Funke, in Non-Equilibrium Phenomena in Supercooled Fluids, Glasses, and Amorphous Materials, edited by M. Giordano, D. Leporini and M.P. Tosi, World Scientific, Singapore (1996), pp.3-22.
29. K.L. Ngai and R.W. Rendell, in Experimental and Theoretical Approaches to Supercooled Liquids: Advances and Novel Applications, edited by J. Fourkas, D. Kivelson, U. Mohanty and K. Nelson American Chemical Society, Washington, DC(1997).
30. G.P.Tsironis, private communication.
31. V.Z. Gochiyaev, V.K. Malinovsky, V.N. Novikov and A.P. Sokolov, *Phil.Mag.B* **63**, 777 (1991).
32. G. Winterling, *Phys.Rev.B* **12**, 2432 (1975).
33. J. Jäckle in Ref.3.
34. U. Buchenau et al. *Phys.Rev.Lett.* **60**, 1318 (1988).

35. V.N. Novikov, submitted to Phil.Mag.B.
36. S. Flach and J. Siewert, Phys.Rev. B **47**, 14910 (1993).
37. S. Flach and J. Siewert, J.Phys.:Condens.Matter **4**, L363 (1992).
38. S. Flach and G. Mutschke, Phys.Rev.E **49**, 5018 (1994).
39. R.J. Roe, J.Chem.Phys. **100**, 1610 (1994).
40. G.F. Signorini, J.L. Barrat, and M.L. Klein, J.Chem.Phys. **92**, 1294 (1990).
41. L.J. Lewis and Wahnström, Phys.Rev.E **50**, 3865 (1994).
42. W. Smith, W. Gillen, and G.N. Greaves, J.Chem.Phys. **103** (1995).
43. C.A. Angell, W. Poole, and J. Shao, Nuovo Cimento **16**, 993 (1994).
44. C.M. Roland and K.L. Ngai, J.Chem.Phys. **104**, 2967 (1996).
45. C.M. Roland and K.L. Ngai, J.Chem.Phys. **106**, 1187 (1997).
46. K.L. Ngai and C.M. Roland, J.Phys.Chem. in press (1997).
47. R. Zorn, D. Richter, B. Frick and B. Farago, Physica A **201**, 52 (1993).
48. Kartini, E. et al., Phys. Rev. B, **54**, 6292 (1996).
49. Kiebel M., Bartsch E., Debus O., Fujara F., Petry W. and Sillescu H., 1992, Phys.Rev.B, **45**, 10310.
50. M.J. Lebon, C. Dreyfus, G. Li, A. Aouadi, H.Z. Cummins and R.M. Pick, Phys.Rev.E **51**, 4537 (1995).
51. K.L. Ngai and C.M. Roland, Phys.Rev.E **54**, 6969 (1996).
52. J. Wuttke, W. Petry, G. Coddens and F. Fujara, Phys.Rev.E **52**, 4026 (1995); see Comment on this work by K.L. Ngai and C.M. Roland, Phys.Rev.E **55**, 2069 (1997).
53. P. Sindzingre and M. Klein, J. Chem.Phys. **96**, 4681 (1992).
54. W. Götze and L. Sjögren, Rep.Prog.Phys. **55**, 241 (1992).
55. We put relaxation of the fast relaxation process inside quotation marks when relating it to the  $\beta$ -process of MCT because the latter is not really a relaxation process in the conventional sense.
56. J. Wuttke, W. Petry, and F. Fujara, Phys. Rev. E **55**, 2071 (1997).

## RELAXATION PROCESSES AND THE MIXED ALKALI EFFECT IN ALKALI METASILICATE GLASSES

J. HABASAKI\*, I. OKADA\*\* and Y. HIWATARI\*\*\*,

\* Tokyo Institute of Technology at Nagatsuta, Yokohama, Kanagawa 226, Japan,  
jhabasak@n.cc.titech.ac.jp

\*\* Tokyo Institute of Technology at Nagatsuta, Yokohama, Kanagawa 226, Japan,  
okada@echem.titech.ac.jp

\*\*\* Kanazawa University, Kanazawa 920-11, Japan, hiwatari@hiwa003.s.kanazawa-u.ac.jp

### ABSTRACT

A molecular dynamics simulation (MD) of lithium metasilicate ( $\text{Li}_2\text{SiO}_3$ ) and related mixed alkali system ( $\text{LiKSIO}_3$ ) has been performed. Changes in the mean squared displacement and the corresponding clear two-step ( $\beta$  and  $\alpha 1$ ) relaxations in a density correlation function have been observed at 700 K (self-part) for each ion in  $\text{Li}_2\text{SiO}_3$  following an exponential decay by vibrational motion in a simulation up to 300 ps (run I). The mean squared displacement of the atoms shows the change in the slope at *ca.* 300 ps when the simulation is extended up to 1 ns (run II). Here we call the slowest relaxation (*ca.* 300 ps $\sim$ ) the  $\alpha 2$  region.

Oscillation, which is clearer for O and Si than for Li, is found in the second ( $\beta$ -relaxation) region of the function, which is attributed to the so called "boson peak". Both the  $\beta$ -relaxation and the boson peak are found to be due to the correlated motion.

The slower relaxation ( $\alpha 1$ -relaxation) can be fitted to a stretched exponential form and the origin of this type of decay is confirmed to be waiting time distribution of jump motions. The back-correlated jumps also decrease the decay rate.

Components A and B in  $\alpha 1$  and  $\alpha 2$  regions for Li ion are analyzed, where the Li ion of component A is located within the first neighboring sites and that of component B moves longer than the nearest neighbor distances by cooperative jump motion. The component B shows accelerated dynamics larger than *t*-linear ones ( $\sim t^{1.77}$ ) in the region 50-300 ps, and the dynamics can be characterized as Lévy flight.

We have found that the contribution of the cooperative jumps decreases in the mixed alkali glass. This explains the maximum of the Haven ratio accompanied with the mixed alkali effect.

### INTRODUCTION

During the past years, many studies, both experimental and theoretical, on slow dynamics near the glass transition temperature have been performed mainly for the so-called "fragile" glasses [1], which have no directional bonds and show an abrupt increase in viscosity upon super-cooling. On the other hand, systems having covalent or hydrogen-bonded frameworks are often classified as "strong" glass systems. In the present work, the slow and fast dynamics of lithium metasilicate ( $\text{Li}_2\text{SiO}_3$ ) are examined by means of molecular dynamics (MD) simulation, where the simulation is extended up to a 1 ns region. The system  $\text{Li}_2\text{SiO}_3$  may be regarded as "fragile" for  $\text{Li}^+$  ions and "strong" for Si and O atoms of the chain structure.

The study of the "mixed alkali effect" in the mixed alkali system is also helpful for understanding the mechanism of the dynamics in the glass. We have found that not merely the interception of the jump path of each kind of alkali ion but the cooperative jumps play an important role for the mixed alkali effect. The latter was not paid attention previously.



## METHOD

The MD calculation was performed in the same way as in our previous studies [2, 3, 4, 5, 6, 7]. The periodic cube contained 144 Li, 72 Si and 216 oxygen atoms. In a mixed alkali system, the cube contained 72 Li and 72 K instead of 144 Li. A Gilbert-Ida [8] type potential function plus an  $r^{-6}$  term was used; *i.e.*

$$\phi_{ij} = z_i z_j e^2 / r + f_0 (b_i + b_j) \exp[(a_i + a_j - r) / (b_i + b_j)] - c_i c_j / r^6, \quad (1)$$

where  $z$  is the effective charge number,  $e$  the elementary charge;  $a$ ,  $b$  and  $c$  are the parameters characteristic of each atom and  $f_0$  is a normalization constant ( $4.184 \text{ kJ } \text{\AA}^{-1} \text{mol}^{-1}$ ). The potential parameters used in this work were previously derived from an *ab initio* MO calculation [3], and their validity has been checked in the liquid, glassy and crystal states under constant pressure conditions.

The system was equilibrated at 4,000 K for more than 10,000 time-steps starting from a random configuration, and then each system was cooled down to lower temperatures. Simulation runs were carried out at 3,000, 2,000, 1,673, 1,173, 973, 800 and 700 K. The step time was 1 fs from 4,000 to 2,000 K and 4 fs from 1,673 K to 700 K. The velocities of all particles were initially set to zero at each temperature, and several thousand steps were carried out at constant temperature and pressure (0.1 MPa). Then, the sizes of the periodic cube were fixed to the equilibrated or quasi-equilibrated volumes. The MD runs (I, II) were carried out at 700 K at a constant energy condition from different initial configurations. Steps of the run I and II were 200,000 and 250,000, respectively. For the mixed alkali system, simulation at 800 K was also performed to enhance the jump frequency. Each system consisted of branched-chain structures composed of  $\text{SiO}_4$ -tetrahedral units and alkali ions surrounded by oxygen atoms. The glass transition temperature,  $T_g$  of  $\text{Li}_2\text{SiO}_3$  system obtained by the volume-temperature relation was  $830 \pm 50 \text{ K}$ , which was comparable to the experimental value, 687 K [9].

## RESULTS AND DISCUSSIONS

### Mean Squared Displacements and Density Correlation Function (self-part)

Mean squared displacements,  $R2(t)$ , of the Li, O and Si atoms at 700 K in a simulation  $\sim 300 \text{ ps}$  (run I) are shown on log scales in Fig. 1.

Except for the early time region, non-linear time dependent behavior is observed. The value for Li ion increases between 1 and 10 ps and those for Si and O slightly increase between 1 and 70 ps. An increase in the curve is observed for each atom in a larger  $t$  region. The part of the curve of increased mean squared displacement corresponds to the  $\alpha 1$ -relaxation region discussed below.

The density correlation function (self-part),  $F_s(\mathbf{k}, t)$ , was calculated for the run I, where  $F_s(\mathbf{k}, t)$  is defined as,

$$F_s(\mathbf{k}, t) = \langle \sum_{j=1}^{N_{\alpha'}} \exp\{i\mathbf{k} \cdot d\mathbf{r}_j^{\alpha'}(t)\} \rangle / N_{\alpha'}, \quad (2)$$

where  $\alpha'$  denotes the species indices, and  $\langle \dots \rangle$  denotes an initial time average.

For Li, O and Si at 700 K, a clear two-step relaxation is observed following an exponential decay (Debye type) by vibrational motion.

In the present work, the "first slow-relaxation process" is termed the " $\beta$ -relaxation" and the "second slow-relaxation process" is termed the " $\alpha 1$ -relaxation". The slowest relaxation process (300 ps  $\sim$ ) observed in the longer simulation (run II) is termed the " $\alpha 2$ -relaxation", which will be discussed later.

### $\beta$ -Relaxation Process

An oscillating process was found in the second region (0.1-10 ps) of  $F_s(k, t)$  for Li, O and Si at 700 K.

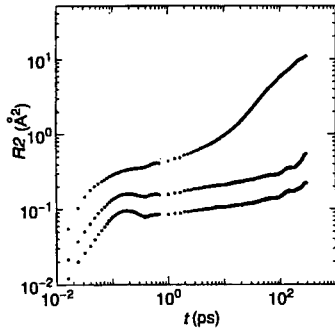


Figure 1: Mean square displacements of the atoms at 700 K on a log-log scale (run I). The curves from top to bottom are for Li, O, and Si, respectively.

The oscillation is deeper for O and Si than for Li. The decay for O and Si during this period is smaller than for Li. Low-frequency vibrational excitation is known to contribute to the dynamics of some glasses near the glass transition temperature. Such excitations are known as the "boson peak" [10], which has not been found in very fragile systems. Motions of the atoms for  $\text{Li}_2\text{SiO}_3$  in this time region were examined.

We have found that some atoms move collectively at the same time. Correlation of the motion of atoms is not restricted to the connected structure ( $\text{SiO}_4$  chain) but includes those of neighboring Li. We have observed the changes in the distinct-part of the van Hove function, which corresponds to this kind of motion. The function is defined by

$$G_d^{\alpha'\beta'}(r, t) = (1/N_{\alpha'}) \sum_{i=1}^{N_{\alpha'}} \sum_{j=1}^{N_{\beta'}} (\delta(\mathbf{r} - \mathbf{r}_i^{\alpha'}(0) + \mathbf{r}_j^{\beta'}(t))), \quad (3)$$

where  $\mathbf{r}_i^{\alpha'}(t)$  denotes the position of particle  $i$  of species  $\alpha'$  at time  $t$  and the self-term  $i = j$  is to

be ruled out if  $\alpha' = \beta'$ .  $N_{\alpha'}$  and  $N_{\beta'}$  are the numbers of particles of species  $\alpha'$  and  $\beta'$ , respectively. In Fig. 3 (a), the van Hove function (distinct-part) for O-O pair is shown, where the time region corresponds to the  $\beta$ -relaxation region ( $< 1.0$  ps).

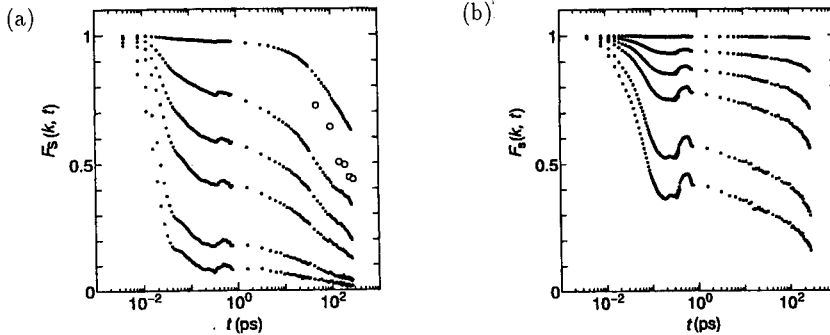


Figure 2: Density correlation function (self-part) of (a) Li and (b) O at 700 K in run (I). The curves from top to bottom are for wavenumbers  $k = 2\pi/n'$  ( $n' = 10, 3, 2, 1.5, 1, 0.8$ ) in the unit of  $\text{\AA}^{-1}$ , respectively. The circles in (a) are obtained from the area under the first peak of the van Hove function (self-part),  $4\pi r^2 G_s(r, t)$  for Li.

We have found that the peak height is not sequenced with the elapse of time but the oscillation of the peak height occurs during 0-1.0 ps. Peak positions remain unchanged

during this period but oscillation of the peak width occurs. Similar behavior is observed for the Si-O, O-Si and Si-Si pairs, which corresponds to the oscillation in the density correlation function. In Fig. 3 (b), the function for the Li-O pair is shown, where the curves overlap and the oscillation is unclear. During this period, the peak position shifts toward higher  $r$ . Similar behavior is observed for Li-Li and O-Li pairs. The shift can be attributed to the  $\beta$ -relaxation. The observed characteristics in the function are due to the correlated motion. Thus the  $\beta$ -relaxation occurs in the same region with the oscillating motions both in space and time. The process seems to have the same microscopic origin as the oscillating motions earlier suggested by Sokolov *et al.* [10] They also suggested that in a strong structure such as chains, an oscillating process is dominant, while in a fragile structure, the relaxation process is dominant.

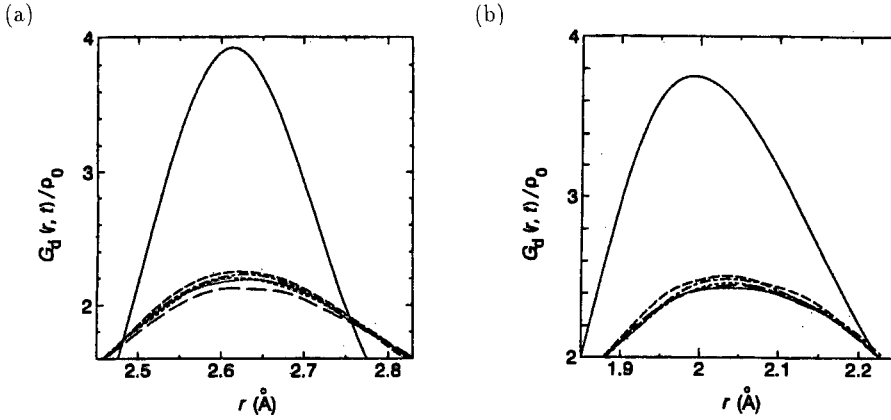


Figure 3: The van Hove function (distinct-part) for (a) O-O pair and for (b) Li-O pair in the  $\beta$ -relaxation region at 700 K. (— :  $t=0$ ; — — :  $t=0.2$ ; - - - :  $t=0.4$ ; - - - :  $t=0.6$ ; - - - :  $t=0.8$ ; ... :  $t=1.0$  (ps))

#### $\alpha$ 1-Relaxation Process

An  $\alpha$ 1-relaxation process can be expressed by a Williams- Watts type function [11].

$$F_s(\mathbf{k}, t) = A \exp(-(t/\tau)^\beta) \quad (4)$$

where  $A$ ,  $\beta$  and  $\tau$  are adjustable parameters. We had fitted the slow decay of  $F_s(\mathbf{k}, t)$  in run (I) by Eq. (4) [2].

The self-part of the van Hove function,  $4\pi r^2 G_s(\mathbf{r}, t)$ , where the function is defined as,

$$G_s^{\alpha'}(\mathbf{r}, t) = (1/N_{\alpha'}) \sum_{i=1}^{N_{\alpha'}} \langle \delta(\mathbf{r}_i^{\alpha'}(t) - \mathbf{r}_i^{\alpha'}(0) - \mathbf{r}) \rangle \quad (5)$$

The number of ions in the original site was calculated from  $\int_0^{r_c} 4\pi r^2 G_s(r, t) dr$ , where  $r_c$  was chosen to be half of the distance of  $g_{\text{Li-Li}}^{\text{max}}(r)$ . The decrease in the area can be well represented by a stretched- exponential form and the fitted parameters for Li are  $A=0.923$ ,  $\beta=0.583$ , and  $\tau_j=448$  (ps). The function shows a second peak due to the jump motions of Li ion. Thus the origin of the stretched exponential form is the distribution of the jump

rate,  $\tau_j$ . The origin of the stretched exponential type decay of Li ion observed in  $F_s(k, t)$  in  $\alpha 1$ -relaxation region is also the jump motion [2, 13].

The number of the ions in the original site also contains the particles returned by back-correlated motion. Such contribution is expected to be large when the the jump path is low dimensional.

The frequency of jumps of O is smaller than those of Li ions. The  $G_d$  functions for Si-Si pair reveal that site-site jumping by Si did not occur during the run (I); however, the short distance-jump of the Si atom is observed, which is clearly correlated with the motion of neighboring O atoms.

The larger  $k$  dependence of  $A$  for Li is also attributable to the highest mobility of the small ion in the large  $k$  area in this time region.

The value of  $\beta$  is found to be less than 1 at 700 K for all the species, with minima at about  $2 \text{ \AA}^{-1}$  for Li and at about  $4 \text{ \AA}^{-1}$  for O. The value for Si seems not to have a minimum in the  $k$  range investigated.

This trend may be interpreted if the  $\beta$  has a minimum value at  $k$  corresponding to the inverse of the jump distance of each species. The order of  $\beta$  is  $\text{Si} > \text{O} > \text{Li}$  for each  $k$  value as expected from the "fragility" of the species, and as the system becomes more "fragile",  $\beta$  seems to decrease.

The relaxation time,  $\tau_k$  was fitted by the linear function of  $k$  on a log-log scale at 700 K, ( $\tau_k \sim k^{-n}$ ) with a larger slope for Si and O than for Li [2].

The larger slope ( $n = 2.67$  for Si,  $n = 2.88$  for O) of  $k$  on the  $\tau_k$  for each Si and O had been found to correspond to the large connectivity. On the other hand, the slope for Li ( $n = 1.41$ ) is less than the value expected for the Debye type relaxation ( $n = 2$ ). The results suggest that the  $k$  dependence of  $\tau_k$  for Li is affected by features of the jump motion. We have attributed the small  $n$  value to the cooperative jump motion of the like alkali ions as will be shown later. Thus the fragility is related to the fractal dimension of both space and time [2].

## $\alpha 2$ -Relaxation Process and Cooperative Jumps

Simulation up to 1 ns has been performed, since we can expect the contribution of the component with a low  $n$  value becomes larger in a longer time region.

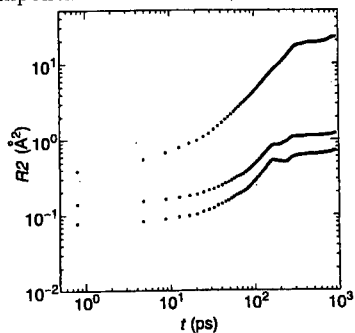


Figure 4: Mean square displacements of the atoms at 700 K on a log-log scale (run II). The curves from top to bottom are for Li, O, and Si, respectively.

Mean squared displacements of the Li, O, and Si atoms at 700 K in a simulation  $\sim 1$  ns (run II) are shown on log scales in Fig. 4, where the behavior of the short time region is omitted.

As long as the distance travelled by the random walkers is smaller than  $R_s$ , diffusion is anomalous and  $R_2(N) \sim N^{2/d_w}$ , where  $d_w$  is fractal dimension of the random walk, which will be defined later.  $R_s$  is a mean radius of clusters of  $s$  sites.

Behavior of the Si and O seems to be quite similar to that of Li ion. However, in the  $\alpha 2$  region, the slope of the mean squared displacements of these atoms is negligibly small. That is, the large slope of these atoms less than  $\sim 150$  ps is attributed to the localized jump motion of the atoms of a small number. The results suggest that the cooperative jump motion plays an important role in the mechanism of the glass transition.

sition.

Now attention is focussed on the motion of alkali metal ions.

For longer time, a random walker cannot escape from the  $s$  cluster, and  $R2_s(N)$  is bounded by  $R_s^2$  if  $N^{2/d_w} > R_s^2$ .

The change in the slope found in Fig.4 (at  $ca. 18 \text{ \AA}^2$ ) clearly corresponds to the squared value of the first minimum distance of the pair correlation function of Li-Li pair ( $g_{\text{Li-Li}}(r)$ ) ( $4.2 \text{ \AA}$ ).

We have divided the walkers into two components. The walkers in component A show squared displacement less than  $R_s^2$  ( $s=2$ ) during a 1 ns run. Namely, the component is located within neighboring sites. The other walkers in component B show squared displacement more than  $R_s^2$  during the 1 ns run. Namely, they contribute to the diffusion of a long time limit.

In Fig. 5, both components are plotted on log-log scales.

The mean squared displacement of the component A shows a maximum and does not show large contribution to the long time diffusive behavior. Mean squared displacement in the  $\alpha 1$  region is the mean value of those for components A and B. The difference of these two components can be explained by the structure of the jump path and by the existence of both single and cooperative jumps.

The jump path of lithium has been found to be low dimensional in localized regions, while the path forms three-dimensional percolation clusters [14].

We have assumed the behavior of the component A is mainly caused by single jumps trapped in low dimensional localized paths, while the behavior of the component B is mainly caused by cooperative jump diffusion travelling three-dimensional connections of these paths, because the characteristic lengths of these motions are different.

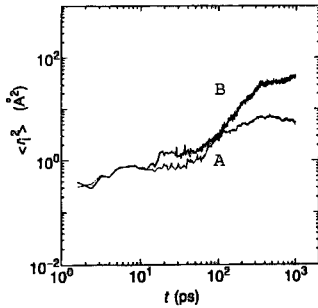


Figure 5: Mean square displacements of the atoms at 700 K of component A (thin line) and B (thick line). The component A is located within neighboring sites. On the other hand, the component B shows squared displacement larger than  $R_s^2$  ( $s=2$ ) during the 1 ns run. Namely, they contribute to the diffusion in longer time region.

To confirm this assumption, we have examined contribution of the single jumps and cooperative jumps to the squared displacements. Positions of lithium ions are checked every 2 ps during arbitrarily chosen 16 ps. The motion with displacement larger than half distance of the first peak ( $2.77/2 \text{ \AA}$ ) of the  $g_{\text{Li-Li}}(r)$  is defined as a jump.

The jumps simultaneously occurring (within 2 ps in some cases) at neighboring sites are judged to be cooperative. In Table I, the numbers of cooperative jumps and the contribution of these motions to mean squared displacements are given. As seen from Table I, even in a short period, contribution of cooperative motion to the mean squared displacement is quite large in spite of the small number of events of cooperative jumps. We have also confirmed that all ions travelling longer distances than first minimum of the  $g_{\text{Li-Li}}(r)$  are concerned with the cooperative jumps.

Therefore, the ions causing cooperative motion must become the main component in a long time region.

A fractal dimension analysis has been per-

formed to characterize these motions [15].

Averaged positions of Li ions every 0.4 ps during 16 ps at 700 K are shown in Fig. 6. The jump path has a low dimensional structure in localized regions, while each path forms percolation clusters of various sizes. The fractal dimension of jump path  $d_f$  is defined by the scaling of the mass  $M$  with their linear size  $L$ :  $M \sim L^{d_f}$  [15]. The fractal dimension of

Table I: (a) Number of single and cooperative jumps during arbitrarily chosen 16 ps. (b) Square displacements of the alkali metal ions during the 16 ps.

(a)			
system	type	number of event	
LiKSiO <sub>3</sub> (700 K)	Li → Li → Li →	1	
	Li →	13	
	K → K → K → K →	1	
	K → K →	2	
	K →	6	
	<hr/>		
LiKSiO <sub>3</sub> (800 K)	Li → Li → Li →	3	
	Li → Li →	1	
	Li →	16	
	Li ↔ Li	1	
	K → K → K → K →	1	
	K → K → K →	2	
	K → K →	9	
	K →	14	
	K → Li →	1	
	Li → K →	2	
	<hr/>		
Li <sub>2</sub> SiO <sub>3</sub> (700 K)	Li → Li →	6	
	Li → Li → Li →	2	
	5Li →*	1	
	Li →	17	
	* complicated collective motion of 5 ions		
<hr/>			
(b)			
system	square displacements total	(Å <sup>2</sup> ) cooperative	ratio(%) cooperative to total
<hr/>			
LiKSiO <sub>3</sub> (700 K)			
Li	94.9	25.3	27
K	190.3	105.9	56
<hr/>			
LiKSiO <sub>3</sub> (800 K)			
Li	245.1	159.8	65
K	385.8	257.8	67
<hr/>			
Li <sub>2</sub> SiO <sub>3</sub> (700 K)			
Li	211.3	166.2	79

clustering  $d_{fc}$  is similarly defined for the clustering region. The fractal dimensions (see Table II) were calculated for the paths shown in Fig. 6.

The  $d_f$  for the local ( $0.7 \sim 2.0$  Å) region is found to be less than 1, (0.22, obtained from the plot of averaged positions of every 0.4 ps during 16 ps run) for this system at 700 K. The value less than 1 means the existence of a long life component and the local path of low dimension.

The modified random network (MRN) model [16] holds well for the local structure in this system; however, the range of the paths which have low dimensionality is very short.

The long range structure of the paths and therefore the dynamics in a long time scale may be characterized by  $d_{fc}$  rather than by  $d_f$ . In  $\text{Li}_2\text{SiO}_3$ ,  $d_{fc}$  is nearly equal to 3, which means that in spite of the low dimensionality of the local structure the whole conduction path has three-dimensional connections. Therefore, the localization is not due to the structure of the cluster but due to the local structure of low dimension as discussed below. Fractal dimension of random walk,  $d_w$  [15], is also related with a back-correlation probability. The fractal dimension of random walk,  $d_w$  is defined by  $L(\sigma) = A \sigma^{1-d_w}$ , where  $L(\sigma)$  is a total length of the trajectory measured by using scale length  $\sigma$  and  $A$  is a constant.

The value of  $d_w$  is directly obtained from the trajectories of Li in run II to avoid the effect of waiting time distribution of jump motions. The values  $d_w$  for the component A and B are found to be 2.83 and 2.47, respectively. Both values are greater than 2 (the value for the free random walk): A higher value for A means that the ions in component A tend to be trapped more in the low dimensional structure.

Combination of the large  $d_w$  and small  $d_f$  values means a localized motion (fracton excitation) [17, 18]. The fractal time distribution of jump motion [2] also contributes to the time dependent behavior. Namely, both components with long life and with high back correlated motion contribute to the slowing-down of the decay of  $F_s(k, t)$ . On the other hand, the mean squared displacement of component B increases sharply in the  $50 \sim 300$  ps region. The slope in a log-log plot during this period is 1.77, which means that  $R_2(t)$  for this component increases faster than  $t$ -linear. That is, the component B shows the accelerated dynamics at least in this time region, which corresponds to the small  $n$  value in the wave number dependence of  $F_s(k, t)$ .

The accelerated dynamics observed can be explained by cooperative motion (jumps in glassy state) of lithium ions [14, 17], because the path of backward jump for an ion is intercepted by the simultaneous jump of an ion which follows. Thus the cooperative jumps should have larger forward correlation probability than the single jumps. The behavior of the cooperative jumps seems to be quite similar to that observed in the kicked rotor or in the Josephson junctions, where the accelerated dynamics (Lévy flight) [19] has been found. In random-walk displacement in Brownian motion grows only in proportion to the square root of time. However, the displacement in Lévy flights grows faster than Brownian motion, as just observed for component B.

The smaller value of  $d_w$  of component B than A can also be explained by the contribution of the small  $d_w$  value of Lévy flight dynamics. As pointed out by Shlesinger *et al.* [19], the sums of the displacement are dominated by their largest terms, hence by rare intermittent events. This feature is important for an understanding of the mechanism of the reproducibility of dynamics in limited time simulation. The difference between the runs (I) and (II) can be attributed to such characteristics of the cooperative jumps.

Comparison of component A and B reveals that without such accelerated dynamics, the walker cannot escape from the nearest neighbor region, because the corresponding backward jump would follow with a high probability in the single jump mechanism. That is, a particle jumping within a local network can switch from time to time to a motion along a global network by forward correlated jumps caused by the cooperative motion.

### Mixed Alkali Effect

In alkali silicate glasses, transport coefficients such as self-diffusion coefficients, markedly fall when single alkali ion is mixed with other alkali ions; this phenomenon is referred to as the "mixed alkali effect" [20, 21]. Interception of the jump path among the unlike alkali ion sites has been shown by means of the van Hove function (distinct part) to occur in the mixed alkali glass [22, 23]. The interception is characteristic of the glass where the relaxation time of motion of alkali metal ion is much shorter than that of the (silicate) frame. The "dynamic structure model" [24] is one of the recent models for explaining the mixed alkali effect where the site memory is assumed. However, the model does not describe the detail of the jump paths and the cooperative motion of atoms, which is found to play an important role in determining transport coefficients both in the pure and mixed alkali glasses.

Averaged positions of Li and K ions every 0.4 ps during 16 ps at 800 K (near the glass transition temperature) are shown in Fig. 6 (b).

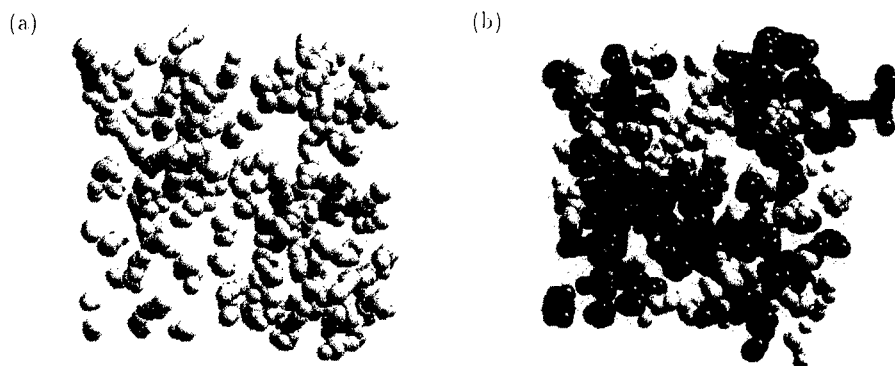


Figure 6: (a) Jump paths for Li during 16 ps within a basic cell for  $\text{Li}_2\text{SiO}_3$  at 700 K. All positions averaged for every 0.4 ps are shown. (b) Jump paths for Li and K during 16 ps within a basic cell for  $(\text{Li,K})\text{SiO}_3$  at 800 K. All positions averaged for every 0.4 ps are shown for Li and K. (Li: white, K: gray).

Each kind of alkali metal ion clearly shows an independent path, which indicates the interception of the mutual jump paths.

The fractal dimensions listed in Table II were calculated for the paths shown in Fig. 6(a) and (b) and from those for  $\text{K}_2\text{SiO}_3$ . The fractal dimension values  $d_f$  obtained for the 0.7-2.0 Å region were less than 1 in every case. The value  $d_{fc}$  decreases on mixing owing to the interception of the mutual path. This explains the change of dynamics in long time behavior.

We have also calculated the fractal dimension of random walk during a 16 ps run of each system. The values for larger than 2 imply a large back-correlation probability. The probabilities for Li and K ions in the mixture are larger than those in the pure systems. This fact contributes to the mixed alkali effect, although the contribution of both single and cooperative jumps are contained in the result.

The Haven ratio is defined as the ratio of the tracer diffusion coefficient to that of the bulk which is calculated from the electric conductivity by the Nernst-Einstein relation. In several mixed alkali systems, the Haven ratio is known to reach a maximum for a composition near the conductivity maximum [26, 27]. This was attributed to a decreased



back-correlation probability on mixing based on a single-jump mechanism, which is, however, opposite to the actual situation, as stated above.

Table I (a) shows that in the mixed system the number ratio of single jumps to cooperative jumps is larger than that in the pure systems. Table I (b) shows that the contribution of the cooperative motion to the total square displacement is quite large. That is, the main mechanism to cause the displacement is cooperative motion and the contribution of the cooperative motion in the mixed system is smaller than in the pure systems.

Table II: (a) Fractal dimension of jump path ( $d_f$ ) and fractal dimension of clustering  $d_{fc}$ . (b) Fractal dimension of random walk,  $d_w$ .

(a)					
system	T(K)	$d_f$ Li	$d_f$ K	$d_{fc}$ Li	$d_{fc}$ K
Li <sub>2</sub> SiO <sub>3</sub>	700	0.22		2.98	
(Li,K)SiO <sub>3</sub>	800	0.31	0.29	2.47	2.72
	700	0.24	0.40	2.21	2.50
K <sub>2</sub> SiO <sub>3</sub>	700		0.95		2.78
(b)					
system	T(K)	$d_w$			
Li <sub>2</sub> SiO <sub>3</sub>	1673	1.77			
	1173	1.92			
	973	2.61			
	700	2.71			
(Li,K)SiO <sub>3</sub>	2000	1.99	1.86		
	800	2.94	2.75		
	700	3.25	2.94		
	700		2.31		

The tracer and bulk velocity autocorrelation functions of the pure and mixed systems at 700 K are examined. The bulk velocity correlation function has been found to have larger and longer oscillation than those for the tracer function. Such a large and long oscillation indicates highly correlated motion of conducting ions, as argued for the fast ion conductors [28]. The amplitude of the oscillation in the bulk correlation functions becomes larger in the mixture than in the pure salts. On the other hand, the change in the tracer correlation function on mixing is relatively small. The result means that interception of the jump paths in the mixture yields larger effect on a collective motion than on a single ion motion.

These findings in the functions are related to the Haven ratio through the following relations if the long time limit is taken.

$$D^t(\nu) = \frac{1}{zN} \int_0^\infty \left( \sum_{i=1}^N v_i(t) \cdot v_i(0) \right) \exp(i2\pi\nu t) dt, \quad (6)$$

$$D^b(\nu) = \frac{1}{zN} \int_0^\infty \left( \sum_{i=1}^N v_i(t) \cdot \sum_{j=1}^N v_j(0) \right) \exp(i2\pi\nu t) dt, \quad (7)$$

where  $z$  is the dimensionality,  $N$  the number of conducting ions and  $\nu$  the frequency. The Haven ratio is equal to  $D^t(0)/D^b(0)$ . These results are consistent with the changes in Table I.

It should be noted that, without cooperative motion, the jump motion could not have large contribution to diffusion or conduction, because the corresponding backward jump would follow with a high probability in the case of the single jumps. Long time behavior is mainly determined by the cooperative jumps. In other words, diffusion and conduction in the pure systems occur with higher efficiency by cooperative jumps than those in the mixed system.

## CONCLUSIONS

A molecular dynamics simulation (MD) of lithium metasilicate glass ( $\text{Li}_2\text{SiO}_3$ ) has been performed. In a density correlation function (self-part) for each atom, we have observed  $\beta$  and  $\alpha$  (1 and 2)-relaxation following an exponential decay by vibrational motion during  $\sim 1$  ns. Oscillation is found in the second ( $\beta$ -relaxation) region of the function. The oscillation is clearer for O and Si than for Li. Namely, in a strong structure an oscillating process is dominant, while in a fragile structure, the relaxation process is dominant. Both the  $\beta$ -relaxation and the oscillation are found to be due to the correlated motion in the same time and space regions. The slower relaxation ( $\alpha$ 1-relaxation) can be well fitted to a stretched exponential form,  $F_s(\mathbf{k}, t) = A \exp(-(t/\tau)^\beta)$ . The small value of  $\beta$  ( $< 1$ ) comes from the waiting time distribution of the jump motions. The large back correlation probability of the jump in the locally low dimensional path also causes the delay of the decay. The relaxation time  $\tau_{\mathbf{k}}$  behaves as  $k^{-n}$  with a larger slope for Si and O than for Li. The value  $n$  is related to the fractal dimension of space in the system. The value of  $n$  smaller than 2 means contribution of the component with accelerated dynamics. The component moves longer than the nearest neighbor distance by the cooperative jump motion and the slowest relaxation ( $\alpha$ 2-relaxation) is mainly characterized by the component.

That is, fractal dimension of the path and of random walk, cooperative motion of the particles as well as the waiting time distribution of the jump determine the behavior of relaxation processes.

The anomalous increase in the Haven ratio in the mixed alkali system can be accounted for by the decreased contribution of the cooperative jumps to the bulk diffusion coefficients. That is, the cooperative jumps are more affected by the interception of the jump paths than the single jumps are. Therefore, fractal dimension of path and random walk and the cooperative motion of like ions play an important role in the mixed alkali effect.

## ACKNOWLEDGEMENTS

The computation in this work has been done using the HITAC M-680 and S-820 computers at the Institute for Molecular Science at Okazaki and FACOM VPP500 computer at the Institute for Solid State Physics, University of Tokyo. The cpu time made available is gratefully acknowledged.

This study was supported by the Original Industrial Technology R & D Promotion Program from the New Energy and Industrial Technology Development Organization (NEDO) of Japan.

## REFERENCES

- [1] C. A. Angell, J. Phys. Chem. Solids, **49**, 863 (1988).
- [2] J. Habasaki, I. Okada and Y. Hiwatari, Phys. Rev. E, **52**, 2681 (1995).
- [3] J. Habasaki and I. Okada, Molec. Simul., **9**, 319 (1992).
- [4] J. Habasaki and I. Okada, Molec. Simul., **8**, 179 (1992).
- [5] J. Habasaki, I. Okada and Y. Hiwatari, Molec. Simul., **9**, 49 (1992).
- [6] J. Habasaki, Molec. Phys., **70**, 513 (1990).
- [7] J. Habasaki, I. Okada and Y. Hiwatari, Taniguchi International Symposium XIII, Springer Series in Solid State Science 103, 'Molecular Dynamics Simulations', Edited by F. Yonezawa, p.98 (1992).

- [8] Y. Ida, *Phys. Earth Planet Interiors*, **13**, 97 (1976).
- [9] M. Tatsumisago, T. Minami and M. Tanaka, *Yogyo-Kyokai-Shi*, **93**, 581 (1985).
- [10] A. P. Sokolov, E. Rössler, A. Kisliuk and D. Quitmann, *Phys. Rev. Lett.*, **71**, 2062 (1993).
- [11] G. Williams and D. C. Watts, *Trans. Faraday Soc.*, **66**, 80 (1970).
- [12] H. Miyagawa, Y. Hiwatari, B. Bernu and J. P. Hansen, *J. Chem. Phys.*, **88**, 3879 (1988).
- [13] Y. Hiwatari, H. Miyagawa and T. Odagaki, *Solid State Ionics* **47**, 179 (1991).
- [14] J. Habasaki, I. Okada and Y. Hiwatari, *J. Non-Cryst. Solids*, in press.
- [15] S. Halvin and D. Ben-Avraham, *Advances in Phys.*, **36**, 695 (1987).
- [16] G. N. Greaves, *J. Non-Cryst. Solids*, **71**, 203 (1985).
- [17] J. Habasaki, I. Okada and Y. Hiwatari, submitted to *Phys. Rev. B*.
- [18] S. Alexander and R. Orbach, *J. Phys. (Paris) Lett.* **43**, L625 (1982).
- [19] M. F. Shlesinger, G. M. Zaslavsky and J. Klafter, *Nature*, **363**, (1993); J. Klafter, M. F. Shledinger, G. Zumofen, *Physics Today*, **February 1996**, 33.
- [20] D. E. Day, *J. Non-Crystal. Solids*, **21**, 343 (1976).
- [21] M. D. Ingram, *Phys. Chem. Glasses* **28**, (1987) 215.
- [22] J. Habasaki, I. Okada and Y. Hiwatari, *J. Non-Cryst. Solids*, **183**, 12 (1995).
- [23] S. Balasubramanian and K. J. Rao, *J. Phys. Chem.*, **97**, 8835 (1993); *J. Non-Cryst. Solids*, **181**, 157 (1995).
- [24] P. Maass, A. Bunde and M. D. Ingram, *Phys. Rev. Lett.*, **68**, 3064 (1992); A. Bunde, M. D. Ingram and P. Maass, *J. Non-cryst. Solids*, **172-174**, 1222 (1994).
- [25] K. Compaan and Y. Haven, *Trans. Faraday Soc.*, **52**, 786 (1956); **54**, 1498 (1958).
- [26] R. Terai, *J. Non-Cryst. Solids*, **6**, 121 (1971).
- [27] H. Jain, N. L. Peterson and H. L. Downing, *J. Non-Cryst. Solids*, **55**, 283 (1983).
- [28] H. L. Tuller, D. P. Button and D. R. Uhlmann, *J. Non-Crystl. Solids*, **40**, 93 (1980).

**Part II**

**Relaxation Dynamics of Glasses  
and Glass Formers**

## Dynamical heterogeneities in glass-forming materials

A. HEUER, S.C. KUEBLER, U. TRACHT, H.W. SPIESS

Max-Planck-Institut für Polymerforschung, Ackermannweg 10, D-55128 Mainz, Germany

K. OKUN

Institut für Physik, Johannes Gutenberg Universität Mainz, Staudinger Weg 7, D-55099 Mainz

### ABSTRACT

Cooperative dynamics around the glass transition leads to complex motional behavior of the individual molecules, resulting in non-exponential relaxation. The nature of this non-exponentiality is clarified theoretically as well as experimentally. The non-exponentiality may be due to heterogeneous relaxation (superposition of exponential processes with different rate constants) or homogeneous relaxation (identical intrinsically non-exponential processes). A precise definition of both limits is given. It is shown that the type of relaxation, i.e. to which degree heterogeneous and homogeneous contributions are present, reflects geometrical properties of the dynamics. The heterogeneous contribution can be further classified according to the timescale of fluctuations within the underlying distribution of relaxation rates, thereby introducing the concept of the rate memory. Determination of the type of relaxation and the rate memory essentially boils down to analysing the properties of multi-time correlation functions. Experimentally they are accessible by multidimensional NMR methods. Alternatively, they can be directly obtained from computer simulations. In order to clarify these concepts, the dynamics of polymers above the glass transition is analysed experimentally as well as numerically. The rotational dynamics of polymer segments turns out to be mainly heterogeneous with only small homogeneous contributions. Interestingly, the fluctuations within the heterogeneous distribution occur on the same timescale as the reorientation process itself.

### INTRODUCTION

For temperatures close to the glass transition the relaxation of most glass-forming materials is strongly non-exponential in time[1]. This reflects the complexity of the highly cooperative dynamics. Recently it was shown that it is possible to obtain additional information about the nature of the dynamics beyond the time-scale and the degree of non-exponentiality without referring to specific models.

One aspect refers the long discussed problem of heterogeneous versus homogeneous relaxation, see e.g. [2, 3, 4, 5]. It will be denoted *type of relaxation*. In the first limit all relaxators display exponential relaxation with different rates, in the second limit identical intrinsic non-exponential relaxation. Of course, in general one expects a superposition of

both contributions. An intuitive sketch for the example of one-dimensional translational dynamics is shown in Fig.1. Homogeneous contributions occur, e.g., by correlated back-and-forth jumps (see theory section).

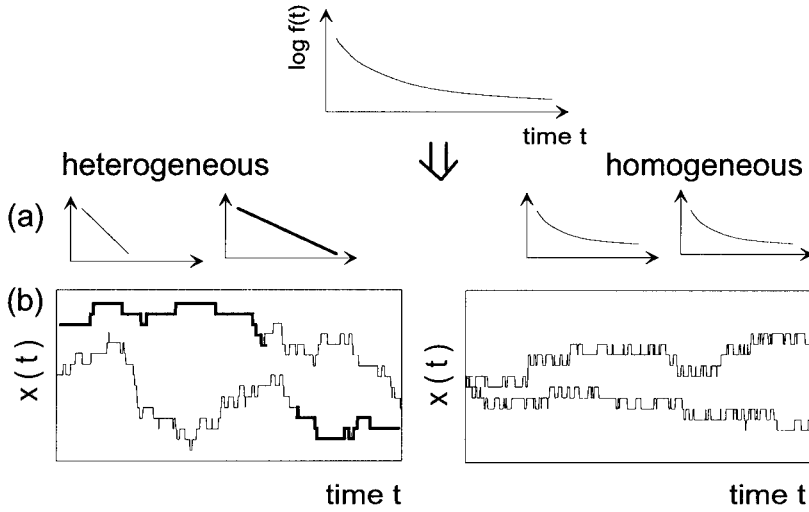


Figure 1: (a) Sketch of the limits of heterogeneous and homogeneous relaxation (heterogeneous: different exponential processes, homogeneous: identical non-exponential processes). The slow processes in the heterogeneous limit correspond to the thicker line. In both limits the simple two-time relaxation functions  $f(t)$  of the whole ensemble are identical. (b) Visualisation of both limits for the example of one-dimensional dynamics. Left: superposition of a slow (thick line) and a fast particle both performing a one-dimensional random walk. Exchange processes between a fast and a slow rate, also indicated, do not change the type of relaxation! Right: identical one-dimensional dynamics with a strong preference for correlated back-and-forth jumps giving rise to homogeneous relaxation.

In case the relaxation contains heterogeneous contributions it is possible to distinguish fast and slow segments (from now on we use the "polymer language"). Then one can ask the question on which timescales a fast segment becomes slow and vice versa, see Fig.2. In recent theoretical work this property has been quantified in terms of a *rate memory parameter* [7], see also [8],[9].

In general, information about the type of relaxation and the rate memory can be obtained from analysis of multi-time correlation functions. Experimentally they are accessible by multidimensional NMR-experiments [10]. This technique has been applied to both, amorphous polymers [4, 5, 9] and low molar mass systems [11]. Very recently, the information about the rate memory has also been obtained by fluorescence spectroscopy [12] and spectral hole burning in dielectric relaxation [13].

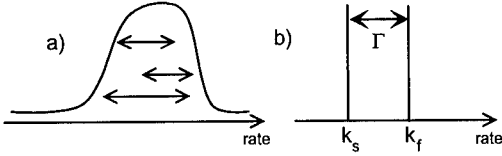


Figure 2: (a) Sketch of fluctuations within the heterogeneous rate distribution. (b) Sketch of a bimodal distribution of rates with an exchange rate  $\Gamma$ .

The purpose of this paper is three-fold. First, it summarizes the theoretical basis of the concepts of the type of relaxation and the rate memory. Second, application of these new concepts is exemplified for multidimensional NMR experiments as well as for computer simulations of a model polymer. Third, a rather detailed picture about the dynamics of polymers is extracted from the experimental and numerical results. Among others it is clarified how freezing influences the dynamics of polymers.

## THEORY

### General

The translational dynamics of polymers is often analysed in terms of the incoherent scattering function

$$p(0; \Delta t_{01}) \equiv \langle \cos \vec{q}(\vec{r}(t_1) - \vec{r}(t_0)) \rangle. \quad (1)$$

$\vec{r}(t_i)$  is the position of a segment at time  $t_i$ , the brackets denote the ensemble average,  $\Delta t_{ij} = t_j - t_i$ , and  $\vec{q}$  denotes a wave vector, see, e.g. [14]. Furthermore we introduce the abbreviation  $\Delta \vec{r}_{ij} \equiv \vec{r}(t_i) - \vec{r}(t_j)$ . Here the properties of the system are correlated at two different times. In general  $p(0; \Delta t_{01})$  displays non-exponential relaxation. Intuitively,  $p(0; \Delta t_{01})$  denotes the fraction of particles moving a distance less than  $2\pi/q$  during  $\Delta t_{01}$ . The index 0 indicates that on average only those segments contribute which are quasi-static, i.e.  $|\vec{r}(t_1) - \vec{r}(t_0)| \ll 2\pi/q$ . In case of rotational dynamics the analogous correlation function, as determined by multidimensional NMR echo methods, is given by

$$p(0; \Delta t_{01}) \equiv \langle \cos t_p(\omega(t_1) - \omega(t_0)) \rangle. \quad (2)$$

where  $\omega(t_i)$  denotes the Larmor frequency at time  $t_i$  and  $t_p$  is an experimentally adjustable time-scale fixing the angular sensitivity of the experiment [10]. The subsequent results are presented for translational dynamics but can be directly transferred to rotational dynamics. This reflects the general analogy between scattering and two-dimensional exchange NMR [10].

For later purposes we also define the three-time correlation function

$$p(0, 0; \Delta t_{01}, \Delta t_{12}) \equiv \langle \cos \vec{q} \Delta \vec{r}_{01} \cos \vec{q} \Delta \vec{r}_{12} \rangle, \quad (3)$$

and the four-time correlation function

$$p(0, ?, 0; \Delta t_{01}, \Delta t_{12}, \Delta t_{23}) \equiv \langle \cos \vec{q} \Delta \vec{r}_{01} \cos \vec{q} \Delta \vec{r}_{23} \rangle. \quad (4)$$

The '?' indicates that the correlation function is not sensitive on the dynamics during the time interval  $\Delta t_{12}$ .

Experimentally also the multi-time correlation functions introduced above can be measured via multidimensional NMR echo methods.

#### Type of relaxation

From a theoretical point of view the type of relaxation can be defined on the basis of the properties of the conditional probability  $\mathcal{P}_3(\hat{q}\Delta\vec{r}_{01}, \Delta t_{01} | \hat{q}\Delta\vec{r}_{12}, \Delta t_{12})$  [6]. The structure of this probability function reflects that the dynamics is projected on the direction of the wave vector  $\vec{q}$ . It describes the probability for a change in position along  $\vec{q}$  by  $\hat{q}\Delta\vec{r}_{12}$  during  $\Delta t_{12}$  under the condition that the segment displacement during  $\Delta t_{01}$  was  $\hat{q}\Delta\vec{r}_{01}$ . The crucial step of our analysis is to separately consider the dependence on the *distance*  $|\hat{q}\Delta\vec{r}_{01}|$  and the *direction*  $\hat{q}\Delta\vec{r}_{01} / |\hat{q}\Delta\vec{r}_{01}|$ . Both quantities can be treated independently of each other. We define the dependence on the distance  $|\hat{q}\Delta\vec{r}_{01}|$  as the *heterogeneous* and the dependence on the direction  $\hat{q}\Delta\vec{r}_{01} / |\hat{q}\Delta\vec{r}_{01}|$  as the *homogeneous* contribution. This definition agrees with the intuitive picture of Fig.1. In the heterogeneous limit fast segments will be fast during both time intervals which directly implies a correlation between  $|\hat{q}\Delta\vec{r}_{12}|$  and  $|\hat{q}\Delta\vec{r}_{01}|$ . This correlation totally vanishes in the purely homogeneous limit. There the non-exponentiality is due to the correlation of the direction of motion during  $\Delta t_{12}$  with the direction during the previous time interval. This dependence is typically related to the occurrence of correlated back-and-forthjumps. A more detailed discussion can be found in Ref.[6].

It is crucial that fluctuations within the heterogeneous distribution do not affect the type of relaxation. Although the time-averaged relaxation of a single particle on the left side of Fig.1 is non-exponential due to the fluctuations between the fast and the slow state, its type of relaxation remains purely heterogeneous. The underlying reason is that according to the present definition homogeneous contributions are exclusively related to geometric correlations of the dynamics. There is no trivial "homogenisation" due to fluctuations of rates. Rather these fluctuations will be expressed in terms of the rate memory, see below.

Simple conditions can be formulated for both limits in terms of two-time and three-time correlation functions [6]. A condition for the homogeneous limit can be formulated as

$$p(0, 0; \Delta t_{01}, \Delta t_{12}) / p(0; \Delta t_{01}) = p(0; \Delta t_{12}). \quad (5)$$

Intuitively this relation means that during  $\Delta t_{12}$  the dynamics of the subensemble of segments with only little motion during  $\Delta t_{01}$  is identical to the dynamics of the full ensemble. This implies a lack of heterogeneous contributions.

Alternatively, a strict condition for the heterogeneous limit reads

$$p(0; \Delta t_{01} + \Delta t_{12}) = p(0, 0; \Delta t_{01}, \Delta t_{12}). \quad (6)$$

Also for this relation a simple intuitive interpretation can be formulated. Every segment which significantly moves during  $\Delta t_{01}$  and moves back to the original position during  $\Delta t_{12}$  contributes to  $p(0; \Delta t_{01} + \Delta t_{12})$  but not to  $p(0, 0; \Delta t_{01}, \Delta t_{12})$ . Hence both correlation functions are only identical if no tendency for back-and-forthjumps is present.



In general one expects (using now  $t$  instead of  $\Delta t$ ) [6]

$$p(0; t/2)^2 \leq p(0, 0; t/2, t/2) \leq p(0; t). \quad (7)$$

In case of purely homogeneous relaxation the first two functions are identical, whereas for purely heterogeneous relaxation the second and the third function are identical. Hence comparison of the three functions directly allows to judge whether the type of relaxation is more homogeneous or heterogeneous. As will be seen below the type of relaxation may depend on the length scale  $2\pi/q$ .

Finally we mention that  $p(0; t)$  and  $p(0, 0; t/2, t/2)$  can be analytically calculated in the framework of the Rouse model which describes the dynamics of sufficiently short polymer chains [15]. One obtains

$$p(0; t) = \exp(-\sqrt{t/\tau_0(q)}) \quad (8)$$

which is well-known from the polymer literature and

$$p(0, 0; t/2, t/2) = (1/2) \left[ \exp\left(-\sqrt{t/\tau_0(q)}\right) + \exp\left(-(2\sqrt{2}-1)\sqrt{t/\tau_0(q)}\right) \right]. \quad (9)$$

with some temperature and  $q$ -dependent timescale  $\tau_0(q)$  which depends on the local mobility as well as temperature [15, 6].

#### Rate memory

Assuming the existence of some heterogeneous contribution to the non-exponential relaxation, the relaxation rate of a segment may fluctuate within the heterogeneous rate distribution [4, 5], see also Fig.2. The timescale of fluctuations can be obtained from comparing the relaxation rates of a segment at two different times. The definition of a rate itself involves the determination of the position at two different times. Hence in total one needs a four-time correlation function with four successive times  $t_0, \dots, t_3$ , corresponding to three successive time intervals.

The correlation function  $p(0, ?, 0; \Delta t_{01}, \Delta t_{12}, \Delta t_{23})$  introduced above contains the relevant information. It denotes the fraction of segments which do not move significantly during the first and the third time interval. The properties of this correlation function have been extensively analysed in [7]. Here we summarize the main results.

The correlation function can be interpreted such that during  $\Delta t_{01}$  a slow subensemble is selected by a filter which then may evolve during  $\Delta t_{12}$ . Afterwards again the slow part of the evolved subensemble is selected. For reasons of simplicity we set  $\Delta t_{01} = \Delta t_{23}$ . For  $\Delta t_{12} \rightarrow 0$  the subensemble does not have time to equilibrate its rate distribution. Hence the whole subensemble will pass the final filter during  $\Delta t_{23}$ . In contrast, for  $\Delta t_{12} \rightarrow \infty$  the dynamical properties of the selected slow subensemble have approached equilibrium so that the corresponding part of the slow subensemble will be filtered out during  $\Delta t_{23}$ , hence reducing the value of the correlation function. The timescale of fluctuations can then be related to the time  $\Delta t_{12}$  for which the correlation function displays a crossover between both limiting values.

For the simplest non-trivial model of a bimodal and equal distribution of relaxation rates three rate parameters are involved: the slow and fast relaxation rates  $k_s$  and  $k_f$  and the exchange rate  $\Gamma$  between both states. This model is sketched in Fig.2b. For this model all correlation functions can be calculated analytically. The relaxation of this model, as probed by  $p(0;t)$ , is biexponential with *effective* rate constants  $\kappa_s$  and  $\kappa_f$ . For  $\Gamma \neq 0$  they are different to  $k_s$  and  $k_f$ .  $\kappa_s$  is approximately given by  $k_s + \Gamma$ . It is enhanced as compared to  $k_s$  since the exchange process to the fast state and the subsequent fast relaxation opens another relaxation channel. The relation  $\kappa_s \approx k_s + \Gamma$  implies that the exchange rate  $\Gamma$  cannot be larger than the effective slow rate  $\kappa_s$ .

Since the value of  $\Gamma$  is only of interest in comparison to the other timescales of the system one may introduce the dimensionless rate memory parameter

$$Q \equiv \kappa_s/\Gamma \approx 1 + k_s/\Gamma \geq 1. \quad (10)$$

The value of  $\kappa_s$  may be obtained from a fit of the two-time correlation function  $p(0;t)$  and the value of  $\Gamma$  from including the additional information of the four-time correlation function [5]. Hence  $Q$  can be obtained from combining the information from  $p(0;t)$  and  $p(0,?,0;\Delta t_{01},\Delta t_{12},\Delta t_{23})$ .

In general one has a continuous rather than a bimodal distribution of relaxation rates. From a theoretical point of view it may seem hopeless to quantify the fluctuations for the general case. However, it has been shown that even for a continuous rate distribution a single rate memory parameter  $Q \geq 1$  can be defined, which in analogy to the bimodal case can be basically extracted from knowledge of  $p(0;t)$  and  $p(0,?,0;\Delta t_{01},\Delta t_{12},\Delta t_{23})$  [7]. In the limit of a bimodal distribution it reduces to  $Q = \kappa_s/\Gamma$ . The general interpretation is that after  $Q$  relaxation processes the present dynamical state of a segment is uncorrelated to its initial state.

For the determination of  $Q$  we define

$$\frac{F(\Delta t_{01}, \Delta t_{12}, \Delta t_{23}) \equiv p(0, 0, 0; \Delta t_{01}, \Delta t_{12}, \Delta t_{23}) + [p(0; \Delta t_{01}) - p(0, 0; \Delta t_{01}, \Delta t_{12})][p(0; \Delta t_{23}) - p(0, 0; \Delta t_{12}, \Delta t_{23})]}{1 - p(0; \Delta t_{12})} \quad (11)$$

where the correlation function  $p(0, 0, 0; \Delta t_{01}, \Delta t_{12}, \Delta t_{23})$  is defined in analogy to  $p(0, 0; \Delta t_{01}, \Delta t_{12})$  as

$$p(0, 0, 0; \Delta t_{01}, \Delta t_{12}, \Delta t_{23}) \equiv \langle \cos \vec{q} \Delta \vec{r}_{01} \cos \vec{q} \Delta \vec{r}_{12} \cos \vec{q} \Delta \vec{r}_{23} \rangle. \quad (12)$$

It can be shown that the rate memory parameter  $Q$  fulfills to a very good approximation the relation

$$p(0, ?, 0; \Delta t_{01}, \Delta t_{12}, \Delta t_{23}) \approx F(\Delta t_{01}, \Delta t_{12}/Q, \Delta t_{23}). \quad (13)$$

Since all correlation functions entering Eq.13 are accessible by simulations or NMR experiments Eq.13 allows a straightforward determination of the rate memory parameter  $Q$ . In case that the relaxation is purely heterogeneous the definition of  $F$  can be further simplified by using relations like Eq.6.

In general the rate memory parameter  $Q$  may depend on the wave vector  $q$ . For reasons of simplicity let us assume that regions of fast dynamics and slow dynamics have a spatial extension of  $2\pi/q_{crit}$ . Then for  $q < q_{crit}$  a system experiences fast as well as slow environments, yielding  $Q = 1$  (of course, for  $q \ll 1$  the relaxation becomes exponential). In the opposite limit  $q > q_{crit}$  an initially fast(slow) segment is still fast(slow) after moving the short distance  $2\pi/q$  which, in our language, implies  $Q > 1$ . Analogously, in the rotational case one expects a dependence of  $Q$  on the time  $t_p$ , hence on the angular sensitivity of the filter.

## EXPERIMENTAL RESULTS

To analyze homogeneous and heterogeneous contributions to the  $\alpha$ -relaxation, two-time and three-time correlation functions have been measured for polystyrene (PS- $d_3$ ) isotopically labeled at the main chain. The temperature was 389 K ( $T_g + 13$  K). The time constant  $t_p$  was  $30\mu s$ . Fig.3 displays the three functions  $[p(0; t/2)]^2$ ,  $p(0, 0; t/2, t/2)$ , and  $p(0; t)$ . The

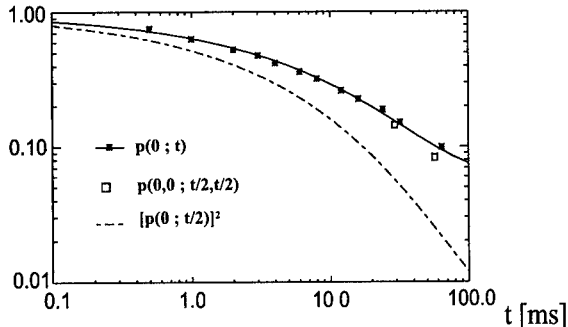


Figure 3: *Determination of the type of relaxation for PS from NMR exchange experiments above the glass transition.*

solid lines for  $[p(0; t/2)]^2$  and  $p(0; t)$  were determined on the basis of a fit of the experimental  $p(0; t)$  (stars) with a stretched exponential  $\exp(-(t/\tau_0)^\beta)$ , yielding  $\tau_0 = 6.5$  ms and  $\beta = 0.45$ . The experimental data for  $p(0, 0; t/2, t/2)$  have been determined by the 4D echo [5] for  $t = 4.3\tau_0$  and  $t = 8.7\tau_0$ . Due to the dependence of the absolute signal intensity on the employed pulse sequence a straightforward normalization had to be performed [9].

The close agreement between  $p(0, 0; t/2, t/2)$  and  $p(0; t)$  indicates that the relaxation is mainly heterogeneous. Hence the spatial heterogeneity in amorphous polymers directly translates into dynamic heterogeneities as observed by the present method. As discussed in Ref. [9] the deviations from the purely heterogeneous case can be explained by a small fraction of correlated back- and forthjumps.

The determination of the rate memory is exemplified for PVAc selectively labeled with  $^{13}C$  at the carbonyl site, which is a convenient sensor of structural relaxation. In Fig.4

$F_2(t) \equiv p(0; t)$  and  $F_4(t) = p(0, ?, 0; t_{m0}, t, t_{m0}) / p(0, ?, 0; t_{m0}, t = 0, t_{m0})$  are shown for measurements at  $T = 313$  K ( $T_g + 13$  K). In all cases the evolution time  $t_p$  was set to  $180 \mu\text{s}$ .

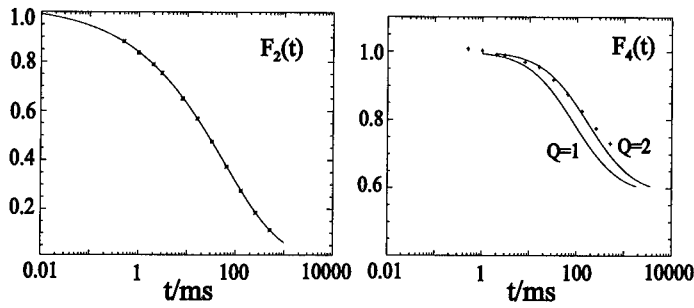


Figure 4: The results of the NMR echo experiments for PVAc above the glass transition: (a) two-time correlation function  $F_2(t)$  and (b) normalized four-time correlation function  $F_4(t)$ . The solid lines in (a) represent a fitted stretched exponential, the solid lines in (b) the theoretical curves for both indicated values of the rate memory parameter  $Q$ .

The two-time correlation function recorded as a function of  $t_m$  as shown in Fig.4a has been fitted with a Kohlrausch parameter  $\beta = 0.39$  and a relaxation constant of  $\tau_0 = 60.5$  ms. Comparison between  $F_4(t)$  and the theoretical curves yields  $Q \approx 2$ . After two relaxation processes a segment has forgotten its dynamic history. The strong fluctuations among the relaxation rate distribution quantitatively agree with results obtained previously for PVAc at a somewhat higher temperature ( $T_g + 20$ K) [5] and qualitatively with the other polymeric systems PS [9] and PMMA [16] as well as the low molecular glass-former ortho-terphenyl [11] where the results could be explained with  $Q = 1$ . Interestingly, only for PVAc a value of  $Q$  significantly larger than 1 has been measured by NMR until now (see, however, Ref.[12] for the photobleaching experiment on ortho-terphenyl).

## NUMERICAL RESULTS

### The bond fluctuation model

The bond fluctuation model has been proposed as a polymer lattice model to represent the dynamics of polymer melts on timescales longer than the microscopic timescale [17, 18]. An effective bond can be interpreted as some kind of Kuhn segment. Due to an interplay of entropic and energetic effects the system tends to be frustrated at low temperatures, resulting in a glass transition. From a fit of typical relaxation times to a Vogel-Fulcher law the Vogel-Fulcher temperature, which is supposed to be slightly lower than the glass transition temperature  $T_g$ , can be estimated to lie between 0.12 and 0.13 in temperature units of the energy scale of the bond fluctuation model, see [18, 19] where also details of the bond fluctuation model and the definition of the energy and distance units can be found. The lowest temperature used for the present simulations will be  $T = 0.19$  and hence still

much above the glass transition temperature  $T_g$ . The maximum of the structure factor is for  $q = 3$  in units of the lattice. Larger values cannot be simulated because then the dynamics starts to be dominated by lattice effects. For a detailed listing of the parameters of the simulation, see [6].

### Results

In Fig.5a  $p(0;t)$ ,  $p(0,0;t/2,t/2)$ , and  $p(0;t/2)^2$  are shown for different values of the wave vector  $q$  at the temperature  $T = 0.25$ . Naturally, the timescale of relaxation strongly de-

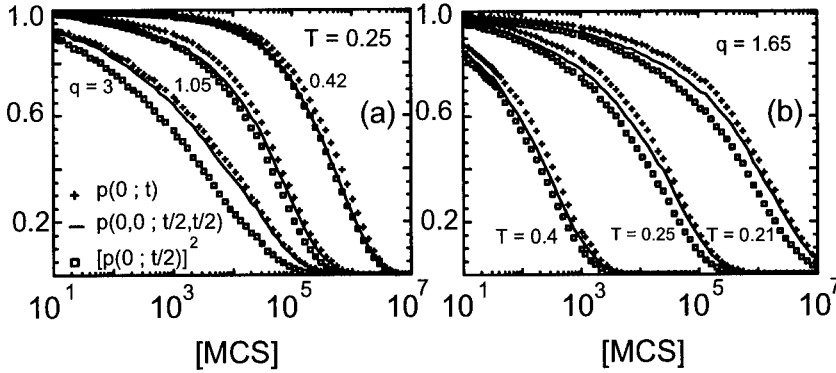


Figure 5: The correlation functions  $p(0;t)$ ,  $p(0,0;t/2,t/2)$ , and  $p(0;t/2)^2$  for (a) different wave vectors  $q$  at temperature  $T = 0.25$  and (b) different temperatures for  $q = 1.65$ . [MCS] means Monte Carlo Steps.

pend on the lengthscale. From comparing the three correlation functions one can clearly see that for  $q = 0.42$  the dynamics is mainly homogeneous because  $[p(0;t/2)]^2 \approx p(0,0;t/2,t/2)$  except for very long times where heterogeneous contributions become visible. Even quantitatively this behavior is identical to the predictions of the Rouse model as can be checked from analysis of Eqs.8,9. However, when going to shorter lengthscales the behavior dramatically changes. For  $q = 3.0$  the dynamics is mainly heterogeneous.

In Fig.5b the same analysis is performed for constant  $q = 1.65$  but for different temperatures. For  $T = 0.21$  the dynamics is significantly more heterogeneous than for  $T = 0.4$ . Hence temperature has a pronounced influence on the degree of heterogeneity and only for the highest temperatures one can expect a very good agreement with the predictions of the Rouse model.

We just mention that the sensitivity of this analysis depends on the difference between  $[p(0;t/2)]^2$  and  $p(0;t)$  and hence on the degree of non-exponentiality.

The determination of the rate memory parameter has been performed in analogy to the NMR case. For all temperatures  $T > 0.19$  and all wave vectors  $q < 3$ , i.e. for all wave vectors smaller than the maximum of the structure factor, we obtained  $Q = 1$ .

## DISCUSSION

The present multidimensional NMR experiments probe rotational dynamics whereas the simulation of the fluctuating bond model is sensitive to the translational dynamics. Hence a priori the results presented above are difficult to compare. However, the type of relaxation and the rate memory are very fundamental properties of the dynamics on a local scale and hence should be comparable for rotational and translational dynamics, although a quantitative comparison always has to be performed with great care, see e.g. discussion in Ref.[21]. For a qualitative comparison the rotational behaviour should be related to translational behaviour on length scales significantly smaller than the maximum of the structure factor.

A general advantage of simulations is the possibility of significant changes in temperature and lengthscale. In contrast, the NMR experiments are restricted to a small temperature interval of about 20 K. The reason is that the whole dynamics, on the one hand, has to be faster than the  $T_1$ -relaxation (of the order of seconds) and, on the other hand, slower than the evolution time (several hundred microseconds) [10]. Note that the temperature of the NMR experiments is very close to the glass transition. It is not possible to analyse this temperature regime via computer simulations because the dynamics becomes much too slow.

Analysis of the bond fluctuation model in dependence of lengthscale and temperature indicates a picture of the freezing of a polymer melt which is summarized in Fig.6. Coming

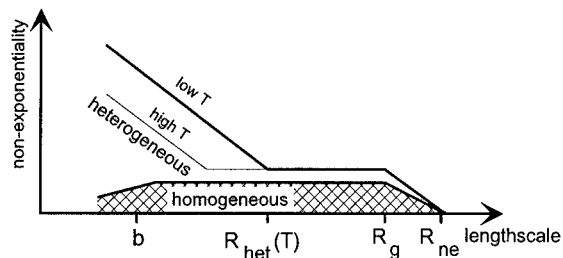


Figure 6: Sketch of the type of relaxation for a polymer melt in dependence of temperature and lengthscale as indicated by the results of the simulations of the fluctuating bond model.  $b$  is the microscopic average segment-segment distance,  $R_g$  the radius of gyration.

from very long lengthscales the first effects of non-exponential relaxation are expected to appear at a lengthscale  $R_{ne}$  somewhat larger than the end-to-end distance. Going further to the radius of gyration both homogeneous and heterogeneous contributions start to increase with the homogeneous contribution much larger than the heterogeneous. Between  $R_g$  and some temperature dependent lengthscale  $R_{het}(T)$  the non-exponentiality as well as the type of relaxation is unchanged. This regime is in quantitative agreement with the Rouse model which only takes into account intramolecular interactions. Going from  $R_{het}(T)$  to

the microscopic lengthscale the dynamical heterogeneities increase. This effect is more pronounced for low temperatures probably because of increasing cooperativity close to the glass transition. Since the heterogenous contributions are related to intermolecular interactions, the local relaxation close to the glass transition is no longer sensitive to the connectivity within a polymer chain.

Like the simulated translational behaviour on very short length scales the rotational dynamics experimentally also turns out to be mostly heterogeneous. Hence for translational as well as rotational dynamics the structural heterogeneities locally translate into dynamical heterogeneities. This supports the idea that fast translational dynamics is connected with fast rotational dynamics [20].

As discussed above, for the translational dynamics one expects some critical lengthscale  $q_{crit}$  such that  $Q > 1$  for  $q > q_{crit}$ . The simulations have shown that  $q_{crit}$  is larger than the maximum of the structure factor, i.e. the inverse lengthscale of typical segment-segment distances  $d_{s-s}$ . In this respect it is interesting that for PVAc one observes  $Q > 1$ . This indicates that the timescale of single rotational processes indeed corresponds to translational lengthscales significantly shorter than  $d_{s-s}$ .

## CONCLUSIONS

We propose a new way to analyse the dynamics of systems displaying non-exponential relaxation. The cooperative multi-particle dynamics results in a very complicated single-particle dynamics which we analyse in terms of its type of relaxation and its rate memory. This information can be interpreted without resorting to any specific model. From a practical point of view this analysis requires the determination of multi-time correlation functions.

One of the beauties of multidimensional NMR is that it allows the determination of all relevant correlation functions. So far unknown information about the type of relaxation and the rate memory became available. The experiments have shown that for all the systems analysed so far the dynamics is mainly heterogeneous with only minor homogeneous contributions and the rate memory is close its theoretical minimum, indicating strong fluctuations within the heterogeneous distribution.

In general, the experimental determination of multi-time correlation functions is very difficult if not impossible. In contrast, they can be easily implemented in all kinds of simulations. The present bond fluctuation model simulation shows that new information can be obtained which is not contained in the analysis of the standard correlation functions. In the present work a closer understanding of the freezing process of polymers became possible.

## Acknowledgement

This work was supported by the DFG (SFB 262). Furthermore we would like to acknowledge helpful discussions with K. Binder, M. Wolfgardt, J. Baschnagel, M. Wilhelm, H. Sillescu, R. Böhmer, and G. Diezemann. U.T. gratefully acknowledges the financial support from the BMBF and the "Stiftung Stipendien-Fonds des Verbandes der Chemischen Industrie".

## References

- [1] J. Jäckle, Rep. Prog. Phys. **49**, 171 (1986).
- [2] R.H. Austin et al., Phys. Rev. Lett. **32**, 403 (1974).
- [3] R. Richert, Chem. Phys. Lett. **216**, 223 (1993).
- [4] K. Schmidt-Rohr and H.W. Spiess, Phys. Rev. Lett. **66**, 3020 (1991).
- [5] A. Heuer, M. Wilhelm, H. Zimmermann, H. W. Spiess, Phys. Rev. Lett. **75**, 2851 (1995).
- [6] A. Heuer, K. Okun, to be printed in J. Chem. Phys. (1997).
- [7] A. Heuer, to be printed in Phys. Rev. E (1997).
- [8] H. Sillescu, J. Chem. Phys. **104**, 4877 (1996).
- [9] S.C. Kuebler, A. Heuer, H.W. Spiess, submitted to Phys. Rev. E.
- [10] K. Schmidt-Rohr, H.W. Spiess, Multidimensional Solid-State NMR and Polymers, Academic Press, London (1994).
- [11] R. Boehmer, G. Hinze, G. Diezemann, B. Geil, H. Sillescu, Europhys. Lett. **36**, 55 (1996).
- [12] M. T. Cicerone and M. D. Ediger, J. Chem. Phys. **103**, 5684 (1995).
- [13] B. Schiener, A. Loidl, R. Böhmer, R.V. Chamberlin, Science **274**, 752 (1996).
- [14] S.W. Lovesley, Theory of Neutron Scattering from Condensed Matter, Oxford Univ. Press, Oxford (1984).
- [15] M. Doi and S. F. Edwards, The Theory of Polymer Dynamics, Oxford Science Publications, Oxford (1986).
- [16] A. Heuer, S.C. Kuebler, U. Tracht, H.W. Spiess, to be printed in Appl. Magn. Res.
- [17] I. Carmesin and K. Kremer, Macromolecules **21**, 2819 (1988).
- [18] K. Binder (Ed.) Monte Carlo and Molecular Dynamics Simulations in Polymer Science, Oxford University Press, New York (1995).
- [19] K. Okun, M. Wolfgardt, J. Baschnagel, K. Binder, to be printed in Macromolecules.
- [20] M.T. Cicerone and M.D. Ediger, J. Chem. Phys. **104**, 7210 (1996).
- [21] I. Chang, F. Fujara, B. Geil, G. Heuberger, T. Mangel, and H. Sillescu, J. Non-Cryst. Solids **172-174** 248 (1994).



## **SLOW DIELECTRIC RELAXATION OF SUPERCOOLED LIQUIDS INVESTIGATED BY NONRESONANT SPECTRAL HOLE BURNING**

R. V. Chamberlin<sup>\*</sup>, B. Schiener<sup>†</sup>, R. Böhmer<sup>‡</sup>

<sup>\*</sup>Department of Physics and Astronomy, Arizona State University, Tempe, AZ 85287-1504

<sup>†</sup>Institut für Festkörperphysik, Technische Hochschule, D-64289 Darmstadt, Germany

<sup>‡</sup>Institut für Physikalische Chemie, Johannes Gutenberg Universität, D-55099 Mainz, Germany

### **ABSTRACT**

When supercooled propylene carbonate and glycerol are subjected to a large-amplitude, low-frequency electric field, a spectral hole develops in their dielectric relaxation that is significantly narrower than their bulk response. This observation of nonresonant spectral hole burning establishes that the non-Debye response is due to a distribution of relaxation times. Refilling of the spectral hole occurs abruptly, indicative of a single recovery rate that corresponds to the peak in the distribution. The general shape of the spectral hole is preserved during recovery, indicating negligible interaction between the degrees of freedom that responded to the field. All relevant features in the behavior can be characterized by a model for independently relaxing domains that are selectively heated by the large oscillation, and which recover via connection to a common thermal bath, with no direct coupling between the domains.

### **INTRODUCTION**

One of the most prominent features in the response of many diverse materials is their slow nonexponential relaxation. Although slow mechanical creep was known to Robert Hooke more than 300 years ago,<sup>1</sup> and similar nonexponential relaxation has been found to occur in thousands of different measurements on hundreds of diverse substances,<sup>2</sup> there is still no widely accepted explanation for the observed behavior. In fact, there is still considerable debate<sup>3-6</sup> about the fundamental source of the spectral broadening: is it intrinsic, where all regions of the sample exhibit similar nonexponential relaxation? or is it due to a heterogeneous distribution of local relaxation times? For supercooled liquids near their calorimetric glass transition temperature  $T_g$ , several studies<sup>7,8</sup> have concluded that heterogeneity occurs on length scales of 1 to 5 nm, yet competing models proposed to describe the slow dynamics have often been based (at least in spirit) on opposite assumptions regarding the nature of the intrinsic local response. Such uncertainty punctuates the need for additional experimental evidence.

Only in the past few years have techniques been developed that can characterize the intrinsic local response of supercooled liquids. These techniques generally utilize a local probe, and a spectral filter, to investigate selected constituents of the net response. A multi-dimensional NMR technique, developed by Schmidt-Rohr, Spiess and co-workers,<sup>9</sup> uses nuclear magnetic moments as the local probe, and a spin-echo sequence as a low-pass filter for selecting slowly rotating molecules for subsequent investigation. Another technique, developed by Cicerone and Ediger,<sup>10</sup> uses dilutely dispersed dye molecules as the local probe, and a photobleaching procedure as a low-pass filter for subsequent investigation of selected slowly rotating probe molecules. Recently<sup>11</sup> we introduced the technique of nonresonant spectral hole burning (NSHB), where a large-amplitude, low-frequency electric field is used to distinguish selected dielectric response for subsequent measurements. Two key advantages of NSHB are that the frequency of the oscillating field provides an easily tuneable

band-pass filter, and that the responding degrees of freedom are used directly as their own local probe.

Observation of spectral hole burning generally requires a heterogeneously broadened spectrum, a strong external perturbation that can modify selected parts of the spectrum, and a resulting "hole" that is persistent enough to allow subsequent measurement of the modified spectrum. Although first observed in magnetic resonance spectroscopy,<sup>12,13</sup> the technique is now most commonly applied to optical resonances utilizing the intense monochromatic beams available from modern lasers. NSHB had not previously been observed, mainly because spectral holes in slow nonresonant response are often difficult to achieve, and not very persistent.

The basic idea of NSHB in supercooled liquids is easiest to picture in a plot of the dielectric loss ( $\epsilon''$ ) as a function of frequency, Fig. 1. On a logarithmic frequency scale, the full-width-at-half-maximum of single relaxation rate (Debye-like) behavior is 1.14 decades wide, whereas observed loss peaks are usually significantly broader. According to the Boltzmann superposition principle, linear macroscopic measurements that do not modify the spectrum of response cannot distinguish between intrinsically broadened local response (Fig. 1A), or a heterogeneous distribution of relaxation times (Fig. 1B). Thus, any direct investigation of the constituents in the net response of a bulk sample requires that the spectrum of response must be modified nonlinearly. Consider an oscillating field at frequency  $\Omega$  with sufficient intensity to shift the responding degrees of freedom to higher frequencies. If energy from the field is absorbed homogeneously (Fig. 1A), the entire spectrum is shifted uniformly to higher frequencies; whereas if energy is absorbed heterogeneously (Fig. 1B), the energy absorbed depends on the local response, and a spectral hole develops. If the absorbed energy simply heated the thermal bath, it would diffuse out of the absorbing region (assuming a diameter of  $< 5$  nm) in less than a nanosecond. Instead we find that local modifications induced by the electric field persist long enough to reveal the heterogeneity in the slow relaxation, and to be observed using time-domain spectroscopy.

## MEASUREMENTS

We measure time-dependent dielectric polarization using a Sawyer-Tower bridge<sup>14</sup> consisting of a parallel-plate sample capacitor and an integrating capacitor connected in series across a computer controlled high-voltage supply. The distance between the sample plates is maintained at  $d=50$   $\mu\text{m}$  using quartz fibers, yielding a nominal empty-cell capacitance of 30 pF. The sample capacitor is immersed in the dielectric liquid, whose temperature is controlled by a closed-cycle refrigeration system to an absolute accuracy of  $\pm 1$  K, with relative stability of  $\pm 3$  mK. A high-impedance amplifier measures changes in voltage across the integrating capacitor, which are proportional to changes in polarization of the sample.

NSHB is measured using a pump-and-probe procedure (Fig. 2) that combines the frequency selectivity of an oscillating field, with the ability to measure the entire spectrum of time-dependent response after a single step in the applied field. The sample is selectively modified by a sinusoidal pump voltage of  $N$  oscillations at frequency  $\Omega$  and amplitude  $V_0$ . After a recovery time  $t_r$ , a probe step of amplitude  $+v$  is applied, yielding the time-dependent polarization of the selectively modified sample,  $P_+^*$ . Unless otherwise noted,  $V_0=900$  V and  $+v=150$  V. The large, but less interesting linear response from the pump voltage is removed by means of a phase-cycling scheme in which an identical pump oscillation and recovery time is followed by a negative probe step  $-v$ , yielding  $P_-^*$ . The difference  $P_+^*-P_-^*$  is proportional to the transient dielectric constant of the sample after it was selectively modified by the pump voltage,  $\epsilon^*(t)$ , which can be compared to the unmodified response,  $\epsilon(t) \propto P_+-P_-$ . Care is taken to always allow full recovery of the sample after each relaxation. When repeated accurately,

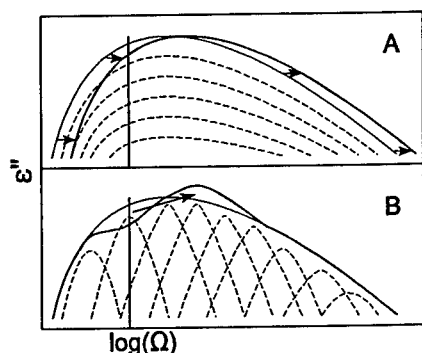


Fig. 1. Sketch of the dielectric loss as a function of logarithm of frequency from the intrinsic degrees of freedom in a sample exhibiting (A) homogeneously broadened response and (B) response due to a distribution of relaxation times. In an applied field at frequency  $\Omega$ : for (A), energy is absorbed homogeneously and the spectrum is shifted uniformly; whereas for (B), only the domains with significant absorption at  $\Omega$  are heated and a spectral hole develops.

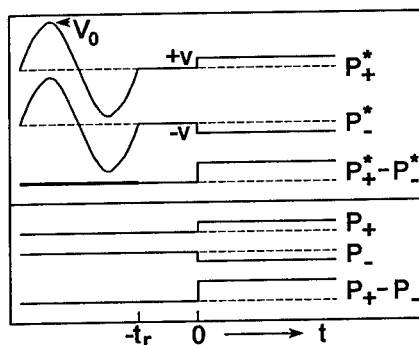


Fig. 2. Voltage sequences that yield modified ( $P_+^*$ ,  $P_-^*$ ) and unmodified ( $P_+$ ,  $P_-$ ) time-dependent polarizations. Unless otherwise indicated, the amplitudes are  $V_0=900$  V for the pump oscillation and  $+v=150$  V for the probe step. If not for dielectric heating during the pump oscillation, the differences  $P_+^*-P_-^*$  and  $P_+-P_-$  would be identical.

the phase-cycling scheme also eliminates spurious nonlinear effects that often interfere with traditional measurements of nonlinear response.<sup>15</sup> Specifically, extrinsic effects such as electrode polarization, sample electrostriction and viscoelastic deformation will be identical after identical pump oscillations, hence they are cancelled by the subtraction process; only intrinsic modifications in the dielectric constant change sign with the probe step, so that they are enhanced by the subtraction process. Although extrinsic effects may be induced by the probe step itself, they are immeasurably small, and further reduced by a factor of  $(+v/V_0)^2=1/36$  compared to the intrinsic changes induced by the pump oscillation. The reported results occur reproducibly in the raw data, but sometimes the cancellation is incomplete due to slight temperature drifts. Thus, some of the data presented here have been corrected by a small factor (always less than 0.1%) times the response from the pump oscillation ( $P_+^*+P_-^*$ ). The pump-and-probe procedure with phase-cycling scheme facilitates the investigation of spectra with relatively small and transient modifications.

Most data shown here are for propylene carbonate (PC), which was chosen for its extraordinarily large dielectric loss and highly temperature-dependent relaxation rate near its  $T_g$  of 156 K.<sup>16</sup> Glycerol, with a smaller dielectric loss and less pronounced temperature dependence near its  $T_g$  of 190 K, exhibits weaker but otherwise similar NSHB behavior. The solid curves in Fig. 3A show the unmodified dielectric constant of PC at a measurement temperature of  $T=157.4$  K, while the dashed curves show the modified response after a single oscillation at three different frequencies. Close inspection of the original data reveals that the 2 Hz oscillation modifies the spectrum most at short times and that the 0.01 Hz oscillation modifies the spectrum most at long times, while the 0.05

Hz oscillation modifies the response most in the middle. The result is amplified in Fig. 3B by taking the difference in the dielectric constant at each time,  $\Delta\epsilon(t) = \epsilon^*(t) - \epsilon(t)$ , as defined in the inset of Fig. 3A. Note that the response which is modified most by the 2 Hz oscillation is virtually unchanged by the 0.01 Hz oscillation, and vice versa, unambiguously establishing that the spectrum is heterogeneously broadened. Perhaps a more physically meaningful way to show how the pump

oscillation has changed the relaxation rate of selected domains is to plot the change in the logarithm of the relaxation time as a function of time,  $\Delta(t)$ , also defined in the inset of Fig. 3A. Recall that if the response were homogeneous, the relaxation rates of all domains would be shifted uniformly, yielding a constant value for  $\Delta(t)$ . Instead, Fig. 3C shows that the different frequencies modify different parts of the spectrum, providing a most direct demonstration that the slow dielectric relaxation is heterogeneously broadened. Although PC has one of the narrowest loss peaks of any supercooled liquid, with net response that is only about 1.3 times the Debye width, the intrinsic local response is significantly narrower.

We find that the spectral modification is more strongly dependent on the power (amplitude) than the energy (number of oscillations) of the electric field. Figure 4 shows that the size of the spectral hole increases

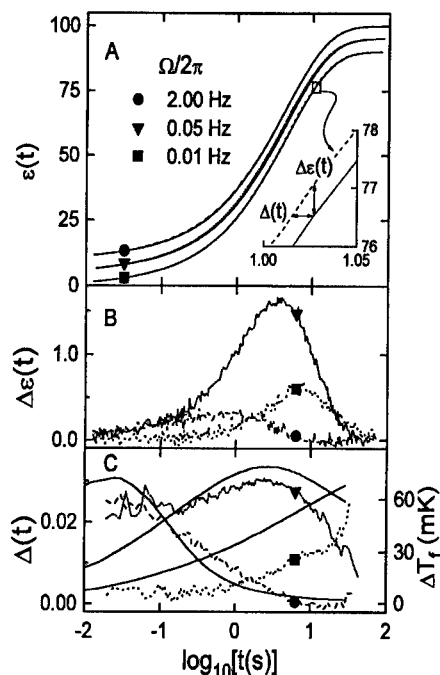


Fig. 3. (A) Time-dependent dielectric constant of PC at 157.4 K. Solid curves are the unmodified response, dashed curves are the response after modification by a single oscillation of 900 V at 2.0 Hz (upper), 0.05 Hz (middle), and 0.01 Hz (lower). The upper and lower curves have been offset for clarity. (B) Time-dependent difference between modified and unmodified dielectric constants,  $\Delta\epsilon(t)$ , as defined in the inset of (A). (C) The difference in the logarithm of the relaxation time at each time,  $\Delta(t)$ , also defined in the inset of (A). The smooth curves in (C) are calculated using a distribution of relaxation times with no adjustable parameters

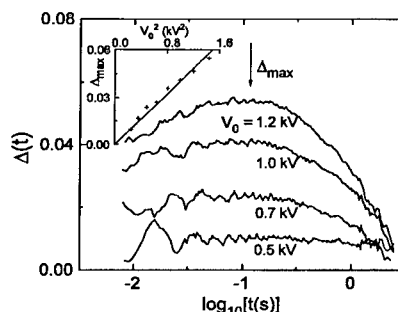


Fig. 4. Time-dependent modification of the relaxation times in PC after a single 1 Hz oscillation with various amplitudes  $V_0$ . An accurate value for the maximum in each spectral hole was obtained by fitting to several points in the spectrum near the maximum modification (arrow), yielding  $\Delta_{\max} = 4 \times 10^{-8} V_0^2$  (inset).

quadratically with increasing oscillation amplitude. Indeed, the maximum modification, as determined by fitting to several points in the spectrum near the maximum modification, is given by  $\Delta_{\max} = 4 \times 10^{-8} V_0^2$  (inset); thus confirming that the modification increases linearly with the power absorbed from the oscillating field. Figure 5 shows that the size of the spectral hole saturates as a function of the energy from multiple oscillations at fixed amplitude, indicating that energy flows out of the responding degrees of freedom on roughly the same time scale as it is absorbed from the field. Hence NSHB, where local fictive temperatures are monitored as heat flows into the thermal bath, is consistent with the behavior observed by specific heat spectroscopy,<sup>17,18</sup> where the thermal bath is monitored as heat flows into the local degrees of freedom.

Further details in the mechanism of spectral recovery are revealed by changing the recovery time ( $t_r$ ) between the pump oscillation and probe step. Identifying the equilibrium distribution of relaxation times as the ergodic state, these measurements probe the spectral recovery after a large electric field has induced non-ergodic response. Although similar to traditional bulk aging experiments,<sup>19</sup> NSHB has some distinct advantages. First, the minimum time for measuring a modified spectrum is limited only by the speed of the high-voltage supply, not a thermal quench rate. Our present apparatus has a minimum  $t_r$  of  $\sim 2$  ms, allowing "aging" experiments at temperatures well above  $T_g$ . More importantly, however, NSHB provides details about spectral shape during recovery, and specific constituents can be emphasized by changing the frequency ( $\Omega$ ) at which the sample was modified. Figure 6 shows the residual modification for several different  $t_r$  after a single oscillation at 0.2 Hz. Within experimental resolution, the shape of the spectral hole is preserved during recovery. Indeed, all parts of the sample recover monotonically, indicating that the selectively heated domains do not significantly modify their neighboring regions during recovery, indicative of negligible direct coupling between domains. Furthermore, all parts of the sample recover at essentially the same rate, independent of the modification frequency, demonstrating that a uniform recovery process acts in conjunction with the heterogeneous linear response.

Figure 7 is a comparison between the distribution of relaxation times in the linear response, and the uniform recovery rate for spectral hole refilling. Refilling is consistent with a single exponential,  $\Delta_{\max} \propto e^{-\gamma t_r}$ , with recovery rates of  $\gamma = (0.083 \text{ s})^{-1}$  and  $(4.2 \text{ s})^{-1}$  for PC at 161.0 and 157.6 K respectively, and  $(0.73 \text{ s})^{-1}$  for glycerol at 194.7 K. Characteristic relaxation times for the linear response,  $\bar{\tau}$ , which for  $\beta = 0.7$  are within 9% of the peak in the distribution of relaxation times,<sup>20</sup> are

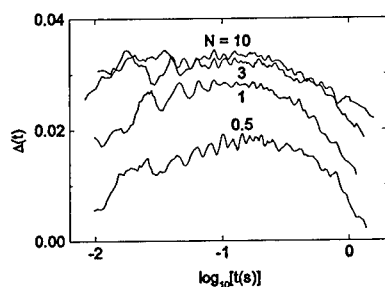


Fig. 5. Time-dependent modification of the relaxation times in PC at 159.3 K after N oscillations at 1.0 Hz.

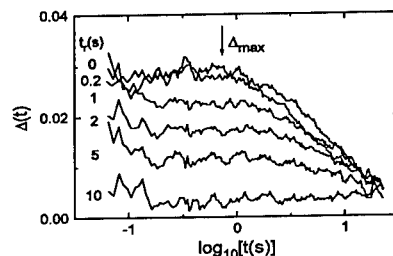


Fig. 6. Time-dependent modification of the relaxation times in PC at 157.6 K after a 0.2 Hz pump oscillation for various recovery times. Again, each  $\Delta_{\max}$  was obtained by fitting to several data points in the vicinity of the maximum modification, arrow.

0.082 and 4.1 s for PC at 161.0 and 157.6 K respectively, and  $\bar{\tau}=0.71$  s for glycerol at 194.7 K. Such similar values for  $\bar{\tau}$  and  $1/\gamma$  may be contrasted with what is observed for photobleaching of probe molecules in orthoterphenyl,<sup>10</sup> where a typical probe molecule must rotate 100 times before the equilibrium distribution of rotation rates is recovered; but our observation of similar relaxation and recovery rates is consistent with the close connection found for the rotation and exchange rates in the dynamics of various substances as measured by multi-dimensional NMR.<sup>9,21</sup>

## THEORY

We model the observed behavior assuming that the sample contains discrete domains that relax exponentially,  $e^{-t/\tau_i}$ , with distinct relaxation times  $\tau_i$  enumerated by index  $i$ . The net relaxation is the weighted sum over all possible relaxation times,  $\epsilon(t)=\sum_i g_i e^{-t/\tau_i}$ . Here, the distribution of relaxation times ( $g_i$ ) is established empirically by fitting to the equilibrium bulk response; these same  $g_i$  are then used to characterize the spectral hole. NSHB involves adding energy to selected domains, thereby modifying their local relaxation times. As noted above, if this energy simply flowed into the thermal bath, it would diffuse out of a typical domain in less than a nanosecond. The fact that NSHB can be observed indicates that some of the added energy must remain localized long enough to change the local dynamics, which may be described in terms of a change in the local fictive temperature,  $T_{fi}$ . In ergodic liquids, the fictive temperature is equal to the thermodynamic temperature, whereas quenched samples often exhibit aging in their response as fictive temperature approaches  $T$ .<sup>22</sup> Although there is no consensus about the mechanism that governs relaxation times in supercooled liquids, proposed scenarios include local response (and hence  $T_{fi}$ ) that depends on the size,<sup>7,8,23-25</sup> density,<sup>26</sup> or structure<sup>27</sup> of the relaxing region. Empirically, over the temperature range of our investigation, changes in relaxation times may be approximated by an Arrhenius law,  $\tau_i \propto e^{B/T_{fi}}$ , which for bulk fictive temperature is known as the Narayanaswamy-Moynihan equation. Here  $B$  is an effective energy barrier that indicates how rapidly the  $\tau_i$  decrease as the sample is warmed above  $T_g$ . Thus, for small changes in local fictive temperature, changes in local relaxation times may be written as  $\ln(10)\Delta\log(\tau_i)=(-B/T^2)\Delta T_{fi}$ .

After  $N$  oscillations of an electric field of amplitude  $E$  and frequency  $\Omega$ , the energy absorbed (via Joule heating) in a domain characterized by dielectric loss  $\epsilon_i'' \propto \Omega\tau_i/[1+(\Omega\tau_i)^2]$  is  $Q_i=N\pi\epsilon_0\epsilon_i''E^2$ , where  $\epsilon_0$  is the permittivity of free space. Assuming that this energy remains in the degrees of freedom that responded to the field, the local fictive temperature will increase by an amount  $\Delta T_{fi}=Q_i/\Delta c_p$ , where  $\Delta c_p$  is the specific heat of the responding degrees of freedom, which may be deduced from the difference in  $c_p$  from above and below  $T_g$ . Depolarization effects reduce the

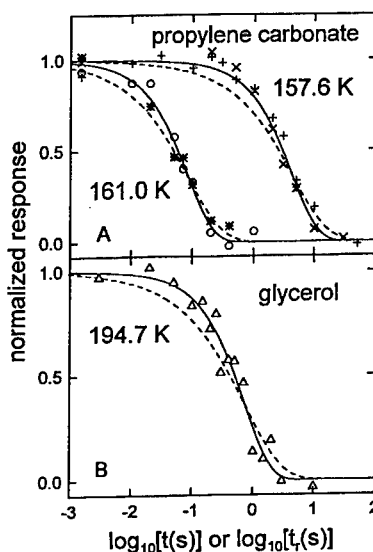


Fig. 7. Normalized dielectric constant as a function of time (dashed curves) and  $\Delta_{\max}$  as a function of recovery time (symbols) for (A) PC at 161.0 and 157.6 K, and (B) glycerol at 194.7 K. Symbols are for recovery after modification by 10 Hz (\*), 1 Hz (o), 0.3 Hz (x), 0.06 Hz (+), and 0.5 Hz ( $\Delta$ ). Solid curves are the best single-exponential fits to the symbols that characterize spectral hole refilling.

net internal field. Assuming the Lorentz formula for spherical domains in a thin sample between parallel plates,  $E = (V_0/d)(\epsilon' + 2)/3\epsilon'$ , where the net in-phase response is  $\epsilon' = \sum g_i / [1 + (\Omega\tau_i)^2] + \epsilon_\infty$  with  $\epsilon_\infty \approx 5$ . After a single cycle of amplitude  $V_0$  at the maximum loss frequency in PC at  $T \approx T_f \approx T_g \approx 156$  K where  $\epsilon' \approx \epsilon'' \approx 40$ , using published thermodynamic data<sup>28</sup> for  $\Delta c_p = 7.7 \times 10^5$  J/(m<sup>3</sup>-K) and  $B/T_g = 230$ , the maximum hole depth is calculated to be  $\Delta_{\max} = 4.1 \times 10^{-8} V_0^2$ . In light of all the approximations involved, such excellent agreement with the amplitude dependence shown in the inset of Fig. 4 is somewhat fortuitous, but still provides quantitative support for our interpretation that NSHB involves local dielectric heating. Further support for our interpretation that the sample contains a distribution of distinct relaxation times is shown by the generally good agreement with the amplitude and shape of the spectral modification shown in Fig. 3C, with no adjustable parameters. Discrepancies between calculated and observed behavior, most evident at long times and after the 0.01 Hz modification, can be attributed to energy flow out of the localized degrees of freedom, as demonstrated in Figs. 5-7, and discussed below.

Figure 8 shows a specific model for energy flow in NSHB that combines the heterogeneous distribution of relaxation times with a uniform recovery rate. We describe the model in terms of the phonon bottle-neck theory from magnetic resonance,<sup>29</sup> but further investigation is necessary to fully establish the actual microscopic picture. Distinct domains are characterized by a local fictive temperature,  $T_{fi}$ , that is modified by selective dielectric heating as described above. (By analogy to the local spin-temperature in magnetic resonance, the  $T_{fi}$  may correspond to a local "dipole-temperature" for each distinct domain in the sample.) Each domain couples directly to only a subset of phonons, with an energy flow rate,  $1/\tau_i$ , that is governed by the local relaxation time. These select phonons couple to the rest of the phonon bath by a uniform rate,  $\Gamma$ . An important parameter in the model is the ratio of the heat capacity of the domains to that of the subset of phonons,  $b = \Delta c_p / c_{ph}$ . If  $b \leq 1$ , then the subset of phonons have sufficient heat capacity so that the coupling to the uniform phonon bath can be ignored, but this assumption yields a distribution of recovery rates, similar to the distribution of relaxation times, that is not supported by the data. Whereas if  $b \gg 1$ , the recovery rate is governed primarily by the uniform coupling rate, which gives good agreement with the shape of the spectral holes (Fig. 9) and the spectral recovery as a function of  $t$ , (Fig. 10). Assuming the Debye model for  $c_{ph}$  and Ising dipoles for  $\Delta c_p$ , gives<sup>30</sup>  $b \approx (\theta/T)^2 k_B \theta / (36 \hbar \Delta \omega)$ , where  $\theta$  is the Debye temperature and  $\Delta \omega$  is the intrinsic width of the dielectric loss. Using<sup>31</sup>  $\theta \approx T_g$  and  $\Delta \omega \sim 1$  rad/s yields  $b \sim 10^{12}$ , implying a severe bottle-neck in the net recovery rate  $\gamma \approx \Gamma/b$ , which may explain how typical phonon scattering rates ( $\Gamma \sim 10^{12}$  s<sup>-1</sup>) can influence spectral hole burning and recovery in the slow relaxation near  $T_g$ . Again, confirmation of such a bottle-neck process requires more detailed investigation, but the concept of slow degrees of freedom coupled to the bath through a small subset of phonons offers one explanation for the sluggish transfer of energy observed by NSHB. Finally, we note that the overall agreement with NSHB shown in Figs. 9 and 10 is worsened by assuming any significant non-Debye local response, or by adding any significant direct coupling between the domains.

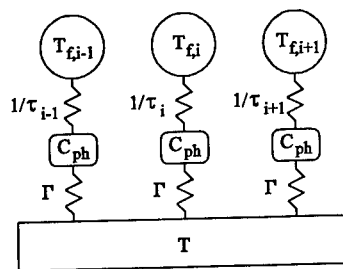


Fig. 8. Model for heat flow from local domains to the thermal bath during NSHB recovery. Each distinct domain, characterized by fictive temperature  $T_{fi}$ , is coupled through a subsystem with heat capacity  $c_{ph}$  to the thermal bath at temperature  $T$ . The flow of heat is governed by the local relaxation time  $\tau_i$  and a uniform coupling rate,  $\Gamma$ .

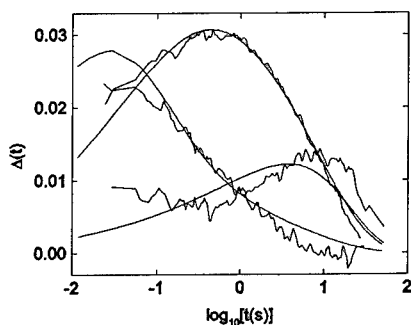


Fig. 9. Time-dependent change in the relaxation times in PC at 157.4 K after modification at three different frequencies, similar to Fig. 3C. The solid curves are from the model shown in Fig. 8, with an amplitude factor of 2.1 as the only adjustable parameter, showing reasonable agreement with all data.

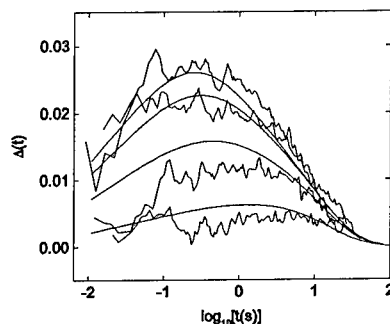


Fig. 10. Time-dependent change in the relaxation times in PC at 157.6 K after a 0.3 Hz pump oscillation, and recovery times of 0, 1, 3 and 10 s, from top to bottom, respectively. The solid curves are from the model shown in Fig. 8, using the same amplitude factor as in Fig. 9.

## CONCLUSIONS

Nonresonant spectral hole burning is a powerful new technique for characterizing intrinsic local response in systems that exhibit nonexponential relaxation. Important advantages of NSHB include that it is the first technique to incorporate a tuneable band-pass filter for distinguishing selected constituents in the net spectrum of response, and that the responding degrees of freedom are used directly as their own local probe. Here we have shown that the broadened dielectric response of supercooled liquids is comprised of a distribution of relaxation times, indicative of a distribution of discrete domains. We have further shown that the return to the ergodic distribution of relaxation times in these liquids involves a uniform recovery rate that is independent of the frequency at which the sample was modified. All relevant features in the observed behavior are modeled assuming a heterogeneous distribution of independently relaxing domains, that couple to the phonon bath, but not directly to each other.

## ACKNOWLEDGEMENTS

We have benefitted from discussions with C.A. Angell, G. Diezemann, J. Hemberger, A. Heuer and H. Sillescu. The research was supported by the Deutsche Forschungsgemeinschaft through SFB 262. RVC has the pleasure of thanking R. Böhmer, A. Loidl and H. Sillescu for their hospitality during the course of this work.

## REFERENCES

1. See H. Scher, M.F. Shlesinger, J.T. Bendler, *Phys. Today* **44** (1), 26-34 (1991).



2. See e.g., *Relaxations in Complex Systems*, edited by K.L. Ngai and G.B. Wright, J. Non-Cryst. Solids **172-174** (1994).
3. K.S. Cole and R.H. Cole, J. Chem. Phys. **9**, 341 (1941).
4. G. Williams, M. Cook, P.J. Hains, J. Chem. Soc. Faraday Trans. 2 **68**, 1045 (1972).
5. A.K. Jonscher, *Dielectric Relaxation in Solids* (Chelsea Dielectrics Press, London, 1982).
6. R. Richert, Chem. Phys. Lett. **216**, 223 (1993).
7. E. Donth, J. Non-Cryst. Solids **53**, 325 (1982).
8. C.T. Moynihan and J. Schroeder, J. Non-Cryst. Solids **160**, 52 (1993).
9. K. Schmidt-Rohr and H.W. Spiess, Phys. Rev. Lett. **66**, 3020 (1991); A. Heuer, M. Wilhelm, H. Zimmermann, H.W. Spiess *ibid* **75**, 2851 (1995).
10. M.T. Cicerone and M.D. Ediger, J. Chem. Phys. **103**, 5684 (1995).
11. B. Schiener, R. Böhmer, A. Loidl, R.V. Chamberlin, Science **274**, 752 (1996).
12. N. Bloembergen, E.M. Purcell, R.V. Pound, Phys. Rev. **73**, 679 (1948).
13. P.L. Kuhs and M.S. Conradi, J. Chem. Phys. **77**, 1771 (1982).
14. R. Böhmer, B. Schiener, J. Hemberger and R.V. Chamberlin, Z. Phys. B **99**, 91 (1995); *ibid* p. 624 (1996).
15. See e.g. T. Furukawa and K. Matsumoto, Jpn. J. Appl. Phys. **31**, 840 (1992).
16. C.A. Angell, L. Boehm, M. Oguni, D.L. Smith, J. Mol. Liq. **56**, 275 (1993).
17. P.K. Dixon and S.R. Nagel, Phys. Rev. Lett. **61**, 341 (1988).
18. H. Fujimori and M. Oguni, J. Non-Cryst. Solids **172-174**, 601 (1994).
19. I.M. Hodge, Science **267**, 1945 (1995).
20. C.P. Lindsey and G.D. Patterson, J. Chem. Phys. **73**, 3348 (1980).
21. R. Böhmer, G. Hinze, G. Diezemann, B. Geil, and H. Sillescu, Europhys. Lett. **36**, 55 (1996).
22. I.M. Hodge, J. Non-Cryst. Solids **169**, 211 (1994).
23. G. Adams and J.H. Gibbs, J. Chem. Phys. **43**, 139 (1965).
24. J.R. Macdonald, J. Appl. Phys. **62**, R51 (1987).
25. R.V. Chamberlin and D.W. Kingsbury, J. Non-Cryst. Solids **172-174**, 318 (1994).
26. J.E. Andersen and R. Ullman, J. Chem. Phys. **47**, 2178 (1967).
27. J.C. Phillips, Rep. Prog. Phys. **59**, 1133 (1996).
28. R. Böhmer, K.L. Ngai, C.A. Angell and D.J. Plazek, J. Chem. Phys. **99**, 4201 (1993).
29. *Electron Paramagnetic Resonance of Transition Ions*, A. Abragam and B. Bleaney, Oxford University Press, New York (1970), pgs. 574-583.
30. B.W. Faughnan and M.W.P. Strandberg, J. Phys. Chem. Solids **19**, 155 (1961).
31. C.A. Angell, J. Am. Ceram. Soc. **51**, 117 (1968).

## DYNAMIC HETEROGENEITY BY HIGHER MOMENTS OF A RELAXING QUANTITY

R. RICHERT

Max-Planck-Institut für Polymerforschung, Ackermannweg 10, D-55128 Mainz, Germany

### ABSTRACT

A relaxation experiment usually acquires a measure for the mean energetic distance of the system from the thermodynamic equilibrium and its temporal evolution. For sufficiently small perturbations necessary to assure linear responses such data is bound to remain undecided as regards the spatial nature of the relaxation process, heterogeneous or homogeneous. The technique of solvation dynamics near the glass transition can probe the entire distribution of site specific energies and its approach towards equilibrium, so that apart from the mean solvation energy  $\nu(t)$  also higher moments in terms of the inhomogeneous optical linewidth  $\sigma_{inh}(t)$  become accessible. While  $\nu(t)$  maps the dielectric relaxation behaviour of the liquid,  $\sigma_{inh}(t)$  is found to be sensitive to the spatial nature of the underlying process. Contrasting experiment and simulation leads to the conclusion, that the relaxation time is a site specific quantity, i.e. the heterogeneous nature is found to dominate.

### INTRODUCTION

A common feature of supercooled liquids is their approach  $\phi(t)$  towards equilibrium in a non-exponential fashion, even if the perturbation is small enough such that the response is linear with respect to the amplitude of the perturbation [1,2]. For the ensemble averaged structural relaxation or  $\alpha$ -process temporal patterns which are approximated by the stretched exponential or Kohlrausch-Williams-Watts (KWW) decay function

$$\phi(t) = \phi_0 \cdot \exp \left[ - (t/\tau_{WW})^\beta \right], \quad 0 < \beta \leq 1, \quad (1)$$

are often found. Observations of dispersive relaxation patterns, i.e.  $\beta < 1$ , can equally be cast into a distribution of relaxation times or the concomitant probability density  $G(\ln\tau)$  for finding a site associated with the time constant  $\tau$ . The ensemble averaged decay in this formulation reads

$$\phi(t) = \phi_0 \cdot \int_{-\infty}^{+\infty} G(\ln\tau) e^{-t/\tau} d\ln\tau, \quad \phi(0) = \phi_0. \quad (2)$$

Because any monotonic decay can be described by an appropriate choice of  $G(\ln\tau)$ , the coincidence of eqn. (2) with experimental findings is in no way decisive regarding the nature of the underlying processes. It should be emphasized that  $G(\ln\tau)$  becomes physically meaningless whenever the integral kernel  $\exp[-t/\tau]$  is conceptually inappropriate. Similarly, the stretching exponent  $\beta$  in eqn. (1) gives no hint towards the relaxation mechanism, since there is no unique theory related to the KWW expression. Therefore, an experimental relaxation pattern can equally be associated with different microscopic pictures regarding the spatial heterogeneity of the relaxation times. The heterogeneous case is meant to describe the situation of uncoupled relaxors,

each associated with a single and static relaxation time  $\tau_i$ , which is then assumed to be a site specific quantity with its statistical occurrence being outlined in  $G(\ln\tau)$ . The homogeneous situation refers to every site relaxing identically according to the ensemble averaged dispersive decay  $\phi(t)$ . These two situations represent only the extreme cases of the spatial nature of relaxation phenomena, combined with the simplification of disregarding possible temporal fluctuations of site specific relaxation scenarios [3]. Fig. 1 illustrates that the inevitable ensemble average applied to these microscopically different pictures eventually leads to identical decay functions  $\phi(t)$ .

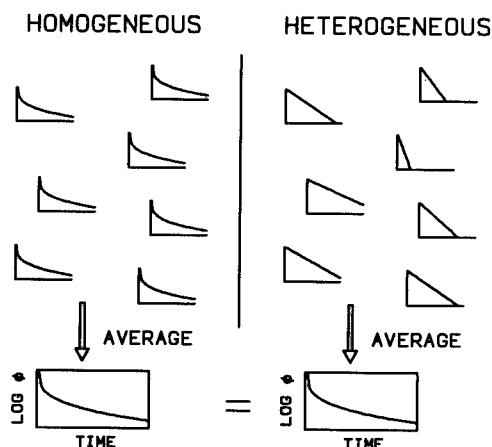


**Fig. 1.** Outline of a simplified discrimination between homogeneous and heterogeneous character of a relaxation process. The small graphs are ment to display single site decay patterns as plotted in terms of  $\log[\Phi(t)]$  versus time. The ensemble averaged relaxations (lower frames) can be indistinguishable, even though the two scenarios are quite different in nature.

Under special experimental conditions it is possible to select or remove certain portions of the distribution of relaxation times, such that the spatial nature of the relaxation process can be derived [4]. Here we examine the possibility of discriminating between dynamical homogeneity and heterogeneity on the basis of the time dependent inhomogeneous linewidth  $\sigma_{inh}(t)$  of emission spectra. This optical experiment not only observes the approach of the average energy  $\nu(t)$  towards equilibrium but also the distribution of site specific energies in terms of the entire emission profile. Note that other relaxation experiments have access only to the mean energetic offset from equilibrium conditions, e.g. the polarization decay in a dielectric experiment, without information on the corresponding spatial distribution. The situation in a dielectric experiment equivalent to measuring  $\sigma_{inh}(t)$  would be the possibility of observing the temporal evolution of individual molecular orientations,  $\cos\theta(t)$ , of spatially distinct dipoles.

## EXPERIMENT AND RESULTS

Solvation dynamics experiments on supercooled liquids record the emission spectra of chromophoric guest molecules as a function of time [5]. At time zero the probe molecules are excited from their electronic ground state  $S_0$  to the long lived state  $T_1$ , thereby inducing a change  $\Delta\mu = \mu_E - \mu_G$  of the permanent dipole moment. Assuming equilibrium conditions regarding the

ground state  $\mu_G$  at times  $t < 0$ , the effect of the  $\mu_G \rightarrow \mu_E$  transition is to initiate a dielectric relaxation process of the adjacent liquid towards the equilibrium with respect to the excited state dipole moment  $\mu_E$  [6]. The quantities observed by phosphorescence spectroscopy are the energy differences  $\nu(T_1) - \nu(S_0)$ . Polarizing the liquid by the electric field created by  $\Delta\mu$  lowers the energy level of the excited state and increases that of the ground state, such that the emission energy  $\nu_i(t)$  of each probe molecule 'i' becomes a function of time whenever orientational polarization is active within the lifetime  $\tau_{ph}$  of the excited state  $T_1$ .

The average emission energy  $\nu(t) = \langle \nu_i(t) \rangle_i$  reflects the dynamics of the Stokes shift which is quantitatively dictated by the dielectric properties of the solvent regarding both the temporal pattern and the absolute energy values [7,8]. At time  $t = 0$  the emission spectrum is a gaussian profile characterized by its mean  $\nu(0)$  and standard deviation  $\sigma_{inh}(0)$  and in the equilibrium state the spectrum is again of gaussian shape with standard deviation  $\sigma_{inh}(\infty) = \sigma_{inh}(0) = \sigma_0$  but with a red-shifted mean value at  $\nu(\infty)$  [8]. The entire Stokes shift is given by  $\Delta\nu = \nu(0) - \nu(\infty)$  and the normalized decay is represented by the so called Stokes shift correlation function

$$C(t) = [\nu(t) - \nu(\infty)] / [\nu(0) - \nu(\infty)] \quad (3)$$

Detailed solvation data is available for quinoxaline (QX) as a phosphorescent chromophore with a lifetime  $\tau_{ph} \approx 0.3$  s dissolved in the glass-former 2-methyltetrahydrofuran (MTHF) [6-8]. For this example at temperatures near the glass transition at  $T_g \approx 91$  K it has been found that  $\Delta\nu = 246$   $\text{cm}^{-1}$ ,  $\sigma_{inh}(\infty) = \sigma_{inh}(0) = 160$   $\text{cm}^{-1}$ , and that  $C(t) = \exp[-(t/\tau_{WW})^\beta]$  with  $\beta \approx 0.5$ , in favorable agreement with the dielectric properties  $\epsilon^*(\omega)$  of the solvent [6-8]. For the particular case  $T = 95.1$  K shown in Fig. 2 a fit to  $C(t)$  yields  $\beta = 0.5$  and  $\tau_{WW} = 25$  ms. The further observation of a transient increase of  $\sigma_{inh}(t)$  peaking at  $\sigma_{max} = 183$   $\text{cm}^{-1}$  is plotted in Fig. 3 as  $\sigma_{inh}(t)/\sigma_{inh}(0)$ . Because  $\sigma_{max} - \sigma_0$  scales with the polarity of the solvent the contribution of the homogeneous linewidth  $\sigma_{hom}$  should be negligible and has been estimated not to exceed 10 % of the observed width [8].

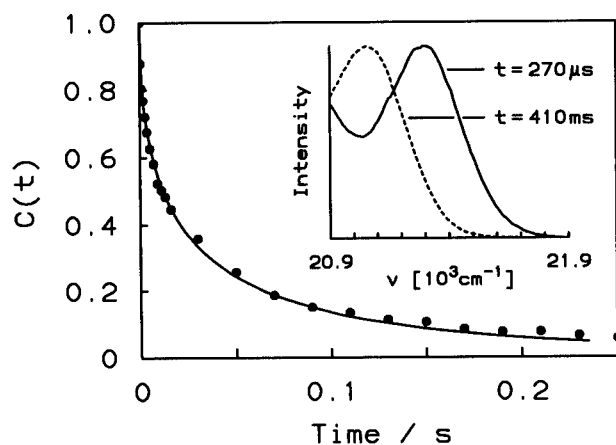


**Fig. 2.** Solvation dynamic data of QX in MTHF at  $T = 95.1$  K. Symbols indicate the experimental  $C(t)$  results for times  $0 \leq t \leq 250$  ms as derived from time resolved  $S_0 \leftarrow T_1$  emission spectra, the solid line is a KWW fit with  $\beta = 0.5$  and  $\tau_{WW} = 25$  ms. The inset shows the related  $S_0 \leftarrow T_1$  (0-0) emission profiles for short and long times separated by  $\Delta\nu = 246$   $\text{cm}^{-1}$ , with  $C(t = 270 \mu\text{s}) \approx 1$  and  $C(t = 410 \text{ ms}) \approx 0$ , both having a gaussian width of  $\sigma_{inh} = 160$   $\text{cm}^{-1}$ .

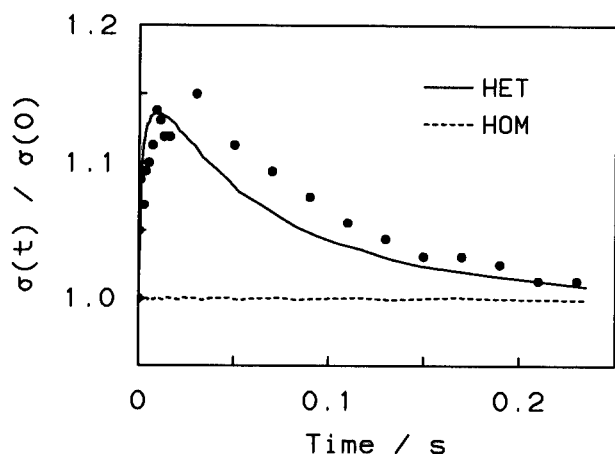


**Fig. 3.** Experimental data for the inhomogeneous line width  $\sigma_{inh}(t)$  (dots) as evaluated from the  $S_0 \leftarrow T_1$  (0-0) spectra leading to the  $C(t)$  results of Fig. 2. The lines are simulation results assuming  $\Delta\nu = 246 \text{ cm}^{-1}$ ,  $\sigma_0 = 160 \text{ cm}^{-1}$ , and dynamics of the form  $C(t) = \exp[-(t/\tau_{ww})^\beta]$  with  $\beta = 0.5$  and  $\tau_{ww} = 25 \text{ ms}$ . The solid line refers to dynamic heterogeneity (HET), the dashed line is for the case of homogeneity (HOM).

## DISCUSSION

In order to rationalize the observed  $\sigma_{inh}(t)$  behaviour, the energetic relaxation of the individual probe molecules are simulated according to the two distinct pictures outlined in Fig. 1, which both lead to the same decay pattern as regards  $C(t)$ . The initial and final energies for each chromophore,  $v_i(0)$  and  $v_i(\infty)$ , are assumed perfectly correlated, i.e. we set  $v_i(\infty) = v_i(0) - \Delta\nu$  for each molecule. Relaxing this condition has been shown not to affect the conclusions drawn in the following [9]. For the case of homogeneous (HOM) dynamics, every site is expected to decay energetically according to the non-exponential ensemble averaged pattern  $C(t)$ . In contrast, dynamical heterogeneity (HET) refers to the situation of each site 'i' decaying exponentially as  $\exp(-t/\tau_i)$  along the energy scale, but with the time constants  $\tau_i$  being subject to a probability density  $g(\tau)$ , which has to satisfy the relation  $C(t) = \int g(\tau) \exp(-t/\tau) d\tau$ .

The above two different cases for modeling the details of energetic relaxation in the course of a solvation dynamics experiment have been simulated by the following method. For the total number of  $i = 1 \dots N = 5 \cdot 10^6$  sites random numbers  $v_i(0)$  are taken according to the probability density  $(2\pi\sigma_0^2)^{-1/2} \cdot \exp[-(v-\Delta\nu)^2 / 2\sigma_0^2]$  with  $\Delta\nu = 246 \text{ cm}^{-1}$  and  $\sigma_0 = 160 \text{ cm}^{-1}$  in order to mimic the unrelaxed gaussian density of energies at  $t = 0$  with  $\langle v_i \rangle(0) = \Delta\nu$ . The relaxed gaussian profile is then determined by  $v_i(\infty) = v_i(0) - \Delta\nu$ , thereby setting  $\langle v_i \rangle(\infty) = 0$ . The relaxation is introduced by associating each site with an energy decay function of the form  $v_i(t) = v_i(\infty) + [v_i(0) - v_i(\infty)] \cdot \phi_i(t)$ . For the HOM type dynamics we chose the KWW type decay  $\phi_i(t) = C(t) = \exp[-(t/\tau_{ww})^\beta]$  identically for all sites. The HET case is given by  $\phi_i(t) = \exp[-t/\tau_i]$  with the  $\tau_i$  generated at random according to the generalized gamma probability density

$$g(\tau) = \Gamma^{-1}(\alpha) \cdot \gamma \cdot (\tau/\tau_{GG})^{\alpha\gamma} \cdot \exp[-(\tau/\tau_{GG})^\gamma] \quad (4)$$

For the present choice of the KWW parameters  $\beta = 0.5$  and  $\tau_{\text{WW}} = 25$  ms we have  $\alpha = 0.5$ ,  $\gamma = 1$ , and  $\tau_{\text{GG}} = 4 \cdot \tau_{\text{WW}} = 0.1$  s such that  $\exp[-(t/\tau_{\text{WW}})^\beta] = \int g(\tau) \exp(-t/\tau) d\tau$  holds exactly [10]. In this manner we can easily obtain the manifold of  $v_i(t)$  which defines the emission spectrum at time  $t$ , and a further statistical analysis yields the quantities  $v(t)$  or  $C(t)$  and  $\sigma_{\text{inh}}(t)$ .

According to the numerical concept outlined above the simulated  $v(t)$  curves for both cases, HOM and HET, are practically identical to the KKW fit to  $C(t)$  in Fig. 2. However, the resulting patterns for  $\sigma_{\text{inh}}(t)$  display qualitatively different behaviours, where the case HOM yields  $\sigma_{\text{inh}}(t) \equiv \sigma_0$  for trivial reasons. These simulated  $\sigma_{\text{inh}}(t)$  curves are included in Fig. 3 after normalization to the base value  $\sigma_{\text{inh}}(0) = \sigma_0$ , indicating that only the case of dynamical heterogeneity (HET) is capable of accounting for the observed  $\sigma_{\text{inh}}(t)$  data. Modeling the solvation process by correlated initial and final energies,  $v_i(\infty) = v_i(0) - \Delta v$ , is in accord with the notion that the entire average Stokes shift  $\Delta v$  is only a fraction of the full width of the emission spectrum. Moreover, the situation of uncorrelated limiting energy values would imply that a substantial amount of sites experience a blue shift, in contrast to physical reasonings.

An instructive summary of the solvation phenomenology near the glass transition  $T_g$  is obtained by considering  $v(T)$  and  $\sigma_{\text{inh}}(T)$ , i.e. for an arbitrarily preset time window and with the temperature as a variable. Fig. 4 shows such data for a fixed integration time in the range  $1 \text{ ms} \leq t \leq 2 \text{ ms}$ , again with a clear indication of  $\sigma_{\text{inh}}(T)$  peaking at  $\sigma_{\text{max}}$ . Fig. 4 also indicates the increase of the homogeneous linewidth  $\sigma_{\text{hom}}(T)$ , which becomes a significant factor for  $T \geq 100$  K. Consequently, an analogous interpretation of emission profiles at elevated temperatures must become meaningless.

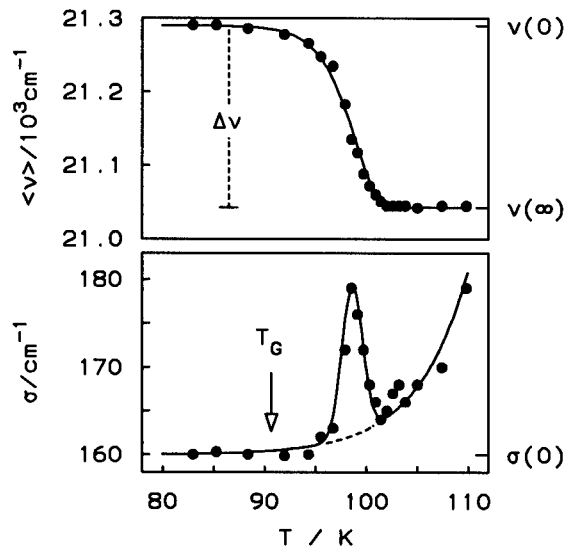


**Fig. 4.** Solvation data for QX/MTHF for a fixed time window of  $1 \text{ ms} \leq t \leq 2 \text{ ms}$  and for temperatures in the range  $80 \text{ K} \leq T \leq 110 \text{ K}$ . The upper panel shows the mean emission energy  $v(t)$ , the lower panel displays the observed line width  $\sigma(t)$ ,  $\sigma$  being the convolution of inhomogeneous ( $\sigma_{\text{inh}}$ ) and homogeneous ( $\sigma_{\text{hom}}$ ) contributions. Above  $T \approx 100 \text{ K}$   $\sigma_{\text{hom}}$  is no longer negligible. The plots also indicate the quantities  $v(0)$ ,  $v(\infty)$ ,  $\Delta v$ , and  $\sigma_0$ , used in the text. Lines serve as guides only.

On the basis of the simulation data obtained for the inhomogeneous linewidth, we conclude that  $\sigma_{\text{inh}}(t)$  data are sensitive quantities regarding the discrimination between homogeneous and heterogeneous nature of the relaxation process. This contrasts the mean energy  $\nu(t)$ , whose simulation result remained independent on the particular dynamic case, HOM or HET, as would be the case for most relaxation results. Since  $\sigma_{\text{inh}}(t)$  inherently refers to the energetic statistics of spatially distinct sites, this higher moment of the relaxing quantity contains information which can not be derived from the mean value  $\nu(t)$  alone.

The present observation of dynamical heterogeneity in a low molecular weight glass-forming liquid at  $T \approx T_g + 4$  K conforms well with analogous results obtained from other methods. Conclusionss on the dynamical nature of relaxation processes in glass-forming materials have also been inferred from 4D-NMR experiments [4,11], from non-linear dielectric relaxation methods [12], and from data on probe molecule reorientation and translation [13,14], with the common result that the time scale of molecular dynamics being a spatially varying quantity dominates over dynamic homogeneity. The present method of elucidating the spatial distribution of relaxation processes differs conceptually from the previous examples compiled above, which exploit the possibility of selecting dynamical sub-ensembles. Probing the dielectric relaxation in terms of the  $S_0 \leftarrow T_1$  (0-0) emission spectra does not involve dynamical sub-ensembles, but the energetically different contributions to the inhomogeneous linewidth are inherently associated with spatially distinct emitters. Note also that the emission energy of a certain probe molecule reflects the solvent state only at the moment of the electronic transition  $S_0 \leftarrow T_1$  (0-0), i.e. no time averaging over various solvent states within the excited state lifetime is in effect. As a consequence,  $\sigma_{\text{inh}}(t)$  will indicate dynamic heterogeneity even if the site specific relaxation times are subject to temporal fluctuations.

## REFERENCES

1. M.D. Ediger, C.A. Angell, and S.R. Nagel, *J. Phys. Chem.* **100**, 13200 (1996).
2. Disorder Effects on Relaxational Processes, edited by R. Richert and A. Blumen (Springer, Berlin, 1994).
3. A. Heuer, *J. Chem. Phys.* (submitted).
4. K. Schmidt-Rohr and H.W. Spiess, *Phys. Rev. Lett.* **66**, 3020 (1991); A. Heuer, M. Wilhelm, H. Zimmermann, and H.W. Spiess, *Phys. Rev. Lett.* **75**, 2851 (1995).
5. M. Maroncelli, *J. Mol. Liquids* **57**, 1 (1993).
6. R. Richert, *Chem. Phys. Lett.* **199**, 355 (1992).
7. R. Richert, F. Stickel, R.S. Fee, and M. Maroncelli, *Chem. Phys. Lett.* **229**, 302 (1994).
8. R. Richert and A. Wagener, *J. Phys. Chem.* **97**, 3146 (1993); **95**, 10115 (1991).
9. R. Richert, *Phys. Rev. Lett.* (submitted).
10. C. Burger, Ph.D. thesis, Marburg University (1994).
11. R. Böhmer, G. Hinze, G. Diezemann, B. Geil, and H. Sillescu, *Europhys. Lett.* (to be published).
12. B. Schiener, R. Böhmer, A. Loidl, and R.V. Chamberlin, *Science* **274**, 752 (1996).
13. M.T. Cicerone, F.R. Blackburn, and M.D. Ediger, *Macromol.* **28**, 8224 (1995).
14. M.T. Cicerone and M.D. Ediger, *J. Chem. Phys.* **104**, 7210 (1996).

## FLUCTUATION MODEL FOR STRUCTURAL RELAXATION AND THE GLASS TRANSITION

C. T. MOYNIHAN, J.-H. WHANG

Materials Science and Engineering Dept., Rensselaer Polytechnic Institute  
Troy, NY 12180-3590, moynic@rpi.edu

### ABSTRACT

The fluctuation or independently relaxing nanoregion model attributes the distribution of structural relaxation times in a glassforming melt to a physical distribution of nanoregions which vary in their properties. A quantitative test of this model is described, in which parameters derived from relaxational data on  $B_2O_3$  glass are shown to be capable of predicting the anomalous light scattering in the glass transition region. It is also shown that the local inhomogeneities which lead to the distribution of structural relaxation times make only a very minor contribution to the distribution of electrical relaxation times in ionically conducting glasses and melts.

### INTRODUCTION

Models for the kinetics of the structural relaxation process associated with glass transition require a distribution of relaxation times [1-3]. Anomalous light scattering seen during cooling, heating or annealing in the transition region indicates that this distribution may correspond to a physical distribution of nanoregions (density or entropy fluctuations) which vary in their properties. A model based on this assumption - the fluctuation or independently relaxing nanoregion model - was able to explain qualitatively, e.g., the anomalous maxima in the light scattering intensity during heating through the transition region [4]. In the present paper this model is tested quantitatively.

### QUANTITATIVE TEST OF THE FLUCTUATION MODEL

The Tool-Narayanaswamy (TN) model for structural relaxation [1-3] uses the following expression for the  $i$ th relaxation time in the distribution:

$$\ln \tau_i = \ln \tau_{i0} + x\Delta H^*/RT + (1-x)\Delta H^*/RT_f \quad (1)$$

where  $\Delta H^*$  is an activation enthalpy,  $x$  a constant which parameterizes the nonlinearity, and  $T_f$  the fictive temperature. In the TN model the relaxation times differ in their pre-exponential constants  $\tau_{i0}$ . For the fluctuation model an appropriate modification of the TN equation is:

$$\ln \tau_i = \ln \tau_0 + x\Delta H^*/RT + (1-x)\Delta H^*/RT_{si} \quad (2)$$

Here the distribution arises from a distribution of local "structural" temperatures  $T_{si}$  which reflect local fluctuations in free volume or configurational entropy. The mean value of the  $T_{si}$ ,  $\langle T_s \rangle$ , is constrained to equal the fictive temperature  $T_f$  at any instant.

Intrinsic light scattering in a melt is due to local fluctuations in the refractive index  $n$ . Since the kinetics of structural relaxation are not precisely identical when measured for different macroscopic properties [1], a calculation of the variation in the light scattering



during structural relaxation should use kinetic parameters derived from relaxation experiments in which  $n$  is the property which is monitored. Using procedures detailed in Refs. [1-3], Eq. (2) with a KWW distribution was used to fit the data of Boesch et al. [5] for the isothermal relaxation of the refractive index  $n$  of  $B_2O_3$  glass in the transition region. These fits are shown in Figs. 1 and 2, where  $T_{fn}$  is the fictive temperature assessed from the refractive index  $n$ . The best fit parameters were:

$$\begin{aligned}\tau_0 &= 3.1 \times 10^{-33} \text{ s} \\ \Delta H^*/R &= 45,300 \text{ K} \\ x &= 0.51 \\ \beta &= 0.78\end{aligned}$$

where  $\beta$  ( $0 < \beta \leq 1$ ) is the exponent in the KWW or stretched exponential relaxation function,  $\exp[-(t/\tau)^\beta]$ . These parameters were then used to calculate the variance  $\langle \Delta^2 T_{sn} \rangle (= \langle T_{sn}^2 \rangle - \langle T_{sn} \rangle^2)$  in the refractive index "structural" temperature of  $B_2O_3$  glass during rate heating following rate cooling and isothermal annealing just below the transition region for the thermal histories reported by Bokov and Andreev [6]. These  $\langle \Delta^2 T_{sn} \rangle$  curves are compared in Fig. 3 with the corresponding light scattering intensities  $I$  (arbitrary units) measured by Bokov and Andreev [6]. Since  $I$  is proportional to the mean square fluctuation  $\langle \Delta^2 n \rangle$  in  $n$ , it should similarly be proportional to  $\langle \Delta^2 T_{sn} \rangle$ . The agreement between the shapes of the experimental  $I$  curves and the calculated  $\langle \Delta^2 T_{sn} \rangle$  curves in Fig. 3 is excellent, and the changes in the temperatures and heights of the maxima in the experimental  $I$  curves with increases in sub- $T_g$  annealing time are accurately reflected in the calculated curves.

The principal discrepancy between the experimental and calculated curves in Fig. 3 is that the  $I$  curves are displaced toward lower temperatures by about 9K relative to the  $\langle \Delta^2 T_{sn} \rangle$  curves. This discrepancy was neither surprising nor unexpected. The viscosity and structural relaxation times of  $B_2O_3$  are extremely sensitive to small amounts of water in the melt [7]. The relaxation experiments of Boesch et al. [5] were done on extremely dry specimens, while there is no indication of special drying procedures in the study of Bokov and Andreev [6]. Since water decreases the viscosity and structural relaxation time of  $B_2O_3$ , it is expected that the region of relaxational behavior in the  $I$  vs.  $T$  curves, which were measured on samples of presumably higher water content, will be displaced to lower temperatures relative to the  $\langle \Delta^2 T_{sn} \rangle$  curves calculated using data from samples of lower water content.

The shift of 9K between the  $I$  and  $\langle \Delta^2 T_{sn} \rangle$  curves of Fig. 3 can be caused by a difference of only about 0.1 mol% in the  $H_2O$  contents of the two samples [7]. In Fig. 4 "corrected" values  $I_{corr}$  of the light scattering intensity during rate heating obtained by shifting the experimental  $I$  curves upwards by 9K along the temperature axis are compared with the calculated  $\langle \Delta^2 T_{sn} \rangle$  curves. This shift of 9K is in very good agreement with a shift of 15K at about 573K between the log viscosity vs. temperature curves reported by Bokov and Andreev [6] for their  $B_2O_3$  melts and by Macedo and Napolitano [8] for the extremely dry  $B_2O_3$  used in the experiments of Ref. [5]. Indeed, given that the best reproducibility reported in the literature [7,8] for isoviscosity temperatures near  $T_g$  for  $B_2O_3$  melts of a given water content is about  $\pm 2K$  and that we are now comparing data from four separate experiments on  $B_2O_3$  (the  $n$  relaxation data, the light scattering data, and two sets of viscosity data), the agreement between these two temperature shifts of 9K

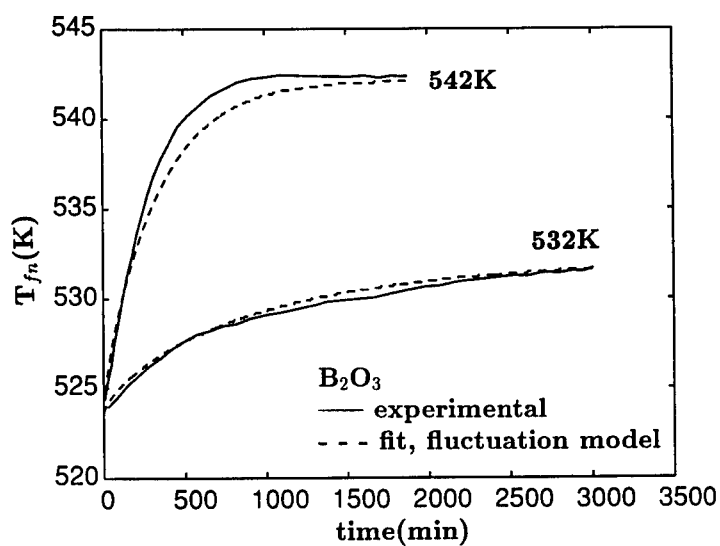


**Figure 1.** Fictive temperature  $T_{fn}$  for refractive index  $n$  vs. time during isothermal annealing of  $B_2O_3$  glass at 532K and 542K following an upward temperature jump from equilibrium at 523K. Data from Ref. [5].

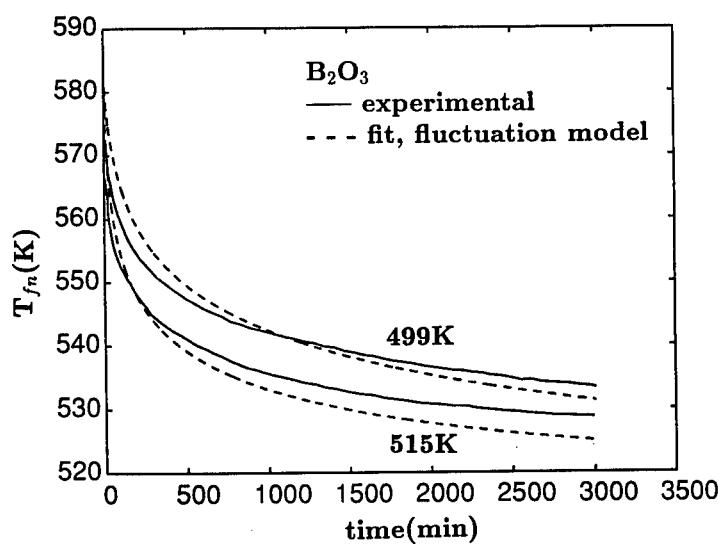


**Figure 2.**  $T_{fn}$  vs. time during isothermal annealing of  $B_2O_3$  glass at 499K and 515K following a downward temperature jump from equilibrium at 584K. Data from Ref.[5].

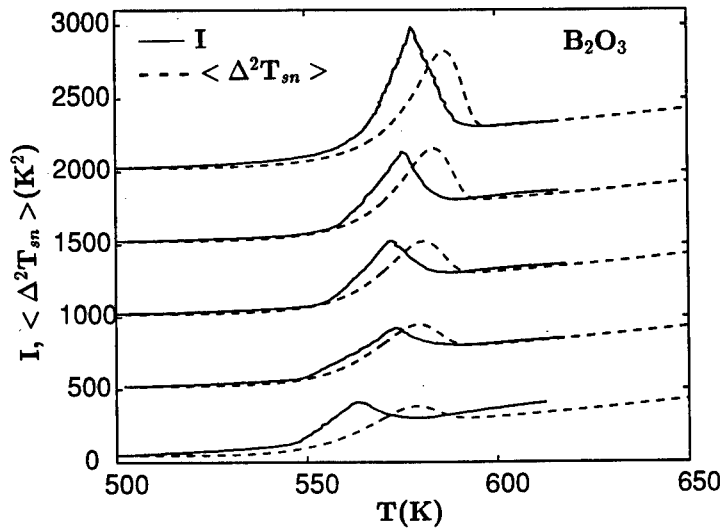


**Figure 3.** Temperature dependence of experimental light scattering intensity  $I$  (arbitrary units) [6] and of  $\langle \Delta^2 T_{fn} \rangle$  calculated from fits to data in Figs. 1 and 2 for  $B_2O_3$  glass during rate heating at 4 K/min after rate cooling at 4 K/min and isothermal annealing at 498K for (bottom to top) 0.5, 7, 15.5, 36 and 68 hours. Vertical scale is correct for bottom curves; other curves are displaced upwards for clarity.

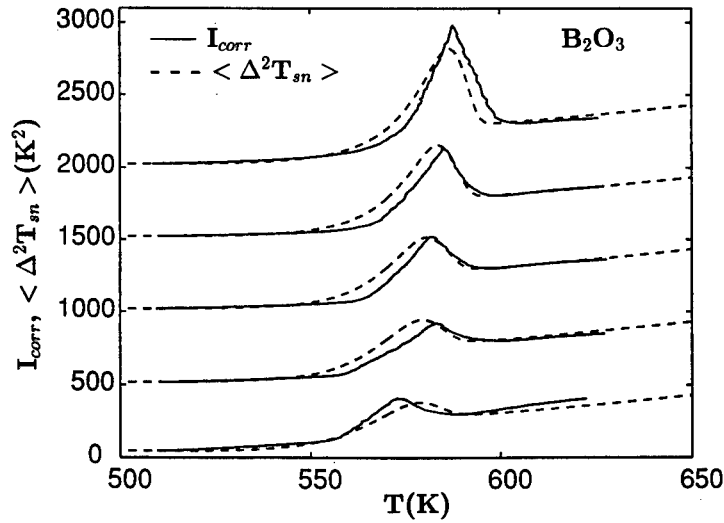


**Figure 4.** Temperature dependence of corrected light scattering intensity  $I_{corr}$  and of  $\langle \Delta^2 T_{fn} \rangle$  during rate heating of  $B_2O_3$  glass at 4 K/min after rate cooling at 4 K/min and isothermal annealing at 498K for (bottom to top) 0.5, 7, 15.5, 36 and 68 hours. Vertical scale is correct for bottom curves; other curves are displaced upwards for clarity.

and 15K is almost certainly within experimental error.

Given the quality of the fits in Figs. 1 and 2 and the uncertainties inherent in comparing data taken on different B<sub>2</sub>O<sub>3</sub> melts, the agreement between the  $I_{corr}$  and  $\langle \Delta^2 T_{sn} \rangle$  curves in Fig. 4 is also within experimental uncertainty and constitutes a quantitative test of the correctness of the fluctuation model for structural relaxation. It should be noted that the fluctuation model used here, which attributes all of the observed distribution of relaxation times to local differences in relaxation times due to entropy or free volume fluctuations, can only yield predictions that agree with or overestimate the intensity of the anomalous light scattering. The reason for this is that, if the distribution were due primarily to some inherently nonexponential character of the relaxation process and not due to free volume or configurational entropy differences between local regions, all of the nanoregions would relax at nearly the same rate. This would cause the observed intensity of the anomalous light scattering to be very small (cf. Figs. 1 and 2 in Ref. [4]) compared to that predicted from the fluctuation model.

#### APPLICATION OF THE FLUCTUATION MODEL TO NONEXPONENTIAL ELECTRICAL RELAXATION IN IONICALLY CONDUCTING GLASSES

In ionically conducting glasses and melts relaxation of the electric field due to transport of mobile ions is also nonexponential, but near  $T_g$  is highly decoupled from and typically many orders of magnitude faster than the structural relaxation process (see [9,10] and references cited therein). A longstanding question is whether the nonexponentiality of this electrical relaxation is due to (a) correlations between diffusive motions of ions or (b) nonuniformity or local inhomogeneity in the glass or melt structure. The fluctuation model for structural relaxation suggests that explanation (b) is in part responsible for the nonexponential electrical relaxation, since local nanoregions with different structures and densities (different  $T_{si}$ ) should have different local ionic conductivities, leading to a spatial distribution of electric field relaxation times. We explore this question here.

Using Eq. (2) we can write an expression relating the variance in the logarithms of the structural relaxation times  $\tau_i$  to the variance in the reciprocal of the local structural temperatures,  $1/T_{si}$ :

$$\langle \Delta^2 \ln \tau \rangle = [(1-x)\Delta H^*/R]^2 \langle \Delta^2 (1/T_s) \rangle \quad (3)$$

Note that  $(1-x)\Delta H^*$  is the difference between the structural relaxation activation enthalpy for the equilibrium liquid ( $\langle T_s \rangle = T$ ) and that for the glass below  $T_g$  ( $\langle T_s \rangle = \text{constant}$ ). A similar expression can be written for the contribution of local structural fluctuations to the variance in the logarithms of the electric field relaxation times  $\tau_{\sigma i}$ :

$$\langle \Delta^2 \ln \tau_{\sigma} \rangle = [(\Delta H_{\sigma,eq}^* - \Delta H_{\sigma,gl}^*)/R]^2 \langle \Delta^2 (1/T_s) \rangle \quad (4)$$

where  $\Delta H_{\sigma,eq}^*$  and  $\Delta H_{\sigma,gl}^*$  are respectively the activation enthalpies for the electrical conductivity  $\sigma$  for the equilibrium liquid above  $T_g$  and for the glass below  $T_g$ . Combining Eqs. (3) and (4), we get an expression relating  $\langle \Delta^2 \ln \tau \rangle$  and  $\langle \Delta^2 \ln \tau_{\sigma} \rangle$ :

$$\langle \Delta^2 \ln \tau_{\sigma} \rangle = \left[ \frac{\Delta H_{\sigma,eq}^* - \Delta H_{\sigma,gl}^*}{(1-x)\Delta H^*} \right]^2 \langle \Delta^2 \ln \tau \rangle \quad (5)$$

Note that the values of  $\langle \Delta^2 \ln \tau \rangle$  and  $\langle \Delta^2 \ln \tau_{\sigma} \rangle$  can be related to the KWW  $\beta$  and  $\beta_{\sigma}$

parameters commonly used to describe the nonexponential character of the relaxation [11]. A large value of  $\langle \Delta^2 \ln \tau \rangle$  corresponds to a small value of  $\beta$ .

Because the electric field relaxation in most ionically conducting melts is highly decoupled from the structural relaxation process near  $T_g$  (decoupling index =  $R_\tau \equiv \langle \ln \tau \rangle / \langle \ln \tau_\sigma \rangle \gg 1$ ), the term containing the activation enthalpies in Eq. (5) is considerably smaller than unity. This leads to the prediction in terms of the fluctuation model that the distribution of electric field relaxation times  $\langle \Delta^2 \ln \tau_\sigma \rangle$  should be much narrower than  $\langle \Delta^2 \ln \tau \rangle$  for the structural relaxation process. This is contrary to what is observed experimentally, as illustrated below with some data [11-14] for a typical ionically conducting melt of composition (mol%) 25Na<sub>2</sub>O-75SiO<sub>2</sub>.

$$\begin{aligned}
T_g &\approx T = 758K \\
(1-x)\Delta H^* &= 123 kJ/mol \\
\langle \Delta^2 \ln \tau \rangle &= 2.14 & (\beta = 0.66) \\
\Delta H_{\sigma,eq}^* &= 96 kJ/mol \\
\Delta H_{\sigma,gl}^* &= 67 kJ/mol \\
\langle \Delta^2 \ln \tau_\sigma \rangle_{exp} &= 3.25 & (\beta_{\sigma,exp} = 0.58) \\
\langle \Delta^2 \ln \tau_\sigma \rangle_{calc} &= 0.12 & (\beta_{\sigma,calc} = 0.97)
\end{aligned}$$

The width of the experimentally observed distribution of electric field relaxation times,  $\langle \Delta^2 \ln \tau_\sigma \rangle_{exp}$ , is much broader for 25Na<sub>2</sub>O-75SiO<sub>2</sub> than the width,  $\langle \Delta^2 \ln \tau_\sigma \rangle_{calc}$ , obtained from Eq. (5). (Correspondingly,  $\beta_{\sigma,exp} \ll \beta_{\sigma,calc}$ .) This means that local spatial inhomogenities in a melt near  $T_g$  or a glass, which are "frozen in" on the timescale of the ionic transport process, make only a very minor contribution to the nonexponentiality of the electric field relaxation. Rather, the nonexponential electric relaxation is likely due mostly to correlations in the motions of the mobile ions. This conclusion is very much in line with comments made in Ref. [10] on electrical relaxation experiments on glass and polycrystalline specimens of LiAlSi<sub>2</sub>O<sub>6</sub> [15]. The distribution of electric field relaxation times for the glass ( $\beta_\sigma = 0.47$ ) was comparable to, but somewhat broader than, the distribution for the polycrystal ( $\beta_\sigma = 0.54$ ). Part, but probably not much, of this difference in the  $\beta_\sigma$  values may, in the current perspective, be due to thermally induced fluctuations in the local structure which are present in the glass but absent in the crystal.

## CONCLUSIONS

As noted previously [4], the anomalous time dependence of light scattering in the glass transition region appears to be the first result to offer evidence on the physical origin of the nonexponentiality of structural relaxation kinetics. Indications are that the apparent distribution of relaxation times has a physical correspondence to a distribution of thermally induced regions of varying local density, entropy and structure. In the present paper we report a quantitative test of this hypothesis. It should be noted that the results in Fig. 4 meet rather rigid standards for testing of a scientific hypothesis, namely, employment of one set of experimental measurements to predict quantitatively the results of an independent and totally different experiment. In addition, the fluctuation model, using an approach different from any previously employed, provides evidence that the nonexponential electrical relaxation in ionically conducting melts and glasses is due mainly to correlated ionic motions, rather than to local inhomogenities in the melt or glass structure.

## REFERENCES

1. C. T. Moynihan et al., Ann. NY Acad. Sci. **279**, 15 (1976).
2. I. M. Hodge, J. Non-Cryst. Solids **169**, 211 (1994).
3. C. T. Moynihan, S. N. Crichton and S. M. Opalka, J. Non-Cryst. Solids **131-133**, 420 (1991).
4. C. T. Moynihan and J. Schroeder, J. Non-Cryst. Solids **160**, 52 (1993).
5. L. Boesch, A. Napolitano and P. B. Macedo, J. Am. Ceram. Soc. **53**, 148 (1970).
6. N. A. Bokov and N. S. Andreev, Sov. J. Phys. Chem. Glass **15**, 243 (1989).
7. T. J. M. Visser and J. M. Stevels, J. Non-Cryst. Solids **7**, 401 (1972).
8. P. B. Macedo and A. Napolitano, J. Chem. Phys. **49**, 1887 (1968).
9. C. A. Angell, Chem. Rev. **90**, 523 (1990).
10. W. C. Hasz, C. T. Moynihan and P. A. Tick, J. Non-Cryst. Solids **172-174**, 1363 (1994).
11. C. T. Moynihan, L. P. Boesch and N. L. Laberge, Phys. Chem. Glasses **14**, 122 (1973).
12. R. H. Doremus, Glass Science, 2nd ed. (Wiley, New York, 1994), p. 272.
13. L. P. Boesch and C. T. Moynihan, J. Non-Cryst. Solids **17**, 44 (1975).
14. C. T. Moynihan, A. J. Easteal, D. C. Tran, J. A. Wilder and E. P. Donovan, J. Am. Ceram. Soc. **59**, 137 (1976).
15. B. Munro, M. Schrader and P. Heitjans, Ber. Bunsenges. Phys. Chem. **96**, 1718 (1992).

## COOPERATIVE LENGTH SCALE OF AROCLOR NEAR ITS DYNAMIC GLASS TRANSITION

A. K. RIZOS\*, K. L. NGAI\*\*

\*University of Crete, Department of Chemistry and Foundation for Research & Technology-Hellas (FORTH), P.O. Box 1527, Heraklion 71409, Greece, rizos@talos.cc.uoh.gr

\*\*Naval Research Laboratory, Washington, D.C. 20375-5347, USA, ngai@estd.nrl.navy.mil

### ABSTRACT

Photon correlation spectroscopy in the depolarized mode has been used to monitor the reorientational dynamics of Aroclor (A1248) (polychlorinated biphenyls) that contain in solutions various amounts of low and high molecular weight ( $M_w$ ) polymers. For the high  $M_w$  polymer/A1248 solutions we observe a very small dependence of the stretched exponential parameter  $\beta$  on temperature. In contrast, the low  $M_w$  polymer/A1248 solutions display a pronounced temperature dependence of  $\beta$ . These preliminary experiments allow us to use the effect of modification of the solvent dynamics by added polymer to estimate the length scale of cooperative motion in glass forming systems from the size of the polymer chain.

### INTRODUCTION

The dynamic glass transition is an old basic problem in condensed matter physics and it is a subject of continued discussion. Among the models that have been advanced to comprehend the dynamic behavior of a supercooled liquid, the concept of molecules rearranging themselves cooperatively within regions of characteristic size which increases with decreasing temperature has been found to be the most appealing. Adam and Gibbs [1] emphasized the definitive role of the configurational entropy by introducing cooperatively rearranging regions (CRR), defined as the smallest regions that can experience a transition to a new configuration without a required simultaneous change outside its boundary. Donth [2,3]

estimated the characteristic length of the CRR from calorimetric data to be of the order of 10-20 Å.

In the present report our objective is to provide supporting evidence for the concept of cooperativity in glass forming polymer solutions by using Photon Correlation Spectroscopy in the depolarized mode and Dielectric Relaxation Spectroscopy. In previous studies [4,5] we have used a modification of the Adam-Gibbs theory [1] according to the coupling model [6] to take into account interactions among the CRR's.

## EXPERIMENT

Solutions of polyisoprene (*PI*) ( $M_w=1000$ , 8000, 20000 and 43000) in Aroclor and 1,4-polybutadiene (*PB*) ( $M_w=1000$ , 2500 and 100000) in Aroclor were filtered in a cylindrical light scattering cell and the samples were finally sealed under vacuum. Depolarized dynamic light scattering measurements were made using the technique and apparatus described earlier equipped with an Ar<sup>+</sup> laser (Spectra Physics) emitting vertically polarized light with wavelength at 488 nm and an ALV-5000 full digital correlator. The scattered light passed through a Glan-Thompson polarizer with an extinction better than  $10^{-7}$ . Measurements of the complex dielectric function have been made in the frequency range from  $10^{-2}$  Hz to  $10^6$  Hz within the temperature range from 210 to 273 K. The samples were kept between two gold-plated stainless steel plates of 20 mm in diameter with a separation of 100  $\mu m$ .

## RESULTS

The dynamic light scattering experimental correlation functions were treated in the homodyne limit. The measured intensity autocorrelation function  $G(q,t)$  is related to the desired normalized field correlation function  $g(q,t)$  (where  $q = (4\pi n/\lambda) \sin(\theta/2)$  is the scattering vector,  $n$  is the refractive index of the bulk polymer,  $\theta$  is the scattering angle and  $\lambda$  the laser wavelength) by:

$$G(q,t) = A \left[ 1 + f |ag(q,t)|^2 \right] \quad (1)$$

where  $f$  is the instrumental factor, calculated by means of a standard,  $a$  is the fraction of the total scattered intensity associated with orientation fluctuations with correlation times longer



than  $10^{-6}$ s and  $A$  is the baseline. Analyses have been performed for the  $g(q,t)$  correlation functions using the form of the Kohlrausch-Williams-Watts (*KWW*) function,

$$\alpha g(q,t) = A_f \exp\left[-(t/\tau_f)^\beta\right] \quad (2)$$

with parameters  $A$ ,  $\tau$  and  $\beta$  that give the contrast, relaxation time and shape of the relaxation process, respectively. Typical depolarized intensity-intensity correlation functions for a scattering angle of  $90^\circ$  are shown in Figure 1 for a PB(2500)/A1248 solution at various temperatures.

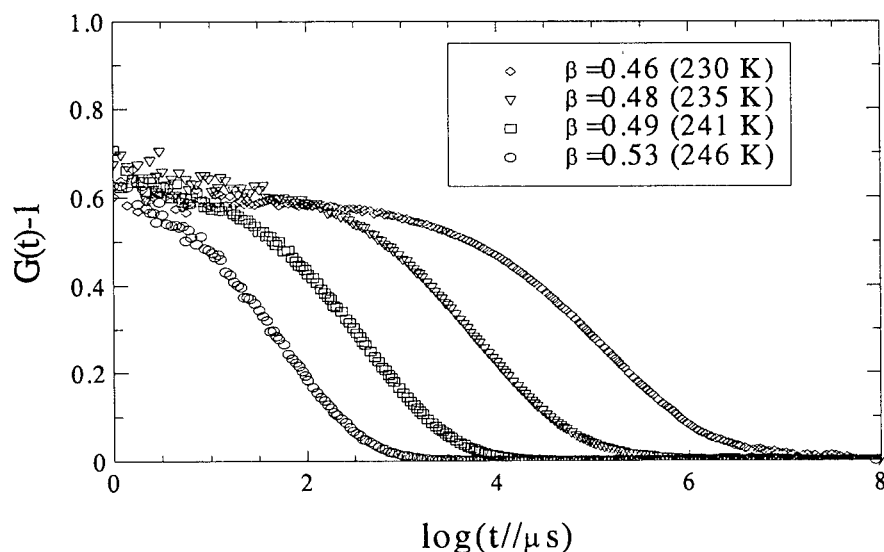


Figure 1 Depolarized experimental correlation functions for the low  $M_w$ (=2500) 13% PB/Aroclor mixture at different temperatures.

Aroclor dynamics in the presence of the polymer is probed for convenience only.  $\beta$  should not be identified with the coupling parameter of the coupling model because fluctuations contribute additionally to the measured dispersion characterized by  $\beta$ .

Depolarized dynamic light scattering measurements were recorded in the temperature range between 218 and 257 K. The fit of the data to the *KWW* function gave a temperature dependent distribution parameter  $\beta$ . We found a pronounced temperature dependence of  $\beta$  for the low  $M_w$  *PI* and *PB* solutions. On the other hand for the high  $M_w$  polymer solutions there is only a slight change in  $\beta$  with temperature. Typical results are shown in Figure 2. This

interesting behavior found here by PCS is confirmed by dielectric relaxation spectroscopy. The observed spectra were well represented by a single Havriliak-Negami function over a broad temperature range which in turn after a half-sided cosine transformation into the time domain was fitted to the KWW stretched exponential from which the shape parameter  $\beta$  was extracted. The agreement with the light scattering data is clear from Figure 2.

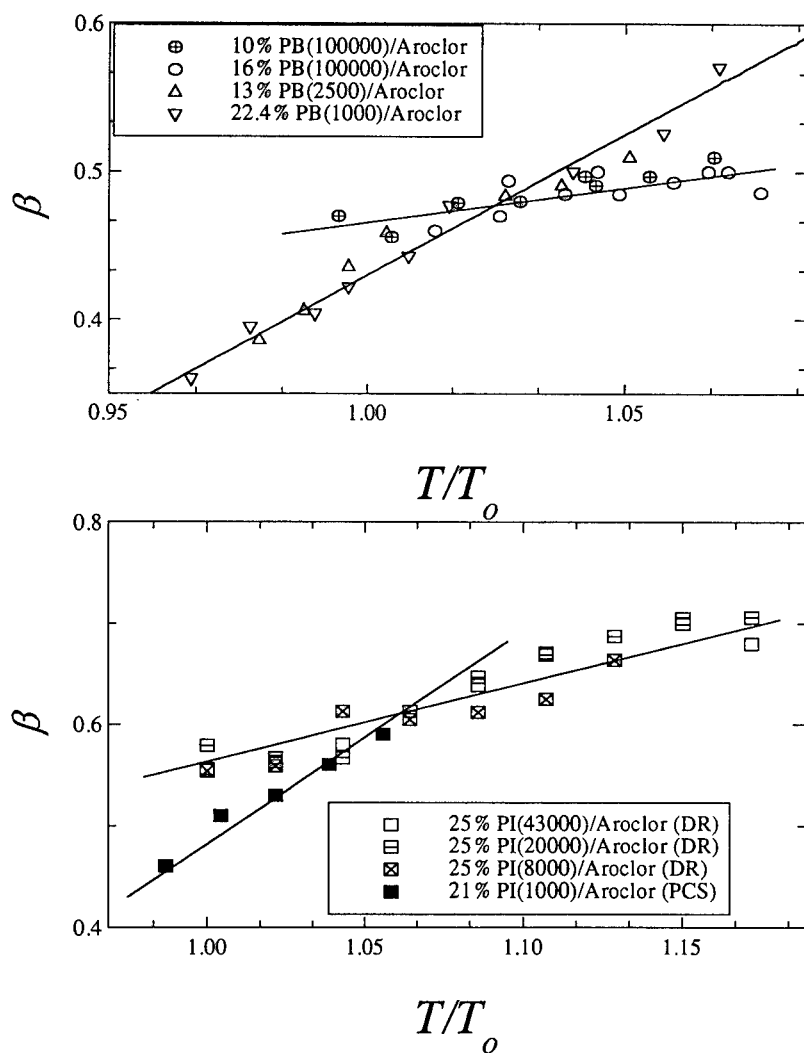


Figure 2 The distribution parameter  $\beta$  as a function of the reduced temperature  $T/T_o$ , where  $T_o$  is the temperature at which  $\tau = 1s$ .

These results indicate that there is definitely a relevance between the change in  $\beta$  with temperature and the size of the polymer chain. The radius of gyration ( $R_g$ ) changes almost by a factor of 10 from  $\sim 10$  Å to 100 Å as one goes from PB ( $M_w=1000$ ) to PB ( $M_w=1\times 10^5$ ). This suggests the pronounced temperature dependence of  $\beta$  is caused by the large fluctuations in the modification of the polymer on the Aroclor when the size of the polymer  $R_g$  becomes comparable to the cooperative rearranging regions. Figure 3 shows the molecular weight dependence of the slope  $d\beta/T$  for PI and 1,4-PB. It appears that there is a narrow range between  $1000 < M_w < 3000$  ( $10 \text{ Å} < R_g < 20 \text{ Å}$ ) where this behavior is observed

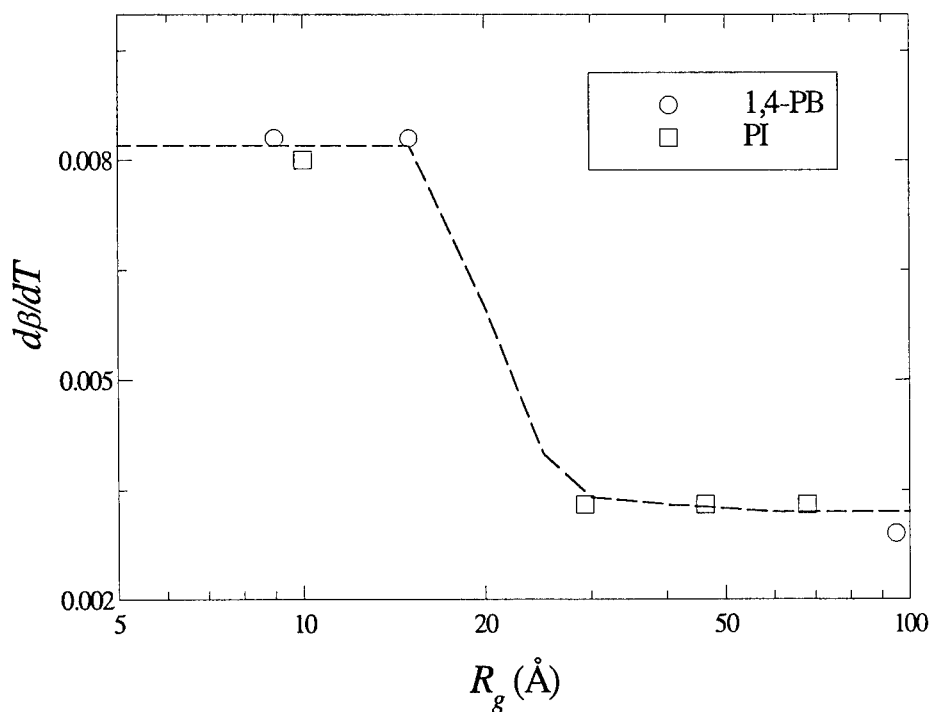


Figure 3 The dependence of the slope  $d\beta/T$  on molecular weight.

The effect we observed can be used as a method to determine the length scale of the glass transition near  $T_g$ , when Aroclor solutions of polymers with a range of  $M_w$ 's are studied in the way demonstrated here. We can give an estimate that such a lengthscale is approximately equal to  $R_g$  ( $M_w=3000$ ) or  $\sim 15$  Å.

## CONCLUSIONS

The behavior of the Aroclor orientational motion in Aroclor solutions of high molecular weight *PI* and *PB* is distinctively different from that in solutions of low molecular weight polymers. When the  $M_w$  of *PI* or *PB* becomes small the photon correlation function shows large broadening. We believe this is caused by the radius of gyration of the polymer being now comparable to the size of the cooperative rearranging regions. When this condition holds, concentration fluctuations become enhanced resulting in a concomitant dramatic broadening of the observed Aroclor reorientational relaxation spectrum. We have exploited this effect to determine the lengthscale of cooperativity near  $T_g$ .

## ACKNOWLEDGEMENTS

The authors are grateful to Prof. Keiichiro Adachi for supplying the polyisoprene samples.

## REFERENCES

1. G. Adams and J. H. Gibbs, J. Chem. Phys., **43**, p. 139, (1965).
2. E. Donth, J. Non-Cryst. Sol., **131-133**, p. 204, (1991).
3. E. W. Fischer, E. Donth and W. Steffen, Phys. Rev. Lett., **68**, p. 2344, (1992).
4. A. Rizos, G. Fytas, T.P. Lodge and K. L. Ngai, J. Chem. Phys., **95**, p. 2980, (1991).
5. A. K. Rizos, K. L. Ngai and G. Fytas, Progr. Colloid Polym. Sci., **91**, p. 135, (1993).
6. K. L. Ngai, R. W. Rendel and D. J. Plazek, J. Chem. Phys., **94**, p. 3018, (1991).

## POSSIBLE CAUSES OF THE CHANGE OF DYNAMICS IN GLASS-FORMING MATERIALS SUBJECTED TO REDUCED DIMENSION

K.L. NGAI \*, A.K. RIZOS \*\*

\*Naval Research Laboratory, Washington, DC 20375-5320 USA, ngai@estd.nrl.navy.mil

\*\*Department of Chemistry, University of Crete, and Foundation for Research & Technology-Hellas (FORTH), P.O. Box 1527, Heraklion 71409, Crete, Greece, rizo@talos.cc.uh.gr

### ABSTRACT

There is currently many ongoing investigations of the change in the glass transition temperature when a material is reduced in dimension from the normal bulk state. The reduction in dimension can be accomplished by casting the material as thin films with or without a substrate or putting it in nanometer size pores. In this work, we explore possible causes of the change in dynamics of the bulk material when the glass-former is subjected to such modifications. The existence of a growing cooperative length scale  $L(T)$  with decreasing temperature in bulk fragile glass-forming liquids reaching the size of approximately 1.5-2.0 nm at the glass transition temperature is the basis of our consideration. When the reduced dimension is comparable to  $L(T_g)$ , cooperative dynamics within a lengthscale equal to  $L(T_g)$  can no longer be maintained in all three dimensions throughout the sample. The imposed reduction of the cooperative length scale speeds up the dynamics and causes a reduction of the glass transition temperature. For polymeric glass-formers particularly at higher molecular weights, reduction of one dimension in thin films engenders orientation of the polymer chains when their radius of gyration becomes comparable to the film thickness. The latter is known to cause also a reduction of the glass transition temperature.

### INTRODUCTION

The dynamics of glass transition is currently the subject of intensive study as evidenced by the papers published in this Volume. The current trend of research which extends the research to short microscopic times and temperatures much higher than  $T_g$  means a solution has to provide an understanding of the dynamics over immense time (frequency) and temperature ranges. Thus the problem of glass transition in bulk glass-formers at present days has become very difficult to solve due to the presence of many complicating factors. First and foremost is the many-body nature of the dynamics (sometimes loosely referred to as *cooperativity*) which makes it difficult to be accurately described, particularly over a large time range from microscopic times of the order of a picoseconds to macroscopic times of the order of  $10^2$  s. It is expected, at least from some models including the coupling model [1-4], that the many-body effects are responsible at least partly for the nonexponentiality [1,2], dynamically heterogeneous nature [5] and slowing down with decreasing temperature of the dynamics [6]. The many-body effects are thought of being responsible also for the relation between short-time and long-time dynamics observed experimentally. Second is the nontrivial effect caused by the significant change of a thermodynamic variable such as density and entropy which take place over the large temperature range. These large changes of thermodynamic variables are the basis of the free volume theory [7] and the configurational entropy theory [8,9]. It seems a complete description of glass transition requires a synthesis of all these relevant factors into a theory.

Development of a satisfactory theory of dynamics for glass-forming liquids in the bulk state can be accelerated by paying attention to experimental facts coming out from recent works on the changes of the dynamics when the liquid is subjected to reduced dimension or dimensionality. Concept or theory proposed for bulk dynamics must be consistent with the change observed in reduced dimension. Confinement of the material in nanometer size pores reduce its dimension and formation of a thin film with or without a substrate reduced its dimensionality. There are complications encountered sometimes in these studies caused by the modification of the surface layers of the liquid near the substrate or the confining material. However, when this complication is either eliminated or taken into consideration, the dynamics of the liquid with reduced dimension seems to be sped up compared with the bulk at the same temperature [10-12]. A consequence of this change is that the glass transition temperature falls with reduced dimension. In this paper we propose the principal cause of this effect is due to the cooperative length scale of the dynamics  $L(T)$  being comparable with the reduced dimension  $d$ . For polymeric glass-formers with high molecular weight and large radius of gyration  $R_g$ , the reduced dimension when comparable with  $R_g$  cause orientations of the polymer chains which are Gaussian coils in the bulk. The induced orientation of polymer chains in a thin film has the effect of speeding up the local segmental dynamics. The two effects,  $L(T) \approx d$  and  $R_g \approx d$ , act in concert in accelerating the dynamics of polymer thin film and may explain the large shifts in  $T_g$  reported for high molecular weight polymers [ ].

#### COOPERATIVE LENGTH SCALE $L(T)$

The Gibbs-DiMarzio [8] and Adam and Gibbs [9] description of relaxation and glass transition using configurational entropy imply the existence of some length-scale for their cooperative rearranging region (CRR). The many-body nature of relaxation in fragile glass-formers imply that motions of the basic units have to be cooperative meaning that some units can move first and others have to wait for their turn. This dynamic heterogeneous relaxation may also engenders some cooperative length-scale [13]. Donth [14] has suggested also the existence of a length-scale of the order of a few nm for polymers. In a paper of this Volume [15] we have used an effect to determine the cooperative length-scale  $L(T)$  of a fragile glass-former Aroclor (polychlorinated biphenyl) near  $T_g$ . The value  $L(T)$  found is about 15 to 20 nm when the relaxation time is within the time window of photon correlation spectroscopy ( $10^{-1} < t < 10^{-6}$  s) and the temperature is above  $T_g$ . Thus,  $L(T_g)$  can be larger than 15 nm. As far as we know this is the first direct experiment determination of  $L(T)$  for  $T$  slightly larger than  $T_g$ . In this work we are interested in the existence of  $L(T)$  and the consequence when it is modified by reduced dimension or dimensionality. We are not concerned with the exact interpretation or physical origin of  $L(T)$ . The result of this paper is independent of theoretical models for  $L(T)$ .

#### REDUCTION OF $L(T)$ AND CORRESPONDING DECREASE OF $T_g$

The cooperative nature of the dynamics determines both  $L(T)$  and the relaxation time  $\tau_\alpha(T)$ . Even without following in detail of any theory, it is intuitively obvious that  $L(T)$  like  $\log \tau_\alpha(T)$  is a monotonic increasing function with decreasing temperature as the dynamics becomes slower.  $\tau_\alpha(T)$  and  $L(T)$  are not independent of each other because both are determined by the many-body dynamics. A change of one is accompanied by a corresponding change of the other. In particular, at constant  $T$ , a decrease of  $L(T)$  effected by some means is necessarily followed by a decrease of  $\tau_\alpha(T)$ . When the glass-forming liquid is reduced in dimension or in dimensionality and one of its length  $d$  (radius of the unmodified liquid in the pore or the thickness of the unmodified

liquid of the thin film) becomes comparable to  $L(T)$ , portion of the liquid near the interface can no longer maintain a cooperative length-scale equal to  $L(T)$  entirely within the liquid. As a result, this portion of the liquid has to contend with a smaller cooperative length-scale which causes its structural relaxation time  $\tau_\alpha(T)$  to be shortened and its glass transition temperature reduced. Experimentally this has been observed in fragile small molecule glass-formers [10] contained in nanometer size pores and in polymer thin films [11,12].

#### INDUCED CHAIN ORIENTATION IN POLYMER THIN FILM

Thin high molecular weight polymer films with the thickness of the unmodified polymer layer of the order of nanometers have another effect that also accelerates the local segmental relaxation in the film compared with that in the bulk. The polymer chains are Gaussian coils in the bulk. The size of the Gaussian coil is measured by its radius of gyration  $R_g$ . For high molecular weight polymers it can be of the order of  $10 \geq R_g \geq 1$  nm. Therefore when the film thickness  $d$  is of the order 10 nm or less, we can expect that the polymer chains contained therein can no longer assume the Gaussian coil configuration in three dimensions. The coils are compressed to be more pancake like as  $d$  is further reduced. Consequently, the polymer chains have acquired some orientations in the plane of the film. It has previously been found experimentally by mechanical relaxation measurements in glassy polymers [4] that the induced orientation of the polymer chains by large deformation speeds up the local segmental motion. There is further experimental evidence that the effect is due to the reduction of dynamic constraint (or the degree of cooperativity) consistent with the coupling model [1-4]. By analogy with the mechanical data of deformed glassy polymers, we expect that the induced orientations of the chains in thin polymer film will also speed up the local segmental motion and decrease the glass transition temperature. For thin films formed by high molecular weight polymers, the condition  $R_g > L(T)$  holds. When  $d$  is reduced to approach  $L(T)$ , both effects due to induced orientation and decrease of  $L(T)$  discussed in the previous section act in concert to accelerate the local segmental relaxation and reduce the glass transition temperature. They reinforce each other, leading to a large combined effect in polymer thin films which may explain the large shift in glass transition temperature reported [11,12].

#### CONCLUSION

Our recent experimental work has located the size of the length-scale  $L(T)$  in a typical fragile glass former to be of the order of 1.5-2.0 nm above and near  $T_g$ . It is expected that  $L(T)$  at  $T=T_g$  can be even larger. Such size of  $L(T)$  indicate that full cooperativity of structural relaxation in the bulk fragile glass-forming liquids cannot be maintained throughout the same liquid when confined in nanometer size pores and in thin films with thickness of nanometers. The degree of cooperativity is a measure of the slowing down of the relaxation or the structural relaxation time. The reduction in  $L(T)$  or degree of cooperativity is therefore expected to speed up the relaxation and accounts for the experimental observations. For thin films formed by high molecular weight polymers, an additional effect due to induced orientation in the plane of the film enhances the effect.

#### ACKNOWLEDGMENTS

This work at the Naval Research Laboratory is supported by the Office of Naval Research. The authors thank Tadeusz Pakula for a discussion of induced orientations in polymer thin films.

## REFERENCES

1. K.L. Ngai, *Comments Solid State Phys.* **9**, 121 (1979).
2. K.L. Ngai in Disorder Effects on Relaxational Properties, edited by R. Richert and A. Blumen (Springer, Berlin 1994), p.89-150.
3. K.Y. Tsang and K.L. Ngai *Physical Review E* **54**, R3067 (1996).
4. K.L. Ngai, C.M. Roland and A.F. Yee, *Rubb.Chem.Tech.* **66**, 817 (1993).
5. K.Schmidt-Rohr, *Phys.Rev.Letters* **66**, 3020 (1991).
6. R. Böhmer, K.L. Ngai, C.A. Angell and D.J. Plazek, *J.Chem.Phys.* **94**, 3018 (1994).
7. J.D. Ferry, Viscoelastic Properties of Polymers, (Academic, New York) 3rd ed. (1980).
8. J.H. Gibbs and E.A. DiMarzio, *J.Chem.Phys.* **43**, 139 (1965).
9. G. Adam and J.H. Gibbs, *J.Chem.Phys.* **28**, 373 (1958).
10. A. Patkowski et al. to be published.
11. J.A. Forrest, K. Dalnoki-Veress, J.R. Stevens and J.R. Dutcher, *Phys.Rev.Lett.* **77**, 2002 (1996).
12. A.F. Yee and D. Gidley, private communication.
13. K.L. Ngai, J. Colmenero, A. Arbe, and A. Alegria, *Macromolecules* **25**, 6727 (1992).
14. E. Donth, *J.Non-Cryst.Solids* **131-133**, 204 (1991).
15. A.K. Rizos and K.L. Ngai, in this Volume.



## DYNAMICS IN A NONFRAGILE GLASS-FORMING LIQUID

B. Rufflé, S. Beaufils, J. Etrillard, J. Gallier, B. Toudic, C. Ecolivet

*Groupe Matière Condensée et Matériaux, UMR CNRS 6626, Université de Rennes I, 35042 Rennes, France*

G. Coddens, J.P. Ambroise

*Laboratoire Léon Brillouin, CE Saclay, 91191 Gif Sur Yvette, France*

E. Guéguen, R. Marchand

*Groupe Verres et Céramiques, URA CNRS 1496, Université de Rennes I, 35042 Rennes, France*

### ABSTRACT

The dynamics of  $\text{Na}_{0.5}\text{Li}_{0.5}\text{PO}_3$  ( $T_g = 515$  K,  $T_m = 749$  K) a non fragile glass forming liquid has been investigated over a large temperature range (300 - 1000 K) and in a wide energy window using various experimental techniques. The susceptibility spectra obtained by coherent neutron scattering and depolarized light scattering between 1 and  $10^4$  GHz show mainly two contributions: a low frequency vibrational peak, the so-called Boson peak and a quasielastic component, referred to the  $\beta_{\text{fast}}$  process in the mode coupling theory (MCT).

The data are discussed in relation to the mode coupling theory for the liquid glass transition. In particular, the temperature evolution of the susceptibility height in the  $\beta_{\text{fast}}$  region is compatible with a crossover temperature  $T_c \sim 620$  K which is also deduced from a power law temperature dependence of the structural relaxation timescale. As a secondary  $\beta_{\text{slow}}$  process, observed by  $^{31}\text{P}$  NMR, decouples from the structural relaxation timescale also below 600 K, a real change in the dynamics seems to occur around  $T_c \sim 620$  K =  $1.2 T_g$  in this non fragile glass forming liquid.

### INTRODUCTION

During the last years, the mode coupling theory [1] has been shown to successfully describe neutron and light scattering data [2-9] for the dynamics of some weakly supercooled liquids which are called fragile [10]. Indeed, a two step ( $\beta_{\text{fast}}$  and  $\alpha$ ) relaxation behavior for the correlation function of the density fluctuations is observed and a crossover temperature  $T_c > T_g$  is identified as predicted by the MCT. In the idealized version of the theory, an ergodic-nonergodic transition occurs at  $T_c$  where the density fluctuation modes arrest with decreasing temperature. In an extended version, temperature activated hopping processes have been taken into account to restore ergodicity below  $T_c$  as experimentally observed.

However, it seems that in less fragile systems, the MCT fails to describe the dynamics at high frequencies. It has been related to the stronger vibrational contribution, present in these glass formers. Indeed, it is now well known that the Boson peak contribution to the dynamical structure factor  $S(q, \omega)$  strongly increases when going from fragile towards strong glass forming liquids [11]. Thus in non fragile systems, this inelastic contribution strongly distorts the dynamical susceptibility above the susceptibility minimum [12-15] between the  $\alpha$  and  $\beta_{\text{fast}}$  processes which is just the frequency range concerned by some predicted scaling laws of the MCT. The Boson peak contribution could thus be responsible for the departure of the asymptotic exponent from the constraint imposed by the MCT, as already slightly observed in fragile liquids and strongly amplified in less fragile systems [16].

### EXPERIMENTAL RESULTS

$\text{Na}_{0.5}\text{Li}_{0.5}\text{PO}_3$  is the eutectic composition ( $T_g = 515$  K,  $T_m = 749$  K) based on the two alkali phosphate compounds  $\text{NaPO}_3$  and  $\text{LiPO}_3$ . The structure consists of covalent twisted chains of phosphate tetrahedra  $\text{PO}_4$  linked through ionic bonds between non-bridging oxygen and alkali ions. In the crystalline state,  $\text{NaPO}_3$  and  $\text{LiPO}_3$  are characterized by a very different conformational state of the phosphate chain. As the cations are supposed to be randomly distributed in the mixed structure, it results in a random microstructure which prevents the

supercooled liquid from crystallizing in the whole temperature range between  $T_g$  and  $T_m$ , thus over more than 200 K.

As it is clearly shown in Fig. 1, the temperature dependence of the viscosity for this glass forming liquid has an intermediate behavior between fragile and strong liquids in the Angell classification. Recently, it has been shown that in this glass forming system, a secondary  $\beta_{\text{slow}}$  process was probed around  $T_g$  by low frequency techniques like  $^{31}\text{P}$  NMR [19] and DMA [21], whereas at higher temperatures, the structural relaxation process was analyzed. Thus below 600 K ( $\sim 1.2 T_g$ ) occurs a decoupling between the structural relaxation timescale and the secondary  $\beta_{\text{slow}}$  process as shown in Fig. 2.

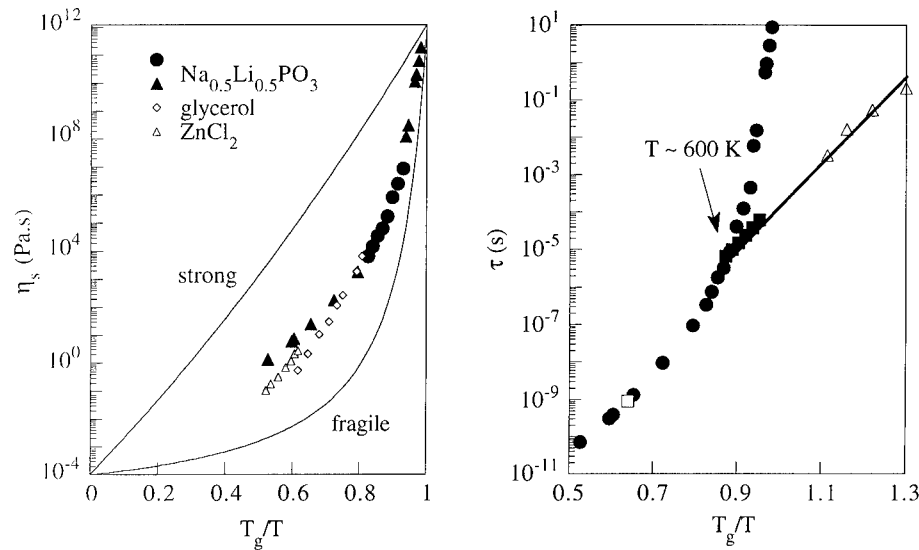


Fig. 1. (left) Temperature dependence of the viscosity for  $\text{Na}_{0.5}\text{Li}_{0.5}\text{PO}_3$  ( $\blacktriangle$  from [17],  $\bullet$  from [18]) as compared to glycerol ( $\diamond$ ) and  $\text{ZnCl}_2$  ( $\triangle$ ) from [10].

Fig. 2. (right) Temperature dependence of the structural relaxation timescale  $\tau_s$  from viscosity measurements ( $\bullet$  [17-18]) and relaxation times from  $^{31}\text{P}$  NMR ( $\blacksquare$  [19],  $\square$  [20]) and DMA ( $\triangle$  [21]) probing the same  $\beta_{\text{slow}}$  process.

Neutron scattering spectra have been obtained on the time-of-flight spectrometer MIBEMOL at the LLB (Saclay, France). With an incident wavelength fixed to 6.2 Å, a resolution of 84  $\mu\text{eV}$  has been achieved. As MIBEMOL is characterized by a resolution function of triangular shape, inelastic and broad quasielastic scattering can be observed down to 0.1 meV.  $\text{Na}_{0.5}\text{Li}_{0.5}\text{PO}_3$  is a coherent scatterer (93.4 %) and furthermore, 87.2 % of the total scattering cross section is due to the coherent scattering from the phosphate chains. Thus neutron scattering is a very convenient probe to analyze the collective dynamics of the liquid glass transition in this system.

In Fig. 3 is shown a representative set of the coherent neutron scattering susceptibility spectra,  $\chi''(q, \omega, T) = S(q, \omega, T) / n(\omega, T)$  where  $n(\omega, T)$  is the Bose factor, from  $T_g$  up to above  $T_m$ . Around 6 meV is found a large vibrational contribution, the Boson peak which is very weakly temperature dependent as clearly observed in the figure. At lower energy, a relaxational component

is detected (MCT  $\beta_{\text{fast}}$  process) with an increasing intensity when temperature is increased. As shown in the figure, the susceptibility spectra above  $T_g$  are strongly influenced by the presence of the Boson peak. Furthermore, the structural relaxation remains sufficiently slow to not enter the energy window scanned by our experiment even for the highest temperature studied 773 K, just above  $T_m$ .

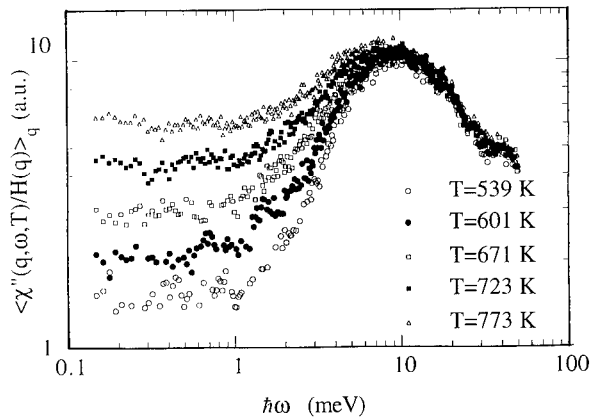


Fig. 3. Temperature dependence of the susceptibility spectra for some temperatures above  $T_g$  from neutron data. At high energy, the Boson peak is clearly seen even for temperatures above  $T_m$  (749 K) whereas at lower energy the  $\beta_{\text{fast}}$  region remains almost flat with an increasing amplitude with temperature.

All these features result in almost flat susceptibility spectra in the  $\beta_{\text{fast}}$  region without any prominent minimum and with observed power law frequency dependences which do not agree with the predictions of the MCT. In particular, the slope at high energies is rather close to a  $\approx 1$  as for other non fragile glass forming liquids investigated [12-13,15]. This value is noticeably higher than the limiting value of 0.395 given by the MCT. So the lack of pronounced susceptibility minima in these spectra prevents from a complete line shape analysis within the framework of the MCT. On the other hand, the factorization property of the dynamic susceptibility in  $q$  and  $\omega$  function  $\chi''(q, \omega, T) = \chi''(\omega, T) H(q)$  predicted by the MCT in the  $\beta$  regime has been verified in the whole temperature range investigated. Furthermore, the data for different wavevectors overlap within experimental accuracy not only in the  $\beta$  regime but also for the Boson peak leading to  $q$ -independent susceptibility spectra.

Nevertheless, a prediction which can be tested, as it does not require any determination of a critical exponent, is the temperature dependence of the susceptibility plateau height. Its temperature dependence for  $T > T_g$  is reported in Fig. 4 showing a steeper increase above about 650 K. These data are compatible with a MCT analysis leading to a crossover temperature  $T_c$  near 620 K. As shown in Fig. 5, the  $\alpha$  relaxation timescale which is related to the shear viscosity  $\eta_s$  via the Stokes-Einstein relation  $\tau_\alpha \propto \eta_s/T$  can also yield to the same crossover temperature  $T_c \sim 620$  K as predicted by the MCT. However, the  $\gamma = 3$  value used to obtain the linear dependence in Fig. 5 cannot be checked against the MCT constraint as the other critical exponents  $a$  and  $b$  are unknown in this supercooled liquid and cannot be safely determined from the susceptibility spectra.

It is very interesting to note that the crossover temperature  $T_c \sim 620$  K found within this simple MCT-like analysis is very close to the temperature of the decoupling phenomenon of the relaxation timescales observed by  $^3\text{P}$  NMR on this glass former below 600 K [19] and shown in

Fig. 1a. Indeed, for fragile liquids, the temperature where the decoupling phenomenon between the structural relaxation and a secondary slow process as observed by NMR or dielectric spectroscopy occurs, is often found just below the crossover temperature  $T_c$  deduced from MCT analysis [22].

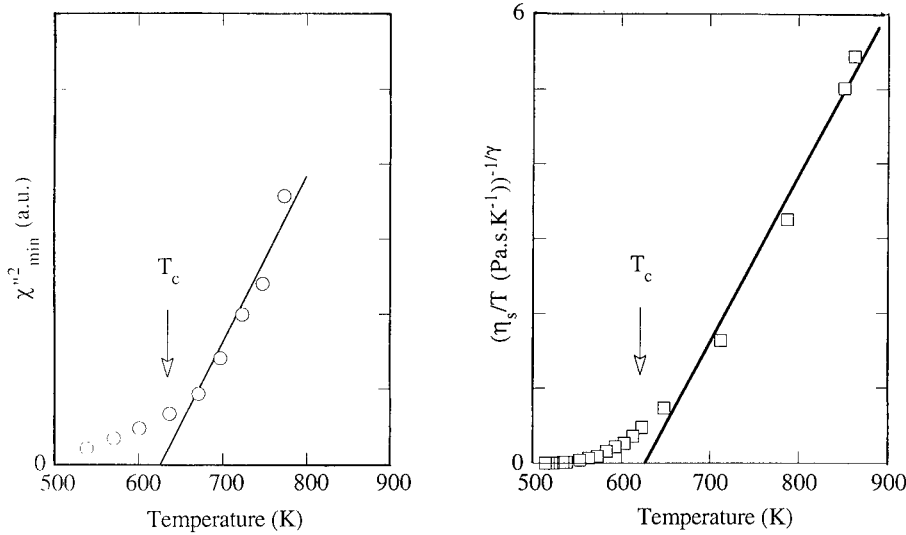


Fig. 4. Temperature dependence of the susceptibility plateau height deduced from the susceptibility spectra of Fig. 3 leading to a possible crossover temperature  $T_c \sim 620$  K.

Fig. 5. Critical scaling of the structural relaxation timescale  $\tau_\alpha \propto \eta_s/T$  also leading to the same crossover temperature  $T_c \sim 620$  K with  $\gamma = 3$ .

## CONCLUSION

In this paper, we have shown that the temperature dependence of the fast process intensity can be accounted for by the predictions of the simplest version of the MCT. It leads to a crossover temperature  $T_c \sim 620$  K ( $\sim 1.2 T_g$ ) in the supercooled liquid phase in good agreement with scaling analysis of the structural relaxation timescale deduced from viscosity data. Furthermore, it is also close to the temperature where a decoupling phenomenon between the  $\alpha$  process and a secondary slow process occurs in this system as already observed by  $^{31}\text{P}$  NMR. However, it has not been possible to use the susceptibility spectra for a line shape analysis and thus a more quantitative comparison with the MCT predictions. In particular, the susceptibility spectra in  $\text{Na}_{0.5}\text{Li}_{0.5}\text{PO}_3$  are strongly distorted by the low lying vibrational modes, the Boson peak, not really taken into account by the MCT.

As it has been previously shown [23] that in this system the quasielastic component could be also related to the damping of the Boson peak via a convolution model for example, these results suggest that in less fragile systems, the fast relaxational intensity could be the result of two equally weighted contributions: one from the  $\alpha$  process as described by the MCT and the other one from the damping of the Boson peak of negligible intensity in more fragile liquids.

## REFERENCE

- [1] Götze W., Sjögren L., Rep. Prog. Phys. **55**, 241 (1992).
- [2] Fujara F., Petry W., Euro. Phys. Lett. **4**, 921 (1987).
- [3] Knaak W., Mezei F., Farago B., Euro. Phys. Lett. **7**, 529 (1988).
- [4] Frick B., Farago B., Richter D., Phys. Rev. Lett. **64**, 2921 (1990).
- [5] Petry W., Bartsch E., Fujara F., Kiebel M., Sillescu H., Farago B., Z. Phys. B **83**, 175 (1991).
- [6] Li G., Du W.M., Chen X.K., Cummins H.Z., Tao N.J., Phys. Rev. A **45**, 3867 (1992).
- [7] Du W.M., Li G., Cummins H.Z., Fuchs M., Toulouse J., Knauss L.A., Phys. Rev. E **49**, 2192 (1994).
- [8] Steffen W., Patkowski A., Gläser H., Meier G., Fischer E.W., Phys. Rev. E **49**, 2992 (1994).
- [9] Rössler E., Sokolov A.P., Kisliuk A., Quitmann D., Phys. Rev. B **49**, 14967 (1994).
- [10] Angell C.A., in *Relaxations in complex systems*, K.L. Ngai and G.B. Wright, eds (NRL Washington, 1984) p. 3.
- [11] Sokolov A.P., Rössler E., Kisliuk A., Quitmann D., Phys. Rev. Lett. **71**, 2062 (1993).
- [12] Brodin A., Börjesson L., Engberg D., Torell L.M., Sokolov A.P., Phys. Rev. B **53**, 11511 (1996).
- [13] Lebon M.J., Dreyfus C., Li G., Aouadi A., Cummins H.Z., Pick R.M., Phys. Rev. E **51**, 4537 (1995).
- [14] Patkowski A., Steffen W., Meier G., Fischer E.W., J. Non-Cryst. Solids **172-174**, 52 (1994).
- [15] Wuttke J., Hernandez J., Li G., Coddens G., Cummins H.Z., Fujara F., Petry W., Sillescu H., Phys. Rev. Lett. **72**, 3052 (1994).
- [16] Sokolov A.P., Steffen W., Rössler E., Phys. Rev. E **52**, 5105 (1995).
- [17] Rufflé B., Thesis, University of Rennes I (1996).
- [18] Wäsche R., Brückner R., Phys. Chem. Glasses **2**, 80 (1986) and **2**, 87 (1986).
- [19] Rufflé B., Beaufils S., Gallier J., Chem. Phys. **195**, 339 (1995).
- [20] Green P., private communication.
- [21] Green P., Sidebottom D., Brow R., J. Non-Cryst. Solids **172-174**, 1353 (1994).
- [22] Rössler E., Warschewske U., Eiermann P., Sokolov A.P., Quitmann D., J. non Cryst. Solids **172-174**, 113 (1994).
- [23] Rufflé B., Beaufils S., Delugeard Y., Coddens G., Etrillard J., Toudic B., Bertault M., Even J., Gallier J., Ecolivet C., MRS Symp. Proc. Series **407** (1996).



## ROTATIONAL DYNAMICS OF A MOLECULAR PROBE IN TRI-CRESYL PHOSPHATE: FROM "STICK" TO "SLIP" BOUNDARY CONDITIONS

M.G. BAGLIESI<sup>1</sup>, F. CIANFLONE<sup>1,2</sup>, D. LEPORINI<sup>1,2</sup>

<sup>1</sup> Dipartimento di Fisica, Università di Pisa, Piazza Torricelli 2, I-56100 Pisa ITALY

leporini@ipifidpt.difi.unipi.it

<sup>2</sup> INFN, UdR Pisa

### ABSTRACT

The rotational dynamics of a molecular probe dissolved in the glass-former tri-cresyl phosphate has been studied by linear and non-linear Electron Spin Resonance spectroscopy. At the highest temperatures the Debye-Stokes-Einstein (DSE) law with *stick* boundary conditions holds. On cooling, a transition region is crossed and then a new regime sets in which is accounted for by the DSE law provided that *slip* boundary conditions are assumed. At the lowest temperatures the rotational diffusion and the shear viscosity are decoupled. The onset of the decoupling takes place close to  $T_c$ , the critical temperature predicted by the Mode Coupling Theory.

### INTRODUCTION

The translational and the rotational diffusion of a macroscopic object in a fluid are accounted for by the Stokes-Einstein (SE) and the Debye-Stokes-Einstein (DSE) laws, respectively [1,2]. For axially symmetric ellipsoids the latter takes the form [3,4]:

$$D_i = kT / (6\eta v \kappa f_i) \quad i = \parallel, \perp \quad (1)$$

$D_{\parallel}$  and  $D_{\perp}$  are the rotational diffusion coefficients and refer to spinning around the symmetry axis and tumbling of the symmetry axis of the ellipsoid, respectively.  $v$ ,  $\eta$ ,  $k$  and  $T$  are the volume of the ellipsoid, the shear viscosity, the Boltzmann constant and the temperature, respectively. The dimensionless coefficients  $f_i$   $i = \parallel, \perp$  depend only on the ratio between the two semiaxes of the ellipsoid.  $\kappa$  is a factor depending on the boundary conditions. Two limit cases are usually considered. The *slip* boundary conditions assume that the angular velocity of the layer adjoining the particle is determined by its displacement in the path of the rotating particle, while in the *stick* case it is equal to the angular velocity of the particle. For *slip* boundary conditions  $\kappa$  is less than one and depends on the ratio of the two semiaxes. For *stick* boundary conditions  $\kappa = 1$  [4].

Both SE and DSE are customarily derived via the fluctuation-dissipation theorem, relating the diffusion coefficient to the friction coefficient, and the hydrodynamics, relating the latter to the viscosity. In spite of these severe assumptions, in fluids with low viscosity they work fairly well down to molecular length scales. Anyway, since suitable molecules have finite diffusion constants in solid hosts, a breakdown of the SE and DSE laws may be anticipated in highly viscous fluids where a change from liquid-like transport to activated, solid-like transport is expected [5].

Failures of both the DSE and SE laws in polymers [6,7] and supercooled molecular fluids were reported [8-12]. There are indications that a new diffusion regime may set in close to the critical temperature  $T_c$  predicted by the mode coupling theory of the glass transition (MCT) [8]. In that regime the viscosity and the diffusion are partially decoupled, the latter being less temperature dependent. One intriguing aspect is that the decoupling is described by power laws [6-9, 12,13]. In particular, the DSE law takes the fractional form (FDSE)  $D_r \propto \eta^{-\xi}$  with  $0 \leq \xi \leq 1$ .

The molecular origin of the decoupling is not clear. From the theoretical point of view MCT does not make quantitative predictions on the molecular reorientation. Furthermore, even if there is

wide evidence of the *translational* decoupling, the experiments on the *rotational* diffusion are less conclusive. The reorientation of *o*-terphenyl ( OTP ) follows DSE according to NMR [9] . The study of the rotation of different tracers in OTP by time resolved optical spectroscopy reached the same conclusion [11]. Anyway, the quantity  $D_r \eta / T$  was found to increase of one order of magnitude for DANS when the glass transition is approached [11]. NMR observed a similar decoupling for benzene in tri-cresyl phosphate (TCP) [10]. The onset was at  $T_c$  . One of the present author (DL) and coworkers evidenced the FDSE of TEMPO and CHOLESTANE in OTP by Electron Spin Resonance [12, 13]. The comparison between results from different techniques is delicate and will be discussed elsewhere. However, we believe that the coherent interpretation of the above results also relies on the consideration of the molecular symmetry [13] and the related aspect of the boundary conditions between the tagged molecule and the host environment [1].

Being motivated by these remarks, this paper presents preliminary results on the investigation of the rotational motion of molecular probes dissolved in TCP via linear [14] and non linear Electron Spin Resonance [15, 16]. It is found that at the highest temperatures the reorientation process is accounted for by the DSE law with *stick* boundary conditions. By decreasing  $T$ , after a transition region, a new regime is observed which is described by the DSE law with *slip* boundary conditions [4]. The phenomenon seems to be a precursor of the decoupling between the rotational diffusion and the viscosity. The onset of the decoupling takes place close to  $T_c$  .

## EXPERIMENT

### Rotational Diffusion: Linear and Non-Linear Electron Spin Resonance Spectroscopies

The Electron Spin Resonance spectroscopy is extensively used to study the rotational motion of paramagnetic molecules, so called *spin probes*, dissolved in simple liquids [14], liquid crystals, polymeric materials [7] and supercooled fluids [12-14, 17]. It must be noted that the signal is a sum of single particle contributions. In the present study, in addition to the customary linear Electron Spin Resonance spectroscopy (ESR ), we used the Longitudinally Detected ESR technique ( LODESR ). Details on both the spectroscopies are given elsewhere [14-16]. The linear ESR measurement were carried out on a Bruker ER 200D SRL spectrometer equipped with an X-band microwave bridge. The home built LODESR spectrometer is described elsewhere [15]. The two techniques provide complementary information on the power spectrum of the random orientation of the probe molecule  $J(\omega)$ , *i.e.* the Fourier transform of the correlation functions of the spherical harmonics. The ESR spectroscopy is sensitive to  $J(0)$  in viscous materials, whereas the LODESR spectroscopy provides a direct measurement of the longitudinal relaxation time  $T_1$  and then of  $J(\omega_0)$ ,  $\omega_0$  being the electron Larmor angular frequency ( $\omega_0 = 2\pi 10^{10}$  Hz rad ). Consequently, both the high- and the low-frequency behaviour of  $J(\omega)$ , *i.e.* both the short- and long-time behaviour of the correlation function, are probed. The time scales which may be investigated by linear ESR are in the range  $10^{-12}$  s  $< \tau < 10^{-7}$  s. Slower time scales are accessible to LODESR whose range is  $10^{-11}$  s  $< \tau < 10^{-5}$  s.

Owing to the size and the cylindrical shape of the spin probe under study, the reorientation of the latter has been pictured as the anisotropic rotational diffusion of an axially symmetric ellipsoid. Not surprisingly, the diffusion coefficients which are drawn by ESR and LODESR are different, the former yielding lower values than the latter. This may be understood since, as noted above, ESR and LODESR are sensitive to  $J(0)$  and  $J(\omega_0)$ , respectively. In the presence of non exponential relaxation the apparent diffusion coefficient being drawn from  $J(0)$  is smaller than the one from  $J(\omega_0)$ . For example, if the orientation relaxes via a two step process with rates  $6D_s$  and  $6D_l < 6D_s$ , the ESR apparent diffusion coefficient is  $D^{ESR} \approx D_l^{-1} + D_s^{-1}$ , whereas in the LODESR case  $D^{LODESR} \approx D_l + D_s > D^{ESR}$ . The deviations from the exponential decay of the rotational correlation function are not investigated in the present paper.



## Materials

The isomer mixture tricresyl phosphate ( m-TCP: 64%, p-TCP: 35%, o-TCP: 1% ) and the spin probe CHOLESTANE ( fig.1 ) were bought from Aldrich and used without further purification. TCP exhibits a calorimetric glass transition at about  $T_g = 215\text{ K}$ . The spin probe was dissolved in TCP with concentration lower than  $8 \cdot 10^{-4}\text{ M/l}$  to avoid the plasticization of TCP. The solution was degassed and sealed in quartz tubes in presence of  $N_2$  atmosphere. No particular tendency to crystallization was observed in the doped samples.

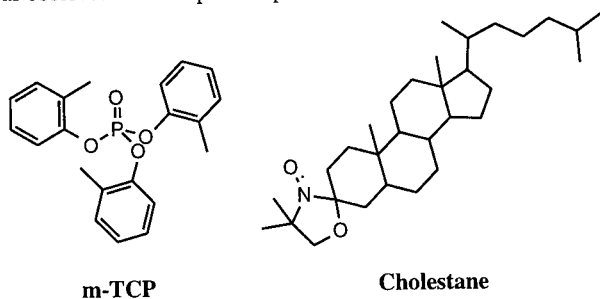


Fig.1. Molecular structures of m-TCP and the spin probe cholestane.

The magnetic parameters of the spin probe do not show appreciable temperature dependence and were drawn by simulation of the ESR powder lineshape [17]. The components of the Zeeman and hyperfine tensors in the magnetic frame are  $g_x = 2.0080$ ,  $g_y = 2.0057$ ,  $g_z = 2.0017$ ,  $A_x = 0.57\text{ mT}$ ,  $A_y = 0.38\text{ mT}$ ,  $A_z = 3.338\text{ mT}$ , respectively. Having set the magnetic parameters, the theoretical ESR and LODSR curves were fitted to the experimental lineshapes by adjusting only the diffusion coefficients  $D_{||}$  and  $D_{\perp}$ .

## RESULTS

Fig.2 is the Arrhenius plot of the diffusion coefficients  $D_{||}^{\text{ESR}}$  and  $D_{\perp}^{\text{ESR}}$ , which are drawn from ESR. In absence of large sets of data on the viscosity of TCP, they were compared to the rotational correlation time of TCP  $\tau_{iso} = 1/6D_{iso}$ , as measured via NMR [10]. Being  $D_{iso}$  the rotational diffusion constant of TCP, eq.1 implies  $\tau_{iso} \propto \eta/T$ . Nonetheless, a small continuous decrease of  $\tau_{iso}/\eta$  with  $T$  was observed in m-TCP for  $T < 320\text{ K}$  which may be recovered by taking  $\tau_{iso} \propto \eta$  [10]. We will analyse first our data in terms of  $\tau_{iso} \propto \eta/T$ . Five regions are identified in fig.2. In region I ( $T > 322\text{ K}$ ) the diffusion coefficients are proportional to  $1/\tau_{iso}$ . In region II ( $286\text{ K} < T < 322\text{ K}$ )  $D_{||,\perp}^{\text{ESR}}$  and  $1/\tau_{iso}$  exhibit temperature dependences which are partially different. For  $D_{||}^{\text{ESR}}$  the discrepancy is smaller. In region III ( $265\text{ K} < T < 286\text{ K}$ )  $D_{||,\perp}^{\text{ESR}}$  are proportional to  $1/\tau_{iso}$  again but the proportionality constants are larger than the corresponding ones of region I. In region IV ( $250\text{ K} < T < 265\text{ K}$ ) the rotational motion decouples from the viscosity time scale. The decoupling is more apparent for  $T < 250\text{ K}$  ( region V ) where the temperature dependence of  $D_{||,\perp}^{\text{ESR}}$  is activated ( $\Delta E \approx 28\text{ kJ/mol}$ ). In region V the rotational motion of cholestane may be thought as occurring in a virtually frozen TCP environment. A similar behaviour was observed for other spin probes in *o*-terphenyl [12, 17].

It is tempting to note that the decoupling between  $\tau_{iso}$  and the rotational diffusion of benzene in TCP was seen by NMR at  $T \approx 269\text{ K}$  [10] which should be compared with  $T \approx 265\text{ K}$  of the present study on cholestane, a largely different molecule. The fact that those temperatures are close to the mode-coupling critical temperature of TCP  $T_c \approx 260\text{ K}$  has been pointed out [10].

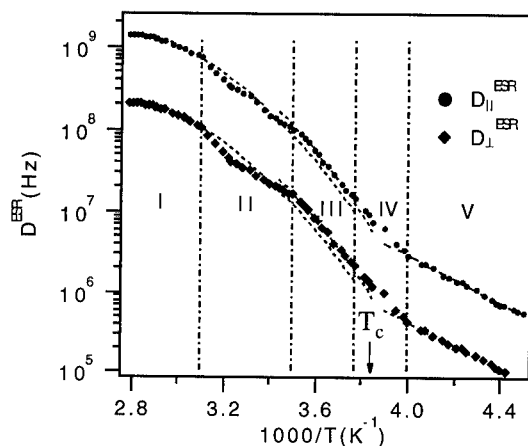


Fig.2. Arrhenius plot of the ESR rotational diffusion coefficients. Superimposed lines in regions I, III and V are the best fits according to  $D_i^{ESR} = \alpha_i / \tau_{iso}$   $i = \parallel, \perp$  and the Arrhenius law, respectively.  $T_c \approx 260$  K is the critical temperature predicted by the mode coupling theory.

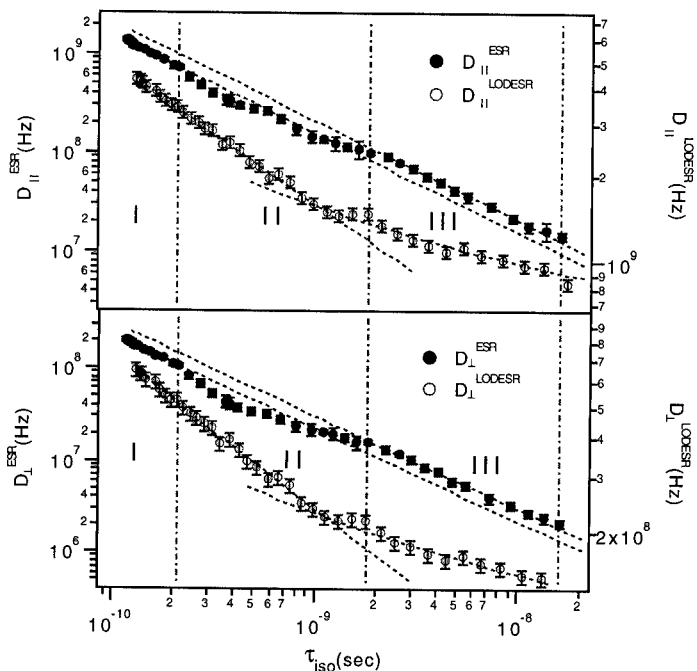


Fig.3. Comparison between the ESR and LODESR rotational diffusion coefficients and the rotational correlation time of TCP  $\tau_{iso} \propto \eta / T$ . The superimposed lines to the ESR and LODESR data are the best fits according to  $D_i^{ESR} = \alpha_i / \tau_{iso}$   $i = \parallel, \perp$  and guides for the eye, respectively.

Fig.3 shows a view of the regions I, II and III. The four straight lines are best-fit according to the law  $D_i^{ESR} = \alpha_i^m / \tau_{iso}$  where  $i = \parallel, \perp$  and  $m = I, III$ . We find  $\alpha_{\parallel}^I = 0.147 \pm 0.004$ ,  $\alpha_{\perp}^I = 0.0215 \pm 0.0006$ ,  $\alpha_{\parallel}^{III} = 0.197 \pm 0.01$ ,  $\alpha_{\perp}^{III} = 0.029 \pm 0.0013$ . By inspecting fig.3 and the quantities  $\alpha_i^m$ , it is apparent that the DSE law which is found in region I underestimates the rotational coefficients in region III. The discrepancy cannot be explained by a change of the ratio of the apparent molecular sizes of the spin probe. In fact, according to eq.1, the ratio  $D_{\parallel}^{ESR} / D_{\perp}^{ESR} = f_{\parallel} / f_{\perp}$  depends only on the ratio  $a/b$  of the semiaxes of the equivalent prolate spheroid approximating the shape of cholestane [3]. In region I and III it is found  $f_{\parallel}^I / f_{\perp}^I = \alpha_{\parallel}^I / \alpha_{\perp}^I = 0.146 \pm 0.006$  and  $f_{\parallel}^{III} / f_{\perp}^{III} = 0.147 \pm 0.01$ , respectively, which correspond to  $a/b = 0.20 \pm 0.01$ . A molecular model of cholestane ( Chem3D®, Cambridge Scientific Computing ) yields the ratio between the Van der Waals radii as  $0.25 \pm 0.01$ .

The above findings suggested that the reorientation of the spin probe in region I and III takes place differently. At the highest temperatures the spin probe, which is relatively large, should rotate by dragging TCP molecules ( stick bc ). Instead, the cholestane rotations taking place without hooking TCP molecules ( slip bc ) are expected to be favoured in the supercooled phase due to the increased viscosity . Since the  $\kappa$  factor of DSE ( eq.1 ) incorporates the effects due to the boundary conditions, they were evaluated in region I and III. It was found  $\kappa_{\parallel}^{III} / \kappa_{\parallel}^I = \alpha_{\parallel}^I / \alpha_{\parallel}^{III} = 0.74 \pm 0.04$  and  $\kappa_{\perp}^{III} / \kappa_{\perp}^I = \alpha_{\perp}^I / \alpha_{\perp}^{III} = 0.74 \pm 0.04$ . Prolate spheroids with  $a/b = 0.20 \pm 0.01$  have  $\kappa_{\perp}^{slip} / \kappa_{\perp}^{stick} = \kappa_{\parallel}^{slip} / \kappa_{\parallel}^{stick} = 0.66 \pm 0.01$ . The ratios are in good agreement irrespective of the assumptions being inherent in extending hydrodynamics down to molecular scales.

The above analysis took  $\tau_{iso} \propto \eta/T$ . Nonetheless,  $\tau_{iso} / \eta$  is a weak function of  $T$  in m-TCP for  $T < 320$  K [10]. Taking  $\tau_{iso} \propto \eta$  does not change the ratio of the semiaxes of the equivalent ellipsoid (  $a/b = 0.2$  ) and yields  $\kappa_{\parallel}^{III} / \kappa_{\parallel}^I = \kappa_{\perp}^{III} / \kappa_{\perp}^I = 0.66$  in full agreement with theory.

Further insight is provided by LODESR. As discussed above, LODESR measures the high-frequency wing of the spectral density  $J(\omega_0)$  with  $\omega_0 \approx 10^{11} \text{ rad s}^{-1}$ . Rotational diffusion coefficients  $D_{\perp}^{LODESR}$  and  $D_{\parallel}^{LODESR}$  are drawn from  $J(\omega_0)$  via the anisotropic diffusion model [14]. The model predicts for  $J(\omega)$  a Debye form, which could be questioned in supercooled fluids. However, refined forms, e.g. Cole-Davidson, Havriliak-Negami, add additional adjustable parameter and do not change our conclusions. In fig. 3  $D_{\perp}^{LODESR}$  and  $D_{\parallel}^{LODESR}$  are shown. A change in the rotational diffusion is detected close to the boundary between the regions II and III ( $T = 286$  K). The change is clear even in the raw data on the longitudinal spin relaxation  $T_1$  and, therefore, cannot be ascribed to artifacts due to the model of the reorientation.

Table I. Comparison between the independent measurements of the ratio  $D_{\parallel}^{ESR} / D_{\perp}^{ESR}$  via the fit procedure and the Redfield theory.

T ( K )	$(D_{\parallel}^{ESR} / D_{\perp}^{ESR})_{\text{Redfield}}$	$(D_{\parallel}^{ESR} / D_{\perp}^{ESR})_{\text{fit}}$
345.15	$6.6 \pm 0.4$	$6.5 \pm 0.4$
333.75	$6.7 \pm 0.5$	$6.8 \pm 0.3$
322.25	$6.9 \pm 0.4$	$6.8 \pm 0.4$
313.75	$7.6 \pm 0.5$	$7.7 \pm 0.7$
304.85	$8.2 \pm 0.6$	$8.7 \pm 0.6$

The LODESR data points to a well defined change of the rotational motion occurring close to  $T = 286$  K. This is consistent with the ESR data, especially the ones on  $D_{\parallel}^{ESR}$  which show only small deviations from the DSE with stick boundary conditions in region II. To understand if the deviations of  $D_{\perp}^{ESR}$  from the DSE in region II ( see fig.3 ) are artifacts due to the fit procedure of the ESR lineshape, we have measured the ratio  $D_{\parallel}^{ESR} / D_{\perp}^{ESR}$  independently by resorting to the Redfield theory of spin relaxation which holds in region II [14]. The results concerning selected

temperatures in region II are listed in table I. They agree with the fit within the errors.

## CONCLUSIONS

We have discussed the preliminary results of an extensive LODESR/ESR investigation on the rotational dynamics of cylindric tracers dissolved in the glass former tri-cresyl phosphate. Below  $T \approx 265\text{ K}$  the diffusion and the viscosity are decoupled. The decoupling occurs close to the critical temperature of TCP  $T_c \approx 260\text{ K}$  [8-10]. For  $T > 265\text{ K}$  the diffusion is well coupled to the viscosity and the DSE (eq.1) holds. Combining the LODESR and ESR data evidences a change of the reorientation process at  $T \approx 286\text{ K}$ . The phenomenon has been interpreted quantitatively in terms of a change from stick to slip boundary conditions between the tracer and the host phase occurring when the rotational diffusion of the former decreases but it is always well coupled to the viscosity (eq.1). In a sense, changing the boundary conditions may be seen as a precursor of the decoupling observed at  $T \approx 265\text{ K}$ . Measurements of the viscosity of TCP are planned to reach clearer evidence of the above findings.

Finally, we would like to comment on the missing evidence of temperature regions where the DSE law takes the fractional form (FDSE)  $D_r \propto \eta^{-\xi}$  with  $0 \leq \xi \leq 1$  [6-9, 12,13]. FDSE is observed in a range between the two regions where the supercooled fluid exhibits clear liquid-like and solid-like features [5]. In the present case FDSE should be observed in region IV. However, this region is not large (see fig.2) and difficult to characterize in absence of viscosity data.

## REFERENCES

- 1) D.Kivelson in Rotational Dynamics of Small and Macromolecules, edited by Th.Dorfmler, R.Pecora (Springer, Berlin, 1987), p.1.
- 2) P.A. Egelstaff An Introduction to the Liquid State (Clarendon Press, Oxford, 1994).
- 3) F.Perrin, J.Phys.Radium **5**, 497 (1934); L.D.Favro Phys.Rev. **119**, 53 (1960).
- 4) C. M. Hu, R. Zwanzig J.Chem.Phys. **60**, 4354 (1974).
- 5) M.D.Ediger, C.A.Angell, S.R.Nagel, J.Phys.Chem. **100**, 13200 (1996).
- 6) D. Ehlich, H. Sillescu, Macromolecules **23**, 1600 (1990).
- 7) L. Andreozzi, C.Donati, M.Giordano, D.Leporini in Disordered Materials and Interfaces, edited by H.Z.Cummins, D.J.Durian, D.L.Johnson, H.E.Stanley (Mater.Res.Soc.Proc.**40**, Pittsburgh, PA, 1996) pp. 233-238.
- 8) E.Rössler, Phys.Rev.Lett. **65**, 1595 (1990).
- 9) F.Fujara, B.Geil, H.Sillescu, G.Fleischer, Z.Phys.**B88**, 195 (1992).
- 10) E. Rössler, J.Tauchert, P.Eiermann J.Phys.Chem. **98**, 8173 (1994); E. Rössler, P.Eiermann J.Chem.Phys. **100**, 5237 (1994).
- 11) M.T.Cicerone, F.R.Blackburn, M.D.Ediger J.Chem.Phys. **102**, 471 (1995); M.T.Cicerone, M.D.Ediger J.Chem.Phys. **103**, 5684 (1995); **104**, 7210 (1996);
- 12) L.Andreozzi, A.Di Schino, M.Giordano, D.Leporini J.Phys.:Condens.Matter **8**, 9605 (1996). L.Andreozzi, M.Giordano, D.Leporini in Non Equilibrium Phenomena in Supercooled Fluids, Glasses and Amorphous Materials, edited by M.Giordano, D.Leporini, M.P.Tosi (World Scientific, Singapore, 1996).
- 13) L.Andreozzi, A. Di Schino, M.Giordano, D.Leporini, submitted.
- 14) Electron Spin Relaxation in Liquids edited by L.T.Muus, P.W.Atkins (Plenum, NY 1972); Spin Labeling: Theory and Applications, edited by L.J.Berliner (Academic, NY 1976).
- 15) M.Giordano, D.Leporini, M.Martinelli, L.Pardi, S.Santucci, C.Umeton J.Chem.Phys. **88**, 607 (1988).
- 16) D.Leporini Phys.Rev.A,**49**, 992 (1994).
- 17) L.Andreozzi, F.Cianflone, C.Donati, D.Leporini J.Phys.:Condens.Matter **8**, 3795 (1996).

## A UNIFIED THEORY FOR THE GLASS TRANSITION DYNAMICS AND ITS SINGULARITIES

T. ODAGAKI, J. MATSUI, M. FUJISAKI AND M. HIGUCHI  
Department of Physics, Kyushu University, Fukuoka 812-81, Japan

### ABSTRACT

Vitrification is a gradual freezing process of supercooled liquids, during which a slow process is separated from the fast diffusive and microscopic motions. The slow process is identified as a non-trapped jump motion and can be characterized by the waiting time distribution (WTD) of the elementary relaxation process. We first show that the WTD can be expressed as a power law function in the long time limit in general with modest assumptions. Defining the glass transition temperature by vanishing diffusivity or the divergence of the mean waiting time, we relate the exponent to the Adam-Gibbs parameter  $Ts_C(T)$  where  $T$  is the temperature and  $s_C(T)$  is the excess entropy. We also show that the divergence of the fluctuation of WTD leads to a cross over in the non-Gaussianity and present a unified view of the dynamics in the vitrification process.

### INTRODUCTION

The most important feature of glass formers from the point of view of application is the gradual change in viscosity and other dynamical properties with temperature. This is a clear contrast to crystallization in which the structural arrest takes place suddenly at the freezing point. In this gradual "freezing" process, various characteristic temperatures have been observed, defined or suggested from experiments: From the lowest, the Vogel-Fulcher temperature  $T_0$  [1] at which the viscosity measured near the glass transition temperature is extrapolated to diverge as  $\sim \exp[DT_0/(T-T_0)]$ , the Kauzmann temperature  $T_K$  [2], close to  $T_0$ , at which the excess entropy in the supercooled state is extrapolated to vanish, the glass transition temperature  $T_g$  at which some thermodynamic quantities exhibit anomalies and a cross over temperature  $T_x$  where liquid-like dynamics changes to solid-like dynamics[3].

In this paper we first present the gradual transition from liquid to amorphous solid state for the dynamical properties of a supercooled binary soft-sphere system obtained by molecular dynamics (MD) simulation. We attribute the slowest mode to a concerted jump motion from the trapped site and the fast motion to the trapped diffusion and rapid oscillation in a trapped region. To characterize the slowness, we introduce the waiting time distribution (WTD) which can be shown to be a power-law function of time in the long time limit. We show the power can be related to a scaled parameter  $[Ts_C(T) - T_g s_C(T_g)]/T_g s_C(T_g)$ , where  $s_C(T)$  is the excess entropy of the system at temperature  $T$ . We also present unique behavior of the non-Gaussianity parameter which may be used as a technique to identify the cross over point. We summarize our results by proposing a unified view of the change in dynamics in the vitrification process.

## SEPARATION OF SLOW PROCESS

We first present the result of MD simulation for a binary soft-sphere mixture composed of  $N_1$  atoms of mass  $m_1$  and diameter  $\sigma_1$  and  $N_2$  atoms of mass  $m_2$  and diameter  $\sigma_2$  in a volume  $V$ , which interact through the purely repulsive soft-sphere potentials [4]:

$$v_{\alpha\beta}(r) = \epsilon \left( \frac{\sigma_{\alpha\beta}}{r} \right)^{12}, \quad (1)$$

where  $\alpha, \beta = 1$  or  $2$  denotes species indices,  $\epsilon$  is the energy unit, and we assume that  $\sigma_{\alpha\beta} = (\sigma_\alpha + \sigma_\beta)/2$ . It is known that the thermodynamic state of the system is well specified by the effective coupling constant  $\Gamma_{\text{eff}}$ :

$$\Gamma_{\text{eff}} = \frac{N}{V} \left( \frac{k_B T}{\epsilon} \right)^{-1/4} \sigma_{\text{eff}}^3, \quad (2)$$

$$\sigma_{\text{eff}}^3 = \sum_{\alpha} \sum_{\beta} x_{\alpha} x_{\beta} \sigma_{\alpha\beta}^3. \quad (3)$$

where  $N$  and  $V$  are the total number of atoms  $N (= N_1 + N_2)$  and the volume, and  $x_1 (= N_1/N)$  and  $x_2 (= 1 - x_1)$  are concentrations. [We set  $\sigma_2/\sigma_1 = 1.2$ ,  $m_2/m_1 = 2.0$ ,  $x_1 = x_2 = 0.5$  and  $N = 500$ .] It has been shown that the freezing point and the glass transition point are at  $\Gamma_{\text{eff}} = 1.15$  and  $1.58$ , respectively. It has also been argued that the mode-coupling critical point, the crossover temperature and the Vogel-Fulcher temperature are at  $\Gamma_{\text{eff}} = 1.32$ ,  $1.45$  and  $1.89$ , respectively [5,6].

Following the procedure reported elsewhere [4,7], we performed MD simulation from the liquid state to the amorphous state and obtained the imaginary part of the self-part of the generalized susceptibility  $\chi_s''(\mathbf{q}, \omega)$ , which is related to the dynamical structure factor by  $S_s(\mathbf{q}, \omega) = \omega \chi_s''(\mathbf{q}, \omega)$ .

Figure 1 shows the frequency dependence of  $\chi_s''(\mathbf{q}, \omega)$  for  $\Gamma_{\text{eff}} = 0.8$  (liquid),  $1.4$  (supercooled liquid) and  $2.0$  (amorphous solid), where  $|\mathbf{q}| = 2\pi/\sigma_1$ . This figure clearly shows that the dynamics does not change suddenly from the liquid- to solid-type as in the crystallization, but a slow process characterized by the so-called  $\alpha$ -peak is separated from the microscopic motions and the position of the  $\alpha$ -peak represents the slowness of the dynamics. We identify the microscopic peak as the trapped motions consisting of oscillatory and trapped diffusive motion and the  $\alpha$ -peak as the non-trapped motion. In fact we can reproduce the characteristics of the susceptibility from a simple ideal-three mode model consisting of these three modes of dynamics [8]. Therefore, it is now possible to characterize the gradual transition by observing at the non-trapped dynamics which will be done in the next section.

## WAITING TIME DISTRIBUTION

The characteristic feature of the slow dynamics can be well described by the waiting time distribution (WTD)  $\psi(t)$  for the non-trapped motion, which is defined as the probability density that an atom makes an elementary relaxation process at time  $t$  with no such processes between time  $t = 0$  and  $t$ . Note that one can define the WTD only when the trapped and non-trapped motions can be distinguished.

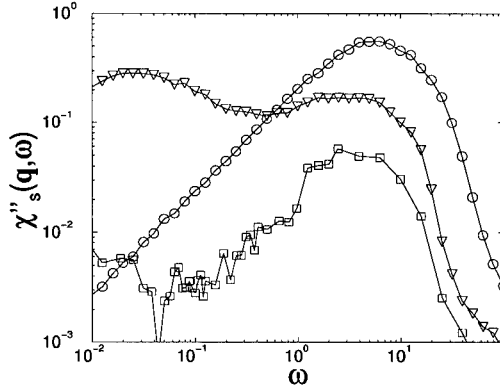


Figure 1:  $\chi''_s(\mathbf{q}, \omega)$  is plotted against  $\omega$  in log-log scale. Circles :  $\Gamma_{\text{eff}} = 0.8$  (liquid), triangles :  $\Gamma_{\text{eff}} = 1.4$  (super-cooled liquid) and squares:  $\Gamma_{\text{eff}} = 2.0$  (amorphous solid), which are the average for two species.

The elementary relaxation process can occur in an area which can provide the critical excess entropy  $S_0^*$  required for the process. The critical excess entropy  $S_0^*$  is supposed to be close to  $k_B \ln 2$ , as proposed first by Adam and Gibbs[9]. Now, suppose the excess entropy per atom for a given system to be  $s_c(T)$ . Then, the number of atoms in the area is given by  $n = S_0^*/s_c(T)$ . The existence of this kind of region has been proposed by many authors[10]. In these regions, atoms perform two types of diffusive motion: trapped diffusion and non-trapped motion. The jump rate of the non-trapped motion can be determined by the following argument. If one focuses on one particular atom in the domain, its jump rate  $w$  leading to the structural relaxation at a given temperature  $T$  and pressure would be written as

$$w = w_0 \exp[-n\Delta\mu/k_B T], \quad (4)$$

where  $w_0$  is the product of the attempt frequency comparable to the jump rate producing the trapped diffusive motion and the efficiency of moving out from the excited state[11], and  $\Delta\mu$  is the excitation chemical potential per atom. Note that  $w \leq w_0$  holds in general since  $\Delta\mu \geq 0$ .

Noting that the distribution  $p(\Delta\mu)$  of the excitation chemical potential  $\Delta\mu$  can be written as[12]

$$p(\Delta\mu) = C \sigma(\Delta\mu) \exp(-\bar{\sigma} \Delta\mu), \quad (5)$$

where  $C$  is a normalizing constant and  $\bar{\sigma} = \int_0^{\Delta\mu} \sigma(\epsilon) d\epsilon / \Delta\mu$  is the mean value of the distribution of excited energy (chemical potential) levels of the region  $\sigma(\epsilon)$ , we can easily show that the distribution function  $P(w)$  for the jump rate  $w$  is given by

$$P(w) = \begin{cases} \frac{(\rho+1)w^\rho}{w_0^{\rho+1}} & \text{when } w \leq w_0 \\ 0 & \text{when } w > w_0 \end{cases}. \quad (6)$$

with

$$\rho = \frac{k_B T \bar{\sigma} s_c(T)}{S_0^*} - 1. \quad (7)$$

Here, the dependence of  $\bar{\sigma}$  on  $\Delta\mu$  has been neglected and  $\sigma[\Delta\mu(w)]$  was approximated by  $\bar{\sigma}$  since  $\sigma[\Delta\mu(w)]$  depends on  $w$  through  $\ln w$ .

It has been shown[13] that the WTD corresponding to the jump rate distribution (6) is given by

$$\psi(t) = (\rho + 1)w_0\Gamma(\rho + 2)\gamma^*(\rho + 2, w_0t), \quad (8)$$

where  $\Gamma(x)$  and  $\gamma^*(a, x)$  are the Gamma function and the Tricomi incomplete Gamma function, respectively. As  $t \rightarrow \infty$ ,  $\psi(t)$  is shown to behave as

$$\psi(t) \sim t^{-(\rho+2)}. \quad (9)$$

The waiting time distribution determines physical properties related to the slow relaxation. In particular, the diffusion constant is in proportion to the inverse of the mean waiting time  $\langle t \rangle$  which is given by

$$\langle t \rangle = \frac{\rho + 1}{\rho} w_0^{-1} \quad \text{for } \rho > 0. \quad (10)$$

Therefore, the diffusivity vanishes for  $\rho \leq 0$  and thus we can identify  $\rho = 0$  as the glass transition temperature. It is thus noted from Eq. (7) that the parameter  $\rho$  is regarded as the scaling parameter

$$\rho = \frac{T s_c(T) - T_g s_c(T_g)}{T_g s_c(T_g)}. \quad (11)$$

## NON-ERGODICITY AND NON-GAUSSIANITY

When the mean waiting time diverges, the system cannot explore the entire phase space within a given observation time, and the system appears non-ergodic, although the system can still relax. This concept of non-ergodicity is different from the one known in the statistical mechanics, and we call it quasi-non-ergodicity. In this sense, the glass transition can be considered as the ergodic - quasi-non-ergodic transition.

Equation (11) indicates that when the excess entropy vanishes at  $T_K$  i.e. at  $\rho = -1$ , the WTD cannot be normalized and the system becomes non-ergodic in the conventional sense. Note that the main relaxation time diverges exponentially at  $\rho = -1$  in the trapping diffusion model[7] and thus  $T_K$  coincides with  $T_0$ .

The non-Gaussian parameter  $A(\rho, t) \equiv 3 \langle \mathbf{r}^4 \rangle / 5 \langle \mathbf{r}^2 \rangle^2 - 1$  takes a maximum as a function of time when the mean square displacements due to oscillatory motion and due to jump motion cross. Figure 2 shows the non-Gaussianity at a fixed time as a function of parameter  $\rho$  for the trapping diffusion model[14].

Since the dependence of the mean square displacement on  $t$  behaves differently for  $\rho < 0$ ,  $0 < \rho < 1$  and  $1 < \rho$ , the  $\rho$  dependence of  $A(\rho, t)$  at a fixed  $t$  is expected to have different behavior in these regions. To see this, we show in Fig. 3  $dA(\rho, t)/d\rho$  as a function of  $\rho$  for four different observation times. It is clear that (1) For  $\rho > 1$ , the derivatives at different times have more or less the same  $\rho$  dependence, and (2) the dependence deviates



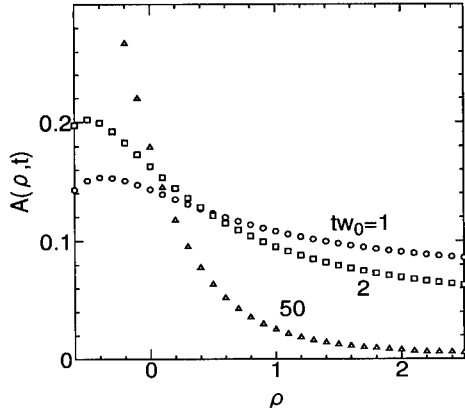


Figure 2: The non-Gaussianity is plotted against parameter  $\rho = [Ts_C(T) - T_g s_C(T_g)]/T_g s_C(T_g)$  at three different observation times.

significantly from each other for  $\rho < 1$ , and (3) the derivatives take minimum at a certain  $\rho$  below the glass transition point.

The singular behavior of the non-Gaussianity for  $0 < \rho < 1$  is due to the subanomalous diffusion where the mean square displacement acquires a divergent term with exponent less than unity beside a  $t$ -linear term[15]. This subanomalous behavior is related to the divergence of the fluctuation of the WTD. In fact, the fluctuation  $\langle \delta t^2 \rangle^{1/2} = [\langle t^2 \rangle - \langle t \rangle^2]^{1/2}$  is given by

$$\langle \delta t^2 \rangle^{1/2} = \frac{1}{\rho} \sqrt{\frac{\rho+1}{\rho-1}} w_0^{-1} \quad (12)$$

which diverges at  $\rho = 1$ .

## SUMMARY

We have presented two concepts to understand the gradual transition from supercooled liquids to amorphous solids, one is the non-ergodicity and the other is the non-Gaussianity. Here, the non-ergodicity is not the same concept as in the statistical mechanics, but it denotes the fact that the observation time becomes shorter than some characteristic time which determines a certain dynamical property. This definition must be more relevant in the analysis of dynamics in glass forming materials.

We also defined the non-Gaussianity as a measure of the deviation from the simple Gaussian dynamics. From the long time behavior of  $A(\rho, t)$ , one can identify three regions (1)  $\rho < 0$ , non-Gaussian region where  $A(\rho, \infty) \neq 0$ , (2)  $0 < \rho < 1$ , quasi-non-Gaussian region where  $A(\rho, t)$  decays as  $\sim t^{-\theta}$  with  $\theta < 1$ , and (3)  $1 < \rho$ , Gaussian region. The

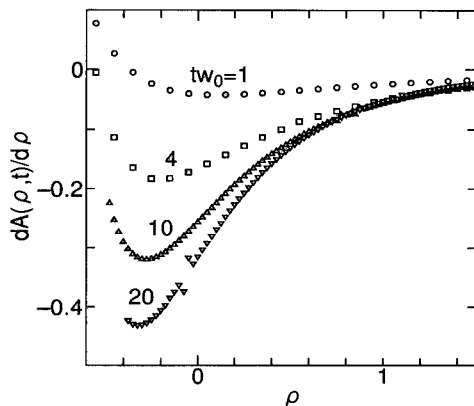


Figure 3:  $d \log A(\rho, t)/d\rho$  is plotted as a function of  $\rho$  at four different observation times.

non-Gaussianity can now be measure by experiments[16] and thus the present concept can be tested by experiments.

We now state a unified view for the scenario of the gradual transition in the vitrification process. When a liquid is cooled down below its freezing point, the single peak in the generalized susceptibility breaks up into two peaks, indicating that trapped and non-trapped motions can be distinguished. The  $\alpha$ -peak moves continuously to lower frequencies as the temperature is reduced, while the microscopic peak changes its nature from the highly damped dynamics to well-defined oscillatory motion. During this process, a fast process may be identified as the diffusive motion of the local potential minima[6]. From the slow relaxation process, Gaussian to quasi-non-Gaussian transition occurs at the cross over temperature and to non-Gaussian transition occurs at the glass transition point. The system transforms itself from the ergodic to quasi-nonergodic state at  $T_g$  and to the non-ergodic state at  $T_0$ .

#### ACKNOWLEDGEMENT

This work was supported in part by the grants from the Ministry of Education, Science, Sports and Culture, and Izumi Science and Technology Foundation.

#### REFERENCES

- [1] H. Vogel, Phys. Zeit. **22**, 641 (1921); G. S. Fulcher, J. Am. Cer. Soc. **8**, 339 (1925).
- [2] W. Kauzmann, Chem. Rev. **43**, 219 (1948).

- [3] C. A. Angell, J. Phys. Chem. Solids **49**, 863 (1988).
- [4] J. Matsui, H. Miyagawa, T. Muranaka, K. Uehara, T. Odagaki and Y. Hiwatari, Mol. Sim. **12**, 305 (1994); J. Matsui, T. Odagaki and Y. Hiwatari, Phys. Rev. Lett. **73**, 2452 (1994).
- [5] J. L. Barrat and A. Latz, J. Phys. : Cond. Matt. **2** 4289 (1990).
- [6] M. Fujisaki, J. Matsui and T. Odagaki, Proceedings of YKIS'96, to be published.
- [7] T. Odagaki, J. Matsui and Y. Hiwatari, Mat. Res. Soc. Symp. Proc. vol. 367 (1995), 337.
- [8] M. Higuchi and T. Odagaki, Proceedings of YKIS'96, to be published.
- [9] G. Adam and J. H. Gibbs, J. Chem. Phys. **43**, 139 (1965).
- [10] E. Donth, J. non-Cryst. Sol. **53**, 325 (1982); E. W. Fischer, E. Donth and W. Steffen, Phys. Rev. Lett. **68**, 2344 (1992); K. L. Ngai, R. W. Rendell and D. J. Plazek, J. Chem. Phys. **94**, 3018 (1991).
- [11] H. Eyring, "*The Theory of Rate Processes*", (McGraw-Hill, New York, 1964).
- [12] T. Odagaki, Phys. Rev. Lett. **75**, 2452 (1995).
- [13] T. Odagaki and Y. Hiwatari, J. Phys.: Cond. Matt. **3**, 5191 (1991).
- [14] T. Odagaki, J. Matsui and Y. Hiwatari, Physica A**204** (1994), 464.
- [15] T. Odagaki, Phys. Rev. B**38** (1988), 9044.
- [16] T. Kanaya, I. Tsukushi and K. Kaji, Proceedings of YKIS'96, to be published.

## FRAGILITY OF POLYMERIC LIQUIDS: CORRELATIONS BETWEEN THERMODYNAMIC AND DYNAMIC PROPERTIES

DINA M. COLUCCI and GREGORY B. McKENNA, Polymers Division, National Institute of Standards and Technology, Gaithersburg, MD 20899

### ABSTRACT

The effect of polymer structure on fragility was determined by relating the apparent fragility to the relaxation response, heat capacity, and thermal expansion. For the 14 polymers studied, the fragility estimates based on the relaxation behavior ( $\log a_T$ ) correlated well with the thermodynamic estimates of  $\Delta C_p/M_o$ , and  $\Delta\alpha$ . In general, polymers with less sterically hindered repeat unit structures exhibited strong behavior. Polymers with sterically hindered backbones containing oxygen or ringed structures in the backbone were consistently fragile using  $\log a_T$ ,  $\Delta C_p/M_o$ , and  $\Delta\alpha$  as measures of fragility. On the other hand, using  $C_p^l/C_p^g$  as a fragility criterion resulted in very different fragility classifications.

### INTRODUCTION

Liquid fragility is a concept which is widely used in the materials community to classify glass forming liquids. The concept was developed by Angell<sup>1</sup> for simple liquids to account for the differences in the tendency of materials to form glasses based on the thought that strong liquids would have stable structures (local to intermediate range order) and properties that do not change dramatically in going from the liquid state to the glassy state. On the other hand, for fragile liquids, such structures would be unstable and the property changes in going from the liquid to the glass would be more evident. This is true for both the thermodynamic response, e.g. heat capacity  $C_p$  and transport properties e.g. viscosity  $\eta$ . In the case of the former, either the change in  $C_p$  at the glass transition  $T_g$ ,  $\Delta C_p$ , or the ratio of the liquid to glassy heat capacities,  $C_p^l/C_p^g$ , serve as the measure of fragility. For viscosity, the fragile liquids show non-Arrhenius temperature dependencies as  $T_g$  is approached, while strong liquids show Arrhenius behavior, with the  $T_g$  being ill-defined. An important means of classifying the liquids by viscosity is the so-called fragility or Angell plot which is discussed subsequently.

Here we are interested in both the thermodynamic measures of fragility and the viscosity measures and examine, in particular, polymeric glass formers in this framework. In addition to simply tabulating polymers according to fragility based on the several schemes available, we also look at the chemical structure of the polymers. We suggest for estimates of the fragility that the thermodynamic property/viscosity correlation for polymer glass forming liquids is best maintained using a monomer molecular weight normalized heat capacity  $\Delta C_p/M_o$ .

### RESULTS

#### The Angell Plot for Polymers

One common way to classify liquids as strong or fragile is to plot  $\log \eta$  versus the ratio of the glass transition temperature to the temperature of interest,  $T_g/T$ . The strongest liquids

show near Arrhenius-like behavior ( $\log a_T \sim 1/T$ ), while the fragile liquids show complex non-Arrhenius behavior and larger viscosity changes over the same temperature range.

Figure 1, was constructed for 14 polymers using the following relationship which relates the viscosity  $\eta(T)$  and the viscosity  $\eta(T_o)$  at a reference temperature  $T_o$ , to the temperature shift factor  $a_T$

$$\log \frac{\eta(T)}{\eta(T_o)} = \log a_T - \frac{C_1(T-T_o)}{C_2 + T - T_o} \quad (1)$$

where  $C_1$  and  $C_2$  are material constants in the WLF<sup>2</sup> relationship. We note that the Angell plot is often constructed using  $\log \eta/\text{Pa-s} = 12$  at  $T_g/T = 1$ . Here we obtain a similar scaling by setting  $\log a_T = 0$  at  $T_g$ . Consistent with the definition of Angell, a strong liquid is characterized as one with a fairly linear relationship and a much smaller change in viscosity with increasing temperature when compared to a fragile liquid which shows clearly non-Arrhenius viscosity behavior and a strong initial dependence of viscosity on temperature.

Here we chose to classify the polymers into 3 categories: strong, intermediate, and fragile. The classification results from the shift factor analysis for the 14 polymers analyzed in Figure 1 are given in Table 1. The classifications were defined by considering the changes in shift factor in the range of  $0.6 < T_g/T < 1$ . Strong liquids show a decrease of up to 11.0 decades in  $\log a_T$  over this range; whereas, intermediate strength is defined in the range of -11 to -14 in  $\log a_T$ . Fragile liquids are defined by a decrease of more than 14 decades in  $\log a_T$ . The names of the polymers represented as well as the values of the material constants  $C_1$ ,  $C_2$ ,  $T_o$ , and  $T_g$  used to generate Figure 1 are given in Table 2.

#### Fragility and Heat Capacity

The heat capacity can also be used as a measure of strong or fragile behavior. Angell<sup>1</sup> proposed that small changes in heat capacity in going from the liquid to glassy state indicated strong liquids while larger changes indicated more fragile behavior. In his work, Angell used  $C_p^l/C_p^g$  as a measure of fragility and the values of  $C_p^l/C_p^g$  for various polymers are given in Table 3 with the corresponding behavior classified in Table 1. Clearly the results do not correlate well with the segmental relaxation data. In particular both PE and PBD exhibit a relaxation response characteristic of a strong liquid yet the  $C_p^l/C_p^g$  ratio is consistent with more fragile behavior. Another conflicting result is seen in the case of PC where the relaxation response suggests fragile behavior while the  $C_p^l/C_p^g$  ratio is consistent with a strong liquid.

The change in heat capacity at  $T_g$ ,  $\Delta C_p$ , is often used in glassy physics and can be related to the change in configurational entropy due to freezing in of polymer conformations upon cooling from the liquid to the glassy state. We propose here to use  $\Delta C_p$  as an alternative measure of the fragility and normalize it by the monomer molecular weight,  $M_o$ . This normalization takes into account, in a sense, the effect of repeat unit size (molecular weight). The corresponding values for  $\Delta C_p/M_o$  are given in Table 3 for most of the polymers listed previously. A summary of the classification results is given in Table 1. It is clear from Table 1 that the fragility rankings based on  $\Delta C_p/M_o$  are more consistent with the relaxation data than when based on  $C_p^l/C_p^g$ . In particular, most of the polymers fall into the same category in both the relaxation and  $\Delta C_p/M_o$  schemes. Although we do note that the PP and PVC move from intermediate to strong in going from the relaxation to  $\Delta C_p/M_o$  approach. It is unclear at this point why the polymer repeat unit size provides such a correlation with the normalized

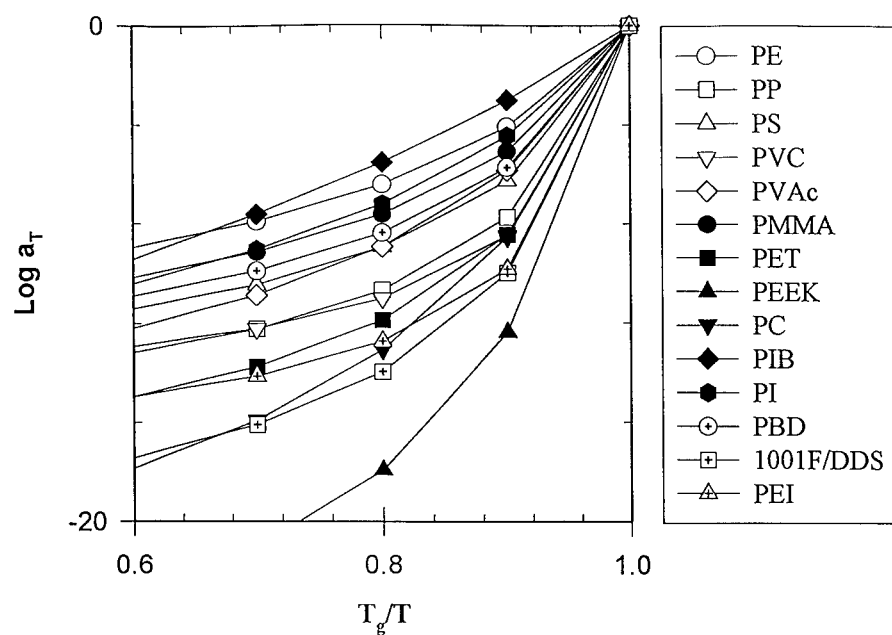


Figure 1: Segmental Relaxation Data Represented in an Angell Plot

Table 1: Fragility Classification for 14 Polymers Using Relaxation and Thermodynamic Criteria.(See Table 2 for polymer designations.)

Criterion	Strong	Intermediate	Fragile
$\log a_T$	PIB, PE, PI, PMMA, PBD	PS, PVAc, PP, PVC	PET, PEI, PC, 1001F/DDS, PEEK
$C_p^l/C_p^s$	PC, PEI, PMMA, PIB	PS, PVC, PET, PP, PI	PVAc, PE, PBD
$\Delta C_p/M_0$	PE, PIB, PVC, PP, PI, PBD, PMMA	PS, PVAc	PC, 1001F/DDS, PET, PEI
$\Delta \alpha$	PE, PMMA	PP, PEI, PVC, PS	PC, 1001F/DDS, PVAc, PET

Table 2: WLF shift factor values used in Angell plot in Figure 1. The values of  $T_g$ ,  $C_1$ ,  $C_2$  and  $T_0$  were obtained from a work by Ngai and Plazek<sup>1</sup>.

Polymer	$T_g$ (K)	$C_1$	$C_2$ (K)	$T_0$ (K)
poly(ethylene) PE	317.0	12.7	63.3	312.3
poly(propylene) PP	262.0	6.86	65.0	298.0
poly(styrene) PS	373.0	13.7	50.0	373.0
poly(vinyl chloride) PVC	338.7	11.2	34.6	346.5
poly(vinyl acetate) PVAc	305.0	8.86	101.6	349.0
poly(methyl methacrylate) PMMA	390.0	12.2	70.1	393.1
poly(ethylene terephthalate) PET	346.6	17.7	42.6	346.6
poly(aryl ether ether ketone) PEEK	417.0	30.0	53.7	412.9
poly(carbonate) PC	418.0	22.9	78.6	418.0
poly(isobutylene) PIB	201.0	8.6	200.4	298.0
poly(isoprene) PI	205.0	8.2	89.5	243.2
poly(butadiene) PBD	180.2	3.0	120.0	273.2
poly(ether imide) PEI	480.7	16.7	37.5	480.7
Diglycidyl ether of bisphenol-A epoxy (DGEBA) with diamino diphenyl sulfone(1001F/DDS)	400.2	19.3	50.0	403.2

Table 3: Data Used in Fragility Analysis

Polymer	$M_0$ (g/mole)	$C_p/C_p^*$	$\Delta C_p/M_0$ (J/mole-K)	$\Delta\alpha \times 10^4$ ( $^{\circ}\text{C}^{-1}$ )
PE	28	1.54 <sup>2</sup>	10.1 <sup>12</sup>	1.93* <sup>3</sup>
PP	42	1.36 <sup>12</sup>	21.8 <sup>12</sup>	3.77* <sup>4</sup>
PS	80	1.24 <sup>12</sup>	37.5 <sup>12</sup>	2.97 <sup>5</sup>
PVC	63	1.31 <sup>12</sup>	20.9 <sup>12</sup>	3.18 <sup>13</sup>
PVAc	86	1.52 <sup>12</sup>	53.7 <sup>12</sup>	4.093
PMMA	100	1.18 <sup>12</sup>	33.7 <sup>12</sup>	2.30 <sup>13</sup>
PET	192	1.31 <sup>12</sup>	78.7 <sup>12</sup>	5.27* <sup>6</sup>
PC	254	1.14 <sup>7</sup>	57.2 <sup>17</sup>	3.72 <sup>10</sup>
PIB	56	1.20 <sup>8</sup>	20.6 <sup>18</sup>	-
PI	68	1.36 <sup>18</sup>	27.2 <sup>18</sup>	-
PBD	54	1.52 <sup>12</sup>	28.6 <sup>12</sup>	-
PEI	592	1.18 <sup>9</sup>	177.6 <sup>19</sup>	3.05 <sup>19</sup>
1001F/DDS	284		73.7 <sup>10</sup>	3.84 <sup>20</sup>

\*for PE, PP, and PET, the  $\Delta\alpha$  was estimated from the change in thermal expansion upon melting

\*\*the  $\Delta\alpha$  values used are those listed in the previous column and the  $T_g$  values were obtained from Table 1

temperature dependence of the relaxation response.

### Fragility and Thermal Expansion

The coefficient of thermal expansion is commonly used to characterize the effect of temperature on dimensional changes. We ask the question does a correlation exist between the change in the coefficient of thermal expansion at  $T_g$ ,  $\Delta\alpha$ , and the relaxation behavior and consequently  $\Delta C_p/M_0$ ? Table 3 contains  $\Delta\alpha$  values for several of the polymers given previously with the resulting classifications shown in Table 1. Similar to the results for the relaxation and  $\Delta C_p/M_0$ , many of the polymers such as PMMA and PE consistently exhibit strong behavior while others such as PET, 1001F/DDS, and PC are consistently fragile.

### Fragility and Structure

The link between the different types of behavior might lie in the chemical structure of each material. Figure 2 correlates the strong to fragile behavior of each of the polymers studied by assigning a classification to each material based on the segmental relaxation,  $\Delta C_p/M_0$ , and  $\Delta\alpha$  results. Clearly, a trend exists. The less hindered repeat unit structure polymers such as PE, PMMA, PIB, PI, PBD, PP, and PVC consistently exhibit strong to intermediate behaviors while the more complicated polymers which have phenol rings or oxygen in the backbone such as PET, PEEK, PC, and 1001F/DDS consistently exhibit fragile behavior. Such a correlation requires further exploration in the future.

### SUMMARY AND CONCLUSIONS

The effect of polymer structure on fragility was determined by relating the apparent fragility to the relaxation response, heat capacity, and thermal expansion. For the 14 polymers studied, the fragility estimates based on the relaxation behavior ( $\log a_T$ ) correlated well with

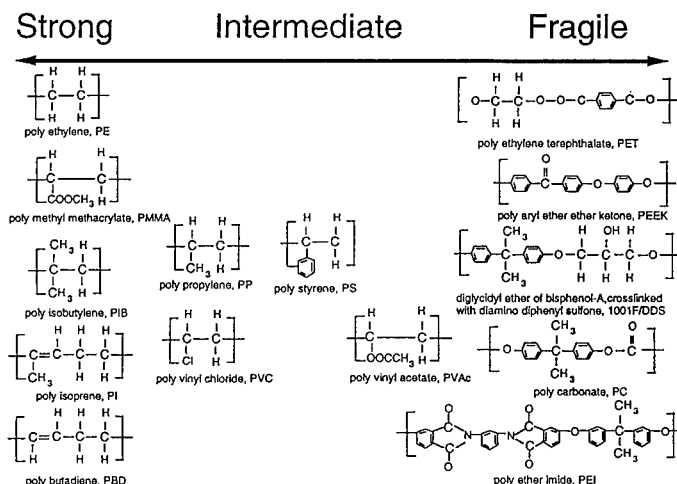


Figure 2: Correlation of Chemical Structure with Fragility



the thermodynamic estimates of  $\Delta C_p/M_o$ , and  $\Delta\alpha$ . In general, polymers with less sterically hindered repeat unit structures such as PE and PMMA exhibited strong behavior. Polymers with sterically hindered backbones such as PET, 1001F/DDS, PC and PEI were consistently fragile using  $\log a_T$ ,  $\Delta C_p/M_o$ , and  $\Delta\alpha$  as measures of fragility. On the other hand, using  $C_p^{1/2}/C_p^*$  as a fragility criterion resulted in very different fragility classifications.

These results lead to an unanswered question: (i) why does  $\log a_T$  versus  $T_g/T$  correlate well with  $\Delta C_p/M_o$  rather than  $\Delta C_p$  or  $C_p^{1/2}/C_p^*$ ? This question illustrates the potential difference between polymers and simple liquids, since Angell found a good correlation between the viscosity and  $C_p^{1/2}/C_p^*$  effects on the fragility. Also, the idea of some local size scale governing the relaxation and thermodynamic responses of polymers is suggested by the correlation of fragility to  $\Delta C_p/M_o$ . Although the fragility framework seems to be rather useful in describing the response of a wide variety of polymers when specific scaling measures are used, there still exist many unanswered questions as to why the specific classification methods described correlate in the same way.

#### REFERENCES

1. C.A. Angell, in "Relaxations in Complex Systems," ed. by K.L. Ngai and G.B. Wright, Workshop Proceedings, Naval Research Laboratory, Washington, D.C., (1984).
2. M.L. Williams, R.F. Landel, and J.D. Ferry, *J. Amer. Chem. Soc.*, 77, 3701, (1955).
3. K.L. Ngai and D.J. Plazek, "Temperature Dependencies of the Viscoelastic Response of Polymer Systems," from Physical Properties Handbook, ed. J. E. Mark, American Institute of Physics Press, Woodbury, NY, pg 341, (1996).
4. J. Wen, "Heat Capacities of Polymers," from Physical Properties Handbook, ed. J. E. Mark, American Institute of Physics Press, Woodbury, NY, pg 101, (1996).
5. H. Domininghaus, Plastics for Engineers: Materials, Properties, and Applications, Hanser Publishers, New York (1993). (value from analysis of PVT data contained in book).
6. P. Zoller, *J. Appl. Poly. Sci.*, 23, 1057, (1979).
7. A. Quach and R. Simha, *J. Appl. Phys.*, 42, 12, (1971).
8. P. Zoller and P. Bolli, *J. Macromol. Sci. - Phys.*, B18, 3, 555, (1980).
9. General Electric Database, <http://www.ge.com/datasheets/LEXANLS2.html>
10. H. Wilski, "Heat Capacities of High Polymers Part A: Experimental Curves, Polymer Handbook, 3rd ed., eds. J. Brandrup and E.H. Immergut, J. Wiley and Sons, N. Y. C. (1989).
11. S. Simon, University of Pittsburgh, personal communication.
12. D.M. Colucci, PhD Thesis, Purdue University, (1995).

## MODELING DSC ANNEALING PEAKS FOR POLYETHERIMIDE: INCORPORATION OF TEMPERATURE GRADIENTS

Sindee L. Simon

Department of Chemical Engineering, University of Pittsburgh, Pittsburgh, PA 15261

### ABSTRACT

Enthalpy recovery of polyetherimide is measured during heating with differential scanning calorimetry (DSC) after cooling at various rates. The resulting annealing peaks are fit using the Moynihan-Tool-Narayanaswamy model of structural recovery. A self-consistent phenomenological equation is used to describe the experimentally observed structure and temperature dependence of the relaxation time in both glass and equilibrium regimes. Temperature gradients in the DSC sample are incorporated into the model calculations. When no thermal gradients are assumed, model parameters are found to vary with thermal history despite the use of the self-consistent equation for the relaxation time. Accounting for the presence of thermal gradients in the DSC sample is found to affect the values of the model parameters needed to fit the data. However, thermal gradients are unable to account for the thermal history dependence of the model parameters or for the discrepancy between the observed and calculated shapes of the DSC annealing peaks.

### INTRODUCTION

Physical aging, or structural recovery, occurs in all glassy materials due to the nonequilibrium nature of the glassy state, and results in changes in the macroscopic properties of the material, including a decrease in volume and enthalpy, and an increase in brittleness. Prediction of the rate of physical aging and its effects on various properties is important for predictions of the long-term performance of polymeric glasses.

The changes in enthalpy which occur during physical aging cannot be measured in-situ using differential scanning calorimetry (DSC) due to a lack of sensitivity. However, since an aged glass shows an endothermic annealing peak during heating (as the material recovers the enthalpy lost during physical aging), DSC can be used to investigate this enthalpy recovery process.<sup>1,2,3</sup>

The results of enthalpy recovery experiments can be described using a mathematical model of structural recovery based on work done originally by Narayanaswamy<sup>4,5,6,7,8,9,10</sup>, incorporating the ideas of Tool<sup>11</sup>. However, there are several problems with the models<sup>7,10,12,13</sup>, including an apparent dependence of model parameters on thermal history. The problems may result from 1) the presence of thermal gradients<sup>14,15</sup>, 2) an inconsistent equation for describing the effects of temperature and structure on the relaxation time, or 3) incorrect representation of structural recovery using the Kohlrausch-William-Watts (KWW)<sup>16,17</sup> function<sup>7</sup>. It is of interest in this work to examine the effects of the first two issues identified.

The presence of thermal gradients in differential scanning calorimetric measurements have been suggested to be a factor in discrepancies between experimental data and model calculations.<sup>14,15</sup> Using Moynihan's formulation of the Tool-Narayanaswamy model, Hodge and Huvard<sup>14</sup> found good agreement between calculated and observed values for the magnitude and placement of annealing peaks at low degrees of annealing (small overshoot peaks at  $T_g$ ) using a single set of model parameters. However, for high degrees of annealing (large overshoots), calculations using the same model parameters overpredicted the magnitude of annealing peaks. The researchers postulated that these differences might be attributable to thermal lag effects. In later work, O'Reilly and Hodge<sup>18</sup> found that model parameters varied with thermal history even for relatively slow heating rates (1.25°C/min) where thermal gradients were assumed to be negligible. Their results indicate that thermal gradients are not accountable for all of the shortcomings of the model. They do not address, however, the effects of thermal gradients on the shape of enthalpy recovery curves done in the DSC at typical rates (10°C/min) and the degree to which the gradients contribute to discrepancies between experimental data and model calculations.

### Model Calculations

A full description of Moynihan's form of the Tool-Narayanaswamy model of structural relaxation is given elsewhere<sup>6</sup>; only a brief description follows. In Moynihan's formulation, the fictive temperature,  $T_f$ , originally defined by Tool<sup>11</sup>, is used as a measure of the structure of the glass. The relaxation process is both nonlinear and nonexponential and is represented by the generalized KWW function:

$$\frac{dT_f}{dt} = 1 - \exp \int - (t/\tau_0)^\beta dt \quad (1)$$

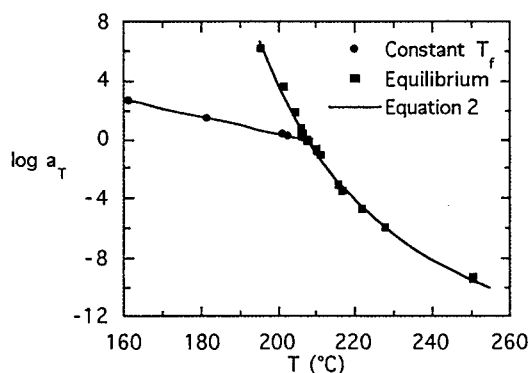
The nonexponentiality of the process is described by  $\beta$ ; the nonlinearity is incorporated into the model by allowing the relaxation time  $\tau_0$  to be a function of both temperature and structure ( $T_f$ ). Equation (1) is solved numerically for a given thermal history which begins at a temperature  $T_0$  above  $T_g$  for a specified thermal history consisting of cooling and heating ramps. To compare the calculation to experimental DSC data, the normalized heat capacity is calculated from the temperature derivative of the fictive temperature.<sup>19</sup>

A phenomenological equation relating the relaxation time  $\tau_0$  to temperature and structure ( $T_f$ ) is needed to perform the model calculations. The Tool-Narayanaswamy equation<sup>4</sup> is an Arrhenius-like equation, and although it is widely used, it is unable to describe the observed Vogel-Tammon-Fulcher<sup>20</sup> (WLF<sup>21</sup>) behavior in the equilibrium limit when  $T_f = T$ . Hence, an equation derived by Scherer<sup>22</sup>, based on Adam and Gibbs' approach<sup>23</sup>, is used in this work:

$$\ln a_T = \ln \frac{\tau_0}{\tau_{0,ref}} = \frac{D}{R \left[ a \ln \left( \frac{T_f}{T_2} \right) + b(T_f - T_2) \right]} - \frac{D}{R \left[ a \ln \left( \frac{T_{ref}}{T_2} \right) + b(T_{ref} - T_2) \right]} \quad (2)$$

where  $D/Ra$ ,  $b/a$ ,  $T_2$ , and  $\ln \tau_{0,ref}$  are treated as fitting parameters, and  $\ln a_T$  is the temperature shift factor. The parameters  $D/Ra$ ,  $b/a$ , and  $T_2$  are determined from data previously published<sup>24</sup> in which enthalpy, volume, and creep recovery measurements for polyetherimide were reported at various temperatures. Time-temperature superposition of the normalized data resulted in reduced curves and gave the temperature dependence of the shift factor ( $\log a_T$ ) in the equilibrium regime where  $T = T_f$ . A time-temperature reduction of the non-normalized enthalpy data also gave a reduced curve and the temperature dependence of the shift factor at constant  $T_f$ . The fit of Scherer's equation (equation 2) to the described shift factor data is shown in Figure 1, where  $D/Ra = 780$ ,  $b/a = -0.0017 \text{ K}^{-1}$ ,  $T_2 = 152.6^\circ\text{C}$ , and  $T_{ref} = 207.5^\circ\text{C}$ . Scherer's equation is considered to

Figure 1



be more self-consistent than the Tool-Narayanaswamy equation since it is able to predict both glassy and equilibrium behavior with one set of parameters.

The presence of a thermal gradient in the sample was incorporated into the Moynihan-Tool-Narayanaswamy model of structural relaxation by calculating the normalized heat capacity at several points in the sample and averaging the response. To this end, the temperature profile and average temperature in the DSC sample were first calculated as a function of program temperature for a given thermal history using a numerical solution to the one-dimensional heat conduction equation in which radial heat transfer is neglected:

$$\frac{\partial}{\partial x} \kappa \frac{\partial T}{\partial x} = \rho C_p \frac{\partial T}{\partial t} \quad (3)$$

where  $\kappa$  is the thermal conductivity,  $\rho$  is the density, and  $C_p$  is the heat capacity of the material. Then the structural recovery was calculated at the average sample temperature and at four other temperatures, two on either side of the average sample temperature, and the responses at these temperatures were averaged to give the sample response at the program temperature  $T_p$ .

The temperature profile in the DSC sample was determined for two cases: i) the ideal case in which the top and bottom of the sample pan are assumed to be maintained at the program temperature ( $T_p$ ), and ii) the non-ideal case in which there is a thermal gradient across the furnace such that the temperature at the top of the sample pan depends on but does not equal the program temperature. Both cases are of interest because the first is a conservative estimate of the temperature gradient and the second, for large temperature differences across the sample, is not. For both cases, the thermal diffusivity ( $k = \kappa/\rho C_p$ ) was assumed to have a downward step change at  $T_g$ , as is observed experimentally. In the glassy state,  $k = 0.00034 \text{ cm}^2/\text{s}$  based on the literature value of the thermal conductivity<sup>25</sup> and the values of the density and heat capacity obtained experimentally. For the equilibrium state,  $k$  is assumed to decrease 50% from the glassy value, based on the fact that polystyrene shows a change of this magnitude according to values of  $\kappa$ <sup>25</sup>,  $\rho$ <sup>26</sup>, and  $C_p$ <sup>27</sup> in the literature.

## EXPERIMENTAL

A polyetherimide (PEI), Ultem 1000 from General Electric, was used for experiments. Its glass temperature is approximately 207°C at a cooling rate of 1°C/min. The material is reported to have a number-average molecular weight of  $30 \pm 10 \text{ kg/mol}$  by the supplier.

A TA Instruments 1910 DSC equipped with a LNCA liquid nitrogen cooling unit was used to measure enthalpy recovery during heating at 10°C/min after cooling from 260°C to 100°C at various rates ranging from 0.1 to 60°C/min. The DSC sample used for these experiments weighed 13.6 mg and was sealed in an aluminum DSC pan. The DSC data obtained is normalized with respect to the glass and liquid heat capacities, which were found to be:

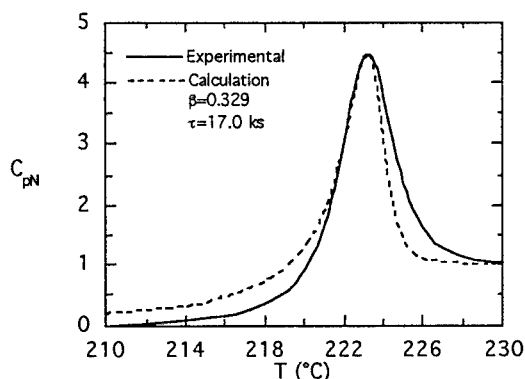
$$C_{pg}(T) = 0.94 + 0.0034 T(^{\circ}\text{C}) \quad \text{from } 125 \text{ to } 165^{\circ}\text{C} \quad (\text{J/g}^{\circ}\text{C}) \quad (4)$$

$$C_{pl}(T) = 1.51 + 0.0017 T(^{\circ}\text{C}) \quad \text{from } 230 \text{ to } 285^{\circ}\text{C} \quad (\text{J/g}^{\circ}\text{C}) \quad (5)$$

## RESULTS

The numerical calculations of the temperature gradient showed a symmetrical temperature profile in a DSC sample 1 mm thick for the ideal case in which the sample temperature was assumed to be the same at the top and bottom of the pan. In the glassy state, the temperature lag in the center of the sample was 0.6°C, with the average sample temperature being 0.4°C lower than the program temperature. In the rubbery state, there is an increase in the thermal lag due to the decrease in  $k$ , with the lag at the center of the sample being 1.2°C, and the average sample temperature being 0.8°C lower than the program temperature. The thermal lag is similar to that determined experimentally, with the difference between the melting temperature of an Indium standard on the bottom and top of the DSC sample pan generally being reported to be on the order

Figure 2

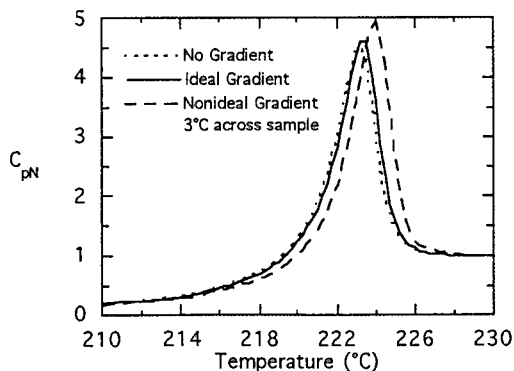


of 1°C.<sup>7,18,28,29</sup> For the non-ideal case, which is a less conservative estimate of the gradient, the temperature profile is asymmetric due to the externally imposed temperature difference across the sample of 3°C and the temperature profile did not change as dramatically through  $T_g$ .

A typical fit of the Moynihan-Tool-Narayanswamy model, without the incorporation of temperature gradients, is shown in Figure 2 for data obtained during heating at 10°C/min after cooling at 0.1°C/min. The values of the two model parameters ( $\tau$  and  $\beta$ ) used to fit the DSC curve were determined such that the height and placement of the calculated annealing peak corresponded to the experimentally observed value. The values depend on thermal history, with  $\beta$  increasing from 0.33 to 0.44 as the cooling rate increased from 0.1 to 30°C/min, despite the fact that a self-consistent equation was used to describe the effects of temperature and structure on the relaxation time. Figure 2 also shows another problem with the model calculations in that there appears to be a deviation between the shapes of the calculated and experimental peaks: the calculated curve is shifted above the experimental curve at temperatures below the peak temperature and vice versa, above the peak. In other words, the calculation predicts that enthalpy recovery will begin and end at a temperature lower than that experimentally observed. It is noted that this latter discrepancy is also present in the calculations of other researchers, although depending on the scale of the presented results, it may not be very noticeable.

The effect of incorporating a thermal gradient in the calculation is shown in Figure 3 for a cooling rate of 0.1°C/min, where all calculations were made using the same set of model

Figure 3

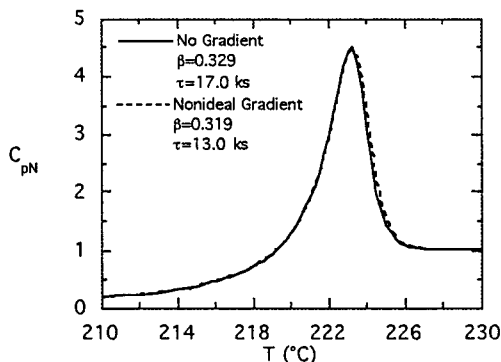


parameters ( $\tau_0(207.5^\circ\text{C}) = 19,000$  s and  $\beta = 0.326$ ). Three curves are shown, corresponding to the absence of a thermal gradient, as well as to the presence of either the ideal thermal gradient or the non-ideal thermal gradient previously shown. More substantial effects are seen for the non-ideal gradient which has an average temperature lag of greater than twice that in the ideal case. The presence of thermal gradients shifts the calculated response to higher temperatures and broadens the response. Thermal gradients also increase the height of the annealing peak. This latter effect was unexpected, and has not been reported in the literature, and results simply from the asymmetry of the calculated annealing peaks. If the calculated peak were symmetric, a thermal gradient would be expected to broaden and flatten the peak.

To determine whether thermal gradients in the sample could account for the deviations observed between the calculated and experimental curves, the model parameters were varied in the non-ideal case in order that the height and placement of the calculated annealing peak corresponded to the experimentally observed values. The difference between the calculation assuming no thermal gradients and the non-ideal case, in which there is  $3^\circ\text{C}$  temperature difference across the sample, is shown in Figure 4 for a cooling rate of  $0.1^\circ\text{C}/\text{min}$ . In order to match the height and placement of the observed annealing peak,  $\tau_0(207.5)$  was decreased to 14,000 s and  $\beta$  was decreased slightly to 0.316, changes of 25% and 3%, respectively, compared to the values used in the calculation without a thermal gradient. Similar changes in model parameters were found for other cooling rates. Besides a change in the value of the model parameters, the only effect of the thermal gradient is a very slight broadening of the peak. Model parameters still depend on thermal history and there is no change in shape of the calculated curve in the area where the calculation and experimental results differ. Hence, the presence of a thermal gradient cannot account for the differences in the shape of the recovery curves predicted by the model and those observed experimentally.

In summary, the two problems with the model calculations (i.e., the thermal history dependence of model parameters and the lack of agreement between experiment and model calculations with respect to the shape of annealing peaks) are found to be unaffected by 1) use of a self-consistent equation for the relaxation time, and 2) accounting for the effects of thermal gradients.

Figure 4



## CONCLUSIONS

Moynihan's formulation of the Tool-Narayanaswamy structural recovery model was used to describe enthalpy recovery DSC data for polyetherimide during heating after cooling at various rates. A self-consistent equation was used to describe the effects of temperature and structure on

the relaxation time with one set of parameters capable of describing both glassy and equilibrium behavior. Despite use of this self-consistent equation, model parameters were still dependent on thermal history and there were differences observed between the shape of experimental DSC annealing peaks and model calculations. The presence of thermal gradients was then incorporated into model calculations. In order to determine these thermal gradients, numerical calculations of the temperature profile within the DSC sample were performed taking into account the step change in thermal diffusivity at the glass transition. Thermal gradients were found to significantly affect values of the model parameters, especially  $\tau$ , needed to fit the experimental curves. However, thermal gradients cannot account for the dependence of model parameters on thermal history or for the lack of agreement between the shape of experimental and calculated DSC annealing peaks.

#### ACKNOWLEDGMENTS

Helpful discussions with Dr. Gregory B. McKenna (NIST) are gratefully acknowledged.

#### REFERENCES

1. C. R. Foltz and P. V. McKinney, *J. Appl. Polym. Sci.* 13, 2235 (1969).
2. S. E. B. Petrie, *J. Polym. Sci., Part A-2* 10, 1255 (1972).
3. L. C. E. Struik, *Physical Aging in Amorphous Polymers and Other Materials*, Elsevier, Amsterdam, 1978.
4. O. S. Narayanaswamy, *J. Am. Ceram. Soc.* 54, 491 (1971).
5. A. J. Kovacs, *Ann. N.Y. Acad. Sci.* 371, 38 (1981).
6. C. T. Moynihan, et al., *Ann. N.Y. Acad. Sci.* 15, 279 (1976).
7. I. M. Hodge, *J. Non-Cryst. Solids* 169, 211 (1994).
8. O'Reilly, *CRC Crit. Rev. in Solid State and Mat. Sci.* 13 (3), 259 (1987).
9. R. W. Rendell, J. J. Aklonis, K. L. Ngai, and G. R. Fong, *Macromolecules* 20, 1070 (1987).
10. G. B. McKenna, in "Comprehensive Polymer Science, Volume 12, Polymer Properties", C. Booth and C. Price, Ed., Pergamon, Oxford (1989).
11. A. Q. Tool, *J. Am. Ceram. Soc.* 29, 240 (1946).
12. G. B. McKenna and C. A. Angell, *J. Non-Cryst. Sol.* 133-133, 528 (1991).
13. C. T. Moynihan, S. N. Crichton, and S. M. Opalka, *J. Non-Cryst. Sol.* 131-133, 420 (1991).
14. I. M. Hodge and G. S. Huvar, *Macromolecules* 16, 371 (1983).
15. J. M. Hutchinson, M. Ruddy, and M. R. Wilson, *Polymer* 29, 152 (1988).
16. F. Kolrausch, *Pogg. Ann. Phys.* 12, 393 (1847).
17. G. Williams and D.C. Watts, *Trans. Faraday Soc.* 66, 80 (1970).
18. J. M. O'Reilly and I. M. Hodge, *J. Non-Cryst. Solids* 131-133, 451 (1991).
19. C. T. Moynihan, et al., *J. Am. Cer. Soc.* 59 (1-2), 12 (1976).
20. H. Vogel, *Phys. Z.* 22, 645 (1921).
21. M. L. Williams, R. F. Landell, and J. D. Ferry, *J. Am. Chem. Soc.* 77, 3701 (1955).
22. G. W. Sherer, *J. Am. Cer. Soc.* 67 (7), 504 (1984).
23. G. Adam and J. H. Gibbs, *J. Chem. Phys.* 43 (1), 139 (1965).
24. I. Echeverria, P.-C. Su, S. L. Simon, and D. J. Plazek, *J. Polym. Sci.: Part B: Polym. Phys.* 33, 2457 (1995).
25. Y. Yang, in "Physical Properties of Polymers Handbook", J. E. Mark, Ed., Chapter 10, American Institute of Physics, Woodbury, NY 1996.
26. R. A. Orwoll, in "Physical Properties of Polymers Handbook", J. E. Mark, Ed., Chapter 7, American Institute of Physics, Woodbury, NY 1996.
27. J. Wen, in "Physical Properties of Polymers Handbook", J. E. Mark, Ed., Chapter 9, American Institute of Physics, Woodbury, NY 1996.

## GLASS TRANSITION AND ULTRASONIC RELAXATION IN POLYSTYRENE

A. SAHNOUNE, L. PICHE

National Research Council Canada, Industrial Materials Institute, 75, de Mortagne, Boucherville,  
Québec J4B 6Y4 CANADA, abdelhadi.sahnoune@nrc.ca

### ABSTRACT

We present measurements of the glass transition and the ultrasonic relaxation modulus in a series of monodisperse polystyrenes. The temperature dependence of the modulus was analyzed using Havriliak-Negami relaxation model (HN) and Vogel-Tammann-Fulcher equation (VTF) for the relaxation time. The results allowed us to determine the fragility index,  $m$ , which decreases with increasing molecular weight,  $M_n$ . Furthermore, the relaxation time was found to saturate at high molecular weights and varies as  $M_n^p$ , in the low molecular weight region. The exponent is  $p \approx 2$  at high temperatures and  $p \approx 7$  at low temperatures close to  $T_g$ .

### INTRODUCTION

Glass transition and relaxation phenomena continue to be the subject of intensive research and many experimental techniques have been applied to gain insight into the properties of glass forming substances [1]. In general, one obtains the glass transition temperature,  $T_g$ , and the relaxation time,  $\tau$ , which are then analyzed within various theories and empirical expressions. The results provide a relatively informative view on the molecular mechanisms in glasses. Recent measurements using ultrasonics [2] have shown the potential of the technique to characterize the relaxation behavior and the glass transition. In particular, ultrasonics constitutes a practical alternative to study fragility in glassy systems. Here, we present ultrasonic measurements on a series monodisperse atactic polystyrenes with number average molecular weight,  $M_n$ , varying from  $615$  to  $1.6 \times 10^6$  g / mole. The main objective is to investigate the influence of molecular weight on the relaxation time and the fragility of polystyrene.

### EXPERIMENT

The polymers were purchased from Pressure Chemicals Co. and were used as received. All samples, about 3.5 grams each, were melted into disks under a pressure of 22.5 MPa and annealed for 15 min at  $\approx T_g + 200$  K. Then, while maintaining pressure, each sample was quenched to well below  $T_g$ . The measurements of the specific volume,  $V$ , the longitudinal sound velocity,  $v$ , and the ultrasonic attenuation,  $\alpha$ , were then immediately taken at a heating rate of 2 K / min from 220 to 520 K. Details of the experimental setup were given elsewhere [3]. All samples were prepared following the same procedure so that the effect of molecular weight could be studied. From the quantities,  $V$ ,  $v$  and  $\alpha$  we compute the complex longitudinal modulus,  $L^* = L' + iL''$ , with the storage,  $L'$ , and loss,  $L''$ , moduli given by [4]:

$$L' = \frac{v^2}{V} \left( 1 - \left( \frac{av}{\omega} \right)^2 \right) / \left( 1 + \left( \frac{av}{\omega} \right)^2 \right)^2 \quad \text{and} \quad L'' = \frac{2av^3}{V\omega} / \left( 1 + \left( \frac{av}{\omega} \right)^2 \right)^2 \quad (1)$$

where  $\omega = 2\pi f$  is the angular frequency; here we used  $f = 2.7$  MHz.



## RESULTS

Representative data of  $L'$  and  $L''$  as a function of temperature are shown in Fig. 1. The symbols represent the experimental data and the solid line is a fit to the theoretical expressions, as explained below. With increasing temperature, the storage modulus decreases first slowly then more rapidly. The break point from slow to rapid change in the modulus is the glass transition temperature,  $T_g$ , where the glass-like structure of the polymer starts to collapse and the system goes into the molten state. In the low- and high-temperature regions,  $L'$  tends toward the same limiting values indicating the independence of the modulus on the molecular weight in the completely glassy state as well as in the liquid state. On the other hand, with increasing  $M_n$  the loss peak shifts to higher temperatures and its height increases steadily before saturating at high molecular weights.

The viscoelastic modulus,  $L^*$ , can also be written in terms of a relaxed modulus,  $L_R$ , and an unrelaxed modulus,  $L_U$ , as:

$$L^* = L_R + (L_U - L_R)L(\omega), \quad (2)$$

$L_U$  and  $L_R$  are the low and high temperature limits of the storage modulus.  $L(\omega)$  is the HN relaxation function,  $L(\omega) = (1 + (i\omega\tau)^\alpha)^{-\gamma}$  [5], where  $\tau$  is the relaxation time and  $\alpha, \gamma$  are shape parameters of the loss peak. The temperature dependence of  $\tau$  is given by the empirical VTF equation [6]:

$$\tau = \tau_0 \exp\left[\frac{B}{(T - T_0)}\right] \quad (3)$$

where  $\tau_0$  is a microscopic time scale which relates to energy barrier crossing which oppose chain rearrangements during structural relaxation and is the same for all samples ( $\sim 10^{-14}$  s) [7]. The Vogel temperature,  $T_0$ , and  $B$  are parameters specific to the material. The experimental data are fitted to the theoretical expression of the modulus from eq. 2. Thus, the unknown parameters are  $B$ ,  $T_0$ ,  $\alpha$ , and  $\gamma$ . The results of the fit are the solid lines in Fig. 1. The agreement is very good

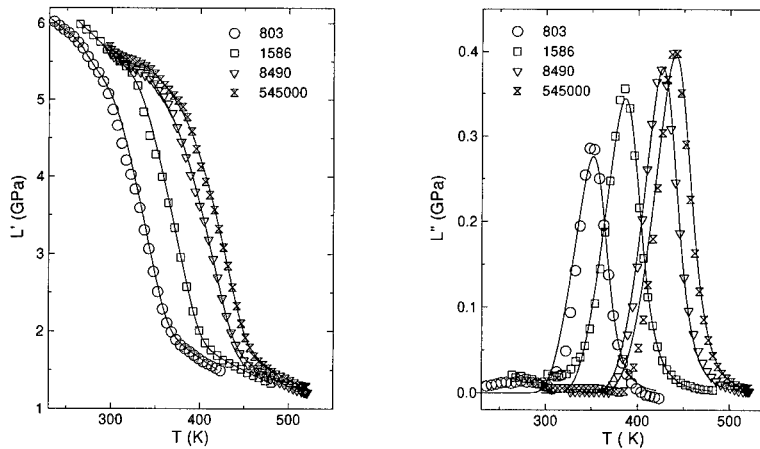


**Figure 1:** Longitudinal storage,  $L'$ , and loss,  $L''$ , moduli of polystyrene as a function of temperature. The symbols are the data and the solid line are fits to HN relaxation model as outlined in the text. The molecular weight is indicated in the figure.

over the entire temperature range and all molecular weights for both storage and loss moduli. Hence, HN model accounts well for the relaxation behavior in polystyrene. The exponents  $\alpha$  and  $\gamma$  vary only slightly with molecular weight and have mean values of  $0.75 \pm 0.03$  and  $0.2 \pm 0.03$ , respectively.

The results for the glass transition temperature, shown in Fig. 2, are analyzed using Fox-Flory equation [8]:

$$T_g = T_g(\infty) - K_g / M_n \quad (4)$$

where  $K_g$  is a constant and  $T_g(\infty)$  is the glass transition temperature for an infinite molecular weight chain. A fit to eq. 4 yields values of  $K_g$  and  $T_g(\infty)$ , see Table I, in excellent agreement with the literature [9]. Thus eq. 4 provides a good description of the glass transition temperature in polystyrene over more than three orders of magnitude of molecular weight.

The behavior of  $T_0$  is shown in Fig. 2 where it is also found to follow the molecular weight dependence given by eq. 4. In fact, not just  $T_0$  but  $T_{\max}$ , the temperature where the loss peak is maximum, also obeys eq. 4. In other words, all three characteristic temperatures;  $T_0$ ,  $T_g$ , and  $T_{\max}$  are described by the same equation. Even more surprising is the behavior of the parameter  $B$  shown in the inset of Fig. 2. It also is governed by eq. 4. The "universality" of Fox-Flory equation is unexpected and at the moment its origin remains unclear. The fit values for  $T_0$ ,  $T_{\max}$  and  $B$  are given in Table I. Finally, as evident from the figure, we point out that the difference  $T_g - T_0$  decreases with decreasing molecular weight. This has important implications for the relaxation behavior and a detailed analysis of this observation will be published elsewhere.

In Fig. 3 we show the relaxation time as obtained from our fits. In Fig. 3.a,  $\tau$  is plotted as a function of  $T_g/T$ . This type of plot, due to Angell [10,11] and often referred to as a "fragility plot", compares the temperature dependence of the relaxation time in different glass-forming materials. Fragility reflects the complexity of the energy landscape of the system: A fragile liquid has a large number of local minima in its energy hypersurface, while a strong liquid has relatively few. It is therefore more difficult for the latter to relax towards a lower energy state than for its

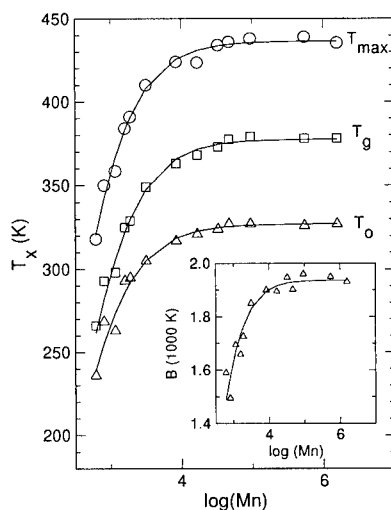


**Figure 2:** The characteristic temperatures  $T_0$ ,  $T_g$ , and  $T_{\max}$  in polystyrene as function of molecular weight. The solid lines are fits to eq. 4. Inset: Parameter  $B$  versus  $\log(M_n)$ .

**Table I:** Fit parameters of the characteristic temperatures and parameter  $B$  using eq. 4.

	$T_x(\infty)$ , $B(\infty)$ (K)	$10^5 K_x$ (mol g <sup>-1</sup> · K)
$T_0$	327	1.03
$T_g$	377	0.74
$T_{\max}$	436	0.97
$B$	1937	3.58

fragile counterpart. The relaxation time of a strong liquid is Arrhenius like and leads to a straight line on a fragility plot whereas a fragile liquid is characterized by a non-Arrhenius temperature dependence as shown in Fig. 3.a. One way to quantify fragility is by calculating the fragility index,  $m$ , defined as [11]:

$$m = d(\log \tau) / d(T_g/T) \Big|_{T=T_g} \quad (5)$$

i.e., the rate at which the relaxation time increases at  $T_g$ . Typically,  $m$  varies from  $\sim 16$  for strong glass formers to 150 or more for very fragile glass formers. For polystyrene,  $m$  is always large (see inset Fig. 3.a) and reflects the overall fragile character of polystyrene as reported previously [2]. However what is more interesting is the increase of  $m$  from  $\sim 120$  to approximately 230 with decreasing molecular weight. This means that at low molecular weight, the relaxation time increases more rapidly with decreasing temperature and would diverge not too far from  $T_g$ . Indeed, this divergence is illustrated in Fig. 3.b where we have calculated the relaxation at the glass transition temperature using VTF equation. We interpret this result as a change in the energy landscape structure of the polymer with decreasing molecular weight. Indeed, for low  $M_n$  and therefore short polymer chains the number of possible configurations is very large resulting in a large number of minima in the energy hypersurface; i.e., a more fragile system. In contrast, the ubiquitous entanglements for high  $M_n$  will restrict the polymer chains to a relatively limited number of configurations; hence fewer energy minima and a less fragile liquid. This view is supported by the fact that in general strong glass formers, such as  $\text{SiO}_2$ , are characterized by a strong network structure and directional bonding which constrains atoms to a limited number of rearrangements [11, 12]. Our result also shows that the definition of the glass transition temperature as the point where a common value of  $\tau$  is reached (e.g.  $\sim 100$  s) may not be generally correct for all systems. Using this criterion for low  $M_n$  samples would lead to values

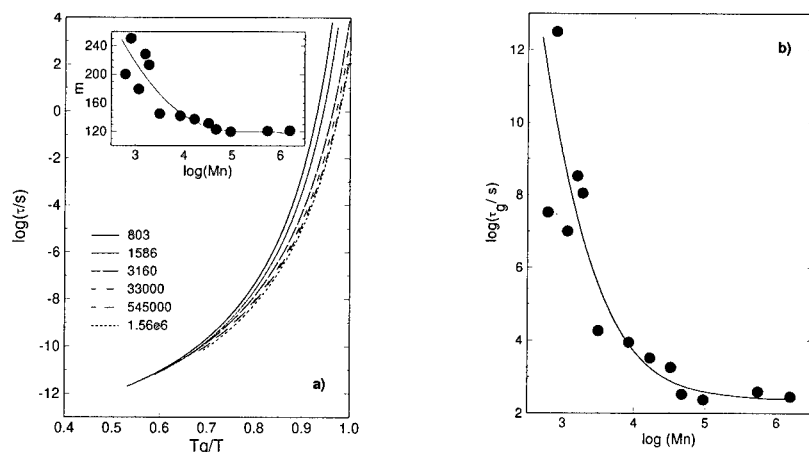


**Figure 3:** The relaxation time in polystyrene. a) as a function of  $T_g/T$ . The curves are generated using VTF equation (eq. 4) and fitted values of  $B$  and  $T_0$  (Table I). The molecular weight is indicated in the figure. Inset: fragility index,  $m$ , as a function of molecular weight (eq.5), the solid line is a guide to the eye; b) the relaxation time at the glass transition temperature. The solid line is a guide to the eye.

of  $T_g$  much different from those obtained from volume or modulus measurements.

In Fig. 4 we show the relaxation time as a function of molecular weight at different temperatures. The first remark is that, independently of temperature,  $\tau$  saturates when the molecular weight exceeds  $M_c \approx 10^4$ . This is due to entanglements which are expected to become important around this molecular weight range. In fact in a polymer such as polystyrene, there are two different mechanisms which affect the relaxation behavior: the interchain interactions and entanglements. Below the entanglements threshold only interchain interactions are important and the chains simply interact through van der Waals forces. For  $M_n > M_c$  however, the entanglements which are topological in nature, will take over and dominate the polymer properties, leading to a very weak molecular weight dependence of the relaxation time as displayed in the figure. We now focus on the behavior of  $\tau$  at low molecular weights. In this region, it varies as  $M_n^p$ , and depending on temperature the exponent evolves from  $p \approx 2.0$  at high temperatures to  $p \approx 7.0$  at low temperatures just above  $T_g$ . According to Rouse model, the relaxation time of chain modes can be written as [13]:

$$\tau_p = (\zeta_0 / M_0) (M_n^2 / \rho R T) \propto \zeta_0 M_n^2 \quad (6)$$

where  $\zeta_0$  is the friction coefficient,  $M_0$  the molecular weight of a repeat unit,  $\rho$  the mass density,  $M_n$  the molecular weight.  $\zeta_0$  is a measure of the force needed for the chain segment to reorient or change position and is assumed to be constant within this model. Thus at high temperatures where interchain correlations are relatively weak we recover the predicted molecular weight dependence of  $\tau$ . The new result is the steady increase of the exponent  $p$  as the temperatures decreases. We believe this is caused by the increasing chain stiffness with decreasing temperature. In this case one expects the chain segments mobility to be greatly reduced and the short length chain to behave like rigid rods. According to Doi and Edwards [14], the relaxation time of such a system is strongly dependent on chain length. In fact, they predict  $\tau \propto M^7$ , the same as our results. The data in Fig. 4 show therefore a complete change in the hydrodynamics of short polymer chains with temperatures from a Rouse type to a rigid chain-like system. The different regimes suggest correspondingly different energy landscapes, thereby connecting to the idea of fragility.

## CONCLUSION

In summary, we have studied the glass transition and the ultrasonic relaxation in polystyrene over a wide range of temperature and molecular weight. The glass transition temperature is well described by the Fox-Flory equation over more than three orders of magnitude of molecular weight. The "universality" of the Fox-Flory equation in describing both the characteristic temperatures and the activation energy is unexpected and is worth further investigation. The fragility index,  $m$ , was calculated using our fit results and was found to increase with decreasing molecular

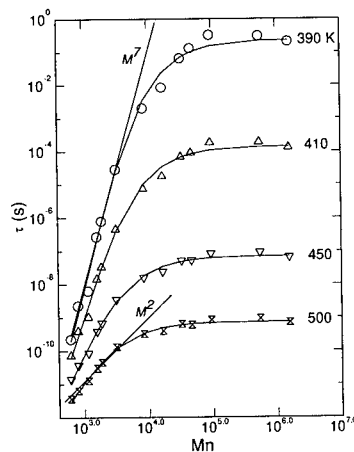


Figure 4: The relaxation time in polystyrene as a function of molecular weight at different temperatures.

weight. Furthermore, the results allowed us to study the molecular weight and temperature dependence of the relaxation time over a very wide range.  $\tau$  is independent of molecular weight for entangled polymers and shows a power law dependence  $M_n^p$  for short polymer chains. In this latter case, there is a progressive cross over with decreasing temperature from a Rouse type relaxation time ( $M_n^2$ ) to a very strong dependence ( $M_n^7$ ) characteristic of rigid chains.

#### REFERENCES

1. Proc. of the 2nd International Discussion Meeting on "Relaxation in Complex Systems", *J. Non-cryst. Solids* **172 - 174**, (1994).
2. A. Sahnoune, F. Massines, and L. Piché, *J. Polym. Sci., Part B: Polym. Phys.*, **34**, 341 (1996).
3. F. Massines, L. Piché, and C. Lacabanne, *Makromol. Chem. Macromol. Symp.*, **23**, 121 (1989).
4. G. J. Gruber and T. A. Litovitz, *J. Chem. Phys.*, **40**, 13 (1964).
5. S. Havriliak and S. Negami, *Polymer*, **8**, 161 (1967).
6. H. Vogel, *Phys. Z.*, **22**, 645 (1921); G.S. Fulcher, *J. Am. Chem. Soc.*, **8**, 789 (1925).
7. C. A. Angell (submitted to *Macromolecules*).
8. A. Eisenberg, in *Physical Properties of Polymers*, 2<sup>nd</sup> ed., American Chemical Society, Washington, 1993, p. 61.
9. T. G. Fox and P. J. Flory, *J. Polym. Sci.*, **14**, 315 (1954).
10. C. A. Angell, *J. Non-cryst. Solids*, **131 - 134**, 13 (1991).
11. R. Bohmer and C. A. Angell, in *Disorder Effects on Relaxational Processes*, R. Richert and A. Blumen (eds.), Springer, Berlin, 1994, p. 11.
12. M. Wilson, P. A. Madden, M. Hemmati, and C. A. Angell, *Phys. Rev. Lett.*, **77**, 4023 (1996).
13. S. Matsuoka, in *Relaxation Phenomena in Polymers*, Hanser Publishers, Munich, 1992, p.160.
14. M. Doi and S. F. Edwards, in *The Theory of Polymer Dynamics*, Clarendon Press, Oxford, 1986, p. 335.

## TIME AND ENSEMBLE AVERAGED DYNAMIC LIGHT SCATTERING IN ORTHOTERPHENYL ABOVE AND BELOW THE GLASS TRANSITION

D.L. SIDEBOTTOM\*\*, C.M. SORENSEN\*

\*Department of Physics, Kansas State University, Manhattan, KS 66506-2601

\*\*Advanced Materials Lab, 1001 Univ. Blvd. SE, Albuquerque, NM 87106

### ABSTRACT

While traditional dynamic light scattering is useful for following structural relaxation in the liquid, in the glassy domain the technique is limited by the ultimate patience of the experimentalist; i.e., the structural relaxation can not be measured when the experimental time scale is less than the structural relaxation time. Nevertheless, we show how useful information regarding structural relaxation can be accessed from light scattering in the glass using a novel ensemble-averaged technique. Dynamic light scattering (DLS) measurements performed on glass forming orthoterphenyl show an inequality between time and ensemble average correlation functions near and below the calorimetric glass transition temperature,  $T_g$ , and hence demonstrate ergodicity breaking. Our ensemble averaged measurements provide a measure of the so-called non-ergodicity parameter,  $f_q$ , below  $T_g$ . Our DLS results for orthoterphenyl indicate that the functional form for  $f_q$  is consistent with Mode Coupling theory predictions, but occurs at the glass transition temperature,  $T_g \approx 243\text{K}$ , rather than at  $T_c \approx 290\text{K}$  as observed in neutron scattering studies.

### INTRODUCTION

Many liquids when cooled through their freezing temperatures can avoid the discontinuous, first-order liquid-to-crystal transition and supercool to an amorphous, glass phase [1-2]. This occurs because the rising viscosity of the liquid which accompanies the falling temperature can become large enough to kinetically inhibit molecular rearrangement into the thermodynamically more stable crystalline phase. This glass transition is imprecise, although calorimetric measurements of the heat capacity  $C_p$  show, in most cases, a definite steplike change over a narrow temperature range the center of which is the glass transition temperature,  $T_g$ , which is cooling rate dependent. Hence the nature of this transition appears to be kinetically arrested thermodynamics, but there has long been suspicion that some more fundamental, phase transition explanation of the glass transition might be viable. This proposed transition is hidden or masked by the kinetics but is the underlying reason for vitrification.

The past decade has seen a new tact taken to describe the glass transition. A Mode Coupling Theory (MCT) describing the behavior of the density correlation function has been developed which has stimulated considerable activity in this field[3-8]. MCT predicts the viscosity to diverge in a power law fashion,  $\eta \sim (T-T_c)^{-\gamma}$  where  $\gamma > 0$ , a behavior that has been seen experimentally at temperatures well above  $T_c$ [9]. A key aspect of MCT is that the glass transition is caused by a fundamental ergodicity breaking transition. Hence it awakens the suspicion of a transition underlying the kinetics as mentioned above. This ergodicity breaking is predicted to occur at the "ideal glass transition" temperature,  $T_c$ , tens of degrees above the

calorimetric  $T_g$  and is marked by a partial "freezing in" of density fluctuations at a level  $f_q$ , the Debye-Waller or nonergodicity factor. Above  $T_c$ , the system is ergodic, that is the system can sample all of its allowed phase space, and time and ensemble averages are equal. Below  $T_c$ , the system becomes nonergodic, molecular motion is constrained, allowed phase space is not completely accessed, and time and ensemble averages are not equal. In the extended version of MCT[5-8], the inclusion of thermally activated hopping processes ultimately restores ergodicity, but the density correlation function continues to be "pinned" near a level  $f_q$  that rises abruptly near  $T_c$  in a cusplike fashion

$$f_q = \begin{cases} f_q^c + (1 - f_q^c)\epsilon^{1/2}; & T < T_c \\ f_q^c; & T > T_c \end{cases} \quad (1)$$

where  $\epsilon = (T_c - T)/T_c$ . Both neutron [10,11] and light [12-15] scattering experiments have provided evidence for ergodicity breaking of the form Eq.(1) at a  $T_c > T_g$ , but no work exists to explicitly demonstrate this through an inequality of ensemble and time averages of the density correlation function.

We have examined the molecular, and so-called fragile glass former, orthoterphenyl (OTP) for temperatures of  $130\text{K} \leq T \leq 267\text{K}$  using dynamic light scattering (DLS). This temperature range is below the conventional, MCT  $T_c \approx 290\text{K}$  for OTP [11,16] and includes the calorimetric glass transition temperature  $T_g \approx 243\text{K}$  [17]. We measured both the time and the ensemble averaged scattered light intensity correlation function,  $g^{(2)}(t)$ , a direct measure of the dynamic structure factor  $f(q,t)$ . We find i) an explicit demonstration of ergodicity breaking; the time and ensemble averages of  $g^{(2)}(t)$  are equal above, but not equal below the calorimetric glass transition temperature  $T_g \approx 243\text{K}$ . This occurs significantly below the ideal glass transition temperature  $T_c \approx 290\text{K}$  found for OTP from both neutron scattering [11] and viscosity [18] measurements. ii) Despite this discrepancy, the nonergodic (i.e., nondecaying) part of the correlation function, the nonergodicity function  $f_q$ , still obeys Eq.(1) with  $T_c = T_g$ .

## EXPERIMENT

Suitable samples of o-terphenyl (OTP) were produced from 99% grade (Aldrich) stock melted at about  $70^\circ\text{C}$  and passed through  $0.22\mu\text{m}$  Teflon filters into the light scattering cell. After degassing, the cells were flame sealed. For work above  $T_g \approx 243\text{K}$ ,  $1\text{cm}^2$  pyrex cuvettes were used and temperature control provided by circulated Methanol from a temperature controlled bath. These cuvettes typically fractured at about  $230\text{K}$ , so smaller samples, contained in thick walled capillary tubing ( $2.5\text{mm}$  ID,  $9\text{mm}$  OD), were used below  $T_g$ . Temperature control below  $T_g$  was provided by a  $\text{LN}_2$ , cold finger cryostat.

An  $\text{Ar}^+$  laser operating at about  $400\text{mW}$  in TEM<sub>00</sub> [19,20] with  $\lambda = 5145\text{\AA}$  provided incident light which was focused by a lens to a beam waist of about  $30\mu\text{m}$  inside the sample. The scattering wave vector was  $q = 25\mu^{-1}$  ( $\theta = 90^\circ$ ). The scattered light was collected by another lens and focused onto a  $100\mu\text{m}$  pinhole located  $50\text{cm}$  in front of the cathode of a photomultiplier tube. Photopulses from the PMT were digitized and fed to an ALV5000 correlator which computed  $g^{(2)}(t)$ , the time averaged, normalized intensity correlation. This is related to the field correlation function,  $f(q,t)$ , through the Siegert relation [21]

$$g^{(2)}(t) = 1 + A_c |f(q, t)|^2, \quad (2)$$

where  $A_c \leq 1$  is an instrumental coherence factor. This field correlation function is the dynamic structure factor, i.e., the spatial Fourier transform of the liquid's density correlation function, the central element in the MCT theory. An important aspect of our work was that the coherence factor was periodically calibrated from an aqueous suspension of latex spheres ( $r=38\text{nm}$ ) for which  $A_c=0.95 \pm 0.03$ .

A theoretical development of light scattering from non-ergodic media was first proposed by Pusey and van Megen (PVM)[19] and developed by others[22-24] in conjunction with the sol/gel transition. The formation of a rigid gel network contributes a static (non-fluctuating) component to the scattered light and leads to both homodyne and heterodyne contributions in  $g_T^{(2)}(t)$ . The heterodyne component produces an effective reduction of the observed amplitude of  $g_T^{(2)}(t)$  and provides a measure of non-ergodic behavior.

Key to success of these approaches is proper evaluation of  $g_T^{(2)}(0)$ . In the case of gels,  $g_T^{(2)}(1\mu\text{s})$  is a suitable choice for  $g_T^{(2)}(0)$  since even the fastest dynamics contributing to  $g_T^{(2)}(t)$ , the so-called "gel mode", generally occurs at times greater than  $1\mu\text{s}$ . However, if the relaxation process being observed involves substantial decay at times less than  $1\mu\text{s}$ , the lower limit of modern correlators,  $g_T^{(2)}(1\mu\text{s})$  no longer provides a measure of the quantity  $g_T^{(2)}(0)$ . Thus in general, changes in  $g_T^{(2)}(1\mu\text{s})$  cannot *a priori* be interpreted as evidence of non-ergodic behavior, since they could instead reflect the partial decay of  $g_T^{(2)}(t)$  occurring at shorter times.

Since MCT predicts an initial decay ( $\beta$ -relaxation) extending from vibrational timescales ( $t \approx 1\text{psec}$ ) to a plateau,  $f_q^c$ , followed by slower collective  $\alpha$ -relaxation[6-8], we opted instead to employ an alternative approach which circumvents the difficulty with  $g_T^{(2)}(0)$ . Ensemble averaged measures of the intensity correlation function,  $g_E^{(2)}(t)$ , were achieved by moving the sample at a fixed rate ( $\sim 8\mu\text{m/sec.}$ ) vertically relative to the optical plane while the correlator was running [23-25]. In this way  $g^{(2)}(t)$  becomes an average over many spatially independent scattering volumes, that is, an ensemble average. We do not mean to imply that only one "ensemble member", i.e., a region of the fluid with an extent of one spatial coherence length, a coherence region, of the system resides in our scattering volume at any given time. Instead, one may envision many such regions inside the scattering volume creating a scattered light speckle pattern at the detector which carries information regarding the numerous coherence regions in the scattering volume. With motion of the sample, new coherence regions pass into the scattering volume and an average is obtained.

## RESULTS

Figure 1 displays some of our results for  $g_T^{(2)}(t)$  and  $g_E^{(2)}(t)$ . For  $T=255\text{K}$  and  $264\text{K}$  the ensemble and time averages are identical indicating ergodicity. For  $T=217\text{K}$ , however, these averages are not equal; an explicit demonstration of nonergodicity at this temperature. We find the transition from ergodic to nonergodic as indicated by comparison of  $g_T^{(2)}(t)$  and  $g_E^{(2)}(t)$  occurs at  $T=243 \pm 5\text{K}$ . This temperature is in close agreement with the calorimetrically determined  $T_g=243\text{K}$  [11,26]. This result is in contrast to earlier versions of MCT which predicted ergodicity breaking at  $T_c > T_g$ , but in accord with more recent versions in which hopping



processes restore ergodicity at and below  $T_g$ . Our results indicate that ergodicity is restored so long as these processes have time scales shorter than the upper range of our experimental dynamic window,  $\sim 10^3$  sec.

The pronounced decay in  $g^{(2)}(t)$  for  $T > T_g$  is the alpha relaxation which we have fit through Eq.(2) to a stretched exponential,

$$f(q, t) = f_q^c e^{-(t/\tau_\alpha)^\beta}.$$

We find a temperature independent  $\beta = 0.57 \pm 0.03$ .

The alpha relaxation time,  $\tau_\alpha$ , shows a strong temperature dependence and becomes unmeasurably long at  $T_g$  and below. The level from which the dynamic structure factor decays is

the nonergodicity factor of the MCT theory which we find to be *constant* at  $f_q^c = 0.56 \pm 0.01$  for  $243 \leq T \leq 267$  K, despite the fact that this temperature range lies well below 290 K where a non-constant  $f_q^c$  is expected.

To understand the  $T < T_g$   $g_E^{(2)}(t)$  spectrum consider again the speckle pattern due to scattering from a group of coherence regions in the liquid within the scattering volume described in the Experimental Section above. For a stationary sample if the relaxation time of these fluctuations is long compared to the experimental time scale, the detector sees a static speckle pattern. If instead the fluctuations have a two-step spectrum with one time scale faster the other slower than the experimental time scale, and if the shorter time scale is also too fast for the correlator, the speckle pattern will appear static but its visibility will be decreased below unity due to the faster time scale. If the system is translated in either case, the speckle pattern will fluctuate on the time scale of the motion. The latter, two time scale case, however, will retain information regarding the faster time scale because of its decreased fringe visibility. This is what we observe. The decay near  $10^{-1}$  sec. is the beam transit time [27] caused by the relative motion and is not fundamentally related to the glass. The height of  $g_E^{(2)}(t)$  at times shorter than the beam transit is physically relevant and represents the decreased speckle visibility due to relaxation at time scales shorter than  $10^{-6}$  sec., the lower limit of our correlator. These relaxations determine  $f_q$  and hence our translating cell method allows us to measure  $f_q$  even when the alpha relaxation time has exceeded the experimental time scale, i.e., when  $T < T_g$ .

Below 243 K we monitored the plateau level while each spectrum was accumulating to insure a sufficient number of "ensemble members" are collected. This plateau approaches a limiting constant value as the number of ensemble members increases as shown in the inset to Fig. (2). Our complete set of results for  $f_q$  for  $130 < T < 267$  K are shown in Fig. (2). The data for  $T < T_g$

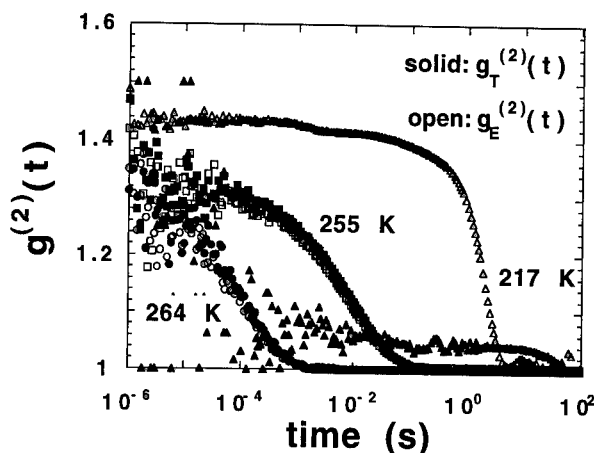


Fig. 1 Normalized intensity autocorrelation functions for light scattered at  $\theta=90^\circ$  from orthoterphenyl. Decays at  $T=255$  and  $264$  K are the alpha relaxation. Decay at  $T=217$  K in  $g_E^{(2)}(t)$  is a beam transit term.

have considerably more error than those for  $T > T_g$ , but the trend of the former and the precise constancy of the latter demonstrate cusp-like behavior at  $T_g \approx 243\text{K}$ . As discussed above, Eq.(1) has been verified in both OTP and other glass systems using other techniques but with  $T_c$  values tens of Kelvin higher than  $T_g$  [10-13]. For OTP the neutron data of Bartch et al. [11] indicate  $T_c = 290 \pm 5\text{K}$ . This value of  $T_c$  is corroborated by the power law behavior of the viscosity [18],

where the MCT prediction of  $\eta^{-1/\gamma} \sim (T - T_c)$  is fit best with  $\gamma = 2.5$ .

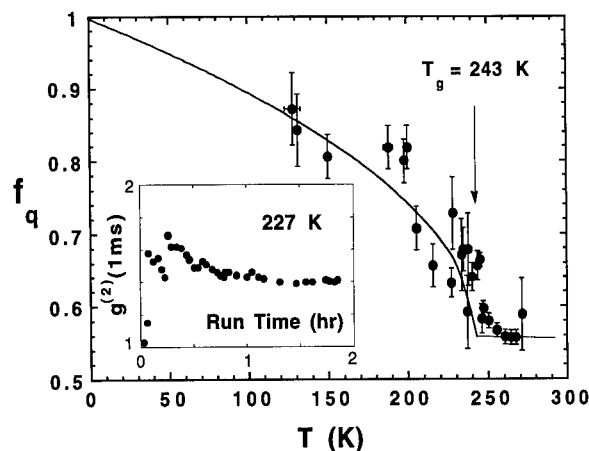


Fig. 2 Nonergodicity parameter  $f_q$  versus temperature. Line is fit to Eq.(1) with  $T_c = 243\text{K}$ . Inset shows plateau of  $g_r^{(2)}(t)$  vs. run time.

## CONCLUSIONS

To summarize, our DLS results verify key aspects of MCT regarding ergodicity: we demonstrate explicitly that ergodicity is broken, and  $f_q$  obeys Eq.(1) as illustrated in Fig. 2. A major discrepancy exists, however, in the temperature where the cusp in  $f_q$  occurs. We see this to occur at  $T_g$  whereas MCT predicts and earlier experiments find broken ergodicity at significantly higher temperatures, 47K higher for neutron scattering from OTP [11].

Acknowledgments: D.L.S. wishes to recognize the kind hospitality of Lee Ann Sidebottom and Dr. Tonette Demagante. The correlator used in this work was purchased with funds obtained through NSF Grant No. CTS 9024668.

## REFERENCES

1. "Relaxations in Complex Systems, Proceedings of the Workshop on Relaxation Processes," Blacksburg VI, 1983, edited by K. Ngai and G.B. Smith (National Technical Information Service, U.S. Department of Commerce, Washington, DC, 1985).
2. Dynamics of Disordered Materials, edited by D. Richter, A.J. Dianoux, W. Petry and J. Teixeira (Springer-Verlag, Berlin, 1989).
3. E. Leutheusser, Phys. Rev. **A29**, 2765 (1984).
4. U. Bengtzelius, W. Gotze and A. Sjolander, J. Phys. **C19**, 5915 (1984).
5. S.P. Das and G.F. Mazenko, Phys. Rev. **A34**, 2265 (1986).
6. W. Gotze and L. Sjogren, J. Phys. **C20**, 879 (1990).
7. L. Sjogren, Z. Phys. **B79**, 5 (1990).
8. W. Gotze and L. Sjogren, Rep. Prog. Phys. **55**, 241 (1992).
9. P. Taborek, R.N. Kleimann, and D.J. Bishop, Phys. Rev. **B34**, 1835 (1986).

10. D. Richter, B. Frick, and B. Farago, Phys. Rev. Lett. **61**, 2465 (1988); and ibid. **64**, 2921 (1990).
11. E. Bartsch, F. Fujara, M. Kiebel, H. Sillescu, and W. Petry, Ber. Bunsenges. Phys. Chem. **93**, 1252 (1989).
12. M. Elmroth, L. Borjesson, and L.M. Torrell, Phys. Rev. Lett. **68**, 79 (1992).
13. C. Dreyfus, M.J. Lebon, H.Z. Cummins, J. Toulouse, B. Bonello, and R.M. Pick, Phys. Rev. Lett. **69**, 3666 (1992).
14. N.J. Tao, G. Li, H.Z. Cummins, Phys. Rev. Lett. **66**, 1334 (1991); G. Li, W.M. Du, X.K. Chen, H.Z. Cummins and N.J. Tao, Phys. Rev. **A45**, 3867 (1992); G. Li, W.M. Du, A. Sakai, and H.Z. Cummins, Phys. Rev. **A46**, 3343 (1992).
15. Y. Yang and K.A. Nelson, Phys. Rev. Lett. **74**, 4883 (1995).
16. W. Steffen, et al., Phys. Rev. **E49**, 2992 (1994).
17. R.J. Greet and D. Turnbull, J. Chem. Phys. **46**, 1243 (1967).
18. W.T. Laughlin and D.R. Uhlmann, J. Phys. Chem. **76**, 2317 (1972); and M. Cukiermann, J.W. Lane, and D.R. Uhlmann, J. Chem. Phys. **59**, 3639 (1973).
19. P.N. Pusey and W. van Megen, Physica **A157**, 705 (1989).
20. P.N. Pusey, J.M. Vaughan and D.V. Willetts, J. Opt. Soc. Am. **73**, 1012 (1983).
21. B. Berne and R. Pecora, Dynamic Light Scattering (Wiley, New York, 1976).
22. S.Z. Ren and C.M. Sorensen, Phys. Rev. Lett. **70**, 1727 (1993).
23. J.G.H. Joosten, J.L. McCarthy, and P.N. Pusey, Macromolecules **24**, 6690 (1991).
24. J.Z. Xue, D.J. Pine, S.T. Milner, W.L. Wu, P.M. Chaikin, Phys. Rev. **A46**, 6550 (1992).
25. K. Schatzel, Appl. Opt. **32**, 3880 (1993).
26. G. Fytas, C.H. Wang, D. Lilge, and Th. Dorfmueller, J. Chem. Phys. **75**, 4247 (1981).
27. T.W. Taylor and C.M. Sorensen, Appl. Optics **25**, 2421 (1986).

## REORIENTATIONAL DYNAMICS AND INTERMOLECULAR COOPERATIVITY OF REACTIVE SYSTEMS

JOVAN MIJOVIC

Department of Chemical Engineering, Chemistry and Materials Science  
Polytechnic University, Six Metrotech Center, Brooklyn, NY 11201 USA  
jmijovic@duke.poly.edu

### ABSTRACT

An investigation was conducted of the effects of the advancement of chemical reactions and the prepolymer molecular weight on the reorientational dynamics and intermolecular cooperativity in reactive epoxy-amine systems. Experimental results were obtained by dielectric spectroscopy over a wide range of frequency (1 MHz to 1 GHz) and temperature (-170 to +200 °C). A strong effect of the progress of reaction on reorientational dynamics was noted and, for the first time, an explanation was put forward within the framework of the coupling theory. It was proposed that the molecular-level characteristics of a reactive system that affect its intermolecular cooperativity can be classified into two categories: 1) molecular architecture - determined by molecular symmetry, rigidity and steric hindrance; and 2) dielectric architecture - determined by the type and concentration of all dielectrically active species.

### INTRODUCTION

Reorientational dynamics of glass-forming polymers and small molecules are currently the subject of extensive experimental and theoretical studies in a number of laboratories worldwide [1]. However, information on the reorientational dynamics in systems that undergo a temporal evolution of structure as a result of chemical reactions is scarce and no comprehensive study on this theme has appeared hitherto in the literature. The advancement of chemical reactions alters the very nature of the material and adds a new component to the study of dynamics of molecular motions in polymers. Changes in the chemical composition, glass transition temperature ( $T_g$ ), crosslink density, and morphology, are accompanied by a continuous variation in the time scale of the segmental motions. Consequently, the origin and the characteristic relaxation times of various molecular processes, their temperature dependencies, activation energies, and the widths and breadths of their distributions, all change with the progress of reaction. The principal goal of this study is to examine how the advancement of chemical reactions in epoxy-amine systems affects the reorientational dynamics within the general framework of intermolecular cooperativity.

### EXPERIMENTAL

**Materials** - The six epoxy prepolymers utilized in this study were all based on diglycidyl ether of bisphenol A (DGEBA). Their chemical structure, degree of polymerization ( $x$ ) and molecular weight (MW) are shown in the inset in Figure 1. The non polymer-forming model epoxy-amine system consisted of 1,2-epoxy-3-phenoxypropane, also known as phenyl glycidyl ether (or PGE), and aniline. The multifunctional polymer-forming formulation consisted of a DGEBA epoxy resin and methylenedianiline (MDA). All

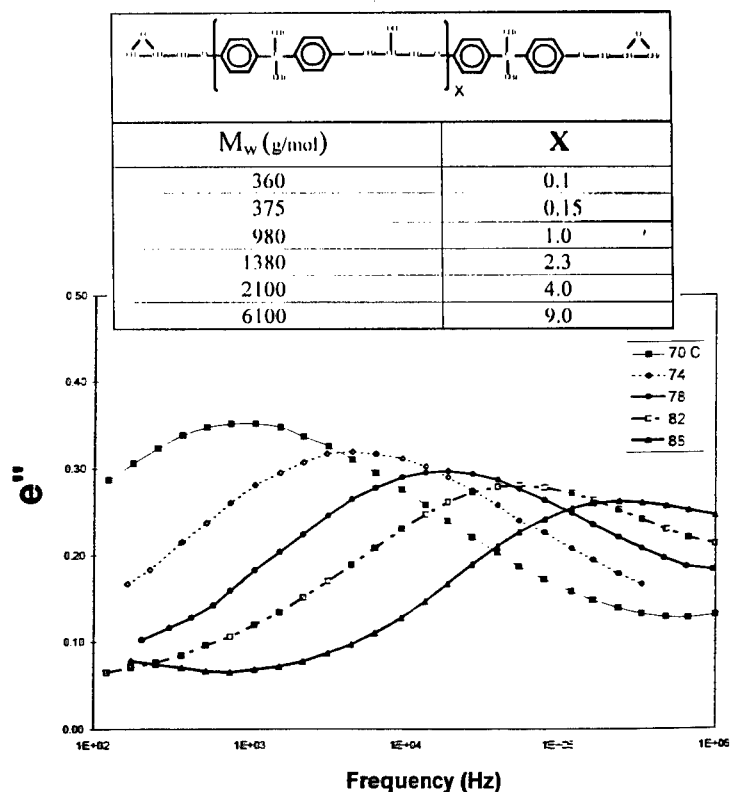
reactive mixtures contained the stoichiometric amount of epoxy group and amine hydrogen.

**Techniques** - Our experimental facility for dielectric measurements consists of modified commercial and custom-made (in-house) instruments [2]. The three commercial instruments are : 1) Solartron 1260 Impedance/Gain Phase Analyzer (10  $\mu$ Hz -32 MHz); 2) Hewlett-Packard 4284A Precision LCR Meter (20 Hz - 1 MHz); and 3) Hewlett-Packard 8752C Network Analyzer (300 kHz- 1.3 GHz). Each instrument was modified by the addition of a temperature controlled chamber and interfaced to a computer.

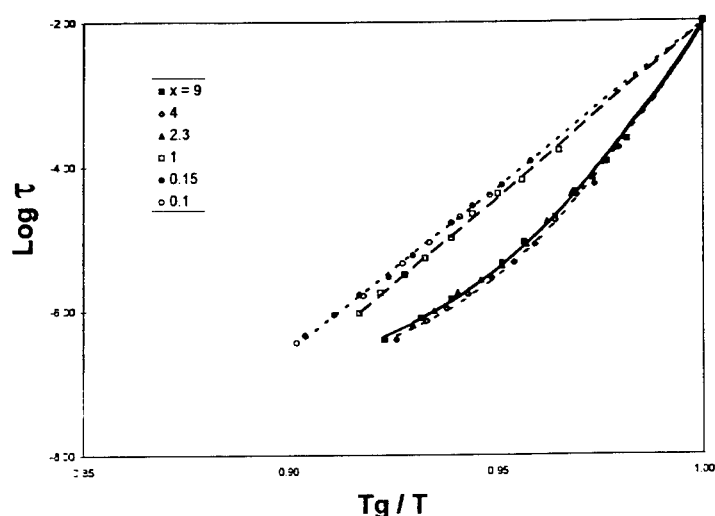
## RESULTS AND DISCUSSION

### 1. Effect of molecular weight of epoxy prepolymer on reorientational dynamics

The first part of our study examines the reorientational dynamics of a homologous series of bifunctional epoxies of different molecular weights. Frequency sweeps at various temperatures were performed on all prepolymers and an example is given in Figure 1 for the prepolymer with the degree of polymerization of 2.3 (MW=690 g/mole). The  $\alpha$  relaxation peak is clearly observed in the frequency domain; with increasing temperature it shifts to higher frequency, while its intensity and dielectric dispersion decrease.



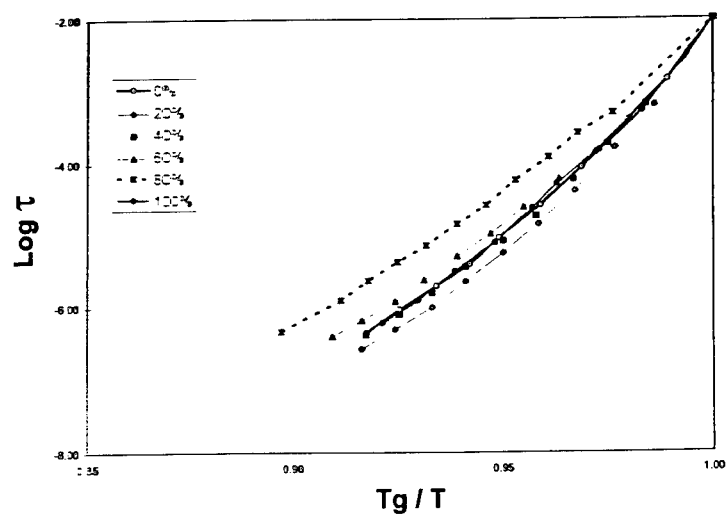
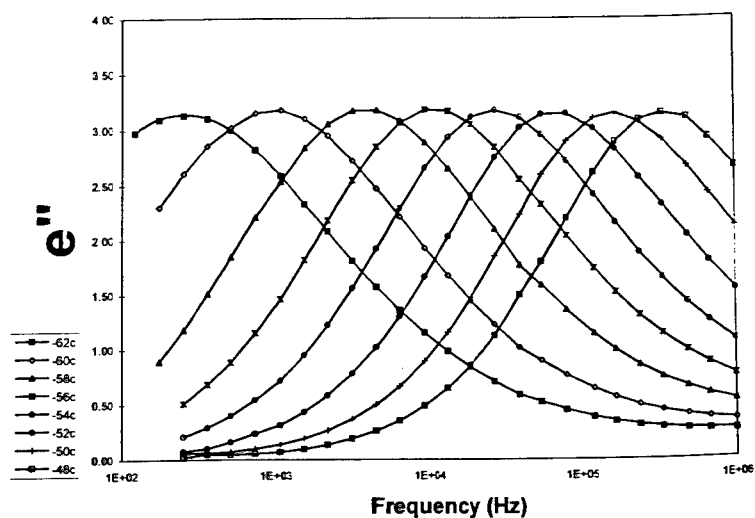
Next, we sought to relate the observed changes in the dielectric response to the molecular and dielectric architecture of prepolymers within the framework of the coupling theory. The interpretation afforded by the cooperativity plot, shown in Figure 2 for all six prepolymers, is most interesting.



We observe an Arrhenius type response for  $x \leq 1$  and a distinctly non-Arrhenius behavior for the higher molecular weight samples. We also note a large increase in cooperativity in going from  $x=1$  to  $x=2.3$  owing to the dominant influence of the dielectric architecture (decrease in the concentration of dielectrically active terminal epoxy groups) over the molecular architecture (increase in intermolecular rigidity).

## 2. Effect of progress of reaction on reorientational dynamics in model system

The effect of the progress of reaction on the reorientational dynamics was investigated by evaluating the dielectric response of a series of samples with precisely determined extent of reaction. A large number of runs were executed on samples with different extent of reaction; in Figure 3 we present data from the frequency sweeps between 0.1 kHz and 1 MHz for a mixture reacted to 20 %. An examination of the cooperativity plot in Figure 4 affords a unique insight into the effect of the advancement of chemical reactions on dipole dynamics. We shall preface our interpretation of the cooperativity plot in Figure 4 by advancing an explanation of the nature of the various phenomena that govern cooperativity in reactive systems. We propose that the molecular-level characteristics of a reactive system which affect its intermolecular cooperativity can be classified into two categories: 1) **molecular architecture** - determined by symmetry, rigidity and steric hindrance; and 2) **dielectric architecture** - determined by the type and concentration of

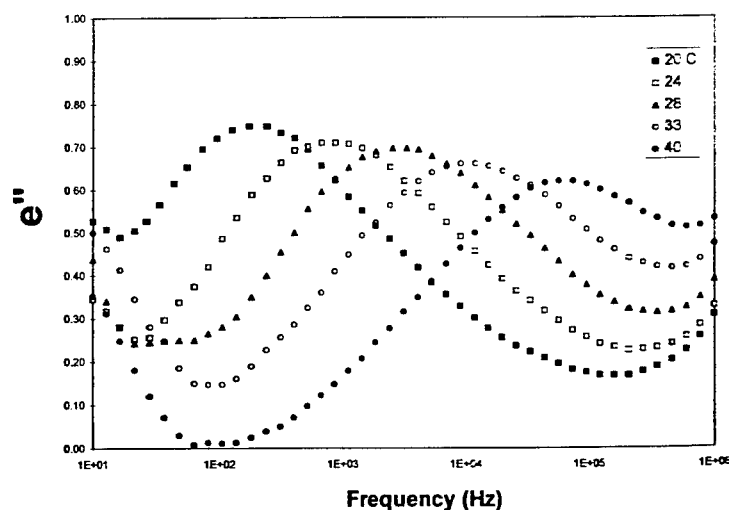


dielectrically active species (mostly dipoles) and the various specific interactions that can affect the reorientational dynamics of dipoles. The overall direction in which the cooperativity shifts in the course of reaction is determined by the interplay of these two phenomena. Let us now examine how this information can be parlayed into the cooperativity plot of Figure 4. The cooperativity of the non-reacted mixture reflects its initial molecular and dielectric architecture, the latter being strongly affected by mixing. Specific interactions in the mixture, namely hydrogen bonding, have an effect on the

spatial distribution of dipoles associated with epoxy and primary amine groups and hence should influence the dielectric response. This view is further supported by infrared spectroscopy, which shows higher absorption by the epoxy (particularly) and primary amine groups in the non-reacted PGE-aniline mixture than in the individual components. Once the reactions begin, however, the effect of specific interactions diminishes rapidly. Between approximately 10 and 90 % reaction there is a systematic decrease in cooperativity, clearly recognized as decreasing curvature in Figure 4. We submit that in this range it is possible to explain the direction in which cooperativity shifts by considering the interplay between molecular and dielectric architecture. We believe that the dominant influence on cooperativity between ca. 10 and 90 % reaction is exerted by dielectric architecture, as the disappearance of major dipolar contributors to  $\alpha$  relaxation (epoxy and primary amine groups) outweighs the continuing demand for more cooperativity from the changing molecular architecture. Near and at the end of reaction (100 %) the origin of dipole relaxations changes completely. The loss peak is still present but its intensity is greatly reduced, as the origin of dipole relaxations now lies with less dielectrically active species, namely tertiary amines and glycidyl ethers.

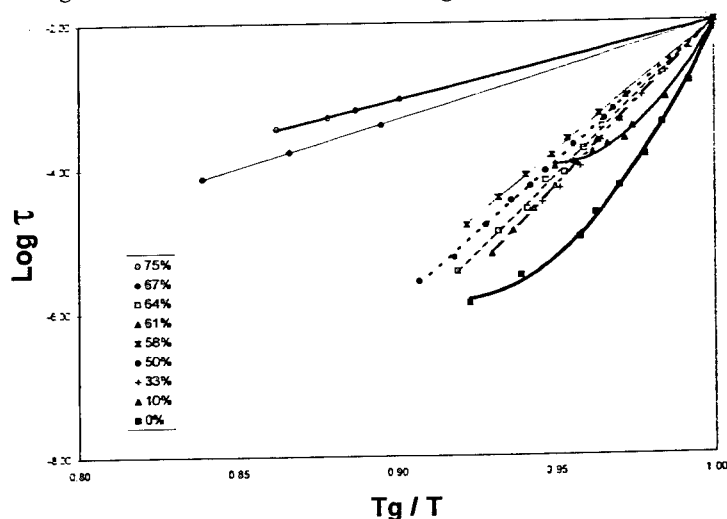
### 3. Effect of progress of reaction on reorientational dynamics in polymer-forming system

Frequency sweeps were performed next on a series of DGEBA-MDA samples of a precisely known degree of cure. An example of dielectric loss in the frequency domain, with temperature as a parameter, is shown in Figure 5 for a sample cured to 50 % conversion.





Data obtained from the frequency sweep of each partially cured sample were used to construct the cooperativity plots. The use of cooperativity plots has again yielded most interesting information as can be surmised from Figure 6.



The initial mixture is characterized by high intermolecular cooperativity and a distinctly non-Arrhenius response. The advancement of cure affects both molecular and dielectric architecture, which, together, determine intermolecular cooperativity. Crosslinking affects molecular architecture by increasing the intermolecular dynamic constraints as a result of the reduced mobility and increased steric hindrance, and also dielectric architecture, as a consequence of the change in the concentration and type of dielectrically active species during reaction. Soon after the onset of reaction the response becomes linear and the steepness of the cooperativity plot decreases. A careful examination of Figure 6 reveals that this situation prevails through 58% of cure. At 61% cure, however, a dramatic change is observed; the curve shifts back toward an increase in cooperativity and reverts to a non-Arrhenius response. This increase in cooperativity is caused by the formation of a hydrogen bonded complex in the vicinity of gel point (corroborated by FTIR) and it is evident that the occurrence of gelation has a strong effect on the cooperativity plot. Above gel point, however, the plot reverts to the Arrhenius form with a rapidly decreasing slope with further cure.

#### ACKNOWLEDGEMENTS

This material is based on work supported by National Science Foundation under Grant No. DMR-9400716.

#### REFERENCES

1. K. L. Ngai and D. J. Plazek, *Rubber Chem. Tech.* **68**, p. 376 (1996).
2. J. Mijovic, S. Andjelic, W. C. F. Yee, F. Bellucci and L. Nicolais, *Macromolecules* **28**, p. 2797 (1995).
3. J. Mijovic, F. Bellucci and L. Nicolais, *J. Electrochem. Soc.* **142**, p. 1176 (1995).

**Part III**  
**Glasslike Systems, Simulations,**  
**and Models**

## FROM SPIN GLASSES TO GLASSES

J.P. BOUCHAUD\*, M. MEZARD\*\*

\* Service de Physique de l'État Condensé, Centre d'Études de Saclay, Orme des Merisiers, 91191 Gif-sur-Yvette Cédex, FRANCE

\*\*Laboratoire de Physique Théorique de l'Ecole Normale Supérieure, \* 24 rue Lhomond, 75231 Paris Cedex 05, FRANCE

**ABSTRACT:** We discuss some aspects of the links between the behaviour and theory of spin glasses and that of structural glasses of the fragile type. We review the present status of the conjecture according to which a certain class of spin glass mean field theories (those with first order transitions) could provide a mean field theory for the glass transition. Recent developments pointing in that direction include the existence of spin glasses without disorder, and the general link between Mode-Coupling Theory (MCT) and the motion of a particle in a random potential. This link enables one to generalize the MCT equations for temperatures below the glass transition, and to describe aging effects. We compare these results with those obtained within more phenomenological 'trap' models.

A priori there exist striking differences between the behaviour and the basic constitutive ingredients of spin glasses on the one hand and structural glasses on the other hand. Let us mention a few of the most obvious ones. The first one that comes to mind is the existence of quenched disorder in spin glasses (for instance the Mn impurities in CuMn do not move on experimental time scales, and therefore the magnetic exchange couplings are frozen), while in glass forming liquids there is *a priori* no quenched disorder: disorder is "self induced" by the gradual freezing of some degrees of freedom. This induces a second difference, namely the existence of a crystalline state in glasses with no counterpart in spin glasses. A third one is the fact that the glass transition is a dynamic effect, basically defined as the temperature or density at which the relaxation times reaches the experimentally accessible order

---

\* Unité propre du CNRS, associée à l'Ecole Normale Supérieure et à l'Université de Paris Sud

of magnitudes of hours. In spin glasses there exists rather good evidence in favour of the existence of a second order phase transition at least in zero magnetic field, with a power law singularity of the non linear magnetic susceptibility.

In spite of these seemingly crucial differences, there is increasing convergence between some of the theoretical ideas developed in the two fields. A first step in this direction is the understanding that there exist two very different types of mean field spin glasses. While the most conventional ones like the Sherrington-Kirkpatrick model provide a good starting point for the description of real spin glasses, there exist a second class, which is characterized by a discontinuous static phase transition at a temperature  $T_s$ . The discontinuity is that of the Edwards-Anderson order parameter, while the transition is second order in the thermodynamic (Ehrenfest) sense. An extreme example of this type of spin glass ordering is provided by the Random Energy model [1], which has zero entropy density in the whole low temperature phase. But there are many other such examples, some of which can also be reinterpreted as a thermalised particle in a random potential, in a large dimensional space. We shall come back to this case later on as it provides a particularly interesting bridge between our two problems, but let us first list some of the basic properties of these spin glass mean field models with discontinuous transitions. These models generally possess a peculiar dynamical behaviour, with a dynamical transition temperature  $T_c$  which is *higher* than the static one (and which coincides with the Mode-Coupling critical temperature -- see below). When approaching  $T_c$  from above, the relaxation time diverges as a power law, but there is no singularity in the static thermodynamic quantity. This behaviour originates from the fact that the system gets trapped in some metastable states, the free energy of which still being extensively higher than the one of the fundamental state. Of course such a scenario can only exist at the mean field level: in a finite dimensional space the nucleation of bubbles of the fundamental state will smear the dynamical singularity. About ten years ago, a series of works by Kirkpatrick, Thirumalai and Wolynes [2] pointed out the existence of these two transitions, the dynamic one above the static one, and conjectured that in a finite dimensional system the relaxation time  $\tau$  will grow rapidly around the mean field  $T_c$ , and diverge only at the static temperature  $T_s$ . Within this conjecture the spin glass models with discontinuous transitions appear as good candidates for describing the glass transition at the mean field level. In this description  $T_s$  appears as a Vogel Fulcher or Kauziman temperature, while the experimental glass temperature, where  $\tau$  reaches a few hours, lies somewhere between  $T_s$  and  $T_c$ . Unfortunately little progress has been made to support this conjecture and derive the behaviour of  $\tau$  when one lowers the temperature, although some arguments in favour of a generalised Vogel-Fulcher law have been proposed [2][3].

The above arguments thus suggest a convergence of phenomenology, and propose a scenario where a dynamical glassy "transition" can appear in discontinuous

spin glasses. As for the fundamental difference about the existence of quenched disorder in spin glasses, it now appears less relevant since recent work has shown the existence of spin glass behaviour without disorder. There exist spin systems with frustration but no disorder which behave in all respects like spin glasses with discontinuous transitions [4] [5]. The simplest example is the problem of low binary autocorrelation sequences, an old and important problem from communication theory which was restated in physical terms ten years ago by Bernasconi as follows: take a one dimensional chain of Ising spins  $\sigma_i$ ,  $i = 1 \dots N$ . Compute the correlation function at distance  $k$ :  $C_k = \sum_i \sigma_i \sigma_{i+k}$ . Define the energy function as  $E = 1/N \sum_k C_k^2$ . The interest in communication is to find configurations of low energy. It was shown by simulations that there exist a finite temperature freezing transition [6] [7]. The analytical study of the problem is in itself interesting. Despite its simplicity we know of no direct solution. A rather indirect, but illuminating, one consists in substituting it with a problem with quenched disorder. This was done in two ways, depending on the type of boundary conditions adopted [4][5]. With fixed boundary conditions, one can introduce a disordered correlation  $C_k^d = \sum_{ij} M^{(k)}_{ij} \sigma_i \sigma_k$ , where  $M^{(k)}$  is a matrix the elements of which are chosen randomly equal to 0 or 1, with the only constraint that  $\sum_{ij} M^{(k)}_{ij} = N - k$ . The original problem is a very special choice of  $M^{(k)}$ , which of course might not be a generic sample. There is in fact quite a bit of educated guesswork in the choice of the class of disordered system in order to ensure that the original, not disordered, system be a generic sample. In the case of fixed boundary conditions, the previous choice turns out to be a good approximation, but it is not exact (as seen from a high temperature expansion). With periodic boundary conditions, there exist another choice of random systems, involving the replacement of the Fourier series  $\sigma(q) = \sum_j \sigma_j \exp(iqj2\pi/N)$  in terms of which the energy can be expressed ( $E = \sum_q |s(q)|^4$ ) - by an appropriate random unitary transformation which apparently leads to an exact solution [5], although this could be shown only in the high temperature phase. What is interesting is that these disordered systems can be solved by spin glass techniques like the replica method. They show precisely a discontinuous type of replica symmetry breaking, with two transition temperature  $T_c > T_s$ , as seen in discontinuous spin glasses. There is in particular an apparent 'entropy crisis' at  $T_s$ , which is resolved by the breaking of replica symmetry, which leaves a small residual entropy in the glass phase (which is linear in  $T$ ).

There exist by now a few such examples of spin glasses without disorder. In particular it is worth to mention the model of Josephson junction array, studied in [8], which can provide an experimental realization, allowing for detailed tests of these ideas.

One of the most fascinating recent developments on the convergence between the theoretical approaches to the discontinuous spin glasses and the structural glasses is the equivalence of the Mode Coupling equations in the two systems. This is most

clearly seen from the study of a particle in a random potential as follows. Let us introduce the following simplified picture of a glass: the motion of a given particle can be thought of as taking place in a random potential created by its neighbours. Since the motion of the molecules is extremely slow at low temperatures, one can assume that this random potential has a static component. The diffusion of a particle in a quenched disordered potential can be studied in different ways. A first approach is to treat the problem in large dimension of space, where one can establish *exact* equations [9] relating the two-time correlation function  $C(t + t_w, t_w) = \bar{r}(t + t_w) \cdot \bar{r}(t_w)$  (where  $\bar{r}(t)$  is the position of the particle at time  $t$ ), and the two-time response to an external force  $R(t + t_w, t_w)$  ( $t_w = 0$  is defined as the moment where the system reaches the temperature  $T$  after a rapid quench from high temperatures). For temperatures higher than a certain  $T_c$ , one finds that  $C$  and  $R$  are actually *time translation invariant* (i.e. these functions only depend on time differences), and furthermore that the fluctuation-dissipation theorem  $R(t) = -\frac{1}{T}\Theta(t)\frac{\partial C(t)}{\partial t}$  is obeyed. In this case, one can then eliminate  $R(t)$  and find an equation for  $C(t)$  which, interestingly, is *precisely the schematic Mode-Coupling equation*, with a kernel which is related to the correlation of the random potential. Hence, the physical content of the (schematic) MCT is clear: it is a mean-field description of a single particle in a static *quenched random* potential. It is very important to identify a well defined Hamiltonian which corresponds to the MCT equations: from this point of view, one should note that the same equations can be obtained starting with some mean-field models of *spin-glasses* [10]. The important point is thus that MCT implicitly assumes the presence of some *quenched disorder* which should rather, as discussed above, be ‘self-induced’ by the dynamics itself.

Coming back to the equations relating  $C$  and  $R$ , one can now investigate the ‘glass’ phase  $T < T_c$  [11]. In this case, the correlation and response function cease to be functions of  $t$  only. More precisely,  $C(t_w + t, t_w)$  can be written as the sum of an ‘equilibrium’ contribution  $C_{eq}(t)$  which only depends on  $t$ , and an ‘aging’ part which depends on the ratio  $u = \frac{t_w + t}{t_w}$ ,  $C(u)$  (actually the ratio could involve a more complicated function  $h$  and read  $u = \frac{h(t_w + t)}{h(t_w)}$ : see refs. [12][9][13] for a more precise discussion of this point). The same decomposition holds for the response function; however, the aging parts of  $C$  and  $R$  are related by an ‘anomalous’ fluctuation dissipation theorem, where  $T$  is replaced by an effective temperature  $\frac{T}{X}$ , with  $X \leq 1$  [12][14]. In more physical terms, this means that for a finite waiting time  $t_w$  after the quench below  $T_c$ , one expects that the susceptibility  $\chi(\omega, t_w)$  still exhibits two peaks: a high frequency  $\beta$ -peak very similar to the high temperature ( $T > T_c$ ) one, and a low frequency  $\alpha$ -peak which reaches a maximum at a frequency  $\omega_\alpha \simeq \frac{1}{t_w}$ , which thus progressively disappears as  $t_w \rightarrow \infty$ . An interesting prediction of this low temperature extension of MCT is that the high frequency part of the ‘aging’  $\alpha$ -peak behaves as  $(\omega t_w)^{-b}$ , while the low frequency ‘foot’ of the  $\beta$ -peak behaves as  $\omega^a$ , with the following relation between  $a$ ,  $b$ , and the ‘anomaly’  $X$  [9][11]:  $X \frac{\Gamma^2[1+b]}{\Gamma[1+2b]} = \frac{\Gamma^2[1-a]}{\Gamma[1-2a]}$ . This

equation generalizes the famous MCT relation [15] between  $a$  and  $b$  for  $T > T_c$ , for which  $X \equiv 1$ .

Another, more phenomenological approach, consists in coarse-graining the random potential, replacing it by ‘traps’, where the potential is locally harmonic, from which the particle can only escape through thermal activation and ‘hop’ to the neighbouring sites. The important quantity here is the distribution of barrier height  $\rho(\Delta E)$ , which in turn determines the distribution of local *waiting times*  $\tau$  through the relation  $\tau = \tau_0 \exp[\frac{\Delta E}{T}]$ , where  $\tau_0$  is a microscopic time scale (typically the oscillation period within the trap).  $\rho(\Delta E)$  describes the strength of the ‘cages’ created by the neighbouring particles. Let us consider the case where  $\rho(\Delta E)$  decreases for large  $\Delta E$  as  $\exp(-\frac{\Delta E}{T_0})$ . (Other possibilities are discussed in [16]). Then one can show [17] [18] that there is a true dynamical phase transition at  $T = T_0$ , separating a high temperature phase where the correlation function  $C_q(t_w + t, t_w) = \langle \exp[i\vec{q} \cdot (\vec{r}(t + t_w) - \vec{r}(t_w))] \rangle$  is time translation invariant and decays to zero for large times, from a low temperature phase where  $C_q(t_w + t, t_w)$  has an ‘aging’ component, decaying on a time scale proportional to the waiting time  $t_w$  itself [16]. For  $T < T_0$ , the asymptotic diffusion constant of the particle is zero [18]. Hence, these simple minded ‘trap’ models, describing the motion of a particle in a random potential in finite dimension, also capture many features of supercooled liquids, and lead to predictions which are very similar to those of the MCT. It is thus natural to wonder whether the above two descriptions are in fact equivalent. This is not so: the motion of a particle in infinite space dimensions (which leads to the schematic MCT equations) is peculiar because the particle actually never reaches the bottom of an energy well: there is always directions along which it can escape and lower its energy [19]. Hence, aging within the low temperature MCT is not related to barrier crossing and activated processes, but rather to a slow, endless descent in phase space. On the other hand, in any finite dimension, the particle reaches local minima of the potential in a finite time, and activation is crucial to leave these minima. The major differences between these two descriptions is that the late ‘in cage’ dynamics (described by the exponent  $a$ ) is intimately related to the early ‘out of cage’ dynamics (described by the exponent  $b$ ) within the MCT description, whereas these two regimes are a priori not related in a precise way within the trap models. This is why we believe that a precise experimental investigation of the age dependent susceptibility spectra  $\chi(\omega, t_w)$  in the glass phase, in order to test Eq. (1), would be valuable to draw a consistent physical picture of supercooled liquids. From a theoretical point of view, it would be extremely interesting to understand how finite dimensional effects and the residual motion of the surrounding particles (which make the random potential time dependent) can be included in a systematic way within the Mode-Coupling framework. It is also possible now to use some of the usual spin glass techniques, combined with standard approximations for the description of the liquid phase like the HNC equations, to give reasonable predictions on the value of the

density where the glass phase appears in e.g. hard sphere systems [20]. One may hope that an improvement of these methods will be able to give quantitative information on the glass phase itself.

ACKNOWLEDGEMENTS. We wish to warmly thank our collaborators on these matters, namely Alain Barrat, Rafaella Burioni, Leticia Cugliandolo, David Dean, Silvio Franz, Jorge Kurchan, Cécile Monthus and Giorgio Parisi. Enlightning discussions with Walter Kob must also be acknowledged.

### References

- [1] B. Derrida, Phys. Rev. Lett. **45** (1980) 79 and Phys. Rev. B **24** (1981) 2613; D.J. Gross, M. Mézard, Nuclear Physics B **240** (1984) 431
- [2] T. R. Kirkpatrick and D. Thirumalai, Phys. Rev. **B36** (1987) 5388; J. Phys. **A22** (1989) L149; T. R. Kirkpatrick, D. Thirumalai and P. G. Wolynes; Phys. Rev. **A40** (1989) 1045; see also A. Crisanti, H. Horner and H-J Sommers, Z.Phys. **B92** (1993) 257
- [3] G. Parisi *Slow dynamics in glasses*, cond-mat **9411115** and **9412034**
- [4] J.P. Bouchaud and M. Mézard; J. Phys. I (France) **4** (1994) 1109
- [5] E. Marinari, G. Parisi and F. Ritort; J. Phys. **A27** (1994) 7615; J. Phys. **A27** (1994) 7647
- [6] J. Bernasconi, J. Physique **48** (1987) 559
- [7] W. Krauth and M. Mézard Z. Phys. **B97** (1995) 127
- [8] P. Chandra, M. Feigelmann and L. Ioffe; cond-mat/9509022, to appear in Phys. Rev. Lett.
- [9] S. Franz, M. Mézard, Europhys. Lett. **26** (1994) 209, Physica **A209** (1994) 1; L. Cugliandolo, P. Le Doussal, Phys. Rev. **E 53** (1996) 1525
- [10] T. R. Kirkpatrick and D. Thirumalai, Phys. Rev. **B36** (1987) 5388; S. Franz, J. Hertz, Phys. Rev. Lett. **74** (1995) 2114
- [11] J.P. Bouchaud, L. Cugliandolo, J. Kurchan, M. Mézard, Physica **A226**, 243 (1996)
- [12] L. Cugliandolo, J. Kurchan, Phys. Rev. Lett. **71** (1993) 173, J. Phys. A **27** (1994) 5749
- [13] E. Vincent, J. Hammann, M. Ocio, J.P. Bouchaud, L. Cugliandolo, *Proceedings of the 1996 Sitges Conference of Glassy Systems*, cond-mat/9607224



- [14] L. Cugliandolo, J. Kurchan, L. Peliti, cond-mat/9611044
- [15] For reviews, see W. Götze, in *Liquids, freezing and glass transition*, Les Houches 1989, JP Hansen, D. Levesque, J. Zinn-Justin Editors, North Holland. See also W. Götze, L. Sjögren, Rep. Prog. Phys. **55** (1992) 241
- [16] C. Monthus, J.P. Bouchaud, J. Phys. A **29** (1996) 3847
- [17] J.P. Bouchaud, D.S. Dean, J. Physique I (France) **5**, (1995) 265
- [18] T. Odagaki, Phys. Rev. Lett. **75** (1995) 3701
- [19] This does not mean, however, that the particle reaches the lowest energy states: it is localised in regions where the energy is still very high: J. Kurchan, L. Laloux; J. Phys. A **29** (1996) 1929; A. Barrat and M. Mézard; J. Physique I (France) **5** (1995) 941
- [20] M. Mézard and G.Parisi, cond-mat 9602002, to appear in J. Phys. A

## A MODEL FOR RELAXATION IN SUPERCOOLED LIQUIDS AND POLYMER MELTS

T. PAKULA, J. TEICHMANN

Max-Planck-Institut für Polymerforschung, Postfach 3148, 55021 Mainz, Germany

### ABSTRACT

A new model for molecular rearrangements in liquids is proposed. The liquids are regarded as dense ensembles of vibrating molecules satisfying the excluded volume condition. A continuity condition is applied on the molecular scale of such systems and is regarded as controlling rearrangements leading to translations of molecules beyond the range of their vibration amplitude. It results in cooperative rearrangements which are considered as taking place in systems with fluctuating density. Rates of rearrangements are considered as being controlled by thermal activation with activation energy barriers dependent on local density. Various dependencies of the activation energy barriers on local density are examined. It is shown, that the model is able to reproduce the extremal cases of temperature dependencies of relaxation times represented on one edge by the Arrhenius relation and on the other edge by the Vogel-Fulcher-Tamman relation. The model can, however, provide a broad spectrum of other dependencies filling the gap between these extremes. All cases are based on the uniform microscopic picture of cooperative molecular rearrangements resulting from system continuity. The model is implemented as a simulation algorithm (Dynamic Lattice Liquid - DLL algorithm) which is used to simulate dynamic properties of liquids and polymer melts. Simulation results obtained for polymers are compared with experimental results obtained by means of the dynamic mechanical measurements on polyisobutylene samples with various molecular weights.

### INTRODUCTION

Due to a dense packing of molecules, the dynamic properties of liquids become complex and the relaxations extend over various, usually well distinguishable, time scales [e.g. 1-3]. On the short time scale,  $\tau_v$ , the molecules oscillate around some quasi-fixed positions being temporarily "caged" by neighbors. It is believed that more extensive translational motions of molecules take place on a much longer time scale,  $\tau_\alpha$ , due to breaking down of cages by cooperative processes. Trajectories of molecules consist, therefore, both of oscillatory components and of occasional longer range translational movements between subsequent quasi-fixed states, as illustrated in Figure 1. The macroscopic flow of the liquid is related to the longer time scale ( $\tau_\alpha$ ), in which the arrangement of molecules becomes unstable because each molecule wanders through the material changing neighbors during the translational motion steps.

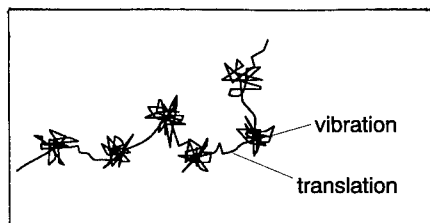


Fig. 1. Schematic illustration of a trajectory of a molecule in a liquid as composed of vibrational and translational parts.

Although the picture of motion in a liquid shown above is commonly accepted and partially documented by computer simulations of dense Lennard-Jones systems [4,5], it is not quite clear under which conditions single diffusion steps can occur. Theories of transport phenomena in liquids do not consider this problem explicitly. In theories based on the picture of Brownian motion [6-8], trajectories of molecules are smoothed out to random walk paths, which means, that time scales at which the molecular movement is observed is much larger than the characteristic time scale of elemental translation steps. Mode coupling theory [9], developed recently, considers various time scales of relaxations but there are still no precise models for the memory function which would consider microscopic details of molecular rearrangements. In phenomenological models, like the free volume model [10] or the Adam-Gibbs model [11], no microscopic picture of elemental dynamic events is postulated at all.

Cooperativity is believed to play an important role in the relaxation mechanism of molecular liquids. It still remains, however, an undefined phenomenon without any related microscopic picture. This situation leads us to reconsider the dynamic properties of liquids in terms of a simple model in which cooperativity of molecular rearrangements would be included.

Lattice liquid models have been quite successful in describing some thermodynamic properties of liquids [12]. There is, however, no dynamics included in this model, except for the vacancy diffusion mechanism. This mechanism predicts that the mobility of elements is proportional to the volume fraction of vacancies, a prediction which is not confirmed by experimental observations. The vacancy diffusion mechanism has mainly been used as a method to achieve a mobility of elements of lattice fluids in MC simulations, usually with a considerable fraction of vacancies. In only few cases [13,14], have other mechanisms of motion been considered that have some similarities to the model we will discuss in this paper.

A number of phenomenological models has been postulated for description of relaxation behavior of liquids versus temperature [9-11,15-19]. Two of them can be considered as the most prominent examples describing extremely different cases corresponding to the so called Arrhenius and non-Arrhenius behavior. In models describing the Arrhenius behavior simple thermally activated processes with constant activation barriers are considered [15] while in the second case a free space left to molecules to assume new positions is regarded as controlling the molecular mobility (free volume model) [10].

Real systems show various types of behavior covering almost the whole range between these extremes [e.g. 20]. Liquids for which temperature dependencies of relaxation times are closer to the Arrhenius case are regarded as "strong" and the other as "fragile". Thermal expansion and density fluctuations are well established experimental facts which have to be considered in any attempts to describe relaxations in liquids. On the other hand, systems kept at constant volume by adjustment of pressure and temperature show a variation of viscosity indicating a necessity of consideration of thermally activated processes [21,22]. Therefore, in this paper, a generalization of the above models is suggested by considering that molecular rearrangements in a liquid are controlled both by the distribution of volume and by thermal activation with potential barriers dependent on the local density.

## THE MODEL

The model we propose here is based on a lattice structure. Positions of molecules are regarded as coinciding with lattice sites. The lattice is, however, considered only as a coordination skeleton defining the presence of nearest neighbors but not precisely the distances between them. Under the condition of uniform and constant coordination ( $q$ ), all lattice sites are assumed to be occupied. It is assumed that the system has some excess volume so that molecules

have enough space to vibrate around their positions defined by lattice sites but can hardly move over larger distances because all neighboring lattice sites are occupied. The vibrations are assumed to take place with a mean frequency  $\nu_v = 1/\tau_v$ , related to the short time scale ( $\tau_v$ ). Each large enough displacement of a molecule from the mean position defined by the lattice is considered as an attempt to move to the neighboring lattice site. For simplicity, the attempts are assumed to take place only along the coordination lines but are independent and randomly distributed among  $q$  directions. Most of the attempts remain unsuccessful because we assume that all the time the system remains quasi continuous, which means that no holes of molecular sizes are generated and multiple occupations of lattice sites are excluded (excluded volume condition). The continuity condition of the system, for the vector field of attempted displacements  $\mathbf{r}$ , can be written as follows

$$\text{div } \mathbf{r} + \frac{d\rho}{dt} = \varepsilon \quad \text{with} \quad \varepsilon \rightarrow 0 \quad (1)$$

where:  $\rho$  is the density and should not deviate considerably from 1 if all lattice sites remain occupied,  $\varepsilon$  is introduced as a small number allowing density fluctuations but excluding generation of holes. Consequently, most of the attempted displacements have to be compensated by a return back to the initial position within the period  $\tau_v$ . Only those attempts can be successful which coincide in such a way that along a path including more than two molecules the sum of displacements is close to zero. In the system considered, only paths in a form of closed loops can satisfy this condition, as illustrated in Figure 2. The probability to find an element taking part in such coincidences will determine the probability of longer range rearrangements and the slower time scale ( $\tau_\alpha$ ).

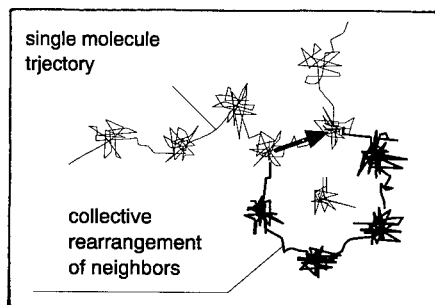


Fig. 2. An illustration of correlated displacements of some neighbors related with a translational step in a trajectory of a single molecule.

A determination of this probability reduces to counting the number of self-avoiding "n-circuits" on a given lattice, i.e. to a problem which has already been extensively considered in the literature [23]. The generally accepted result describing the probability to find the self-avoiding circuits is given by

$$p(n) = Bn^{-h}\mu^n \quad (2)$$

where  $B$  is a lattice dependent constant,  $\mu$  plays a role of an effective coordination number (called "connective constant") of the lattice and the exponent  $h$  is positive and dependent on the dimensionality  $d$  of the lattice, but is believed to be independent on detailed structure of the lattice. Related theories predict only bounds for the exponent  $h$  ( $h \geq d/2$ ). More detailed information is obtained from enumerations performed for various lattices [23].

If  $p(n)$  is known, the relaxation time related to molecular displacements can be determined as

$$\tau = \left( B \sum_{n=3}^{\infty} n^{-h+1} \mu^n \right)^{-1} \quad (3)$$

In the above consideration a full connectivity within the lattice has been assumed. The exclusion of attempted motions has, therefore, only been caused by the continuity condition in a dense system, but all attempts have been regarded as potentially effective. Such a situation can be regarded as an athermal state of the model. Generally, more details of intermolecular interactions will control the dynamics, like potential barriers for displacements, free volume, fluctuations in the coordination number and the kinetic energy of molecules, all influencing the effectivity of motion attempts. It can be considered in the model that at a finite temperature a fraction of connections within a lattice will not be available because of the above effects. This can be described by a respective modification of the connectivity constant  $\mu$ .

Our next task is, therefore, to specify in which way  $\mu$  can depend on temperature. In order to consider this the following assumptions are made:

1. A local volume  $v$  can be assigned to each molecule. This volume can fluctuate assuming values not smaller than a minimum volume  $v_0$ , which corresponds to a hard core picture of the system. The excess volume  $v_e = v - v_0$  can take part in a redistribution of volume in the system according to various rules [24]. Here, only the simplest cases of such distributions are considered as examples, firstly an exponential distribution

$$\phi(v) = \frac{1}{\bar{v} - v_0} \exp\left(-\frac{v - v_0}{\bar{v} - v_0}\right) \quad (4)$$

and secondly a Gaussian distribution

$$\phi(v) = \frac{1}{\sigma\sqrt{2\pi}} \exp\left[-\frac{(v - \bar{v})^2}{2\sigma^2}\right] \quad (5)$$

where  $\bar{v}$  is the mean volume per molecule in the system and  $\sigma$  is the standard deviation of the Gaussian distribution and is assumed here to be proportional to  $(\bar{v} - v_0)$ .

2. The system is considered to expand thermally with an expansion coefficient  $\alpha$ , so that

$$\bar{v} = v_0 [1 + \alpha \cdot (T - T_0)] \quad (6)$$

where  $T_0$  is a temperature corresponding to the closest packing of molecules.

3. Molecular transport is driven by thermal activation processes with potential energy barriers  $E(v)$  dependent on local density. A probability for a molecule to take part in a local rearrangement can then be given by

$$p(v, T) = \exp\left(-\frac{E(v)}{kT}\right) \quad (7)$$

4. Quantities characterizing the molecular transport like the diffusion constant or the relaxation time can be calculated using Eq. (3) with

$$\mu(T) = \mu_0 \langle \phi(v) \cdot p(v, T) \rangle \quad (8)$$

where  $\mu_0$  is the connectivity of the lattice in the athermal case and the averaging is performed over the whole range of local volume changes at a given temperature. It implies that local conditions leading to exclusion of connections within the lattice are noncorrelated.

The model formulated in this way would allow a determination of temperature dependencies of relaxation times if the dependence of  $E$  on  $v$  would be known. This problem requires an extra discussion.

It is interesting to notice, at first, that the two models mentioned at the beginning of this paper, i.e. the Arrhenius and the free volume models, can be defined in terms of the present model constituting particular extremal cases of the  $E$  vs.  $v$  dependence. In the case of the Arrhenius model, a volume independent activation energy is assumed, whereas, in the case of the free volume model, the assumptions made can be interpreted as a discontinuous change of the activation energy at certain  $v_c$ , from an infinite value below  $v_c$  to 0 above  $v_c$ . These two cases are illustrated in Figures 3a and 3b, respectively. They are considered as extremal cases of the present model because each of these assumptions switches off one of the two terms in the Eq. 8.

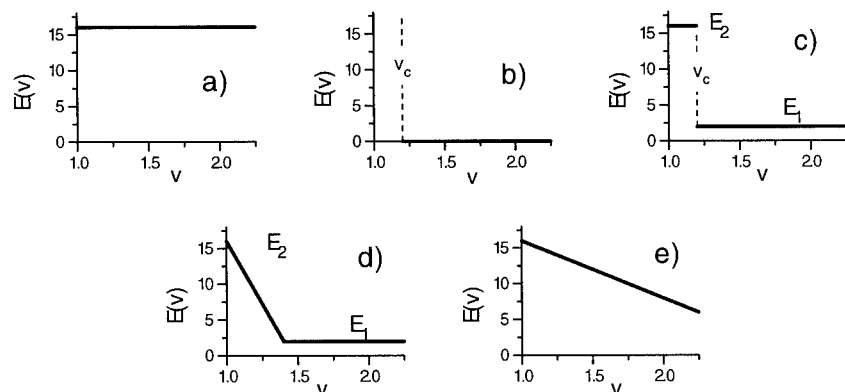


Fig. 3. Various dependencies of the activation energy for local molecular rearrangements vs. local volume: (a) corresponding to the Arrhenius model, (b) corresponding to the free volume model and (c - e) some other possible dependencies.

Generally, however, various types of interactions are distance dependent in various ways and it would be interesting to prove how some other dependencies of  $E$  vs.  $v$  would influence the temperature dependencies of the relaxation times. We consider here some examples of such dependencies which are illustrated schematically in Figures 3c - 3e. The case shown in Figure 3c is analogous to the assumption made in the free volume model with the only difference that the activation energy values below and above  $v_c$  are finite and different from 0. In the case shown in Figure 3d, the discontinuity between the energy levels  $E_1$  and  $E_2$  is replaced by a linear dependence of  $E$  vs.  $v$  in the range between  $v_0$  and  $2v_c$ . The last case, shown in Figure 3e, assumes a linear drop of the activation energy over a broad volume range.

An attempt to consider relative roles of free volume and activation energy in the relaxation of liquids has been already made earlier by Macedo and Litovitz [21]. they assumed that a molecular jump can occur when (1) the molecule attains sufficient energy to overcome attractive forces holding it to its neighbors and (2) an empty site is available into which the molecule can jump. This corresponds to the case considered here in Figure 3c with a finite  $E_1$  and infinite  $E_2$ .

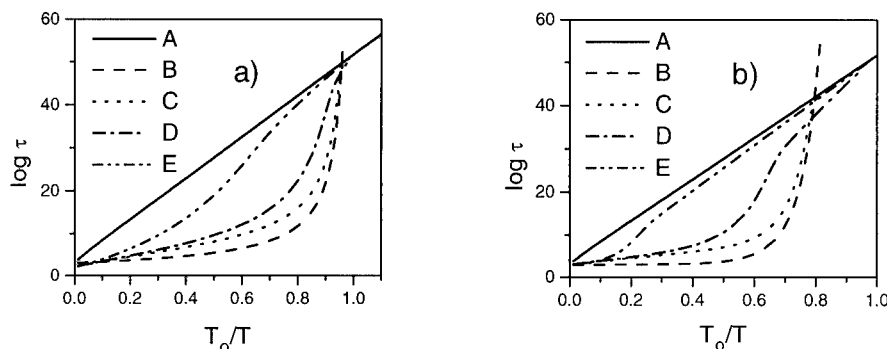


Fig. 4. Temperature dependencies of relaxation times calculated using  $E(v)$  dependencies shown in Figure 3 (lines A - E correspond to cases (a) - (e) of Fig. 3, respectively). The exponential (a) and Gaussian (b) distributions of the excess volume are considered. The following parameters have been used:  $E_1=2$ ,  $E_2=16$ ,  $v_0=1$ ,  $v_c=1.2$ ,  $\alpha=0.3$ ,  $B=0.4$ ,  $h=3.01$ ,  $\mu_0=0.847$  (the last three determined for the fcc lattice by simulation).

The results of temperature dependencies of relaxation times using relations (3) - (8) with the above considered models for  $E(v)$  and  $\phi(v)$  are shown in Figure 4 in the form of the so called Angel plot. These results indicate that within the present model a variation of behavior of the model system can be obtained which approximately corresponds to the variation of properties observed for real systems [20,25]. This can be regarded as promising that the general assumptions made in the model by considering thermally activated processes dependent on the local volume have been chosen appropriately.

Certainly, further considerations concerning the nature of local interactions are necessary in order to obtain  $E(v)$  adequate for particular real systems and for the described form of molecular rearrangements. The results presented here should be regarded only as examples illustrating the possibilities to describe a class of behaviors ranging between the Arrhenius case, on one side, and the typical non-Arrhenius case described by the traditional free volume model, on the other side.

## SIMULATION

### Simple liquids

The model described has been implemented as a dynamic Monte-Carlo algorithm. A system of beads on the fcc lattice is considered. The beads occupy all lattice sites. It is assumed that the beads vibrating with a certain frequency around the lattice sites attempt periodically to change their positions towards nearest neighboring sites. The attempts are represented by a field of unit vectors, assigned to beads and pointing in a direction of attempted motion, chosen randomly. Attempts of all beads are considered simultaneously.

An example of such an assignment of attempted directions of motion is shown in Figure 5, for a system of beads on a triangular lattice, taken here as a two dimensional illustration only. From the field of attempts represented in this way, all vectors that do not contribute to correlated sequences (circuits) satisfying the continuity condition (1) are set to 0. This concerns, for example, such situations as attempts of displacements in opposite directions (e.g. area 1 in Figure 5) or attempts of motion starting from lattice sites towards which any other bead is not trying to

move at the same time (e.g. area 2 in Figure 5). What remains after this operation, are vectors contributing to a number of closed loop traces which are considered as paths of possible rearrangements (areas 3 in Figure 5). If the system is considered as athermal, all possible rearrangements found are performed by shifting beads along closed loop traces, each bead to the neighboring lattice site.

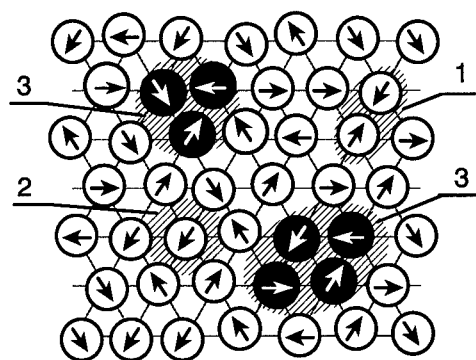


Fig. 5. An illustration of the vector field representing attempts of molecular displacements towards neighboring lattice sites in the lattice liquid model. Shaded areas represent various local situations: (1) unsuccessful attempt when neighboring elements try to move in opposite direction, (2) unsuccessful attempt because the element in the center will not be replaced by any of neighbors and (3) successful attempts in which each element replaces one of his neighbors. Elements taking part in cooperative translational rearrangements are shown as black.

The above procedure, consisting of (1) generation of motion attempts, (2) elimination of non successful attempts and (3) displacing beads within closed loop paths, is considered as a Monte-Carlo step and assumed to take place within the time scale  $\tau_v$ . The procedure is exactly repeated in subsequent time steps always with a new set of randomly chosen attempted directions.

The system treated in this way can be regarded as provided with the dynamics consisting of local vibrations and occasional diffusional steps resulting from the coincidence of attempts of neighboring elements to displace beyond the occupied positions. Within a longer time interval, this kind of dynamics leads to displacements of individual beads along random walk trajectories with steps distributed randomly in time. Details of the algorithm including considerations concerning detailed balance and ergodicity will be discussed elsewhere [27]. The algorithm is called DLL (Dynamic Lattice Liquid) algorithm.

A system of  $n_b = 4000$  beads on the fcc lattice of the size  $10^3$  have been simulated. Periodic boundary conditions in all directions have been assumed. Figure 6 shows the distribution of probabilities of loop lengths determined from the simulated systems. A fit of the simulated data (obtained under athermal conditions) by Eq. 2 is shown by the solid thick line. It indicates that the loop size distribution can be very well described by this equation. The parameters obtained ( $B=0.4 \pm 0.09$ ;  $\mu=0.847 \pm 0.006$  and  $h=3.01 \pm 0.13$ ) are characteristic for the lattice used (fcc with  $q=12$ ) and the dimensionality of the system ( $d=3$ ). The mean probability to move an element by the mechanism used has been determined as 0.0588, indicating that within the model discussed the time scales of vibrational and translational relaxations should differ at least by one order of magnitude.

In order to test a behavior of the model under the condition of limited connectivity within the lattice, simulations have been performed, in which a fraction  $(1-p)$  of all connections in the lattice has been excluded. The exclusion of lattice connections has been performed randomly and independently in each time step. It resulted in a dynamics considerably slowed down with decreasing  $p$ . Results of changes in distributions of rearrangement sizes are shown in Figure 6, in comparison with the athermal case ( $p=1$ ). Figure 6 demonstrates that the distributions of



rearrangement sizes for  $p < 1$  can be well described by the relation analogous to Eq. (2), with only modification in the connective constant  $\mu = \mu_0 \cdot p$ .

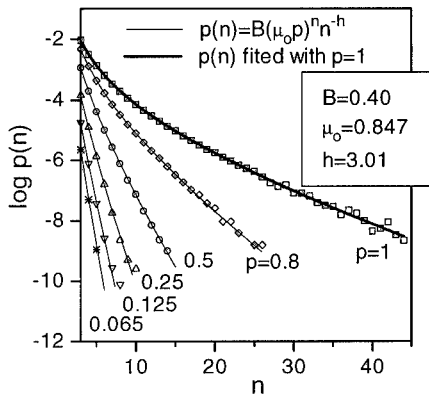


Fig. 6. Distributions of lengths of  $n$ -circuits constituting rearrangement paths in the simulated lattice liquid for the athermal case ( $p=1$ ) and for other cases with reduced lattice connectivity ( $p < 1$ ). Thick solid line represents a fit of Eq. (2) to the simulated results. Fit parameters are given in the inset. Other lines are plotted with the same  $B$  and  $h$  values in Eq. (2), but with the connectivity constant modified by corresponding  $p$  value.

Positions of beads in the simulated systems have been monitored in time. Two quantities characterizing the dynamic behavior of the system have been determined: (1) the mean squared displacement of beads

$$\langle r^2 \rangle = \frac{1}{n_b} \sum_i [r_i(t) - r_i(0)]^2 \quad (9)$$

where  $r_i(t)$  are space coordinates of beads at time  $t$ , and (2) the autocorrelation of beads to their initial position

$$\rho(t) = \frac{1}{n_b} \sum_i m_i(0) \cdot m_i(t) \quad (10)$$

where  $m_i(0)=1$  and  $m_i(t)=1$  or  $0$  depending on whether the bead  $i$  is occupying his original position (at  $t=0$ ) or not, respectively.

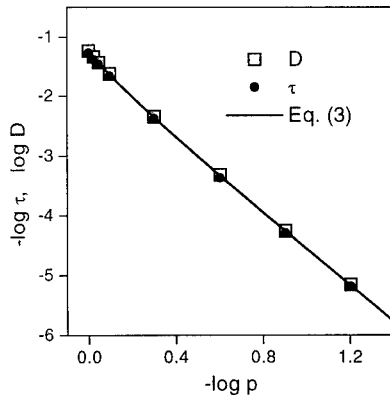


Fig. 7. Relaxation times and diffusion constants of beads in simulated lattice liquid systems in comparison with relaxation times calculated according to Eq. (3) with the connectivity constant ( $\mu$ ) reduced by the factor  $p$ .

Linear dependencies of the mean squared displacements of beads vs. time in logarithmic coordinates indicated a Fickian diffusion and have been used to determine diffusion constants. The correlation functions, showing nearly exponential decay, have been used to determine relaxation times. Values of the relaxation times and diffusion constants obtained for systems with limited lattice connectivity are shown in Figure 7. The relaxation times are very well described by the relation (3) represented in Figure 7 by the solid line. This proves that temperature dependent details of intermolecular interactions can enter the model via the term  $p$ , modifying the connective constant (Eq. 8) and consequently the dynamics of the system. Other systems in which volume distributions and thermal activation have been considered explicitly were simulated as well leading to the same conclusion. Corresponding results will be presented in detail elsewhere [27].

In order to prove whether the results are influenced by the finite size effects, other systems of sizes  $L^3$  with  $L$  in the range 8 to 16 have been simulated. No influence of the systems size on relaxation times as well as on the loop length distribution (as long as  $n < 2L$ ) has been detected. It means that the systems have been within the size range being beyond the range which can be influenced by finite sizes.

### Polymers

The algorithm described above has been applied to simulate dense polymer systems. Linear polymers have as usually been represented as chains of beads connected by non breakable bonds. A presence of bonds between beads imposes additional limits on rearrangement possibilities which can be considered as additional reduction of the connectivity constant of the lattice. This results in a strong effect of the number of bonds and consequently chain length on bead relaxation rates. In application to polymers the DLL algorithm does not require much modification. Only the condition of nonbreakability of intramolecular bonds has to be added.

Both static and dynamic properties of polymer systems with various chain lengths in the range between  $N=2$  and  $N=32$  have been analyzed [26]. It has been shown that longer chains assume conformations characteristic for gaussian chains and that their dynamics is well represented by the Rose model. These results will be described in detail in another publication. We concentrate here only on the local (segmental) dynamics in simulated systems.

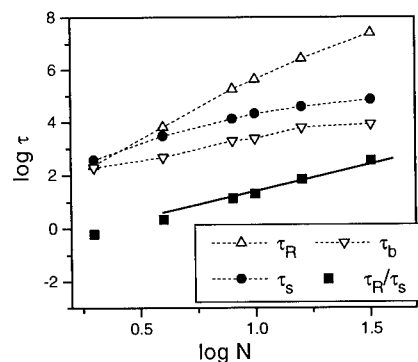


Fig. 8. Chain length dependencies of relaxation times of end-to-end vectors ( $\tau_R$ ), bonds ( $\tau_b$ ) and beads ( $\tau_s$ ). The solid line represents a slope of 2, corresponding to the Rouse-like behavior. Results are obtained for dense monodisperse systems of linear chains simulated by the DLL algorithm.

Figure 8 shows chain length dependencies of relaxation times determined from autocorrelation functions of end-to-end vectors of chains and bonds in comparison with the correlation function of bead displacements (as described by Eq. 10). It can be seen that the chain

length dependence of end-to-end vector relaxation time is much stronger, especially for short chains, than the Rouse model and other simulations predict. On the other hand, when the chain relaxation times are normalized by the segmental mobility described by  $\tau_s$  they nearly satisfy the  $N^2$  dependence as expected for the Rouse chains. This suggests that  $\tau_s$  vs.  $N$  dependence represents the effect of chain length on local dynamics which in the Rouse model is included in the friction coefficient and is not considered explicitly.

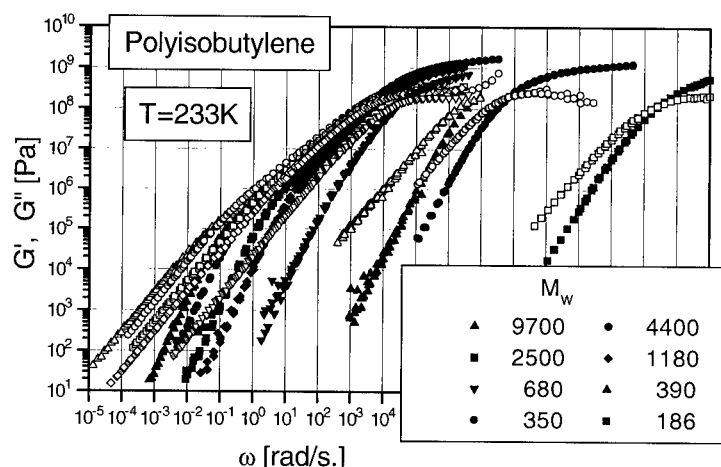


Fig. 9. Frequency dependencies of the storage  $G'$  (filled symbols) and loss  $G''$  (hollow symbols) shear modulus for monodisperse polyisobutylene melts with linear chains of various molecular weight ( $M_w$ ).

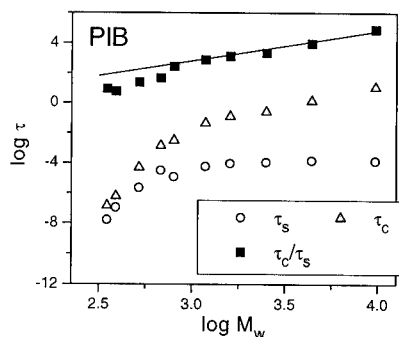


Fig. 10. Segmental ( $\tau_s$ ) and chain ( $\tau_c$ ) relaxation times and their ratio vs. molecular weight of polyisobutylene melts. The solid line represents a slope of 2.

In order to test whether the effects observed in model systems are also seen in real polymer melts, dynamic mechanical measurements have been performed on polyisobutylene samples with chain lengths in a range comparable with that of the simulated systems. Results of the measurements are shown in Figure 9 in the form of master curves of  $G'$  and  $G''$  (real and imaginary parts of the complex shear modulus) reduced to a common reference temperature.

From these dependencies segmental and chain relaxation times have been determined (procedures used will be described elsewhere [27]). Figure 10 shows molecular weight

dependencies of both these relaxation times. The results indicate that also in real systems strong chain length dependence of the dynamics can be observed, especially for short chains. Moreover, as the figure illustrates, the chain relaxation times when normalized by the segmental relaxation times show nearly the  $N^2$  dependence. This is, at least qualitatively, in a very good agreement with the dynamic behavior of simulated melts with short linear chains.

The simulation results used for the above comparison have been obtained for systems at athermal states. It means that the effects of the influence of chain lengths on rates of segmental relaxation are obtained without any additional assumptions, like for example, additional free volume effects at chain ends [28]. In the model described they are only caused by a reduction of the connectivity constant within the lattice involved by introduction of nonbreakable bonds between lattice elements. Nevertheless, the range of changes of segmental relaxation times with the chain length is comparable with the corresponding range of changes observed in experiments.

In application to polymers the DLL algorithm has many similarities with the cooperative motion algorithm (CMA) used previously [14]. There is, however, an important difference, between them consisting in a parallel treatment of all system elements in the case of DLL in contrast to the sequential treatment in CMA. This difference results in differences in distributions of rearrangement sizes and consequently in some specific effects related to the local dynamics as illustrated by the above described example.

## CONCLUSIONS

The simple lattice model described can be regarded as an alternative to the vacancy diffusion mechanism in liquids. The model considers the cooperativity of molecular rearrangements related to their translational motions. The cooperativity in this model is precisely defined as resulting from the continuity condition of the mass transport, applied here on the microscopic scale. The cooperative rearrangements are additionally considered as controlled by thermal activation over potential barriers dependent on local packing density of system elements. Consideration of various models of these dependencies opens a possibility of description of a class of behaviors ranging between "strong" and "fragile" liquids. The model requires further developments based on an analysis of local interactions characteristic to particular systems which can lead to a formulation of more realistic models describing potential barriers for local rearrangements as a function of local packing of molecules.

Based on this model, a simulation algorithm is proposed and successfully tested both for simple liquids and for polymers. In the later case, a good representation of the influence of chain length on local dynamics is obtained as an exceptional property of the proposed simulation method.

## ACKNOWLEDGMENTS

The authors gratefully acknowledge E. W. Fischer, F. J. Stickel and J. Reiter for numerous stimulating discussions.

## REFERENCES

1. S. Brower, Relaxation in Viscous Liquids and Glasses, The Am. Ceramic Soc., Columbus, OH, 1985
2. W. Götze in Liquids, Freezing and Glass Transition, eds. J. P. Hansen, D. Levesque and J. Zinn-Justin, North-Holland, Amsterdam 1991

3. E. Donth, Relaxation and Thermodynamics in Polymers, Akademie Verlag, Berlin 1992
4. J. A. Barker and D. Henderson, Rev. Mod. Phys. 48,587(1976)
5. B.J. Alder and T.E. Wainwright, J. Chem. Phys. 31,459(1969)
6. A. Widom, Phys. Rev. A 3,1394(1971)
7. R. Kubo, Rept. Progr. Phys. 29, 255(1966)
8. R. E. London, J. Chem. Phys. 66,471(1977)
9. W. Götze and L. Sjögren, Rep. Prog. Phys. 55,241(1992)
10. M.H. Cohen and G.S. Grest, Phys. Rev. B, 20,1077(1979)
11. G. Adam and J.H. Gibbs, J. Chem. Phys. 43,139(1965)
12. P. J. Flory, "Principles of Polymer Chemistry", Cornell Univ. Press, Ithaca 1953
13. S.F. Edwards and T. Vilgis, in Physics of Disordered Materials, Eds.: D. Adler, H. Frizsche and S.R. Ovshinsky, Plenum, London 1985
14. T. Pakula, Macromolecules 20,679(1987)
15. S. Glasstone, K.J. Laidler and H. Eyring, The Theory of Rate Processes, McGraw-Hill, New York, 1941
16. H. Vogel, Phys. Z. 22.645(1921); G.S. Fulcher, J.Am.Ceram.Soc. 8,339(1953)
17. M.L. Williams, R.F. Landel and J.D. Ferry, J.Am.Ceram.Soc. 8.339(1953)
18. H. Bässler, Phys.Rev.Lett. 58,767(1987)
19. J. Souletie and D. Bertrand, J.Phys.France 51.1627(1991)
20. C.A. Angel, C. Alba, A. Arzimanoglou, R. Böhmer, J. Fau, Q. Lu, E. Sanchez, H. Senapati and M. Tatsumisaga, in Slow Dynamics in Condensed Matter, ed. K. Kawasaki, M. Tokuyama and T. Kawakatsu, AIP New York 1992
21. P.B. Macedo and T.A. Litovitz, J. Chem. Phys. 42,245(1965)
22. J. Koppelman, in Proceedings of the International Congress on Rheology, 4th, ed. E.H. Lee and A.L. Copley, Wiley, New York 1965.
23. B.D. Hughes, Random Walks and Random Environments, Clarendon Press, Oxford, 1995
24. T.S. Chow, Macromol. Theory Simul. 4,397(1995)
25. F. Stickel, E.W. Fischer and R. Richert, J. Chem. Phys. 102,6251(1995)
26. J. Teichmann, PhD Thesis, Universität Mainz, 1996
27. T. Pakula and J. Teichmann - in preparation
28. T.G. Fox and P.J. Flory, J. Appl. Phys. 21,581(1980)

## TEMPERATURE DEPENDENCE OF SPATIAL AND DYNAMIC HETEROGENEITIES ABOVE THE ISING SPIN GLASS TRANSITION

S.C. GLOTZER\*, P.H. POOLE\*\*, A. CONIGLIO†, N. JAN‡

\* Center for Theoretical and Computational Materials Science, NIST, Gaithersburg, MD, 20899

\*\* Dept. of Applied Mathematics, University of Western Ontario, London, Ontario N6A 5B7, Canada

† Dipartimento di Scienze Fisiche, Univ. di Napoli, Mostra D'Oltremare, Pad. 19, Napoli, Italia, 80125

‡ Department of Physics, St. Francis Xavier University, Antigonish, Nova Scotia B2G 2W5, Canada

### ABSTRACT

The temperature dependence of the microstructure and local dynamics in the paramagnetic phase of the  $d = 2$  and  $d = 3 \pm J$  Ising spin glass model is examined by comparing the equilibrium distributions of local flip-rates and local energies calculated in large-scale Monte Carlo simulations. The emergence in this model of fast processes as the glass transition is approached corresponds with recent experimental results.

### INTRODUCTION

An open question in the quest to understand the glass transition [1] and the relationship between microstructure, local dynamics, and global relaxation in glass-forming materials, is that of the homogeneity of the material as it is cooled. A number of recent experiments on supercooled liquids and polymers have detected dynamic spatial heterogeneities above the glass transition [2], fueling arguments put forth by numerous groups on the presence of clusters, cooperatively rearranging domains, or coexisting fluids, in such systems [3]. It has been known for some time that the global relaxation in equilibrium glass-forming materials above their glass transition temperature is poorly described by a simple exponential, and better described by a stretched exponential at long times. However, it is still not generally known whether individual subdomains relax homogeneously, that is, with each region associated with the same relaxation time and the same stretching exponent, or heterogeneously, that is, with each region having a different relaxation time and/or a different stretching exponent. In systems where the frustration is self-induced, i.e. emerges upon cooling due to packing constraints between the molecules, the relationship between local structure and local dynamics even in computer simulations is difficult to assess due to the time-dependent nature of the local energies and relaxation times.

Recently, we have described a detailed computer simulation study of the high temperature, equilibrium phase of a glass-forming system with *quenched* disorder — the  $\pm J$  Ising spin glass — in both two and three dimensions [4, 5]. This model affords us the opportunity to characterize the temperature dependence of spatial heterogeneities that we know *a priori* exist in the system due to the quenched disorder. Heterogeneities in such quantities as the local site energy, local flip-rates, local relaxation times, local fields, etc. — which are absent in the pure Ising ferromagnet — give rise to complex behavior in the spin glass. For example, we recently reported the emergence of a subset of high-frequency, high-energy excitations that *increase* in magnitude as temperature  $T$  *decreases* toward the spin glass transition temperature  $T_{sg}$ . This phenomenon is a direct consequence of the frustration, and is similar to results of recent measurements of the magnetic susceptibility of an insulating spin glass in which the approach to the glass transition on cooling could be detected from the behavior of the *fastest* dynamics in the system [6].

In this proceedings, we focus on the role of frustration and disorder in producing the wide spectra of energies and dynamics in the high  $T$ , paramagnetic phase of the Ising spin glass, and discuss the temperature dependence of the correlation between these two distributions as the spin glass transition is approached from high temperature.

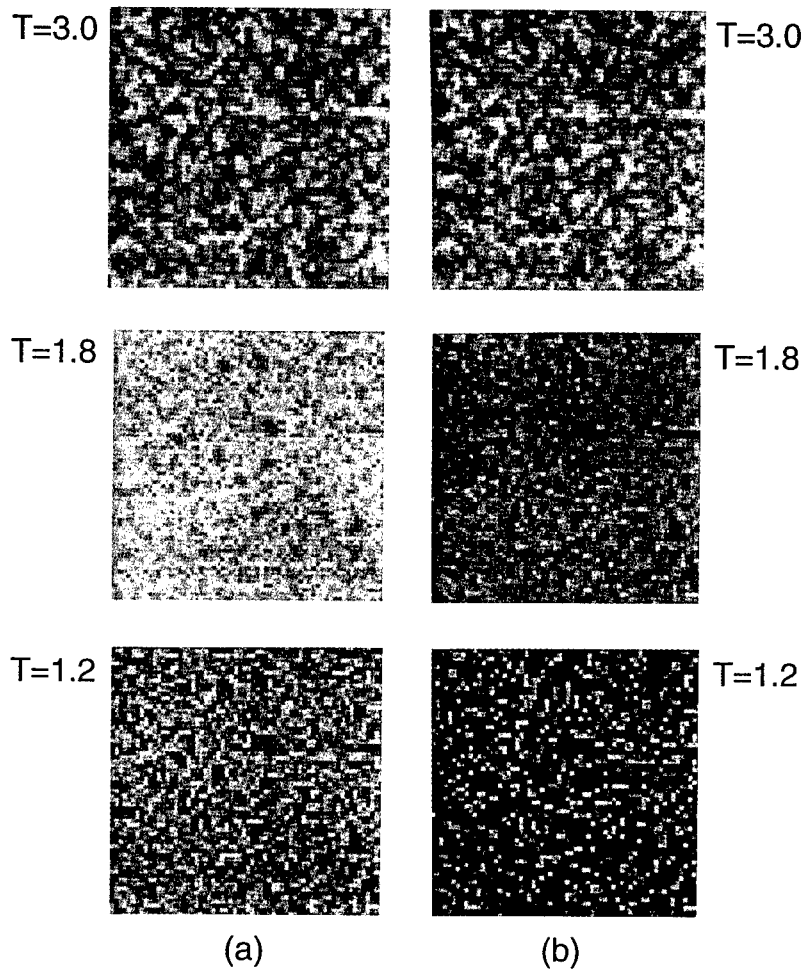


Figure 1: Equilibrium spatial distributions of the (a) local site energy  $\epsilon_i$  and (b) local flip-rate  $\nu_i$  in  $d = 2$ . High values of  $\epsilon_i$  and  $\nu_i$  are shown in white, low values in black. The lowest and highest values of  $\epsilon_i$  possible for  $T$  ranging between zero and infinity are  $-4.0$  and  $0.0$ , respectively. The lowest and highest values of  $\nu_i$  possible are  $0.0$  and  $0.5$ , respectively.

## METHOD

The Ising spin glass model is described by the Hamiltonian  $H = -\sum_{\langle ij \rangle} \sigma_i J_{ij} \sigma_j$ . Square (dimension  $d = 2$ ) and simple cubic ( $d = 3$ ) lattices of size  $64^2$  and  $16^3$  were prepared by randomly assigning exchange interactions  $J_{ij} = \pm J$  to the edges of the lattice, and placing on the vertices (sites) Ising spins  $\sigma$  with values  $\sigma = \pm 1$ . The transition temperature  $kT_{sg}/J = 0$  and  $1.1$  in  $d=2$  and  $d=3$ , respectively [7], where  $k$  is Boltzmann's constant. Monte Carlo computer simulations were performed in zero magnetic field using heat bath dynamics with periodic boundary conditions. Depending on  $T$ , between  $3 \times 10^5$  and  $2 \times 10^7$  Monte Carlo Steps (MCS) were used to equilibrate the system. Simulations were performed for temperatures ranging from  $kT/J = 1.2$  to  $3.0$  in  $d = 2$ , and from  $kT/J = 1.6$  to  $6.0$  in  $d = 3$ . Individual on-site magnetizations and spin autocorrelation functions were carefully monitored to ensure equilibration before commencing the evaluation of the quantities presented below. Time averages for all quantities were evaluated for up to  $2 \times 10^7$  MCS following equilibration. Simulations with different random bond configurations for the quenched disorder confirm that all distributions are converged to their asymptotic, equilibrium form; that is, our conclusions are independent of the particular choice of random  $\{J_{ij}\}$ .

## RESULTS

The spatial arrangement of local energies and local flip-rates in the  $d = 2$  Ising spin glass at selected temperatures is shown in Figure 1. At each site  $i$ , the instantaneous energy  $E_i = -\sum_j \sigma_i J_{ij} \sigma_j$ , where  $j$  labels the nearest neighbors (nn's) of  $i$ . Quenched disorder induces the time average of  $E_i$  in equilibrium,  $\epsilon_i$ , to vary from site to site as shown in Fig. 1a. That is, the local site energy is spatially heterogeneous [8]. The length scale of the heterogeneity is presumably set by the intrinsic length scale of the random quenched disorder, which is present at all  $T$ . The effect of the quenched disorder on the behavior of the system, however, changes strongly with  $T$ . For example, we see from Fig. 1a that in most instances spins which have low energy at high  $T$  continue to decrease their energy with decreasing  $T$ , while spins which have high energy at high  $T$  may also have high energy at lower  $T$ . As shown elsewhere [4, 5], these highest energy spins actually first decrease, and then increase in energy with decreasing  $T$ .

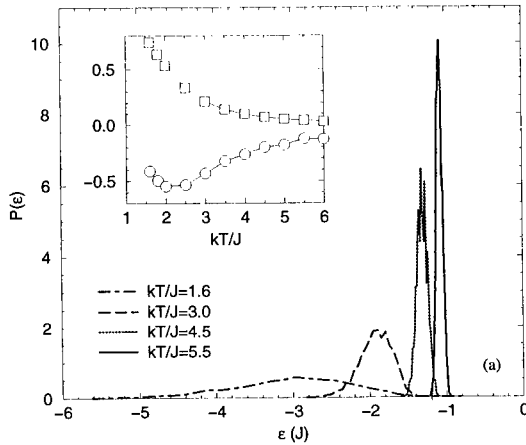


Figure 2:  $P(\epsilon)$  versus  $\epsilon$  for various  $T$  in  $d = 3$ . INSET: Skewness  $\gamma$  and standard deviation  $\sigma$  of the distribution versus  $T$ .



Next we define the local flip-rate  $\nu_i$  to be the number of flips observed for spin  $i$ , divided by the total observation time in equilibrium.  $\nu_i$  is therefore the equilibrium probability, per MCS, for spin  $i$  to flip. Like  $\epsilon_i$ ,  $\nu_i$  is also spatially heterogeneous (Fig. 1b) [8]. Again the effect of the quenched disorder on the behavior of the system changes strongly with  $T$ . For example, we see from Fig. 1b that in most instances spins which have low flip-rate at high  $T$  continue to decrease their flip-rate with decreasing  $T$ , while spins which have high flip-rate at high  $T$  may also have high flip-rate at lower  $T$ . As shown elsewhere [4, 5], these highest flip-rate spins actually first decrease, and then increase, their flip-rate with decreasing  $T$ .

We calculated both the normalized probability density  $P(\epsilon)$  for a given site to have an average energy  $\epsilon$ , as well as the probability density  $P(\nu)$  for a given site to have an average flip rate  $\nu$ , for several  $T > T_{sg}$ . As reported elsewhere [4] and shown for  $d = 3$  in Figs. 2 and 3, we observe that the shape of these distributions changes substantially even for  $T$  well above  $T_{sg}$ , becoming increasingly broad, and in particular developing long tails with decreasing  $T$ . As shown in the insets of Figs. 2 and 3, both the standard deviation  $\sigma$  and skewness  $\gamma$  characterizing the distributions are increasing as  $T \rightarrow T_{sg}$  [9].

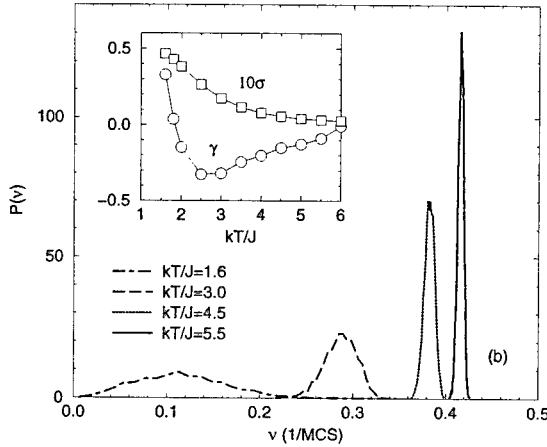


Figure 3:  $P(\nu)$  versus  $\nu$  for various  $T$  in  $d = 3$ . INSET: Skewness  $\gamma$  and standard deviation  $\sigma$  of the distribution versus  $T$ .

To examine the correlation between  $\nu$  and  $\epsilon$ , in Fig. 4 we plot the value of  $\nu$  against  $\epsilon$  for each site in the system, for various  $T$  in  $d = 2$  and  $d = 3$  [10]. As expected from the distributions in Figs. 2 and 3, Fig. 4 shows an increasing spread in the range of both  $\nu$  and  $\epsilon$  as  $T$  decreases. Also, we find that at high  $T$ , a given value of  $\nu$  correlates well to a specific value  $\epsilon$ . As  $T$  decreases, the lowest and highest values of  $\nu$  and  $\epsilon$  remain strongly correlated. However, at intermediate values of  $\epsilon$ , a given  $\epsilon$  corresponds to a broad spectrum of  $\nu$  values, which widens further with decreasing  $T$ . This last effect occurs because the correlation length is increasing as  $T$  decreases toward  $T_{sg}$ , causing local relaxation rates to be influenced by interactions beyond the nn interactions quantified by  $\epsilon$ .

Despite the fact that the global relaxation of the system is becoming increasingly slow [7], we see in Fig. 4 the surprising emergence of spins whose flip-rate and energy are higher than that observed at higher  $T$  for the range of  $T$  simulated. In fact, we showed elsewhere [4, 5] that both the energy and flip-rates of those spins actually first decrease, and then increase, with decreasing  $T$ .

The approach to the glass transition in this system upon cooling can thus be detected by observing the

behavior of the *fastest* dynamics. In a recent experiment by Bitko, et al. [6], the magnetic susceptibility was measured over 8 decades of frequency for an insulating Ising spin glass  $\text{LiHo}_{0.167}\text{Y}_{0.833}\text{F}_4$ . The results showed that the approach to  $T_{\text{sg}}$  upon cooling could be detected from the high frequency behavior alone, similar to that observed here and in several other recent experimental studies [11]-[13].

We see that the complex dynamics that emerge upon cooling in this system [7] is intimately coupled to the local energetic environment, or microstructure. For example, consider the following extreme case: an individual site will have a high flip-rate at low  $T$  if (i) its sites each have a very low flip-rate (which will occur if the time-averaged energy of each of those sites is low), and (ii) half of the interactions with the nn sites are satisfied and half are unsatisfied. On the other hand, a site with an intermediate energy at low  $T$  may have one of many different flip-rates, depending on the environment around the spin beyond the nn's but within the correlation length at that  $T$ . Thus as the system cools, it appears to "partition" the local energies in such a way as to "focus" the frustration on a subset of sites in the system, raising the energy and flip-rate of those sites. This "focusing" allows other spins to locally order and thus lower their energy as much as environmentally allowed, while keeping the system globally in equilibrium.

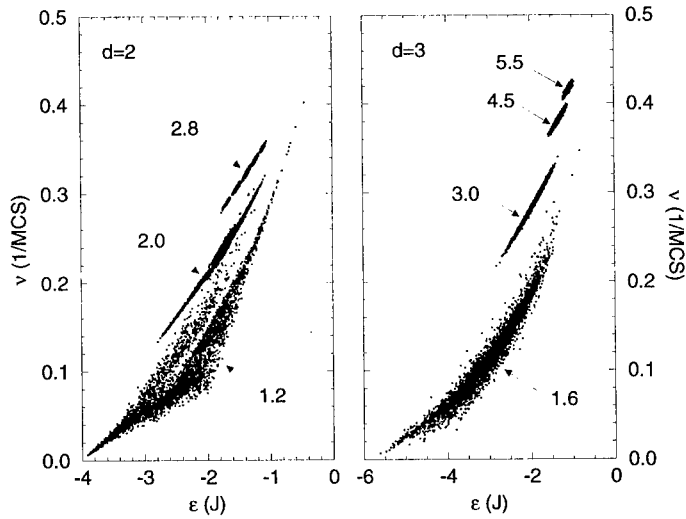


Figure 4: Scatter plot of local fliprate  $\nu$  versus local energy  $\epsilon$  for all sites at various  $kT/J$  (a) in  $d = 2$ , and (b) in  $d = 3$ .

## CONCLUSIONS

In summary, the much-studied "fruitfly" glass-forming spin model of statistical mechanics — the nn Ising spin glass — has much to teach us about the effects of frustration and disorder on equilibrium thermodynamic and dynamic properties as a glass transition is approached. The fact that in this model the disorder is quenched to the lattice — and not annealed, or self-induced as in liquids — provides us with a unique opportunity to measure and characterize the frustration and disorder-induced heterogeneities in such quantities as the local energies and local flip-rates, in a system where we know *a priori* that heterogeneities exist. It is our hope that such a study will provide a useful approach and

benchmark by which to investigate frustration-induced heterogeneities in a wider class of glass-forming materials.

### Acknowledgements

SCG and PHP gratefully acknowledge valuable discussions with C.A. Angell. PHP and NJ are sponsored by NSERC of Canada.

### References

- [1] M.D. Ediger, C.A. Angell and S.R. Nagel, J. Phys. Chem. **100**, 13200 (1996); see also the reviews on glasses in Science **267** (1995), and Proceedings of Workshop on Glasses and the Glass Transition, J. Comp. Mat. Sci **4**, 283-388 (1995).
- [2] M.T. Cicerone and M.D. Ediger, J. Chem. Phys. **104** 7210 (1996); M. Cicerone, F.R. Blackburn, and M.D. Ediger, J. Chem. Phys. **102**, 471 (1995); M.T. Cicerone and M.D. Ediger, J. Chem. Phys. **103**, 5684 (1995). F. R. Blackburn, et al., J. Non-Cryst. Solids **172-174**, 256 (1994); M. Cicerone, F.R. Blackburn, and M.D. Ediger, Macromolecules **28**, 8224 (1995). K. Schmidt-Rohr and H. W. Spiess, Phys. Rev. Lett. **66**, 3020 (1991); H. Heuer, et al., Phys. Rev. Lett. **75**, 2851 (1995).
- [3] See, e.g., G. Adam and J. H. Gibbs, J. Chem. Phys. **43**, 139 (1965); M. Goldstein, J. Chem. Phys. **51**, 3328 (1969); F.H. Stillinger and J.A. Hodgdon, Phys. Rev. E **50**, 2064 (1994) and references therein; D. Kivelson et al., Physica A **219**, 27 (1995); S.C. Glotzer and A. Coniglio, Comp. Mat. Sci. **4**, 325 (1995); J.F. Douglas and J. B. Hubbard, Comp. Mat. Sci **4**, 300 (1995).
- [4] P.H. Poole, S.C. Glotzer, A. Coniglio and N. Jan (preprint).
- [5] S.C. Glotzer, P.H. Poole, A. Coniglio and N. Jan, Proceedings of YKIS '96, submitted.
- [6] D. Bitko, et al, Europhys. Lett. **33**, 489 (1996); D. Bitko, et al, J. NIST Research, *APS Proceedings from Symposium on 40 Years of Entropy Theory and the Glass Transition*, in press.
- [7] The first large-scale simulations focusing on the dynamics of the Ising spin glass model were reported in A.T. Ogielski and I. Morgenstern, Phys. Rev. Lett **54**, 928 (1985); A.T. Ogielski and D.L. Stein, Phys. Rev. Lett. **55**, 1634 (1985); A.T. Ogielski, Phys. Rev. B **32**, 7384 (1985); A.T. Ogielski and D. A. Huse, Phys. Rev. Lett. **56**, 1298 (1986); A.T. Ogielski, Phys. Rev. Lett. **57**, 1251 (1986). See also K. Binder and A. P. Young, Rev. Mod. Phys. **58**, 801 (1986), and H. Reger, Ann. Rev. Comp. Phys. **II**, 295 (World Scientific, Singapore, 1995) for reviews.
- [8] For comparison, note that for a ferromagnetic Ising model  $\epsilon_i$  would approach the same value for all sites. The same is true for  $\nu_i$ .
- [9] If  $P(x)$  describes the distribution of a set of  $N$  values  $\{x_i\}$ , then the standard deviation  $\sigma$  of  $P(x)$  is given by  $\sigma^2 = [1/(N-1)] \sum_{i=1}^N (x_i - \langle x \rangle)^2$  where  $\langle x \rangle$  is the average value of  $x$ . The skewness  $\gamma$  of  $P(x)$  is given by  $\gamma = (1/N) \sum_{i=1}^N [(x_i - \langle x \rangle)/\sigma]^3$ .
- [10] A similar plot for the ferromagnetic Ising model would display a single point for each temperature.
- [11] S. Nagel, et al., Advances in Chem. Phys., in press; P. Dixon, et al, Phys. Rev. Lett. **65**, 1108 (1990); R.D. Deegan and S.R. Nagel, Phys. Rev. B **52**, 5653 (1995) and refs. therein.
- [12] P. Lunkenheimer, et al., Phys. Rev. Lett. **77**, 318 (1996); Proceedings of YKIS '96, in press, and these proceedings.
- [13] A. Sokolov, et al., these proceedings, and references therein.

## GLASSY AND CRYSTALLINE STATES IN A MODEL WITHOUT DISORDER: SPIN ANALOG OF A STRUCTURAL GLASS

LEI GU, BULBUL CHAKRABORTY

Department of Physics, Brandeis University, Waltham, MA 02254, USA,  
bulbul@snow.cc.brandeis.edu

### ABSTRACT

We have analyzed a non-randomly frustrated spin model which exhibits behavior remarkably similar to the phenomenology of structural glasses. The high-temperature disordered phase undergoes a strong first-order transition to a long-range ordered structure. Using Monte Carlo simulations, we have studied the behavior of the supercooled state by quenching to temperatures below this transition temperature. For a range of supercooling, the system remains ergodic and exhibits dynamics characteristic of supercooled liquids. Below a certain characteristic temperature, however, the system freezes into a "glassy" phase. In this phase, the system is non-ergodic and evolves through a distribution of traps characterized by a power-law distribution of trapping times. This change in the dynamic behavior is concurrent with the appearance of a shear instability.

### INTRODUCTION

Understanding of glassy dynamics and the glass transition remains as one of the significant challenges in condensed matter physics. Recent experiments on glasses [1,2] have led to some interesting observations regarding the glass transition in structural glasses and indicated some similarities between spin glasses and structural glasses [2]. On the theoretical side, a lot of interest has been focused on spin models without quenched-in disorder which exhibit glassy dynamics [3]. The glassy dynamics in these models, in some instances, have been related to the behavior of equivalent spin-glass like models [3]. Frustration is a key concept in theories of structural glasses such as the curved-space pictures of metallic glass [4]. The two concepts taken together, glassy dynamics in non-random spin systems and frustration as a key to glassy behavior, suggest that frustrated spin systems could play a role in our quest for an understanding of the nature of structural glasses [5]. The model discussed in this paper belongs to this category.

It has been shown [6,7] that the frustration of a triangular-lattice Ising antiferromagnet can be removed by elastic distortions. In the deformable lattice, the antiferromagnetic couplings between nearest-neighbor spins depend on their separation. In the simplest model, considered here, only uniform distortions of the lattice are allowed and these are characterized by the relative changes  $\epsilon_1$ ,  $\epsilon_2$  and  $\epsilon_3$  of the three nearest-neighbor bonds lengths. In equilibrium, there is a strong first-order transition from the paramagnetic phase to a "striped" structure. The striped phase has alternating rows of up and down spins and a frozen-in shear distortion with one set of bonds (between parallel spins) expanded and the other two (between antiparallel spins) contracted. Monte Carlo simulations have been used to demonstrate that this picture remains virtually unchanged when fluctuations in bond-lengths are allowed [7].

A strong first-order transition accompanied by a shear distortion is reminiscent of the density functional theory of freezing, where volume change plays a similar role, and it seems natural to ask how the supercooled spin system behaves. Upon quenching the system from the

disordered phase to the ordered regime, a phenomenology remarkably similar to structural glasses was observed. Monte Carlo simulations were used to study the dynamics following instantaneous quenches from a high-temperature disordered phase to a range of temperatures below the ordering transition (which was strongly first-order). The dynamics employed was standard spin-exchange dynamics extended to include moves which attempt global changes of the shape and size of the box [7]. These global changes were attempted after a complete sweep of all the spins in the lattice. Three system sizes, 32x32, 48x48 and 64x64 were used to investigate the finite size dependence of physical quantities.

## DISCUSSION AND RESULTS

These simulations lead to an intriguing picture of the supercooled state which could shed some light on the nature of the structural glass transition. Above a certain characteristic temperature,  $T^*$ , the relaxation of the supercooled state can be described reasonably well by a stretched exponential behavior although there are some deviations. The time scale for nucleation of the striped phase is extremely long and the system behaves as if it is in equilibrium in the metastable disordered phase. There is a volume change of the lattice but the shear distortion fluctuates around zero, as seen in Fig 1. Fig. 1 also shows the time evolution of the energy per spin. For  $T > T^*$ , the plateaus in these plots indicate the existence of shallow traps which are sampled by the system as it explores the configurations available to it within the large trap or valley that is the disordered phase with zero shear distortion. Below  $T^*$ , the behavior of the system becomes non-ergodic. Time-translational invariance is lost and there is continuous evolution or “aging” of the system. The plots in Fig 1 show aging of the shear distortion and the energy per spin. The system is no longer trapped within the large valley characterizing the disordered phase. There is a clear evolution towards lower energy states but this evolution is interrupted by trapping into states with varying well depths. The evidence from simulation points towards a power-law distribution of the trapping times in these wells. If the power law is weak enough, this distribution could lead to aging since the system can always find a trap with a trapping time comparable to the observation time [8].

The onset of aging in this model is concurrent with the disappearance of the well characterized by zero shear, or equivalently, with the appearance of a shear instability. It is known that this model has a shear instability at low enough temperatures [6]. This instability is normally not seen because the first-order transition intervenes at a higher temperature. What is a true instability in this mean-field model could become a narrowly avoided critical point [5] when fluctuations of the bond lengths are included. This would, however, not lead to any drastic changes in the scenario. In the mean-field model considered here, the supercooled state loses its stability at  $T^*$ . This, by itself, would have been uninteresting since it would have simply implied that the nucleated path to the striped phase would be replaced by a continuous ordering path. What makes the dynamics non-trivial in this model is the existence of intermediate states which cannot be avoided and are traversed only by barrier-hopping. Therefore, the instability of the supercooled phase leads to the appearance of a glassy phase rather than the striped phase.

One of the characteristics of glass is the lack of ergodicity. A measure of broken ergodicity can be obtained from examining the fluctuation metric [9]. This quantity,  $\Omega(t)$ , measures the integral of the auto-correlation function of the fluctuating quantity and is expected to decay as  $1/t$  for ergodic systems where the autocorrelation function decays to zero. Fig 2 shows

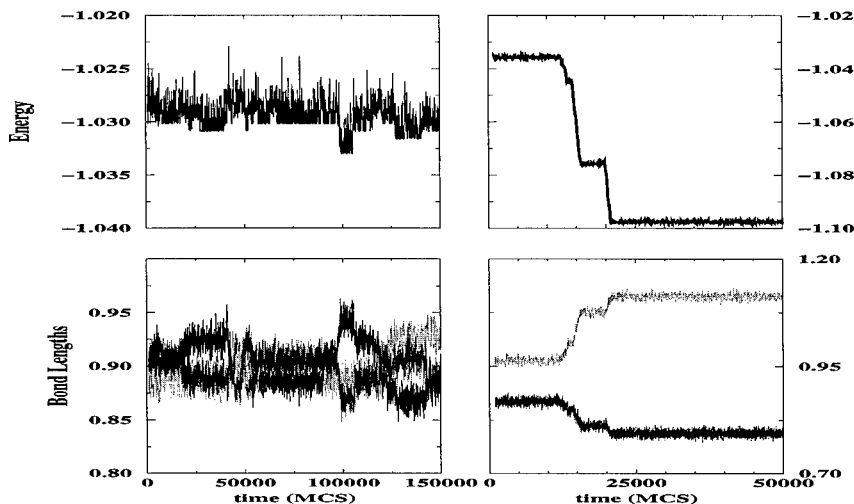


Figure 1: Typical Monte Carlo trajectories showing the energy per spin and the three bond lengths ( $1 + e_\alpha$ ) vs. time. The left-hand panel shows data for a temperature  $T > T^*$  and the right hand panel shows data for  $T < T^*$ . A shear distortion is indicated by  $e_1 > 0$  and  $e_2, e_3 < 0$  in the right-hand panel for  $T < T^*$ . In the left-hand panel, the bond lengths are fluctuating about a common value, and there is no shear distortion. The energy of the completely ordered striped phase is  $-1.27$ .

the inverse of the fluctuation metric for four different quench histories at temperatures above and below  $T^*$ . Above  $T^*$  the system is clearly ergodic and there is no dependence on quench history. This is far from true for temperatures below  $T^*$ . The dependence on quench history shows that the evolution of the system takes place in a rugged landscape. This statement could be made more accurate by analyzing the probability distribution of energy,  $P(E)$  in the two different temperature regimes.

In trying to deduce a picture of the free-energy surface from the simulation data, it is useful to characterize a valley by a region of phase space in which the system spends a macroscopic amount of time, much larger than the microscopic time scale for spin exchange. These valleys can then be characterized by local averages such as the energy per spin or the shear distortion. In equilibrium, the probability of finding a system in a given valley characterized, for example, by energy  $E_\alpha$  is proportional to  $\exp(-\beta F_\alpha)$  where  $F_\alpha$  is the free energy characterizing that state. Since the system is observed to reach quasiequilibrium in the valleys, one can obtain a picture of the free energy landscape by measuring the energy histogram  $P(E)$  and examining the behavior of  $-\ln P(E)$ . These free energy surfaces for  $T > T^*$  and  $T < T^*$  are shown in Fig 3. The difference between the two justifies the picture presented earlier. At the higher temperatures, there is a large valley with a subvalley structure. The system, for large enough system sizes, never escapes this valley and for all intents and purposes, is in equilibrium. The breaking of ergodicity here is akin to that in a ferromagnet and does not lead to glassy dynamics. Simulations at higher temperatures show that the internal structure of this valley is not present at high enough temperatures. This

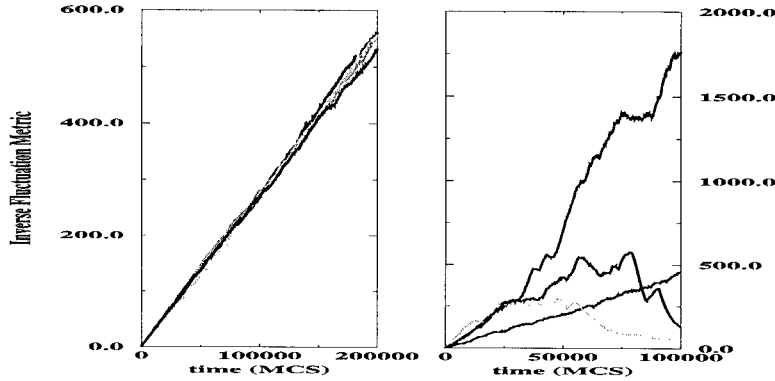


Figure 2: Plot of the inverse of the fluctuation metric for four different Monte Carlo runs. The left panel shows data for  $T > T^*$  and the right panel shows data for  $T < T^*$ .

indicates that as the temperature is lowered, the subvalleys become deeper in relation to the overall depth of the large valley. The relaxation time within this large valley should be affected by the changing internal structure and, it is possible that these structures lead to the unusual dynamics observed in supercooled liquids above the glass transition [2]. This aspect is being investigated at present. The large valley is absent from the free energy surface for  $T < T^*$ . The trend of the subvalleys becoming deeper in relation to the overall depth of the large valley has led to the disappearance of this overall structure. The system is now free to explore a larger region of phase space. However, the subvalleys, which have now acquired the role of the primary valleys, trap the system over all different time scales.

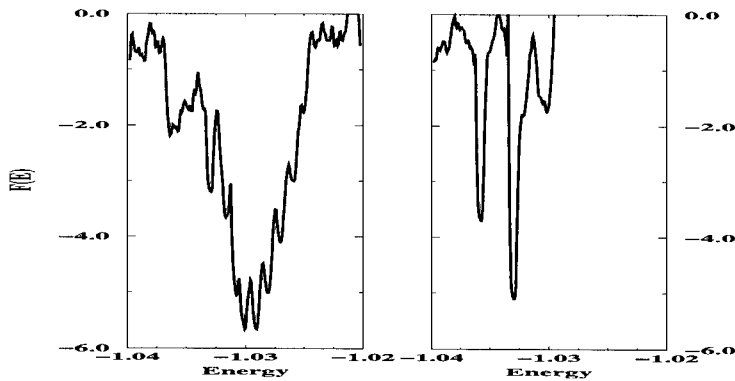


Figure 3: The topology of the free energy surface obtained from  $-\ln P(E)$ . This prescription gives us the free energy differences between different states at a given temperature. Hence, it can provide a description of the topology but not absolute magnitudes or comparison between different temperatures. The left panel is for  $T > T^*$  and the right panel for  $T < T^*$ .

A theory of aging in glasses has been proposed which is based on a broad distribution of trapping times [8]. This distribution can be obtained from the energy versus time data obtained in the simulations. A histogram of trapping times at  $T < T^*$  (Fig. 4) shows a power law distribution and is consistent with the class of power laws discussed in the theory of aging [8]. These power law distributions imply that the *average* trapping time diverges and the system cannot explore all of phase space in a finite amount of time. This phenomenon has been referred to as weak ergodicity breaking [8].

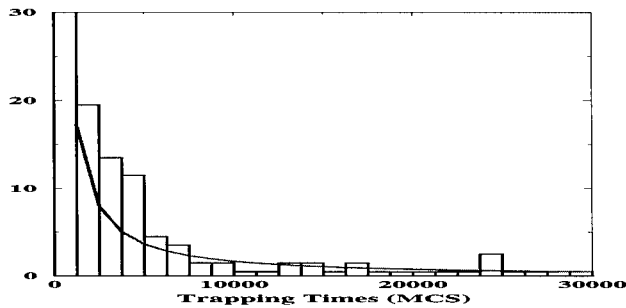


Figure 4: Histogram of trapping times,  $P(\tau)$  for  $T < T^*$ . The solid line is a fit to a power law,  $P(\tau) = (\tau)^{(-1.2)}$ . This distribution law implies a divergent average,  $\langle \tau \rangle$ .

There seems to be a correlation between the trapping times in the various wells and the shear distortion characterizing these states. The larger the shear distortion the longer is the trapping time. An examination of the morphologies of the states in these wells shows that there are regions of locally ordered striped phases in these wells. These locally ordered regions are separated by disordered regions. The disordered regions get squeezed into smaller and smaller channels as the system evolves towards lower-energy valleys. The trapping time increases as these channels get smaller. The aging process, therefore, leads to valleys with larger shear strains and smaller disordered regions. However, since this leads to the system getting trapped in these wells for longer and longer times, the aging process, in effect, never stops.

The height of the barrier, or equivalently, well depth of the large disordered valley was found to scale with the systems size. For  $T < T^*$ , it is more meaningful to talk about the distribution of well depths or trapping times. Preliminary results indicate that this distribution extends to longer times as the system size increases. What is clear, in this temperature regime, is that some barriers do not scale with system size.

## CONCLUSION

The stepwise relaxation seen in Fig 1 is akin to the observed relaxation in the multispin models [10]. As far as the equilibrium properties are concerned, the deformable lattice model considered in this paper can be mapped onto a pure spin model with pair interactions which are short-ranged and four-spin interactions which are long ranged. It is therefore not



surprising that there are similarities between these models. The basic driving force behind the complexity observed in the deformable lattice model is the frustration inherent in the triangular lattice. Coupling to the lattice removes the degeneracies and in its place introduces structure on small and large energy scales. The instability to shear owes its existence to the degeneracy of the triangular lattice groundstate [6]. The coupling between local variables which are frustrated and global variables which are capable of removing the frustration seem to be the essential ingredients of this model. It is possible that this feature is also present in real glasses and is responsible for the remarkable similarity of the phenomenology of our toy model with real systems.

#### ACKNOWLEDGEMENT

The authors would like to acknowledge useful discussions with N. Gross, Bill Klein and Royce Zia. This work has been supported in part by DE-FG02-ER45495.

#### REFERENCES

1. C. A. Angell, Proc. Nat. Acad. Sci. **92**, 6675 (1995).
2. Narayanan Menon and Sidney R. Nagel, Phys. Rev. Lett. **74**, 1230 (1995) ; D. Bitko *et al*, Europhys. Lett **33**, 489 (1996).
3. J. P. Bouchaud and M. Mezard, J. Phys. I **4**, 1109 (1994).
4. For a recent review and simulation studies, see T. Tomida and T. Egami, Phys. Rev. B **52**, 3290 (1995).
5. S. A. Kivelson *et al*, J. Chem. Phys **101**, 2391 (1994).
6. Z. Y. Chen and M. Kardar, J. Phys. C **19**, 6825 (1986).
7. Lei Gu, Bulbul Chakraborty, P. L. Garrido, Mohan Phani and J. L. Lebowitz, Phys. Rev. B **53**, 11985 (1996).
8. J. P. Bouchaud, J. Phys. I **2**, 1705 (1992).
9. D. Thirumalai and Raymond D. Mountain, Phys. Rev. B**47**, 479 (1993).
10. W. Krauth and M. Mezard, Z. Phys. B **97**, 127 (1995).

## SLOW DYNAMICS IN SUPERCOOLED WATER

FRANCESCO SCIORTINO (\*), PIERO TARTAGLIA(\*), PAOLA GALLO (\*\*),  
SOW-HSIN CHEN (\*\*)

(\*) *Dipartimento di Fisica and Istituto Nazionale per la Fisica della Materia, Università di Roma La Sapienza, P.le Aldo Moro 2, I-00185, Roma, Italy, fs@dectar.roma1.infn.it*

(\*\*) *Department of Nuclear Engineering, Massachusetts Institute of Technology, Cambridge, MA 02139*

### ABSTRACT

We review some recent results on the self-dynamics in deep supercooled (simulated) water, obtained by analyzing very long Molecular Dynamics simulations. We discuss the possibility of interpreting the observed slowing down of the dynamics in terms of Mode Coupling Theory for supercooled liquids and, at the same time, of associating the experimentally observed anomalies of the transport coefficients in water on lowering the temperature to the formation of long living cages. The so-called critical Angell temperature  $T_A$  in supercooled water could be interpreted as kinetic glass transition temperature, relaxing the need of a thermodynamic singularity for the explanation of the dynamic anomalies of liquid water. In the end we discuss the possibility that  $T_A$  acts as cross-over temperature from fragile to strong liquid behavior.

### INTRODUCTION

Supercooled water is characterized by an anomalous increase in specific heat and in compressibility on cooling[1]. This thermodynamic anomalous behavior, which originates from the presence of a line of temperatures of maximum density[2], has been associated with the presence of an experimentally inaccessible thermodynamic instability in the region of phase space where the crystal is the stable phase[3, 4]. The temperature dependence of transport coefficients in water is also anomalous. It is strongly non-Arrhenius and it is rather well represented by power-law[5] in  $|T - T_A(P)|^\gamma$ . Here  $T_A(P)$  is the so-called (pressure dependent) Angell temperature and  $\gamma$  is the corresponding exponent. The impressive power-law behavior in the transport coefficient has been one argument in favor of a thermodynamic instability, notwithstanding the observed pressure dependence of the exponent  $\gamma$ [5].

A theoretical framework to interpret the divergences of transport coefficient in supercooled water, which does not require the presence of a thermodynamic instability, would be very valuable in the discussion of the thermodynamics behavior of supercooled water. This topic, recently addressed in Refs. [6, 7, 8, 9], is the main point of this paper. We also present some new results on the relation between translational and rotational correlation functions, which strengthen the interpretation of the slow dynamics in SPC/E water in terms of Mode Coupling Theory (MCT) [11, 12, 13].

### DISCUSSION

The study we review here[7, 10] is based on the analysis of very long (up to 100 ns) molecular dynamics simulations, performed modelling the water-water interaction with a well known effective pair-additive rigid potential, the SPC/E potential[14]. Very deep supercooled states have been simulated along an isobar and results for the self-molecule motion have been carefully compared[7] with the MCT predictions [11, 12, 13]. This study has shown that the dynamics of SPC/E water

in deep supercooled states is characterized by a power-law dependence of  $D$ , i.e.  $D \sim |T - T_{ig}|^\gamma$ , where  $T_{ig}$  is the ideal glass transition temperature[12], not to be confused with the calorimetric glass transition temperature. Moreover, the self-density fluctuation follows a two-step relaxation which becomes more and more evident on lowering the temperature. Correlation functions decay first to a plateau value  $f_{EA}$  (early  $\beta$  regime), followed by a slower decay to zero (late  $\beta$  regime and  $\alpha$  relaxation). As predicted by MCT, the  $\alpha$ -relaxation is characterized by a power-law decay ( $C(t) - f_{EA} \sim -t^b$ ) followed by a stretched exponential decay. As an example, Fig.1 shows the scaled self-intermediate scattering function  $F_s(Q, t/\tau_T(Q))$  at different low temperatures, and it highlights the presence of scaling in the so-called late  $\beta$  and  $\alpha$  region. The inset shows the power-law ( $C(t) - f_{EA} \sim -t^b$ ) in the early  $\alpha$  relaxation.

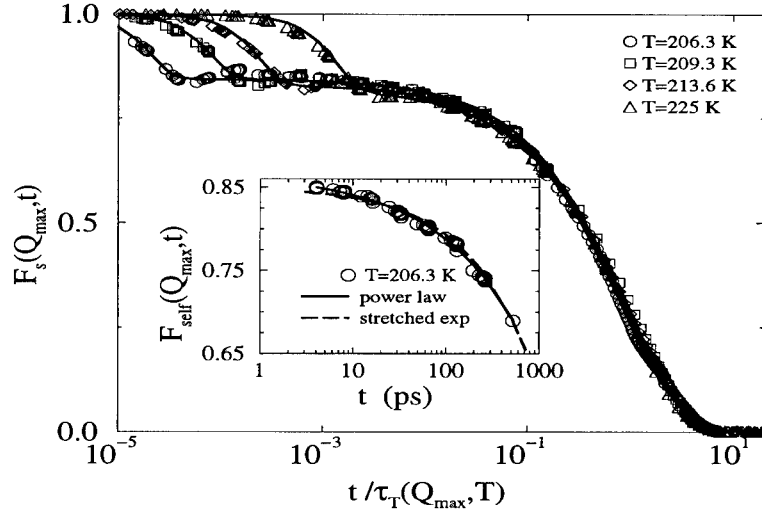


Figure 1: Decay of the intermediate scattering function at  $Q = 18\text{nm}^{-1}$ , corresponding to the position of the structure factor maximum. Curves have been scaled in time by 5230, 1260, 439 and 80 ps respectively. Full lines are fit with a gaussian function, to describe the microscopic dynamics, plus a stretched exponential function with stretching exponent 0.7. The inset shows the late- $\beta$  regime, to highlight that a power-law fits the data better than the stretched exponential form.

Studying the behavior of the stretching exponent in the fit of  $F_s(Q, t/\tau_T(Q))$  as a function of  $Q$  and  $T$  it was noted[7] that the system goes back to “normal” behavior (stretching exponent approaching one) for distances much bigger than the cage size. Indeed, it was found that for small  $Q$ , the stretched exponential behavior tends to the usual simple exponential behavior, diffusion becomes normal, the translational time  $\tau_T(Q)$  scales as  $Q^{-2}$  and the gaussian approximation for  $F_s(Q, t)$  becomes sufficiently good to represent the data. At small  $Q$  vector, the presence of a nearby ideal glass transition appears only via the  $T$  dependence of  $D$ . It was also found[7] that at  $Q$  vectors comparable with the first peak in the structure factor, diffusion is anomalous (it was found that translational times  $\tau_T(Q)$  scale as  $Q^{-1}$ ) while the correlation function is highly non gaussian. The product  $DQ^2\tau_T(Q)^{-1}$ , which is equal to one at small  $Q$  and high  $T$  deviates from one at low  $T$  and high  $Q$  vectors.

The approach to the plateau of any correlation function should follow according to MCT a self-

similar  $t^\alpha$  dynamics[12]. In Ref. [7] it was found that the approach to the plateau is completely masked by the presence of a strongly undamped harmonic dynamics. Molecules are shown to perform undamped oscillations in cages, for times comparable to the approach to the plateau[15, 16]. An underlying  $t^\alpha$  power-law is impossible to detect. The progressive development of a RTN structure, in which all molecules have very similar "monodisperse" cages (all molecule being HB-ed with four neighbors) together with the presence of a strong harmonic dynamics completely mask the possibility of detecting a  $t^\alpha$  power-law in any correlators for this system.

MCT at the present stage of development is a theory for spherical molecules. No theoretical predictions are available for the decay of correlations of orientational degrees of freedom. It is thus particularly interesting to compare, for the case of SPC/E water, orientational and translational correlation functions. Orientational correlations are best studied via the evaluation of the Legendre polynomial  $P_l(x(t))$ , where the argument  $x(t)$  is the cosine of the angle between the studied orientational vector at time  $t$  and the orientation of the same vector at time 0. Fig. 2 shows the first five  $P_l$  for the molecular dipole vector. Also for the orientational degrees of freedom, we observe a two step relaxation, with a stretched exponential  $\alpha$ -decay.

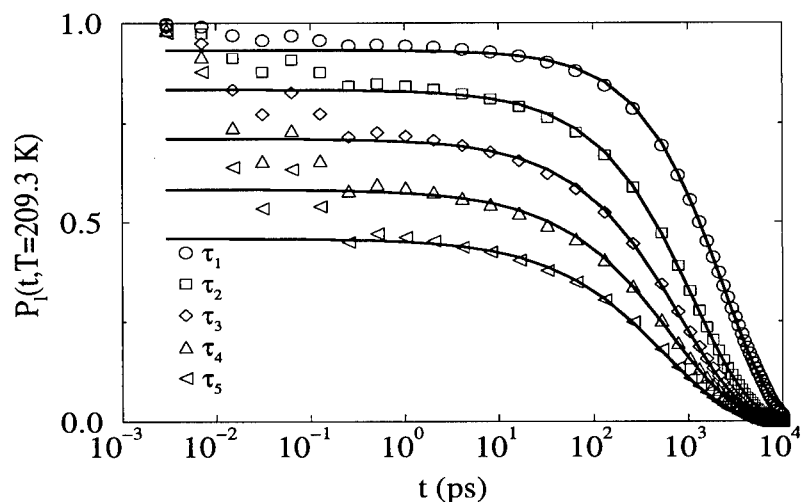


Figure 2: First five Legendre correlation function for the molecular dipole axis at  $T = 209.3K$ . The full curves are stretched exponential fits for times larger than 1 ps. The fitted rotational times are respectively 2310, 1130, 821, 674, 558 ps, while the stretching exponent parameters are 0.84, 0.73, 0.67, 0.63, 0.62

It is important to compare the decay of the translational correlation functions  $F_s(Q, t)$  and of the rotational correlation functions  $P_l(t)$ . Both correlations are fitted to stretched exponential forms  $e^{-(t/\tau)^\beta}$ . In Fig.3 we compare the characteristic times and the stretching exponents for  $P_1$  and  $P_2$  with the same quantities for  $F_s(Q = 10nm^{-1})$  and  $F_s(Q = 16nm^{-1})$ .  $Q$ -vectors have been chosen in such a way to match the characteristic times at one temperature.

The similarities between the two sets of data support the view that orientational dynamics close to the ideal glass transition singularity is strongly coupled to translational dynamics. Rotations and translations are controlled by the same stochastic process and, as a result, are characterized by the same decay laws. Molecules rotate and translate at the same time while jumping out of

their cage. It is important to stress that decorrelation of angular degrees of freedom as measured by  $P_1$  is associated to decorrelation of translational quantities over distances comparable to the nearest neighbor distance. As we said before, in this  $Q$  range  $\tau_T(Q)^{-1}DQ^{-2}$  becomes more and more different from one on decreasing  $T$ . From the equivalence between  $\tau_R$  and  $\tau_T$  at large  $Q$ , it follows that the product  $D\tau_R$  increases on approaching  $T_{ig}$ .

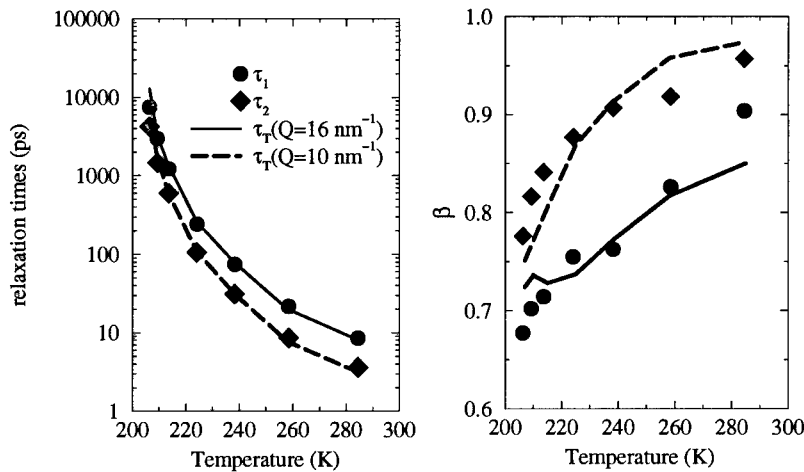


Figure 3: (left) Relaxation times for  $F_s(Q, t)$  ( $\tau_T(Q)$ ) and  $P_l(t)$  ( $\tau_l$ ) as a function of temperature. (right) Stretching exponent  $\beta$  for the same quantities.

Dynamics of simulated water molecule is very well described by MCT. Moreover, it has been shown in Ref.[7] that the relation between the independently calculated exponents  $\gamma$  and  $b$  are consistent with MCT predictions. In other words, according to Ref. [7], the anomalous behavior of the transport coefficients in water could be interpreted in terms of *ideal* MCT. In the simulated system, as well as in real water, the temperature of structural arrest  $T_{ig}$ , evaluated from the power-law temperature dependence of  $D$ , is about 50K below the TMD. This equivalence strongly suggests to interpret the thermodynamic Angell temperature as ideal glass transition temperature  $T_{ig}$ .

The strong slowing down of the dynamics develops in the same  $T$  range where the coefficient of thermal expansion  $\alpha_P$  is negative. More and more hydrogen bonds forms in the system (as monitored by the significant decrease of the potential energy) and the coordination number decreases to almost 4. According to Angell's classification scheme[17], liquid water behaves as a highly fragile liquid in this  $T$  range. Close to  $T_{ig}$ , the structure of simulated liquid water is similar to the structure of a Random Tetrahedral Network (RTN) in which all molecules are tetrahedrally coordinated. If this is the case, then diffusion around and below  $T_{ig}$  can happen only at the expense of breaking *four* HBs. This breaking process could constitute the zeroth-order picture for the description of the elementary processes producing activated diffusion below  $T_{ig}$ . On the other end, it is hard to imagine that the structure of the liquid would keep changing on further cooling once it has reached the RTN structure.

The presence of activated diffusion and the absence of significant structural relaxation are the essential ingredients in the classification of a liquid as a strong one. The speculations on the

behavior of the liquid below  $T_{ig}$  are consistent with the possibility of a kinetic transition from a fragile liquid behavior (above  $T_{ig}$ ) to a strong liquid behavior (below  $T_{ig}$ ) associated with the complete formation of the RTN. Unfortunately, the very slow diffusion close and below  $T_{ig}$ , which could be described only by the *extended* MCT, cannot be studied via computer simulations at the present time, due to the huge cpu time required.

#### ACKNOWLEDGMENT

We thank C.A. Angell and W. Kob for useful discussions.

#### REFERENCES

- [1] C.A. Angell, in *Water: A Comprehensive Treatise*, Ed. F. Franks (Plenum, New York, 1981), Ch. 1. C.A. Angell, *Ann. Rev. Phys. Chem.* **34**, 593 (1983).
- [2] S. Sastry, P. G. Debenedetti, F. Sciortino and H.E. Stanley, *Phys. Rev. E* **53** 6144 (1996).
- [3] R.J. Speedy, *J. Chem. Phys.* **86**, 982 (1982). R.J. Speedy and C.A. Angell, *J. Chem. Phys.* **65**, 851 (1976).
- [4] P.H. Poole, F. Sciortino, U. Essmann, H. E. Stanley, *Nature* **360**, 324 (1992). F. Sciortino, P.H. Poole, U. Essmann, H. E. Stanley, *Phys. Rev. E* **55** 727 (1997).
- [5] E. W. Lang and H. D. Lüdemann, *Angew. Chem. Int. Ed. Engl.* **21**, 315 (1982).
- [6] A. P. Sokolov, J. Hurst and D. Quitmann, *Phys. Rev. B* **51**, 12865 (1995).
- [7] F. Sciortino, P. Gallo, P. Tartaglia, S. H. Chen, *Phys. Rev. E* **54** 6331 (1996).
- [8] D. Paschek and A. Geiger, preprint. (1996).
- [9] H. Weingärtner, R. Haselmeier and M. Holz, *J. Phys. Chem.* **100** 1303 (1996).
- [10] P. Gallo, F. Sciortino, P. Tartaglia, S. H. Chen, *Phys. Rev. Lett.* **76** 2730 (1996).
- [11] E. Leutheusser, *Phys. Rev. A*, **29**, 2765 (1984), U. Bengtzelius, W. Götze and A. Sjölander, *J. Phys. C* **17** 5915 (1984).
- [12] W. Götze and L. Sjögren, *Rep. Prog. Phys.* **55**, 241 (1992).
- [13] W. Götze and A. Sjögren, *Transport Theory and Statistical Physics* **24**, 801 (1995).
- [14] H. J. C. Berendsen, J. R. Grigera and T. P. Straatsma, *J. Phys. Chem.* **91**, 6269 (1987).
- [15] F. Sciortino and P. Tartaglia, *Phys. Rev. Lett.* in press (1997).
- [16] F. Sciortino and P. Tartaglia, *Prog. Theor. Phys.* **121** (1997).
- [17] C. A. Angell in *Relaxations in Complex Systems*, edited by K. Ngai and G. B. Wright. (National Technical Information Service, U.S. Dept. of Commerce: Springfield, VA, 1985) p. 1; C. A. Angell, *J. Non-Cryst. Solids* **13**, 131.

## LOCAL STRUCTURE OF MD SIMULATED SODA-LIME-SILICATE GLASS

XIANGLONG YUAN, ALASTAIR N. CORMACK

Center for Glass Research, NYS College of Ceramics at Alfred University, Alfred, NY 14802

### ABSTRACT

Simulation of soda-lime-silicate (sls) glass has been performed using molecular dynamics (MD). The local structure of each component is analyzed extensively in terms of total radial distribution function and coordination number and found to be insensitive to the composition change. Because of its big size,  $\text{Na}^+/\text{Ca}^{2+}$  shows a behavior rather like  $\text{O}^{2-}$  instead of  $\text{Si}^{4+}$ . It is evident that the CN and local structure of  $\text{Na}^+$  with  $\text{O}^{2-}$  are similar to those in crystalline  $\alpha\text{-Na}_2\text{Si}_2\text{O}_5$ . Finally, the  $\text{Na}^+/\text{Ca}^{2+}$  cluster phenomenon is discussed.

### INTRODUCTION

The complexity of silicate glasses is well known and it has taken a great deal of time and ingenuity, coupled with advanced experimental techniques, to provide the detailed understanding that exists today. Techniques such as x-ray absorption fine structure (XAFS), neutron diffraction, MAS-NMR and x-ray photoemission spectroscopy (XPS) have been very important in elucidating the detailed structure.<sup>1-4</sup> Based on such techniques, a modified random network (MRN)<sup>1</sup> has emerged which is characterized by the microsegregation of glass modifiers and glass formers, the boundaries being defined by non-bridging oxygen ions (NBOs). According to this model, glass modifiers will form clusters between the bridged  $[\text{SiO}_4]$  units, to which they are linked predominantly via NBOs. As the modifier is generally the minority component, it will form channels separated by network regions. The extent of the modified regions is clearly governed by the glass composition. Previous MD simulations<sup>5,6</sup> have provided support for this model.

The coordination number (CN) of glass modifiers in glasses is not easy to determine considering its ill-defined shell. In practice, the CN is defined as the average number of nearest neighbors surrounding the central atom. The nearest neighbors are usually those lying within a given radius. However, this radius for modifiers is not easy to define and reporting CN without referring to radial distance is often inappropriate.

In this study, the local structure and CN of each species and the  $\text{Na}^+/\text{Ca}^{2+}$  cluster are fully discussed in terms of total radial distribution function,  $T(r)$ , bond angle distribution (BAD) and  $\text{CN}(r)$ . The  $\text{Q}_n$  species and ring size distribution (RSD) containing unique ring up to 14 numbers have also been calculated and a detailed analysis will be reported subsequently.

### SIMULATION METHODS

Although silicate glass is mainly thought to be a covalent bonded framework structure, full ionic charges on both silicon and oxygen species are employed for long-range Coulomb potential calculation using Ewald's method. The charges on the ions here should be regarded simply as parameters in the potential model. The covalent character of the Si-O bonds is modelled by using

the Truncated Vessal three-body potential<sup>7</sup> modified by Smith and Greaves.<sup>8</sup> A four-range Buckingham potential based on that of Vessal *et al.*<sup>9</sup> is used to model the short-range interactions. The  $\text{Na}^+-\text{O}^{2-}$  interaction was taken from a study of sodium  $\beta''$  alumina by Wolf *et al.*<sup>10</sup> while  $\text{Ca}^{2+}-\text{O}^{2-}$  comes from Lewis and Catlow.<sup>11</sup>

Simulations were performed on the  $x\text{Na}_2\text{O} (1-x)\text{CaO} 3\text{SiO}_2$  glass systems with same amount of  $\text{O}^{2-}$  (945) and  $\text{Si}^{4+}$  (405) species, 270, 216, 162, 108  $\text{Na}^+$  and 0, 27, 54, 81  $\text{Ca}^{2+}$  for  $x = 1.0, 0.8, 0.6, 0.4$ , respectively. Since the generation of the starting configuration is crucially important and the strategy of starting from the crystal structure and heating to high temperature has been shown not adequate in randomizing the system on a reasonable time scale,<sup>8</sup> the initial position of each atom in this study was randomly generated and put into the initial simulation box with 1/5 room temperature density. The system was first simulated at 9000 K for 10,000 time steps at constant volume. The constant pressure simulation using Nose-Hoover algorithm<sup>12</sup> was then conducted at 2, 4, 6, 8, 8 GPa with corresponding temperature of 7547, 5274, 3686, 2576 and 1800 K for total  $5 \times 10,000$  time steps. Simulation was then performed at 1800, 1258, 879 and 300 K using constant volume simulation (NVE ensemble) with 8000, 8000, 8000 and 10,000 time steps, from which 101 configurations of the last 4000 time steps were sampled at intervals of 40 time steps to calculate  $T(r)$ , RSD, BAD,  $Q_n$  species and NBO/BO ratios.  $\Delta t$  is 1.0 fs for all steps.

## RESULTS AND DISCUSSION

Fig. 1a illustrates the  $T(r)$  for  $x = 0.6, 0.8$  and  $1.0$  sls glass. The curves here are simply the summation of each component and not ready for comparison with neutron diffraction data. It is clear that the difference between different  $T(r)$  is very small except that the intensity ratio of first peak to second peak increases as  $x$  decreases. Fig. 1b decomposes the  $T(r)$  curve for  $x = 0.6$  system. Some pairs whose contributions are relatively small and merge into other peaks are not shown here to give a clearer illustration.

### BO and NBO Ratio

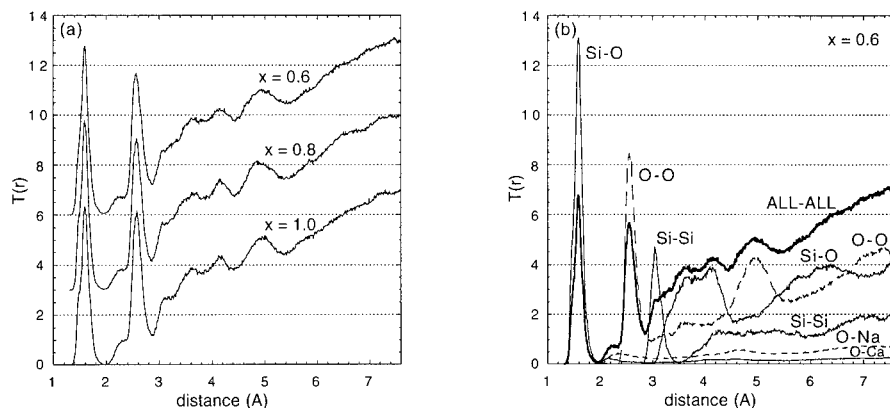


Fig. 1. a).  $T(r)$  for  $x\text{Na}_2\text{O} (1-x)\text{CaO} 3\text{SiO}_2$  glass. b). Decomposed  $T(r)$  for  $x = 0.6$  glass.



TABLE I. BO/NBO ratio for  $x\text{Na}_2\text{O}$  (1- $x$ ) $\text{CaO}$   $3\text{SiO}_2$  glass

This study	BO/NBO	Experimental ( $x = 1.0$ )	BO/NBO
$x = 1.0$	2.47 (673/272)	Jen (ESCA) <sup>4</sup>	2.59
$x = 0.8$	2.47 (673/272)	Bruckner (ESCA) <sup>3</sup>	2.4
$x = 0.6$	2.45 (671/274)	Newell (MD) <sup>13</sup>	2.45 (159/65)
$x = 0.4$	2.44 (670/275)	Theoretical	$2.50[(7-2)/2]$

The alkalis and alkali earths are glass modifiers. Theoretically,<sup>14</sup> two alkali ions or one alkaline earth ion will break a Si-O bridge and attach an oxygen to the broken bridge. Thus, each alkali ion is expected to create one NBO while each alkali earth two NBOs. This suggests that NBOs will be present in proportion to the concentration of alkali and/or alkaline earth in a silicate glass and implies a strong association between NBO and  $\text{Na}^+/\text{Ca}^{2+}$ .

For  $x\text{Na}_2\text{O}$  (1- $x$ ) $\text{CaO}$   $3\text{SiO}_2$  glasses, the calculated ratio of NBOs to total oxygen atoms will be  $2/7 = 0.2857$ . The glass systems we studied contain a total of 945 oxygen atoms and should have 270 NBOs and 675 BOs despite the difference in  $x$ . Both Jen and Kalinowski<sup>4</sup> and Bruckner *et al.*<sup>3</sup> used XPS to study the BO/NBO ratio and obtained results close to theoretical expectations (Table I). BO/NBO ratios of 2.6 and 2.4 were found for  $\text{Na}_2\text{O}$   $3\text{SiO}_2$  glass.

#### Coordination of Silicon and Oxygen

The CN of  $\text{Si}^{4+}$  is easy to determine since it has a well defined first peak which does not overlap with others. Whether a cutoff of 2.3 or 2.6 Å, the CN remains the same: 3.99 over all  $x$ .

As for  $\text{O}^{2-}$ , the calculation of CN is rather complicated. Fig. 2 clearly shows that the first shell of NBO/BO is well defined and only contains one/two  $\text{Si}^{4+}$  species. The second shell, however, is not so well defined but still has a distinguishable minimum around 2.9 Å. Considering that the ionic radius of  $\text{Na}^+/\text{Ca}^{2+}$  is much larger than that of  $\text{Si}^{4+}$  and is comparable to that of  $\text{O}^{2-}$ ,  $\text{Na}^+/\text{Ca}^{2+}$  joins other  $\text{O}^{2-}$  to form the second shell of a central  $\text{O}^{2-}$  and becomes comparable to  $\text{O}^{2-}$  species for a NBO center. Table II shows that for  $x = 0.6$  sfs glass given a cutoff of 2.9 Å, the CN of BO is 8.63, in which  $\text{O}^{2-}$  contributes 6.18 (6 goes from the two  $[\text{SiO}_4]$  the BO connected),  $\text{Si}^{4+}$  2.0 and  $\text{Na}^+/\text{Ca}^{2+}$  0.45. For NBO the CN is 6.78, in which  $\text{O}^{2-}$  contributes 3.64 (3 from the  $[\text{SiO}_4]$  it connected),  $\text{Si}^{4+}$  1.0 and  $\text{Na}^+/\text{Ca}^{2+}$  2.14.

TABLE II. CN of each species in MD simulated  $x\text{Na}_2\text{O}$  (1- $x$ ) $\text{CaO}$   $3\text{SiO}_2$  glass

center specie	composition $x$	cutoff (Å)	Total CN	Partial CN contributed from species		
				$\text{O}^{2-}$	$\text{Si}^{4+}$	$\text{Na}^+/\text{Ca}^{2+}$
$\text{Si}^{4+}$	0.4 ~ 1.0	2.6	3.99	3.99	0.0	0.0
BO	0.6	2.9	8.63	6.18	2.0	0.45
NBO	0.6	2.9	6.78	3.64	1.0	2.14
	1.0	2.9	7.05	3.35	1.0	2.70
$\text{Na}^+$	0.6	2.9	4.44	2.47(NBO) 1.48(BO)	0.08	0.41
$\text{Ca}^{2+}$	0.6	2.9	4.77	3.46(NBO)	0.03	0.13
				1.15(BO)		

Noticeably, the local structure of BO is almost independent of the composition change. The environment of NBO, however, changes slightly since it is more sensible to  $\text{Na}^+/\text{Ca}^{2+}$  species. As the total number of  $\text{Na}^+/\text{Ca}^{2+}$  species increases with  $x$ , the contribution from  $\text{Na}^+/\text{Ca}^{2+}$  increases too and leads to the decrease of that from  $\text{O}^{2-}$ . (Table II) For  $x = 1.0$  sils glass, the CN of NBO goes from 6.78 to 7.05, in which the contribution of  $\text{O}^{2-}$  decreases by 0.29 and that of  $\text{Na}^+/\text{Ca}^{2+}$  increases by 0.56 because more  $\text{Na}^+/\text{Ca}^{2+}$  is added, and it preferentially associates with NBO.

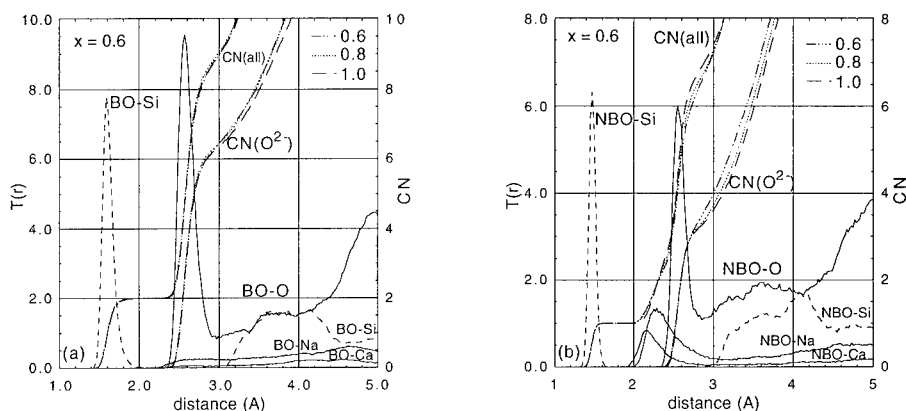


Fig. 2.  $T(r)$  and  $CN(r)$  for a). BO and b). NBO with other species for  $x = 0.6$  glass. The CN for other composition is also shown.

### Coordination of Sodium and Calcium

Determining the CN of  $\text{Na}^+$  or  $\text{Ca}^{2+}$  is quite difficult due to the broad  $\text{Na}^+/\text{Ca}^{2+}$ -BO and almost indistinguishable  $\text{Na}^+/\text{Ca}^{2+}$ -NBO curves, though  $\text{Na}^+/\text{Ca}^{2+}$ -NBO curves shows a sharp peak at  $\sim 2.3$  Å and go to a minimum around 3.0 Å. (Fig. 3) Obviously there is a strong association between NBO and  $\text{Na}^+/\text{Ca}^{2+}$ . Suppose that BO species join NBO to form the first shell of a  $\text{Na}^+/\text{Ca}^{2+}$  center, other  $\text{Na}^+/\text{Ca}^{2+}$  species that form the second shell will trespass into the first one; they are mixed intimately at the boundary. Due to the repulsive force between cations, the connection between a  $\text{Na}^+/\text{Ca}^{2+}$  center and its surrounding  $\text{Na}^+/\text{Ca}^{2+}$  species is loosely connected.

Table II shows that the CN of  $\text{Na}^+$  for  $x = 0.6$  glass is 4.44 to which  $\text{O}^{2-}$  contributes 3.95. The cutoff here is set to 2.9 Å over which the contribution of  $\text{Si}^{4+}$  will increase dramatically. For  $\text{Ca}^{2+}$ , the total CN is 4.77 to which  $\text{O}^{2-}$  species contribute 4.61. Note that the NBO contributes one more to the  $\text{Ca}^{2+}$  center than to the  $\text{Na}^+$  one simply because of the extra charge of  $\text{Ca}^{2+}$  over  $\text{Na}^+$ . For sodium silicate ( $x = 1.0$ ), the CN is counted as 4.88 to which  $\text{O}^{2-}$  contribute 3.99. About one more  $\text{Na}^+$  is included in the first shell of a  $\text{Na}^+$  center. The CN of 4.88 indicates a geometry intermediate between tetrahedral and octahedral. Note that in crystalline  $\alpha\text{-Na}_2\text{Si}_2\text{O}_5$ ,  $\text{Na}^+$  are fivefold coordinated. The substitution of  $\text{Na}^+$  with  $\text{Ca}^{2+}$  lowers the CN of  $\text{Na}^+$  slightly and thus somewhat looses its local structure. On the other hand,  $\text{Ca}^{2+}$  is insensitive to the composition change. It is clear from Fig. 3b that  $CN(r)$  curves of  $\text{Ca}^{2+}$  and its partial  $CN(r)$  contributed from  $\text{O}^{2-}$  (not shown here) for different  $x$  are almost the same in each case. Here the combined effort of  $\text{Na}^+/\text{Ca}^{2+}$  is considered to be the same, though the individual contribution of  $\text{Na}^+$  or  $\text{Ca}^{2+}$  is surely changed as composition changes.

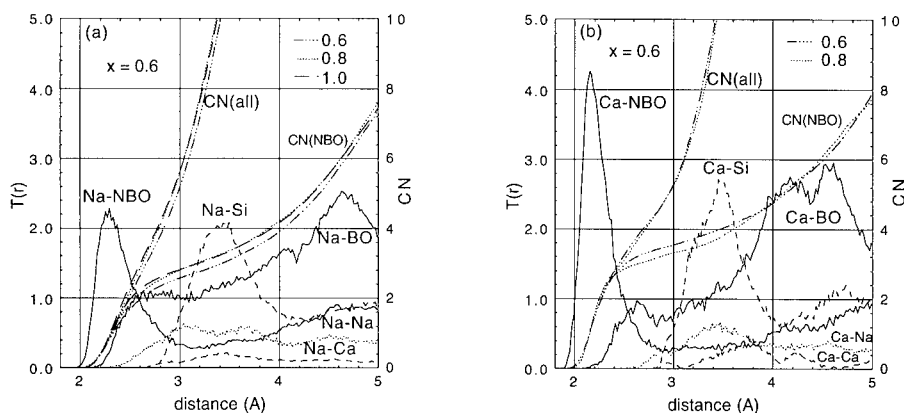


Fig. 3.  $T(r)$  and  $CN(r)$  for a).  $\text{Na}^+$  and b).  $\text{Ca}^{2+}$  with other species for  $x = 0.6$  glass. The CN for other composition is also shown.

#### BAD for O-Na-O Linkage and RDF for First Neighbor of Na/Ca Center

Between 2.6 and 5.0 Å peak of  $\text{O}^{2-}\text{-O}^{2-}$   $T(r)$  curve there is a small peak around 3.6 Å, (Fig. 1b) which as Smith *et al.*<sup>8</sup> suggested, arises from correlations involving NBOs. If this peak is due to O-Na-O linkages, this implies an angle of  $\sim 96^\circ$ , typical of the trigonal bipyramidal units found in crystalline  $\alpha\text{-Na}_2\text{Si}_2\text{O}_5$ . We hence calculated the BAD of such linkages using a cutoff of 3.0 Å, and, truly enough, a peak appears around  $\sim 93^\circ$  which confirms that the 3.6 Å peak is due to the O-Na-O linkage. (Fig. 4a) The sharp peak at  $57.5^\circ$  has been identified, as shown in figure, mainly due to the BO- $\text{Na}^+$ -BO linkage the BOs of which belong to the same  $[\text{SiO}_4]$ . Note that in  $\alpha\text{-Na}_2\text{Si}_2\text{O}_5$ ,  $\text{Na}^+$  are 5-coordinated, which is similar to what we calculated for  $\text{Na}^+$  in sls glass.

We also calculated the BAD for O-Ca-O linkage and found a similar behavior. It implies that  $\text{Ca}^{2+}$  is also responsible for the 3.6 Å peak in  $\text{O}^{2-}\text{-O}^{2-}$   $T(r)$  and it behaves similarly to  $\text{Na}^+$  since they have a similar ionic radius. This result is consistent with our previous discussion.

The relationship between  $\text{Na}^+/\text{Ca}^{2+}$  species is analyzed using radial distribution function (RDF) for the first neighbors of a  $\text{Na}^+/\text{Ca}^{2+}$  center. Fig. 4b shows that the first neighbor  $\text{Na}^+/\text{Ca}^{2+}$  species of either  $\text{Na}^+$  or  $\text{Ca}^{2+}$  center is certainly within 5.0 Å and is mostly around 3 Å that is larger than 2.3 Å for  $\text{Na}^+/\text{Ca}^{2+}\text{-O}^{2-}$  peak due to the coulomb force between cations. It thus leads to a loose structure within  $\text{Na}^+/\text{Ca}^{2+}$  rich region.

The clustering of  $\text{Na}^+/\text{Ca}^{2+}$  predicted by the MRN model is supported in this study. Fig. 4b suggests that  $\text{Na}^+/\text{Ca}^{2+}$  tend to cluster together. Most  $\text{Na}^+/\text{Ca}^{2+}$  species can find their first neighboring  $\text{Na}^+/\text{Ca}^{2+}$  species around 3 Å and, if not, will do within 5 Å for sure. As a reference, the distance between each Na/Ca species pair, provided that they are evenly distributed throughout the whole system, will be around 4.36 Å for  $x = 1.0$  and 4.64 Å for  $x = 0.6$ ; that is  $\sim 1.5$  Å greater. For  $x = 0.8$  sls glass, setting a cutoff distance as 4.0 Å, within which most first neighbor  $\text{Na}^+/\text{Ca}^{2+}$  of a  $\text{Na}^+/\text{Ca}^{2+}$  center can be found (Fig. 4b), we calculated the CN for  $\text{Na}^+/\text{Ca}^{2+}$  to be 3.5 and 2.5 for  $\text{Ca}^{2+}\text{-Na}^+/\text{Ca}^{2+}$  pair. It shows a strong correlation between  $\text{Na}^+/\text{Ca}^{2+}$  species and thus support the MRN cluster model.

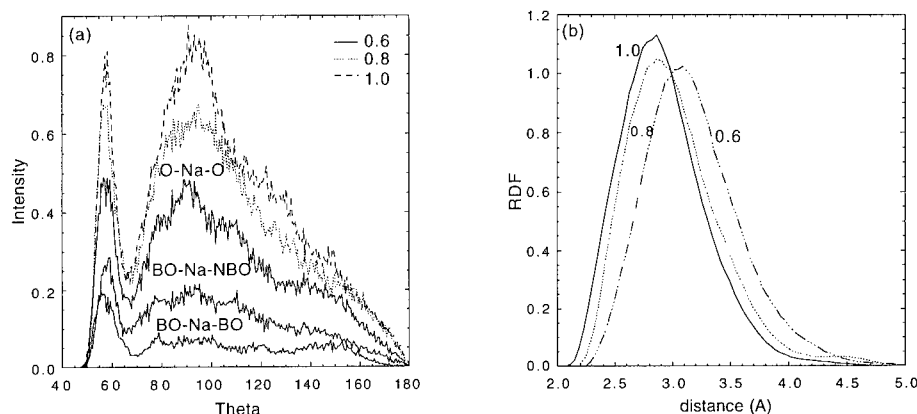


Fig. 4. a). BAD of O-Na-O linkage and the decomposed BAD for  $x = 0.6$  glass with a cutoff of 3.0 Å. b). RDF of first neighboring Na/Ca ions around a Na/Ca center.

## CONCLUSIONS

The local structure of each species in soda-lime-silicate glass has been analyzed and found to be insensitive to the composition change. Because of its large size,  $\text{Na}^+/\text{Ca}^{2+}$  shows a behavior rather like  $\text{O}^{2-}$  instead of  $\text{Si}^{4+}$ . It is evidenced that the CN and local structure of  $\text{Na}^+$  with  $\text{O}^{2-}$  are similar to that of crystalline  $\alpha\text{-Na}_2\text{Si}_2\text{O}_5$ . A strong correlation between  $\text{Na}^+/\text{Ca}^{2+}$  species was found and thus further supports the MRN cluster model.

## ACKNOWLEDGMENTS

We gratefully acknowledge the Center for Glass Research, NYS College of Ceramics at Alfred University, for financial support. Some of the calculations were performed at Cornell Theory Center.

## REFERENCES

1. G.N. Greaves, *Journal of Non-Crystalline Solids* **71**, p. 203 (1985).
2. Alan J. Leadbetter, *Journal of Non-Crystalline Solids* **179**, p. 116 (1994).
3. Rolf Bruckner, Hans-Ulrich Chun and Hans Goretzki, *Glastechn. Ber.* **51**, p. 1 (1978).
4. J.S. Jen and M.R. Kalinowski, *J. Non-Cryst. Solids* **38-39**, p. 21 (1980).
5. Cheng Huang and A.N. Cormack, *J. Chem. Phys.* **93**, p. 8180 (1990).
6. A. N. Cormack and Yuan Cao, *Molecular Engineering* **6**, p. 183 (1996).
7. Behnam Vessal, *Journal of Non-Crystalline Solids* **177**, p. 103 (1994).
8. W. Smith, G. N. Greaves and M. J. Gillan, *J. Chem. Phys.* **103**, p. 3091 (1995).
9. B. Vessal, M. Amini, D. Fincham and C. R. A. Catlow, *Philosophical Magazine B* **60**, p. 753 (1989).
10. M. L. Wolf, J. R. Walker and C. R. A. Catlow, *Solid State Ionics* **13**, p. 33 (1984).
11. G V Lewis and C. R. A. Catlow, *J. Phys. C: Solid State Phys.* **18**, p. 1149 (1985).
12. W. G. Hoover, *Phys. Rev.* **A31**, p. 1695 (1985).
13. R. G. Newell, B. P. Feuston and S. H. Garofalini, *J. Mater. Res.* **4**, p. 434 (1989).
14. Arun K. Varshneya *Fundamentals of Inorganic Glasses*; Academic Press, Inc: San Diego, 1994.

# The coupling model of relaxation: An alternative for the study of an interacting system of small particles

J. Castro

Departamento de Física Aplicada. Universidad de Santiago de Compostela. E-15706, Spain

## Abstract

It is shown that the coupling model of relaxation accounts for the main experimental results of the magnetic relaxation in an assembly of interacting fine particles.

## 1 Introduction

The coupling model for relaxation in complex systems was first introduced by Ngai in 1979 [1]. Since then, it has been found to offer an accurate description of a wide variety of systems [2]. The theoretical foundation of the model has been given recently [3]. However, its use in magnetism is more recent. See reference [4] and other references therein

The fundamental difference between the coupling model and previous models of relaxation is that these earlier models treat the effect of complexity on the relaxation as being essentially static, in the sense that the effect of complexity is to change the relaxation time or to produce a distribution of relaxation times. In contrast to this, in the coupling model, the relaxation in complex systems, is dynamical in nature.

From this view-point, according to Ngai [5], a relaxing complex system consists of three parts:

- i) Individual primary species (PS), which are of interest for the relaxation.
- ii) A heat-bath, whose interaction with the PS provides a primary mechanism of relaxation.
- iii) Other relaxing species, X, whose interaction with PS, the PS-X coupling, slows down the relaxation process. This is the main manifestation of complexity.

In this paper we propose another application of the coupling model to a magnetic system: namely that of an interacting fine-particle assembly. In this system, the PS are the individual particles whose dipolar coupling with the other particles in the assembly slows down the relaxation process. This is the main difference with preceding attempts to tackle this problem [6,7,8], where the only effect of the presence of inter-particle interactions is a change in the relaxation times.

In this paper we show how the model can explain, in a natural way the observed differences for a system of interacting and non-interacting particles via the variation of the inverse of the blocking temperature with the logarithm of the measuring time and the values of the relaxation times (table 1). The organization of the paper is as follows: After a brief review of the coupling model for the relaxation in a complex system (section 2), in section 3 we apply this model to a system of interacting particles and show that their observed behaviour can be accounted for by this model.

## 2 The coupling model

In this section we summarize briefly the salient features of the coupling model. For more details about the theoretical derivations and the successful experimental applications of the model we refer to references [2]-[5].

The coupling model [5] proposes the existence of a temperature-insensitive crossover time,  $t_c$ , separating two regimes in which the dynamics of the relaxation are different. The relaxation function is a linear exponential  $\exp(-\frac{t}{\tau_0})$  for  $t < t_c$  and cross-over at  $t \approx t_c$  to a stretched exponential form  $\exp(-(\frac{t}{\tau^*})^{1-n})$  for  $t > t_c$ . The coupling parameter  $n$  lies in the range  $0 < n < 1$ . Notice the appearance of two different characteristic time-scales,  $\tau_0$  and  $\tau^*$ , for the two regimes. These two time-scales are not independent, but continuity of the relaxation function at  $t = t_c$  implies that:

$$\tau^* = (t_c^{-n} \tau_0)^{\frac{1}{1-n}} \quad (1)$$

## 3 Application of the coupling model to the relaxation of a system of small interacting particles

The study of the relaxation of a system of small non-interacting magnetic particles was started by Neel[9] and later reconsidered by Brown[10]. There are several excellent treatments of the magnetic properties of an ensemble of particles. Thus, we need only to review here the main ideas[11].

We consider, firstly, an ensemble of non-interacting particles of equal volume  $V$ . For simplicity we assume that the particle anisotropy is uniaxial and that the particle's easy axis of magnetization is parallel to the field direction. Then the energy of one of the particles in a field  $H$  will be [11]:

$$E = KV \sin^2 \theta - M_s V H \cos \theta \quad (2)$$

where  $K$  is the anisotropy constant,  $M_s$  is the bulk saturation magnetization and  $\theta$  measures the orientation of the magnetic moment of the particle with respect to the field. This energy gives rise to two energy minima separated by an energy barrier:

$$E_A = \frac{V}{2} M_s H_K (1 - \frac{H}{H_K})^2 = e_A V \quad (3)$$

where  $H_K = \frac{2K}{M_s}$ . At a finite temperature, we have thermally activated motion over the energy barrier. The predicted time dependence[9] has a linear exponential form with a characteristic time given by the expression:

$$\tau_0 = \tau_\infty \exp(E_A/kT) \quad (4)$$

Recent estimates give  $\tau_\infty \approx 10^{-10} - 10^{-11}$  s [12].

For such a system, in the presence of dipolar interactions between the particles, the coupling model predicts the existence of a cross-over time,  $t_c$ , independent of temperature, to be determined from the experiment, separating two different regimes of the dynamics

of the relaxation. The relaxation function is a linear exponential  $\exp(-t/\tau_0)$  for  $t < t_c$  and has a stretched exponential form  $\exp(-(t/\tau^*)^{1-n})$  for  $t > t_c$ , where  $0 < n < 1$ . The relation between  $\tau^*$  and  $\tau_0$  is given by equation 1.

An important consequence of equation 1, if  $\tau_0$  describes the physics of some motion over an energy barrier with a characteristic time given by equation (2), is:

$$\tau^* = \tau_\infty \exp\left(\frac{E_A^*}{kT}\right) \quad (5)$$

where:

$$E_A^* = \frac{E_A}{1-n} \quad (6)$$

$$\tau_\infty^* = \tau_\infty^{\frac{1}{1-n}} t_c^{\frac{n}{n-1}} \quad (7)$$

and note that  $E_A^* > E_A$ .

The characteristic time scale of the relaxation defines the blocking temperature  $T_B$ . At temperatures  $T > T_B$ , the particle's magnetic moment reaches thermal equilibrium during the time of measurement, and thus exhibits superparamagnetic behaviour. At  $T < T_B$ , the particle moment is blocked.

An important consequence of the model can be now pointed out if, as a definition of the blocking temperature ( $T_B$ ), we use the usual criterion that the characteristic time-scales of the relaxation will be of the order of the measuring time ( $t_m$ ), i.e.  $t_m = \tau_\infty \exp(E_A/kT_B)$  for  $t_m < t_c$  and  $t_m = \tau_\infty^* \exp(E_A^*/kT_B)$  for  $t_m > t_c$ . We then expect that the logarithm of the measuring time plotted as a function of the inverse of the blocking temperature will be a "piece-wise" straight line with two different slopes,  $\frac{E_A}{k_B}$  for  $t_m < t_c$  and  $\frac{E_A^*}{k_B(1-n)}$  for  $t_m > t_c$  and intersecting the  $\log t_m$  axis at  $\log \tau_\infty$  and  $\log \tau_\infty^*$  respectively. The slope of the line corresponding to the small measuring times will be smaller than that corresponds to the longer measuring times.

A comparison between theory and the experiment can be made with the data of Dormann et al[13] in a system consisting of  $\gamma - Fe_2O_3$  particles dispersed in a polymer matrix (figure 1). By varying the aggregation state these authors have a series of samples with approximately the same size and different interparticle distances, therefore different interactions, including the case of zero interaction (sample IF). In figure 1, the interaction increases from right to left and the labels on the figure corresponds to the different samples of reference[13]. In the figure we have lengthened the straight line corresponding to  $t_m > t_c$  as a guideline for the eye (dashed line). We observe that, when the interaction is present, the data point corresponding to the smallest measuring time deviates from this line. However, this cannot be taken as demonstration of the presence of two slopes in the  $\log t_m$  versus  $1/T_B$  data. The main reason is that the first measuring point corresponds to a Mössbauer experiment. In analyzing Mössbauer spectroscopy there are two difficulties: the measuring time is not precisely defined and the blocking temperature is very difficult to determine because it depends on the line shape under relaxation. Therefore the position of this data point is not without controversy. As a demonstration of this fact, we mention that this point is not located in an unique way in the references under [16] in the paper.

However, the stringent condition for the applicability of the coupling model is the presence of two different regimes of the dynamics of the relaxation with two different time scales related by equation (1). We shall demonstrate the presence of this crossover in an

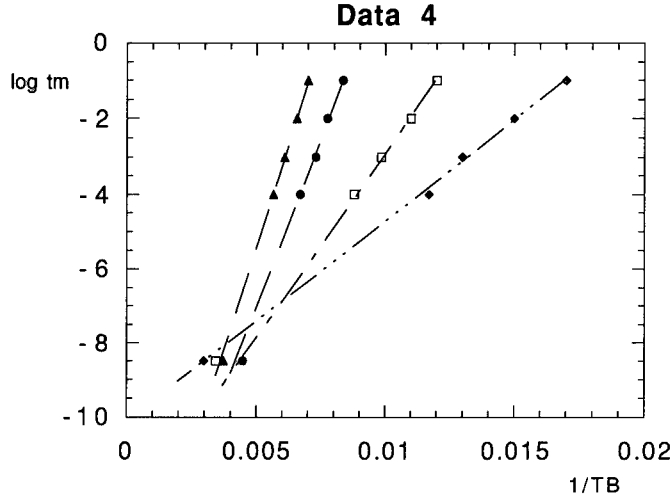


Figure 1: Variation of the blocking temperature,  $T_B$ , with the logarithm of the measuring time for different samples of  $\gamma - Fe_2O_3$  particles, according to [16]. The interparticle interaction strength increases from right to left. The average particle size is held constant.

analysis of the  $t_m > t_c$  data. The characteristic time scale for the dynamics of the sample without interactions (sample IF) is given by equation (4). Therefore from an analysis of the  $\log t_m$  versus  $1/T_B$  for this sample we can estimate  $\tau_\infty \approx 10^{-10}s$  and  $E_A/k = 1050K$ . The characteristic time scale for the dynamics of the other samples is given by equation (5). Therefore from an analysis of the  $\log t_m$  versus  $1/T_B$  for these we can estimate  $\tau_\infty^*$  and  $E_A^*$  for each sample. Notice that  $E_A/E_A^* = 1 - n$  and thus we can calculate the value of  $n$ . The experimental values of  $\tau_\infty^*$ ,  $\tau_\infty^*(exp)$ , and  $n$  for each sample are given in table 1. In the coupling model the two time scales  $\tau_\infty$  and  $\tau_\infty^*$  are related by equation (7), and therefore to demonstrate the applicability of the coupling model to our system we can calculate  $\tau_\infty^*$ ,  $\tau_\infty^*(th)$ , from  $\tau_\infty$  and  $n$  and compare it with the experimental results. The only free parameter of the theory is  $t_c$ . The  $\tau_\infty^*(th)$  values, for  $t_c \approx 10^{-8}s$ , are compared with the experimentally obtained ones in table 1. We observe that there is excellent agreement between theory and experiment.

Here we wish to stress the importance of this observed fact. The existence of the cross-over time, which separates two different time dependences with times-scales related by equation 5, is the most important aspect for verification of the coupling model. As far as we know, this is the first time that this cross-over has been found in a magnetic system.

The coupling model does not provide a prescription of estimating the crossover time. Although, within the conceptual framework of the coupling model, it is expected that the crossover time should increase with weaker interactions. At very least, the time scale



Sample	$n$	$\tau_{\infty}^*(th)(s)$	$\tau_{\infty}^*(exp)(s)$
CH	0.4	$4 \times 10^{-12}$	$10^{-12}$
IN	0.73	$4 \times 10^{-16}$	$10^{-16}$
FLOC	0.76	$3 \times 10^{-17}$	$10^{-17}$

Table 1: Comparison between the theoretical and experimentally obtained values for  $\tau_{\infty}^*$ . See text.

at which crossover takes place depends on the characteristics of the particular system considered. Recently it has been found by Colmenero et al [14] and Zorn et al [15] that in glass formed polymers the crossover time is of the range of picoseconds. In these systems the interactions are between monomer units and are of the Van der Waals type at molecular distance. In the present system the interactions are of the magnetic dipolar kind and the distance involved is significantly larger than molecular distance in polymers. Therefore the interaction is much weaker in our system and as a result the crossover time found is four orders of magnitude larger.

## 4 Conclusions

In this work we have shown that the coupling model of relaxation can account for the main experimental findings in the studies of the magnetic relaxation in an assembly of interacting fine particles. This encouraging development leads us to expect that this model will be used more in the future in the analysis of magnetic relaxation in assemblies of small particles.

## 5 Acknowledgements

The author is indebted to Dr. D. Fiorani for making available to me his experimental results and for many valuable discussions. Critical reading of the manuscript by Prof. K. L. Ngai, Dr. H. J. Blythe and Prof. J. Rivas is also acknowledged.

## References

- [1] K. L. Ngai. Comments Solid State Physics, **9**, 127, 1979.
- [2] For a review, see K. L. Ngai, in "Disordered Effects in Relaxation Processes", edited by A. Blumen and R. Richert (Springer-Verlag, Berlin 1994).
- [3] K. Y. Tsang and K. L. Ngai, Phys. Rev. E54, R3067, 1996.
- [4] J. Colmenero, A. Alegria, I. Telleria, K. L. Ngai, Phys. Rev. B47, 5041, 1993.
- [5] K. L. Ngai and D. J. Plazek, Rubber Chem. Tech. Reviews, 68, 376, 1995.

- [6] R. W. Chantrell and E. P. Wohlfarth, *Journal. Magn. Magn. Mat.* 40, 1, 1983.
- [7] J. L. Dormann, L. Besais and D. Fiorani, *J. Phys. C*21, 2015, 1988.
- [8] J. L. Dormann and D. Fiorani in “Relaxation in Complex Systems and Related Topics”, Edited by J. A. Campbell and C. Giovanella, Plenum Press, New York, 1990.
- [9] L. Neel, *Ann. Geophys.* 5, 99, 1949.
- [10] W. F. Brown Jr. *Phys. Rev.* B45, 7805, 1992.
- [11] E. Kneller in “Handbuch der Physik”, volume XVIII(2) Ed. by S. Flugge, Springer Verlag, 1966.
- [12] L. Bessais, L. Ben Jaffel and J. L. Dormann, *Phys. Rev* B45, 7805, 1992. See also W. T. Coffey, D. S. F. Crothers, Yu. P. Kalmykov, E. S. Massawe and J. T. Waldron, *Phys. Rev.* E49, 1869, 1994
- [13] J. L. Dormann, F. D’Orazio, F. Lucari, M. Nogues, R. Cherkaoui, P. Prene, E. Tronc, J. P. Jolivet and D. Fiorani, presented at the International Conference on Magnetism ICM94 and *ibid. Phys. Rev.* B21, 1491, 1996. See also E. Tronc, P. Prene, J. P. Olivet, F. D’Orazio, F. Lucari, D. Fiorani, M. Gordinho, R. Cherkaoui, M. Nogues and J. L. Dormann *Hiperfine Interactions* 95, 129, 1995.
- [14] J. Colmenero, A. Arbe and A. Alegria, *Phys. Rev. Lett.* 71, 2603, 1993.
- [15] R. Zorn, A. Arbe, J. Colmenero, B. Frick, D. Richter and U. Buchenau, *Phys. Rev.* E52, 781, 1995.

## 1/f Dielectric Fluctuations at the Glass Transition

N. E. Israeloff and W. Wang

Department of Physics and Center for Interdisciplinary Research on Complex Systems,  
Northeastern University, Boston, MA 02115

### Abstract

The temperature and frequency dependence of thermal dielectric polarization noise was investigated in glycerol and PVC in the vicinity of their glass transitions. Polarization fluctuations were observed via voltage noise which was produced within a sample capacitance cell. The high sensitivity and accuracy of the technique provides a powerful probe of dynamics in low-loss regimes of various materials. Noise spectra had  $1/f^\beta$  form at lower temperatures just below the glass transition. In glycerol, the spectral exponent decreased smoothly with temperature, extrapolating to 1, i.e.  $1/f$  noise, near  $T_0$  where relaxation times diverge. The results support the idea that a glassy phase transition occurs in the static limit.

### Introduction

Glasses have been intensively investigated not only because they are ubiquitous in nature, but also because they are prototype complex systems [1]. Yet generic *glassy* behaviors such as non-exponential relaxation and glass transitions have yet to be fully explained. The transition from a liquid to an amorphous solid, such as ordinary window glass, occurs at a temperature,  $T_g$ , at which the average relaxation time in the material becomes longer than the measurement time. The measured  $T_g$  decreases with measuring frequency, however, it extrapolates to a nonzero value,  $T_0$ , in the zero frequency limit for many materials [1]. Scaling behavior is observed over a wide range in temperature and frequency [2]. The question of whether a thermodynamic phase transition can occur at  $T_0$  remains a major unsolved mystery.

Recently Menon and Nagel [3] have argued, based on dielectric susceptibility measurements which exhibit scaling behavior that the static dielectric susceptibility may have a logarithmic divergence at  $T_0$ , indicative of a true phase transition. An important consequence of this picture is the expectation of dielectric polarization noise with precisely a  $1/f$  spectral dependence over a wide range of frequency at  $T_0$ . Recently we showed that dielectric polarization noise can be systematically observed and studied near the glass transition in glycerol [4]. The noise, measured as current fluctuations produced by a sample capacitor, obeyed predictions of the fluctuation-dissipation theorem (FDT), connecting noise and susceptibility, even when the material was weakly out-of-equilibrium. With higher sensitivity voltage noise techniques [5], dielectric fluctuation measurements can be extended to low noise (low loss) regime below the glass transition where power-law spectral dependences are expected [2] and more subtle predicted violations of FDT [6] can be checked.

Because  $1/f$  noise has been observed in a wide variety of conducting materials as well as other diverse problems a number of exotic theories have been invoked to account for the apparent "universality" of the  $1/f$  spectral dependence [7]. In fact the spectral dependence in conducting materials is a non-universal,  $1/f^\beta$ , with  $0.6 < \beta < 1.5$  [7]. The variations with temperature of  $\beta$  together with the temperature dependence of the noise magnitude can often be self consistently explained by thermally activated kinetics with a broadened distribution of activation energies [7]. In this picture, a precisely  $1/f$  spectrum ( $\beta = 1$ ) appears only briefly (if at all) over narrow ranges of temperature (and frequency) in a given material. This is consistent with the observed noise spectra in many materials, with one notable exception: metallic spin glasses [8]. In that instance

$\beta$  was not measurably different from 1.00 over at least a decade in temperature below the spin glass transition. This implies, in an activated kinetics picture,  $1/f$  noise over an extremely broad range of frequency, e.g. many more decades than can be measured. The question is whether this is a generic signature of a thermodynamic glass phase and whether it occurs in structural glasses.

In this paper detailed measurements of dielectric polarization noise as a function of temperature and frequency in glycerol and PVC are described. Thermal equilibrium noise in the electric polarization of a lossy dielectric material is expected based on the fluctuation-dissipation theorem. Johnson noise of the conduction electrons in a resistor is a well known analog. Thermal noise was observed in the magnetization of spin-glasses using very sensitive SQUID detectors[9].

A systematic investigation of thermal dielectric polarization noise and FDT in glycerol was recently reported[4,5]. The FDT voltage noise produced by dielectric polarization fluctuations within a sample-filled capacitor is given by:

$$S_V = 4 k_B T \epsilon'' C_0 / |C|^2 \omega \sim 4 k_B T (\epsilon''/\epsilon') / |C| \omega \quad (1)$$

where  $k_B$  is the Boltzmann constant,  $T$  is temperature,  $\omega$  is angular frequency,  $C$  is the capacitance of the sample-filled cell,  $C_0$  is the empty cell geometrical capacitance,  $\epsilon'$ ,  $\epsilon''$  are the real and imaginary components of the dielectric susceptibility.

## Experimental Methods

The capacitance sample cell consisted of copper plates separated by teflon or polypropylene spacer rings (0.1 - 0.4mm thickness, 0.5-4.0 cm<sup>2</sup> area). The geometrical capacitances,  $C_0$ , ranged from 5 pF to 45pF ( $\pm 10\%$ ). The sample cell was attached to a copper cold finger in vacuum within a liquid-nitrogen cooled cryostat which sits on a vibration isolation table within an RF shielded room. The operational temperature range was 80K-400K. A custom built preamplifier utilizing an Analog Devices 549L ultra-low current noise JFET op-amp, and a  $10^{11}$  ohm (Victoreen) input resistor, was mounted inside the cryostat adjacent to the sample [5] (See fig. 1 inset). The stray capacitance in this arrangement was limited to  $< 1$  pF. The preamplifier could be used for low temperature measurements by maintaining it at a much higher temperature than the sample using its self heating and deliberately poor thermal grounding. The preamp output was further amplified with a Stanford Research pre-amp and then digitized using a personal computer-based data acquisition card and spectrum analyzer.

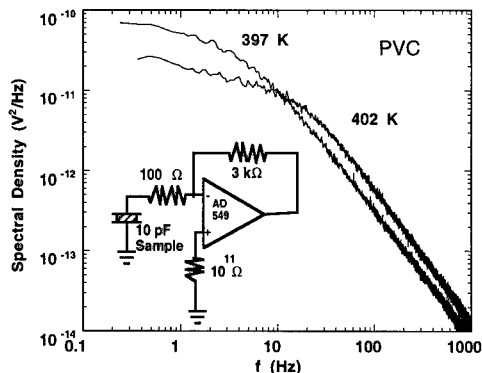


Figure 1. Voltage noise spectra for PVC at two temperatures in the vicinity of its glass transition. Inset: the measurement circuit located within the cryostat

One must be careful in dealing with the amplifier background. Amplifier current noise produces voltage noise inversely proportional to the sample capacitance at low frequencies with a  $1/f^2$  dependence. The relative proportion of background noise at high frequencies due to amplifier voltage noise scales as sample capacitance. Thus an optimal capacitance which gave a large dynamic range was of order 10 pF. The background can be determined accurately by replacing the sample with a vacuum capacitor equal in size to the sample at a specific temperature. Additionally the background was checked by measuring the sample spectrum at lower temperatures.

## Results

Measurements of the dielectric polarization noise were performed on glycerol and polyvinyl-chloride (PVC) through their respective glass transitions. Glycerol is one of the most highly studied materials while PVC is considered one of the most *fragile* [1] glass formers. The PVC was fine mesh powder while the glycerol was liquid at room temperature. Figure 1 shows noise spectra in the vicinity of the glass transition for PVC. Similar spectra are observed for glycerol near  $T_G$  (fig. 2 a). Both exhibit the characteristic broadened lorentzian spectrum with a

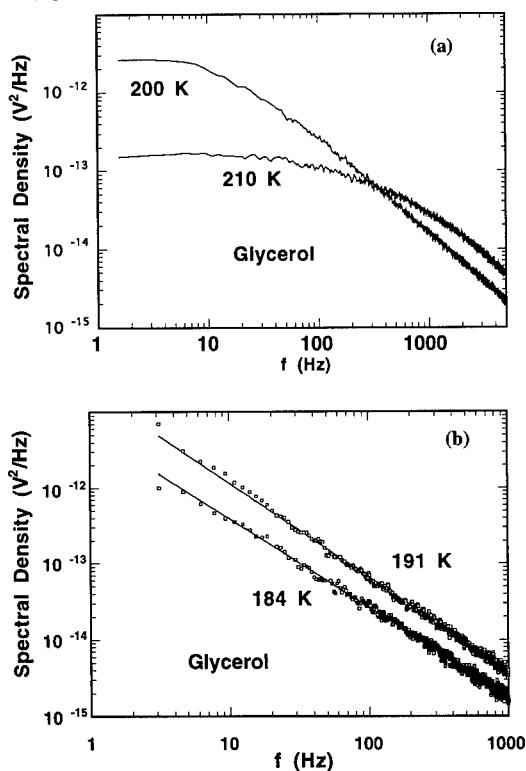


Figure 2. Noise spectra for glycerol at the glass transition (a) and at lower temperatures (b) where power-law spectra are observed.

knee marking the dominant relaxation frequency, which moves rapidly to lower frequencies with decreasing temperature.

The noise spectrum attains a  $1/f^\beta$  power-law at lower temperatures in both materials. See fig. 2 (b). This corresponds to the high frequency tail of the spectra seen in fig. 2 (a) for glycerol at higher temperatures. Detailed temperature dependence studies have only been completed in glycerol thus far. We found that the exponent,  $\beta$ , decreases smoothly with temperature. A simple linear extrapolation of the data crosses  $\beta = 1.00$  near 147 K (fig. 3). The extrapolated static-limit glass transition temperature was previously found to be  $T_0 = 137 \pm 10$  K for glycerol [10]. At the same time, the spectral density appears to extrapolate to a non-zero value at this temperature. Together these two results strongly suggest that a  $1/f$  spectrum with finite spectral density over a broad range in frequency occurs near  $T_0$ . Since the static susceptibility is proportional to the noise spectrum integrated over all frequency, it will diverge for a spectrum which is  $1/f$  down to zero frequency. Our results support the notion that the static susceptibility diverges logarithmically indicating a phase transition in the static limit [3].

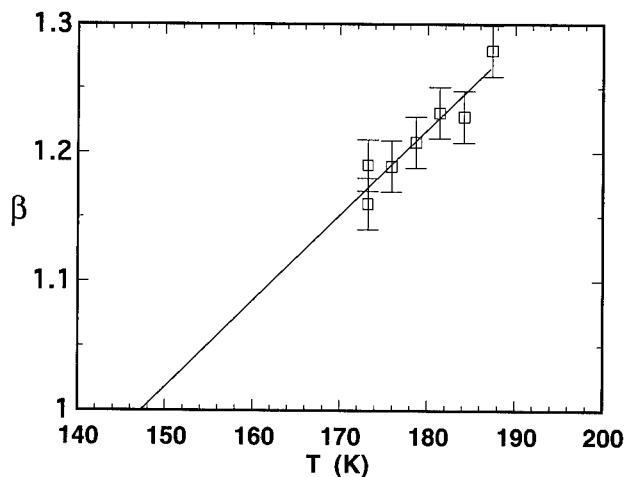


Figure 3. Spectral exponent vs. temperature for glycerol. A linear fit (shown) extrapolates to 1.0 near  $T_0$ .

## Conclusions

We have studied dielectric polarization noise in PVC and glycerol near their glass transitions. The voltage noise spectra had power-law form below the glass transition and in glycerol extrapolated to a  $1/f$  form at a temperature near the presumed critical temperature,  $T_0$ . This should be investigated in non-polar materials such as ortho-terphenyl, and more fragile materials such as PVC and toluene and [1], for which the measurements can be extended closer to  $T_0$ .

The noise measurements offer certain advantages over conventional dielectric spectroscopy for many materials. Namely, no applied fields which might potentially influence dynamics are needed. The frequency dependence is obtained naturally in a single measurement. And greater accuracy is possible at low values of the imaginary component of susceptibility since there is no

need to determine systematic phase shifts in the measurement circuit. At present we can accurately resolve noise spectra and spectral exponents in materials with  $\epsilon'' \sim 10^{-3}$  [5]. Another interesting question which can be studied involves the possible breakdown of the fluctuation-dissipation theorem in aging glasses [6].

### Acknowledgments

I thank G. B. Alers, S. R. Nagel, M. B. Weissman, M. Tinkham, and S. Sridhar for helpful discussions. This work was supported by the National Science Foundation (NYI program) through Grant No. DMR-9458008.

### References

1. C. A. Angell, *Science* **267**, 1924 (1995) and following articles in the same issue.
2. P. K. Dixon, et. al., *Phys. Rev. Lett.* **65**, 1108 (1990).
3. Narayanan Menon and Sydney R. Nagel, *Phys. Rev. Lett.* **74**, 1230 (1995), S.R. Nagel, private communication.
4. N. E. Israeloff, *Phys. Rev.* **B53**, R11913 (1996).
5. N. E. Israeloff, and W. Wang, *Rev. Sci. Instr.* in press.
6. L. F. Cugliandolo and J. Kurchan, *Phys. Rev. Lett.* **71**, 173 (1993).
7. M. B. Weissman, *Rev. Mod. Phys.* **60**, 537 (1988).
8. N. E. Israeloff, M. B. Weissman, G. J. Nieuwenhuys, and J. Kosiorowska, *Phys. Rev. Lett.* **63**, 794 (1989); N. E. Israeloff, G. B. Alers, and M. B. Weissman, *Phys. Rev.* **B 44** (Rapid Comm.), 12613 (1991).
9. M. Ocio, H. Bouchiat, and P. Monod, *J. Physique Lett.* L-647 (1985); W. Reim, R. Koch, A. P. Malozemoff, M. B. Ketchen, and H. Maletta, *Phys. Rev. Lett.* **57**, 905 (1987); H. Bouchiat and M. Ocio, *Comments Cond. Mat. Phys.* **14**, 163 (1988) and ref. therein.
10. N. O. Birge, *Phys. Rev.* **B34**, 1631 (1986).





## MOLECULAR DYNAMICS SIMULATION OF ALKALI BORATE GLASS USING COORDINATION DEPENDENT POTENTIAL

Byeongwon Park and Alastair N. Cormack  
New York State College of Ceramics at Alfred University, Alfred, NY 14802,  
parkbw@bushbaby.alfred.edu & cormack@bigvax.alfred.edu

### ABSTRACT

The structure of sodium borate glass was investigated by molecular dynamics simulation using coordination dependent potential model. The simulated alkali borate glass consists of basic units,  $\text{BO}_3$  triangle,  $\text{BO}_4$  tetrahedra and structural groups such as boroxol ring and triborate units. The coordination of boron is converted from 3 to 4 by adding alkali oxide.

### INTRODUCTION

The molecular dynamics (MD) simulations have become a useful tool in studying amorphous materials. [1] [2] [3] [4] Whilst the determination of the structure of a crystalline solid is relatively easy because of its periodicity, in glasses, there is no straightforward way to determine the structure, because of the lack of long range periodicity. In MD computer simulations, information about individual ion configurations may be analyzed and various properties of the materials may be predicted. The technique has seen a widespread successful application to silica based glasses. [1] [2] [3] [5] [6] The principal limitation of the technique is the need for a viable interatomic potential model.

This paper describes MD simulation of alkali (Na) borate glass. Alkali borate glasses have held the attention from many researchers because of the so called 'borate anomaly', besides its practical usage as superionic conductor. We are to explain the structural properties of alkali borates by MD simulation using coordination dependent potential which has been quite successful in modelling pure boron oxide glass. [7] [8]

### ALKALI BORATE GLASS

#### Structure of Alkali Borate

When modifier (alkali oxide) is added to pure borate glass, it brings one of two possibilities; 1) convert the coordination state of boron from 3 to 4; 2) create a nonbridging oxygen. This coordination conversion occurs over certain range of addition and the amount of 4 fold coordinated boron can be expressed  $x/(1-x)$  where  $x$  is mole fraction of modifier. This assumption has been confirmed by  $^{11}\text{B}$  NMR up to 40% alkali oxide. [9] [10] [11] People have tried to connect this coordination conversion to the boron anomaly. However, by careful experiment, the boron anomaly may be related to the manifestation of the various atom groups. [12] Krogh-Moe [13] has asserted that borate glasses are not merely a random network of  $\text{BO}_3$  triangles and  $\text{BO}_4$  tetrahedra joined at corner but, instead, they actually contain well defined and stable groups as segments of the disordered framework, the so called superstructural groups. Jellison and Bray [9] [14] has shown that there are five distinct boron site in sodium borate glasses containing up to 35 mol%  $\text{Na}_2\text{O}$ . The three coordinated boron signal in boroxol rings disappear as amount of alkali oxide increases and regular local structures as diborate, tetraborate and metaborate complex groups are conceived.

#### MD Simulation of Pure Borate and Alkali Borate Glass

Recently, there have been several studies using MD calculations of systems containing  $\text{B}_2\text{O}_3$  [7] [8] [15] [16] [17] [18] [19] [20] [21] In contrast to the success of MD simulations in silicate systems, most MD simulations of borate systems show some discrepancies with experimental data. Though pair potential models can reproduce the RDFs derived from x-ray and neutron scattering data at short distance, there still remain discrepancies in the intermediate region structure, including

B-O-B angles which are often far from the average of the estimated values of around  $130^\circ$ . These models always generate continuous random networks without any boroxol rings, even when a three body potential was included for some simulations. Hirao et al. [22] have performed MD simulation of sodium borate glasses containing a small amount of  $\text{Eu}_2\text{O}_3$ . They showed that each Na ion introduced into borate glass converts a trigonally connected boron to a tetrahedrally connected one. They found two local maxima in the B-O-B angle distribution; one around  $120^\circ$  and the other  $145^\circ$ . The first one may be attributed to the connection of boroxol groups and the second to connections involving  $\text{BO}_4$  tetrahedra. Abramo et al. [19] [23] have simulated  $\text{Ag}_2\text{O-B}_2\text{O}_3$  glasses. The addition of silver oxide increases the coherence of network by converting tricoordinated boron to tetrahedrally coordinated. However, they were unable to find evidence for boroxol, diborate, triborate and pentaborate groups in the simulated glass. The average B-O-B angle was  $150^\circ$ . Soppe et al. [24] have simulated lithium borate glasses. Structure of lithium borate glass consists of randomly connected  $\text{BO}_3$  and  $\text{BO}_4$  units. They disputed the possibility of the existence of boroxol rings in borate glass. Verhoef et al. [25] have studied the alkali (Li, Cs) borate glass by MD simulation. Their calculation yields a glass structure consisting of  $\text{BO}_3$  triangles and  $\text{BO}_4$  tetrahedra with no boroxol rings at all. They claimed that experimental Raman peaks at  $805\text{ cm}^{-1}$  and  $770\text{ cm}^{-1}$  are reproduced by symmetric breathing modes of  $\text{BO}_3$  and  $\text{BO}_4$  units.

Almost all MD simulations of borate systems have failed to generate structural grouping such as boroxol rings in pure borate and triborate, diborate group in alkali borates except Inoue et al. [17], Takada et al. [7] and Park et al. [8], though conversion from  $\text{BO}_3$  to  $\text{BO}_4$  has been successfully reproduced. These discrepancies may come from inadequate potential parameters and hence force calculation between atoms. The development of adequate theoretical models for borate is much more difficult than for silicates due to the complexity of boron-oxygen bonding, where coordination of boron can be easily changed by adding modifiers. Therefore, it is necessary to improve the interatomic potential model in order to get more reliable simulation results. Recently, Takada et al. [7][26] developed a new interatomic potential model for the two crystalline phases of boron oxide; it depends on the coordination number of oxygen atoms and was applied to vitreous  $\text{B}_2\text{O}_3$  using a molecular dynamics simulation. They have successfully reproduced the boroxol group in pure borate glass. They suggested that the use of partial charges, and the inclusion of a B-O-B bond bending, three body term are necessary to reproduce the boroxol rings in  $\text{B}_2\text{O}_3$  glass. This scheme has been implemented in a conventional MD simulation.

## EXPERIMENTAL PROCEDURE

### Potential Parameters

Potential models based on those of Takada et al. [7] were implemented. The MD program used is FUNGUS [27]. The original source code, and especially the force calculation subroutine, had to be heavily modified to implement the coordination dependent potential model. The distances between atoms are evaluated at every time step and the number of neighbors for each atom within a cutoff distance is calculated. Then the appropriate label for each atom is assigned, e.g. three fold, two fold or intermediate coordination, and the proper interatomic potential is chosen according to the label. In alkali borate glass simulation, the alkali ions and boron are counted for determining coordination number of oxygen. Three body bonding are also calculated. The equilibrium angle for B-O-B is set to  $120^\circ$  and for O-B-O,  $130^\circ$ . The long range Coulombic interaction is calculated using the usual Ewald method; the potential parameters are given in Table 1. A larger transition range of  $0.4\text{ \AA}$  was used.

### Simulation Procedure for Alkali borate Glass

The MD simulations were run on Silicon Graphic workstations. A total of 402 (234 O, 150 B, 18 Na) atoms,  $0.1\text{Na}_2\text{O} \cdot 0.9\text{B}_2\text{O}_3$  was used in the simulation. The initial coordination is randomly given. The simulation box size was adjusted to give the experimental density ( $2.041\text{ g/cm}^3$ ), under constant volume conditions. At high temperatures, the box size was enlarged to account for thermal expansion of the material. Initially, the atoms were heated to a target temperature of 5000 K and equilibrated for 10,000 time steps (each timestep = 1 fs). This process destroyed the crystallinity of

the starting structure and gave a random, disordered structure. After melting, the system was cooled to room temperature through several steps: 3000K, 1500K, 600K and finally to 300K using 10,000 timesteps for each temperature. The positions of the atoms, averaged over the last 1,000 timesteps were used to obtain the radial distribution function, bond angle distribution, and coordination number. Graphical visualization was achieved using commercial software; Cerius<sup>2</sup> and InsightII from Molecular Simulation Incorporated.

Table 1  
Potential Parameters for sodium borate glass

Parameter	
<u>Charge</u>	
q(B)	+1.2
q(O)	-0.8
<u>Morse Potential for B-O</u>	
for two fold Oxygen atom :O2	
D[eV]	1.84
b[1/Å]	2.7
ro[Å]	1.35
for three fold Oxygen atom: O3	
D[eV]	0.98
b[1/Å]	2.7
ro[Å]	1.475
<u>Buckingham potential for O-O</u>	
A[eV] for O2-O2	1990.8
A[eV] for O2-O3	1650.9
A[eV] for O3-O3	692.3
r[Å]	0.30
C[eV Å <sup>6</sup> ]	0.0
<u>Buckingham potential for B-B</u>	
A[eV]	323.1
r[Å]	0.30
C[eV Å <sup>6</sup> ]	0.0
<u>Three body term for O-B-O(<math>q_0=120^\circ</math> for three fold, <math>q_0=109.47</math> for four fold)</u>	
for three fold Boron atom	
k[eV/rad <sup>2</sup> ]	0.0
for three fold Boron atom	
k[eV/rad <sup>2</sup> ]	1.66
<u>Three body term for B-O-B(<math>q_0=120^\circ</math>)</u>	
for two fold Oxygen atom	
k[eV/rad <sup>2</sup> ]	6.38
for three fold Oxygen atom	
	4.22
<u>Buckingham potential for Na-O</u>	
A[eV]	208.556
r[Å]	0.3065
C[eV Å <sup>6</sup> ]	0.0
R=1.8Å D=0.2Å	

## RESULTS AND DISCUSSIONS

For comparison with alkali borate glass, the simulated total distribution function(TDF) of pure borate is given in Fig. 1 with neutron diffraction data. [28] The simulated TDF is folded with a peak function to allow broadening of the peaks due to limited  $Q_{\max}$ . [29] [30] The overall behavior is quite well matched with neutron experiment, especially peak at 3.63 Å which comes from boroxol group structure in the borate glass. Therefore we extend our simulation to sodium borate with confidence that potential was reasonable.

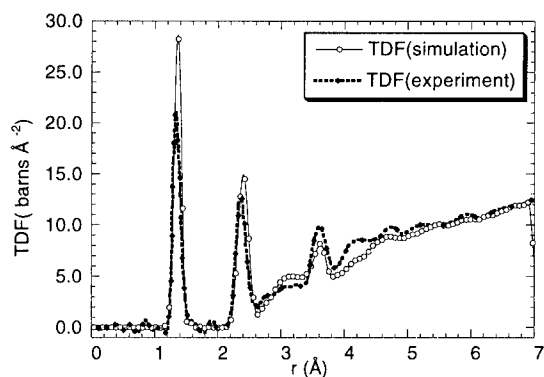


Fig. 1. Total distribution function of pure borate glass with neutron diffraction data. [28] The simulated peaks are folded with peak function to explain limit of  $Q_{\max}$  in experiment

A typical structure of our simulated sodium borate glass is given in Fig. 2 with circle which shows the structural units. As mentioned earlier, each oxygen of modifier added into pure boron oxide glass can convert one  $\text{BO}_3$  trigonal to  $\text{BO}_4$  tetrahedron at low concentration modifier, increasing the fraction of four fold boron,  $N_4$ , subsequently generation of nonbridging oxygen causes to decrease  $N_4$ . In the simulated sodium borate glass with low concentration of sodium oxide, the structural units are  $\text{BO}_3$  triangle and  $\text{BO}_4$  tetrahedra can be found clearly in Fig. 2.

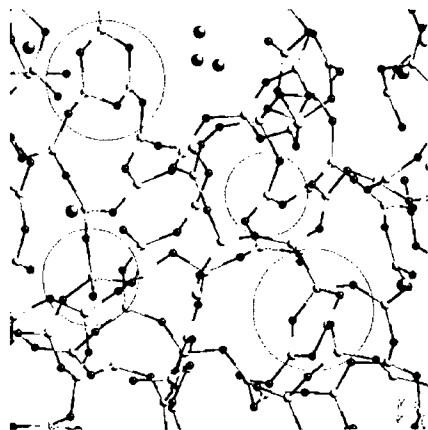


Fig. 2. Typical structure of simulated sodium borate glass. Big dark gray is Na; black ball, O, light gray is B. Structural groups are shown by drawing circle around them.

The existence of large structural units in borate glass was proposed by Krogh-Moe. [13] [31] NMR work by Jellison et al. [9][14] and Bray et al. [11] clearly shows the existence of larger structural unit. Our simulated sodium borate glass also shows the conversion from  $\text{BO}_3$  to  $\text{BO}_4$  and large structural units such as boroxol groups and triborate groups can be found. Verhoef et al. [21] [25] failed to generate such large structural units in their MD simulations of pure boron oxide and alkali borate glass. They were only able to generate  $\text{BO}_3$  triangle and  $\text{BO}_4$  tetrahedra. They argued that it is not necessary to have any larger structural unit to explain the experimental data even though the discrepancy exists. [28] Almost all the MD simulations of borate glass have failed to reproduce these kinds of structural units. We believe that it may come from the inadequate potential parameters which cannot describe the complexity of borate glass bond characteristics.

The individual pair correlation function is given in Fig. 3. Our simulation can reproduce the nearest neighbor distance  $\text{O-B}=1.36 \text{ \AA}$ ,  $\text{O-O}=2.36 \text{ \AA}$  and  $\text{B-B}=2.43 \text{ \AA}$ , but the distance between Na-O is a little larger than the expected value,  $2.31 \text{ \AA}$ . It comes from a slightly too large repulsive potential term between Na-O.

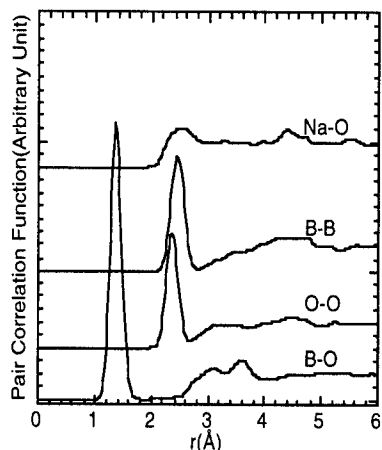


Fig. 3. Individual pair correlation functions for Na-O, B-B, O-O and B-O in simulated sodium borate glass

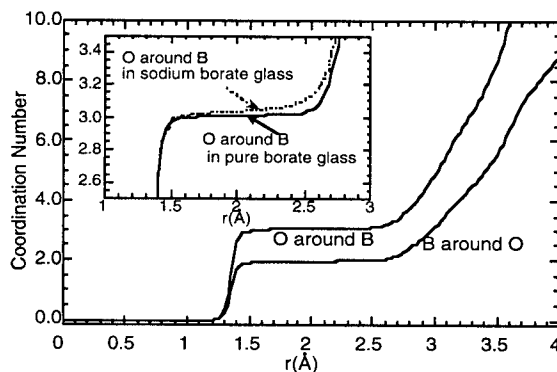


Fig. 4. Distribution of coordination number for Simulated alkali glass. The graph inside is to comparison of  $n_{\text{B-O}}$  for pure boron oxide glass and sodium borate glass.

The coordination number by distance is given in Fig. 4. The fraction of four fold boron is

given by  $N_4 = x/(1-x)$  where  $x$  is the mole fraction of modifying oxide. In our system,  $0.1 \text{ Na}_2\text{O} \cdot 0.9 \text{ B}_2\text{O}_3$ , the expected value of  $N_4$  is 11% and coordination of oxygen around boron,  $n_{\text{B-O}}$ , 3.11.

However the value we have for  $N_4$  is 3% and our  $n_{\text{B-O}}$  is 3.03. These numbers are somewhat lower than that measured in the real glass. It suggested that we don't have optimized potential parameters, especially for Na-O which was simply transferred from  $\text{Na}_2\text{O}$  oxide. The bond angle distributions for B-O-B and O-B-O are given in Fig. 5. The most probable angle for B-O-B is  $128^\circ$  and for O-B-O,  $120^\circ$ . For the  $\text{BO}_4$  tetrahedron, the equilibrium angle is to be  $109.5^\circ$ , but we see no peak at that angle. This is probably due to the low concentration of  $\text{BO}_4$  tetrahedral units in our simulations.

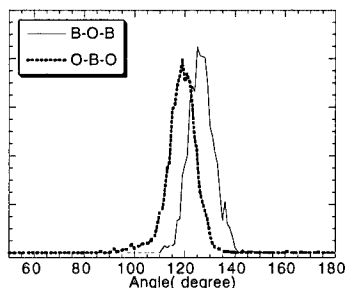


Fig. 5. Bond angle distribution for B-O-B and O-B-O in simulated sodium borate glass

We note that the conventional MD code doesn't account for changes in instantaneous coordination during the simulation. With the instantaneous coordination dependent potential for pure boron oxide glass, we were able to reproduce the superstructural units. Therefore, we believe that for alkali borate glass simulation, it will be necessary to consider the coordination change of boron during the simulation and to use different equilibrium angles and force constants for O-B-O bond angle of  $\text{BO}_3$  and  $\text{BO}_4$ , separately.

## CONCLUSION

Superstructural units in sodium borate glass were reproduced by molecular dynamics simulation using coordination dependent potential model. In contrast to conventional MD codes which failed to reproduce them. In addition  $\text{BO}_4$  units are seen, although fraction of four fold boron,  $N_4$ , is lower than the expected values. This may come from non-optimized potential parameter and potential calculation scheme. We believe that the coordination change of boron should be included in subsequent simulations

## REFERENCES

- [1] C. Huang and A. N. Cormack, *J. Chem. Phys.*, **93**, 8180(1990).
- [2] C. Huang and A. N. Cormack, *J. Chem. Phys.*, **95**, 3634(1991).
- [3] C. Huang and A. N. Cormack, *J. Mater. Chem.*, **2**, 281(1992).
- [4] W. Smith, G. N. Greaves, and M. J. Gillan, *J. Chem. Phys.*, **103**, 3091(1995).
- [5] P. Vashishta, R. K. Kalia, W. Jin, and A. Nakano, in *Diffusion in amorphous materials*, H. Jain and D. Gupta, Eds.: The Mineral, Metal & Materials Society, 1994, p. 129.
- [6] B. Vessal, M. Amini, and C. R. A. Catlow, *J. Non-Cryst. Solids*, **159**, 184(1993).
- [7] A. Takada, C. R. A. Catlow, and G. D. Price, *J. Phys.:Condens. Matter*, **7**, 8693(1995).
- [8] B. Park and A. N. Cormack, presented at The second international conference on borate glasses, crystals & melts, Abingdon, UK, 1996.
- [9] G. E. Jellison and P. J. Bray, *J. Non-Cryst. Solids*, **29**, 187(1978).

- [10] S. A. Feller, W. J. Dell, and P. J. Bray, *J. Non-Cryst. Solids*, **51**, 21(1982).
- [11] P. J. Bray, *J. Non-Cryst. Solids*, **75**, 29(1985).
- [12] D. L. Griscom, in Borate Glasses: Structure, Properties, Applications, vol. 12, Materials science research, L. D. Pye, V. D. Frechette, and N. J. Kreidl, Eds. New York: Plenum Press, 1978, p. 11.
- [13] J. Krogh-Moe, *Phys. Chem. Glasses*, **3**, 101(1962).
- [14] G. E. Jellison, S. A. Feller, and P. J. Bray, *Phys. Chem. Glasses*, **19**, 52(1978).
- [15] T. F. Soules, *J. Chem. Phys.*, **78**, 4032(1980).
- [16] M. Amini, S. K. Mitra, and R. W. Hockney, *J. Phys. C: Solid State Phys.*, **14**, 3689(1981).
- [17] H. Inoue, N. Aoki, and I. Yasui, *J. Am. Ceram. Soc.*, **70**, 622(1987).
- [18] Q. Xu, K. Kawamura, and T. Yokokawa, *J. Non-Cryst. Solids*, **104**, 261(1988).
- [19] M. C. Abramo and G. Pizzimenti, *J. Non-Cryst. Solids*, **85**, 233(1986).
- [20] W. Soppe, C. v. d. Marel, W. F. v. Gunsteren, and H. W. d. Hartog, *J. Non-Cryst. Solids*, **103**, 201(1988).
- [21] A. H. Verhoef and H. W. d. Hartog, *J. Non-Cryst. Solids*, **146**, 267(1992).
- [22] K. Hirao and N. Soga, *J. Am. Ceram. Soc.*, **68**, 515(1985).
- [23] M. C. Abramo, G. Carini, and G. Pizzimenti, *J. Phys. C: Solid State Physics*, **21**, 527(1988).
- [24] W. Soppe, C. v. d. Marel, and H. W. d. Hartog, *J. Non-Cryst. Solids*, **101**, 101(1988).
- [25] A. H. Verhoef and H. W. d. Hartog, *J. Non-Cryst. Solids*, **182**, 235(1995).
- [26] A. Takada, C. R. A. Catlow, and G. D. Price, *J. Phys.:Condens. Matter*, **7**, 8659(1995).
- [27] J. R. Walker, in Computer simulation of solids, vol. 166, Lecture notes in Physics, C. R. A. Catlow and W. C. Mackrodt, Eds. Berlin: Springer-Verlag, 1982.
- [28] A. C. Hannon, D. I. Grimley, R. A. Hulme, A. C. Wright, and R. N. Sinclair, *J. Non-Cryst. Solids*, **177**, 299(1994).
- [29] P. A. V. Johnson, A. C. Wright, and R. N. Sinclair, *J. Non-Cryst. Solids*, **50**, 281(1982).
- [30] A. C. Clare, G. Etherington, A. C. Wright, M. J. Weber, S. A. Brawer, and D. D. Kingman, *J. Chem. Phys.*, **91**, 6380(1989).
- [31] J. Krogh-Moe, *J. Non-Cryst. Solids*, **1**, 269(1969).

## MOLECULAR DYNAMICS SIMULATIONS OF FRACTURE IN AMORPHOUS SILICA

JINGHAN WANG, ANDREY OMELTCHENKO, RAJIV K. KALIA, AND PRIYA  
VASHISHTA

Concurrent Computing Laboratory for Materials Simulations  
Department of Physics & Astronomy and Department of Computer Science  
Louisiana State University  
Baton Rouge, LA 70803-4001

### ABSTRACT

Fracture in amorphous silica is studied using million-atom molecular dynamics simulations. The dynamics of crack propagation, internal stress fields, and the morphology of fracture surfaces are examined as a function of temperature and strain rate. At 300K and 600K we observe brittle fracture: internal stress increases to a critical value (typically 2 - 3 GPa) and then turns over when the crack reaches a terminal speed on the order of half the Rayleigh wave speed. At 900K crack propagation slows down dramatically due to plastic deformation and the material becomes ductile.

### INTRODUCTION

Silica is one of the most interesting materials found in nature. It occurs in various crystalline forms such as quartz, cristobalite, tridymite, and the high-pressure phase known as stishovite. Silica also exists in the vitreous form, which can be viewed as a frozen-in supercooled liquid. Vitreous silica is a network glass of corner-sharing  $\text{SiO}_4$  tetrahedra. It displays medium-range order, whose fingerprint is the first sharp diffraction peak (FSDP) in the static structure factor.<sup>1,2</sup> Crystalline and vitreous forms of silica have unique mechanical, thermal, electrical, and optical properties. As a result, this material has numerous technological applications<sup>3</sup>: in sensors and accelerometers and in microelectronic devices. Porous silica is an excellent material for thermal insulation and passive solar energy collection devices.

In this paper, we investigate mechanical failure in vitreous silica at the microscopic level. Despite a great deal of experimental, theoretical, and computer simulation work, there is very little knowledge about the microscopics of crack-front propagation in amorphous  $\text{SiO}_2$ . Five years ago, Ochoa, Swiler and Simmons<sup>4</sup> carried out molecular-dynamics (MD) simulations to investigate brittle failure in vitreous silica. Their simulations were based on a simple Born-Mayer-Huggins potential and the system they simulated was of a modest size.

Using large scale molecular-dynamics simulations, we investigate dynamic fracture in vitreous  $\text{SiO}_2$  at temperatures between 300 and 900K. These fracture simulations, involving 1.18 million particle systems, are based on interatomic potentials<sup>5</sup> which include effects of charge transfer, electronic polarizabilities, steric repulsion, and covalency. From these simulations we find that the amorphous silica systems at 300 and 600K undergo cleavage fracture. The crack tips reach terminal speeds of 1.40 km/s at 300K and 0.85 km/s at 600K. At 300K the terminal speed is close to half the Rayleigh wave speed in this material ( $V_R = 2.84$  km/s). The critical strains at



which the amorphous systems at 300 and 600K fracture are 8% and 9%, respectively. In contrast, at 900K the amorphous silica system shows plastic behavior up to 17% strain.

## MOLECULAR DYNAMICS SIMULATIONS

MD simulations of silica are performed using an empirical interatomic potential<sup>5</sup> which includes two- and three-body terms. The two-body part contains the effects of charge transfer, electronic polarizability, and steric repulsion. Three-body terms incorporate bending and stretching of covalent bonds. This potential has been successfully used in simulations of crystalline, amorphous and molten silica.<sup>1,5-8</sup> For amorphous silica the calculated static structure factor, including the height and position of the FSDP, agree very well with neutron diffraction experiments.<sup>1</sup> This potential predicts correctly the transition to octahedral phase of silica at high pressures exceeding 42 GPa.<sup>6,9</sup> The calculated phonon density of states and elastic moduli of the normal density system are also in good agreement with experiment.<sup>8</sup>

Amorphous silica for fracture simulations is prepared as follows. Starting from a bulk system with  $\beta$ -cristobalite lattice structure, the system is gradually heated to 3000K (well above the melting temperature) and thermalized for 90,000 time steps (the time step is 1.5 femto second). Amorphous system at 0K is produced by quenching the molten system over 183,000 time steps. Periodic boundary conditions are subsequently removed, and conjugate gradient minimization is applied to allow surface relaxation.

Mechanical failure is studied in a  $300\text{\AA} \times 300\text{\AA} \times 200\text{\AA}$  amorphous silica system consisting of 1.18 million atoms. The system is heated to 300K and stretched uniformly by 6% in the x-direction. A  $50\text{\AA}$  long triangular notch is inserted to initiate crack propagation in the y-direction. At the same time, we keep increasing the strain. The simulations are performed at three temperatures: 300K, 600K, and 900K. Different strain rates have been used, ranging from 0.013% to 2% per pico second.

The simulations have been performed on 16 nodes of the DEC Alpha cluster at the Concurrent Computing Laboratory for Materials Simulations at LSU. Our molecular dynamics code has a parallel efficiency  $\sim 90\%$ . We use a multiple time step approach<sup>10</sup> to accelerate the computations.

## RESULTS

Figure 1 shows snapshots of crack propagation in silica at different temperatures. At 300K the crack propagates through the entire sample in a cleavage-like manner. At the same time, we observe crack branching and meandering due to disordered structure of the material. At a higher temperature of 600K, we find somewhat of a different scenario (see Ref. 11). Tensile stress concentrated near the crack tip gives rise to a low-density region in front of the crack tip. As a result, a secondary crack forms which later coalesces with the main crack. Similar behavior has been observed in MD simulations of  $\alpha$ - $\text{Si}_3\text{N}_4$ .<sup>12</sup> The situation is completely different at 900K, where the crack gets arrested and the system does not fracture even when the strain is increased to 17%.

Figure 2 shows local stress distributions in the notched sample at two different temperatures, 300 and 900K. At 300K, the tensile stress is concentrated in front of the crack tip and the shear stress is the largest around the crack tip in the direction of  $45^\circ$  with respect to the x-axis. This is in agreement with the linear elasticity predictions. Detailed form of the stress distribution is quite different from the elastic theory because of finite system size and material

inhomogeneity. Similar behavior is observed at 600K. However, at 900K, the stress is much smaller (see gray-scale code bars beneath each of the snapshots) and is no longer concentrated in any particular region.

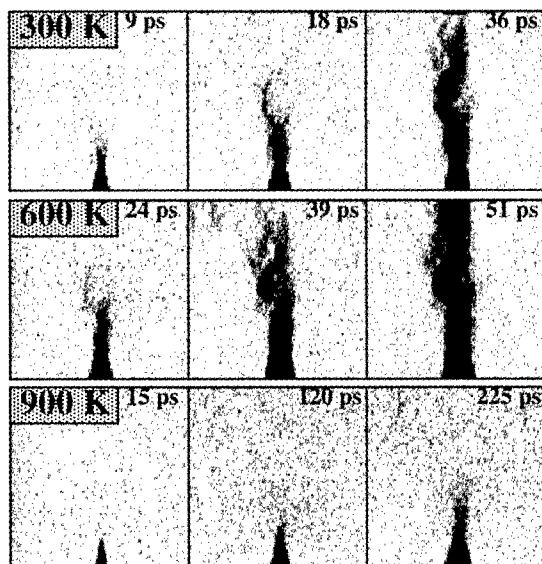


Figure 1. Snapshots of crack propagation in amorphous silica.

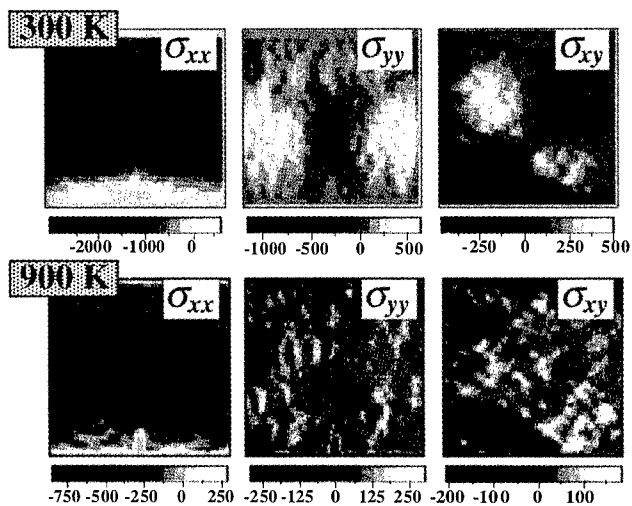


Figure 2. Local stress distributions during fracture in amorphous silica.

Crack tip positions are plotted in figure 3(a) as a function of time at 300 and 600K. Initially, the crack tip has a finite acceleration. After some time (indicated by arrows in fig. 3(a)), it reaches a terminal speed and then continues to propagate with nearly constant speed. The terminal speeds are found to be 1.40 km/s at 300K and 0.85 km/s at 600K. The terminal speed,  $V$ , at 300K is about half the calculated Rayleigh wave speed,  $V_R = 2.84$  km/s, and at 600K  $V \sim 0.33 V_R$  ( $V_R = 2.57$  at 600K).

Figure 3(b) shows the corresponding evolution of the  $\sigma_{xx}$  component of tensile stress. For both temperatures, the stress increases to a maximum value and then turns over and starts decreasing. Comparing fig. 3(a) and fig. 3(b), one can see that the turnover point in the stress curve corresponds to the crack reaching its terminal speed. This behavior is indicative of mechanical failure followed by brittle fracture.

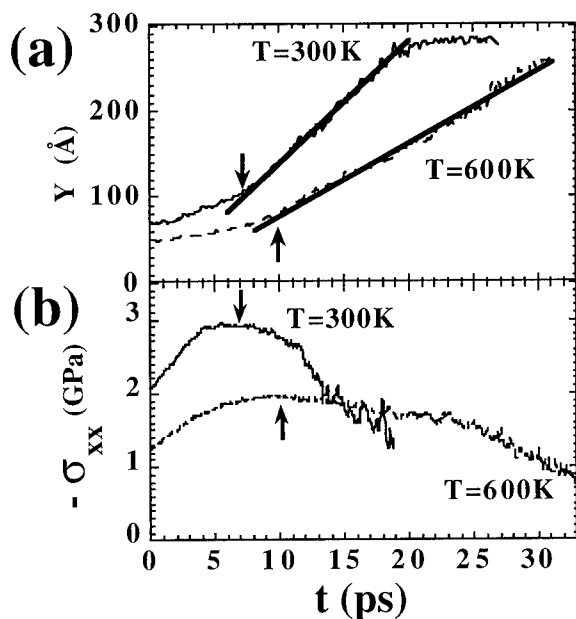


Figure 3. Dynamics of crack propagation: (a) crack-tip position; (b) calculated stress component,  $\sigma_{xx}$ .

We have also investigated the effects of different strain rates. From fig. 4 one can see that for all three temperatures the terminal speed increases roughly linearly with the strain rate. Extrapolating the linear fit to zero strain rate we get finite speeds of 1.1 km/s and 0.6 km/s at 300K and 600K, respectively, while at 900K the crack tip speed extrapolates to zero. This means that at 900K the notch cannot propagate without a finite strain rate providing continuous influx of energy.

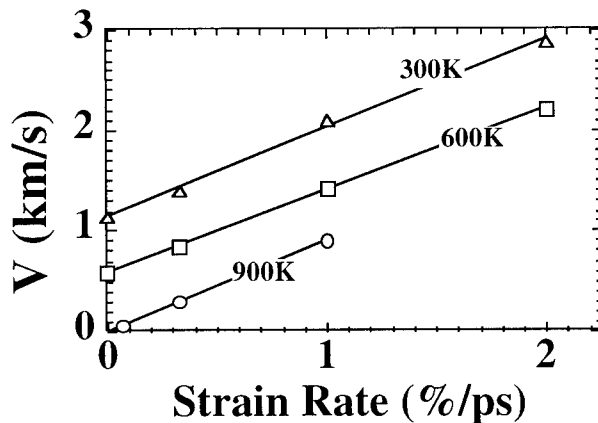


Figure 4. Terminal crack speed as a function of strain rate.

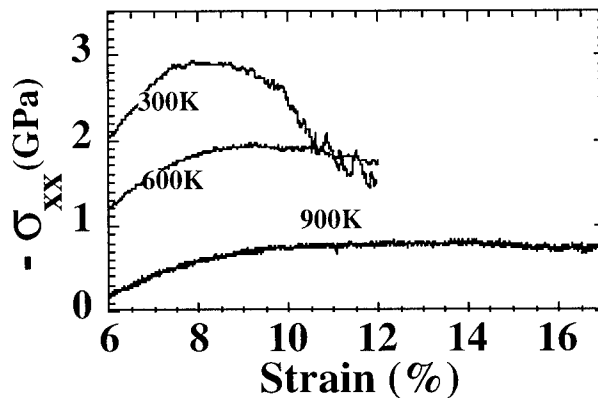


Figure 5. Stress-strain curves at 300, 600, and 900K

In figure 5 we compare the calculated stress-strain curves at three different temperatures. At 300K we observe typical brittle fracture: the stress reaches its maximum value of 2.9 GPa at a strain of 8% and then starts decreasing rapidly. The material is less brittle at 600K, and the mechanical failure occurs at a higher strain (9%) and lower stress (2.0 GPa). Finally, at 900K the stress simply saturates to a constant value of 0.8 GPa, which indicates that the material has become ductile.

## CONCLUSION

In conclusion, we have investigated fracture in vitreous silica at three temperatures. Brittle behavior is found at 300K and 600K; however, at 900K the material is essentially ductile. For brittle fracture, mechanical failure occurs when the stress reaches a critical value and the crack

reaches a terminal speed which is approximately half of the Rayleigh wave speed. In the ductile fracture regime at 900K, the stress saturates to a constant value and crack propagation cannot be sustained without constantly increasing the strain.

## ACKNOWLEDGMENTS

This work was supported by the U.S. Department of Energy (Grant No. DE-FG05-92ER45477), National Science Foundation (Grant No. DMR-9412965), Air Force Office of Scientific Research (Grant No. F 49620-94-1-0444), Army Research Office (Grant No. 36347-EL-DPS), Louisiana Education Quality Support Fund (LEQSF) (Grant No. LEQSF96-99-RD-A-10), and USC-LSU Multidisciplinary University Research Initiative (Grant No. F 49620-95-1-0452). Some of these simulations were performed on the 128-node IBM SP computer at Argonne National Laboratory. The computations were also performed on parallel machines in the Concurrent Computing Laboratory for Materials Simulations (CCLMS) at Louisiana State University. The facilities in the CCLMS were acquired with the equipment enhancement grants awarded by the Louisiana Board of Regents through LEQSF.

## REFERENCES

1. S. Susman, K. J. Volin, D. L. Price, M. Gridsditch, J. P. Rino, R. K. Kalia, and P. Vashishta, *Phys. Rev. B* **43**, 1194 (1991).
2. P. A. V. Johnson *et al.*, *J. Non-Cryst. Solids* **58**, 109 (1983).
3. *The Physics and Technology of SiO<sub>2</sub>*, edited by R. A. B. Devine (Plenum, New York, 1988).
4. R. Ochoa, T. P. Swiler, and Joseph H. Simmons, *J. Non-Cryst. Solids* **128**, 57 (1991).
5. P. Vashishta, R. K. Kalia, and J. P. Rino, *Phys. Rev. B* **41**, 12197 (1990).
6. W. Jin, R. K. Kalia, and P. Vashishta, *Phys. Rev. Lett.* **71**, 1387 (1993).
7. A. Nakano, R. K. Kalia, and P. Vashishta, *Phys. Rev. Lett.* **73**, 2336 (1994).
8. W. Jin, P. Vashishta, and R. K. Kalia, *Phys. Rev. B* **48**, 9359 (1993).
9. C. Meade, R. J. Hemley, and H. K. Mao, *Phys. Rev. Lett.* **69**, 1387 (1992).
10. M. Tuckerman, B. J. Berne, and G. J. Martyna, *J. Chem. Phys.* **97**, 1990 (1992).
11. K. Ravi-Chadar and W. G. Knauss, *International Journal of Fracture* **26**, 141 (1984).
12. A. Nakano, R. K. Kalia, and P. Vashishta, *Phys. Rev. Lett.* **75**, 3138 (1995).

## SLOW DYNAMICS AND GLASS-LIKE BEHAVIOR OF LIQUID CRYSTALS DISPERSED IN NANOPOROUS MEDIA

F.M. ALIEV and G.P. SINHA

Department of Physics and Materials Research Center, PO BOX 23343, University of Puerto Rico, San Juan, PR 00931-3343, USA

### ABSTRACT

We have investigated the dynamic behavior of liquid crystals (LC), which are not glass formers when in bulk form, confined in porous matrices with randomly oriented, interconnected pores as well as in parallel cylindrical pores with different pore sizes by photon correlation (time range: 20 ns-10<sup>3</sup>s) and dielectric spectroscopies (frequencies: 0.1 Hz-1.5GHz). We observed that in random pores (pore size is 10 nm and 100 nm) LC does not crystallize at temperatures about 25° C below bulk crystallization temperature and the non-Debye relaxational processes studied by both photon correlation and dielectric experiments were found not to be frozen. Slow relaxational process which does not exist in bulk LC and a broad spectrum of relaxation times (10<sup>-8</sup> – 10)s appear not only for LC in random pores but in cylindrical pores as well. However in matrices with random pores of 100 Å, glass-like behavior of slow mode ( $\tau > 1ms$ ) was observed. The relaxation time (determined in photon correlation experiment) of this slow process strongly increases when temperature decreases from 300 K up to 270 K varying from 0.2ms to 14 s and it's temperature dependence is described by the Vogel-Fulcher law.

### INTRODUCTION

The effect of confinement and the influence of a very developed interface in porous media on fluids has brought about great deal of achievements and controversies over the past years. The confinement of fluids can lead to such prominent changes in their properties, that even in the case of one component isotropic fluid the physical picture of these changes is far from well understanding [1-4]. This has stimulated intensive research of solids, liquids and liquid crystals confined in different geometries. A variety of new properties and phenomena were discovered and studied in these materials. Although there has been great success in the investigations of the physical properties of confined fluids [1-4] and liquid crystals [5-10], there are still open questions in the understanding of the influence of confinement on the dynamical behavior of both ordinary and anisotropic liquids. Confinement of fluids to porous media leads to changes in the phase and glass transition temperature and molecular mobility, and to a substantial broadening of the distribution of relaxation times [4].

In this paper we present some evidence of glass like behavior in confined and filled liquid crystals. These systems are anisotropic (at least at short scales) and heterogeneous materials characterized by a very developed interface. We performed dynamic light scattering and dielectric measurements in nematic LC confined in porous matrices. We have investigated pentylcyanobiphenyl (5CB) confined in porous glasses with interconnected randomly oriented pores, and in Anopore membranes with parallel cylindrical pores. The experiments show significant changes in physical properties of confined LC and suggest that there is some evidence for glass-like dynamical behavior, although bulk liquid crystal does not have glassy properties in both anisotropic and isotropic phases.

### EXPERIMENT

We performed photon correlation measurements using a 6328 Å He-Ne laser and the ALV-5000/Fast Digital Multiple Tau Correlator (real time) operating over delay times from 12.5 ns up to 10<sup>3</sup> s with the Thorn EMI 9130/100B03 photomultiplier and the ALV preamplifier. The depolarized component of scattered light were investigated. All dynamic light

scattering data we discuss below were obtained at the scattering angle  $\Theta=30^\circ$ . Measurements of the real ( $\epsilon'$ ) and the imaginary ( $\epsilon''$ ) parts of the complex dielectric permittivity in the frequency range 0.1 Hz - 3 MHz were carried out at different temperatures using a computer controlled Schlumberger Technologies 1260 Impedance/Gain-Phase Analyzer. For measurements in the frequency range 1MHz - 1.5GHz we used HP 4291A RF Impedance Analyzer with a calibrated HP 16453A Dielectric Material Test Fixture. We used matrices with randomly oriented, interconnected pores (porous glasses with average pore sizes of 10 nm and 100 nm) and parallel cylindrical pores (Anopore membranes with pore diameters of 20 nm and 200 nm). These matrices were impregnated with 5CB. The phase transition temperatures of bulk 5CB are  $T_{CN}=295$  K and  $T_{NI}=308.27$  K. We also used filled nematic liquid crystals [11]. This material is a suspension of small silica particles, which are about 10-17 nm in diameter and the concentration of these particles in LC was 2.8 % of the volume. These filled nematics were prepared by Dr. M. Kreuzer.

## PHOTON CORRELATION SPECTROSCOPY OF CONFINED AND FILLED NEMATIC LIQUID CRYSTALS

First of all from static light scattering experiments we obtained that the nematic - isotropic phase transition in 1000 Å random pores, 200 Å and 2000 Å cylindrical pores is smeared out, the transition is not as sharp as in the bulk LC, it occupies a finite temperature region, and the temperature of this transition is depressed compared to the bulk value. We determine nematic- isotropic phase transition temperatures for 5CB in pores as: 307.5 K (100 nm random pores), 307.6 K (200 nm cylindrical pores) and 307.0 K (20 nm cylindrical pores). In 10 nm pores we did not observe phase transition from ordered phase to the phase in which long range order is completely absent, or reversely from disordered phase to the phase with perfect long range orientational order.

In the dynamic light scattering experiment, one measures the intensity-intensity autocorrelation function  $g_2(t) = \langle I(t)I(0) \rangle / \langle I(0) \rangle^2$ . This function  $g_2(t)$  is related to dynamic structure factor  $f(q,t)$  of the sample by  $g_2(t) = 1 + k f(q,t)^2$ , where  $k$  is a contrast factor that determines the signal-to-noise ratio and  $q = 4\pi n \sin(\Theta/2)/\lambda$ , ( $n$  is the refractive index, and  $\Theta$  - the scattering angle). The spatial confinement has a strong influence on the relaxational properties of LC investigated in photon correlation experiments. Slow relaxational process which does not exist in the bulk phase appears in both confined and filled LC. Dynamic light scattering in bulk nematic liquid crystals is very well understood, and the main contribution to the intensity of scattered light is due to the director fluctuations. In the single elastic constant approximation, if we assume that the six Leslie coefficients have the same order of magnitude and are  $\sim \eta$  ( $\eta$  is an average viscosity), then the relaxation time is  $\tau = \eta/Kq^2$  and is of order of magnitude  $\sim 10^{-5}s$ . The corresponding decay function is exponential:

$$f(q,t) = a \cdot \exp(-t/\tau). \quad (1)$$

The difference between the dynamic behavior of bulk nematic multidomain 5CB and 5CB in 10 nm random pores as well as in cylindrical pores can be seen by comparing curves (1), (2) and (3) in Fig. 1. Slow relaxational process which does not exist in the bulk LC and a broad spectrum of relaxation times ( $10^{-8} - 10$ )s appear for 5CB in both random and cylindrical pores if LC is in anisotropic phase. It is clear from Fig. 1 that the relaxation processes in 5CB confined in the both matrices are highly nonexponential, as it is usually observed in glasses and glass-like systems [12]. The long time tail of relaxational process for 5CB in pores can not be described by using standard form of dynamical scaling variable ( $t/\tau$ ). It is reasonable for so slow dynamics and such a wide spectrum to use ideas [6, 13, 14] of activated dynamical scaling with the scaling variable  $x = \ln t / \ln \tau$ . We are not able to find the correlation function (or a superposition of correlation functions) which would satisfactorily and quantitatively describe the whole experimental data from  $t = 10^{-4}ms$  up to  $t = 10^6ms$ . However we found that in the time interval  $10^{-3}ms - 10^3ms$  (6 decades on the time scale) the decay function :

$$f(q,t) = a \cdot \exp(-t/\tau_1) + (1-a) \cdot \exp(-x^z), \quad (2)$$

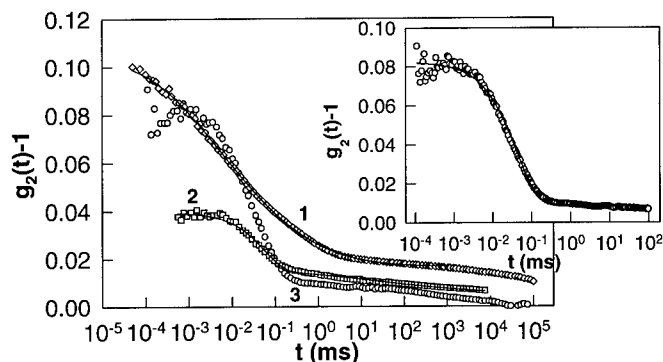


Figure 1: Intensity/intensity autocorrelation functions for 5CB: (1) - in 10 nm random pores,  $T=295.8$  K, (2) - in 20 nm cylindrical pores,  $T=306.9$  K, (3) - in 200 nm cylindrical pores at  $T = 307.3$  K. Inset - fitting for 5CB in 200 nm pores. Opened symbols-experimental data, solid lines-fitting.

where  $x = \ln(t/\tau_0)/\ln(\tau_2/\tau_0)$ , and in our case  $\tau_0 = 10^{-8}$  s provides suitable fitting for 5CB in narrow (10 nm and 20 nm pores). For 5CB in 10 nm random pores the second term in relationship (3) dominates, whereas for 20 nm pores the contribution from the first term is much more visible. The fitting parameters corresponding to curves (1) and (2) in Fig. 2 are: (2) -  $z=2.3$ ,  $\tau_2=0.04$  ms (exponential decay is neglected); (3) -  $\tau_1=0.07$  ms,  $z=3.6$ ,  $\tau_2=3$  s.

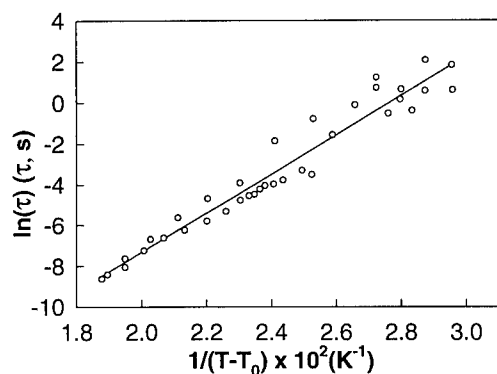


Figure 2: 5CB in 10 nm random pores. Relaxation time as function of inversed temperature.

The relaxation time of the slow process for 5CB in 10 nm pores strongly increases, as shown in Fig.2, when temperature decreases from 300 K up to 270 K varying from  $1.7 \times 10^{-4}$  s to 14 s in this temperature range.

The data analysis shows that the temperature dependence of the relaxation times for 5CB in 100 Å random pores, in the temperature interval (270-300) K, follows the Vogel-Fulcher law:  $\tau = \tau_0 \exp(B/(T - T_0))$  with parameters:  $\tau_0 = 1.4 \cdot 10^{-11}$  s,  $B = 847$  K and  $T_0 = 246$  K.

The dynamical behavior of 5CB confined in large pores (100 nm and 200 nm) was closer to the bulk behavior as we expected. However a slow decay, origin of which is still under question [1-5, 8], appears in the anisotropic phase (Fig.1). For LC confined in these matrices bulk-like relaxation of director fluctuations is observed. However, decay corresponding to



the director fluctuations in confined LC has features typical for relaxation in glass forming systems. It is not single but is stretched exponential. So the first term in the formula (2) should be replaced by  $(a \times \exp(-(t/\tau_2)^\beta))$ . The stretched exponential decay adequately describes the experimental data in the restricted time range  $t < 0.1$  s. The data presented in the inset of Fig. 1 have parameters  $\tau = 0.1$  ms and  $\beta = 0.8$ . In the nematic phase fast decay due to order parameter fluctuations vanishes and stretched exponential decay due to director fluctuations dominates.

We have also observed glass-like non-exponential relaxational process in filled LC. This material has some properties [11] common to LC confined in random pores. Both of them have disordered structure and highly developed solid-liquid crystal interface. A typical non-exponential relaxational process that we have observed in photon correlation experiments for filled LC is shown in Fig. 3. The relaxational curve in this figure is described by the

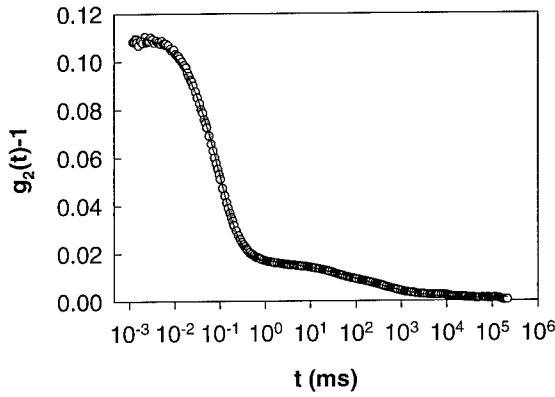


Figure 3: Intensity/intensity autocorrelation functions for filled LC,  $T = 355$  K. Opened circles-experimental data, solid lines-fitting.

superposition of single exponential decay functions with parameters:  $\tau_1=0.14$  ms,  $\tau_2=1.3$ s,  $\beta=0.34$ . We attribute the first decay to the director fluctuations of nematic liquid crystal. The origin of the second glass-like decay is not clear but it could be related to director dynamics in surface layers at aerosil - LC interface.

## LOW FREQUENCY GLASS-LIKE DIELECTRIC RELAXATION

The dielectric behavior of confined LC that we investigated is different from its bulk behavior. We observe at least three identified relaxational processes, low frequency process (1 Hz - 10 KHz) which does not exist in the bulk, a very clear process in MHz frequency range and the last one in the frequency range  $f > 30$  MHz. In Fig. 4 the low frequency process is illustrated for 5CB dispersed in 100 nm random pores at  $T = 13.0$  °C and 19.0 °C, which are below the bulk crystallization temperature. The data analysis shows that the all observed processes can not be described by Debye equation and there is a distribution of relaxation times. The best description of the experimental results is provided by Cole and Cole formula for a system which has more than one relaxational process:

$$\epsilon^* = \epsilon_\infty + \sum_{j=1} (\epsilon_{js} - \epsilon_\infty) / (1 + i2\pi f \tau_j)^{1-\alpha_j} - i\sigma / 2\pi\epsilon_0 f^n, \quad (3)$$

where  $\epsilon_\infty$  is the high-frequency limit of the permittivity,  $\epsilon_{js}$  the low-frequency limit,  $\tau_j$  the mean relaxation time, and  $j$  the number of the relaxational process. The term  $i\sigma / 2\pi\epsilon_0 f^n$  takes into account the contribution of conductivity  $\sigma$  and  $n$  is a fitting parameter ( $n \simeq 1$ ).

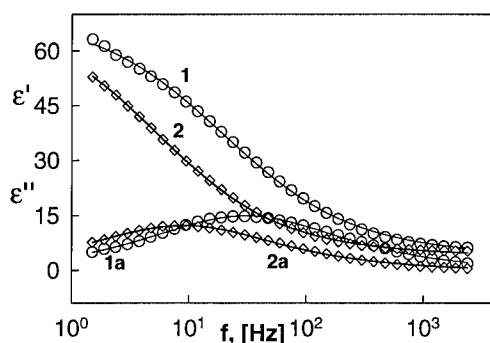


Figure 4: Low frequency dielectric relaxation of 5CB in 100 Å random pores,  $T = 19.0\text{ }^{\circ}\text{C}$  (1, 1a) and  $T = 13.0\text{ }^{\circ}\text{C}$  (2, 2a). 1,2 -  $\epsilon'$ , (1a, 2a) -  $\epsilon''$ . Open symbols - experimental data, solid lines - fitting.

The solid lines in Fig.4 represent the results of using formula (5) for the description of the observed dielectric spectra. The parameters describing these low frequency relaxation processes are for (1) -  $\tau = 0.005\text{ s}$ ,  $\alpha=0.3$  and for (2) -  $\tau = 0.02\text{ s}$ ,  $\alpha=0.3$ .

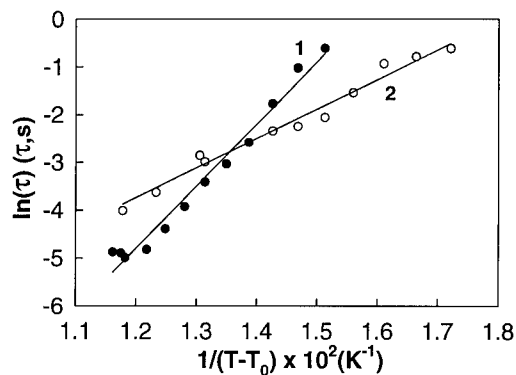


Figure 5: 5CB in 100 nm (1) and 10 nm (2) random pores. Low frequency dielectric relaxation time as function of inversed temperature. Symbols - experimental data, solid lines - fitting.

The data analysis shows that the temperature dependence of the relaxation times of the first (slow) relaxational process in both random pores, in the temperature interval (275-295) K for 1000 Å pores and in (275-305) K for 10 nm pores (Fig.5), follow the Vogel-Fulcher law, and this is a relaxation of interfacial polarization not due to Maxwell-Wagner effect but rather due to a formation of the surface layers with polar ordering on the pore wall [9].

## CONCLUSION

The photon correlation and dielectric experiments show significant changes in the physical properties of liquid crystals confined in porous media. We found that the relaxational processes in confined LC are highly non-exponential and they are not frozen even about  $20^{\circ}\text{C}$  below bulk crystallization temperature. The temperature dependence of relaxation times of

the slow process is described Vogel-Fulcher law. The slow dynamics in the anisotropic phase of confined LC and the extremely wide spectrum of relaxation times still remain unexplained.

#### ACKNOWLEDGEMENTS

This work was supported by US Air Force grant F49620-95-1-0520 and NSF grant OSR-9452893.

#### REFERENCES

1. Molecular Dynamics in Restricted Geometries, ed. by J. Klafter and J.M. Drake (Wiley, New York, 1989).
2. J. Schuller, Yu.B. Mel'nichenko, R. Richert, and E.W. Fischer, *Phys. Rev. Lett.* **73**, 2224 (1994).
3. M. Arndt and F. Kremer in: Dynamics in Small Confining Systems II, edited by J.M. Drake, J. Klafter, R. Kopelman, S.M. Troian, (Mater. Res. Soc. Proc. 363, Pittsburgh, PA 1995), p. 259-263.
4. Yu. Mel'nichenko, J. Schuller, R. Richert, B. Ewen and C.-K. Loong, *J. Chem. Phys.* **103**, p. 2016 (1995).
5. G.P. Crawford and S. Zumer, Liquid crystals in complex geometries, Taylor & Francis, London, 1996).
6. X.-I. Wu, W.I. Goldburg, M.X. Liu, and J.Z. Xue, *Phys. Rev. Lett.*, **69**, 470, (1992).
7. T. Bellini, N.A. Clark, D.W. Schaefer, *Phys. Rev. Lett.*, **74**, 2740, (1995).
8. F.M. Aliev and V.V. Nadtotchi in: Disordered Materials and Interfaces, edited by H.Z. Cummins, D.J. Durian, D.L. Johnson, and H.E. Stanley, (Mater. Res. Soc. Proc., **407**, Pittsburgh, PA, 1996), p. 125-130.
9. F.M. Aliev and G.P. Sinha in: Electrically based Microstructural Characterization, edited by R.A. Gerhardt, S.R. Taylor, and E.J. Garboczi (Mater. Res. Soc. Proc. 411, Pittsburgh, PA 1996), p. 413-418.
10. S.R. Rozanski, R. Stanarius, H. Groothues, and F. Kremer, *Liquid Crystals* **20**, p. 59 (1996).
11. M. Kreuzer and R. Eidenschink in Liquid crystals in complex geometries, edited by G.P. Crawford and S. Zumer (Taylor & Francis, London, 1996), p. 307-324.
12. J.C. Phillips, *Rep. Prog. Phys.* **59**, p. 1133 (1996).
13. D. Huse, *Phys. Rev. B.* **36**, p. 5383 (1987).
14. M. Randieria, J. Sethna, and R.G. Palmer, *Phys. Rev. Lett.* **54**, p. 1321 (1985).

## SIMULATION OF PRESSURE EFFECTS ON GLASSES

Y. KOGURE, M. DOYAMA

Teikyo University of Science & Technology, Uenohara, Yamanashi 409-01, Japan, kogure  
ntu.ac.jp

### ABSTRACT

Glass transition and effects of pressure and shear stress on atomic configuration are investigated by means of molecular dynamics simulation. An embedded atom method potential is used for the atomic interaction. A model crystal for Cu is melted and quenched to realize the glass state. Atomic configuration in the glass is examined through the radial distribution function. External stress is applied and displacement of atoms is monitored to investigate the mechanism of mechanical relaxation. Larger displacement of atoms is observed under a shear stress.

### INTRODUCTION

In a glass state, especially at lower temperatures, material shows anomalous behavior in mechanical and in thermal properties. The resonance absorption of sound at very low temperature ( $< 1\text{K}$ ) and the mechanical relaxation at higher temperatures ( $10 - 30\text{ K}$ ) are characteristic phenomena of glass. These are considered to be due to the motion of atoms through the potential barriers by the quantum mechanical and the thermal activation processes. The purpose of the present study is to investigate the atomic configuration responsible to the double well potential, which may be formed on the course of glass transition. As a model material copper is chosen because the atomic interaction is expressed by a simple function.

### METHOD OF SIMULATION

The atomic interaction in metals has non-central characters due to the existence of conduction electrons, and can be expressed by a  $n$ -body potential. Recently, the embedded atom method (EAM) potentials have been developed by many authors[1-3]. An EAM potential for copper atoms developed by the present authors [4,5] are used for the simulation. The potential function is expressed as

$$E_{\text{tot}} = \sum_i F(\rho) + \frac{1}{2} \sum_{ij} \phi(r_{ij}), \quad (1)$$

$$F(\rho) = D\rho \ln \rho, \quad \rho = \sum_{j \neq i} f(r_{ij}). \quad (2)$$

where,  $F(\rho)$  is the embedding energy for  $i$ -th atom,  $\rho$  is the electron density, and  $r_{ij}$  is the distance between  $i$ -th and  $j$ -th atom. The functions  $\phi(r)$  and  $f(r)$  are

$$\phi(r) = A(r_c - r)^2 \exp(-c_1 r), \quad (3)$$

$$f(r) = B(r_c - r)^2 \exp(-c_2 r), \quad (4)$$

where,  $r_c$  is a cut off distance of the potential. These functions contain five parameters  $A, B, C_1, C_2$ , and  $D$ . They are determined by fitting the potential to experimental values of physical properties for copper. The determined values are  $A = 789.92[\text{eV}]$ ,  $B = 0.037794$ ,  $C_1 = 7.8893r_0$ ,  $C_2 = 0.026582$ , and  $D = 14.005\text{eV}$ , where  $r_0$  is the nearest neighbour distance.

As an initial configuration atoms are arranged in the fcc structure, and a velocity with random distribution is given to each atom to melt the crystal. The mean value of the velocity  $v_m = \sqrt{\langle v_i^2 \rangle}$  is related to reference temperature  $T^*$  as

$$mv_m = 3k_B T^*, \quad (5)$$

where,  $m$  is the atomic mass and  $k_B$  is the Boltzmann's constant. The time interval  $\Delta t$  for the molecular dynamics was chosen to be  $5 \times 10^{-15}\text{sec}$ . An initial velocity corresponds to 2000 K was given to atoms in the crystal. Judging from the velocity distribution the liquid state was stabilized after 3000 MD steps. Then the system was quenched by setting the velocity of all atoms to be 0, and the molecular dynamics simulation was restarted to relax the quenched liquid, and quasi-equilibrium configuration for glass was obtained.

## RESULTS AND DISCUSSION

The radial distribution function (RDF) for a crystal, a liquid and a glass state are shown in Figure 1. It is seen that the sharp peaks in the RDF of the crystal state are broadened in the liquid state. The first peak of the liquid state becomes narrower and the second peak split in the RDF of glass state. The split second peak is a characteristic feature of the RDF of metallic glass and it is observed in amorphous  $\text{Ni}_{76}\text{P}_{24}$  experimentally, and in random closed pack model[6].

After a glass state was realized a effect of external stress was investigated. The stress was applied by giving a finite displacement to each atom according to the strain, and the atomic system was relaxed. The displacement of individual atom from the original position under the typical stress modes was calculated. Distribution of the magnitude of displacement under four kinds of stress mode is summarized in Figure 2. Case (a) and case (b) correspond to the positive and the negative pressure, respectively, which produce isotropic compression and expansion of the atomic system. Case (c) and (d) correspond to pure share stresses with no volume changes. A marked difference between hydrostatic pressure and share stress is seen. Under the hydrostatic pressure only a small number of atoms move more than  $0.2 \text{ \AA}$ . On

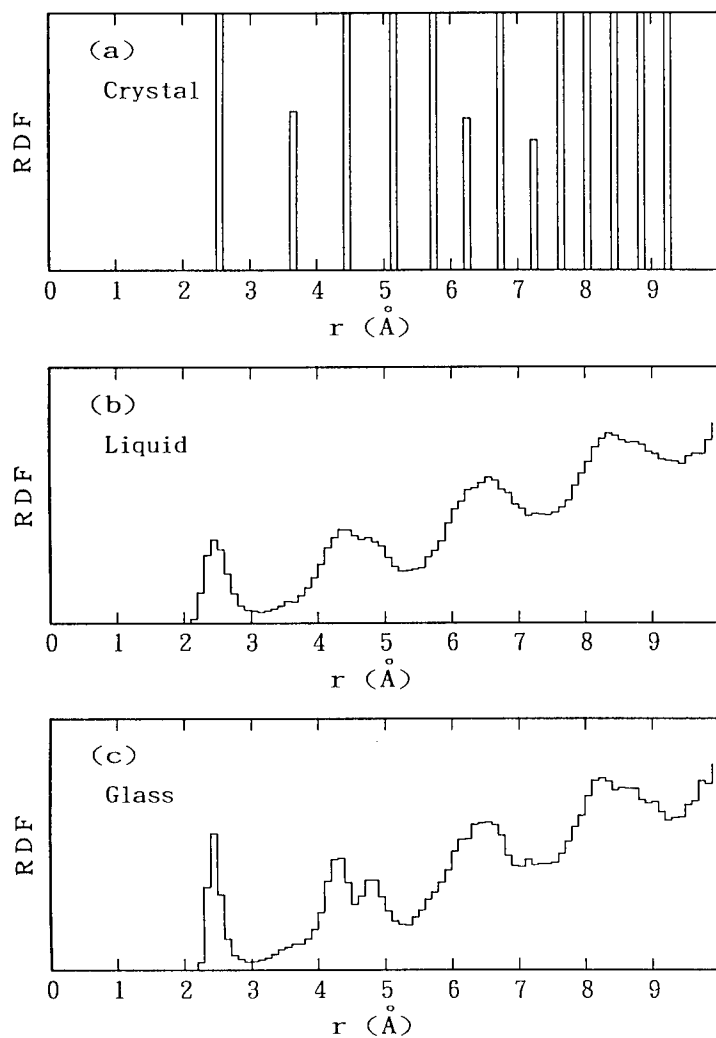


Fig. 1. Radial distribution function. (a) crystal; (b) liquid; and (c) glass state of copper.

the other hand, larger displacement of appreciable number of atoms is observed under the shear stress.

Figure. 3 shows atoms which moved more than  $0.3 \text{ \AA}$ . It is seen that the largely displaced atoms are randomly distributed in the glass.

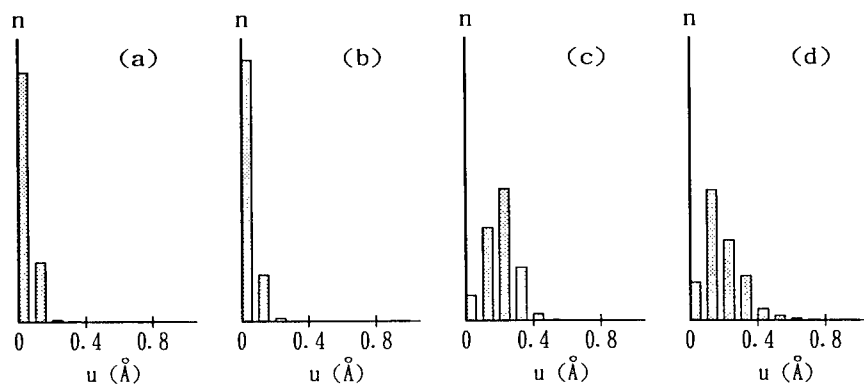


Fig. 2. Distribution of atomic displacement under the applied stress. (a) strain components are  $\epsilon_{xx} = \epsilon_{yy} = \epsilon_{zz} = -0.05$ , (b)  $\epsilon_{xx} = \epsilon_{yy} = \epsilon_{zz} = 0.05$ , (c)  $\epsilon_{xy} = 0.05$ , (d)  $\epsilon_{xx} = 0.1$ ,  $\epsilon_{yy} = \epsilon_{zz} = -0.05$ .

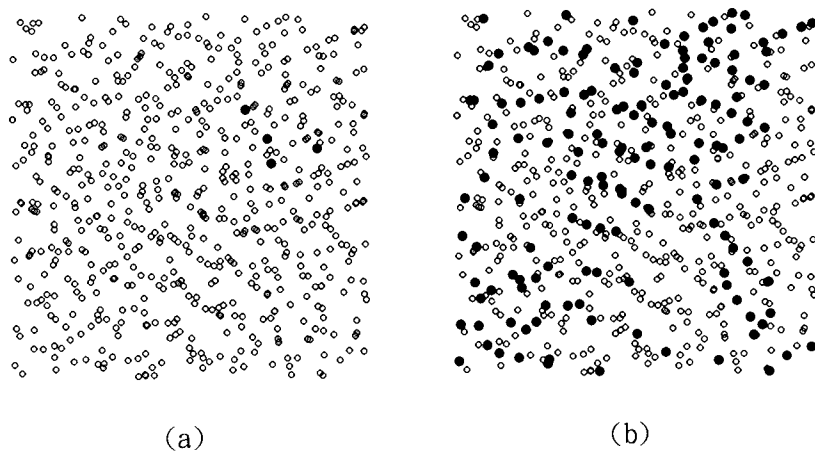


Fig. 3. Position of atoms in a glass projected on a plane. Solid circles show the atoms moved more than 0.3 Å under stresses, (a) hydrostatic pressure, (b) pure shear stress.

Although the present simulation is purely mechanical and is not directly related with the thermal activation process, above results seem to demonstrate the motion of atoms through the mechanical relaxation. A typical example of mechanical relaxation is the Snoek peak due to the point defects with non-spherical strain fields, which can be treated as the elastic dipole. The elastic dipole interacts with the shear stress and changes its orientation, which accompanies the motion of atoms. The response of the elastic dipoles to the stress of a sound wave through the thermal activation process causes mechanical loss, and an internal friction peak is observed. The internal friction peaks in glasses are frequently observed in a variety of materials, and they have been analysed on the basis of the theory of point defect relaxation peak, where widely distributed relaxation time is assumed.

Observed motion of atoms in the present simulation may be due to the interaction of the elastic dipole with the shear stress. The change of the potential energy of individual atom is especially important, because it relates with the thermal activation process.

More detailed study on the motion of atoms may reveal the fundamental mechanism of the relaxation in glasses.

## REFERENCES

1. M.S. Daw and M.I. Baskes; Phys. Rev. B, **29** (1984) 6443.
2. M.W. Finnis and J.E. Sinclair; Phil. Mag. A, **50** (1984) 45.
3. D.J. Oh and R.A. Johnson; J. Mater. Sci., **3** (1988) 471.
4. Y. Kogure, K. Kunitomi, Y. Nakamura and M. Doyama; MRS Symp. Proc. **407** (1996) pp. 185-190.
5. Y. Kogure, H. Masuyama and M. Doyama; MRS Symp. Proc. **407** (1996) pp. 245-250.
6. R. Zallen; *The Physics of Amorphous Solids* (John Wiley and Sons, New York, 1983) pp. 73-85.



# SEPARATION OF DIFFUSIVE JUMP MOTION AND TRAPPED MOTION OF ATOMS IN A GLASS FORMING PROCESS VIA MOLECULAR DYNAMICS SIMULATION

J. MATSUI, M. FUJISAKI AND T. ODAGAKI

Department of Physics, Kyushu University, Fukuoka 812-81, Japan

## ABSTRACT

We have carried out the molecular dynamics (MD) simulation for a binary soft-sphere system and calculated the self part of the generalized susceptibility  $\chi_s(q, \omega)$  at various temperatures. At higher temperatures in liquid state, only one peak appears in the imaginary part of  $\chi_s$ , which tends to split into two peaks, the so-called  $\alpha$ - and  $\beta$ - peaks, as the temperature is reduced. The temperature dependence of the peak frequency is well described by the Vogel-Fulcher law for the  $\alpha$ - peak, and the peak frequency does not change much for the  $\beta$ - peak. We have also measured the trajectory volume of a tagged atom  $V(t)$ , which is related to the dynamical order parameter, the "generalized capacity", in structural glass transitions recently proposed by J. F. Douglas. These results show the transition temperature which is in good agreement with that determined by the trapping diffusion model.

## INTRODUCTION

The viscosity of supercooled fluids increases gradually as the temperature decreases, which can be well fitted by the empirical law, so-called Vogel-Fulcher law, known in glass blowers. In a microscopic point of view, solidification is thought to be a transformation of the diffusive random motions of atoms in the liquid state into the localized oscillatory motions in the solid state. Such a transformation of atomic motion occurs gradually in glass forming processes, while it occurs drastically at the melting point in crystallization. Furthermore, the structure is disordered in supercooled liquids and glasses, while periodic in crystals. Therefore, the localization of atomic motion seems to be a good criterion for defining such transition.

The aim of the present paper is to investigate how the dynamics transforms in vitrification process and to quantify the localization of atomic motion which indicates the order of transition. First, we calculate the self part of the generalized susceptibility  $\chi_s(q, \omega)$  via the molecular dynamics (MD) simulation, and to see how the characteristic time scale of the dynamics changes in the vicinity of the transition point. Next we try to measure the trajectory volume  $V(t)$ , namely the first visit volume where the tagged atom has passed during the time  $t$ , here the re-visited volume where the tagged particle had visited already between the time  $t = 0$  and  $t$  is not counted more than once. In liquid state, the trajectory volume  $V(t)$  in the long time  $t$  increases in proportion to  $t$ , where atoms move randomly without localization. On the other hand,  $V(t)$  in solid state, both crystals and glasses, takes a constant value at large  $t$ , where the atomic motion is completely localized in a certain area. According to J. F. Douglas' proposal in Ref. 1, the long time limit of  $V(t)/t$ , which

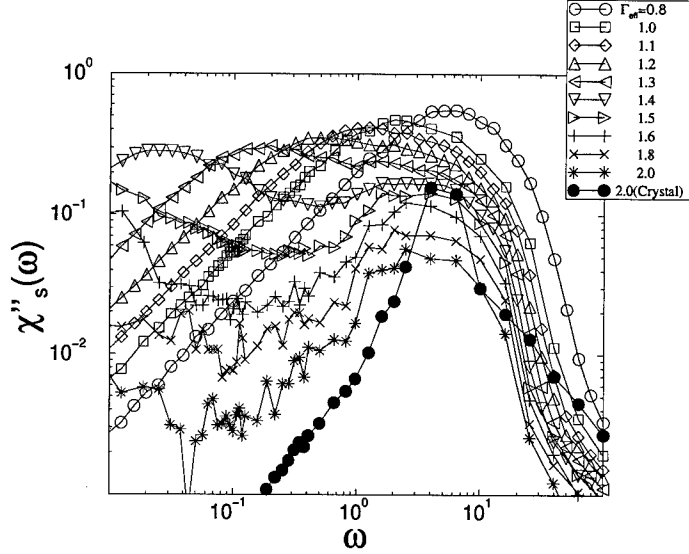


Figure 1: The frequency dependence of  $\chi''_s(q, \omega)$  at different temperature in liquid states, supercooled states and glassy states at wave number  $q = 2\pi/\sigma_{11}$  which corresponds to the inverse interparticle distance. All the data are averaged for two species.

is called the "generalized capacity"  $C(T)$  as the function of temperature  $T$ , is one of the dynamical order parameter pointing such transition from a structurally disordered liquid state ( $C(T) > 0$ ) to a structurally disordered solid (glass) state ( $C(T) = 0$ ). We show the analysis based on the "generalized capacity" and deduce the glass transition point.

## MODEL FOR SIMULATION

We briefly present the model for MD simulation: we use a binary soft-sphere system, the total number of particles  $N (= N_1 + N_2) = 500$ , the ratio of mixture  $N_1/N_2 = 1$ , radius  $r_1/r_2 = 1.2$  and mass  $m_1/m_2 = 2.0$ . The interparticle potential is purely repulsive,

$$\phi_{\alpha\beta}(r) = \epsilon \left( \frac{\sigma_{\alpha\beta}}{r} \right)^{12}; \alpha, \beta = 1, 2, \quad (1)$$

where  $\sigma_{\alpha\beta} = r_\alpha + r_\beta$ .

All parameters can be effectively reduced to one parameter,

$$\Gamma_{eff} = (N/V) \sigma_{eff}^3 (\epsilon/k_B T)^{\frac{1}{4}}, \quad (2)$$

where  $\sigma_{eff}^3 = (\sigma_{11}^3 + \sigma_{12}^3 + \sigma_{21}^3 + \sigma_{22}^3)/4$ .

The simulation starts from a liquid state at  $\Gamma_{eff} = 0.8$  by using the constant temperature simulation. Next, the system is quenched to each temperature for measurement and

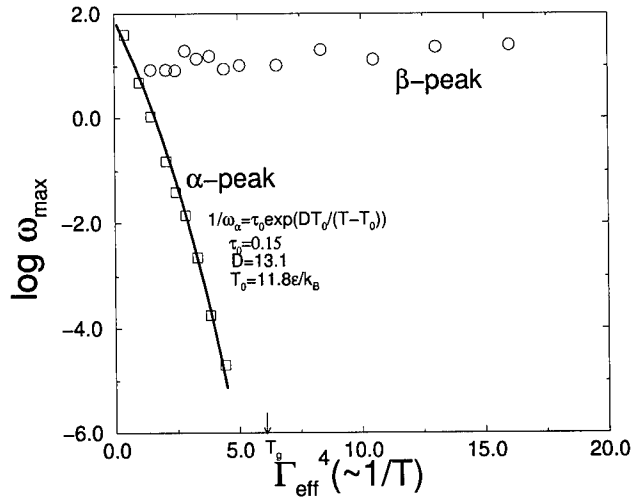


Figure 2: The temperature dependence of peak frequency. Squares and circles represent for the  $\alpha$ - and  $\beta$ -peaks respectively. The fitted curve for  $\alpha$ -peak is drawn by solid curve, which is well described by Vogel-Fulcher law:  $\omega_{max} = \omega_0 \exp[-DT_0/T - T_0]$ . The fitted values are  $\omega_0 = 0.15$ ,  $D = 13.1$ ,  $T_0 = 11.8\epsilon/k_B$  and  $\Gamma_0 = 1.89$ .

annealed. Then we start the calculation of the generalized susceptibility and the trajectory volume by using the micro canonical simulation.

In previous works, it has been shown that the freezing point and the glass transition point are at  $\Gamma_{eff} = 1.15$  and  $1.58$ , respectively[2]. It has also been argued that the mode-coupling critical point and the crossover temperature are at  $\Gamma_{eff} = 1.32$  and  $1.45$ , respectively[3].

## THE SELF PART OF THE GENERALIZED SUSCEPTIBILITY

To calculate the self part of the generalized susceptibility  $\chi(q, \omega)$ , we have used the following equation [2],

$$\chi_s(\mathbf{q}, \omega) = 1 + \frac{i\omega}{T_{total}} \left\langle \sum_j \int_0^{T_{total}} dt_0 e^{i\mathbf{q} \cdot \mathbf{r}_i(t_0)} e^{-i\omega t_0} \int_0^{t_0} dt e^{-i\mathbf{q} \cdot \mathbf{r}_j(t)} e^{i\omega t} \right\rangle_i \quad (3)$$

where  $\mathbf{r}_i(t)$  is the position of the  $i$  th atom at time  $t$ , which is computed in MD simulation.  $T_{total}$  is the total time steps of the integration in Eq.(3), which has to be sufficiently large. In our calculation we have integrated up to 1,000,000 time steps, which corresponds to the order of 10 nano second. The merit of this method is that the calculation works without storing the data of  $\mathbf{r}_i(t)$  in the previous time steps. Therefore, it does not require a huge memory.

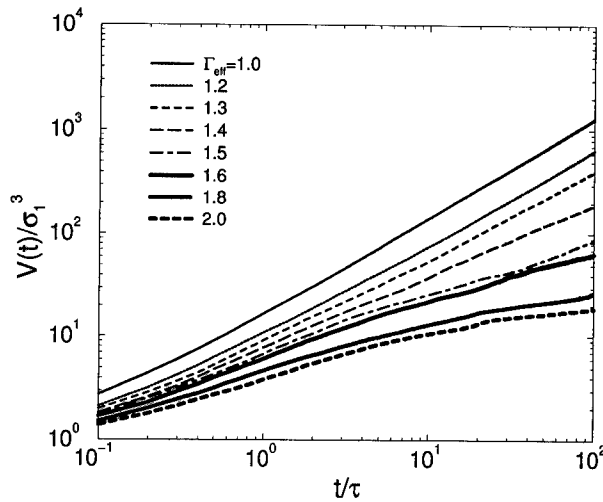


Figure 3: The trajectory volume of the tagged particle as a function of time  $t$  at various temperatures.

In Fig.1 we show the frequency dependence of  $\chi_s''(q, \omega)$  at various temperatures [4]. At high temperatures ( low  $\Gamma_{eff}$  ) only one peak appears in  $\chi_s''(q, \omega)$ , which corresponds to the random motion of atoms in the liquid state. When the temperature is reduced, the so-called  $\alpha$ -peak tends to separate out from the main peak at  $\Gamma_{eff} \approx 1.2$ , and to shift to lower frequencies. It means that the one kind of atomic motion corresponding to the  $\alpha$ -peak, which is thought to be the diffusive jump motion, becomes slow down with decreasing the temperature.

In Fig. 2 we plot the peak frequencies of both the  $\alpha$ - and  $\beta$ - peaks against the inverse temperature. For the  $\alpha$ -peak, it is well fitted by the Vogel-Fulcher law  $\sim \exp[DT_0/T - T_0]$  as represented by solid line in Fig. 2.  $T_0$  is called the Vogel-Fulcher temperature where the viscosity and the relaxation time seem to diverge asymptotically, and  $D$  implies the fragility. From the fitted curve, we estimate these values,  $T_0 = 11.8\epsilon/k_B$ ,  $\Gamma_0 = 1.89$  and  $D = 13.1$ . The peak frequency of the  $\alpha$ -peak can be supposed to be the inverse relaxation time, the diffusive jump motion of atoms is the slowest microscopic motion in supercooled state. On the other hand, for the second peak called the  $\beta$ -peak appearing in higher frequencies, the peak position does not move much. It is thought to be the localized oscillatory motions which can be roughly approximated by harmonic oscillators. Therefore, the time scale of the microscopic dynamics does not change under quenching.

Now, it is clear that the vitrification is a gradual solidification where the localization of the atomic motion becomes significant more and more, then the jump motion from a trap to a trap takes place rarely and its mean time scale becomes longer. At the lowest temperature in the rigid solid state, it becomes out of our time window, thus, the localized motion is only observed.

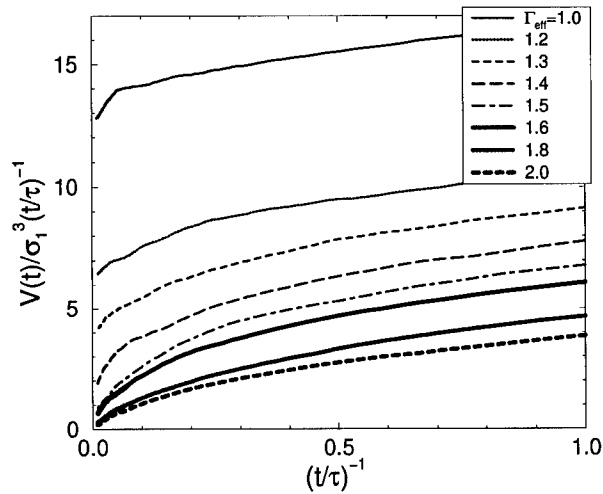


Figure 4: The trajectory volume divided by time  $t$  against the inverse time.

In the following section, we try to quantify the localization of the atomic motion as a dynamical order parameter for disordered solidification.

### TRAJECTORY VOLUME OF A TAGGED ATOM

To measure the trajectory volume  $V(t)$ , we consider the small cubes which is divided the simulation cell into  $64 \times 64 \times 64$ , for the both inside and outside of the boundary, and each cube will be marked when the center of mass of the tagged particle visit in time between  $t = 0$  and  $t$ . Then, the summation of the marked cubes is equal to  $V(t)$ .

In Fig. 3 we show the time dependence of  $V(t)$  at various temperatures, where the data are averaged over all the particles. The long time behavior of  $V(t)$  is asymptotically proportional to  $t$  for higher temperatures  $\Gamma_{eff} = 1.0$  and  $1.2$ , in power law  $\sim t^\delta$  ( $0 < \delta < 1$ ) in lower temperatures  $\Gamma_{eff} = 1.3 \sim 1.6$ , and constant in lowest temperature  $\Gamma_{eff} = 1.8 \sim 2.0$ .

We plot  $V(t)/t$  against the inverse time  $t$  in Fig. 4. From the long time limit  $1/t \rightarrow 0$ , we estimate the "generalized capacity"  $C(T)$ , whose temperature dependence are plotted in Fig. 5. As the temperature is reduced,  $C(T)$  decreases gradually and finally vanishes at a lower temperature. Although our time window is limited, it is clearly seen that the transition occurs near  $\Gamma_{eff} = 1.58$ . The glass transition temperature of our model is  $\Gamma_{eff} = 1.58$ , which has been determined by comparison of the non-Gaussian parameter obtained by MD simulation to that of the trapping diffusion model. Therefore, the glass transition defined by the "generalized capacity"  $C(T)$  is in good agreement with that determined by the trapping diffusion model [5,6].

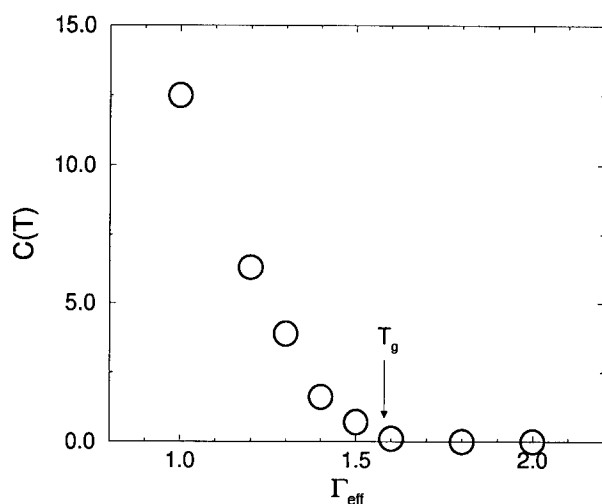


Figure 5: The temperature dependence of the generalized capacity.

## SUMMARY

We have presented two calculations to quantify the gradual transition from a supercooled liquid to an amorphous solid, one is the generalized susceptibility and the other is the generalized capacity. As we have seen in the results of the generalized susceptibility, while the system shows a similar localized atomic motion in the both crystalline state and glass state, each path of the transition is quite different. The generalized capacity  $C(T)$  has been obtained by the trajectory volume measurement, and the transition temperature has been estimated at  $\Gamma_{\text{eff}} = 1.58$  within this approximation. The value is in quite good agreement with the analysis based on the trapping diffusion model.

## ACKNOWLEDGEMENT

This work was supported in part by the grants from the Ministry of Education, Science, Sports and Culture.

## REFERENCES

1. J. F. Douglas, Computational Material Science **4**, 292 (1995).
2. J. Matsui, H. Miyagawa, T. Muranaka, K. Uehara, T. Odagaki and Y. Hiwatari, Mol. Sim. **12**, 305 (1994); J. Matsui, T. Odagaki and Y. Hiwatari, Phys. Rev. Lett. **73**, 2452 (1994).

3. J. L. Barrat and A. Latz, J. Phys. : Cond. Matt. **2** 4289 (1990).
4. M. Fujisaki, J. Matsui and T. Odagaki, Proceedings of YKIS'96, to be published.
5. T. Odagaki, J. Matsui and Y. Hiwatari, Mat. Res. Soc. Symp. Proc. vol. 367 (1995), 337; T. Odagaki, J. Matsui and Y. Hiwatari, Physica A**204** (1994), 464; T. Odagaki and Y. Hiwatari, J. Phys.: Cond. Matt. **3**, 5191 (1991).
6. T. Odagaki, Phys. Rev. Lett. **75**, 2452 (1995).

**Part IV**

**Contrasting Metallic, Ionic,  
Bio, and Polymer Systems**



## CRYSTALLIZATION PATHWAY IN THE BULK METALLIC GLASS $\text{Zr}_{41.2}\text{Ti}_{13.8}\text{Cu}_{12.5}\text{Ni}_{10}\text{Be}_{22.5}$

S. SCHNEIDER<sup>†</sup>, P. THIYAGARAJAN<sup>‡</sup>, U. GEYER<sup>†</sup> and W.L. JOHNSON<sup>\*\*\*</sup>

<sup>†</sup>I. Phys. Institut and SFB 345, Universität Göttingen, 37073 Göttingen, Germany

<sup>‡</sup>Argonne National Laboratory, Argonne, IL 60439, USA

<sup>\*\*\*</sup>California Institute of Technology, Pasadena, CA 91125, USA

### Abstract

A new family of multicomponent metallic alloys exhibits an excellent glass forming ability at moderate cooling rates of about 10K/s and a wide supercooled liquid region. These glasses are eutectic or nearly eutectic, thus far away from the compositions of competing crystalline phases. The nucleation of crystals from the homogeneous amorphous phase requires large thermally activated composition fluctuations for which the time scale is relatively long, even in the supercooled liquid. In the  $\text{Zr}_{41.2}\text{Ti}_{13.8}\text{Cu}_{12.5}\text{Ni}_{10}\text{Be}_{22.5}$  alloy therefore a different pathway to crystallization is observed. The initially homogeneous alloy separates into two amorphous phases. In the decomposed regions, crystallization probability increases and finally polymorphic crystallization occurs. The evolution of decomposition and succeeding primary crystallization in the bulk amorphous  $\text{Zr}_{41.2}\text{Ti}_{13.8}\text{Cu}_{12.5}\text{Ni}_{10}\text{Be}_{22.5}$  alloy have been studied by small angle neutron. Samples annealed isothermally in the supercooled liquid and in the solid state exhibit interference peaks indicating quasiperiodic inhomogeneities in the scattering length density. The related wavelengths increase with temperature according to the linear Cahn-Hilliard theory for spinodal decomposition. Also the time evolution of the interference peaks in the early stages is consistent with this theory. At later stages, X-ray diffraction and transmission electron microscopy investigations confirm the formation of nanocrystals in the decomposed regions.

### Introduction

A unique family of multicomponent metallic glasses exhibits an excellent glass forming ability and a wide supercooled liquid region [1,2]. Their high thermal stability against crystallization has opened for the first time the opportunity to investigate thermodynamic and atomic transport properties in the supercooled liquid state of a metal [3-5]. Since these glasses exhibit high reduced glass temperatures, nucleation of crystalline phases from the homogenous multicomponent systems is suppressed to a great extent. Instead, their thermal stability is probably limited by alternative processes. We have reported phase separation with succeeding polymorphic nanocrystallization in the decomposed regions occurring in  $\text{Zr}_{41.2}\text{Ti}_{13.8}\text{Cu}_{12.5}\text{Ni}_{10}\text{Be}_{22.5}$  earlier [6,7]. This paper gives additional information on small-angle neutron scattering (SANS) investigations of the

time- and temperature evolution of the decomposition process. In particular, we show that above a critical temperature crystallization behavior changes significantly.

## Experimental

Amorphous samples were prepared from a mixture of the pure elements by induction melting on a water-cooled silver boat under Ti gettered Ar atmosphere. The ingots were remelted in a silica tube with an inner diameter of 10mm and then quenched with a cooling rate of about 10K/s. For the SANS investigations disks with a thickness of 2.7mm were cut from the these rods and isothermally annealed at temperatures between 608K and 673K for different times. The SANS measurements were carried out at the Intense Pulsed Neutron Source at Argonne National Laboratory.

## Results and Discussion

Figure 1 shows SANS data of an as prepared  $\text{Zr}_{41.2}\text{Ti}_{13.8}\text{Cu}_{12.5}\text{Ni}_{10}\text{Be}_{22.5}$  alloy and samples isothermally annealed for different times at 613K. The data for the as- prepared sample only depict background scattering, for the aged ones broad maxima appear. For early stages a maximum of scattering intensity is observed at  $q=0.05\text{\AA}^{-1}$ , indicating spatially correlated chemical inhomogeneities in the amorphous state.

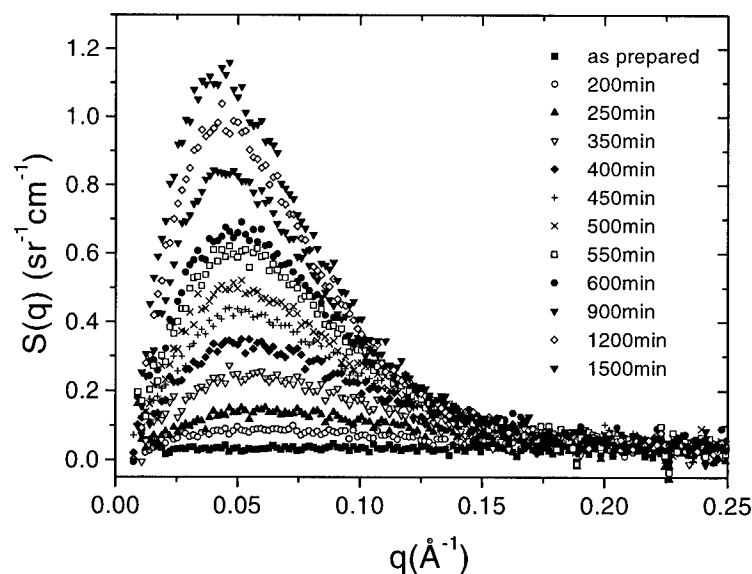


Fig. 1: SANS data of the  $\text{Zr}_{41.2}\text{Ti}_{13.8}\text{Cu}_{12.5}\text{Ni}_{10}\text{Be}_{22.5}$  alloy aged at 613K for different times.

The wavelength corresponding to the maximum intensities is about 125Å. The position of  $q_{\max}$  shifts slightly towards smaller values with increasing annealing duration suggesting a coarsening of the chemical inhomogeneities during isothermal heat treatment. We assume a decomposition process being responsible for the scattering contrast [7]. From estimations of the increase of scattering intensity and  $^{62}\text{Ni}$  isotope experiments we conclude that the initial increase is mainly associated with a decomposition process of Ti and Be atoms [8]. Two different time laws are involved in the process (Fig. 2). First, the scattering cross section for a constant  $q$  value grows exponentially during annealing, and the interference peak shifts slightly to lower  $q$ . In the very early stages of decomposition the slowly rising exponential time law mimics an incubation time of about 150min at 613K. During that time no changes in structure or composition are observed by SANS or thermal analysis [7]. Then the scattered intensity increases very rapidly. Later a much slower process overtakes control on the increase of scattering cross section. It is not clear yet whether the time dependence for the later stages is also exponential or a power law.

Cahn's theory of spinodal decomposition gives such an exponential growth law [9] but does not predict a shift of the interference peak to lower  $q$  with increasing time. Such a behavior is proposed in [10]. During phase separation, composition and short-range atomic order [11] in at least one of the decomposed regions approach those of a competing crystalline phase and the nucleation probability increases rapidly. Due to the exponential time law of decomposition and the rapid increase of nucleation probability with composition and structural changes, the onset of polymorphic nucleation of nanocrystals in the Ti-rich regions is very sharp [7]. The second slower time law probably represents the growth of the periodically arranged nanocrystals.

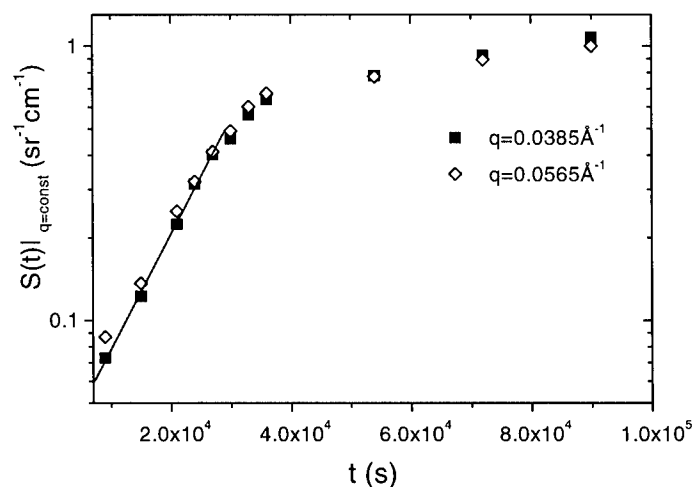


Fig. 2: Annealing time dependence of the scattering cross section of  $\text{Zr}_{41.2}\text{Ti}_{13.8}\text{Cu}_{12.5}\text{Ni}_{10}\text{Be}_{22.5}$  samples aged at 613K for two wavenumbers near the maximum.

The crystal size calculated from Guinier analysis increases slightly from 20Å to 40Å after annealing for 600min and 1500min, respectively. The growth of the nanocrystals is related to Ni diffusion [8]. In this stage no further shift of the scattered intensity maximum to lower  $q$  is detected. This suggests a primary crystallization of the Ti rich regions occurring in the maxima of the composition wave and the pinning of a certain wavelength in the early stages of decomposition.

SANS spectra of samples annealed at different temperatures below and above the glass transition are shown in Fig. 3. All spectra exhibit an interference peak indicating a quasiperiodic arrangement of scattering inhomogeneities. The peak positions shift to lower  $q$  values with increasing temperature and the related wavelengths increase from about 125Å to some 350Å. The wavelengths follow a relation  $\lambda^2 \propto T$  (Fig. 4), as suggested by Cahn's linear theory of spinodal decomposition [9]. The extrapolated coherent spinodal temperature  $T_{cs}$  for  $\lambda \rightarrow \infty$  is about 670K. In accordance with that, samples annealed at 673K do not exhibit an interference peak but a strong increase of intensity with decreasing  $q$ , indicating thermally activated crystallization without precursory decomposition of the amorphous matrix. The change of crystallization behavior might be related to the rapidly decreasing viscosity which destabilizes the periodic composition modulation with increasing temperature.

From the SANS data there is evidence that a miscibility gap opens in the undercooled liquid region near the glass transition temperature. Related to the limited mobility in this temperature range the as prepared samples do not show any indications of decomposition with respect to Ti. But during isothermal annealing below the miscibility gap a Ti composition wave can grow with time. Its wavelength is determined by the aging temperature. Samples annealed above the coherent spinodal temperature do not develop quasiperiodic composition waves and do not exhibit SANS interference peaks.

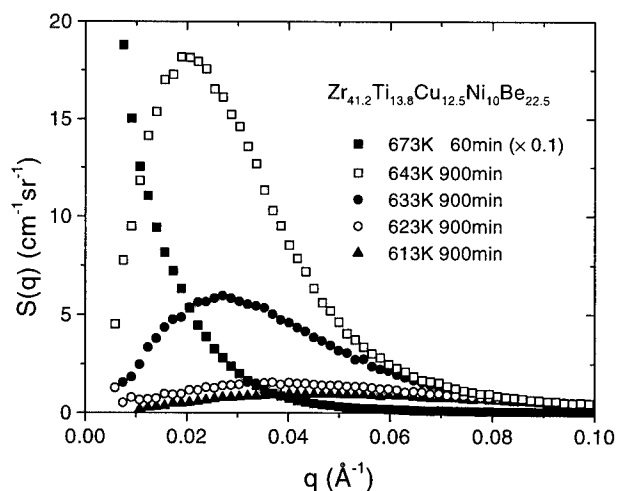


Fig. 3: SANS data of  $Zr_{41.2}Ti_{13.8}Cu_{12.5}Ni_{10}Be_{22.5}$  samples annealed for 900min at different temperatures.

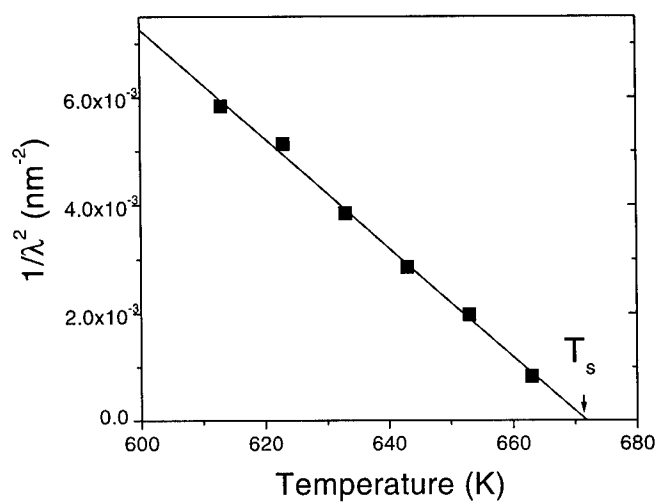


Fig. 4: Temperature dependence of the composition wavelength in  $\text{Zr}_{41.2}\text{Ti}_{13.8}\text{Cu}_{12.5}\text{Ni}_{10}\text{Be}_{22.5}$

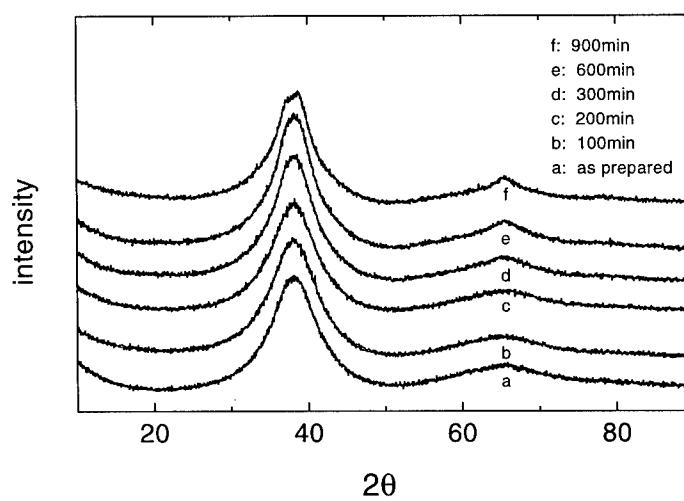


Fig. 5: Wide angle X-ray spectra of  $\text{Zr}_{41.2}\text{Ti}_{13.8}\text{Cu}_{12.5}\text{Ni}_{10}\text{Be}_{22.5}$  samples annealed at 613K for different times.

X-ray diffraction analysis of samples annealed at 613K does not show crystalline contributions for aging times below 400min (Fig. 5). After 600min, when according to Fig. 2 the first stage of decomposition is finished and a slower time law is observed, a slight sharpening of the second diffraction maximum occurs. At this time cross section TEM clearly reveals the existence of nanocrystals in the sample. After 900min of heat treatment also the first diffraction peak indicates the nanocrystals.

### Summary

Our analysis of  $Zr_{41.2}Ti_{13.8}Cu_{12.5}Ni_{10}Be_{22.5}$  samples isothermally annealed near the glass transition temperature of the alloy reveals a chemical decomposition, succeeded by the formation of nanocrystals. The decomposition process shows several properties typical for spinodal decomposition: a quasiperiodic arrangement of chemical inhomogeneities, an exponential growth with time of the amplitude of the composition wave, and a critical temperature beyond which the crystallization behavior changes to a different mechanism. With progressing phase separation composition and short-range atomic order in one of the decomposed regions approach those of a competing crystalline phase. Thus the interfacial energy between a crystalline nucleus and the amorphous matrix decreases with time and the nucleation probability increases rapidly.

### Acknowledgments

Financial support from the Department of Energy (Grant No. DE-FG03-86ER45242) and the DFG via SFB 345 is gratefully acknowledged. This work has benefited from the use of IPNS which is funded by U.S. DOE under Contract No. W-31-109-ENG-38 to the University of Chicago.

### References

- [1] A. Inoue, T. Zhang and T. Masumoto, *Mater. Trans. JIM* **31**, 177 (1990)
- [2] A. Peker and W.L. Johnson, *Appl. Phys. Lett.* **63**, 2342 (1993)
- [3] R. Busch, Y.J. Kim and W.L. Johnson, *J. Appl. Phys.*, **77**, 4039 (1995)
- [4] U. Geyer, S. Schneider, Y. Qiu, et al., *Phys. Rev. Lett.* **75**, 2364 (1995)
- [5] R. Rambousky, M. Moske and K. Samwer, *Mat. Sci. Forum* **179-181**, 761 (1995)
- [6] S. Schneider, U. Geyer, P. Thiyagarajan, and W.L. Johnson, *Mat. Sci. Forum*, in press (1997)
- [7] S. Schneider, P. Thiyagarajan, and W. L. Johnson, *Appl. Phys. Lett.* **68**, 493 (1996)
- [8] S. Schneider et al., to be published
- [9] E.L. Huston, J.W. Cahn, and J.E. Hilliard, *Acta Met.*, **14**, 1053 (1966)
- [10] J.S. Langer, M. Baron, and H.D. Miller, *Phys. Rev.* **A11**, 1417 (1974)
- [11] S. Schneider and P. Schaaf, to be published

## SMALL ATOM DIFFUSION AND BREAKDOWN ON STOKES-EINSTEIN RELATION IN THE SUPERCOOLED LIQUID STATE OF Zr-Ti-Cu-Ni-Be ALLOYS

U. GEYER\*, S. SCHNEIDER\* Y. QIU\*\*, M.-P. MACHT\*\*\*,  
T.A. TOMBRELLO\*\*, W.L. JOHNSON\*\*

\*I. Phys. Institut and SFB 345, Universität Göttingen, 37073 Göttingen, Germany

\*\*California Institute of Technology, Pasadena, CA 91125, USA

\*\*\*Hahn-Meitner-Institut Berlin, Abt. Strukturforschung, 14109 Berlin, Germany

### ABSTRACT

Be diffusivity data in the bulk metallic glass forming alloys  $Zr_{41.2}Ti_{13.8}Cu_{12.5}Ni_{10}Be_{22.5}$  and  $Zr_{46.7}Ti_{8.3}Cu_{7.5}Ni_{10}Be_{27.5}$  are reported for temperatures between 530K and 710K, extending up to 80K into the supercooled liquid states of the alloys. At the glass transition temperature,  $T_g$ , a change in temperature dependence of the data is observed in both alloys, and above  $T_g$  the diffusivity increases faster with temperature than below. The data in the supercooled liquid can be described by a modified Arrhenius expression containing the communal entropy of the supercooled liquid and based on a diffusion mechanism suggested earlier. The comparison with viscosity data in the supercooled liquid state of  $Zr_{46.7}Ti_{8.3}Cu_{7.5}Ni_{10}Be_{27.5}$  reveals a breakdown of the Stokes-Einstein relation, whereas  $D(T)$  and  $\eta(T)$  follow a relation close to van den Beukel's. The breakdown of the Stokes-Einstein relation indicates a cooperative diffusion mechanism in the supercooled liquid state of the ZrTiCuNiBe alloys.

### INTRODUCTION

Recent investigations of multicomponent deep eutectic metallic systems have led to the development of bulk metallic glasses [1-5] with superior glass forming abilities and an excellent stability with respect to crystallization. This has opened new opportunities for fundamental study of the supercooled liquid state above the glass transition temperature,  $T_g$ , as well as of the glass transition in metallic systems, which both were experimentally almost inaccessible before.

For the ZrTiCuNiBe alloy system [4] atomic diffusion [6-8] and viscosity [9], the time-temperature-transformation (TTT) diagram for nucleation and growth of crystals [10] and other thermophysical properties [11] of the supercooled melt have already been investigated. Studies of crystallization in the  $Zr_{41.2}Ti_{13.8}Cu_{12.5}Ni_{10}Be_{22.5}$  alloy around  $T_g$  reveal that crystallization is preceded by phase separation [12, 13]. Further, the availability of bulk specimens has made possible serious mechanical testing which demonstrates that the new alloys are very promising for engineering applications, even more as they can easily be processed and formed in the supercooled liquid state.

This paper reports investigations of atomic diffusion in the glassy and supercooled liquid states of the  $Zr_{41.2}Ti_{13.8}Cu_{12.5}Ni_{10}Be_{22.5}$  (V1) [6, 7] and  $Zr_{46.7}Ti_{8.3}Cu_{7.5}Ni_{10}Be_{27.5}$  (V4) [8] alloys, using Be as the diffusing species. Consequences of phase separation for these and other investigations of the supercooled liquid state of V1 are briefly discussed, and diffusivity, entropy and viscosity data are compared with regard to the diffusion mechanism in the supercooled liquid state of these metallic alloys.

## EXPERIMENT

Experimental details of sample preparation and Be diffusion profile measurements by high energy backscattering spectrometry have been given before [6, 14]. In the course of our investigations the onset of a time dependence of diffusivity values after increased annealing times became obvious. This observation initiated more detailed small angle neutron scattering studies of the thermal stability of V1 during isothermal annealing near the glass transition temperature [12, 13], revealing phase separation followed by nanocrystallization. Isothermal annealing of the samples thus must be restricted to the early stages of phase separation where the composition changes grow very slowly and the system stays almost homogeneous. In case of fast Be diffusion we were able to apply annealing times short enough to avoid influence of decomposition and long enough to produce measurable diffusion profiles (Fig. 1). However, investigations on diffusion of the slower diffusors Co and Al in V1 show a decrease of diffusivity with time [15]. In general, one must consider possible influence of compositional changes due to phase separation in ZrTiCuNiBe and other multicomponent glass forming alloys during all isothermal experiments around the glass transition temperature.

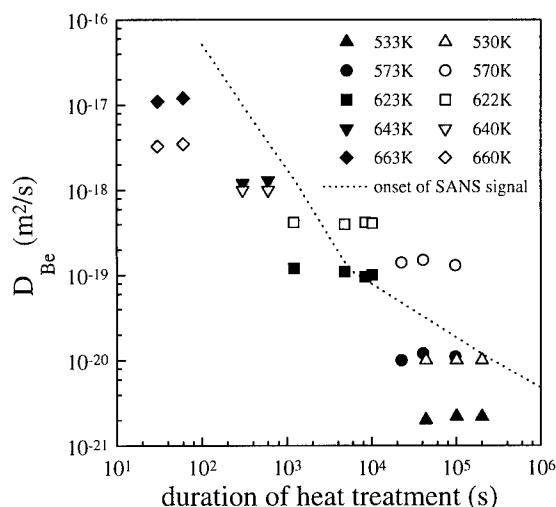


Fig. 1:

Self diffusivity of beryllium in V1 (solid symbols) and V4 (open symbols) as a function of annealing time. The dotted line indicates onset of decomposition in V1, as revealed by small angle neutron scattering (SANS).

## RESULTS AND DISCUSSION

In rapidly quenched conventional metallic glasses diffusion is known to be sensitive to the relaxation state of the samples. In a nonrelaxed sample diffusivity drops as a function of time due to structural relaxation and annealing of excess free volume. It approaches a constant value when the sample is fully relaxed. It is thus essential to check for relaxation effects in evaluating diffusion data. As shown in Fig. 1 no dependence of Be diffusivity on the duration of heat treatment could be found within the experimental time-temperature window in both alloys. This ensures that no significant relaxation effects occur. At 623K annealing times ex-



ceeding the early stages of decomposition have been applied to V1, but no significant influence of decomposition on Be diffusivity is visible.

Figure 2 shows an Arrhenius plot of Be diffusivity in V1 and V4. For both alloys, the respective data can be divided into two subsets. The subsets for temperatures below about 625K fit an Arrhenius law  $D_{\text{Be}}(T)=D_0 \times \exp(-Q/k_b T)$  with  $D_0=1.8 \times 10^{-11} \text{ m}^2/\text{s}$  and  $Q=1.05 \text{ eV}$  (V1) and  $D_0=8 \times 10^{-16} \text{ m}^2/\text{s}$  and  $Q=1.1 \text{ eV}$  (V4), respectively. Above 625K an enhanced temperature dependence of  $D_{\text{Be}}$  is observed in both alloys. If interpreted in terms of Arrhenius behavior, this leads to higher activation energies of 4.47 eV (V1) and 1.9 eV (V4), and to much higher  $D_0$  values of  $1.1 \times 10^{17} \text{ m}^2/\text{s}$  (V1) and  $1.7 \times 10^3 \text{ m}^2/\text{s}$  (V4).

The change in temperature dependence is associated with the glass transition which in both alloys occurs at about 625K for isothermal annealing experiments. The present data extend 40K into the supercooled liquid state of V1 and 80K into that of V4. This again demonstrates that V4 is more stable against phase separation and crystallization than V1.

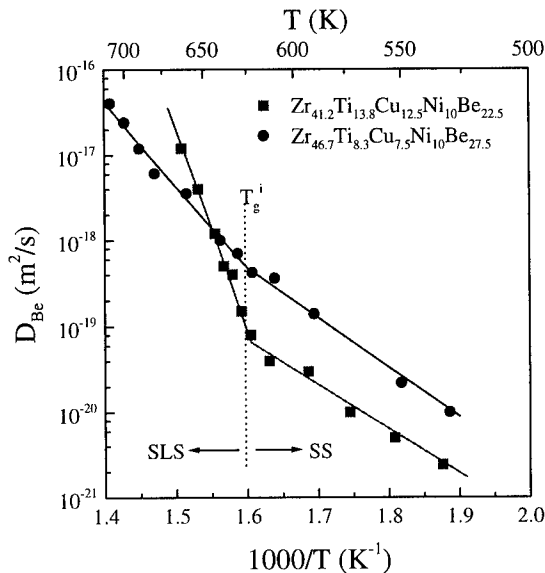


Fig.2: Arrhenius plot of Be diffusivity in V1 and V4.  $T_g^i$  is the glass transition temperature for isothermal annealing. The solid lines represent best Arrhenius fits to the data. The fitting parameters are given in the text.

The small  $D_0$  and  $Q$  values for Be diffusion in the solid states of both alloys suggest single atomic jumps of the small Be atoms in the amorphous matrix. The about one order of magnitude higher diffusivity in the solid state of V4 indicates a higher fraction of free volume in this alloy, in accordance with the higher average atomic size in V4 [8]. In the supercooled liquid states (SLS) of both alloys the Arrhenius parameters show increased values. Particularly for V1 the respective numbers seem unphysically high. This indicates that interpretation of the data in the SLS in terms of thermally activated single atomic jumps is not appropriate and a different diffusion mechanism must be involved. We have suggested that diffusion of Be (and probably of other small atoms) in the SLS can be explained by single atomic jumps of the diffusing atoms in a slowly changing configuration of neighboring atoms [6]. The continuous atomic rearrangements in the SLS support the atomic jumps by providing a higher frequency of critical free volume fluctuations. The respective contribution to Be diffusivity is related to the configura-

tional entropy of the supercooled liquid. By taking into account the temperature dependent entropy change  $\Delta S^{\text{SLs}}(T)$  due to the glass transition, the data can be fitted by the following modified Arrhenius expression:

$$D^{\text{SLs}}(T) = D_0^{\text{SS}} \cdot \exp\left(-\frac{\Delta H_M^{\text{SS}}}{k_B T}\right) \cdot \exp\left(\frac{\frac{N}{N_A} \cdot \Delta S^{\text{SLs}}(T)}{k_B}\right),$$

where  $D_0^{\text{SS}}$  and  $\Delta H_M^{\text{SS}}$  are the preexponential factor and migration enthalpy for diffusion in the solid state,  $N$  is a typical number of neighbor atoms supporting the single jumps by viscous rearrangements, and  $\Delta S^{\text{SLs}}(T)$  is the temperature dependent configurational entropy per mole of the supercooled liquid. Only the fraction  $N/N_A$  of the total configurational entropy which is related to the rearrangements of  $N$  nearest and next-nearest neighbor atoms is considered in this expression. Near the glass transition temperature,  $T_g$ , the entropy can be approximated by a linear expression,  $\Delta S^{\text{SLs}}(T) \approx \Delta c_p(T_g) \times (T - T_g) / T_g$ , with  $\Delta c_p(T_g)$  the specific heat capacity difference at  $T_g$  of the supercooled liquid and crystalline states. Figure 3 shows that this expression fits the Be diffusion data of both alloys if one takes  $N=22$  for V1 and  $N=13$  for V4, respectively. For V1 the fit is based on the fully experimentally determined entropy function [11], in the case of V4 it is based on the linear approximation. Beryllium diffusivity in the SLS of the ZrTiCuNiBe alloys scales with the slope of the entropy function above  $T_g$ , and the large activation energies above  $T_g$  are mimicked by the increase of configurational entropy with temperature. Since  $\Delta c_p(T_g)$  is by 2.9 smaller in V4 than in V1 [8], the slope of the entropy vs. temperature function of V4 is smaller and the change in temperature dependence of  $D_{\text{Be}}(T)$  is less. The smaller number of neighbor atoms involved in Be diffusion in V4 again points to a higher fraction of free volume in this alloy. The change in temperature dependence at  $T_g$  with decreasing temperature is related to the rapidly increasing viscosity of the system: below  $T_g$  mainly single atomic jumps contribute to diffusion, above  $T_g$  cooperative atomic rearrangements dominate the scenario. This change of diffusion mechanism at  $T_g$  should only occur for atoms that are able to perform single atomic jumps. Ni diffusivity in  $\text{Zr}_{55}\text{Al}_{10}\text{Ni}_{10}\text{Cu}_{25}$  also shows a distinct increase in temperature dependence above  $T_g$  [16], and data in [17] indicate a small increase in temperature dependence at  $T_g$  of Ni diffusivity in V1. No effect is observed for Co diffusion in V1 and Co and Al diffusion in V4 [15], the Arrhenius parameters being comparable to those of Be in the SLS.

The present diffusivity data and the equilibrium viscosity data of V4 in the SLS [9] overlap in the temperature regime 650-710K. Thus, we can check both, the Stokes-Einstein relation [18] and van den Beukel's relation [19], for atomic transport in the SLS of V4 at these temperatures. Figure 4 shows our measured data in the SLS of V4 and the diffusivity as predicted by the Stokes-Einstein relation for translational diffusion,  $D(T) = k_B T / 6\pi\eta(T) \times R$ , by choosing the atomic radius of Be, 1.1Å, for the molecular radius  $R$  and using the calculated  $\eta(T)$  from the Vogel-Fulcher fit to the experimentally determined viscosity. According to Fig. 4, the Be diffusion is much faster in comparison to the prediction of the Stokes-Einstein relation. We believe that the observed breakdown of the Stokes-Einstein relation is another indication for the proposed cooperative diffusion mechanism [6] in the SLS of ZrTiCuNiBe bulk glass formers [8].

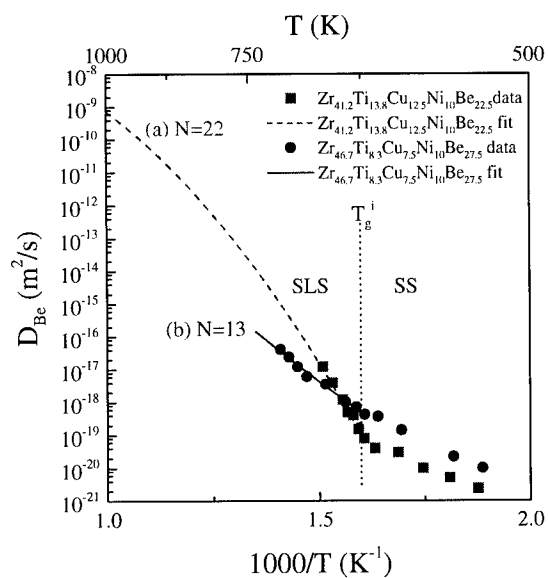


Fig. 3:

$D_{Be}$  data and fit curves to the modified Arrhenius law for data in the supercooled liquid. The fit for V1 is based on the fully experimentally determined entropy function [11], the fit for V4 is based on a linear approximation of the entropy function.

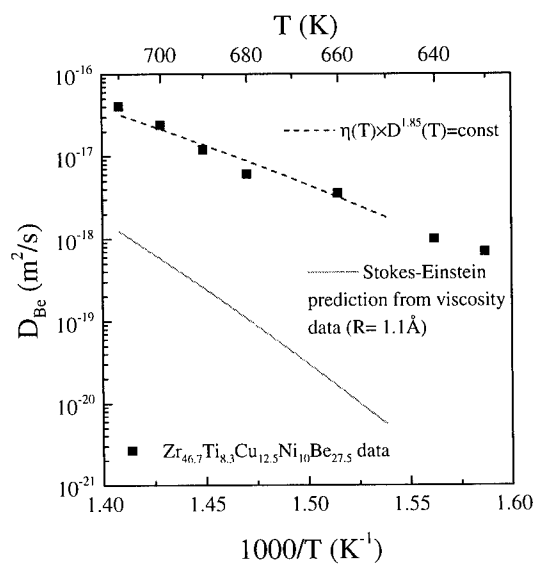


Fig. 4:

Stokes-Einstein prediction for diffusivity ( $R=1.1\text{\AA}$ ), as calculated from the Vogel-Fulcher fit for V4 viscosity data [9] (solid line) and result of a fitting procedure of  $\eta(D/\text{m}^2\text{s}^{-1})^n=\text{const}$  to the data (dashed line,  $n=1.85$ ,  $\text{const}=3.8\times 10^{-13}\text{poise}$ ).

Based on  $D(T)$  and  $\eta(T)$  measurements on conventional metallic glasses, van den Beukel suggested the relation  $\eta \times D^2 = \text{const}$  for the correlation of diffusivity and viscosity data [19]. In terms of the free volume model it can be derived by assuming two different defect types with different concentrations responsible for diffusion and viscosity. The present data on V4 follow a relation  $\eta \times D^{1.85} = \text{const}$  which is close to van den Beukel's suggestion (Fig. 4). The interpretation of this experimentally found relation needs to be clarified.

#### ACKNOWLEDGMENTS

This work was supported by the U.S. Army Research Office [Grant DAAH04-95-1-0233], by the U.S. Dept. of Energy under Grant No. DE-FG03-86ER45242, by the DFG via SFB 345, and by the National Science Foundation [Grant DMR93-18931].

#### REFERENCES

- 1 A. Inoue, T. Zhang, and T. Masumoto, *Mater. Trans. JIM* **31**, 177 (1990).
- 2 A. Inoue, A. Kato, T. Zhang, *et al.*, *Mater. Trans. JIM* **32**, 609 (1990).
- 3 A. Inoue, T. Nakamura, T. Sugita, *et al.*, *Mater. Trans. JIM* **34**, 351 (1993).
- 4 A. Peker and W. L. Johnson, *Appl. Phys. Lett.* **63**, 2342 (1993).
- 5 X. H. Lin and W. L. Johnson, *J. Appl. Phys.* **78**, 6514 (1995).
- 6 U. Geyer, S. Schneider, W. L. Johnson, *et al.*, *Phys. Rev. Lett.* **75**, 2364 (1995).
- 7 U. Geyer, S. Schneider, Y. Qiu, *et al.*, *Mat. Science Forum*, (in press) (1996).
- 8 U. Geyer, S. Schneider, W. L. Johnson, *et al.*, *Appl. Phys. Lett.* **69**, 2492 (1996).
- 9 E. Bakke, R. Busch, and W. L. Johnson, *Appl. Phys. Lett.* **67**, 3260 (1995).
- 10 Y. J. Kim, R. Busch, W. L. Johnson, *et al.*, *Appl. Phys. Lett.* **68**, 1057 (1996).
- 11 R. Busch, Y. J. Kim, and W. L. Johnson, *J. Appl. Phys.* **77**, 4093 (1995).
- 12 S. Schneider, W. L. Johnson, and P. Thiyagarajan, *Appl. Phys. Lett.* **68**, 493 (1996).
- 13 S. Schneider, U. Geyer, P. Thiyagarajan, *et al.*, *Mat. Science Forum*, in press (1997).
- 14 Y. Qiu, U. Geyer, S. Schneider, *et al.*, *Nucl. Instr. Meth. B* **117**, 151 (1996).
- 15 E. Budke, P. Fielitz, M.-P. Macht, *et al.*, in *Intl. Conf. on Diffusion in Materials - DIMAT 96*, edited by H. Mehrer (Transtec Publications Ltd., Nordkirchen, Germany, 1996), in press.
- 16 H. Nakajima, W. Sprengel, and K. Nonaka, in *Intl. Conf. on Diffusion in Materials - DIMAT 96*, edited by H. Mehrer (Transtec Publications Ltd., Nordkirchen, Germany, 1996), in press.
- 17 F. Wenwer, K. Knorr, M.-P. Macht, *et al.*, in *Intl. Conf. on Diffusion in Materials - DIMAT 96*, edited by H. Mehrer (Transtec Publications Ltd., Nordkirchen, Germany, 1996), in press.
- 18 A. Einstein, *Investigations on the theory of Brownian motion* (Dover, New York, 1956).
- 19 A. v. d. Beukel, *Scripta Metall.* **22**, 877 (1988).

## METASTABILITY AND PROPERTIES OF METALLIC BULK GLASS FORMING ALLOYS

H.-J. FECHT

University Ulm, Faculty of Engineering, Department of Materials  
Albert-Einstein-Allee 47, D-89081 Ulm, Germany

### ABSTRACT

Glasses are generally produced from the highly undercooled liquid state by rapid quenching methods or quasi-statically at slow cooling by the effective control of potent heterogeneous nucleation sites. For metallic systems the latter method recently has led to the development of bulk metallic glass with a complex multicomponent chemistry and advanced engineering properties. With these alloys crystallization can be avoided over a broad temperature / time window. As such, the relevant thermodynamic properties of the metastable glassy and undercooled liquid states can be directly measured below and above the glass transition temperature, respectively. The obtained data give new insight into the nature of the glass transition suggesting that it is not a phase transition in the classical sense but kinetic freezing triggered by an underlying entropic instability to avoid crystallization. Further measurements of the mechanical and wear properties point to the unique engineering properties of these highly disordered materials for technological applications.

### INTRODUCTION

Metallic bulk amorphous alloys with a fully non-crystalline glassy atomic structure and dimensions of several hundred cubic-centimeters can be produced at relatively slow cooling rates using conventional casting techniques [1,2,3]. These new materials on the basis of multi-component eutectics have a huge potential as advanced engineering materials due to their excellent processing capabilities in the undercooled liquid state and excellent mechanical properties, such as wear resistance and mechanical strength. The pseudo-ternary alloy  $(Zr_{41}Ti_{13})(Cu_{13}Ni_{10})Be_{23}$  which is most stable against crystallization has been the main focus of the investigations described here and is compared with the undercooling characteristics of pure metals and other good glass forming alloys.

Furthermore, these materials are sufficiently stable against crystallization in the state of the highly undercooled liquid in the range of about 100 K above the glass transition temperature  $T_g$  and give new insight into the dynamical and thermal properties of the highly undercooled liquid state and the glass transition itself [4]. The properties of interest include the temperature dependent thermodynamic properties, such as entropy, enthalpy and Gibbs free energy, volume (density), viscosity and mechanical properties such as the elastic moduli, and hardness.

These new alloys have considerable potential as advanced engineering materials due to their excellent processing capabilities of the undercooled liquid, improved wear resistance, low coefficient of friction, high strength and excellent corrosion resistance.

## EXPERIMENT

Eutectic alloys with the composition  $\text{Zr}_{41}\text{Ti}_{13}\text{Cu}_{13}\text{Ni}_{10}\text{Be}_{23}$  have been prepared by induction melting in a special chamber under ultra clean conditions [5]. By controlled cooling procedures the samples could be crystallized below the eutectic temperature or undercooled over the entire undercooling range resulting in a glass. Typical cooling rates in this case were about 100 K / sec with a sample size of several  $\text{cm}^3$ .

After preparation, these samples were annealed in different time and temperature steps and investigated in terms of their thermal and mechanical properties. Scanning electron microscopy and X-ray diffraction allowed to characterize the microstructural development. Further thermal analysis (Perkin Elmer DSC7) and Dynamic Mechanical Analysis (Perkin Elmer DMA 7e) has been employed to measure the specific heat  $c_p$  and heat of crystallization as well as thermal expansion behavior and the temperature dependent elastic modulus. These investigations of microstructure - property relationships were extended to hardness measurements using conventional microhardness and nanoindentation techniques.

## RESULTS

### Structural Properties

Heating the glass up to temperatures higher than about 80 K above the glass transition temperature leads eventually to crystallization. The crystallization occurs in three distinct exothermic steps. More details on the phase analysis are given elsewhere [6,7]. In brief, the TEM and X-ray diffraction analysis indicates that the crystallization step I corresponds to the formation of nanometer sized f.c.c. crystallites (lattice parameter  $a = 0.4 \text{ nm}$ ) within the liquid matrix. A liquid / liquid phase separation however precedes the crystallization as observed by SANS and FIM analysis [8,9]. This phase separation into Ti- and Be-enriched areas occurs on a length scale of about 50 nm, i.e. at approximately the same length scale as the following crystallization. This crystallization sequence is also shown in Figure 1 exhibiting *in situ* X-ray diffractograms at various temperatures.

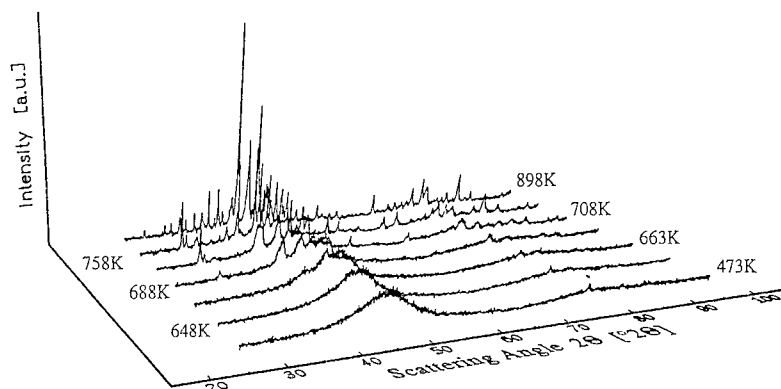
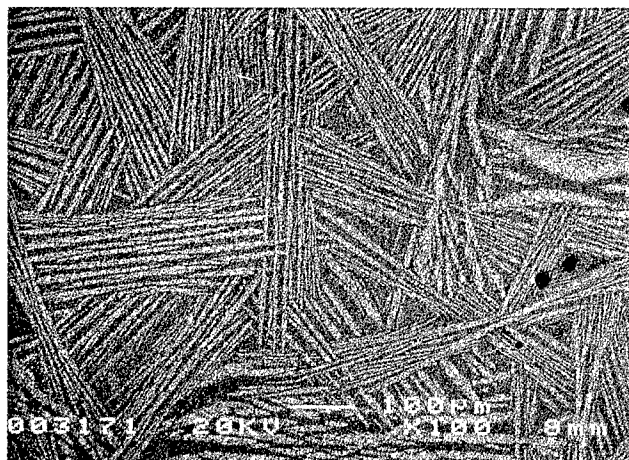


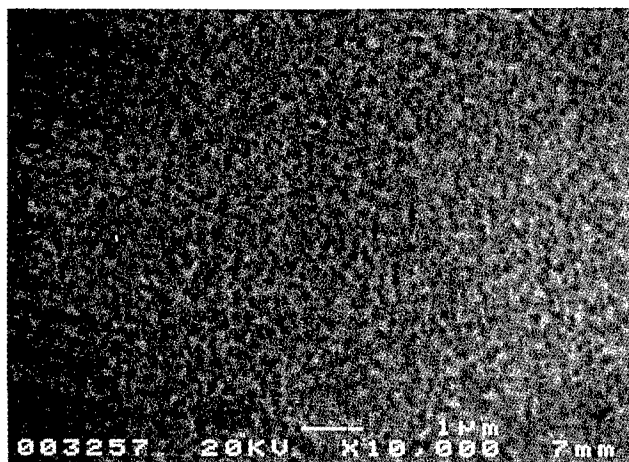
**Figure 1:** In situ X-ray diffractograms (Co-K $\alpha$  radiation) as a function of temperature exhibiting the crystallization sequence of the initially liquid / amorphous sample.

In step II crystallization of a hexagonal "MgZn<sub>2</sub>"-type Laves phase occurs from the (Liquid + f.c.c.) phase mixture. During further heating, three more complex intermetallic compounds are formed which are similar to Be<sub>2</sub>Zr, CuZr<sub>2</sub> and CuZr, respectively [7].

Analyzing the different microstructures which can develop in the pseudo-ternary (Zr<sub>41</sub>Ti<sub>13</sub>)(Cu<sub>13</sub>Ni<sub>10</sub>)Be<sub>23</sub> after crystallization reveals a broad range of length scales. They are controlled by nucleation and growth at the appropriate processing conditions. For example, Figure 2 exhibits two completely different microstructures. They are obtained by a eutectic crystallization reaction at low undercooling just below the eutectic temperature (length scale of 100  $\mu$ m, Figure 2a), and by nucleation and retarded growth at high undercooling resulting in a nanocrystalline microstructure (length scale of typically 50 nm, Figure 2b).



(a)



(b)

**Figure 2:** Variation of the microstructural length scales of Zr<sub>41</sub>Ti<sub>13</sub>Cu<sub>13</sub>Ni<sub>10</sub>Be<sub>23</sub> alloys as obtained by scanning electron microscopy for a eutectic microstructure crystallized at very low undercooling (a) and a nanocrystalline state obtained by crystallization at high undercooling (b).

### Thermal Properties and Metastability

The specific heat of this alloy is shown in Figure 3 for the stable crystal, the fully relaxed glass, the undercooled liquid and the stable liquid obtained at a heating rate of 8 K / min. The glass transition can be clearly distinguished and the data in the undercooled liquid can be interpolated as indicated by the dashed line to the eutectic temperature. The specific heat curve shown in Figure 3 has the typical signature of a "strong" glass, i.e. the lack of a peak at the glass transition.

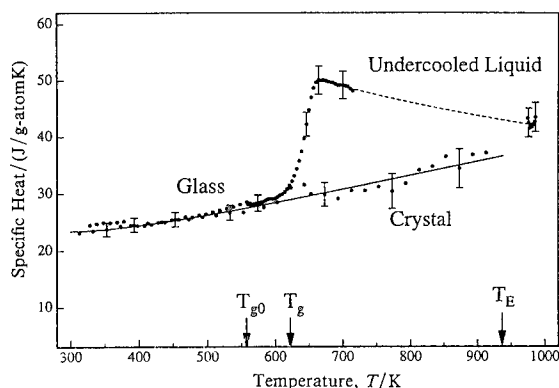


**Figure 3:** Specific heat  $c_p$  of  $Zr_{41}Ti_{13}Cu_{13}Ni_{10}Be_{23}$  alloys in the glassy, undercooled liquid, stable liquid and crystalline state as a function of temperature.

In order to quantify the glass forming ease of these "strong" glass formers we have compared their thermodynamic properties with those of metallic elements and another bulk glass forming alloy ( $Pd_{40}Ni_{40}P_{20}$ ). Reviewing the literature for measured specific heat data of undercooled liquids, it becomes obvious that only very few systematic studies are available. Some of the best data so far, are based on droplet samples with relatively low melting temperatures which can be undercooled significantly during slow cooling bypassing crystallization [10]. In Figure 4 experimental results of specific heat measurements for pure metals as well as glass forming alloys are shown as a function of the reduced melting temperature  $T / T_m$ . For the purpose of analyzing crystallization processes and glass formation, it is generally sufficient to consider the difference in specific heat  $\Delta C_p$  between the undercooled liquid and the corresponding crystalline stable solid. For pure metals with melting points less than 900 K, i.e. Bi, Sn and In [8] specific heat values have been measured by Perepezko and coworkers over a maximum undercooling range of about  $0.4 T_m$ . For other glass forming alloys the specific heat has been measured close to the melting point at low levels of undercooling by standard calorimetric measurements on undercooled bulk samples or by drop calorimetry with undercooling levels of less than typically 10%. It is apparent that for the glass forming alloys the crystal / liquid specific heat difference exhibits a relatively large discontinuity at the eutectic temperature whereas for pure metals the discontinuity at the melting point is small in comparison.



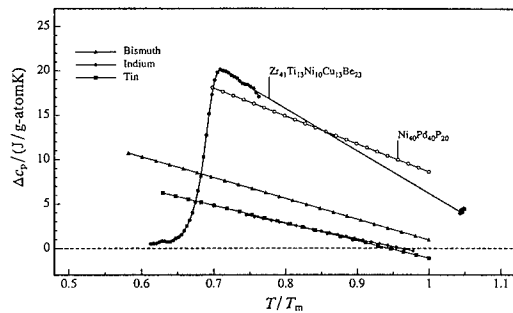


**Figure 4:** The crystal / liquid specific heat difference  $\Delta c_p$  as a function of undercooling below the reduced melting (eutectic) temperature for several metallic elements and glass forming alloys.

Furthermore, from these specific heat data the thermodynamic functions of the undercooled liquid can be obtained as well. For example, the entropy and enthalpy differences between liquid and crystal correspond to  $\Delta S$  and  $\Delta H$ , respectively, with

$$\Delta S = \int \Delta c_p / T \, dT \quad \Delta H = \int \Delta c_p \, dT \quad (1)$$

As such, an isentropic temperature is found where the extrapolated entropy difference between liquid and crystal would be vanishing. This temperature corresponds to  $561 \pm 10$  K for  $Zr_{41}Ti_{13}Cu_{13}Ni_{10}Be_{23}$ . With regard to the isentropic condition Kauzmann already pointed out that with progressive undercooling, the entropy of a liquid tends towards the entropy of the crystalline state as indicated by the increase of  $\Delta c_p$  during cooling [11]. Thus, one would be faced with the paradox that, at temperatures below  $T_{g0}$ , the entropy of the ordered, thermodynamically most stable crystal would exceed that of the disordered liquid. This situation is averted by the occurrence of the glass transition.

In order to further compare the thermodynamic properties of the elements with the "strong" eutectic glass formers, the corresponding entropy  $\Delta S$  (integration over  $\Delta c_p / T$ ), enthalpy  $\Delta H$  (integration over  $\Delta c_p$ ) and Gibbs free energy functions  $\Delta G = \Delta H - T \Delta S$  have been calculated and exhibited in Figure 5. The results are presented as a fraction of the entropy and enthalpy of fusion, respectively. Two examples characteristic for metallic elements and bulk metallic glasses are being compared: Indium representing a typical example of a pure metal with an entropy of fusion of  $7.62$  J / g-atomK (dashed line) and  $Zr_{41}Ti_{13}Cu_{13}Ni_{10}Be_{23}$  as a typically example of bulk glass formation having an entropy of fusion of  $8.72$  J / g-atomK (full line). It is interesting to note that the entropy of fusion of the "strong" glass corresponds to about half of that of the "fragile" glass Au-Pb-Sb.

The liquid - solid entropy difference is shown in Figure 5a. If the entropy values are extrapolated beyond the experimentally determined range an isentropic temperature  $T_K$  is found at about  $0.3 T_m$  for the metallic element ( $T_K^e$ ) and at  $0.6 T_m$  ( $T_m$  is equivalent to the eutectic temperature  $T_E$ ) for the bulk metallic glass ( $T_{g0}$ ). Further experimental results varying the heating rate over two decades indicate that this isentropic condition at  $561$  K (see Figure 14) corresponds to the glass transition temperature for indefinitely slow heating (ideal glass transition temperature  $T_{g0}$ ) [7].

As such, for "strong" glasses the isentropic temperatures sets a limit to the maximum level of undercooling as well. However, in comparison with the "fragile" glass the isentropic instability can not be approached as closely.

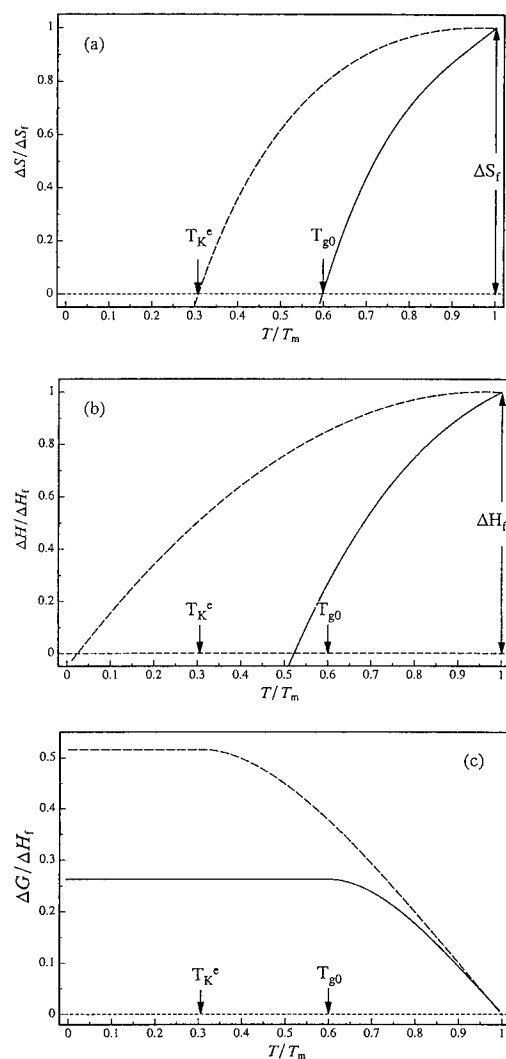


**Figure 5:** The crystal / liquid entropy differences (a), enthalpy differences (b) and Gibbs free energy differences (c) for pure metals (such as Indium or Tin, dashed line) and bulk glass forming alloys (solid line).

Based on the same specific heat data the enthalpy difference  $\Delta H$  is obtained and shown in Figure 5b. It is obvious that enthalpy is frozen out during undercooling. Due to the smaller specific heat the enthalpy reduction for the elemental metal is much less than for the bulk glass with increasing undercooling.

The excess enthalpy for the Zr-based glass forming alloys at the ideal glass transition temperature  $T_{go}$  corresponds to 0.26 of the enthalpy of fusion  $\Delta H_f$  and represents the smallest value a fully relaxed glass with zero residual entropy could have. Experimentally, larger values for the heat of crystallization have been measured in agreement with the estimate (Figure 5b). The crystallization in these alloys occurs at temperatures typically 150 K above  $T_{go}$ , e.g. at approximately  $0.75 T_m$  depending on the heating rate. These considerations appear to be of general relevance and indicate the deviation from the state of an ideal glass when enthalpies of crystallization are measured.

A further important parameter is the Gibbs free energy difference  $\Delta G$  shown in Figure 5c as a fraction of the enthalpy of fusion  $\Delta H_f$ . Since the entropies of fusion, i.e. the slopes of the  $\Delta G$  curves at  $T / T_m = 1$ , for the bulk glass is only slightly reduced in comparison with the pure elements the main contribution to the reduction in the Gibbs free energy results from the different specific heat values.

Thus, for the metallic element the driving force for crystallization is reduced to about half of that close to the melting point. For the bulk glass former the driving force is reduced by another factor of two in comparison with the element. Thus, the resistance to crystallization of bulk glasses is inherently coupled with a reduction of the driving force for crystallization  $\Delta G$  and is reflected in the corresponding increase in excess specific heat.

Since the ease of metallic glass formation is generally related to the formation of eutectic alloys further conclusions can be drawn about the principles of the stabilization of "strong" bulk glasses. For example, by comparing the average melting temperature of the  $Zr_{41}Ti_{13}Cu_{13}Ni_{10}Be_{23}$  alloy with its measured eutectic temperature a reduction in the melting point from 1832 K to 937 K obviously has been achieved due to a eutectic reaction. The eutectic temperature of this "strong" glass forming alloy corresponds to approximately half of the melting point of the constituent elements. The estimated ideal glass transition temperatures ( $0.3 T_m$  for the elements and  $0.6 T_{eut}$  for the bulk metallic glass) indicate approximately the temperature range of glass formation.

Varying the heating rate between 0.5 K/min. and 250 K/min. results in a shift of the experimentally determined reduced glass transition temperature  $T_r = T_g / T_E$  from 0.65 to 0.70  $T_E$ , with  $T_E$  being the eutectic temperature.

The corresponding relaxation times can be obtained by numerical integration of these experimental data as function of heating rate. These results can be fitted within the accuracy of the measurement according to the following equation [12]:

$$\tau^{-1}(T) = \tau_0^{-1} \cdot \exp \left( - \frac{E}{R(T - T_c)} \right) \quad (2)$$

with  $\tau_0 = 1.8 \cdot 10^{-5}$  sec,  $E = 8.4$  kJ / g-atom and  $T_c = 546 \pm 15$  K. It is interesting to note that the critical temperature  $T_c$  coincides with the isentropic temperature  $T_{go}$  within the experimental error of the specific heat measurement. This approach is based on a standard Landau free energy expansion similar to spin ordering of a ferromagnet above its critical point. However, neglecting the data for heating rates larger than 100 K / min. this function could be equally well fitted to a linear dependence of  $\log t$  versus  $1 / T$ . Therefore, a clear distinction between Arrhenius and Vogel-Fulcher type behavior

based on caloric measurements seems rather difficult for these alloys. Further measurements of the temperature dependence of the shear viscosity indicate a behavior which is rather "strong" [10,13,14].

A further important aspect concerning the nature of the glass transition as well as the crystallization relates to the volume changes of the different stable or metastable phases formed as a function of temperature. Figure 6 exhibits the sample volume of the glass and undercooled liquid in comparison with the fully crystallized stable configuration obtained from dilatometric measurements at a heating rate of 4 K / min.

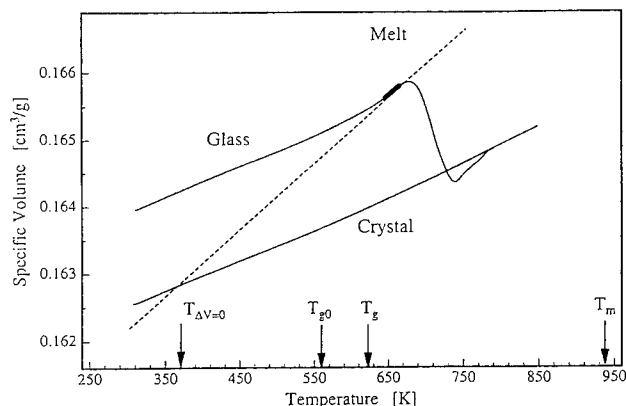


**Figure 6:** The sample volume of the Zr-based bulk metallic glass, the undercooled melt and the crystalline phase as a function of temperature with the isochoric temperature  $T_{\Delta V=0}$ , the isentropic (ideal glass transition temperature)  $T_{g0}$ , the experimental glass transition temperature  $T_g$  and eutectic melting temperature  $T_m$ .

The corresponding linear thermal expansion coefficients  $\alpha$  have been measured as well using the DMA in the dilatometer mode. For the glass and the fully crystallized samples, basically the same value  $\alpha = 9.5 \cdot 10^{-6} \text{ K}^{-1}$  is determined, whereas  $\alpha$  for the fully relaxed undercooled liquid shows a non-linear temperature increase up to a value of  $2 \cdot 10^{-5} \text{ K}^{-1}$  before crystallization sets in. These data are in agreement with other measurements [15]. The volume change during crystallization corresponds to 1.4% and is considerably smaller than typical values for the melting transition under equilibrium conditions. Furthermore, extrapolating the volume of the undercooled liquid back to lower temperatures would indicate an isochoric temperature of 370 K where a density catastrophe would be expected. This temperature is certainly lower than the measured glass transition temperature  $T_g$  of 625 K and lower than the estimated isentropic temperature  $T_{g0}$  of 561 K. This experimental result contradicts theoretical predictions relating the glass transition to an isochoric transition [16]. Here, it is suggested that during cooling of the liquid the glass transition is triggered by an underlying isentropic instability of the undercooled liquid before the density catastrophe would take place [17].

### Mechanical Properties

As a result of the different crystallization steps the microstructure of the amorphous sample in comparison with the nano / microcrystalline material can be controlled on a

nanometer scale over several orders of magnitude. Due to the lack of dislocations mechanical deformation mechanisms different from conventional polycrystalline metals and alloys are becoming relevant. As such, the mechanical strength and wear resistance [18] can be considerably improved in comparison with conventional crystalline materials.

For example, the room temperature Young's modulus  $E$  has been measured on three-point bending samples in a DMA. These data have been measured on samples with 1 mm x 1 mm in thickness and 12 mm length using a DMA under dynamic three-point bending conditions with a static load of 400 mN and a dynamic load of 250 mN at a frequency of 1 Hz. The Young's modulus  $E$  is found to vary between 88 GPa for the glass sample to 116 GPa for the fully crystallized sample.

For example, Figure 7 shows the Young's modulus of the glass sample in the unrelaxed and the fully relaxed state as a function of temperature. A decrease of the Young's modulus with increasing temperature can be clearly discerned. Strong softening is observed above about 600 K, i.e. close to the glass transition temperature. Additional measurements of the phase shift between the applied modulated force and the corresponding extension gives further insight into the structural relaxation of the glass and its viscoelastic properties. For the fully amorphous Zr-based bulk glassy alloy a change in the phase shift (dashed line, loss angle) for a fully relaxed sample is observed close to the glass transition temperature determined by specific heat measurements (see Figure 3).

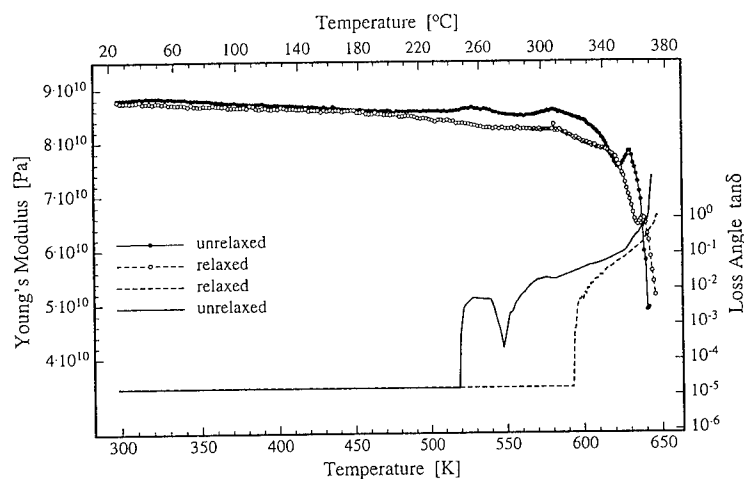


**Figure 7:** Young's modulus and loss angle of glassy alloys in the unrelaxed and fully relaxed states as a function of temperature.

Further room temperature measurements of the Young's modulus for different levels of thermal annealing and at frequencies between 1 and 10 Hz are exhibited in Figure 8. The Young's modulus at room temperature is frequency independent and thus, exhibits no effect of mechanical damping. With increasing crystallization the Young's modulus

is generally increased with the highest value of 1.15 GPa obtained for a sample annealed at 873 K for 4 hours.

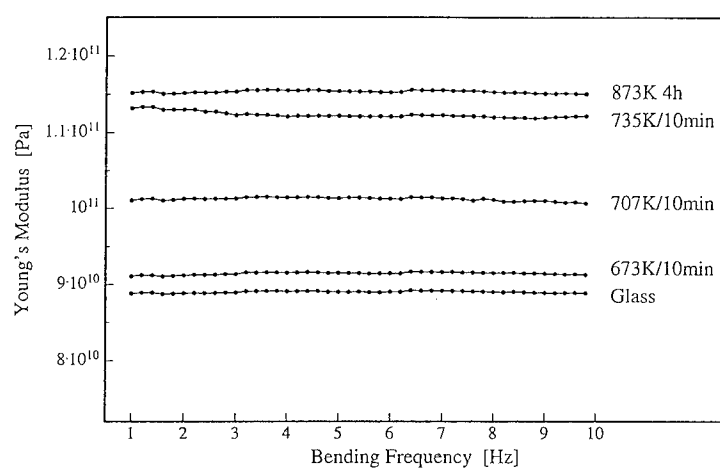


**Figure 8:** The experimentally determined Young's modulus of initially glassy bulk samples at room temperature for different bending frequencies and thermal annealing treatments.

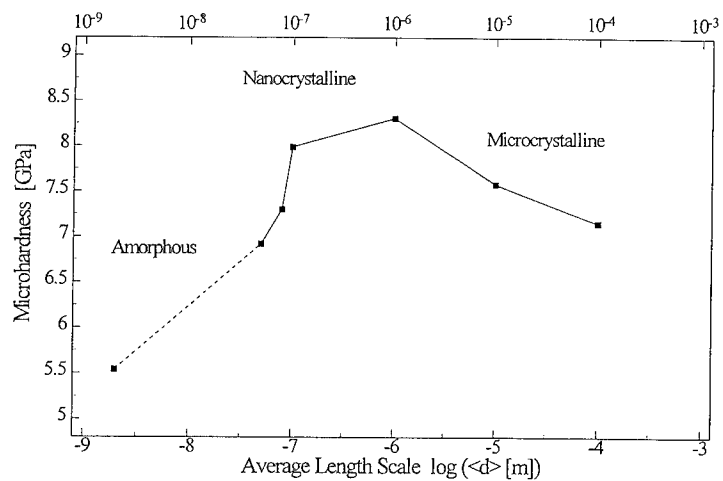


**Figure 9:** Microhardness measured by a nanoindenter as a function of average logarithmic length scales of the micro / nanostructure.

In comparison, the microhardness and local hardness by nanoindentation techniques has been measured for samples with different microstructures as well. The hardness values varied from 5.5 GPa for the fully relaxed glass to 8 GPa for the fully crystallized sample similar to other bulk metallic glasses, such as Zr-Al-Cu-Ni [19]. These results are shown in Figure 9 with an average length scale  $d$  of the microstructure determined by X-ray diffraction and / or electron microscopy. The maximum hardness of 9.5 GPa has been obtained after annealing at 930 K for 2 hours.

As such, a maximum yield strength  $\sigma_f$  can be estimated which corresponds to typically 1 / 3 of the microhardness. It corresponds to 2 - 3 GPa in agreement with earlier experimental results on tensile samples [20]. Thus, the ratio  $\sigma_f / E$ , the elastic limit, is about 2 - 2.5 % which is very high for metallic materials and is typical for refractory ceramics or single-crystalline metal whiskers. So far, such improvements in the elastic limit have not been observed for metallic crystalline bulk samples [21].

## CONCLUSIONS

The described alloy is representative for a new family of bulk glass formers. These alloys are unique in allowing access to the highly undercooled metastable liquid state, the measurement of the thermodynamic and dynamic properties of different liquid and solid metastable states and the control of the crystallization and microstructure developing over a wide range of length scales. Accurate control of the conditions of glass formation and crystallization sequences further will lead to the development of advanced engineering materials with particular shape design and improved physical and mechanical properties.

## ACKNOWLEDGEMENTS

The financial support by DARA (grant 50-WM-9431-1), the Deutsche Forschungsgemeinschaft (Schwerpunkt Unterkühlte Metallschmelzen Fe 313 / 6-3 and Fe 313 / 8-2) and Amorphous Technologies Int. (USA) as well as technical support and discussions with C. Ettl, S. Klose, M.P. Macht, A. Sagel, F. Wanderka, R. Wunderlich and W.L. Johnson are gratefully acknowledged.

## REFERENCES

1. A. Inoue, T. Zhang, N. Nishiyama, K. Ohba and T. Masumoto, *Mater. Trans. JIM* 34 (1993) p. 1234.
2. A. Peker and W. L. Johnson, *Appl. Phys. Lett.* 63 (1993) p. 2342
3. S. Klose, P.S. Frankwicz and H.J. Fecht, *Mat. Sci. Forum*, 179 -181 (1995) p. 729
4. H.J. Fecht, *Mater. Trans. JIM* 36 (1995) p. 391
5. M.P. Macht, N. Wanderka, A. Wiedenmann, H. Wollenberger, Q. Wei, S.G. Klose, A. Sagel und H.J. Fecht, *MRS-Proc.*, Boston (1995) in print
6. F. Wanderka, H.P. Macht, Wei, S. Klose and H.J. Fecht, *Mat. Sci. Forum*, in print
7. S. Klose, Ph.D. Thesis, Technical University Berlin (1995)
8. R. Busch, S. Schneider, A. Peker and W.L. Johnson, *Appl. Phys. Lett* 67 (1995) p. 1544

9. S. Schneider, P. Thiyagarajan and W.L. Johnson, *Appl. Phys. Lett.* 68 (1996) 493
10. J. H. Perepezko and J.S Paik, *J. Non-Crystall. Solids* 61&62, (1984) 113
11. W. Kauzmann, *Chem. Rev.* 43 (1948) p. 219
12. W.M. Saslow, *Phys. Rev. B* 37 (1988) p. 676
13. C.A. Angell, *J. Phys. Chem. Solids*, 49 (1988) p. 863
14. E. Bakke, R. Busch and W.L. Johnson, *Appl. Phys. Lett.* 67 (1995) p. 3260
15. Y. He, R.B. Schwarz, D.G. Mandrus and L. Jacobson, *J. Non-Cryst. Solids*, 205 - 207 (1996) (in print)
16. J.L. Tallon, *Nature* 342 (1989) p. 658
17. H.J. Fecht and W.L. Johnson, *Nature* 334 (1988) p. 50
18. A. Seidel, Diploma Thesis, Technical University Berlin (1995)
19. P.S. Frankwicz, S. Ram and H.J. Fecht, *Appl. Phys. Lett.* 68 (1996) p. 2825
20. H.A. Bruck, T. Christman, A.J. Rosakis and W.L. Johnson, *Scripta Metall.* 30 (1994) p. 429
21. M.F. Ashby, *Materials Selection in Mechanical Design*, Pergamon Press, Oxford (1993)



## CRYSTALLINE, GLASSY AND MOLTEN ELECTROLYTES: CONDUCTIVITY SPECTRA AND MODEL CONSIDERATIONS

K. Funke

Institut für Physikalische Chemie, Westfälische Wilhelms-Universität, Schlossplatz 4/7,  
D-48149 Münster, Germany. E-mail address: k.funke@uni-muenster.de

### ABSTRACT

Conductivity spectra of crystalline, glassy and molten electrolytes are presented and discussed. The spectra cover fourteen decades on the frequency scale as well as wide temperature ranges. In some crystalline ion conductors, the translational and vibrational contributions to the conductivity are well separated on the frequency scale. This is not observed in glasses and melts. In these cases, the vibrational components can, however, often be removed from the total spectra, yielding the translational component. We find that in crystalline, glassy, and molten electrolytes the conductivity caused by translational motion of the ions exhibits plateaux at both low and high frequencies, with a dispersive regime in between. The dispersive sections of the conductivity isotherms always cover a triangular area in a log-log plot of conductivity times temperature versus frequency. For an interpretation, the jump relaxation model turns out to be appropriate for crystalline electrolytes. The existence of different kinds of site is typical of glasses. For fragile molten electrolytes, a simple semimicroscopic model is presented which explains the experimental findings including the Vogel-Fulcher-Tammann temperature dependence of the dc conductivity.

### I. INTRODUCTION AND SURVEY OF SPECTRA

Complete experimental conductivity spectra of solid or molten electrolytes are still rare. This is a consequence of the limited availability of radio, microwave, and far-infrared equipment in most laboratories. Complete conductivity spectra extending from dc to far-infrared frequencies do, however, contain valuable time-resolved information on the mechanisms of ionic motion. They generally consist of a low-frequency part, typically below some 100 GHz, where the conductivity is essentially due to the translational motion of the mobile ions, and of a high-frequency part where it is mainly caused by the vibrational modes of motion.

The crystalline fast ion conductor  $\text{RbAg}_4\text{I}_5$  provides an excellent example. A set of conductivity spectra taken at different temperatures is presented in Fig. 1 [1]. In the following, we will be less concerned with the vibrational components of the spectra, but rather with the hopping conductivity, which is observed below some 150 GHz. The latter is found to consist of three regimes, denoted I, II, III in the figure. I and III are the high- and low-frequency plateau regimes, respectively. In both of them, the temperature dependence of the conductivity is strictly Arrhenius, the activation energy being larger in III than in I. Dispersion is observed in the intermediate regime II, which covers a triangular area in the plot of Fig. 1. The III to II crossover line has a slope of one, while the power-law exponent encountered in II is less than one [2].

Other crystalline electrolytes like Na- $\beta$ -alumina [3], Na- $\beta''$ -alumina [4], and  $\beta$ -AgI [5] have similar sets of conductivity spectra. Their essential features are well explained in terms of the jump relaxation model [6], see Section IV. They are also in general agreement with the predictions of the Coupling Concept [7,8]. Fig. 2 shows a set of spectra obtained from the jump relaxation model. Comparison of Figs. 1 and 2 highlights the striking similarity between the experimental and the model spectra.

High-frequency plateaux of the hopping conductivity are not readily observed in glassy electrolytes. An example is given in Fig. 3 [9,10].

Glassy  $B_2O_3 \cdot 0.56Li_2O \cdot 0.45LiBr$ , see Fig. 3, is a lithium ion conductor. As in crystalline electrolytes, there is an Arrhenius temperature dependence of the dc conductivity, and the III to II crossover line has a slope of one. Shifting the spectra taken at different temperatures along this line, we obtain one master curve, provided the frequencies included are not too high. This feature is called the time/temperature superposition principle; it was also encountered in Figs. 1 and 2.

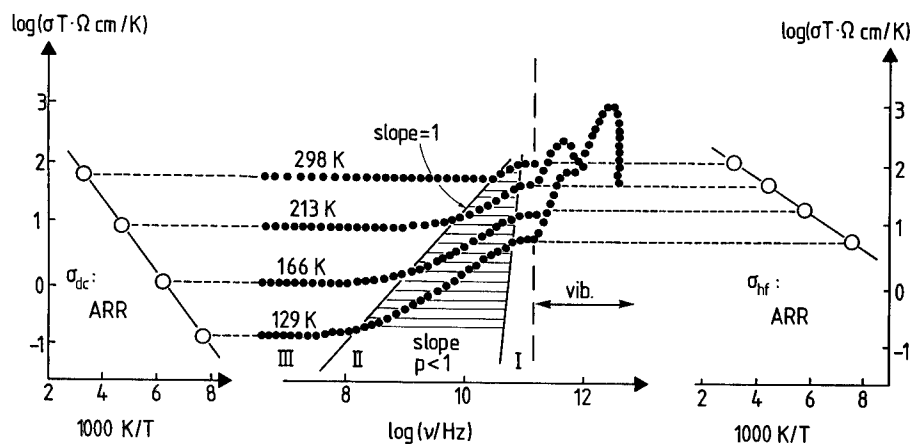


Fig. 1 Conductivity spectra of  $RbAg_4I_5$  at different temperatures; temperature dependence of  $\sigma_{dc}$  and  $\sigma_{hf}$ .

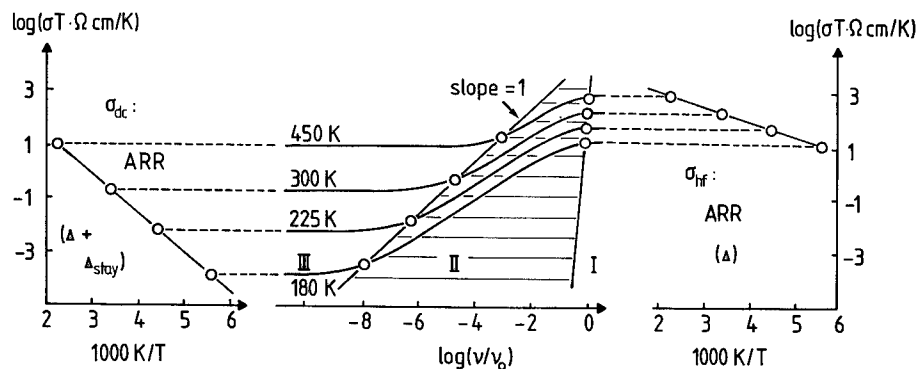


Fig. 2 Set of conductivity spectra as derived from the jump relaxation model [6].

Contrary to Figs. 1 and 2, however, there is no II to I crossover line. Rather, the dispersive hopping conductivity is found to merge into the broad vibrational contribution. The latter has a low-frequency flank with a slope of two and almost no temperature dependence.

Proceeding to a fragile glass-forming molten salt we once again observe similarities and differences in comparison to the previous examples. The spectra of Fig. 4 [11,12] have been taken

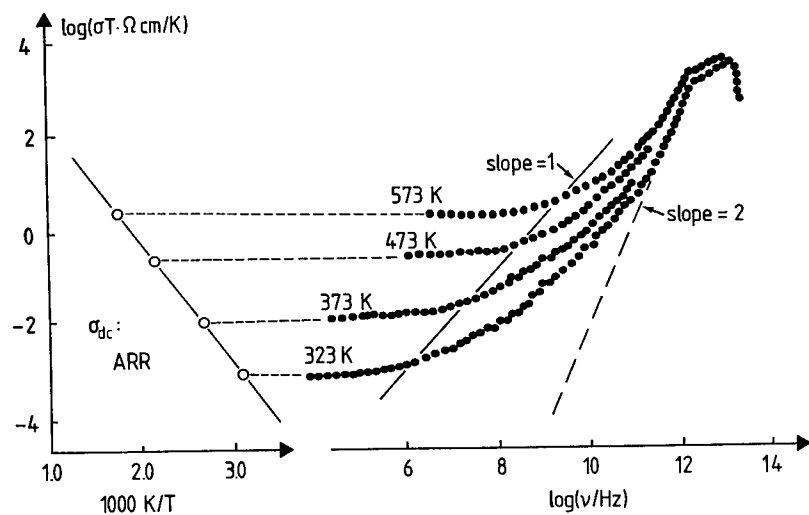


Fig. 3 Conductivity spectra of glassy  $B_2O_3 \cdot 0.56Li_2O \cdot 0.45LiBr$  at different temperatures; temperature dependence of  $\sigma_{dc}$  [9].

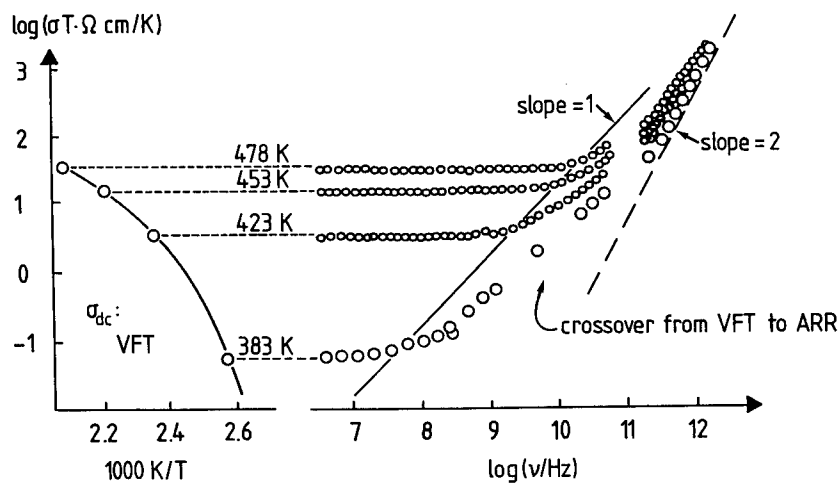


Fig. 4 Conductivity spectra of the fragile glass-forming melt  $0.6 KNO_3 \cdot 0.4 Ca(NO_3)_2$ ; temperature dependence of  $\sigma_{dc}$ .

from  $0.6 \text{ KNO}_3 \cdot 0.4 \text{ Ca(NO}_3)_2$ , abbreviated as CKN. At far-infrared frequencies, the excitation of vibrational motion once again results in a frequency dependent conductivity that obeys a power law with an exponent of two. This becomes more and more apparent as the temperature is decreased. At lower frequencies, the shape of the spectra is at first sight similar to those of the glass in Fig. 3. Contrary to the glass, however, the dc conductivity now has a different temperature dependence which can be described by the empirical Vogel-Fulcher-Tammann law. Most remarkably, there is a gradual crossover from Arrhenius to Vogel-Fulcher-Tammann as the frequency is decreased from the dispersive into the dc regime [13]. Nevertheless, the time/temperature superposition principle is fulfilled, resulting in a III to II crossover line with a slope of one.

## II. HIGH-FREQUENCY PLATEAUX

Today, the most accurate conductivity spectra of an ion conducting glass are probably those of  $\text{B}_2\text{O}_3 \cdot 0.56\text{Li}_2\text{O} \cdot 0.45\text{LiBr}$ , see Fig. 3 [9,10]. Like in other glasses, there is no marked separation between the low-frequency hopping part and the high-frequency vibrational part of the spectrum. However, a separation can be achieved [9,10]. This is possible because the vibrational part varies as frequency squared, with virtually no temperature dependence, whereas the hopping part has a different frequency dependence and varies strongly with temperature. This is demonstrated in Fig. 5 [9,10]. The most striking feature of the remaining hopping part is the appearance of a high-frequency plateau.

Generally, hopping models predict high-frequency plateaux. It has been claimed that these models do not apply for glasses, because they predict a plateau which has never been observed. This argument is now invalidated. The reason for high-frequency plateaux not being directly visible in experimental conductivity spectra of glass is the existence of a broad vibrational component which swamps the high-frequency part of the hopping conductivity.

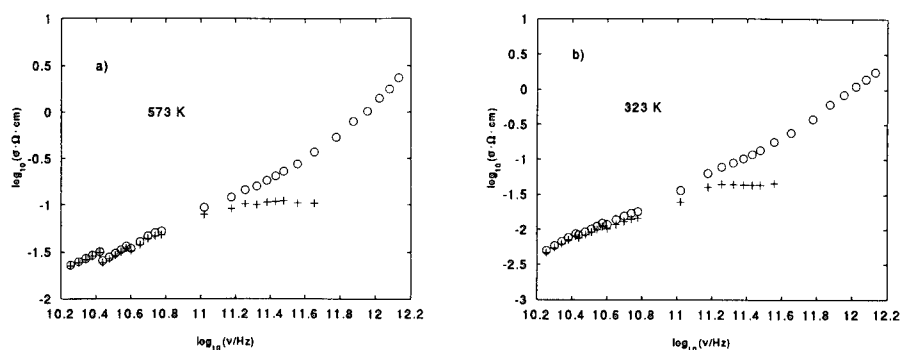


Fig. 5 Microwave and far-infrared conductivity of glassy  $\text{B}_2\text{O}_3 \cdot 0.56\text{Li}_2\text{O} \cdot 0.45\text{LiBr}$ ; o and + denote total experimental spectra and hopping spectra obtained after removing the vibrational contributions [9,10].

In spite of the existence of a high-frequency plateau of the hopping conductivity, the spectra of  $\text{B}_2\text{O}_3 \cdot 0.56\text{Li}_2\text{O} \cdot 0.45\text{LiBr}$  are not well described by the jump relaxation model. Fig. 6 shows data points of the hopping conductivity at 273 K. The low-frequency part of this spectrum has been fitted by the model. The figure includes model spectra thus derived for a set of different

temperatures. Evidently, the experimental data deviate from the model prediction on the high-frequency side. Remarkably, an excellent fit is obtained by

$$\sigma_{\text{hop}}(\omega) - \sigma_{\text{dc}} = A \left(1 + \frac{1}{\omega t_1}\right)^{-0.6} + B \left(1 + \frac{1}{\omega t_1}\right)^{-1.3}. \quad (1)$$

In Eq. (1), the first term on the right hand side results from the jump relaxation model, see Section IV. The second term, featuring a  $\sigma(\omega)$  power law with the unusual exponent 1.3, is additional and will be discussed in Section V.

Let us now revert to the spectra of the CKN melt presented in Fig. 4. Like in glassy  $\text{B}_2\text{O}_3 \cdot 0.56\text{Li}_2\text{O} \cdot 0.45\text{LiBr}$ , the translational and vibrational parts of the conductivity spectra are easily separated from each other [11,12]. A set of translational conductivity spectra of molten CKN is reproduced in Fig. 7, along with Arrhenius-type plots of  $\sigma_{\text{dc}}$  and  $\sigma_{\text{hf}}$ . Unlike  $\sigma_{\text{dc}}$ , the high-frequency conductivity is found to depend on temperature in an Arrhenius fashion. As noted earlier, an Arrhenius temperature dependence is also observed in the dispersive regime II.

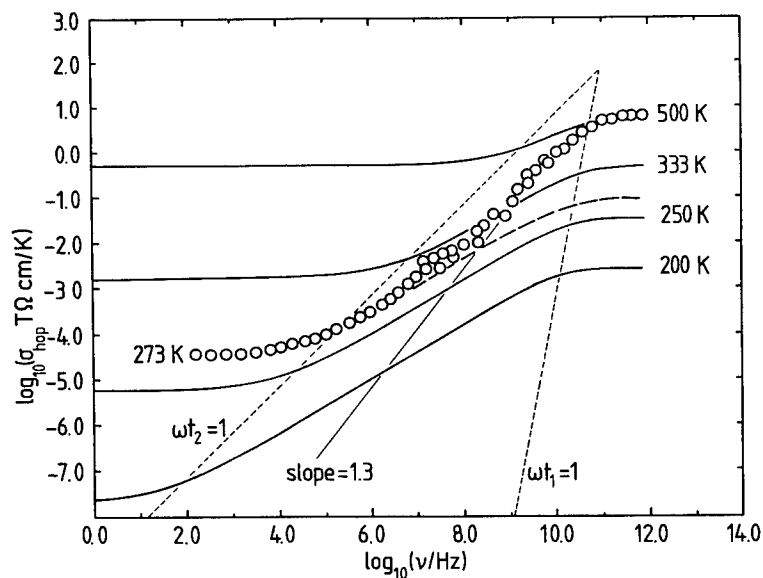


Fig. 6 Hopping conductivity spectrum of glassy  $\text{B}_2\text{O}_3 \cdot 0.56\text{Li}_2\text{O} \cdot 0.45\text{LiBr}$  at 273 K, along with a set of spectra obtained from the jump relaxation model.

Other supercooled glass-forming molten salts, e.g.  $\text{LiCl} \cdot 7\text{H}_2\text{O}$  and  $\text{Ca}(\text{NO}_3)_2 \cdot 4\text{H}_2\text{O}$ , have similar characteristics [13]. All the main features of Fig. 7 are nicely reproduced in a very simple semimicroscopic approach which bears analogy to jump relaxation, but does not presuppose the existence of fixed sites. Fig. 8 is a plot of model spectra and temperature dependences thus obtained. The model will be outlined in Section VI.

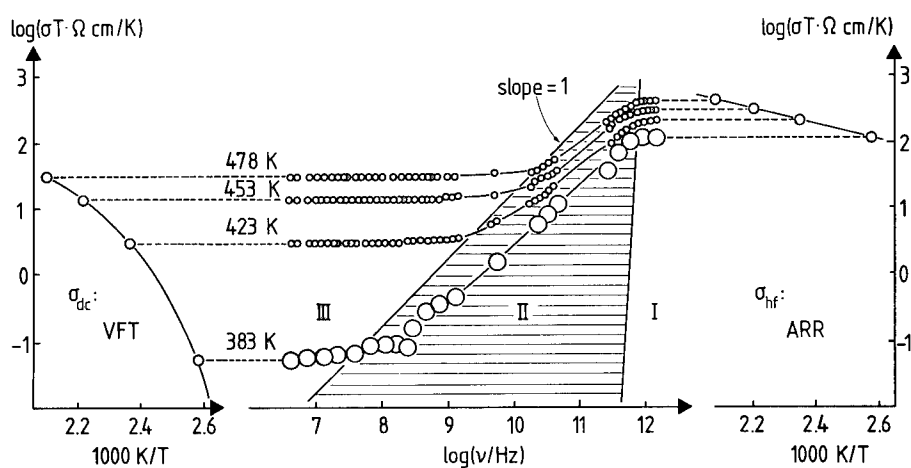


Fig. 7 Translational components of conductivity spectra of CKN. The size of the symbols indicates the possible experimental error; temperature dependence of  $\sigma_{dc}$  and  $\sigma_{hf}$ .

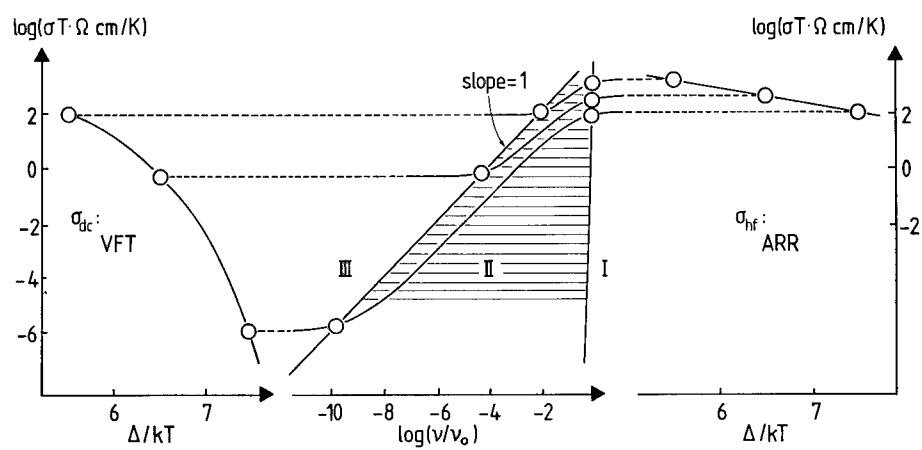


Fig. 8 Model spectra for a molten salt, see Section VI.

### III. MISMATCH AND RELAXATION

In this Section, we consider the relaxation of mismatch which becomes necessary after each elementary step of translational ionic motion. The situation is particularly clear-cut in solid electrolytes. In the following, the discussion is, therefore, largely focused on the hopping of ions in solids. Later on, the main result of this Section will be generalized to apply also in the case of supercooled molten electrolytes.

Suppose an ion performs a hop from site A to site B at time zero. When the ion arrives at B, its neighborhood is still relaxed with respect to A, not B. This causes a backward driving force on the ion. The force may be interpreted as negative gradient of a cage-effect potential provided by the neighborhood. Normalizing it to unity just after the hop, we now introduce a mismatch function,  $g(t)$ . If the ion stays at B, the neighbors will shift and rearrange, and  $g(t)$  will decay from  $g(0) = 1$  to  $g(\infty) = 0$ . In other words, the cage-effect minimum will be shifted from A to B.

The mismatch at site B causes enhanced backward hopping. Denoting the time dependent correlation factor, i.e. the probability for the ion not to have returned to A, by  $W(t)$ , we have a backhop rate of  $-\dot{W}(t)$ . If the ion is still at B at time  $t$ , its backhop rate is  $-\dot{W}(t)/W(t)$ . This is the "conditional" or "normalized" rate.

The rearrangement of the neighbors and the backward hopping of the "central" ion are competing ways of relaxing. They are assumed to be balanced at all times:

$$-\frac{\dot{W}(t)}{W(t)} \propto -\dot{g}(t). \quad (2)$$

Eq. (2) claims that, provided the ion is still at B, its tendency to hop back to A and the tendency of the neighborhood to relax are proportional to each other. Considering the boundary conditions at  $t = 0$  and at long times, we find:

$$-\frac{\dot{W}(t)}{W(t)} = -\dot{g}(t) \cdot \ln(1/W(\infty)), \quad (3)$$

where  $W(\infty)$  is the correlation factor, i.e., the total fraction of "successful" hops.

In the next Sections, Eq. (2) is used for deriving dispersive conductivities in crystalline, glassy, and molten electrolytes, with a reinterpretation of  $W(t)$  for melts. In fact, combining Eq. (2) with crystal-like / glass-like / melt-like properties will be shown to reproduce the characteristics of the conductivity spectra in either case.

### IV. JUMP RELAXATION IN A CRYSTAL

Spectra like those of Fig. 1 are well explained in terms of the jump relaxation model [6]. The model does not discern between different kinds of site, but assumes that there are vacant neighboring sites in the immediate neighborhood of each mobile ion. This is fulfilled in  $\text{RbAg}_4\text{I}_5$ , where there are 48 energetically similar sites (called Ag 1 and Ag 2) for the 16 silver ions in the unit cell [1,15].

The treatment of the model as presented in the brief outline of this Section is simpler than the original one. Nevertheless, the notations and equations are the same.

In a system where diffusion is via sites, all hopping processes are thermally activated. This does not only hold for individual hops over barriers, but also for the completion of successful hops. Consider an ion performing a successful hop from A to B. In a first step, it has to surmount the energy barrier  $\Delta$  between these sites, which is the high-frequency activation energy,  $\Delta_{\text{hf}}$ . The

ensuing site relaxation at B involves further activated hops of other ions. Necessitating a number of individual activated steps, the total process of a successful hop has a total activation energy,  $\Delta_{dc}$ , which is larger than  $\Delta_{hf}$ . With the help of the total correlation factor,  $W(\infty)$ ,  $\Delta_{dc}$  can be written as

$$\Delta_{dc} = \Delta_{hf} + \Delta_{stay} = \Delta_{hf} + kT \ln(1/W(\infty)) \quad (4)$$

It is important to realize that the Arrhenius law of  $\sigma_{dc}$  and the power law of the dispersive conductivity are mutual consequences of each other. We first show how the power law is derived from the Arrhenius behavior. The reciprocal argument will then be given at the end of this Section.

To derive the time dependent correlation factor and the frequency dependent conductivity, let us consider the energy  $\epsilon(t)$  required for the ion to return from B to A successfully, if it is at B at time  $t$ . Starting out from a comparatively small value,  $\epsilon(0) < \Delta$ ,  $\epsilon(t)$  will increase as  $g(t)$  decreases, becoming  $\epsilon(\infty) = \Delta_{dc}$  in the long-time limit. Relating  $\epsilon(t)$  to  $g(t)$ , the simplest assumption is

$$g(t) = \frac{\epsilon(\infty) - \epsilon(t)}{\epsilon(\infty) - \epsilon(0)} \quad (5)$$

Eq. (5) corresponds to an harmonic shape of the cage-effect potential.

Combining Eqs. (3) to (5), we obtain two relations which are extremely useful for understanding conductivity spectra of solid electrolytes:

$$-\frac{\dot{W}(t)}{W(t)} = p \cdot \frac{\dot{\epsilon}(t)}{kT} \quad (6)$$

$$p = \frac{\epsilon(\infty) - \Delta}{\epsilon(\infty) - \epsilon(0)} = \frac{-\dot{W}/W}{\dot{\epsilon}/kT} \quad (7)$$

$$= \frac{\text{normalized backhop rate}}{\text{normalized site relaxation rate}}$$

Note that  $p$  is smaller than one and temperature independent.

The final steps towards  $W(t)$  and  $\sigma(\omega)$  are now simple. At short times, when onward hops are still irrelevant, thermal activation is introduced by

$$-\frac{\dot{W}(t)}{W(t)} = \frac{1}{t_0} \exp[-\epsilon(t)/kT] \quad (8)$$

yielding

$$W(t) = \left(1 + \frac{t}{t_1}\right)^{-p} \text{ at short times} \quad (9)$$

with



$$t_1 = p t_0 \cdot \exp[\varepsilon(0)/kT] \quad (10)$$

At long times, Eq. (8) can be suitably modified to account for the effect of onward hops. As a result, we obtain a crossover from the power law of Eq. (9) into the long-time value of  $W(\infty)$ . An approximate description is

$$W(t) \approx W(\infty) + [1 - W(\infty)] \cdot \left(1 + \frac{t}{t_1}\right)^{-p} \quad (11)$$

The conductivity spectrum,  $\sigma(\omega)$ , is proportional to the Fourier transform of the autocorrelation function of the velocity, which in turn is proportional to the time derivative of  $W(t)$ . As long as power laws are involved, with exponents less than two,  $W(t)$  and  $\sigma(\omega)/\sigma(\infty)$  are almost exact mirror images of each other when represented in log-log plots. This is seen in Fig. 9. At the same time,  $\sigma(\omega)$  is well approximated by

$$\sigma(\omega) \approx \sigma_{dc} + [\sigma_{hf} - \sigma_{dc}] \cdot \left(1 + \frac{1}{\omega t_1}\right)^{-p} \quad (12)$$

$$\sigma(\omega) - \sigma_{dc} \propto \left(1 + \frac{1}{\omega t_1}\right)^{-p}$$

This result has already been used in Eq. (1). In Eq. (12), the constant  $p$  of Eq. (7) turns out to be the Jonscher power-law exponent [2].

Regimes I, II, III have again been marked in Fig. 9. Evidently, every hop contributes to  $\sigma(\omega)$  in regime I, while in regime III only successful hops contribute. In regime II, at angular frequency  $\omega$ , only those hops are seen which are still successful at time  $t = 1/\omega$ .

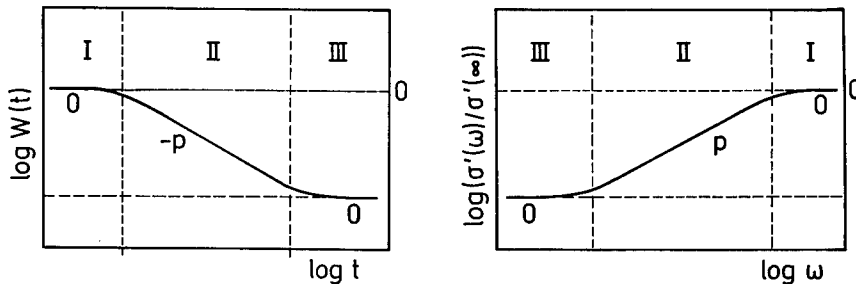


Fig. 9 Time dependent correlation factor and normalized hopping conductivity as obtained from the jump relaxation model.

At the crossover from II to III, when  $W(t)$  approaches  $W(\infty)$ , the mean square displacement is about one hopping distance squared. The crossover angular frequency may, therefore, be approximately identified with the rate of successful hops. This rate increases with increasing temperature, causing an increased conductivity. As a consequence, the II to III crossover line of Fig. 2 has to have a slope of one.

The crossover lines in Fig. 2 being linear, the power-law behavior in regime II implies that the Arrhenius law of  $\Delta_{hf}$  transforms into an Arrhenius law of  $\Delta_{dc}$ . In the case of a vertical I to II crossover line, which is often not a bad approximation, we have  $\Delta_{dc} = \Delta_{hf} / (1-p)$ .

## V. JUMP RELAXATION IN A GLASS

A typical hopping conductivity spectrum of glassy  $B_2O_3 \cdot 0.56Li_2O \cdot 0.45LiBr$  was shown in Fig. 6. An excellent fit was provided by Eq. (1). The first term on the right hand side of Eq. (1) was expected on the basis of the jump relaxation model, the second is additional. The most puzzling feature is the observation of a power law exponent which is larger than one, but smaller than two.

A consistent explanation is given by the "Unified Site Relaxation Model", which is an extension of the jump relaxation model including essential features of the dynamic structure model.

One of the basic ideas of the dynamic structure model is the following. The mobile  $A^+$  ions (here:  $Li^+$  ions) create optimally configured  $\bar{A}$  sites for themselves when the glass is formed from the melt, while less favorable  $\bar{C}$  sites also exist. Translational diffusion is essentially via  $\bar{A}$  sites which play the role of "stepping stones" for the mobile ions.

The original jump relaxation model can, therefore, explain the hopping via  $\bar{A}$  sites, resulting in  $\sigma_{dc}$  and in the first term on the right hand side of Eq. (1). On the other hand, the second term calls for a separate explanation.

In Fig. 10 we present a sketch of the effective potentials felt by ions hopping from  $\bar{A}$  to  $\bar{A}$  and from  $\bar{A}$  to  $\bar{C}$  sites. The construction of Fig. 10 is made by superimposing site sensitive and cage-effect potentials.

The exponent 1.3 in the second term of Eq. (1) is now interpreted on the basis of Eq. (7). Although the site relaxation rate,  $dc(t)/dt$ , may be similar at  $\bar{A}$  and  $\bar{C}$ , the backhop rate will be larger after an  $\bar{A}$  to  $\bar{C}$  hop than after an  $\bar{A}$  to  $\bar{A}$  hop. This results in a larger ratio in Eq. (7) and, hence, in a larger exponent for the  $\bar{A}$  to  $\bar{C}$  (and back to  $\bar{A}$ ) hops, even surpassing unity.

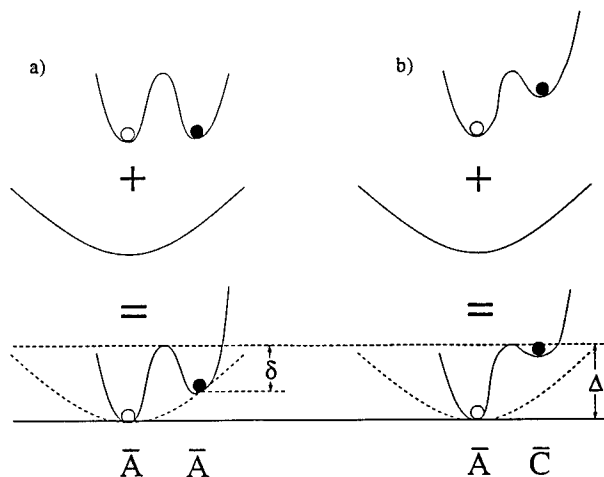


Fig. 10 Sketch of single-particle potentials encountered by hopping ions (at  $t = 0$ ) in a)  $\bar{A}$  to  $\bar{A}$  and b)  $\bar{A}$  to  $\bar{C}$  hops. Each of the effective potentials consists of two contributions: a site-sensitive potential (on top) and a cage-effect potential.

An alternative explanation is provided by the assumption that the  $\bar{A}$  and  $\bar{C}$  sites differ in the rates at which their respective neighborhoods relax. This would mean that the neighborhood of a  $\bar{C}$  site is typically more rigid and less yielding than that of an  $\bar{A}$  site.

On the basis of Eq. (7), either description of  $\bar{C}$  sites has the same consequence, viz., a larger power-law exponent. The ratio of Eq. (7) being larger than one implies that the backward hopping is faster than the "digging" of a deeper potential minimum at site  $\bar{C}$ .  $\bar{A}$  to  $\bar{C}$  hops are, therefore, not normally successful, but followed by a backward hop.

## VI MOTION AND RELAXATION IN A MELT

Let us now consider the change in spectral shape that occurs, when a glass transforms into an undercooled melt, i.e. at the glass transition temperature,  $T_G$ . According to the few examples that are presently known, the applicability of Eq. (1) is restricted to temperatures below  $T_G$ . Above  $T_G$ , non-constant intermediate values of the apparent power-law exponent are observed. Like in Fig 7, the exponent typically increases with frequency, but never surpasses unity. Eventually, the translational conductivity attains its high-frequency plateau.

The model spectra of Fig. 8 have the same characteristics as the experimental ones. For their construction we have again used Eq. (2). The argument is, however, different from the last two Sections, as fixed sites and site energies do not exist in a melt.

At very short times, corresponding to frequencies in the high-frequency plateau regime, individual ions are assumed to perform thermally activated elementary steps of motion in an otherwise essentially rigid environment. The activation energy for these "hops" determines the temperature dependence of  $\sigma_{hf}$ , which is Arrhenius.

At longer times, functions  $W(t)$  and  $g(t)$  are considered. However, there is a slight change in the meaning of  $W(t)$  as compared with the previous Sections. As fixed sites do not exist,  $W(t)$  is now the average fraction of the original displacement still encountered at time  $t$ . As before,  $g(t)$  is the mismatch function.

The model spectra result from two simple rate equations. The first is Eq. (2). The second is

$$-\dot{g}(t) \propto g(t) \cdot W(t) \quad (13)$$

The underlying conception is the following. The rate of reduction of the mismatch felt by the "central" ion is proportional to the rate of the induced rearrangement of its neighbors. The latter rate is, in turn, proportional to a convolution of the driving force,  $g(t)$ , and the velocity autocorrelation function,  $\langle v(0) \cdot v(t) \rangle \propto \dot{W}(t)$ . The approach is so simple that a distinction between different kinds of ions is not even made. As  $g(t)$  varies with time much more slowly than  $W(t)$  does, the convolution  $g * \dot{W}$  is well approximated by the product  $g \cdot \dot{W}$ , yielding Eq. (13).

The combined rate equations, Eqs. (2) and (13), are now solved with the help of the exponential integral function  $E_1(x)$ . The result is

$$t \propto E_1 \left[ \ell n \left( \frac{W(t)}{W(\infty)} \right) \right] - E_1 \left[ \ell n \left( \frac{W(0)}{W(\infty)} \right) \right] \quad (14)$$

Like in solid electrolytes,  $\langle r^2(t) \rangle$  has to surpass a certain value until the mobile ion loses all memory of its initial displacement and ordinary diffusion sets in. As a consequence, the II to III crossover line has to have a slope of one. Transforming  $W(t)$  into  $\sigma(\omega) / \sigma_{hf}$  and arranging spectra  $\sigma(\omega)$  in a way that complies with a II to III crossover line with a slope of one and with

the Arrhenius law at high frequencies, we automatically obtain results like in Fig. 8. The resulting temperature dependence of  $\sigma_{dc}$  is

$$\ln(\sigma_{dc} T) = A - \frac{\Delta}{kT} - B \cdot \exp\left(\frac{\Delta}{kT}\right) \quad (15)$$

Choosing the parameter values  $A = 11.45$ ,  $B = \exp(-4.55)$ ,  $\Delta/k = 2580$  K, we obtain conductivity spectra close to those of CKN. At the same time, the temperature dependence of the dc conductivity of CKN is also nicely reproduced.

Comparing solid and molten electrolytes, we now realize that the existence or non-existence of fixed sites makes the entire difference. If the hopping is via sites, the average amount of energy required for the relaxation process after a hop is well defined, and  $\sigma_{dc}$  obeys the Arrhenius law. On the other hand, if the rate of mismatch reduction cannot be related to the rate of site relaxation at a fixed site, then the argument of this Section applies and  $\sigma_{dc}(T)$  is well described by Eq. (15) or by the empirical Vogel-Fulcher-Tammann law.

#### ACKNOWLEDGEMENTS

I should like to thank A. Bunde, C. Cramer, W. Dieterich, M.D. Ingram, P. Maass, K.L. Ngai, B. Roling and T. Saatkamp for many fruitful discussions. The present work was largely funded by the Deutsche Forschungsgemeinschaft. Financial support by the DAAD and by the Fonds der Chemischen Industrie is also gratefully acknowledged.

#### REFERENCES

1. K. Funke, T. Kloidt, D. Wilmer, and C.J. Carlile, *Solid State Ionics* **53-56**, 947 (1992).
2. A.K. Jonscher, *Nature* **267**, 673 (1977).
3. U. Strom and K.L. Ngai, *Solid State Ionics* **5**, 167 (1981).
4. C. Cramer, R. Graeber, M.D. Ingram, T. Saatkamp, D. Wilmer, and K. Funke, *Mat. Res. Soc. Symp. Proc.* **369**, 233 (1995).
5. K. Funke, D. Wilmer, T. Lauxtermann, R. Holzgreve, and S.M. Bennington, *Solid State Ionics* **86-88**, 141 (1996).
6. K. Funke, *Prog. Solid St. Chem.* **22**, 111 (1993).
7. K.L. Ngai, *Comments Solid State Phys.* **9**, 127 (1979) and **9**, 141 (1980).
8. K. Funke, *J. Non-Cryst. Solids* **172-174**, 1215 (1994).
9. C. Cramer, K. Funke, T. Saatkamp, D. Wilmer, and M.D. Ingram, *Z. Naturforsch.* **50a**, 613 (1995).
10. K. Funke, C. Cramer, B. Roling, T. Saatkamp, D. Wilmer, and M.D. Ingram, *Solid State Ionics* **85**, 293 (1996).
11. T. Saatkamp, Thesis, Münster 1997.
12. K.L. Ngai, Cramer, T. Saatkamp, and K. Funke in *Non equilibrium phenomena in super-cooled fluids, glasses and amorphous materials*, edited by M. Giordano, D. Leporini, and M.P. Tosi (World Scientific, Singapore, 1996), p. 3.
13. C. Cramer, K. Funke, M. Buscher, A. Happe, T. Saatkamp, and D. Wilmer, *Phil. Mag. B* **71**, 713 (1995).
14. C.A. Angell, *J. Phys. Chem.* **68**, 1917 (1964).
15. W.F. Kuhs and G. Heger, Experimental Report, Institut Laue-Langevin, Grenoble, 1981.

## SPACE-TIME-CORRELATIONS FOR CATION MOTION IN ALKALI SILICATES

John KIEFFER

Department of Materials Science & Engineering, University of Illinois, Urbana IL 61801

### ABSTRACT

The motion of structural components in alkali silicates has been studied using molecular dynamic simulations. The relevant time correlation functions have been recorded over periods of up to 0.5 nanoseconds. The van Hove correlation functions reveal that alkali cation diffusion occurs by hopping between rather well defined sites, even at temperatures far above the melting point. The accessibility of such sites is controlled by the relaxation of the surrounding network, and constitutes the mechanism of coupling between the motion of network and modifier elements. The intermediate scattering functions exhibit a stretched exponential behavior, with a wavevector dependent stretching exponent. This is the result of a distribution of residence times at individual cation sites. When the diffusion process is examined on a coarser scale, at which Brownian motion is applicable, this distribution remains undetected. As an alternative to the Kohlrausch function, several mechanistic approaches for describing the relaxation behavior of these structures are discussed.

### INTRODUCTION

Network glasses have a potential for application as electrolytes in fuel cells and batteries or as sensors.<sup>1-6</sup> The efficiency and responsiveness of these devices depends to a large degree on the mobility of the charge carrying species. Ionic conduction is largely understood in the context of the supporting network structure, and can be semi-quantitatively described by models such as the modified random network model<sup>7,8</sup> and the cluster bypass model.<sup>9</sup> One of the constraints in the design of materials that exhibit enhanced conductivity stems from the fact that an increase in the concentration of mobile cations also results in a larger extent of network modification. Not only does the glassy electrolyte then lose its mechanical and chemical stability, but more loosely bonded network segments can dynamically couple to the alkali cations and reduce their mobility.<sup>10,11</sup>

Molecular dynamic (MD) simulations provide an ideal tool for studying kinetic processes on an atomic scale. With the present investigation we attempted to elucidate the issue of cation-network interactions, by analyzing the cation motion for possible correlation effects. In analogy with transport mechanisms in crystalline materials, such correlations are likely to reveal details about how cation migration is facilitated or constrained by the surrounding structure.

### COMPUTATIONAL PROCEDURE

We chose binary alkali-disilicates as model substances for network glasses. We have developed reliable semi-empirical interaction potentials for these systems. The potentials include a repulsive Born-Mayer term, a Coulomb term, whose long-range effects were handled by an Ewald summation, and three-body terms to represent the directional covalent bonding.<sup>12</sup> The potential parameters were optimized such as to reproduce experimental data for crystalline silica at room temperature and zero pressure, including density, Si-O bond distance, as well as infrared and Raman spectra. The simulations of all systems were started from random configurations, which were thermalized at 6000 K by withdrawing excess energy. After the proper coordinations were established, the structure was further relaxed at constant pressure. Subsequently, the configurations were cooled to 3000K over a period of 8 to 10 ps, using the procedure described by Andersen.<sup>13</sup> At the target temperature the structures were then further relaxed during an additional 10 ps, before the accumulation of the data for the computation of intermediate scattering functions

and dynamic structure factors was begun. All systems contained 648 particles. The nature of the alkali cation was varied to include Li, Na, and K.

The mobilities of the alkali cations were evaluated using several different formalisms, including the mean squared displacement and the velocity autocorrelation function of the species. For either method, averages were taken over many time origins and for a large number of atoms. When following atomic trajectories over extended periods of time, larger than about 60 ps, the diffusion coefficients furnished by either method are in excellent agreement.

A third method, easily accessible by MD simulations, involves the calculation of self-intermediate scattering functions,

$$F_s(\mathbf{q}, t) = \frac{1}{N} \left\langle \sum_{j=1}^N e^{i\mathbf{q}(\mathbf{r}_j(t) - \mathbf{r}_j(0))} \right\rangle. \quad (1)$$

This function describes the decay of density fluctuations with a wavelength given by  $\mathbf{q}$ . In case these fluctuations are controlled by random diffusion, one can derive the expression,

$$F_s(\mathbf{q}, t) = e^{-q^2 D t}, \quad (2)$$

which relates the intermediate scattering function to the diffusion coefficient of the mobile species.  $F_s(\mathbf{q}, t)$  corresponds to the Fourier-Laplace transform of the dynamic structure factor,  $S_s(\mathbf{q}, \omega)$ , the signal obtained from an incoherent scattering experiment. Further transformation of  $F_s(\mathbf{q}, t)$  with respect to  $q$  yields the van Hove correlation function,  $G_s(\mathbf{r}, t)$ , which describes the probability of a particle to be at a distance  $\mathbf{r}$  from its initial position, after some time  $t$ .

## RESULTS AND DISCUSSION

It is essential to be able to characterize the process governing the temporal evolution of the density fluctuations as random, for eq.(2) to be applicable. For the systems studied here, this is better observed, the smaller the wavevector magnitude. For larger wavevectors, the rate of decay of the  $F_s(\mathbf{q}, t)$  becomes less than exponential, i.e., it exhibits a stretched long-time tail. This indicates that on a short length scale, motion of the cations is non-random. Direct observation of atomic trajectories, as well as the shape of the van Hove correlation function, clearly indicate that cation diffusion occurs via a jump process, even at a temperature of 3000K. The jump itself takes no longer than an oscillatory period, and the time of residence in each site shows a wide distribution.

The deviation from random implies that the motion of cations is correlated. We therefore focus our analysis on identifying the mechanisms that are responsible for this correlation. First we will examine the time domain, and see whether the deviation from exponential in the intermediate scattering function can be attributed to the oscillatory components in particle motion. This would then point to the near-range structural environment, as it determines the force field with which particles are caged in at their sites. The oscillatory nature of atomic motion is most obvious in the velocity autocorrelation function. Taking this into account, one can compute a mean squared displacement function,<sup>14</sup>

$$\rho_1(t) = \int_0^t (t - t') \langle \mathbf{v}(t') \cdot \mathbf{v}(0) \rangle dt', \quad (3)$$

and substitute this for the product  $Dt$  in eq. (2). In Fig. 1 we compare the function  $e^{-q^2 \rho_1(t)}$  obtained by this procedure for the case of sodium diffusion in sodium disilicate, along with  $\rho_1(t)$ , the velocity autocorrelation function which was used to evaluate  $\rho_1(t)$ , and the intermediate scattering function calculated using eq. (1). The wavevector magnitude was  $12.6 \text{ nm}^{-1}$ . We see that there is poor agreement between  $F_s(\mathbf{q}, t)$  and its approximation based on the mean squared displacement function,  $e^{-q^2 \rho_1(t)}$ . The reason for this is quite obvious when examining the velocity correlation function. Accordingly, cation motion becomes uncorrelated after half a picosecond.

This is a much shorter period than the average residence time of the cations at a given site. The rapid loss of memory about its preceding motion is due to the fact that the structure surrounding the cation also fluctuates, thus continuously changing the force field which controls the cation's motion.

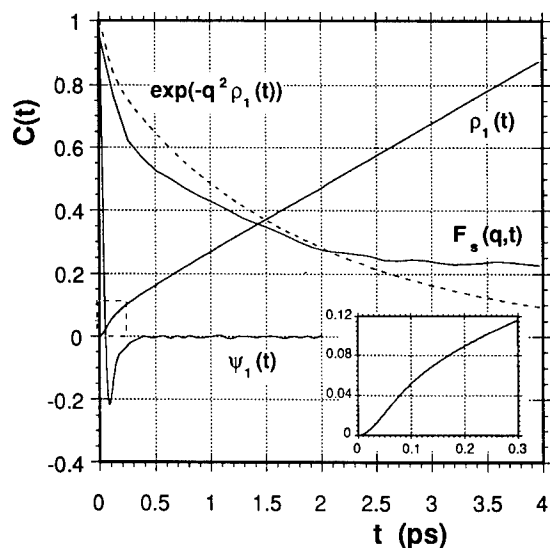


**Fig. 1**

Comparison between the intermediate scattering function derived from the corrected Gaussian approximation and that determined from the density fluctuations of the simulated structure. The mean squared displacement function,  $\rho_1(t)$ , has been calculated from the VACF,  $\psi(t)$ , and was used to calculate the corresponding intermediate scattering function. Inset: Magnification of the initial portion of  $\rho_1(t)$ .

The long-range migration of the cations, on the other hand, is a process which involves a number of adjacent network interstices. In order to identify possible correlations in the jumps of the cations to neighboring sites, one must first find the location of such sites relative to a given cation. To this end, we added 'ghost' particles to the MD configuration. By ways of their interaction potential, ghost particles experience their surroundings exactly as the alkali cations do. The actual structure, however, remains unaware of the presence of these ghost atoms. At first, a large number of ghost atoms were placed at random into the structure. The structure was allowed to evolve dynamically for several hundred iterations, until all ghost atoms have settled into accessible interstices. All but one ghost atom occupying the same interstice were eliminated, except if the interstice was sufficiently large for two cations to exist in, despite strong repulsion between each other.

Surprisingly, only a small number of ghost atoms remained in the system, indicating that either there are very few vacant sites for alkali cations, or, if unoccupied, the structure surrounding these sites collapses. Since even those ghost particles that remained were typically at a rather high energy, it seems that the network structure dynamically adjusts to the presence of modifying cations. One can determine a void distribution function like a regular pair correlation function between actual cations and the ghost atoms, with the restriction that the trajectory between the cation and the ghost site must not be obstructed by other structural entities. Here we simply excluded as countable voids any ghost sites for which the straight line between its center and that of the cation came within an exclusion distance to a third, real atom. The exclusion distance was chosen as the radius at which the repulsive energy of the interatomic potential between this third atom and the ghost crosses zero.

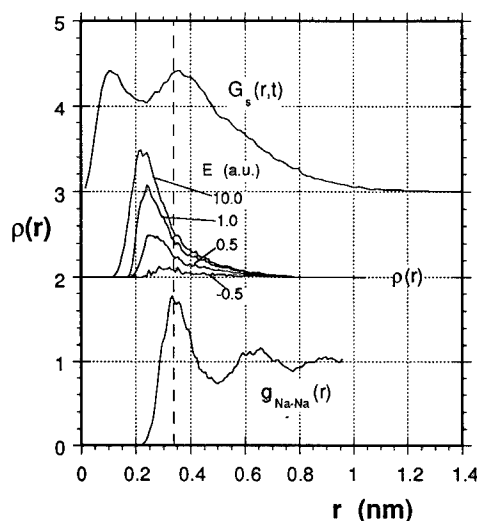


**Fig. 2**

Normalized cation-void distribution functions,  $\rho(r)$ , relative to sodium positions in sodium disilicate, as determined by using ghost particles that have the same thermodynamic characteristics as the alkali cations, but are invisible to the atoms of the actual structure. Labels indicate the maximum energies of the ghost particles. The sodium-sodium pair correlation function,  $g_{Na-Na}(r)$ , and the van Hove self correlation function,  $G_s(r,t)$  (multiplied by  $4\pi r^2$ ), for  $t = 1.5$  ps, are offset for clarity.

Fig. 2 shows the void distribution function determined in this way for sodium in sodium disilicate. Curves are labeled with the ghost particle energy, which shows how unlikely it is to find large unoccupied network interstices. The sodium-sodium pair correlation function and the van Hove self-correlation function for this system are plotted on the same graph. The void density distribution functions show a prominent peak, and decay almost monotonically towards large distances. With decreasing threshold energy the prominent peak shifts towards larger distances, approaching that of the first coordination shell in the sodium-sodium pair correlation function. Accordingly, the largest density of void space exists in the immediate vicinity of the cation, and is part of the same interstice. Obviously, when located within the same interstice, the ghost particle is strongly repelled by the real alkali cation, and finds itself at a high energy. The real cation in turn has no problem to move to the corresponding positions, which shows that alkali cations have great flexibility to move about their current site. It is this flexibility which causes the motion of the cations to become so rapidly uncorrelated.

Void space characterized by a low ghost particle energy, on the other hand, can be considered as stable sites, where the cation could jump to without being drawn back to its original site. It is not surprising that the stable sites are located at about the distance of the first cation-cation coordination shell. The fact that these really are the sites to which the alkali cation jump finds further support in the structure of the corresponding  $G_s(r,t)$ , where a distinct second peak develops after a short period of time, at about the same distance. On the other hand, the density of vacant cation sites is rather small, typically not more than a few percent of the total number of cations. Consequently, the migration of alkali cations depends on the opening of suitable interstices as it moves along. This constitutes the coupling mechanism between cation motion and network relaxation.

Finally, the signature of this coupling can be found in the relaxation kernel which can be used to express the intermediate scattering function in the framework of the generalized Langevin formalism. Accordingly, the evolution of any time correlation function can be expressed as a convolution of this function itself with a relaxation kernel (or memory function),  $\kappa(q,t)$ ,<sup>14-16</sup>

$$\frac{dF_s(q,t)}{dt} = -\int_0^t \kappa(q,t') F_s(q,t-t') dt' \quad (4)$$



This equation is conveniently solved by ways of its Laplace transform, to yield  $F_s(q, s) = [s + \kappa(q, s)]^{-1}$ , which in the limit of  $s = i\omega$  corresponds to the self-dynamic structure factor,  $S_s(q, \omega)$ . This structure factor can be evaluated using atomic trajectories from MD simulations. In Fig. 3  $S_s(q, \omega)$  for sodium in sodium disilicate is plotted as function of the frequency, for different  $q$ -values. The symbols represent simulation data. In case of random diffusion  $S_s(q, \omega)$  assumes a Lorentzian functional form, and on the log-log plot the structure factor decreases with increasing frequency at a slope of  $-2$ . The data in Fig. 3 clearly shows deviations from this behavior. Especially for large  $q$ -values,  $S_s(q, \omega)$  exhibits a shoulder at high frequencies, which is consistent with the observation of  $\beta$ -relaxation processes. The solid lines in Fig. 3 are model solutions of eq. (4) assuming as a functional form for the relaxation kernel  $\kappa(q, t) = (A\delta(t-0) + Be^{-t/\tau} \cos \Omega t)$ . The fit of the data by this model is not entirely satisfactory, and hence no claim is made here for completeness of the model describing this process. However, the comparison allows one to at least identify the necessary components of  $\kappa(q, t)$ , and their physical meaning. The first term in  $\kappa(q, t)$  amounts to a Brownian diffusion model. It dominates at low  $q$ -values, and the factor  $A$  corresponds to  $q^2 D$ . The second term represents a non-diffusive thrust, such as a pressure wave which oscillates with a frequency  $\Omega$ , and is damped as characterized by a relaxation time  $\tau$ . This second term is required to reproduce the high-frequency shoulder in  $S_s(q, \omega)$ , which can then be understood as the result of structural relaxation in the wake of phonon collisions. The diffusive component in  $\kappa(q, t)$  describes the long-range migration of the cations, on a scale which is unaffected by the correlations imposed by the local environments. The latter correlations are reflected in the damped oscillatory thrust, which reflects the impediment imposed on cation motion due to the more slowly relaxing network.

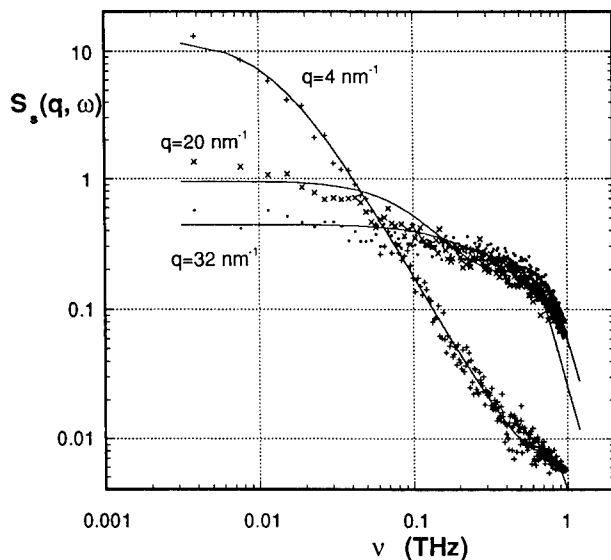


**Fig. 3**  
Self-dynamic structure factors,  $S_s(q, \omega)$ , for sodium in sodium disilicate at 3000 K, and for various wavevector magnitudes. Symbols are simulation results, and lines show the approximation by a model, as described in the text.

## CONCLUSION

Cation migration in alkali silicate melts occurs via a jump diffusion mechanism. The diffusion process is random on a large scale, but it increasingly deviates from randomness on a scale comparable to the size of structural units. The long-range migration of cations has to be facilitated by structural relaxations of the supporting network, which result in the opening of sites accessible to the cations upon a jump. While in a given site, the cation motion becomes rapidly uncorrelated, as is reflected by its velocity correlation function. The coupling between cation motion and network relaxation can be observed as a shoulder in the self-dynamic structure factor. By comparison with simple models for a memory function approach to the description of the diffusion process, one can conclude that the deviation from random motion is due to a damped oscillatory thrust imposed by non-diffusive relaxation of the surrounding network, and which is part of the  $\beta$ -relaxation process.

Acknowledgments: This research was supported by the National Science Foundation, and the US Department of Energy by providing computational resources at Argonne National Laboratory.

## References:

- <sup>1</sup> C.A. Angell, *Solid State Ionics* **18/19**, 72 (1985)
- <sup>2</sup> H.L. Tuller, D.P. Button and D.R. Uhlmann, *J. Non-Cryst. Solids* **40**, 93 (1983)
- <sup>3</sup> J.M. Reau and M. Poulain, *Mat. Chem. Phys.* **23**, 189 (1989)
- <sup>4</sup> F. Rocca and A. Fontana, *Phil. Mag.* **B59**, 57 (1989)
- <sup>5</sup> A. Pradel and M. Ribes, *Mat. Chem. Phys.* **23**, 121 (1989)
- <sup>6</sup> T. Minami and N. Machida, *Mat. Chem. Phys.* **23**, 63 (1989)
- <sup>7</sup> B.E. Warren, J. Bischoe, *J. Am. Cer. Soc.*, 21(1938) 259
- <sup>8</sup> G.N. Greaves, S.J. Gurman, C.R.A. Catlow, A.V. Chadwick, S.N. Houde-Walter and B. Dobson, *Phil. Mag.* **64**, 1059 (1991)
- <sup>9</sup> M.D. Ingram, *Mat. Chem. Phys.* **23**, 51 (1989)
- <sup>10</sup> C.A. Angell, "Materials for Solid State Batteries", B.V.R. Chowdari and S. Radhakrishna, eds., pp. 31
- <sup>11</sup> C.A. Angell, *Solid State Ionics* **18&19**, 72 (1986)
- <sup>12</sup> D.C. Anderson, J. Kieffer, S. Klarsfeld, *J. Chem. Phys.* **98**(1993) 8978.
- <sup>13</sup> H.C. Andersen, "Molecular dynamic simulation at constant pressure and/or temperature", *J. Chem. Phys.*, **72**, 2384 (1980)
- <sup>14</sup> J.P. Boon and S. Yip, "Molecular Hydrodynamics", Dover Publications, New York 1980
- <sup>15</sup> J.P. Hansen and M.L. Klein, *Phys. Rev.* **B13**, 878 (1976)
- <sup>16</sup> N.H. March and M.P. Tosi, "Atomic Dynamics in Liquids", Dover Publications, New York 1991

## PROTEIN DYNAMICS FROM INTRAMOLECULAR ELECTRON TRANSFER

G. U. Nienhaus<sup>\*,\*\*</sup>, B. H. McMahon<sup>\*\*</sup>, J. D. Müller<sup>\*\*</sup>, C. A. Wraight<sup>\*\*\*</sup>

<sup>\*</sup> Dept. of Biophysics, University of Ulm, D-89069 Ulm, Germany, uli@uiuc.edu

<sup>\*\*</sup> Dept. of Physics, University of Illinois, Urbana IL 61801, USA

<sup>\*\*\*</sup> Dept. of Plant Biology, University of Illinois, Urbana IL 61801, USA

### ABSTRACT

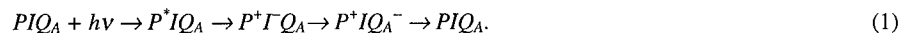
Proteins are complex systems that share essential properties with viscous liquids and polymers. Structure, dynamics, and function of proteins are strongly interrelated, and structural and dynamic aspects can be revealed by studying protein function. Here we report measurements of the kinetics of intramolecular electron transfer (ET) from the primary quinone ( $Q_A$ ) to the special pair ( $P$ ) of reaction center (RC) proteins from *Rhodobacter sphaeroides* as a function of temperature (5 to 300 K) and illumination protocol (cooled in the dark and under illumination from 280 K). From the data, information about structural heterogeneity, relaxations and fluctuations of these molecules is obtained.

### INTRODUCTION

Proteins are unbranched linear polymers of amino acids. Despite their small sizes (typically a few nanometers in diameter), they exhibit structural and dynamic properties similar to glass-forming liquids and synthetic polymers, such as structural heterogeneity, non-exponential relaxations and non-Arrhenius temperature dependencies of characteristic rates [1-3]. Proteins do not possess a unique state of minimal free energy but assume a large number of conformational substates (CS) that can be represented by nearly isoenergetic local minima in a complex energy landscape [4,5]. The CS are separated by free energy barriers that have to be surmounted during a conformational transition. The barriers differ widely in height, and consequently, protein motions are characterized by time scales ranging over many orders of magnitude [6-8].

Protein function depends strongly on structure and dynamics. Therefore, the properties of the conformational energy landscape can be studied with temperature-dependent measurements of the kinetics of functional processes. At low temperatures, many degrees of freedom are thermally arrested, and distributions of reaction rates reflect a heterogeneous ensemble of protein molecules frozen in different CS. At intermediate temperatures, conformational transitions occur on the time scale of the reaction, which allows one to investigate protein motions through studies of reaction kinetics. At sufficiently high temperatures, each protein molecule fluctuates among the CS on time scales shorter than that of the reaction, and fluctuational averaging leads to single-exponential kinetics. This interplay between protein dynamics and biological function has been studied extensively in ligand binding to heme proteins [9-14].

We have investigated the coupling of protein motions to long-range electron transfer (ET) in reaction centers (RC) of purple bacteria (*Rhodobacter sphaeroides*). In these bacteria, the photon energy absorbed by light harvesting complexes or RC cofactors is transferred to the special pair, a bacteriochlorophyll dimer ( $P$ ) on the periplasmic side of the RC protein, and the electronic system is promoted to the first excited singlet state,  $P^*$ . An electron is subsequently transferred from  $P^*$  to a bacteriopheophytin ( $I$ ) and further to the primary quinone ( $Q_A$ ), located 25 Å away from the special pair, closer to the cytoplasmic side [15]. In the absence of the secondary quinone ( $Q_B$ ), the electron then recombines with the hole on the special pair after ~100 ms, and the RC is restored to the ground state:



The charge separation during this cycle generates a strong electric field inside the protein, and the molecule responds to this substantial perturbation with conformational motions to solvate the new charge distribution [15-18]. We have investigated the last and slowest ET step in the sequence,  $P^+Q_A^- \rightarrow PQ_A$ , by measuring its kinetics as a function of temperature after cooling the sample in the dark. We have also examined the influence of illumination on the ET kinetics by switching on a strong light source during cooling to keep the protein in the charge-separated state. The experiments give evidence that, after light-induced charge separation, the protein relaxes from a dark-adapted conformation to a light-adapted conformation which can be trapped at low temperatures. In this contribution, we present a qualitative discussion. A manuscript describing a detailed physical model of the interplay between protein dynamics and electron transfer in reaction centers is in preparation [19].

## EXPERIMENT

Freshly isolated RCs from *Rhodobacter sphaeroides* were quinone-extracted to less than 1 %  $Q_B$ , placed in 0.1 % LDAO, TRIS-buffered to pH 8, and mixed to 75 % glycerol : 25 % water (vol : vol). The sample was loaded in a plastic cuvette which was kept in thermal contact with a Cu sample holder in a storage cryostat. The temperature was maintained within  $\pm 0.3$  K of the desired temperature with a digital temperature controller.

Photoinitiation of the electron transfer cycle was accomplished with a 6 ns pulse from a frequency-doubled, Q-switched Nd-YAG laser. Optical absorbance changes at 440 nm were monitored with light from a tungsten lamp passed through a monochromator. The intensity was measured with a photomultiplier tube and digitized with a home-made logarithmic time-base digitizer (Wondertoy II) from 2  $\mu$ s to 10 s. For a single transient, the noise was  $\sim 200$   $\mu$ OD on the millisecond time scale.

The loaded RC samples were cooled at a rate of  $\sim 20$  K/min until the cryostat was flooded with liquid helium. To cool under illumination, light from a 250-W tungsten lamp, filtered with an infrared filter and a 650 nm long pass filter, was switched on at 280 K. With this setup, an excitation rate  $k_L$  of the RC molecules of  $\sim 200$  s $^{-1}$  was achieved, as determined by comparison of the flash signal amplitude with and without continuous background illumination.

After cooling either under light or in the dark, the sample was warmed up in the dark, and the ET kinetics were measured at fixed temperature intervals. With the sample cooled in the dark, five traces were taken at each temperature. In the experiments where the sample was cooled under illumination, the sample was subsequently warmed at a constant rate of 1.3 mK/s, and 15 traces were averaged for each temperature.

## RESULTS

Fig. 1 shows experimental data of the  $P^+Q_A^- \rightarrow PQ_A$  ET for various temperatures between 5 and 280 K. Small amounts ( $\sim 15$  % of the total amplitude) of an interfering process are visible on the 100  $\mu$ s time scale, arising from the decay of the triplet state of the special pair. However, this process is exponential and well separated from the  $P^+Q_A^- \rightarrow PQ_A$  ET.

For the data plotted with diamonds in Fig. 1 a and b, the sample was cooled in the dark. Subsequently, the temperature was increased in a step-wise fashion, and the kinetics were measured in 5 K intervals. For clarity, we show only data for 5, 60, 120, and 160 K in Fig. 1 a, and 200 and 280 K in Fig. 1 b. The solid and dashed lines are fits of the ET with a theoretical model that will not be discussed here. The triangles represent data taken on the same sample after cooling from  $T_L = 280$  K under illumination. With the excitation rate  $k_L \approx 200$  s $^{-1}$  and an average recombination rate of  $\sim 10$  s $^{-1}$ , illumination keeps the proteins in the charge-separated

state for ~95% of the time. From the comparison of the two data sets, it is obvious that illumination traps the protein in a conformation different from that obtained when it is cooled in the dark. These differences persist as the protein is warmed in the dark. At the higher temperatures, the kinetic differences become successively smaller, demonstrating that the changes are reversible. Only at the highest temperatures ( $T > 260$  K) can the  $P^+Q_A^- \rightarrow PQ_A$  ET be adequately described by a single exponential.

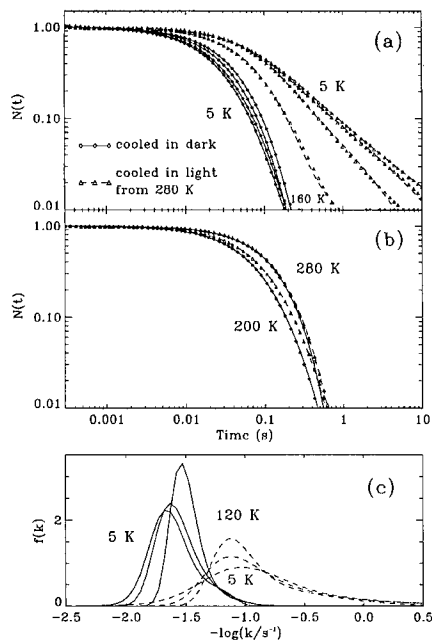


**Figure 1:** Normalized absorbance change,  $N(t)$ , representing  $P^+Q_A^- \rightarrow PQ_A$  electron transfer at (a) 5, 60, 120, 160 K and (b) 200 and 280 K for reaction center samples cooled from 280 K in the dark (diamonds) and under illumination (triangles). The lines are fits with a theoretical ET model. (c) Rate distributions of the 5, 60, and 120 K kinetics, calculated with the maximum entropy method.

The non-exponential kinetics,  $N(t)$ , is related to a rate distribution function,  $f(k)$ , which is conveniently defined on a logarithmic scale,

$$N(t) = \int f(k) \exp(-kt) d \log k. \quad (2)$$

In Fig. 1 c, rate distributions are shown for 5, 60, and 120 K. They were calculated by inverting Eq. 2 using the maximum entropy method (MEM) [20]. The slowing of the kinetics with increasing temperature, observed after cooling in the dark, is reflected by a shift of the rate distributions toward smaller rate coefficients. In contrast, for the sample cooled under illumination,  $f(k)$  narrows and shifts slightly toward faster rates with increasing temperature.

A simple parameterization of the logarithmic rate distributions is provided by the means and widths, defined respectively as

$$\langle \log k_{ET} \rangle = \int f(k) \log k d \log k, \quad (3)$$

$$\sigma_k = [ \int f(k) (\log k - \langle \log k \rangle)^2 d \log k ]^{1/2}. \quad (4)$$

Fig. 2 shows  $\langle \log k_{ET} \rangle$  and  $\sigma_k$  of the distributions, calculated from the kinetic data of the RC sample cooled in the dark (diamonds) and cooled under illumination from 280 K (triangles).

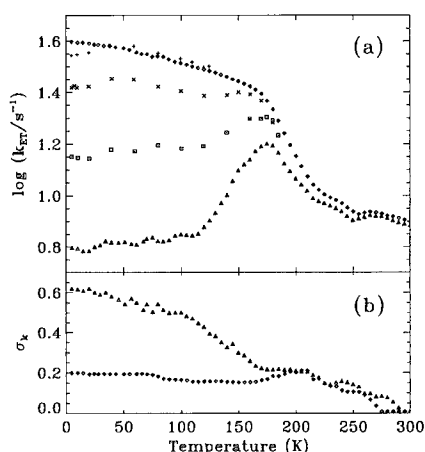


**Figure 2:** (a) Average (logarithmic) rate coefficients of electron transfer, measured while annealing (warming) after cooling under illumination from 280 K (triangles) and in the dark (diamonds), calculated with Eqs. 3 and 4 from the rate distributions. (b) Widths (in decades) of the rate distributions.

## CONCLUSIONS

The ET kinetics in Fig. 1 are non-exponential at all temperatures below 260 K, both for cooling in the dark and under light. A theoretical model has been developed that explains the non-exponential ET kinetics by a distribution in the energy gap,  $\epsilon$ , between the states  $P^+Q_A^-$  and  $PQ_A$  that arises from structural heterogeneity in the protein sample [19]. Moreover, the analysis reveals that the much broader rate distributions observed after cooling under light (Fig. 1 c) do not arise from larger structural heterogeneity but are a consequence of the varying dependence of the rate  $k(\epsilon)$  on the energy gap  $\epsilon$ . The present investigation is closely related to earlier work on heme proteins where the existence of conformational substates (CS) was inferred from the presence of non-exponential ligand binding after photodissociation at low temperatures [4,5].

When cooling RC samples in the dark, the recombination process is slowest at room temperature and speeds up several-fold as the temperature is lowered to 5 K [21]. As shown in Fig. 2 a, the major part of this acceleration occurs over a narrow window from 170 to 250 K. The steepness of this temperature dependence is not accounted for by any simple theoretical description of electron transfer. When cooling under light from 280 K, the behavior of the kinetics is markedly different. At low temperatures ( $T < 125$  K), the average rate coefficient ( $\sim 6$  s $^{-1}$ ) is similar to that seen at room temperature. However, as the sample is rewarmed in the dark, the recombination process accelerates to a maximum at about 175 K. Thereafter, it follows a similar pattern as the dark-adapted sample.

The different temperature dependencies of the ET rates for cooling under light and in the dark arise from relaxation processes between two conformationally different ensembles, one that is adapted to the charge-recombined state and one that is adapted to the charge-separated state. At room temperature, protein molecules in a sample kept in the dark will fluctuate among CS that have a minimal free energy in the uncharged (recombined) state. Upon cooling, a distribution of these dark-adapted structures is frozen in. If, however, the sample is cooled under illumination, the molecules are kept in the charge-separated state, and consequently, a distribution of light-adapted structures is frozen in. Comparing the rates in Fig. 2 a reveals that the average ET rates of the light-adapted sample at 5 K are smaller than those of the dark-adapted sample.

Immediately after photoinduced charge separation, the dark-adapted molecules are in a non-equilibrium state, and conformational relaxation toward the equilibrium charge-separated state

will set in if the thermal energy is sufficiently high to overcome the free energy barriers in the path of these motions. Since charge separation persists for only 100 ms, only motions with characteristic times of less than 100 ms will affect the ET kinetics. Below 170 K, the change in ET rate is only due to the intrinsic temperature dependence of the rate coefficient. The steep temperature dependence around 200 K indicates that, in this temperature interval, motions become sufficiently fast that the proteins can relax appreciably toward the light-adapted state (with smaller ET rate) in the 100 ms following photoexcitation. Without any quantitative analysis, the observation that the relaxation occurs over a temperature interval of ~80 K already implies that the barriers that have to be surmounted are widely different in height. The behavior of the width in Fig. 2 b is consistent with this relaxation scenario: Below 170 K, the width of the distribution is reasonably constant. Around 200 K, a maximum is seen, which is indicative of a distribution that shifts towards slower rates on the time scale of the reaction. Above 260 K, the rate distribution collapses to a delta function because fast fluctuations on the time scale of charge separation (~100 ms) lead to kinetic averaging, analogous to "motional narrowing" in NMR spectroscopy.

As the light-adapted sample is warmed up in the dark, the average rate is constant up to 120 K. The speed-up above that temperature reflects the onset of protein relaxation toward the dark-adapted state (with greater ET rate) on the time scale of heating, which is  $\sim 10^4$  s for the heating rate used in our experiment. The unfreezing of motions at 120 K is quite interesting because previous studies with heme proteins always showed this effect near the glass transition of the viscous solvent used [3-6]. Presumably because of the larger size of the RC protein, there is less coupling of interior protein motions with motions of the solvent. As the temperature is ramped up, protein motions become faster, and more and more relaxation occurs, as indicated by the approach of the lower curve toward the curve of the dark-adapted sample (Fig. 2 a). At 175 K, however, the curve turns down again, which implies that a significant fraction of relaxational motions is becoming faster than 100 ms. These degrees of freedom will be in the dark-adapted state before photoexcitation and attempt to relax towards the light-adapted state within the duration of charge separation. This fraction will thus behave similar to the dark-adapted sample. However, the gap between the curves for the light-adapted and dark-adapted sample up to about 260 K shows that motions still exist in this time/temperature range that are slow compared with the  $10^4$  s time scale of heating. The simultaneous observation of relaxations with characteristic times of below 100 ms and more than  $10^4$  s stresses the fact that protein motions are characterized by rate distributions extending over many orders of magnitude. The temperature dependence of the width (Fig. 2 b) is consistent with the behavior of the average rate: Below 120 K, the width is fairly constant. Above 120 K, it approaches that of the dark-adapted sample because of the onset of relaxation. A maximum at ~200 K is present, and at higher temperatures, we again see a decrease in width due to fluctuational averaging, as in the dark-adapted sample.

In summary, we have shown that the study of a functional process, the ET reaction in RCs, allows us to observe heterogeneous populations of proteins in different conformational substates at low temperatures, relaxations between two ensembles of states in the intermediate temperature range, and the averaging effect of fast fluctuations at high temperatures. From these data, quantitative information about protein motions can be extracted, which is necessary for obtaining a deep understanding of protein function.

#### ACKNOWLEDGMENTS

This work was supported by grants from the National Institutes of Health (PHS5 T32 GM08276 and PHS2 R01 GM18051) and the National Science Foundation (PHY95-13217).

## REFERENCES

1. I. E. T. Iben, D. Braunstein, W. Doster, H. Frauenfelder, M. K. Hong, J. B. Johnson, S. Luck, P. Ormos, A. Schulte, P. J. Steinbach, A. H. Xie and R. D. Young, *Phys. Rev. Lett.* **62**, 1916 (1989).
2. V. I. Goldanskii, Yu. F. Krupyanskii and V. N. Fleurov, *Phys. Scr.* **33**, 257 (1986).
3. H. Frauenfelder, N. A. Alberding, A. Ansari, D. Braunstein, B. R. Cowen, M. K. Hong, I. E. T. Iben, J. B. Johnson, S. Luck, M. C. Marden, J. R. Maurant, P. Ormos, L. Reinisch, R. Scholl, A. Schulte, E. Shyamsunder, L. B. Sorensen, P. J. Steinbach, A. H. Xie and R. D. Young, *J. Phys. Chem.* **94**, 1024 (1990).
4. H. Frauenfelder, F. Parak and R. D. Young, *Annu. Rev. Biophys. Biophys. Chem.* **17**, 451 (1988).
5. G. U. Nienhaus and R. D. Young, Protein Dynamics, in *Encyclopedia of Applied Physics*, Vol. 15, ed.: G. Trigg, VCH Publishers, New York, 1996, pp. 163.
6. R. D. Young, H. Frauenfelder, J. B. Johnson, D. C. Lamb, G. U. Nienhaus, R. Philipp and R. Scholl, *Chem. Phys.* **158**, 315 (1991).
7. T. A. Jackson, M. Lim and P. A. Anfinrud, *Chem. Phys.* **180**, 131 (1994).
8. J. L. Green, J. Fan and C. A. Angell, *J. Phys. Chem.* **98**, 13780 (1994).
9. R. H. Austin, K. W. Beeson, L. Eisenstein, H. Frauenfelder and I. C. Gunsalus, *Biochemistry* **14**, 5355 (1975).
10. N. Agmon and J. J. Hopfield, *J. Chem. Phys.* **79**, 2042 (1983).
11. P. J. Steinbach, A. Ansari, J. Berendzen, D. Braunstein, K. Chu, B. R. Cowen, D. Ehrenstein, H. Frauenfelder, J. B. Johnson, D. C. Lamb, S. Luck, J. R. Maurant, G. U. Nienhaus, P. Ormos, R. Philipp, A. Xie and R. D. Young, *Biochemistry* **30**, 3988 (1991).
12. G. U. Nienhaus, J. R. Maurant and H. Frauenfelder, *Proc. Natl. Acad. Sci. USA* **89**, 2902 (1992).
13. A. Ansari, C. M. Jones, E. R. Henry, J. Hofrichter and W. A. Eaton, *Biochemistry* **33**, 5128 (1994).
14. N. Agmon, W. Doster and F. Post, *Biophys. J.* **66**, 1612 (1994).
15. J. P. Allen, G. Feher, T. O. Yeates, H. Komiya and D. C. Rees, *Proc. Natl. Acad. Sci. USA* **84**, 6162 (1987).
16. P. P. Noks, E. P. Lukashev, A. A. Kononenko, P. S. Venediktov and A. B. Rubin, *Mol. Biol.* **11**, 1090 (1977).
17. D. Kleinfeld, N. Okamura and G. Feher, *Biochemistry* **23**, 5781 (1984).
18. J. M. Peloquin, J. C. Williams, X. Lin, R. G. Alden, A. K. W. Taguchi, J. P. Allen and N. W. Woodbury, *Biochemistry* **33**, 8089 (1994).
19. B. H. McMahon, J. D. Müller, C. A. Wraight and G. U. Nienhaus, manuscript in preparation.
20. P. J. Steinbach, K. Chu, H. Frauenfelder, J. B. Johnson, D. C. Lamb, G. U. Nienhaus, T. B. Sauke and R. D. Young, *Biophys. J.* **61**, 235 (1992).
21. W. W. Parson, *Biochim. Biophys. Acta* **153**, 248 (1967).



## PROTEINS AND GLASSES

HANS FRAUENFELDER

Center for Nonlinear Studies, MS B258, Los Alamos National Laboratory, Los Alamos, NM  
87545, frauenfelder@LANL.GOV

### ABSTRACT

The structure, the energy landscape, and the dynamics of proteins and glasses are similar. Both types of systems display characteristic nonexponential time dependencies of relaxation phenomena. Experiments suggest that both, proteins and glasses, are heterogeneous and that this fact causes the observed time dependence. This result is discussed in terms of the rough energy landscape characteristic of complex systems.

### INTRODUCTION

At first look, proteins and glasses are dissimilar. Proteins are built from 20 different building blocks, amino acids.<sup>1</sup> Of the order of a hundred amino acids are covalently linked together to form a linear polypeptide chain. If the sequence satisfies some not fully understood conditions, the linear polypeptide chain folds into an often globular structure, the working protein. Textbooks picture the folded protein as a unique ordered structure. Glasses (amorphous or noncrystalline solids), on the other hand, are in essence thermally arrested ("frozen") liquids, without crystalline order.<sup>2</sup> Nevertheless, proteins and glasses display similarities that distinguish both from crystalline solids.<sup>3</sup> Two, in particular, are conspicuous. The first concerns the time dependence of relaxation phenomena. These are usually nonexponential in time, and can often be described by a stretched exponential function,

$$\Phi(t) = \exp[-\{k(T)t\}^\beta], \quad (1)$$

where  $\Phi(t)$  describes the relaxing observable and is often normalized to  $\Phi(0) = 1$ . The exponent  $\beta$  is essentially temperature independent over a broad range of  $T$ , is less than 1, and can be as small as 0.1.<sup>4 5 6 7</sup> The nonexponential time dependence can also be characterized by the expansion

$$\Phi(t) = \int f(k) \exp[-k(T)t] dk, \quad (2)$$

where  $f(k)$  is the probability density for having a rate coefficient between  $k(T)$  and  $k(T) + dk$ . In a simple system,  $f(k)$  is a delta function. In glasses and proteins, however,  $f(k)$  can extend over a broad range of rate coefficients and can often be approximated by a Gaussian. The second observation concerns the temperature dependence of the rate coefficient  $k(T)$ . In glasses and proteins,  $k(T)$  usually does not follow an Arrhenius law, but can be approximated by a Tamann-Vogel-Fulcher or a Ferry equation.

Experiments thus show that proteins and glasses share two properties, non-exponential time dependence and non-Arrhenius temperature dependence. These properties can be traced

back to the fact that both, proteins and glasses, have an aperiodic and frustrated structure. Aperiodicity and frustration, in turn, lead to the existence of conformational substates and of a rough energy or conformation landscape.

### CONFORMATIONAL SUBSTATES AND THE ENERGY LANDSCAPE

The concept is simple. Neither glasses nor proteins have a unique structure. In the process of being arrested ("frozen"), a glass can assume a very large number of nearly isoenergetic structures. These are valleys in the energy landscape which characterizes the potential energy of the system in terms of the coordinates of all atoms. Similarly, when a protein folds, it does not reach a unique conformation, but one of a very large number of somewhat different conformations, valleys in the energy landscape of the protein. We call each valley a conformational substate (CS). For glasses, the existence of an energy landscape was postulated by Goldstein<sup>8</sup>; for proteins, it was deduced from the nonexponential time dependence of the binding of CO to myoglobin below about 200 K.<sup>9</sup> The existence of a rough energy landscape in proteins has by now been verified by many experiments and by simulations.<sup>10</sup> A schematic cross section through such an energy landscape is shown in Fig. 1.

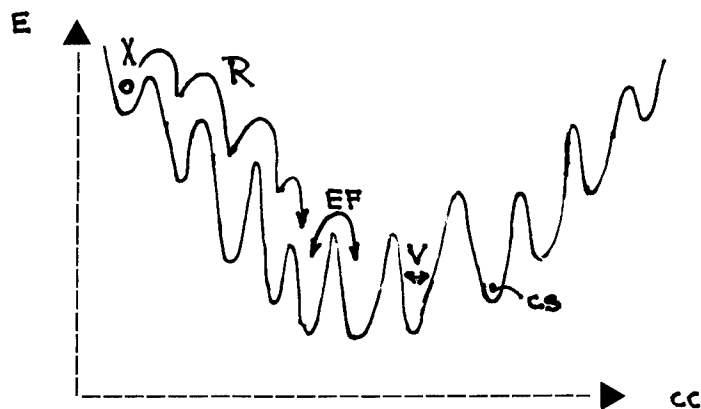


**Figure 1.** One-dimensional cross section through a rough energy landscape.  $E$  denotes the potential energy of the system,  $cc$  a conformation coordinate. Each valley represents a conformational substate, a specific conformation of the system. Within a given substate, the system can vibrate ( $V$ ). In equilibrium, the system can jump from substate to substate by equilibrium fluctuations ( $EF$ ). If the system is brought to a nonequilibrium state ( $X$ ), it can return to equilibrium by a relaxation process ( $R$ ).

The energy landscape sketched in Fig. 1 implies that a protein can perform three different, but related types of motions. Within a given substate, the protein vibrates. At a sufficiently high temperature, the protein executes equilibrium fluctuations from one CS to another. If the protein

is promoted to an excited (non-equilibrium) state (X), it relaxes towards equilibrium as indicated by R. The three motions are sketched in Fig. 1.

### ARE PROTEINS AND GLASSES HOMOGENEOUS OR HETEROGENEOUS?

The crucial experimental observation, mentioned in the introduction, is that the relaxation processes in glasses and proteins are nonexponential in time, as described by Eqs. (1) and (2). Two examples illustrate the situation. The first example concerns the rebinding of small ligands such as carbon monoxide or dioxygen to heme proteins such as myoglobin (Mb). In the experiment, MbCO is photodissociated by a laser flash and the subsequent rebinding is followed in time and characterized by  $N(t)$ .  $N(t)$  is the fraction of Mb molecules that have not rebound a CO at the time  $t$  after photodissociation. Below about 200 K,  $N(t)$  is nonexponential in time.<sup>9</sup> The second example is the relaxation of the protein structure after photodissociation. Immediately after photodissociation, the protein is in the structure corresponding to the bound state, MbCO and we denote this structure by Mb\*. The protein then relaxes toward the deoxy structure, Mb.<sup>11</sup> The relaxation Mb\*  $\rightarrow$  Mb is highly nonexponential in time ( $\beta \approx 0.1$ ) even at room temperature.<sup>12</sup> These results, and similar results in glasses, can be explained with two different models. In the homogeneous case, all proteins are identical and rebinding and relaxation are nonexponential in each protein. In the heterogeneous case, rebinding and relaxation in each individual protein are exponential in time ("the individual systems are thermodynamically simple"), but the proteins are not identical. While theory and simulation can provide some guidance, the decision between the two cases must ultimately rest on experiment.

In glasses, the discussion homo versus hetero has a long history, but recent papers<sup>13 14 15 16</sup> demonstrate that the nonexponential time dependence of the relaxation in glasses and supercooled liquids is caused by a distribution of relaxation times, Eq.(2). Glasses thus are most likely heterogeneous and composed of thermodynamically simple "nanoregions".

In proteins, the experiments also favor heterogeneity. To discuss this evidence, consider the two processes mentioned above, CO rebinding and the relaxation Mb\*  $\rightarrow$  Mb. In the rebinding process, the heterogeneity is proven by multi-flash experiments.<sup>17</sup> By rephotolyzing repeatedly before all CO molecules had rebound it has been shown unambiguously that each protein rebinds exponentially, but that proteins in different substates can have vastly different rebinding rates.<sup>9</sup> The fact that each protein can be characterized by a unique barrier height for rebinding does not exclude the possibility that the relaxation in an individual protein proceeds through a number of substates as sketched in Fig. 1, and is therefore nonexponential in time. A detailed study of the process Mb\*  $\rightarrow$  Mb shows, however, that the relaxation occurs in a single step.<sup>18</sup> Experiments on single molecules<sup>19</sup> also suggest single steps.<sup>20</sup> The proper way to describe both rebinding and relaxation is consequently by an integral over rate coefficients [ Eq. (2)] or activation enthalpies<sup>9</sup>, and not by a diffusion process in the conformation space.<sup>21</sup>

### RELAXATION IN THE ENERGY LANDSCAPE

The energy landscape shown in Fig.1 suggests that relaxation from a highly excited conformational substate should occur by a sequence of steps, a diffusion in the conformation space. Relaxation should therefore be nonexponential in time. Why then does the experiment yield single-step relaxation? The answer to this question lies in the nature of the energy

landscape: The landscape is not one-dimensional, but it exists in a hyperspace of a few thousand coordinates. Such a landscape can best be explored by computer, but even a two-dimensional cross section, sketched in Fig. 2, shows why relaxation phenomena can occur in single steps.

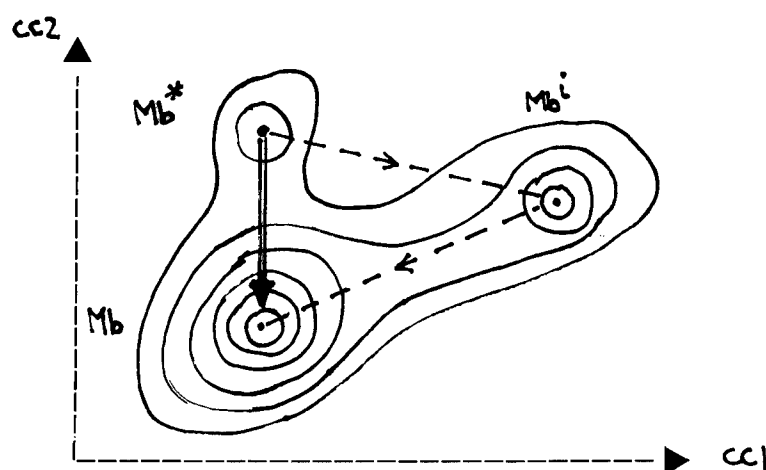


**Figure 2.** Two-dimensional cross section through the energy landscape of a protein. Three substates are shown as craters. The one-dimensional cross section  $Mb^* \rightarrow Mb^i \rightarrow Mb$ , is similar to the cross section shown in Fig. 1. The direct transition,  $Mb^* \rightarrow Mb$ , however, occurs in a single step.

Fig. 2 shows three conformational substates:  $Mb^*$ , a substate immediately after photodissociation,  $Mb^i$ , an intermediate substate, and  $Mb$ , a substate corresponding to the deoxy structure. Relaxation from  $Mb^*$  to  $Mb$  can occur either directly,  $Mb^* \rightarrow Mb$ , or through  $Mb^i$ . For fixed well shapes and positions, the barrier between the wells generally decreases with increasing energy difference between the wells (Brönsted correlation).<sup>22 23</sup> The single-step transition will therefore dominate and relaxation in an individual protein will be exponential. The argument can be generalized to the realistic hyperspace where it is likely that there will be a direct transition from an excited to the lowest substate. The experimental observation of one-step relaxation finds a straightforward interpretation in the energy hypersurface.

#### GLASSES VERSUS PROTEINS

The experimental features considered so far suggest that proteins and glasses share similarities. There are, however, also profound differences. A brief sketch of some of the differences follows: (1) Proteins perform functions; glasses do not. (2) To perform particular functions, proteins must possess specific static and dynamic structures. They therefore show long-range order; glasses do not. (3) While both proteins and glasses have a rough energy landscape, the organization of the EL of proteins is more complex than that of glasses.<sup>24 25 26 27</sup> (4) Some of the relaxation processes in proteins and glasses can be characterized by a glass

transition. The glass transition temperature in glasses is independent of the material that surrounds the glass. In proteins, however, the transition temperature for the protein is often nearly the same as that of the solvent and we can call the transition a slaved glass transition.<sup>28 29</sup> These brief remarks show that, while proteins share essential properties with glasses and also spin glasses, crucial differences exist that are connected with the unique roles that proteins play in life.

## ACKNOWLEDGMENTS

This work was performed under the auspices of the U. S. Department of Energy.

- <sup>1</sup> L. Stryer, *Biochemistry*, Fourth ed., (W. H. Freeman and Company, New York, 1995).
- <sup>2</sup> C. A. Angell, *Science* **267**, 1924 (1995).
- <sup>3</sup> I. E. T. Iben, D. Braunstein, W. Doster, H. Frauenfelder, M. K. Hong, J. B. Johnson, S. Luck, P. Ormos, A. Schulte, P. J. Steinbach, A. H. Xie, and R. D. Young, *Phys. Rev. Lett.* **62**, 1916 (1989).
- <sup>4</sup> J. Jaekle, *Rep. Progr. Phys.* **49**, 171 (1986).
- <sup>5</sup> G. W. Scherer, *Relaxation in Glass and Composites*, (John Wiley, New York, 1986).
- <sup>6</sup> P. J. Steinbach et al., *Biochemistry* **30**, 3988 (1991).
- <sup>7</sup> S. J. Hagen and W. A. Eaton, *J. Chem. Phys.* **104**, 3395 (1996).
- <sup>8</sup> M. Goldstein, *J. Chem. Phys.* **51**, 3728 (1969).
- <sup>9</sup> R. H. Austin, K. W. Beeson, L. Eisenstein, H. Frauenfelder, and I. C. Gunsalus, *Biochemistry* **14**, 5355 (1975).
- <sup>10</sup> H. Frauenfelder, S. G. Sligar, and P. G. Wolynes, *Science* **254**, 1598 (1991); H. Frauenfelder, G. U. Nienhaus, and R. D. Young, in *Disorder Effects on Relaxational Processes*, edited by R. Richert and A. Blumen (Springer-Verlag, Berlin, 1994) pp. 591-614.
- <sup>11</sup> N. Agmon and J. J. Hopfield, *J. Chem. Phys.* **79**, 2042 (1983).
- <sup>12</sup> M. Lim, T. A. Jackson, and P. A. Anfinrud, *Proc. Natl. Acad. Sci. USA* **90**, 5801 (1993); T. A. Jackson, M. Lim, and P. A. Anfinrud, *Chem. Phys.* **180**, 131 (1994).
- <sup>13</sup> R. V. Chamberlin and D. W. Kingsbury, *J. Non-Cryst. Solids* **172-174**, 318 (1994).
- <sup>14</sup> B. Schiener, R. Boehmer, A. Loidl, and R. V. Chamberlin, *Science* **274**, 752 (1996).
- <sup>15</sup> C. T. Moynihan and J.-H. Whang, this volume.
- <sup>16</sup> R. V. Chamberlin, B. Schiener, A. Loidl, G. Diezmann, and R. Boehmer, this volume.
- <sup>17</sup> H. Frauenfelder, in *Methods of Enzymology LIV* (Academic Press, New York, 1978), pp. 506-532.
- <sup>18</sup> G. U. Nienhaus, J. R. Mourant, K. Chu, and H. Frauenfelder, *Biochemistry* **33**, 13413 (1994). K. Chu, R. M. Ernst, H. Frauenfelder, J. R. Mourant, G. U. Nienhaus, and R. Philipp, *Phys. Rev. Lett.* **74**, 2607 (1995).
- <sup>19</sup> E. Geva, P. D. Reilly, and J. L. Skinner, *Accounts Chem. Res.* **29**, 579 (1996).
- <sup>20</sup> L. Edman, Ü. Mets, and R. Rigler, *Proc. Natl. Acad. Sci. USA* **93**, 6710 (1996).
- <sup>21</sup> N. Agmon and G. M. Sastry, *Chem. Phys.* **212**, 207 (1996).
- <sup>22</sup> R. E. Weston, Jr. and H. A. Schwarz, *Chemical Kinetics* (Prentice-Hall, Englewood Cliffs, 1972), p. 191.
- <sup>23</sup> N. Alberding et al., *Biochemistry* **17**, 43 (1978).
- <sup>24</sup> A. Ansari et al., *Proc. Natl. Acad. Sci. USA* **82**, 5000 (1985).
- <sup>25</sup> H. Frauenfelder, *Nature structural biology* **2**, 821 (1995).
- <sup>26</sup> J. Gafert, H. Pschierer, and J. Friedrich, *Phys. Rev. Lett.* **74**, 3704 (1995).
- <sup>27</sup> K. Fritsch, J. Friedrich, F. Parak, and J. L. Skinner (submitted).
- <sup>28</sup> D. Beece et al., *Biochemistry* **19**, 5147 (1980).
- <sup>29</sup> A. Ansari, C. M. Jones, E. R. Henry, J. Hofrichter, and W. A. Eaton, *Biochemistry* **33**, 5128 (1994).
- <sup>30</sup> E. Mayer, *Biophys. J.* **67**, 862 (1994).
- <sup>31</sup> S. J. Hagen, J. Hofrichter, and W. A. Eaton, *J. Phys. Chem.* **100**, 12008 (1996).

## **ELECTRON SPECKLE AND HIGHER-ORDER CORRELATION FUNCTIONS FROM AMORPHOUS THIN FILMS**

J. MURRAY GIBSON, M.M.J. TREACY\* AND D. LORETTO\*\*

University of Illinois, Department of Physics, 1110 W Green St, Urbana, IL 61801

\* NEC Research Institute, 4 Independence Way, Princeton, NJ 08540

\*\* Division of Applied Sciences, Harvard University, Cambridge, MA 02138

### **ABSTRACT**

We obtain valuable information about medium-range order in amorphous semiconductors from variable coherence microscopy, a new quantitative approach to TEM. The technique reveals three-body and higher-order atomic correlation functions, which are sensitive to medium-range order. Preliminary experimental evidence for structural changes on annealing has been found for amorphous semiconductor films, with pronounced medium-range order seen only in unannealed films.

### **INTRODUCTION**

Understanding of the properties of amorphous materials, although well-developed, is hindered by incomplete knowledge of atomic structure. The experimental data about atomic structure in disordered materials is substantially limited to the pair correlation function. Although we have a good idea of the statistically averaged structure and local bonding from diffraction studies, we do not fully understand the medium-range (~1nm scale) configuration and defects. The absence of experimental evidence of three-body and higher correlation functions has been recognized e.g. by Cusack (p23)<sup>1</sup>, as the most serious limitation to progress in structural understanding of this important class of materials. Here we discuss a novel experimental approach which can experimentally illuminate these elusive three-body correlation functions based on statistical analysis of transmission electron micrographs.

The study of structure in amorphous materials and glasses dates back over 50 years. Initial diffraction work with electrons<sup>2</sup>, neutrons<sup>3</sup> and x-rays<sup>4</sup> were all found to be closely consistent with the continuous random network model first proposed by Zachariasen<sup>5</sup>. The basis for comparison in these studies was the first order atom-atom correlation function - the radial distribution function (RDF). RDF's were obtained initially from hand-built CRN models for a-SiO<sub>2</sub><sup>6</sup> and a-Ge<sup>7</sup>, and later from computer-generated models<sup>8,9</sup>. Agreement was very good, implying that the fundamental structure on the short-range scale looks like a random network. However, it is widely recognized that the radial distribution function is not very sensitive to medium range order. Evidence for medium-range order in some amorphous solids, which is unaccounted for by the CRN model, comes from vibrational spectra, e.g. in Raman spectroscopy of a-GeSe<sup>10</sup>. Diffraction data also shows in many solids an anomalous diffraction pre-peak, attributed to ordering on the 1-2nm length scale<sup>11</sup>.

With a new approach based on statistics of images from electron microscopy, it will be possible to obtain higher-order structural correlation information<sup>12</sup>, such as the three atom correlation function. We show that these are sensitive to medium-range order. Cluster-like structures have been proposed in glasses<sup>13</sup>, which would be detectable in medium-range order. An alternative method to obtain the three-body correlation function from x-ray absorption spectroscopy has been proposed<sup>14</sup>, although it appears difficult to obtain medium-range information.

When high-resolution electron microscopy became possible for materials such as Si in the 1970's, one of the first areas which received attention was amorphous materials<sup>15</sup>. Direct images of disordered materials could, in principle, reveal detailed atomic structure which was not subject to the macroscopic averaging of diffraction experiments. Early work by Rudee and Howie<sup>15</sup> appeared to show highly-correlated regions in amorphous Ge, but further analysis revealed that these were indistinguishable from random effects<sup>16</sup>, called "speckle" for the case of dark-field imaging. Even an object without atomic correlations will give chance fluctuations in an analogous manner to laser speckle from dust, or radar "ghost" images from the surface of the sea. It was recognized that even though macroscopic averaging is avoided in high-resolution transmission electron microscopy, there is a form of microscopic averaging through a volume characterized laterally by the microscope resolution, and vertically by the specimen thickness. This volume typically contains a thousand atoms. Statistical fluctuations in the scattered intensity from such volumes cannot be readily distinguished from random effects without the kind of careful analysis proposed here, except for the case of crystalline materials.

Other interesting approaches to microscopy of disordered materials have been considered. A phase-randomization method was first attempted optically by Krivanek et. al.<sup>17</sup>, and more recently in a quantitative fashion with digital images by Fan and Cowley<sup>18</sup>. These have relied on bright-field imaging with relatively coherent illumination. Others have considered statistical analysis of microdiffraction from very small volumes, which appears promising<sup>19,20</sup>. The essence of our approach is systematic variation of coherence as an experimental parameter, and the non-linear aspects of dark-field imaging. Because of this non-linearity, higher-order correlations are detectable from simple statistical properties, such as variance.

Our approach, which we call "Variable Coherence Microscopy" basically involves measurement of a simple statistical property of images (variance) as a function of a well-controlled experimental parameter (coherence). The partial coherence is controlled through the use of "hollow-cone" illumination in the TEM. Although we are extracting only a small fraction of the information in our micrographs through this approach, it is a sensible step towards quantitative analysis. This simple method illuminates the fascinating 3-body correlation function.

## THEORY OF TEM DARK-FIELD IMAGE FORMATION

The important aspect of dark-field imaging which we exploit in these experiments is non-linearity. This non-linearity makes the speckle more sensitive to structural fluctuations than, say, linear bright-field images. The theory here follows Treacy and Gibson<sup>12</sup>. The coherent dark-field image intensity seen at object position  $\underline{r}$  from atoms (assumed identical for simplicity) at positions  $\underline{r}_j$  and scattering factor  $f$  is approximated by:

$$I(\underline{r}, \underline{\kappa}) = |f(\underline{\kappa})|^2 \sum_j \sum_i a_j(\underline{r} - \underline{r}_j) a_i^*(\underline{r} - \underline{r}_i) \exp(-2\pi i \underline{\kappa} \cdot \underline{r}_{ji}) \quad (1)$$

where  $\underline{\kappa}$  is the wavevector associated with scattering into the objective aperture center and  $a_j$  is the image amplitude of the atom  $j$ , given by

$$a_j(\underline{r} - \underline{r}_j) = i \lambda \iint_{obj} \exp(2\pi i \underline{q} \cdot (\underline{r} - \underline{r}_j)) d^2 \underline{q} \quad (2)$$

$$= i \lambda \pi Q^2 A_j$$

where  $A_j$  is the familiar Airy intensity distribution from a circular aperture of radius  $Q$ , given in terms of the Bessel function of the first kind  $J_1$ :

$$A_j = 2 J_1[2\pi Q|\underline{r} - \underline{r}_j|] / (2\pi Q|\underline{r} - \underline{r}_j|) \quad (3)$$

These equations make several simplifying assumptions, which are valid for the regime that we will consider. We have assumed that the kinematical approximation can be made, which is good for amorphous samples of Si, Ge up to 200 Å in thickness<sup>21,22</sup>. In addition, we have neglected the effect of the microscope aberration function, since we will employ small objective apertures producing diffraction-limited resolution ( $\sim 1/Q > 5$  Å) which is well above the instrumental resolution limitations (typically  $< 2$  Å). The latter assumption of a small objective also is required to separate the scattering factor  $f$  from the  $a_j$  in equation (1), but this is valid under most practical conditions<sup>23</sup>.

The mean image intensity in the coherent dark-field case is given by averaging equation (1) over a large image area to give

$$\langle I(\underline{\kappa}) \rangle = [\pi Q^2 \lambda^2 f^2(\underline{\kappa}) / M] \sum_j \sum_i A_{ji} \exp(-2\pi i \underline{\kappa} \cdot \underline{r}_{ji}) \quad (4)$$

where  $A_{ji}$  is the Airy intensity at distance  $r_{ji}$ . It is easily shown that eqn. (4) is no more than the average diffracted intensity into the objective aperture, and thus gives no additional information. However, the situation is more interesting for higher-order moments of the intensity. The simplest is the second moment, simply related to the variance  $V$  of the speckle. We can show that

$$\langle I^2(\underline{\kappa}) \rangle / \langle I(\underline{\kappa}) \rangle^2 - 1 = V = N_0 \frac{\sum_{j,l,m,n} A_{jn} A_{nl} A_{mn} F_{jl} F_{mn}}{\left( \sum_{p,q} A_{pq} F_{pq} \right)^2} - 1 \quad (5)$$

The function  $F_{jl}$  represents the coherence function which is a property of the illumination. For coherent illumination  $F_{jl} = e^{-2\pi i \underline{\kappa} \cdot \underline{r}_{jl}}$ . It is desirable to localize  $F_{jl}$  by



reducing spatial coherence in a controlled manner. Spatial coherence can be reduced by averaging over a range of incident illumination angles, and a particularly effective way of doing so is to use hollow-cone illumination. The illumination is scanned over the surface of a cone during exposure, and the function  $F_{jl}$  becomes more localized, with a width that depends on the hollow-cone angle ( $\alpha$ ). For hollow-cone illumination the form of  $F_{jl}$  is:

$$F_{jl} = \left\{ \int_{k_1}^{k_2} J_0(2\pi k \sigma_{jl}) e^{2\pi i \gamma z_{jl}} f^2(k) k dk \right\} / \left\{ \int_{k_1}^{k_2} f^2(k) k dk \right\} \quad (6)$$

where  $\sigma_{jl}$  is the in-plane component of  $\mathbf{r}_{jl}$  and  $z_{jl}$  is the normal component, and  $k$  is in-plane component of the wave-vector, with  $\gamma$  its normal component<sup>12</sup>.

Looking at equation (5) we can see that the variance depends on the four-body correlations between atoms  $j, l, m, n$ , whereas the diffracted, or mean, intensity depends only on the pair correlation between atoms  $j, l$ . By following reasonable approximations we can show that  $V$  is dependent only on the three-body correlation function. This function is discussed below, and is far more sensitive to structural details than the better-known two-body pair-correlation function. Experimentally, we can vary the coherence function  $F_{jl}$  in hollow-cone illumination by changing the half-angle of illumination  $\alpha$ , which controls  $k$  in equation (6) ( $k = \alpha/\lambda$ ). In this way we can probe the higher-order correlation functions. The theory shows that the image is sensitive to these functions, but it requires further advances to allow direct determination of their properties.

The hollow-cone TEM method is equivalent to annular detector imaging in the STEM. It should be noted that the well-known Z-contrast technique for imaging incoherently utilizes significantly higher angles than in these experiments, where the partial coherence is reduced to a negligible level<sup>24</sup>. Speckle in Z-contrast experiments should be controlled only by incoherent statistical fluctuations in the number of atoms locally, which do not reveal atomic correlations.

## CORRELATION FUNCTIONS

It is well-known that the average kinematically diffracted intensity is the Fourier transform of the pair correlation function, on the assumption that the structure is on average homogeneous and isotropic<sup>25</sup>. There are several functions closely related by normalization to the radial distribution function. We consider the pair correlation function  $\rho(r)d^3r$  (PCF) which is defined as the probability per unit volume of finding an atom at distance  $r$  from another, normalized by the average probability. The pair correlation function, shown by example in figure 2(a), is very revealing about the short-range order in glasses. For example, the tetrahedral structure of a-Si is clearly visible in the positions of the first and second nearest-neighbor peaks in fig. 2(a). This is a strong clue to the continuous random network structure. However, the detail visible in the PCF fades rapidly with increasing distance from the origin. It is this missing detail which is most sensitive to medium-range order. We can dramatically illustrate the insensitivity of the PCF to medium-range order from a simple calculation of the PCF from a highly disordered crystal. A uniformly distributed static disorder of maximum value  $1\text{\AA}$  was added

randomly to each atom in a diamond Ge crystal. The result is a severe attenuation of peaks in the PCF beyond 10 Å (see fig. 1), even though we know that the crystal still has infinite long-range periodicity (the Bragg peaks are still infinitely sharp). The absence of structure comes from the overlap of an increasing number of possible inter-atom correlations at large distances.

The three-body correlation function  $\rho(r_1, r_2) d^3 r_1 d^3 r_2$  (the normalized probability density of finding two atoms at  $r_1$  and  $r_2$  from an atom at the origin) is shown for comparison. Since

this is a complicated 3-D function of  $r_1$  and  $r_2$ , we show the results only for  $r_1$  parallel to the edge of a local tetrahedron of Ge atoms (cubic  $\langle 110 \rangle$  directions), with  $r_2$  parallel to the same direction. This function (fig. 1) clearly reveals the long-range periodicity.

Thus, although the PCF has proven valuable in deducing the random network model of amorphous materials, it has serious limitations in determining medium-range order. The calculations reported here show the improved sensitivity of higher-order correlation functions to medium-range order. Since these correlation functions determine statistical properties of TEM dark-field images they make a natural next step in the study of medium-range order.

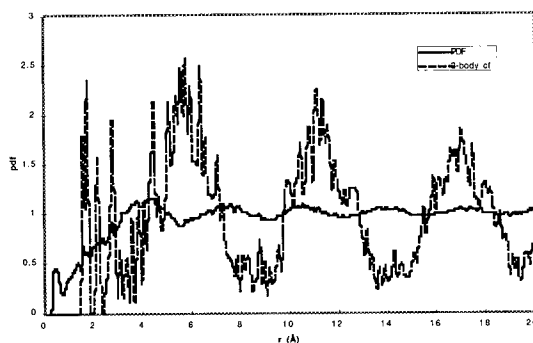


Figure 1: The 2-body pcf and the 3-body cf (dashed line) for a highly disordered diamond Ge crystal, with random displacements up to 1 Å. Although the pcf for this arbitrarily disordered structure shows little medium-range or long-range order, the three-body correlation function is much more sensitive. The direction of this 3-body function is along the edge of a local Ge tetrahedron.

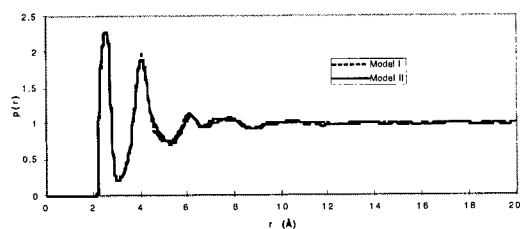


Fig. 2(a): Comparison of pair correlation functions from two models of Pawel Keblinski. Model I is a continuous random network. Model II was based on nanocrystalline silicon, which was energy-minimized in a molecular dynamics simulation. The two pcf's are almost identical, and agree well with the experimental data for amorphous Ge, even though visual inspection of model II shows clear ordered regions.

The three body correlation function can be readily calculated for a known structure, and fig. 2 (b) shows a comparison of the three-body correlation functions along the bond direction for two models of amorphous Ge whose PCF's are shown in fig. 2(a) (coordinates courtesy of Pawel Keblinski at Argonne National Labs). It is clear that the three-body correlation function of either model is different from the pair correlation function, as

would be expected. For example a peak is seen in the three-body function at  $\sim 9.8 \text{ \AA}$ , which is absent in the pair correlation functions. This distance represents the unit cell spacing of the diamond-cubic lattice in the bond direction. The existence of such pronounced peaks indicates the sensitivity of the three-body function to medium-range order, absent from the PCF. Furthermore, the PCF's of the two models are indistinguishable, whereas significant differences are seen in the three-body correlation functions. In particular, the aforementioned peak at  $9.8 \text{ \AA}$  is much more pronounced in model II. This is consistent with the origin of model II in molecular dynamics relaxation of a crystalline nanophase Si material, whereas model I was generated from a liquid-like

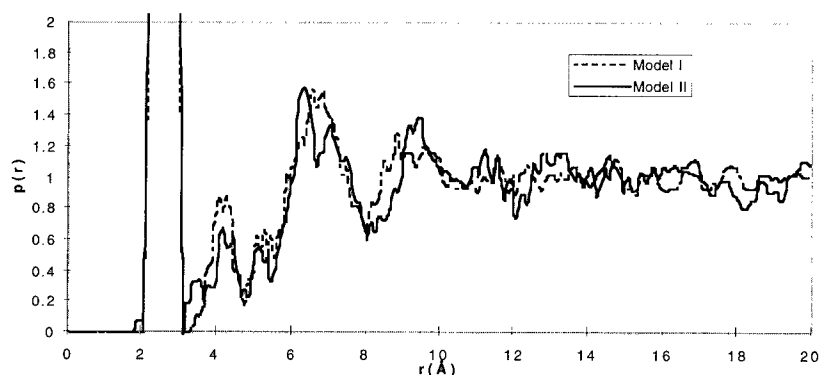


Fig. 2(b): The three body correlation functions for the two models of fig. 1(a). The information shown is centered along the nearest-neighbor bond direction, integrated over a cone of semi-angle 4 degrees. The three body correlation function distinguishes between the models, in particular revealing a clear peak in the more ordered model II at the diamond (111) spacing for crystalline Ge ( $9.8 \text{ \AA}$ ). This peak is invisible in the radially averaged pcf function.

structure. Visual inspection of these models, or analysis of the distribution of energy per atom, reveals the remnant of "crystallinity" in model II, although it is absent from the PCF which could not be distinguished from a random network. The sensitivity of the 3-body function is compelling, especially since our theory shows that the function is directly responsible for details of the electron speckle, and thus can be examined, albeit indirectly at present. Note that the large noise in these calculations is a function of the finite size of the models, and would not be a major issue experimentally.

## PRELIMINARY RESULTS

We have made preliminary studies of amorphous Si and Ge films grown by vacuum deposition. Figure 3 shows a typical image from an amorphous Ge film, in which speckle is observed. Figure 4 shows measurements of the speckle variance as a function of coherence parameter  $k$  (which is equivalent to reciprocal distance) under nominally identical experimental conditions for a UHV evaporated Ge film before (a) and after (b) in-situ thermal annealing at  $350^\circ\text{C}$  for 30 minutes. A theoretical prediction of the speckle observed from a Ge random network due to Wooten<sup>9</sup> was reported in our earlier paper<sup>12</sup>.

The results show that the amorphous Ge film does not look like the Wooten random network in this measurement, particularly in medium-range order. Note that calculations by Filipponi et. al.<sup>14</sup> show that the model of Biswas et. al.<sup>26</sup> provides better agreement with their data than the Wooten model. We have obtained coordinates from Biswas, and will investigate that model in detail. Simulations, and the simple theoretical analysis of eqns (5),(6), show that the existence of strong peaks in the speckle at the relatively low  $k$ -vectors here indicate structural features on a length scale of the Airy-disc of the objective aperture, 16 Å in these measurements. The variance peaks are not present for Airy disc sizes less than 10 Å. The existence of medium range order on these length scales was confirmed by several other experiments and simulations including inspection of speckle sizes in the real images.

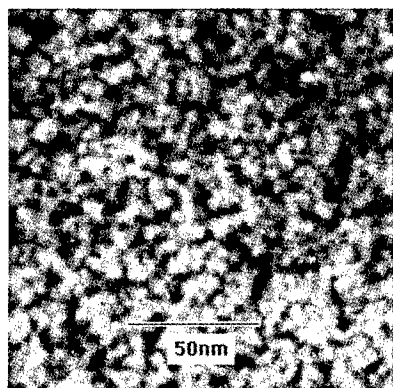


Figure 3: A typical speckle image in hollow-cone illumination from UHV deposited a-Ge.

It should be noted that small-angle scattering can be distinguished from the results shown here because it can be detected in the pair-correlation function, and also is observed in bright-field images. There is no obvious change in small-angle scattering with thermal annealing of a-Ge.

In a recent paper, we summarized some earlier results on the analysis of speckle from amorphous-Ge thin films. The work showed that the CRN model could not account for all the features that we saw in the speckle from thin evaporated films. The disagreement was most pronounced on the medium-length scale from 10-20 Å. We deduced this length scale from the dependence of the speckle on the

diameter of the Airy disc, which is in turn dependent on the radius of the objective aperture. More recent experiments mentioned above on both amorphous-Si and

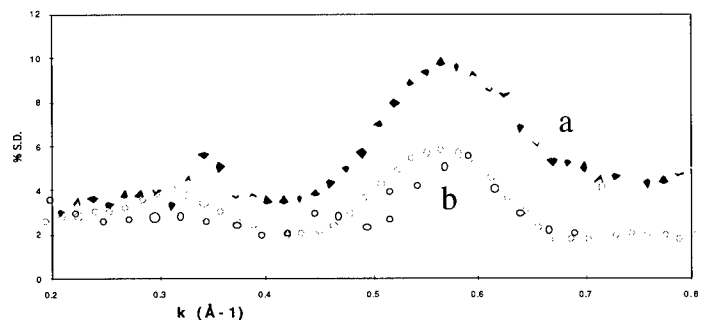


Figure 4: The effect of thermal annealing on the speckle standard deviation (% S.D.) measured experimentally from a 200 Å thick a-Ge film. The diamonds are before annealing (a), the circles after (b). Open and closed symbols represent different experimental runs. The Ge film was deposited on rock-salt, and floated off. The average intensity is negligibly changed.

amorphous-Ge have confirmed these suppositions. In addition, the more recent samples were prepared in ultra-high-vacuum, by molecular beam epitaxy, to avoid concerns of excessive impurities. Data from a-Ge is shown in fig. 4. We draw attention to the comparison between sample a) which is as-grown, and sample b) which has been thermally-annealed in-situ at 350°C. Although there is very little detectable difference in the diffraction patterns (and therefore in the PCF's) after this annealing step, the speckle results show a reduction in the average speckle which is striking and reproducible.

We conclude that there is evidence for structure on the medium-range length scale in the data. The results lead to the intriguing suggestion that the annealed phase has less medium-range structure, i.e. is more perfectly a random network, than the as-deposited film. It will be interesting to reconcile this with Raman and diffraction measurements that show reduction in short-range bond distortions on annealing<sup>27,28</sup>.

We gratefully acknowledge the assistance of Peggy Bisher at NEC, and the kind provision of atomic coordinates from F. Wooten, R. Biswas and P. Keblinski.

## REFERENCES

1. N.E. Cusack, *The Physics of Structurally Disordered Matter* (Adam Hilger, Bristol, U.K., 1987).
2. S.C. Moss and J.F. Graczyk, *Phys. Rev. Lett.* **23**, 1167 (1969).
3. G. Etherington, A.C. Wright, J.T. Wenzel *et al.*, *J. Non-Cryst. Sol.* **48**, 265 (1982).
4. R.J. Temkin, W. Paul, and G.A.N. Connell, *Adv. Phys.* **22**, 581 (1973).
5. W.H. Zachariasen, *J. Am. Chem. Soc.* **54**, 3841 (1932).
6. R.J. Bell and P. Dean, *Nature* **212**, 1354 (1966).
7. D.E. Polk, *J. Non-Cryst. Sol.* **5**, 365 (1971).
8. N.J. Schevchik and W. Paul, *J. Non-Cryst. Sol.* **8-10**, 381 (1972).
9. F. Wooten, K. Winer, and D. Wearie, "Computer Generation of Structural Models of Amorphous Si and Ge," *Phys. Rev. Lett.* **54**, 1392-1395 (1985).
10. R. J. Nemanich, S.A. Solin, and G. Lucovsky, *Sol. State Comm.* **21**, 273 (1977).
11. S.R. Elliot, "Origin of the First Sharp Diffraction Peak in the Structure Factor of Covalent Glasses," *Phys. Rev. Lett.* **67**, 711-714 (1991).
12. M.M.J. Treacy and J.M. Gibson, "Variable Coherence Microscopy: a Rich Source of Structural Information from Disordered Materials," *Acta Cryst. A* **52**, 212 - 220 (1996).
13. J.C. Phillips, *J. Non-Cryst. Sol* **43**, 37 (1981).
14. A. Filipponi, F. Evangelisti, M. Benfatto *et al.*, "Structural investigation of a-Si and a-Si:H using x-ray absorption spectroscopy at the Si K edge," *Phys. Rev. B* **40**, 9636-9643 (1989).
15. M.L. Rudee and A. Howie, *Phil. Mag.* **25**, 1001 (1972).
16. S. Herd and P. Chaudhari, *Phys. Stat. Sol. (a)* **26**, 627 (1974).
17. O.L. Krivanek, P.H. Gaskell, and A. Howie, *Nature* **262**, 454-457 (1976).
18. G.Y. Fan and J.M. Cowley, *Ultramicroscopy* **24**, 49-60 (1988).
19. J.M. Cowley, "Electron Microdiffraction and Microscopy of Amorphous Solids," in *Diffraction Studies on Non-Crystalline Substances* (Hungarian Academy of Sciences, 1980).
20. J.M. Rodenburg, "A STEM Technique for quantifying angular correlations in amorphous specimens," presented at the EMAG '85, Newcastle, U.K., 1985, **78**, 103-104, *Inst. Phys. Conf. Ser.*
21. L.D. Marks, *Ultramicroscopy* **25**, 25 (1988).
22. J.M. Gibson, "Breakdown of the WPO in amorphous objects and measurement of HREM optical parameters," *Ultramicroscopy* **56**, 26-31 (1994).
23. M. M. J. Treacy and J. M. Gibson, *J. Microscopy* **180**, 2-11 (1995).
24. S. J. Pennycook, "Z-contrast STEM for Materials Science," *Ultramicroscopy* **30**, 58-69 (1989).
25. B.E. Warren, *X-Ray Diffraction* (Addison-Wesley, Reading, MA, 1959).
26. R. Biswas, I. Kwon, A.M. Bouchard *et al.*, *Phys. Rev. B* **39**, 5101 (1989).
27. J. Fortner and J.S. Lannin, "Structural Relaxation and order in ion-implanted Si and Ge," *Phys. Rev. B* **37**, 10154-10158 (1988).
28. *ibid.* **39**, 5527 (1989).

## NETWORK STRUCTURE OF OXIDE GLASSES CONTAINING ALKALI & OTHER IONS BY DIFFRACTION AND MD SIMULATIONS

Itaru YASUI\*, H. NAGASAWA\*\*, H. MATSUMOTO\*\*\*, T. MABUCHI\*\*

\*Center for Collaborative Research, University of Tokyo yasui@iis.u-tokyo.ac.jp

\*\*Institute of Industrial Science, University of Tokyo

\*\*\*Faculty of Engineering, Nagoya University

### ABSTRACT

Network structures of several kinds of oxide glasses were analyzed by means of neutron or x-ray diffraction method and molecular dynamics (MD) simulations including silicate, borate and tellurite glasses. The basic scheme of the structure highly depends on the bonding nature of network forming oxide, but the size of the alkali ions is another important factor to control the network structure of the glass. Structures of silicate glasses are rather easily reproduced by means of MD simulation, whereas borate or tellurite glass structures are hard to be constructed by MD calculation with only 2-body potentials. It is necessary to use adequate potentials to control the bonding angles of O-M-O or M-O-M. The network structure of tellurite glass seems very complex because of the shape of structural units with low symmetry, the use of a new kind of potential was found indispensable to reproduce the glass structure by MD.

In addition to the network structure, the polarization of ions seems to be important to understand the whole vision of oxide glass structures. A new kind of MD was developed which took polarization of ions into account to understand the mixed alkali effects in silicate glasses.

### INTRODUCTION

It is normally difficult to obtain detailed structures of glasses, because the observable data by diffraction methods have one-dimensional nature, and even by other methods such as spectroscopy the information can be obtained only for the structural units. It is therefore important to have adequate modeling methods, and proper comparison must be made between observable and theoretical values. The structural theory of glasses has advanced with a tool for modeling such as molecular dynamics simulation and other techniques.

In this report, methods required to construct appropriate models for different kind of glasses with different kind of network formers have been described so as to clarify what is the basic principle to determine the network structure of glasses.

### EXPERIMENT

#### Neutron diffraction

Neutron diffraction was measured by the time of flight method with pulsed neutrons. The structure factor  $S(Q)$  up to  $Q_{\max} = 30 \text{ \AA}^{-1}$  was obtained. The measurement was carried out using the HIT-II facility in the National Institute of High-Energy Physics, Tsukuba. The function  $S(Q)$  was Fourier transformed to yield radial distribution function, which was expressed in the form of  $2\pi^2\rho(r)$ .

#### Molecular dynamics

Structural models of the glasses with the same composition as those for the diffraction measurements were constructed by MD simulation. In the case of silicate glasses, a Born-Mayer type two-body potential set was used. In borate or tellurite glasses, a three-body potential was used in addition to the Born-Mayer type pair potential. The Born-Mayer potential is expressed as,

$$\Phi_{ij} = \frac{1}{4\pi\epsilon_0} \frac{Z_i Z_j e^2}{r_{ij}} + B_{ij} \exp\left(-\frac{r_{ij}}{\rho_{ij}}\right) \quad (1)$$

where  $r$  is interatomic distance,  $Z$  is charge,  $B$  and  $\rho$  are empirical constants.

The three-body potential is explained below for more complex tellurite glasses: In order to consider the anisotropic nature of Te-O, a suitable potential was invented by modifying the Keating type potential [1], which was applied to O-Te-O and Te-O-Te angles. This potential describes the three-body interaction as,

$$\Phi_{ijk} = C(\cos\theta_{ijk} - \cos\theta_0)^2 g(\theta_{ijk}) \exp[\lambda / (r_{ij} - a) + \lambda / (r_{jk} - a)]$$

(for  $r_{ij}, r_{jk} < a$ )

(2)

where,

$$g(\theta_{ijk}) = 1 - q \left( \frac{\cos\theta_{ijk} - \cos\theta_0}{1 + |\cos\theta_0|} \right)^2.$$
(3)

In these two equations,  $C$  is a constant and  $a$  is a cutoff radius of  $r_{ij}$  and  $r_{jk}$ . A variable  $\theta_{ijk}$  represents an angle of a central  $j$ -th atom held between the other  $i$ -th and  $k$ -th atoms, and  $\theta_0$  is the ideal angle. When  $g(\theta_{ijk}) = 1$ , eq. (2) corresponds to the original potential form of Keating, which always has an unstable maximum at  $180^\circ$ . Tellurite glasses are generally thought to consist of  $\text{TeO}_x$  polyhedra with O-Te-O angles of about  $90^\circ$  and  $180^\circ$ , which requires an appropriate modification of the Keating type potential. The factor  $g(\theta_{ijk})$  expressed in eq. (3) was introduced to lower the potential energy at  $180^\circ$ . A parameter  $q$  in  $g(\theta_{ijk})$ , ranging in  $0 \sim 1$ , regulates potential height at the angle.

In order to improve the concept of MD for glasses containing alkali ions, it is necessary to include polarization effect induced at each ion. The concept of polarization is quite important, if the mixed alkali effect is taken into consideration. The potential of induced electronic polarization can be written as

$$\Phi_{\text{IND}} = - \sum_i \frac{1}{2} \alpha_i E_i^2,$$
(4)

assuming point dipoles in local electric fields, where  $\alpha_i$  is isotropic atomic polarizability and  $E_i$  is the local electric field at atom  $i$ . The variable  $E_i$  includes electrostatic interaction from all surrounding atoms, which can be deduced from the gradient of the Coulombic potential, the first term in eq. (1). Atomic forces are obtained directly as the negative gradient of the total potential energy,

$$\mathbf{f}_i = -\nabla_i (\Phi_{\text{PAIR}} + \Phi_{\text{IND}}),$$
(5)

where  $\mathbf{f}_i$  represents the force on atom  $i$ .

## RESULTS and DISCUSSION

### 1. Silicate glasses

The basic structural units for silicate glasses are well established. Current issues in describing the network structure of silicate glasses concern the intermediate structural order, in other words, the mode of connection between the structure units.[2]

With regard to the modeling process of silicate glasses, it has been well established that the simple two-body potential is good enough to reproduce appropriate structure models.

### 2. Borate Glasses

The main difficulty in constructing a good structure model for the network of borate glasses is that a set of simple 2-body potentials is not enough to reproduce macro anions [3], which are known to exist in borate glasses by spectroscopic observation, mainly by NMR. In order to reproduce macro anions with several forms of rings, some form of 3-body potential must be introduced in MD calculation. The main role of 3-body potential is to restrict the bonding angles around B or O atoms.

There are many papers in the literature that report MD calculations of borate glasses[4-8]. Some used 3-body potentials to reproduce macro anions in borate glasses, including rather simple trials to introduce artificial dip in the potential of B-B interaction[6]. It was reported by Verhoef et al.[8], however, that even by the introduction of the three-body potential set to O-B-O, no macro anions were reproduced by MD calculations.

The type of potential function which was introduced in this study can be expressed by eq.(2)  
The term  $\theta_0$  means the ideal bonding angles to specific atomic combinations. The bonding angle around O

atoms can be controlled by the application of eq.(2) with  $g(\theta_{ijk}) = 1$  to the bonds of B-O-B group, and the bonding angle B by the application to O-B-O group.

It has been well established that structural units existing in borate glasses are either  $\text{BO}_3$  triangles or  $\text{BO}_4$  tetrahedra, which can be reproduced in the present study by using only 2-body potentials, because the ionic radius mainly determines the nearest coordination. It was therefore concluded the structure of the basic units can be confirmed by the simple MD calculations reported in the literature.

With regard to the local structure of O atoms, on the other hand, the averaged bonding angle at B-O-B bonds becomes  $140$  to  $165^\circ$  in MD calculation with only 2-body potentials[4,5,8]. The results concerning the bonding angles are summarized in Table 1. This fact may be interpreted such that the bonding angle at  $180^\circ$  is not profitable to increase the packing efficiency of atoms, while the angles less than  $100^\circ$  can not be attained because of steric hindrance between structural units.

Another factor which determines the bonding angle around O atoms is the size of alkali ions included in the glasses. The size of pockets to accommodate alkali ions can be changed by the bonding angles at O atoms, and alkali ions tends to coordinate O atoms as evenly as possible, so an optimum bonding angle for each kind of alkali ion exists. For example, Na ions normally can be accommodated in the pockets consisting of O ions with the bonding angles at around  $140^\circ$ . The bigger the size of the alkali ions, the bigger the bonding angles around O atoms. In order to construct macro anions, the bonding angle at O atoms must be  $120$  to  $130^\circ$ . Therefore it is inevitable to restrict the bonding angles at O atoms to less than  $130^\circ$ .

If a strong three-body potential was applied to O-B-O and B-O-B bonds, it was found that 3 coordinated O atoms were generated, which can be found in some borate crystals. The reason is not clear so far, but it was found that the density of the model tended to increase with three-body potentials and it is also true that crystals with 3 coordinated oxygen have relatively higher densities.

The ideal angle around O may be an important factor, which determines the overall network structure of the models. If the bonding nature of B-O is almost perfectly covalent, then the ideal angle may be  $90^\circ$ , because O atoms uses their p orbital to make chemical bonds.

	Average Angle (deg.)			Average B-O distance (Å)		
	O-B-O	O-B-O	B-O-B	O-B-O	O-B-O	B-O-B
	in $\text{BO}_3$	in $\text{BO}_4$		in $\text{BO}_3$	in $\text{BO}_4$	
Q.Xu[3]	120	110	155~165	—	—	1.367~1.386
W.Soppe[4]	—	—	144~154	—	—	1.41~1.44
Hirao[5]	—	—	120~145	—	—	1.39~1.45
Inoue[6]	120	110	120	1.40	1.48	1.44
A.H.Verhoe[7]	120	109	157	1.37	1.48	—
①	119.4	109.2	127.1	1.35	1.46	1.42
②	119.5	109.2	131.5	1.35	1.46	1.42
③	119.5	109.2	138.8	1.33	1.44	1.40

Table 1. Summary of bonding angles and atomic distances by MD for borate glasses.

- ①: Present Study. Three-body potential for both B-O-B and O-B-O.  
 ②: Present Study. Three-body potential only for B-O-B triangles.  
 ③: Present Study. Only by two-body potential.

The ratio of the strength of 3-body potential to 2-body terms in eq.(2), which can be parameterized by C, is another important factor. C for O should be 5 times as large as that for B atoms. Even when C was assumed



to be zero for B atoms, we reproduced good structure models. The RDF profiles for the model with the case of  $C=0$  are shown in Fig.1(a),(b), where the agreement between the observed and calculated RDF is quite satisfactory. Fig. 2 shows a snapshot of MD results.

The parameter sets used in this study were determined so as to improve the agreement between the observed and calculated RDFs obtained by either neutron diffraction or x-ray diffraction and were summarized in Table 2. The theoretical meaning of the parameter sets were not well understood. Molecular orbital calculation using Gaussian 94 are now being performed to try to give some reasoning to the selected parameter sets.

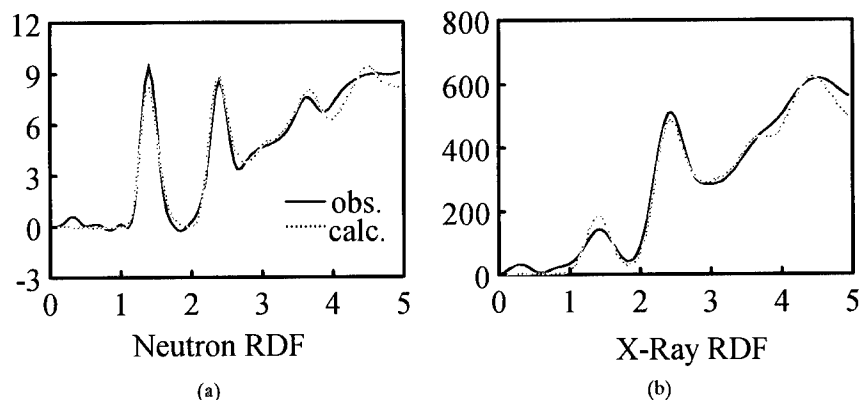


Figure 1 RDFs calculated for the model by MD with three-body potentials for B-O-B triangles (a) Neutron diffraction (b) X-ray diffraction.

Table 2. Summary of MD calculation in the present study.

Parameter Set for Fig.1 and Fig.2

• 2-body potential part

	B-B	B-Ca	B-O	Ca-Ca	Ca-O	O-O
$\rho$	0.25	0.30	0.20	0.30	0.25	0.25
adist	0.50	1.40	1.12	1.60	2.00	1.90

• 3-body potential part

	C	$\theta_0$	a	$\lambda$
B-O-B	3000.0	90°	2.0	2.0

Potential Form:

$$\Phi(r_{ij}) = \frac{z_i z_j}{4\pi\epsilon_0} \frac{e^2}{r} + B_{ij} \exp\left(-\frac{r}{\rho_{ij}}\right)$$

$$\Phi(r_{ij}, r_{ik}, \theta_{jik}) = C(\cos \theta_{jik} - \cos \theta_0)^2 \cdot \exp\left(\frac{\lambda}{r_{ij} - a} + \frac{\lambda}{r_{ik} - a}\right)$$

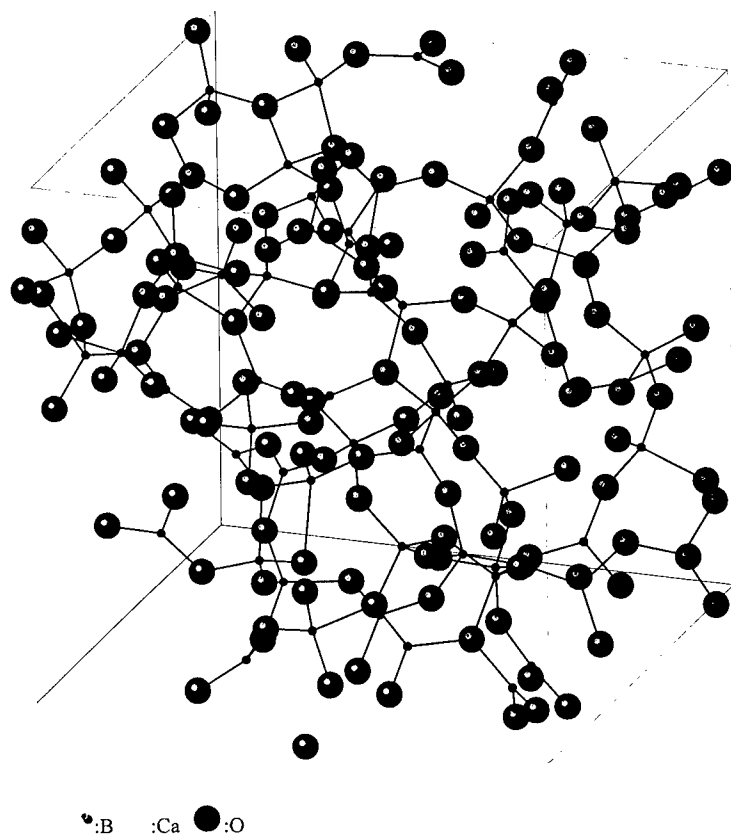


Fig. 2 A snap shot of MD results. Some macro anions with ring structure can be recognized.

### 3. Tellurite Glasses [9][10]

Structure of tellurite glasses has been investigated for some decades. These studies were mostly based on the two principal methods, one being IR or Raman spectroscopy [11-17] and the other neutron or X-ray diffraction[17-19]. The attention in the studies was concentrated on the structural units composing glass network, since very special kinds of  $\text{TeO}_x$  polyhedra could be found in crystalline forms of  $\text{TeO}_2$  and binary tellurites.

In the present work, the structure of  $\text{ZnO} - \text{TeO}_2$  glass system was investigated.

The observed neutron RDFs of  $x \text{ ZnO} - (1-x) \text{ TeO}_2$  glasses ( $x = 0.1, 0.2, 0.3$ ) are shown in Fig. 3. There appeared two clear peaks at  $2.0 \text{ \AA}$  and  $2.8 \text{ \AA}$ . Another small peak around  $3.3 \text{ \AA}$  was observed in the profiles of the three glasses. The first peaks at  $2.0 \text{ \AA}$  were almost alike in heights and areas. The intensity of the second ones at  $2.8 \text{ \AA}$  decreased, and the third feeble peaks at around  $3.3 \text{ \AA}$  increased with  $\text{ZnO}$  content. The latter ones appeared to shift to the smaller  $r$  by introducing  $\text{ZnO}$ .

Figure 4 shows RDF profiles calculated by MD simulation (dotted lines) and those obtained by neutron diffraction (solid lines). The calculated RDFs gave good agreement with the observed curves. The first and

the second peaks were very consistent in the observed and calculated RDFs. The short range order of the glasses are at least well reproduced. The calculation methods adopted in the present simulation are, therefore, thought to be adequate for modeling the tellurite glasses.

Figure 5 (a) shows accumulated coordination numbers of Te-O pairs obtained from the calculated models. These three curves were very similar. In all the structural models, the accumulated coordination curves kept increasing without any flat regions, which could usually be seen in those of strong network glass formers. The clear absence of such high structural order in the model of tellurite glasses is due to the second longer Te-O whose distributions lie in between the first large Te-O peaks and interhedral Te-O distributions. Partial radial distribution of Te-O had a first minimum at about 2.2 Å, as shown in Fig. 6. This critical distance could be regarded as the first coordination of Te-O. When the Te-O pairs closer than 2.2 Å were considered, the values of the Te-O coordination number became 3.12 ~ 3.14. Accordingly, 85 ~ 90 % of tellurium atoms had three-fold coordination and 10 ~ 15 % of tellurium atoms resided in the form of TeO<sub>4</sub> in all three models.

The accumulated coordination numbers of Zn-O pairs obtained from models are shown in Fig. 5 (b). The Zn-O coordination number increased with increasing amount of ZnO. Note that these accumulated coordination curves of Zn-O had rather flat parts when compared to those of Te-O, which implied fairly ordered Zn-O coordination.

It should be noted that coordination state of tellurium is relatively independent of the ZnO content in our structural models. The accumulated coordination curves of Te-O for all three glasses with different ZnO amount seem to be almost coincident as shown in Fig. 5. The present results suggest that the zinc tellurite glasses are composed primarily of TeO<sub>3+1</sub> whose fraction is almost unchanged with the ZnO amount. According to the structural models in the present work, even when the ZnO content is extrapolated to 0 %, the coordination numbers of tellurium will take the same values as those in the models of zinc tellurite glasses. This implies that the coordination state around tellurium atoms of pure TeO<sub>2</sub> glass is similar to that of the zinc tellurite glasses.

Figure 7 shows the average numbers of bridging oxygen in TeO<sub>x</sub> polyhedra derived from the structural models. This figure includes two cases, i.e. zinc was considered as either network modifier or former. A distance of Zn-O less than 2.3 Å was considered as a bond in the latter case. When only tellurium and oxygen atoms were assumed to compose the glass network, the average number of bridging oxygen atoms was small and it became less than two in glasses for  $x = 0.2$  and  $0.3$ . Tellurium - oxygen polyhedra could not form a continuous network in this case. In the latter situation, where both tellurium and zinc were considered as network formers, the number of bridging oxygens became more than two in all compositions. Thus zinc seems to take a network forming role in the zinc tellurite glasses, considering the necessary number of bridging oxygen around tellurium. This idea is supported to some extent by thermal property data of the glasses.

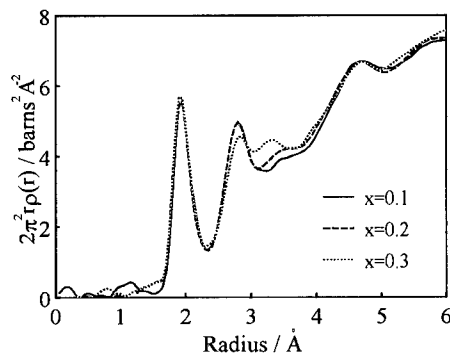


Figure 3 Radial distribution functions of  $x$  ZnO -  $(1-x)$  TeO<sub>2</sub> glasses ( $x = 0.1, 0.2, 0.3$ ) obtained by neutron diffraction.

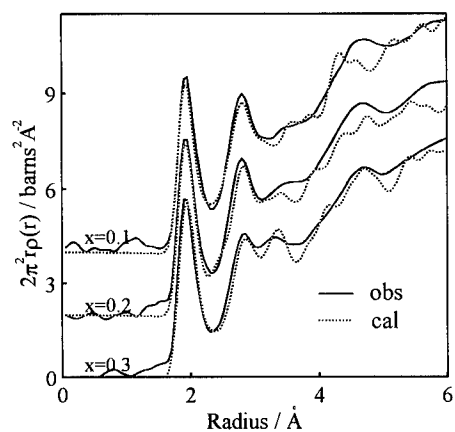


Figure 4 Comparison of the RDFs derived from glass structure models of MD construction (dotted lines) and those obtained by neutron diffraction (solid lines) for  $x$  ZnO -  $(1-x)$  TeO<sub>2</sub> glasses ( $x = 0.1, 0.2, 0.3$ ).

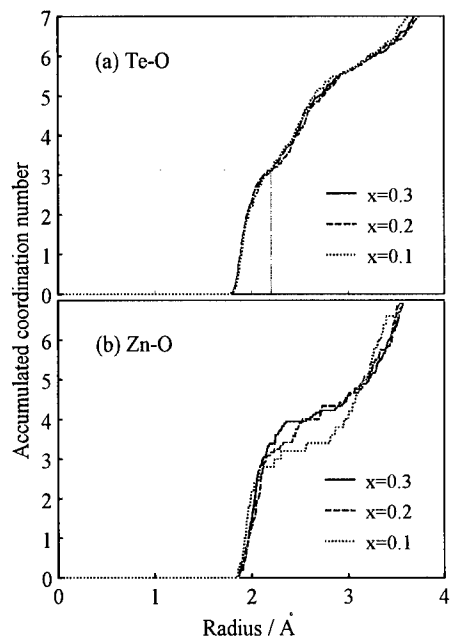


Figure 5 Accumulated coordination numbers of (a) Te-O and (b) Zn-O in the MD structural models for  $x$  ZnO -  $(1-x)$  TeO<sub>2</sub> glasses.

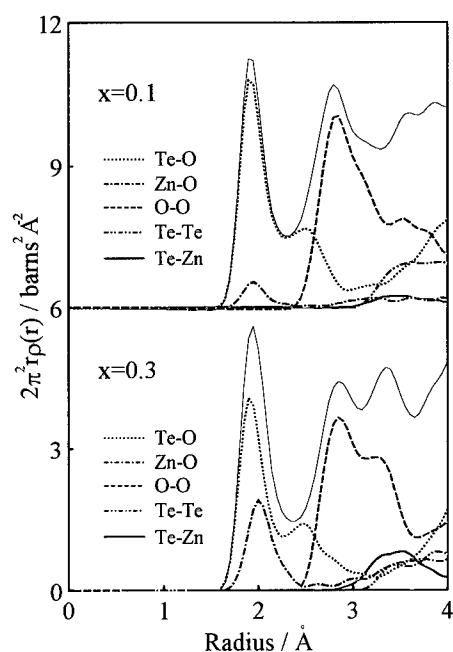


Figure 6 Partial RDFs of Te-O (dotted lines), O-O (broken lines) and other combinations of components for  $x \text{ ZnO} - (1-x) \text{ TeO}_2$  glasses ( $x = 0.1, 0.3$ ) in the structural models constructed by MD.

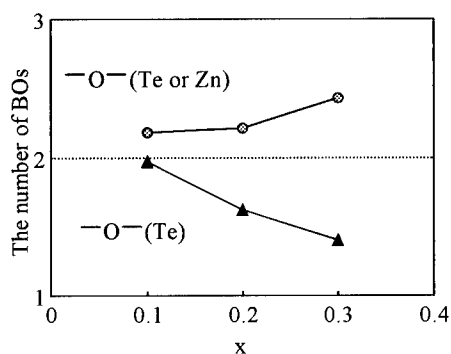


Figure 7 The average number of bridging oxygen atoms around a tellurium atom as a function of  $\text{ZnO}$  amount in the structural models of MD. Triangle marks show the number of bridging oxygen atoms when tellurium is considered as network former; circle ones show the number of oxygen atoms connecting to either tellurium or zinc atoms.

#### 4. Electronic Polarization in Mixed Alkali Silicate Glasses [20]

It is known that mixed alkali glasses show a great reduction in mobility of alkali ions, which is called the mixed alkali effect [21-23]. Though there are several explanations for this anomalous phenomenon [24-27], none of them have been generally accepted.

One of the characteristic features of the mixed alkali glasses is the negative enthalpy of mixing, which may explain the mixed alkali effect [27]. The negative deviation of enthalpy is often explained by electronic polarization which is estimated from the crystalline structure [28-30]. The polarization effect has not been determined for glass, and so it is not known whether, or to what extent the polarization energy is induced in vitrified mixed alkali systems. Polarization of oxygen has been extensively studied using simulation techniques in the field of water structure [31-33]. However, there has been no numerical approach to study of the polarization induced in glass.

In this work, molecular dynamics (MD) involving inductive potential was simulated to examine the effect of electronic polarization on energetic properties of mixed alkali glasses. The MD simulation was performed for lithium - potassium disilicate glasses,  $x \text{Li}_2\text{O} \cdot (1-x) \text{K}_2\text{O} \cdot 2\text{SiO}_2$  ( $x=0, 0.5, 1$ ), in which glass structures were relaxed for inductive polarization as well as for conventional electrostatic and repulsive interactions.

Electronic polarizabilities of 0.029, 0.83 and  $0.0165 \text{ \AA}^3$  were adopted for Li, K and Si, respectively. Although a polarizability of  $1 \sim 3 \text{ \AA}^3$  is usually employed for oxygen [34], we had to use a smaller value. This was because the potential of induced polarization described by eq.(4) was a strongly attractive potential which tends to increase induction infinitely especially when oxygen approaches to any of the surrounding component atoms, which would result in impracticable interatomic approach. To avoid such catastrophic over-induction, an electronic polarizability of  $0.5 \text{ \AA}^3$  was assumed for oxygen in the present calculation, which is sufficient to roughly estimate the polarization energy in mixed alkali glasses. All the parameters for the pair potential were empirically determined to reproduce appropriate interatomic distributions. We have already investigated glasses with the same compositions, in which only the two-body potential was considered [35]. The repulsive parameter  $B_{ij}$  in eq.(1) for oxygen - oxygen and oxygen - cations had to be increased and Si-O bond should have been made tighter by reducing the value of  $r_{\text{Si-O}}$ , due to the strongly attractive nature of the inductive potential.

Table 3 shows a summary of energy data obtained by MD calculation. The inductive electronic polarization energy ( $\Phi_{\text{IND}}$ ) was smaller than that of the pair potential ( $\Phi_{\text{PAIR}}$ ), which was partly due to the presupposed smaller value of polarizability for oxygen.

The electronic polarization energy of each element is shown in Table 3 (b). It was found that oxygen had a far larger energy of induction than the other component cations. This large polarization of oxygen indicates large electric fields located at oxygen atoms, since the polarization energy is proportional to the squared local electric field. Silicon or alkalis are surrounded by oxygen of one sort, whereas oxygen atoms are thought to have coordinations with two or three kinds of cations with different field strengths, which causes a large electric field remaining around and following dipole induction in oxygen atoms.

The non-additivity of the potential energies is shown in Table 3 (c). Deviation of the inductive polarization energy from compositional additivity was negative, while the Coulomb-repulsive pair potential deviated positively. The total deviation was negative,  $-9.47 \text{ kJ} / \text{SiO}_2 \text{ mol}$  ( $-2.26 \text{ kcal} / \text{SiO}_2 \text{ mol}$ ).

Oxygen surrounded by different cations was certainly polarized and the negative deviation from additivity would occur in this calculation as discussed above. However, oxygen atoms are not usually arranged linearly with coordinating cations and more than two cations are expected to surround the oxygen atoms. Thus polarization of oxygen must be considered to be induced by three-dimensional electric field vectors from all the charges around the oxygen. The precise mechanisms of the induction and the corresponding negative deviation need to be clarified by further investigation. On the other hand, oxygen had a smaller polarizability than the ordinary value in the present calculation. It is clear that the electronic polarization energy makes a negative contribution to the non-linearity of potential energy in mixed alkali glasses.

Table 3. Summary of energetic data.

(a) Potential energy of 288-particle system( $10^{-20}$ J/cell)

	Li single	Li-K mixed	K single
$\Phi_{\text{PAIR}}$	-79107.7	-78001.5	-77000.2
$\Phi_{\text{IND}}$	-3369.6	-3506.0	-3336.1
total	-82477.3	-81507.5	-80336.3

(b) Polarization energy of elements( $10^{-20}$ J/atom)

	Li single	Li-K mixed	K single
Si	-0.054	-0.055	-0.051
O	-20.98	-21.65	-20.29
Li	-0.135	-0.172	-
K	-	-1.247	-1.341

(c) non-additivity of potential energy

	$10^{-20}$ J/cell	kJ / SiO <sub>2</sub> mol
$\Delta\Phi_{\text{PAIR}}$	+52.5	+4.94
$\Delta\Phi_{\text{IND}}$	-153.2	-14.41
total	-100.7	-9.47

## CONCLUSIONS

In this report, the application of new kinds of potential functions to the MD calculation is described. Normal two-body potential can produce an appropriate model for silicate glasses, whereas it is necessary to include three-body potential to make suitable models for borate or tellurite glasses. In addition, it is necessary to include polarization effects in MD calculation if we try to explain transport of alkali ions in glasses.

The simulation technique is quite important to describe the true vision of glass structures including both structures of network formers and modifiers.

## REFERENCES

- [1] P.N.Keating, Phys.Rev., 145 (1966) 637.
- [2] Itaru Yasui, Y.Akasaka, H.Inoue, J.Non-Cryst.Solids **177** (194) 91-96
- [3] "Borate Glasses", Material Science Research Vol.12, Ed. L.D.Pye et al. Plenum Press (1978)
- [4] Q.Xu,K.Kawamura and T.Yokokawa, *J. Non-Cryst. Solids* **104** (1988) 261-272
- [5] W.Soppe,C.Van der Marel and H.W. den Hartog, *J. Non-Cryst. Solids* **101** (1988) 101-110
- [6] K.Hirao and N.Soga, *J. Am. Ceram. Soc.* **68** (1985) 515-521
- [7] H.Inoue,N.Aoki and I.Yaui, *J. Am. Ceram. Soc.* **70** (1987) 622-627
- [8] A.H.Verhoef,H.W.den Hartog, *J. Non-Cryst. Solids* **182** (1995) 235-247

- [9] T.Mabuchi, Theses for Master Degree, University of Tokyo (1994)
- [10] H.Matsumoto, T.Mabuchi, Y.Shigesato, I.Yasui, Jpn.J.Appl.Phys. 35 (1996), 694-698
- [11] N. Mochida, K. Takahashi, K. Nakata and S. Shibusawa : Yogyo-Kyokai-Shi, 86 (1978) 316 [in Japanese].
- [12] T. Sekiya, N. Mochida, A. Ohtsuka and M. Tomokawa : J. Ceram. Soc. Jpn., 97 (1989) 1435.
- [13] T. Yoko, K. Kamiya, K. Tanaka, H. Yamada and S. Sakka : J. Ceram. Soc. Jpn., 97 (1989) 289.
- [14] T. Sekiya, N. Mochida, A. Ohtsuka and M. Tomokawa : J. Non-Cryst. Solids, 144 (1992) 128.
- [15] T. Sekiya, N. Mochida and A. Ohtsuka : J. Non-Cryst. Solids, 168 (1994) 106.
- [16] M. Dimitrova-Pankova, Y. Dimitriev and V. Dimitrova : Phys. Chem. Glasses, 30 (1989) 260.
- [17] H. Bürger, K. Kneipp, H. Hobert, W. Vogel, V. Kozhukharov and S. Neov : J. Non-Cryst. Solids, 151 (1992) 134.
- [18] S. Neov, V. Kozhukharov, I. Gerasimova, K. Krezhov and B. Sidzhimov : J. Phys. C. -Solid State Phys., 12 (1979) 2475.
- [19] P. A. V. Johnson, A. C. Wright, C. A. Yarker and R. N. Sinclair : J. Non-Cryst. Solids, 81 (1986) 163.
- [20] H.Matsumoto, Y.Shigesato, I.Yasui, Jpn. J.Appl.Phys., 35 (1996) 2251-2252.
- [21] M. D. Ingram: Phys. Chem. Glasses 28 (1987) 215.
- [22] D. E. Day: J. Non-Cryst. Solids 21 (1976) 343.
- [23] J. O. Isard: J. Non-Cryst. Solids 1 (1969) 235.
- [24] J. R. Hendrickson and P. J. Bray: Phys. Chem. Glasses 13 (1972) 43 and 107.
- [25] M. D. Ingram: J. Am. Ceram. Soc. 63 (1980) 248.
- [26] A. H. Dietzel: Phys. Chem. Glasses 24 (1983) 172.
- [27] M. Tomozawa: J. Non-Cryst. Solids 152 (1993) 59.
- [28] K. Takahashi and T. Yoshio: Zairyo 26 (1977) 72 [in Japanese].
- [29] M. Hattori and M. Kondoh: Yogyo-Kyokai-shi 85 (1977) 180 [in Japanese].
- [30] M. Hattori and M. Kondoh: Yogyo-Kyokai-shi 86 (1978) 326 [in Japanese].
- [31] P. Ahlstrom, A. Wallqvist, S. Engstrom and B. Jossan, Mol.Phys. 68 (1989) 563.
- [32] J. Caldwell, L. X. Dang and P. A. Kollman: J. Am. Chem. Soc. 112 (1990) 9144.
- [33] R. Kutteh and J. B. Nicholas: Comput. Phys. Commun. 86 (1995) 227.
- [34] C. Kittel: Kotai-buturigaku-nyumon (Introduction to Solid State Physics) (Maruzen, Tokyo, 1988) 6th ed., the last vol. p.87 [in Japanese].
- [35] H. Matsumoto, Y. Shigesato and I. Yasui: to be published in Phys. Chem. Glasses (1996).



## STRONG LIQUID BEHAVIOR OF Zr-Ti-Cu-Ni-Be BULK METALLIC GLASS FORMING ALLOYS

Ralf Busch, Andreas Masuhr, Eric Bakke, and William L. Johnson

*Keck Laboratory of Engineering Materials, California Institute of Technology, Pasadena, CA 91125*

### ABSTRACT

The viscosities of the  $Zr_{46.75}Ti_{8.25}Cu_{7.5}Ni_{10}Be_{27.5}$  and the  $Zr_{41.2}Ti_{13.8}Cu_{12.5}Ni_{10}Be_{22.5}$  bulk metallic glass forming liquids was determined from the melting point down to the glass transition in the entire temperature range of the supercooled liquid. The temperature dependence of the viscosity in the supercooled liquid obeys the Vogel-Fulcher-Tammann (VFT) relation. The fragility index  $D$  is about 20 for both alloys and the ratio between glass transition temperature and VFT temperature is found to be 1.5. A comparison with other glass forming systems shows that these bulk metallic glass formers are strong liquids comparable to sodium silicate glass. Furthermore, they are the strongest among metallic glass forming liquids. This behavior is a main contributing factor to the glass forming ability since it implicates a higher viscosity from the melting point down to the glass transition compared to other metallic liquids. Thus, the kinetics in the supercooled liquid is sluggish and yields a low critical cooling rate for glass formation. The relaxation behavior in the glass transition region of the alloys is consistent with their strong glassy nature as reflected by a stretching exponent that is close to 0.8. The microscopic origin of the strong liquid behavior of bulk metallic glass formers is discussed.

### INTRODUCTION

Glass formation is observed in a large variety of materials such as silicates, polymers and ionically bonded systems. In metallic systems glass formation could be observed up to recently only after rapidly quenching the melt with rates of the order of  $10^4$ - $10^6$  K/s<sup>1-2</sup>. This resulted in thin ribbons or sheets with thicknesses of typically 20-50  $\mu$ m. For a long time the only exception was the Ni-Pd-P alloy system where bulk material with thicknesses up to 1cm could be produced by fluxing the surface to avoid heterogeneous nucleation of crystals<sup>3-4</sup>. Recently the judicious choice of the compositions in multicomponent alloy systems made bulk metallic glass (BMG) formation much more common. Examples are La-Al-Ni<sup>5</sup>, Zr-Al-Ni-Cu<sup>6</sup> and Zr-Ti-Cu-Ni-Be<sup>7</sup> of which the latter one is by far the best bulk metallic glass forming alloy system with critical cooling rates as low as 1K/s<sup>8</sup>.

Bulk metallic glasses have promising properties like high yield strength and a high elastic strain limit together with fatigue and corrosion resistance<sup>9-10</sup>. These features make them interesting engineering materials e.g. as high strength, light weight materials, as springs, for bonding, or as composites with ceramics or intermetallic compounds.

BMG forming liquids exhibit very good thermal stability with respect to crystallization in their supercooled state when cooled below the equilibrium melting point as well as when heated above their glass temperature. This high resistance with respect to crystallization allows for the first time to measure thermophysical properties of these supercooled *metallic* liquids in a broad time and temperature range. Results were, e.g., obtained on the specific heat capacity<sup>11</sup>, diffusion coefficients<sup>12</sup>, emissivity<sup>13</sup>, or time-temperature-transformation diagrams<sup>14</sup>.

In this study we focus on the viscosity of  $Zr_{41.2}Ti_{13.8}Cu_{12.5}Ni_{10}Be_{22.5}$  (Vit 1) and  $Zr_{46.75}Ti_{8.25}Cu_{7.5}Ni_{10}Be_{27.5}$  (Vit 4) BMG forming liquids. Viscosity data in the entire temperature range from the melting point down to the glass transition are obtained. The results are

discussed in the framework of the fragility concept<sup>15</sup> comparing the bulk metallic glass forming liquids with the observations in other metallic as well as non-metallic glass forming liquids. We will emphasize that a main contributing factor to the high glass forming ability of the novel bulk metallic glass forming liquids compared to previously known metallic glass formers is their strong liquid behavior similar to supercooled silicate melts.

## EXPERIMENTAL METHODS

Glassy bulk metallic ingots with a composition of  $Zr_{46.75}Ti_{8.25}Cu_{7.5}Ni_{10}Be_{27.5}$  and  $Zr_{41.2}Ti_{13.8}Cu_{12.5}Ni_{10}Be_{22.5}$  were prepared by cooling the melt with a rate of approximately 10 K/s. The viscosity was measured by using four different techniques. (1) High viscosities in the glass transition regime between  $10^{10}$  and  $10^{15}$  poise (1 poise=10 Pa·s) were measured by *three point beam bending*. A beam that is supported at the ends by sharp edges is deflected with a constant force applied in the center of the beam. The viscosity is determined according to Hagy<sup>16</sup>. (2) *Parallel plate rheometry* allows to measure viscosities in the range between  $10^6$  and  $10^{10}$  poise. A cylindrical sample with a small aspect ratio  $h/r$  between radius,  $r$ , and height,  $h$ , flows in between two parallel plates under constant load<sup>17-18</sup>. The viscosity is calculated using an equation derived by Stephan<sup>19</sup>. (3) Viscosity data in the equilibrium liquid were obtained by *capillary flow* measurements<sup>20</sup>. The liquid flows through a capillary driven by a pressure gradient. The viscosity is determined using Hagen-Poiseuille's law for steady flow in a pipe. (4) In the slightly undercooled liquid the viscosity was measured by the *rotating cup* method. A rod is rotating in the liquid and generates a uniform shear flow. The viscosity is derived from the torque on the rod<sup>21</sup>.

## RESULTS

### *Strong Liquid Behavior*

Figure 1 shows the viscosities for Vit 1 and Vit 4 in an Arrhenius plot, obtained from the four different methods. The data cover a range of 14 orders of magnitude and can be fitted well by a Vogel-Fulcher-Tammann (VFT) equation

$$\eta = \eta_0 \cdot \exp[D \cdot T_0 / (T - T_0)] \quad (1),$$

in a modification that was proposed by Angell<sup>15</sup>. In this formulation  $D$  is the fragility parameter and  $T_0$  is the VFT temperature. The best fits to the experimental data yield  $D=18.5$  and  $T_0=412.5$ K for Vit 1 and  $D=22.7$  and  $T_0=372$  K for Vit 4. The value  $\eta_0$  was set as  $4 \cdot 10^{-4}$  poise according to the relation  $\eta_0 = N_A \cdot h / V$ , with,  $N_A$ , Avogadro's constant,  $h$ , Planck's constant and,  $V$ , the molar volume<sup>22</sup>.

Glass formation was observed and studied in a large variety of materials, mostly non-metallic systems. The temperature dependence of viscosity can differ substantially among different materials. The viscosity of  $SiO_2$ , for example, which is an open network glass, can be described well with an Arrhenius law. Other substances such as materials with van der Waals bonds are best described by a VFT relation with a VFT temperature very close to the glass transition. A comprehensive concept to describe the sensitivity of the viscosity to temperature changes for different materials in the supercooled liquid state was developed by Angell (see, for example<sup>15</sup>). The viscosity is plotted normalized to the glass transition temperature,  $T_g$ .

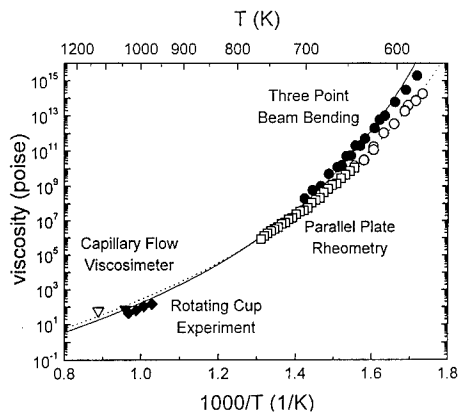


Fig.1: Viscosity of the supercooled liquid for  $Zr_{41.2}Ti_{13.8}Cu_{12.5}Ni_{10}Be_{22.5}$  (Vit 1) (solid symbols) and for  $Zr_{46.75}Ti_{8.25}Cu_{7.5}Ni_{10}Be_{27.5}$  (Vit 4) (open symbols).

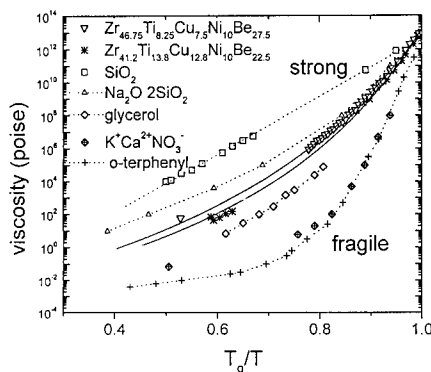


Fig.2: Angell plot of the viscosities of the BMG and several non metallic "strong" and "fragile" glasses (see 15).

Figure 2 compares the data of the BMG forming Vit 1 and Vit 4 with a selection of some non-metallic liquids. Strong glasses, like  $SiO_2$ , are one extreme case. They exhibit very small VFT temperatures and very high melt viscosities. The other extreme are "fragile" glasses that show a VFT temperature close to the glass transition temperature, as well as low melt viscosities. The temperature dependence of the viscosity of the two BMG studied here is found to behave similar to that of the relatively strong sodium silicate glasses. We observe melt viscosities of the order of 50 poise for both alloys. They are much more viscous (three orders of magnitude) than the melts of pure metals, where viscosities of typically  $5 \cdot 10^{-2}$  poise are found.

In the reduced plot of Fig.2 the viscosity curves of Vit 1 and Vit 4 are very close to each others, indicating that their fragility parameters are very similar. The different viscosities in Fig.1 mainly reflect the slightly different glass transition temperatures. The onset of the calorimetric glass transition for a heating rate of 1 K/min is found to be at 602 K and 596 K for Vit 1 and Vit 4, respectively<sup>11</sup>. These temperatures are close to the temperatures where the viscosities of the alloys are at  $10^{13}$  poise [611 K (Vit 1), 592 K (Vit 4)]. The observed glass transition temperatures are considerably higher than the VFT-temperatures. This is consistent with strong liquid behavior. We experimentally find the ratio between glass transition temperature and VFT-temperature to be  $T_g/T_0 = 1.46$  for Vit 1 and  $T_g/T_0 = 1.60$  for Vit 4. This ratio can also be obtained by the equation  $T_g/T_0 = 1 + D/(2.303 \cdot \log \eta_g/\eta_0)$  (2). This is a rewritten form of equation (1) for  $T = T_g$ . By assuming that  $\eta_g$  is  $10^{13}$  poise and with the known values for  $D$  and  $\eta_0$ , we calculate 1.49 and 1.60 for Vit 1 and Vit 4, respectively. This is in good agreement with the values obtained using the calorimetrically determined  $T_g$ .

In order to measure the equilibrium viscosity close to the glass transition the material has to be allowed to undergo relaxation. In general, this relaxation does not proceed exponentially with time. The departure from exponentiality can be described by the Kohlrausch-Williams-Watts (KWW) relaxation function with a stretching exponent  $\beta$ . Figure 3 shows the relaxation of the

viscosity towards equilibrium in isothermal three point beam bending experiments near the glass transition for Vit 4. The relaxation of the viscosity with time is fitted with the stretched exponential function

$$\eta = \eta_{eq} (1 - e^{-(t/\tau)^\beta}) \quad (3).$$

The stretching exponent  $\beta$  is found to be close to 0.8 and increases with temperature. This large stretching exponent is again consistent with strong liquid behavior. Fragile liquids, in contrast, typically exhibit stretching exponents below 0.5 at the glass transition. The stretching exponent can be connected with  $D$ ,  $T_0$ , and  $T_g$  as (see, for example ref. 23)

$$\beta = 1 - \sqrt{\frac{(T_0/T_g)^2}{D}} \quad (4).$$

Using this equation we calculate a stretching exponent of  $\beta=0.86$  which is close to the above value obtained by fitting the viscosity relaxation. It is worthwhile mentioning that the relaxation time in the glass transition region is proportional to the equilibrium viscosity as shown in the insert in Fig. 3. This means that both quantities in first approximation obey the same VFT relation. The high frequency shear modulus  $G_\infty = \eta/\tau$  at the glass transition of Vit 4 is found to be  $6.8 \cdot 10^8$  Pa.

The strong liquid behavior of BMG is reflected by the temperature dependence of the viscosity and the relaxation pattern. It plays an important role in understanding their superior glass forming ability compared to other metallic liquids as will be shown in the following.

#### *Viscosity and Glass Forming Ability*

In Fig. 4, the viscosity of the bulk metallic glass is compared with viscosity data on other *metallic* glass forming liquids. Fragility parameters and the critical cooling rates are indicated in the plot. One observes the general trend that critical cooling rates decrease with increasing fragility parameters. That means the stronger the glass, the lower the critical cooling rate and the higher the glass forming ability.

Strong liquid behavior favors the glass forming ability over the entire supercooled liquid region since the viscosity is a contributing factor to the nucleation rate of crystals. The homogeneous nucleation rate  $I$  as a function of temperature can be described as

$$I(T) = (A/T \cdot \eta) \cdot \exp(\Delta G^* / RT) \quad (5),$$

where  $\eta$  is the viscosity,  $T$  the temperature,  $R$  the gas constant,  $\Delta G^*$  the activation barrier for the formation of nuclei and  $A$  a temperature independent constant. High viscosities in the supercooled melt decrease the nucleation rate and thus enhance the glass forming ability compared to supercooled liquids that exhibit low viscosities. Upon undercooling from the melting point, the viscosities of the BMG forming liquids are about two orders of magnitude larger than for the most fragile liquids (see Fig 4). This decreases the nucleation rate according to equation (5) and decreases the critical cooling rate. On reheating an amorphous BMG into the supercooled liquid the viscosity decreases much slower than in the fragile liquid and the kinetics for crystallization stays sluggish. This contributes to the high thermal stability of the supercooled liquid in BMG forming systems in the glass transition region and allows for the first time to extensively study metallic systems at  $T_g$ .

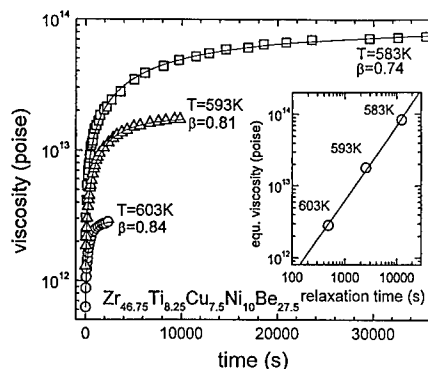


Fig.3: Isothermal measurement of the viscosity of the  $Zr_{46.75}Ti_{8.25}Cu_{7.5}Ni_{10}Be_{27.5}$  alloy (three-point beam bending). The data are fitted with a stretched exponential relaxation function.

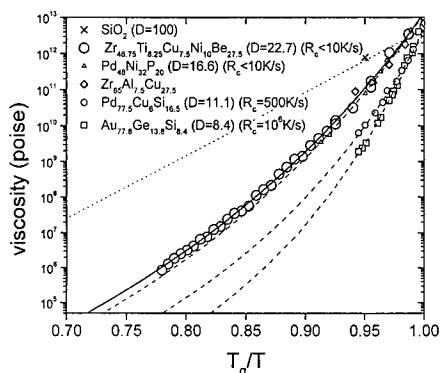


Fig.4: Angell plot of the viscosities of several metallic glasses: (O) this work, (◊) [24] (◊) (Δ) [25], ◻ [26].

The strong liquid behavior of metallic melts is somewhat surprising if one has the picture of a simple liquid without directional bonds. There are however several indications that especially Zr-Ti-Cu-Ni-Be bulk metallic glass forming liquids are not completely disordered simple liquids but exhibit chemical short range ordering that can result in clustering<sup>27</sup> or phase separation<sup>28-29</sup>. Short range order will in fact lead to smaller coordination number of atoms (number of nearest neighbors) and to a narrower distribution of the coordination numbers compared to a hard sphere randomly packed glass. This brings the glass structurally closer to network glasses which exhibit a small coordination number with a very sharp distribution. The chemical short range order makes the BMG stronger than metallic glasses with no tendency to short range order. In addition, the ordering processes decrease the entropy and enthalpy with respect to the competing crystalline phases and thus reduce the thermodynamic driving forces for crystallization<sup>30</sup>.

## CONCLUSIONS

The viscosity of Zr-Ti-Cu-Ni-Be bulk metallic glass forming liquids has been determined in the entire supercooled liquid region. This could be achieved due to their superior thermal stability with respect to crystallization compared to previous alloys. The novel alloys exhibit strong liquid behavior which means that they are much more viscous than previous metallic glass formers or pure metals. Therefore they are kinetically more robust with respect to crystallization. It is most likely that in bulk metallic glass forming system the tendency to short range order or clustering leads to a smaller average number of nearest neighbors with a sharper distribution of configurations. This brings them topologically closer to network glasses and decreases their fragility.

## ACKNOWLEDGEMENT

This work was supported by the U.S. Department of Energy (Grant No. DEFG-03-86ER45242). Partial support for R. Busch was provided by the Alexander von Humboldt Foundation via the Feodor Lynen Program.

## REFERENCES:

1. W. Klement, R. Willens, and P. Duwez, *Nature* **187**, 869 (1960).
2. P. Duwez, *Trans. ASM* **60**, 607 (1967).
3. A.J. Drehman and A.L. Greer, *Acta Metall.* **32**, 323 (1984).
4. H.W. Kui, A.L. Greer, and D. Turnbull, *Appl. Phys. Lett.* **45**, 615 (1984).
5. A. Inoue, T. Zhang and T. Masumoto, *Mater. Trans. JIM* **31**, 425 (1991).
6. T. Zhang, A. Inoue and T. Masumoto, *Mater. Trans. JIM* **32**, 1005 (1991).
7. A. Peker and W. L. Johnson, *Appl. Phys. Lett.* **63**, 2342 (1993).
8. Y.J. Kim, R. Busch, W.L. Johnson, A.J. Rulison, W. K. Rhim, *Appl. Phys. Lett.* **65**, 2136 (1994).
9. H.A. Bruck, T. Christman, A.J. Rosakis, and W.L. Johnson, *Scripta Metall. Mater.* **30**, 429 (1994).
10. H.A. Bruck, A.J. Rosakis, and W.L. Johnson, *J. Mater. Res.* **11**, 503 (1996).
11. R. Busch, Y.J. Kim, and W.L. Johnson, *J. Appl. Phys.* **77**, 4039 (1995).
12. U. Geyer, S. Schneider, W.L. Johnson, Y. Qiu, T. A. Tombrello, and M. P. Macht, *Phys. Rev. Lett.* **75**, 2364 (1995).
13. R. Busch, Y.J. Kim, W.L. Johnson, A.J. Rulison, W. K. Rhim, and D. Isheim, *Appl. Phys. Lett.* **66**, 3111 (1995).
14. Y.J. Kim, R. Busch, W.L. Johnson, A.J. Rulison, W. K. Rhim, *Appl. Phys. Lett.* **68**, 1057 (1996).
15. C.A. Angell, *Science* **267**, 1924 (1995).
16. H.E. Hagy, *J. Amer. Ceram. Soc.* **46**, 93 (1963).
17. G.J. Diennes and H.F. Klemm, *J. Appl. Phys.* **17**, 458 (1946).
18. M.J. Stephan, *Akad. Wiss. Wien. Math.-Natur. Klasse Abt. 2.* **69**, 713 (1984).
19. E. Bakke, R. Busch, and W.L. Johnson, *Appl. Phys. Lett.* **67**, 3260 (1995).
20. E.W. Washburn, *Phys. Rev.* **17**, 273 (1921).
21. I.M. Krieger and S.H. Maron, *J. Appl. Phys.* **23**, 147 (1952).
22. S.V. Nemilov, *Glass Physics and Chemistry* **21**, 91 (1995).
23. R. Böhmer, K.L. Ngai, C.A. Angell, and D.J. Plazek, *J. Chem. Phys.* **99**, 4201 (1993).
24. R. Rambousky, M. Moske, K. Samwer, *Z. Phys. B* **99**, 387 (1996).
25. H.S. Chen, *J. Non-Crystalline Solids* **27**, 257 (1978).
26. H.S. Chen and D. Turnbull, *J. Chem. Phys.* **48**, 2560 (1968).
27. M.K. Miller, K.F. Russell, R. Busch, and W.L. Johnson, *J. de Physique* (in press).
28. R. Busch, S. Schneider, A. Peker, and W.L. Johnson, *Appl. Phys. Lett.* **67**, 1544 (1995).
29. S. Schneider, P. Thiyagarajan, and W.L. Johnson, *Appl. Phys. Lett.* **68**, 493 (1996).
30. R. Busch, E. Bakke, and W.L. Johnson, *Proceedings of the Intl. Symp. on Metastable and Nanocrystalline Materials 1996*, Rome, Italy, *Mater. Sci. Forum*, (1996), in press.

**Part V**

**Structure, Energetics, and  
Polyamorphism**

## LIQUID AND GLASSY STATE POLYAMORPHISM IN THE SYSTEM $Y_2O_3$ - $Al_2O_3$

PAUL F. McMILLAN\*, CHUNG HO\*, SIV AASLAND\*\*, AMIR YEGANEH-HAERI\*, RICHARD WEBER\*\*\*

\* Dept. of Chemistry, Arizona State University, Tempe, AZ 85287-1604 pmcmillan@asu.edu

\*\* Dept. of Inorganic Chemistry, Norwegian Inst. Technology, Trondheim University, Norway

\*\*\* Containerless Research, Inc., 910 University Place, Evanston, IL 60201-3149

### ABSTRACT

During a recent study of supercooled liquids in the system  $Y_2O_3$ - $Al_2O_3$ , a first-order phase transition between two liquid phases with the same composition, but different structure and density, was observed to occur. The transition occurred close to the glass transformation of the two liquids, so that both phases were quenched to metastably coexisting glasses. We report further studies on the liquids and glasses in this system, prepared by rapid (roller) quenching and by containerless levitation techniques.

### INTRODUCTION

We recently reported the occurrence of unusual behavior in undercooled  $Y_2O_3$ - $Al_2O_3$  liquids, close to the high alumina (near 24 mole%  $Y_2O_3$ ) eutectic composition [1]. In that study, a transition occurred between two liquid phases in the metastable regime, as the liquid was quenched from approximately 1400°C. Both liquids were recovered as coexisting glasses, because each passed near-simultaneously through its respective glass transition before the phase transformation was complete. Subsequent chemical and structural analysis revealed that the two liquids had the same composition, within experimental error, but that their densities and structures (as revealed by IR and Raman spectroscopy) were different [1]. This observation constitutes an example of a first-order density-driven liquid-liquid phase transition, long conjectured from theory or indirect experimental evidence [2-4], but never before observed directly. In the present study, we have carried out additional experiments to better characterize the glassy phases, and their crystallization behavior.

### EXPERIMENTAL

Starting samples were prepared by a gel method [5]. Gels were dried and sintered at 1000°C, before melting. Some glasses were prepared by rapid quenching from the melt by a double roller mounted beneath a Xe thermal imaging furnace. Others were melted by  $CO_2$  laser heating, in a containerless levitation experiment in the aero-acoustic levitator at Containerless Research, Inc. [6]. This permitted a controlled cooling rate of ~250°C/s in containerless conditions, and also direct observation of the high temperature liquid behaviour during quenching. Glass could only be prepared at the YAG composition (37.5 mol%  $Y_2O_3$ ) in a preliminary series of runs, due to recrystallization during quench. In the rapid quench experiments, glass was obtained at the 24 mol%  $Y_2O_3$  (AY-24) and AY-34 compositions. The glasses were studied by micro-IR and Raman spectroscopy, and crystallization was followed by X-ray diffraction. Sound wave velocities were determined by Brillouin scattering [7].

### RESULTS AND DISCUSSION

We begin with the YAG composition (AY-37.5). This could not be vitrified in our preliminary roller quench runs. We now know that this is probably related to the very low compressibility (bulk modulus ~180 GPa) for this composition, and further synthesis is ongoing. The glass beads obtained in the levitation experiment contained large (~50  $\mu m$ ) inclusions of the second glassy phase, but no obvious deviation from "normal" liquid cooling behaviour was observed in the video records of cooling down to 1400°C. This sample showed a strong exotherm at 923°C due to metastable crystallization of a  $YAlO_3/Al_2O_3$  mixture [8,9].



A very weak endotherm could just be distinguished in our data at 888°C, which could correspond to a glass transition. The density of the bulk glassy material was measured by pycnometry to be 3.7 g/cm<sup>3</sup>, and the longitudinal and transverse sound wave velocities were 6.826 and 3.740 km/s.

The samples at the AY-24 composition prepared by roller quenching showed several interesting features. One glass was essentially "single phase", but all the others synthesized in this way contained a large fraction of the second (low temperature, lower density) glassy material, as beads dispersed within a glassy matrix of the matrix corresponding to the high temperature liquid (Fig. 1). The sound wave velocities of the homogeneous glass were 7.122

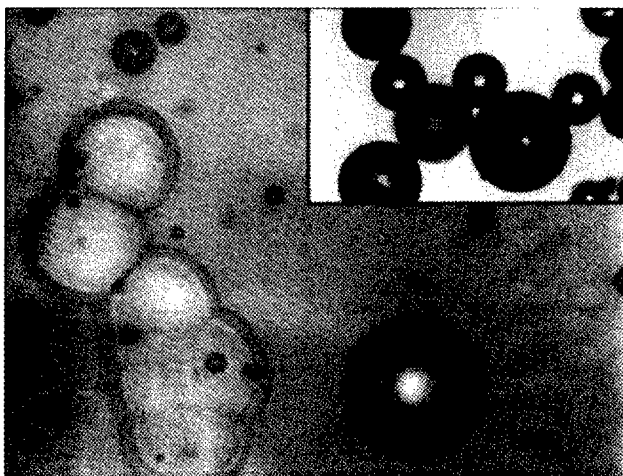


Fig. 1. Optical micrograph of a sample AY-24 prepared by roller quenching, in which liquid-liquid phase transformation occurred during the quench (compare with Fig. 1 in ref. 1). The main photograph (500x) shows the glassy beads in their glassy matrix (both have the same composition). The inset (400x) shows "beads" of the low-density glass phase which have been mechanically separated from the matrix, to form free-standing microspheres. These might have some technological applications.

km/s (longitudinal) and 3.858 km/s (transverse). (To our knowledge, these are the "fastest" oxide glasses yet recorded) [7].

The size of the glassy beads corresponding to the lower temperature liquid phase ranged from 30 to 160 nm, with most beads smaller than 90 nm. It was found that the beads could be mechanically separated from the glassy matrix by applying light (finger) pressure to the glass (Fig. 1) [7]. These could have potential applications in biomedical tracer experiments [10].

The "glassy" materials were examined by X-ray diffraction and by micro-Raman spectroscopy. Both the matrix and the separated glassy beads showed X-ray peaks due to crystalline material, which was indexed as a single phase  $Y_2O_3$ - $Al_2O_3$  solid solution with the garnet structure [11]. The matrix was almost entirely glassy (5-10% crystallinity, estimated from diffraction peak heights), whereas the separated bead fraction contained ~40% crystallinity crystalline material. Micro-Raman spectroscopy revealed that many of the beads were entirely glassy, with a broad band spectrum similar to that described by Aasland and McMillan [1] for the low-density glass phase. Other beads showed peaks for the crystalline garnet solid solution. The spectrum of the matrix glass was featureless, indicating a more "disordered" glass structure [1]. Samples containing coexisting matrix and beads, or matrix and

beads separately, were heated to temperatures in the 900-1100°C range, and examined by optical microscopy, X-ray diffraction, and micro-Raman spectroscopy. On heating to just above 850°C, corresponding to the glass transition temperature measured for this composition by DTA (872°C), spherical voids grew inside the glass beads. The beads then immediately recrystallized to Y<sub>2</sub>O<sub>3</sub>-Al<sub>2</sub>O<sub>3</sub> garnet solid solution.

The X-ray diffraction and Raman spectra of the glassy matrix samples remained unchanged even after 15 minutes annealing at 900°C, indicating that its glass transition lies at higher temperature. This observation indicates that the two glasses are indeed different. On increasing the temperature towards 1000°C, the initially flat pieces of matrix glass began to curve up, indicating that softening had begun. Crystallization to the same Y<sub>2</sub>O<sub>3</sub>-Al<sub>2</sub>O<sub>3</sub> garnet solid solution as observed for the "bead" glass ensued on continued heating. The DTA trace of an unseparated sample shows *two* exotherms (at 939 and 1003°C), for recrystallization of the *same* crystalline phase from the two different glasses.

## CONCLUSIONS

These studies have confirmed the existence of two different glasses quenched from Y<sub>2</sub>O<sub>3</sub>-Al<sub>2</sub>O<sub>3</sub> melts, with the same compositions, but different physical properties. The "matrix" glass corresponding to the high temperature liquid has a *higher* glass transition, indicating that the viscous relaxation curves for the two supercooled liquids must cross in the vicinity of the glass transition.

## ACKNOWLEDGEMENTS

This work was carried out with support by a Small Grant for Exploratory Research awarded by NSF (DMR-9525984).

## REFERENCES

- [1] Aasland S, McMillan PF *Nature* 369, 633-637 (1994).
- [2] Ponyatovsky EG, Barkalov OI. *Mat Sci Rep* 8, 147-191 (1992).
- [3] Angell CA. *Science* 267, 1924-1935 (1995).
- [4] Poole PH, Grande T, Sciortino F, Stanley HE, Angell CA. *J Comp Mat Sci*, in press (1996).
- [5] Douy A, Odier P *Mat Res Bull* 24 1119-1126 (1989).
- [6] Weber JKR, Hampton DS, Merkley DR, Rey CA, Zatarski MM, Nordine PC *Rev Sci Instrum* 65, 456-465 (1994).
- [7] Ho C, McMillan PF, Yeganeh-Haeri A, Weber JKR, in prep.
- [8] Caslavsky JL, Viechnicki DJ *J. Mat. Science* 15 1709-1718 (1980).
- [9] Gervais M, Le Floch S, Rifflet JC, Coutures J, Coutures JP *J. Am. Cer. Soc.* 75 3166-3168 (1992).
- [10] Hyatt MJ, Day DE *Comm. Am. Ceram. Soc.* C-283-287 (1987).
- [11] Le Floch S, Rifflet JC, Coutures J, Gervais M, Coutures JP *Mat. Sci. Engineering A* 173, 185-187 (1993).

## A Crystallographic Guide to THE STRUCTURE OF BORATE GLASSES

Adrian C. WRIGHT\*, Natalia M. VEDISHCHEVA\*\* and Boris A. SHAKHMATKIN\*\*

\*J.J. Thomson Physical Laboratory, University of Reading, Reading, RG6 6AF, U.K.

\*\*Institute of Silicate Chemistry, Russian Academy of Sciences, St. Petersburg, 199155, Russia.

### ABSTRACT

Borate glasses are an enigma in that there is now increasing evidence that their structures are dominated by *superstructural units*, which comprise well defined arrangements of the basic  $\text{BO}_3$  and  $\text{BO}_4$  structural units, with no internal degrees of freedom in the form of variable bond or torsion angles. In the present paper, it is shown that considerable insight into the structure of borate glasses can be gained from a study of the corresponding crystalline polymorphs. A simple, model is proposed to predict the fraction,  $x_4$ , of 4-fold co-ordinated boron atoms in vitreous borate networks and the topological criteria for the formation of such networks are discussed, taking into account the degrees of freedom necessary for conventional glass formation.

### 1. INTRODUCTION

An extremely controversial current issue in the field of glasses and glass formers concerns the role of *superstructural units* in the formation of borate glasses, as indicated by the lively discussion at a recent international conference [1]. Borate glasses are fascinating materials that have not been studied to anything like the extent they deserve, especially taking into account the challenges they present to conventional ideas concerning the structure of network glasses, as embodied in the traditional random network theory. This was first proposed by Zachariasen [2], using structural principles elucidated from crystallography, taking due regard of the additional degrees of topological freedom required by a disordered network appropriate to the vitreous state. The purpose of the present paper is to demonstrate that a similar consideration of the crystal structures of anhydrous borates,  $\text{mM}_x\text{O} \cdot \text{nB}_2\text{O}_3$  (abbreviated mM-nB), leads to a structural theory/model for borate glasses which is consistent with a wide range of experimental data.

### 2. GLASS-FORMING REGIONS

Vitreous  $\text{B}_2\text{O}_3$  itself is a glass former *par excellence* and forms binary glasses with a wide range of other oxides. The single-phase glass-forming regions obtained for binary borate systems using conventional quenching techniques [3-5] are shown as a function of the mole fraction,  $x_M$ , of the second oxide in Fig. 1, together with the crystalline polymorphs occurring in each system [5,6]. For all of the  $\text{M}_2\text{O}-\text{B}_2\text{O}_3$  binary systems in Fig. 1(A), the single-phase glass-forming region commences at zero  $x_M$ , whereas, for all of the  $\text{MO}-\text{B}_2\text{O}_3$  systems {Fig. 1(B)}, single phase glasses are not formed at low modifier contents. Any glass formation in this region results in phase-separated glasses. For example, Shelby [7] records two glass transition temperatures for  $\text{PbO}-\text{B}_2\text{O}_3$  glasses in the region  $0.005 < x < 0.195$ , corresponding to those for the two limiting compositions. Figure 1(C) shows the glass-forming regions for a series of systems where the

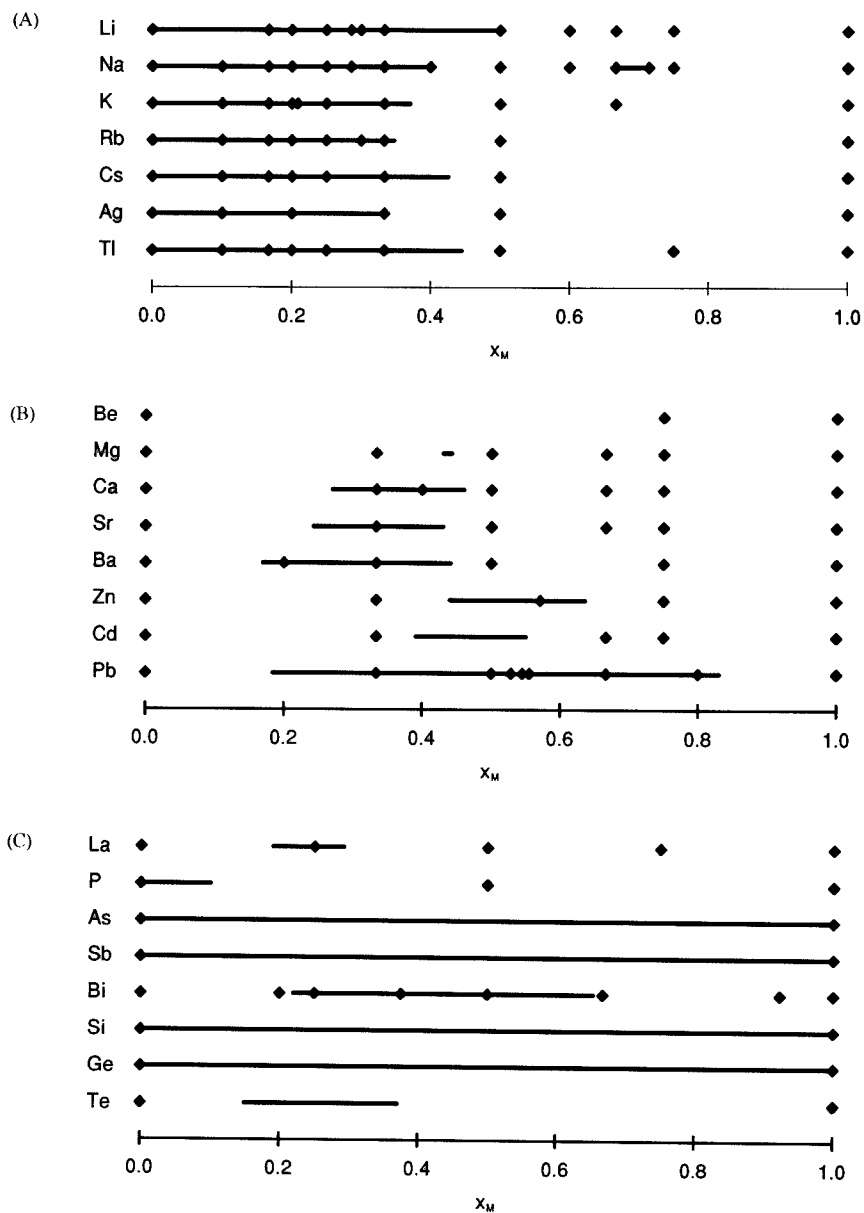


Fig. 1. Conventional glass-forming regions (—) for binary borate systems, together with the corresponding crystalline polymorphs ( $\diamond$ ). (A),  $M_2O-B_2O_3$ ; (B),  $MO-B_2O_3$  and (C), systems containing a rare earth oxide or (conditional) glass former.

second component is either a rare earth ( $\text{La}_2\text{O}_3$ ) or a (conditional) glass-forming oxide. Before discussing the relationship between the glass-forming regions and crystalline polymorphs in Fig. 1, however, it is first necessary to summarise the structural model of borate glasses which has evolved from the early studies of Krogh-Moe and Bray [8].

### 3. BORATE NETWORK STRUCTURES

#### 3.1. Boron Atom Co-ordination Number

For conventional silicate glasses, the various constituents are normally classified as either *network formers* or *network modifiers*, although some materials are intermediate in character and may change their role depending on the composition and/or the other constituents present. The network formers contribute to the basic three dimensional network, whereas the network modifiers are *network breakers*, leading to the formation of non-bridging oxygen atoms. The addition of a network modifier to  $\text{B}_2\text{O}_3$ , on the other hand, initially results mainly in the conversion of  $\text{BO}_3$  triangles into  $\text{BO}_4$  tetrahedra; i.e. it acts as a *network strengthener* via an increase in the B(O) co-ordination number,  $n_{\text{B(O)}}$ , from 3 to 4. In the absence of non-bridging oxygen atoms, the fraction of 4-fold co-ordinated boron atoms,  $x_4$ , is given by [9]

$$x_4 = x_M / (1 - x_M) = m/n, \quad (1)$$

where  $x_M$  is the mole fraction of the modifying oxide and  $m$  and  $n$  refer to the crystalline compound with the general formula given in Section 1. Almost all crystalline structures with  $x_M < 0.5$  have this value of  $x_4$  ( $\alpha\text{-Na}_2\text{B}$  [10] is a notable exception), which indicates that the

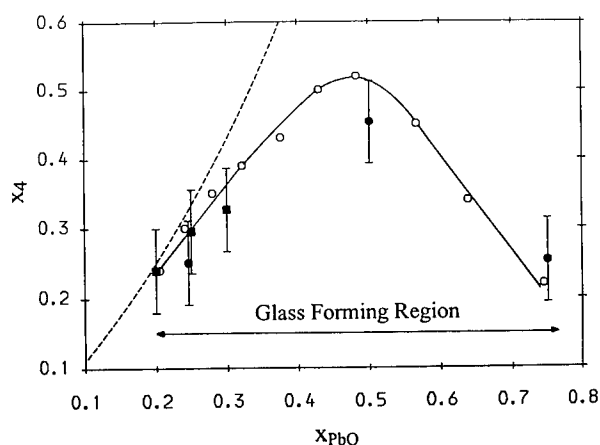


Fig. 2. The fraction of 4-fold co-ordinated boron atoms in  $\text{PbO-B}_2\text{O}_3$  glasses, as a function of composition [12]. Open circles, NMR spectroscopy [13]; closed circles, neutron diffraction and closed squares, thermodynamic prediction [14]. The dashed line denotes Eq. (1) and the glass-forming region [3] is indicated by the horizontal bar. For clarity, the errors on the NMR data are not shown, but range from  $\pm 0.06$  to  $\pm 0.13$ .

conversion of  $\text{BO}_3$  triangles into  $\text{BO}_4$  tetrahedra is energetically more favourable than the breaking of B–O–B bridges to form non-bridging oxygen atoms, but the rich variety of borate structural chemistry is due to the proximity of these two formation energies and, in the glass, extra degrees of freedom can be generated by the formation of non-bridging oxygen atoms. As the modifier concentration increases,  $x_4$  first increases, then passes through a maximum and finally decreases, as may be seen from NMR data (e.g. Figs 1 and 2 of Ref. [11]) and for the  $\text{PbO-B}_2\text{O}_3$  system in Fig. 2.

The classification of components into network formers and network modifiers arises from the fact that the nature of the bonding is different around the two types of cation. The network modifying cations are in general more ionic in character. The negative charge on the  $\text{BO}_4$  tetrahedra means that, in systems containing network modifying cations with a high degree of ionic character, non-bridging oxygen atoms will tend to be confined to the  $\text{BO}_3$  triangles. However, there is insufficient evidence from crystallography to indicate whether non-bridging oxygen atoms will occur preferentially on  $\text{B}^{(3)}$  atoms in superstructural units or on those present as independent  $\text{BO}_3$  triangles. (The  $\alpha\text{-Na}_2\text{B}$  structure [10] contains only superstructural units and no independent  $\text{BO}_3$  triangles.)

### 3.2. Superstructural Units

Following the publication of Zachariasen's paper [2], controversy immediately arose with that of Hägg [15], which postulated the existence in glasses of groupings larger than the basic structural units. More recently, support for Hägg's ideas has come first from the work of Krogh-Moe [16] and then that of Bray and co-workers [17,18], who emphasise the important role of *superstructural units* (Fig. 3) in vitreous borate networks. Superstructural units, which comprise well defined arrangements of the basic  $\text{BO}_3$  and  $\text{BO}_4$  structural units, with no internal degrees of freedom in the form of variable bond or torsion angles, are also found in the corresponding crystalline polymorphs and all of those shown in Fig. 3 have been found in at least one crystalline borate structure. An important reason for the occurrence of these units in borate glasses is the proximity of the equilibrium B–O–B bond angle to that required for planar 3-membered rings, which leads to a favourable formation energy.

In systems containing both  $\text{BO}_3$  and  $\text{BO}_4$  units, four different 3-membered rings are possible, as indicated in Fig. 3, and all four are found in the crystalline borates. The naming convention follows that of Krogh-Moe and, with the exception of the cyclic metaborate anion,  $\text{B}_3\text{O}_6^{3-}$ , refers to the composition which would result if a fully connected network with no non-bridging oxygen atoms contained only the superstructural unit in question. Thus the di-triborate group corresponds to the composition  $2\text{M}\cdot 3\text{B}$ , etc. Larger superstructural units are formed by combining two 3-membered rings by sharing either one (pentaborate series) or two (diborate)  $\text{BO}_4$  tetrahedra. Note that the so-called tetraborate group does not qualify as a superstructural unit since it comprises a triborate and a pentaborate group joined by a single bridging oxygen atom with variable bond and torsion angles.

Irrefutable evidence for the existence of superstructural units in borate glasses is provided by optical spectroscopy; for example the boroxol and triborate groups yield sharp lines in the Raman spectrum at 808 and 770  $\text{cm}^{-1}$ , respectively [19]. More quantitative information is provided by NMR studies [17,18] and potentially from inelastic neutron scattering measurements [20]. In diffraction studies, superstructural units lead to sharp features in the real space correlation function

at higher interatomic distances,  $r$ , than found within the basic structural units and hence, to identify these features, it is necessary to have good real space resolution by making measurements in reciprocal space to high magnitudes of the scattering vector,  $Q$ . The much lower incidence of superstructural units in molecular dynamics simulations suggests that they are present in real borate glasses in significantly greater numbers, as a result of a favourable formation energy, than might be expected on statistical grounds, given an equilibrium B—O—B bond angle of  $\sim 120$ – $130^\circ$ . Conversely, the good glass-forming ability of many borate systems may be linked to the need to break up and reform superstructural units during the crystallisation process, thus leading to a significant activation energy barrier, as in the case of vitreous  $B_2O_3$  (cf. Section 4).

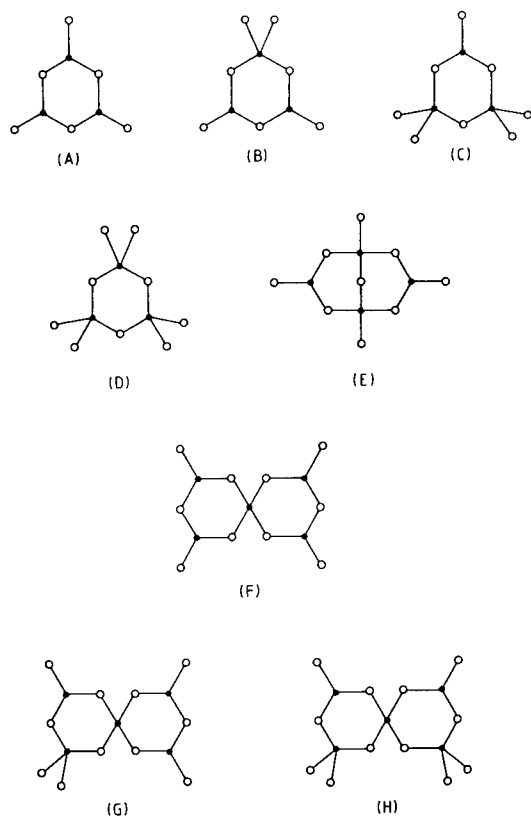


**Fig. 3.** Superstructural units occurring in anhydrous binary crystalline borates. (A) boroxol group,  $B_3O_6$ , or cyclic metaborate anion,  $B_3O_6^{3-}$ ; (B) triborate group,  $B_3O_7$ ; (C) di-triborate group,  $B_3O_8$ ; (D) metaborate group,  $B_3O_9$ ; (E) diborate group,  $B_4O_9$ ; (F) pentaborate group,  $B_5O_{10}$ ; (G) di-pentaborate group,  $B_5O_{11}$ , and (H) tri-pentaborate group,  $B_5O_{12}$ .

### 3.3. Krogh-Moe - Bray Model

The most generally accepted structural model for borate glasses, therefore, comprises a modified Zachariasen-Warren network in which the superstructural units are connected randomly to each other [8], together with the basic  $\text{BO}_3$  and  $\text{BO}_4$  structural units. The question thus arises as to how such units can be connected together topologically to achieve a disordered glass network with no broken bonds, except for non-bridging oxygen atoms, and what are the criteria for their interconnection. As will be demonstrated, much useful information concerning this question can be obtained by studying related crystalline structures.

## 4. VITREOUS BORON OXIDE

The structure of vitreous  $\text{B}_2\text{O}_3$  itself is the subject of considerable controversy in the literature, with regard to the structural role played by the  $\text{B}_3\text{O}_6$  boroxol group {Fig. 3(A)}. The stabilisation energy of the boroxol group, which comprises a 3-membered ring of  $\text{BO}_3$  triangles constrained to be planar by delocalised  $\pi$ -bonding, has been determined from Raman studies of the liquid to be  $6.4 \pm 0.4$  kcal/mol. [21], in good agreement with quantum chemistry calculations [22]. The existence of a stabilisation energy has, however, recently been disputed by Teter [23].

Currently, there are two main models of the structure of vitreous  $\text{B}_2\text{O}_3$ , the boroxol ring model, where the fraction,  $f$ , of boron atoms in boroxol groups is  $\sim 0.8$  [24,25], and the  $\text{BO}_3$  triangle model with  $f \leq 0.1$  [26,27]. The ambient pressure crystalline polymorph,  $\text{B}_2\text{O}_3$ -I [28], does not contain boroxol groups, but is formed from planar ribbons of  $\text{BO}_3$  triangles. However, there are various indications that the structure of vitreous  $\text{B}_2\text{O}_3$  is very different from that of  $\text{B}_2\text{O}_3$ -I. For example, the density of  $\text{B}_2\text{O}_3$ -I is very much (41% [24]) higher than that of the glass and, in addition, a crystal of  $\text{B}_2\text{O}_3$ -I seeded into the anhydrous supercooled melt does not grow, even over a period of several months [29], indicating an extremely high activation energy for crystallisation.

The problem with the  $\text{BO}_3$  triangle model, and in particular the model of Chason and Spaepen [26] which is based on planar ribbons of  $\text{BO}_3$  triangles similar to those found in  $\text{B}_2\text{O}_3$ -I, is that it fails to account for the large density difference between  $\text{B}_2\text{O}_3$ -I and the glass and the lack of crystallisation from the supercooled melt. In addition, to explain a sharp peak at  $3.6\text{\AA}$  in the real space correlation function (See later, Fig. 6), it is necessary for a large fraction of the  $\text{BO}_3$  triangles to be constrained to be approximately coplanar and there is no mechanism for this in the vitreous state. Note that, with inadequate numbers of boroxol groups, the reverse Monte Carlo technique [27] is likely to constrain adjacent  $\text{BO}_3$  triangles to be coplanar in order to reproduce the sharpness of this peak, although the resulting structures will almost certainly be unstable to relaxation with a realistic potential or else occupy too small a region of configuration space to be experimentally accessible by conventional melt quenching.

A detailed analysis of neutron diffraction data for vitreous  $\text{B}_2\text{O}_3$  yields a value for  $f$  of  $0.80 \pm 0.05$  [25], in excellent agreement with NMR data [30] which give  $f = 0.82 \pm 0.08$ . According to the boroxol model, the structure of vitreous  $\text{B}_2\text{O}_3$  may thus be envisaged as a mixed random network of two corner sharing triangular units, one twice the size of the other, as illustrated schematically in two dimensions in Fig. 4, the presence of boroxol groups being inextricably linked to the density and other anomalous properties of vitreous  $\text{B}_2\text{O}_3$ . Further evidence for the boroxol ring model, which explains both the anomalously low density of vitreous  $\text{B}_2\text{O}_3$  and the



extremely high activation energy for crystallisation from the melt, has been summarised elsewhere [24,25] and will not be repeated here. It should be noted that one of the main objections to the boroxol ring model has been that it is extremely difficult to construct a random network model with a sufficiently high number density,  $\rho^\circ$ . However, the problem with all of the random network models of vitreous  $B_2O_3$  to date is that they have been constructed with the preconceived notion that the structure comprises a *single* network, rather than locally independent interpenetrating networks, as is almost certainly the case for the real material. (See discussion in Section 5 and Ref. [31].)

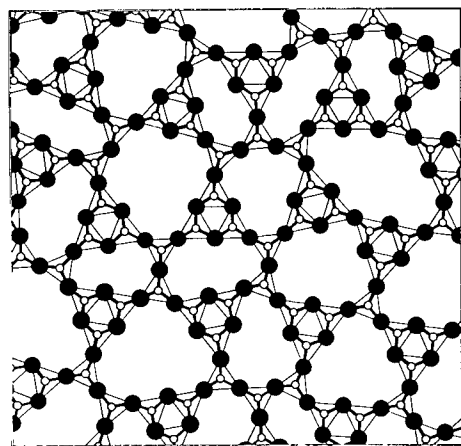


Fig. 4. A 2D representation of a mixed random network of boroxol groups and  $BO_3$  triangles. O, B and  $\bullet$ , O.

## 5. $M_2O$ - $B_2O_3$ SYSTEMS

The lack of crystallographic information for binary borate systems can be seen from the  $Na_2O$ - $B_2O_3$  system, where a full crystal structure determination has only been performed for 7 out of a total of 22 polymorphs listed in the Gmelin Handbook [6]. The superstructural units or borate anions occurring in these 7 polymorphs are summarised in Table 1, which shows the complexity of the crystalline borates in that the first four polymorphs all have structures that include more than one superstructural unit, even when a single superstructural unit would yield a borate network of the correct stoichiometry. Similarly, the various diborate structures also exhibit a wide range of superstructural units, as may be seen from Table 2. Note that, unlike many diborates,  $\alpha$ - $Na_2B$  does not contain the diborate group [10], although this is found in  $\alpha$ - $Na_3B$  [32] which conversely does not have any triborate groups. The fact that the crystalline compounds frequently involve a number of different superstructural units, even at the stoichiometric compositions, indicates that this is likely to be even more true for the corresponding glasses, as indicated by NMR data [17,18]. For the crystalline diborates included in Fig. 1, structures have not been

reported for Cs, Ag and Tl, while, in several non-glass-forming systems, other  $M^{2+}$  diborates exist as networks containing only diborate groups, including Mn, Fe, Co, Ni and Hg. The structures of vitreous Sr-2B and Pb-2B are unlikely to be similar to that of the corresponding crystalline polymorph, since the latter contains 3-fold co-ordinated oxygen atoms, which violate Zachariasen's [2] criteria for glass formation [12].

**Table 1**  
**Superstructural Units in Crystalline  $Na_2O-B_2O_3$  Polymorphs [31]**

Crystal	$B_5O_{10}$	$B_3O_7$	$B_5O_{11}$	$B_4O_9$	$BO_4$	$B_3O_6^{3-}$	$B_2O_5^{4-}$	$BO_3^{3-}$
$\alpha$ -Na-4B	0.5	0.5	-	-	-	-	-	-
$\alpha$ -Na-3B	0.5	-	-	0.5	-	-	-	-
$\beta$ -Na-3B	0.33	0.33	-	-	0.33	-	-	-
$\alpha$ -Na-2B	-	0.5*	0.5	-	-	-	-	-
$\alpha$ -Na-B	-	-	-	-	-	1.0	-	-
2Na-B	-	-	-	-	-	-	1.0	-
3Na-B	-	-	-	-	-	-	-	1.0

\* Has non-bridging oxygen atom on one B<sup>[3]</sup>.

Many crystalline polymorphs containing superstructural units exist as two independent, interpenetrating networks suggesting that, in the presence of significant numbers of superstructural units, the corresponding glasses are locally similar, in order to achieve a sufficiently high borate network density. As pointed out by Krogh-Moe [33], the bond angles and superstructural units of a single borate network do not in general permit efficient atom packing. Instead, a double network is formed so as to avoid a very open, low density structure. Alternatively, as in 5K-19B [34], a normal borate network density can be obtained by the incorporation of larger numbers of independent  $BO_3$  triangles and  $BO_4$  tetrahedra.

**Table 2**  
**Superstructural Units in Crystalline Diborates**

Diborate	$B_3O_7$	$B_5O_{11}$	$B_4O_9$	$B_3O_8$	$BO_3$	$BO_4$	$\langle n_{4(4)} \rangle$
Li,Mg,Zn,Cd	-	-	1.0	-	-	-	1.0
Na	0.5*	0.5	-	-	-	-	0.67
K,Rb	-	-	0.33	0.33	0.33	-	1.0
Ca	0.33	-	0.33	-	-	0.33	1.5
Sr,Pb	-	-	-	-	-	1.0**	-
Ba	-	0.5	-	0.5	-	-	1.5

\* Has non-bridging oxygen atom on one B<sup>[3]</sup>.

\*\* Has 3-fold co-ordinated O atoms.

### 5.1. Bridging Oxygen Atoms

The repulsion between negatively charged  $\text{BO}_4$  tetrahedra means that  $\text{B}^{[4]}-\text{O}-\text{B}^{[4]}$  bridges not within a superstructural unit are energetically unfavourable. Hence, only  $\text{B}^{[3]}-\text{O}-\text{B}^{[3]}$  and  $\text{B}^{[3]}-\text{O}-\text{B}^{[4]}$  bridges are found outside superstructural units in the crystalline state until  $\text{B}^{[4]}-\text{O}-\text{B}^{[4]}$  bridges are unavoidable, which occurs at  $x_M = 0.3$  if there are also none within superstructural units. Note, however, that  $\text{B}^{[4]}-\text{O}-\text{B}^{[4]}$  bridges are found *within* superstructural units for  $x_M < 0.3$  (e.g. in the diborate unit of the  $\alpha\text{-Na}_2\text{B}_2\text{O}_5$  structure - cf. Table 1), presumably as a result of a favourable superstructural unit formation energy. The relative numbers of  $\text{B}^{[i]}-\text{O}-\text{B}^{[j]}$  bridges may be expressed in terms of the co-ordination numbers of  $\text{BO}_i$  around  $\text{BO}_j$  units,  $n_{ij}$ . Thus, for  $x_M \leq 0.3$  and no  $\text{B}^{[4]}-\text{O}-\text{B}^{[4]}$  bridges (i.e.  $n_{4(3)} = 4$  and  $n_{4(4)} = 0$ ),

$$n_{3(3)} = (3 - 10x_M) / (1 - 2x_M) \quad (2)$$

and

$$n_{3(4)} = 4x_M / (1 - 2x_M) \quad (3)$$

while, for  $0.3 \leq x_M \leq 0.5$  and the minimum number of  $\text{B}^{[4]}-\text{O}-\text{B}^{[4]}$  bridges required by the composition (i.e. no  $\text{B}^{[3]}-\text{O}-\text{B}^{[3]}$  bridges;  $n_{3(3)} = 0$  and  $n_{3(4)} = 3$ ),

$$n_{4(3)} = 3(1 - 2x_M) / x_M \quad (4)$$

and

$$n_{4(4)} = (10x_M - 3) / x_M \quad (5)$$

It should be emphasised that Eqs (2-5) refer to the case when there are no non-bridging oxygen atoms present, as in the vast majority of crystalline polymorphs with  $x_M < 0.5$ . At the diborate composition ( $x_M = 1/3$ ),  $n_{4(4)} = 1$ , which is consistent with a network of diborate groups linked only by  $\text{B}^{[3]}-\text{O}-\text{B}^{[4]}$  bridges, as found in the most common diborate structure ( $\text{Li}_2\text{B}_2\text{O}_5$ , etc. - cf. Table 2). The  $\text{Ca}_2\text{B}_2\text{O}_5$  and  $\text{Ba}_2\text{B}_2\text{O}_5$  structures, on the other hand, have a  $\text{B}^{[3]}-\text{O}-\text{B}^{[3]}$  bridge within a superstructural unit (triborate and di-pentaborate, respectively) and an average value for  $n_{4(4)}$  of 1.5, suggesting that the superstructural unit stabilisation energies more than compensate for the increased energy due to the extra  $\text{B}^{[4]}-\text{O}-\text{B}^{[4]}$  bridges. Note that the di-pentaborate composition ( $x_M = 2/7 = 0.286$ ) does not require the presence of  $\text{B}^{[4]}-\text{O}-\text{B}^{[4]}$  bridges, which may explain why no crystalline polymorphs exist with networks comprising only di-pentaborate units. On the other hand, the presence of the diborate group in crystal structures with  $x_M < 0.3$  (e.g.  $\alpha\text{-Na}_2\text{B}_2\text{O}_5$ ) and its common occurrence, both in borate glasses and as the only superstructural unit in many crystalline diborates, suggests a particularly favourable formation energy.

In the vitreous state, the number of  $\text{B}^{[4]}-\text{O}-\text{B}^{[4]}$  bridges may exceed the minimum number required by the composition, in order to attain the degrees of topological freedom necessary for the formation of an experimentally accessible vitreous network. However, it is extremely interesting to note that the  $x_4$  curves for the alkali borate (Figs 1 and 2 of Ref. [11]) and lead borate glass systems start to deviate significantly from Eq. (1) very close to the composition where

$\text{B}^{(4)}\text{--O--B}^{(4)}$  bridges become unavoidable ( $x_M = 0.3$ ), suggesting that the formation of non-bridging oxygen atoms is energetically more favourable than adjacent  $\text{BO}_4$  tetrahedra. Assuming that the charge on a  $\text{BO}_4$  tetrahedron is mainly located on the boron atom, this can be understood in terms of the increased separation of the negative charges for a  $\text{BO}_3$  triangle with a non-bridging oxygen atom adjacent to a  $\text{BO}_4$  tetrahedron (i.e.  $\text{B}^-\text{--O--B--O}^-$  compared to  $\text{B}^-\text{--O--B}^-$ ), especially since the negative charge on a  $\text{BO}_4$  tetrahedron is likely to be more delocalised over the whole structural unit than that from a non-bridging oxygen atom on a  $\text{BO}_3$  triangle. A similar explanation may be put forward for the presence of the non-bridging oxygen atom on one of the  $\text{BO}_3$  triangles of the triborate group in the  $\alpha\text{-Na-2B}$  crystalline structure and hence its reduced value of  $n_{4(4)}$ .

## 5.2. Model for $x_4$ in Glasses

In the case of network modifying cations with predominantly ionic bonding, the arguments of the previous paragraph may be extended to yield a first order model for the variation of  $x_4$  with composition in the vitreous state, based on the following three assumptions:

- (i) The borate network contains the maximum number of  $\text{BO}_4$  tetrahedra ( $\text{B}\varnothing_4^-$  units, where  $\varnothing$  represents a bridging oxygen atom) consistent with assumptions (ii) and (iii). As discussed in Section 3.1, the formation of a  $\text{B}\varnothing_4^-$  unit in a network of  $\text{BO}_3$  triangles ( $\text{B}\varnothing_3$  units) is energetically more favourable than the generation of a  $\text{BO}_3$  triangle with a non-bridging oxygen atom ( $\text{B}\varnothing_2\text{O}^-$  unit).
- (ii) There are no  $\text{B}^{(4)}\text{--O--B}^{(4)}$  bridges (neighbouring  $\text{B}\varnothing_4^-$  units).
- (iii) There are no  $\text{BO}_4$  tetrahedra with non-bridging oxygen atoms; i.e. the addition of a non-bridging oxygen atom to a  $\text{B}\varnothing_4^-$  unit, results in its conversion to a  $\text{B}\varnothing\text{O}_2^{2-}$  unit.

The predictions of this simple model are compared to NMR data for the  $\text{Li}_2\text{O--B}_2\text{O}_3$  system [11] in Fig. 5, the model being denoted by the solid line. For  $x_M \leq 0.3$  (region A in Fig. 5), only  $\text{B}\varnothing_3$  and  $\text{B}\varnothing_4^-$  units are present and  $x_4$  is given by Eq. (1), which represents the maximum  $x_4$  possible for a network of corner-sharing  $\text{BO}_3$  triangles and  $\text{BO}_4$  tetrahedra with no oxygen atoms having a co-ordination number greater than 2. The composition  $x_M = 0.3$  corresponds to a network of alternating  $\text{B}\varnothing_3$  and  $\text{B}\varnothing_4^-$  units and hence the addition of further network modifier leads to the formation of  $\text{B}\varnothing_2\text{O}^-$  units. Thus, in region B, the network involves  $\text{B}\varnothing_3$ ,  $\text{B}\varnothing_4^-$  and  $\text{B}\varnothing_2\text{O}^-$  units until  $x_M = 0.5$ , where the network consists of alternating  $\text{B}\varnothing_4^-$  and  $\text{B}\varnothing_2\text{O}^-$  units. Similarly  $\text{B}\varnothing_4^-$ ,  $\text{B}\varnothing_2\text{O}^-$  and  $\text{B}\varnothing\text{O}_2^{2-}$  units are present in region C, which terminates at  $x_M = 9/14$  (0.643) with a structure comprising  $[\text{B}(\varnothing\text{BO}_2)_4]^{9-}$  anions. Finally, in region D, there is a mixture of  $[\text{B}(\varnothing\text{BO}_2)_4]^{9-}$  and  $\text{BO}_3^{3-}$  anions and  $x_4$  becomes zero at the orthoborate composition (only  $\text{BO}_3^{3-}$  anions;  $x_M = 0.75$ ). Throughout regions B to D,  $x_4$  is given by

$$x_4 = (3 - 4x_M) / [6(1 - x_M)]. \quad (6)$$

The short-dashed line in Fig. 5 denotes an alternative *scenario* for region D, in which  $\text{BO}_3^{3-}$  anions are not formed but the structure comprises a mixture of  $[\text{B}(\text{OBO}_2)_4]^{9-}$  and  $\text{B}_2\text{O}_4^{4-}$  (pyroborate) anions. In this case, the value of  $x_4$  decays to zero at  $x_M = 2/3$  (pyroborate composition), according to the relationship

$$x_4 = (2 - 3x_M) / (1 - x_M). \quad (7)$$

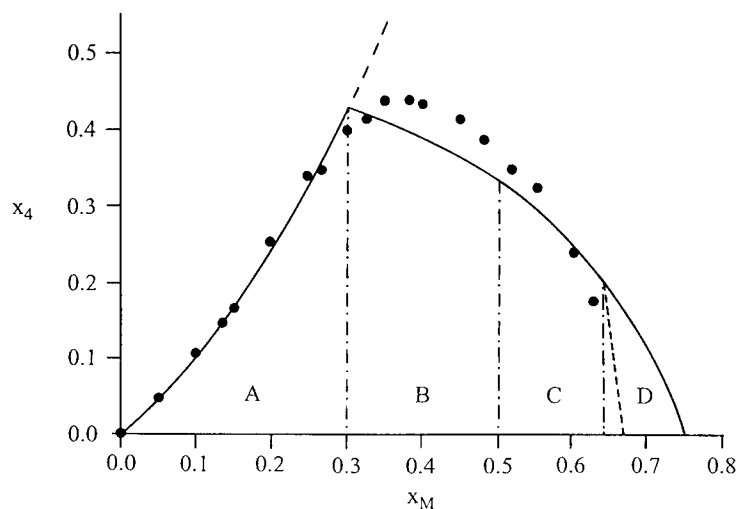


Fig. 5. The fraction of 4-fold co-ordinated boron atoms in lithium borate glasses. Closed circles, NMR data [11]; solid line, present model and dashed line, continuation of Eq. (1). The short-dashed line is discussed in the text, together with the units occurring in each of the regions A to D.

The NMR data in Fig. 5 deviate from the model and follow a smooth curve, without the discontinuity at  $x_M = 0.3$ . The deviations may be explained, as follows: First, it should be realised that a perfect network of alternating  $\text{B}\text{O}_4^-$  and  $\text{B}\text{O}_3$  units (i.e. only even membered rings of  $\text{BO}_n$  units) represents an extremely small region of configuration space and so will not be accessible to a vitreous network using conventional quenching techniques (cf. the discussion of the III-V analogues of  $\text{SiO}_2$  in Section 7). Thus a real network will contain some odd membered rings, which can only avoid  $\text{B}^{(4)}\text{--O--B}^{(4)}$  bridges by incorporating a  $\text{B}\text{O}_2\text{O}^-$  unit, and hence  $x_4$  for the NMR data falls below the value predicted by Eq. (1), as  $x_M$  approaches 0.3. Conversely, some  $\text{B}^{(4)}\text{--O--B}^{(4)}$  bridges are likely to be present *within* superstructural units, which indeed are *based on* odd-membered (i.e. 3-membered) rings, particularly above and just below the diborate

composition ( $x_M = 1/3$ ). This will tend to increase  $x_4$  and explains why  $x_4$  for the NMR data exceeds the model value between  $x_M \sim 0.35$  and  $x_M \sim 0.55$ . Finally, in region D, the alternative pyroborate anion model (short-dashed line) yields a better fit to the experimental data, which seem to approach zero close to the pyroborate composition ( $x_M = 2/3$ ). For the other alkali borate glass systems, it should be noted that the NMR data of Zhong and Bray [35] indicate that, in the region  $0.14 \leq x_M \leq 0.45$ , the value of  $x_4$  falls progressively further below that for the  $\text{Li}_2\text{O}-\text{B}_2\text{O}_3$  system with increasing alkali atomic number and hence the agreement with this simple model will vary as a function of both the alkali cation and  $x_M$ .

### 5.3. Stereochemical Considerations

In addition to the stabilisation energy, there are also stereochemical considerations which influence the detailed distribution of superstructural units in a given glass. The importance of achieving a sufficiently high borate network density has already been discussed in respect of the need for locally independent, interpenetrating networks in glasses with large concentrations of superstructural units but, even under these circumstances, some independent  $\text{BO}_3$  triangles and/or  $\text{BO}_4$  tetrahedra are almost certainly necessary to ensure more efficient packing and the necessary degrees of freedom for glass formation. In the absence of such units, excessive network strain and/or numbers of broken bonds would be likely to be "frozen in" on passing through the glass transition region and would be reflected in a relatively high heat of crystallisation. However, the heats of crystallisation of binary borate glasses are typically in the range  $\sim 2\text{-}4$  kcal/mole [36], indicating the absence of excessive network or (super)structural unit deformation relative to the crystalline state.

Table 3  
Na<sup>+</sup> ion co-ordination in Crystalline  $\text{Na}_2\text{O}-\text{B}_2\text{O}_3$  Polymorphs [31]

Crystal	4	5	6	7	8
$\alpha$ -Na-4B	-	-	-	-	1.0
$\alpha$ -Na-3B	-	0.33	0.67	-	-
$\beta$ -Na-3B	-	-	0.33	0.33	0.33
$\alpha$ -Na-2B	-	-	0.75	0.25	-
$\alpha$ -Na-B	-	-	-	1.0	-
2Na-B	-	0.5	0.5	-	-
3Na-B	0.33	0.67	-	-	-

Another important stereochemical parameter is the effective radius of the network modifying cations, which will depend on the degree of ionicity in their bonding. Simple radius ratio considerations mean that, in the melt and during vitrification or crystallisation, the network modifying cations will attempt to restructure their local environments in order to achieve their optimum first co-ordination shell. This determines the size of the cavities in the borate network in which these ions reside and hence influences the borate network density. However, it is characteristic of borate crystal structures that the co-ordination number,  $n_{M(O)}$ , of a given network

modifying cation varies for different crystalline polymorphs and frequently between different sites in the same structure, as may be seen for the  $\text{Na}^+$  ion from Table 3. Similarly, the oxygen polyhedra surrounding the network modifying cations are often considerably distorted, with a wide range of cation - oxygen distances. Krogh-Moe [37] ascribes this to the effect of the rigid superstructural units and hence similar distorted network modifying cation polyhedra will exist in the vitreous state. In addition, the lack of periodicity in the latter will lead to a considerable variation in the network modifying cation environment, both in terms of the distortion and coordination number.

## 6. $\text{MO-B}_2\text{O}_3$ SYSTEMS

The lack of single phase glass formation for the  $\text{MO-B}_2\text{O}_3$  systems at low modifier contents is extremely interesting and may be connected with the fact that two  $\text{BO}_4$  tetrahedra are required in close proximity to balance the charge on a  $\text{M}^{2+}$  ion. This is supported by the lack (Be) or very small range (Mg) of glass formation for the smallest modifying cations. Conversely, glasses are formed at the lowest modifier contents for the largest and most easily polarised cations (Ba and Pb), the lowest of all being for Ba, which is the only system for which a crystalline tetraborate has been reported {Fig. 1(B)}.

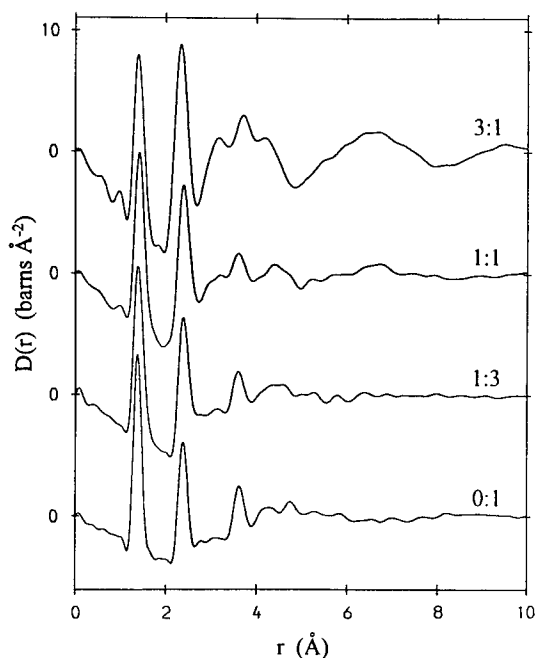


Fig. 6. Differential correlation functions,  $D(r)$ , for a series of glasses in the system  $\text{PbO-B}_2\text{O}_3$ , normalised to a composition unit  $x\text{PbO-B}_2\text{O}_3$  [12]. The nominal glass compositions are indicated as  $m:n$  (i.e.  $m\text{PbO}.n\text{B}_2\text{O}_3$ ), 0:1 being pure vitreous  $\text{B}_2\text{O}_3$ .

The situation where the second oxide has considerable intermediate character and can behave as a network forming oxide, at least at high concentrations, is more complicated, as may be seen from the crystal structure of 6Pb·5B [38] ( $x_M = 0.545$ ), which has the largest isolated borate anion found to date, consisting of two diborate groups connected together by a chain of two  $\text{BO}_3$  triangles. This includes a terminating  $\text{B}^{(4)}\text{--O}$  bond (i.e. a non-bridging oxygen atom in the ionic modifier approximation) on each diborate group, but examination of the Pb–O bonding reveals the presence of considerable covalent character. It is therefore likely that similar groupings or superstructural units also occur in lead borate glasses at high PbO concentrations, as demonstrated by the differential correlation functions,  $D(r)$ , for a series of lead borate glasses in Fig. 6 [12]. With increasing PbO content, the well-defined superstructural unit (boroxol group) peak for vitreous  $\text{B}_2\text{O}_3$  at  $3.6\text{\AA}$  is reduced in intensity, slightly broadened and shifted to higher  $r$ , due to the presence of superstructural units with three-membered rings containing one or more  $\text{BO}_4$  tetrahedra, but a well defined feature remains in the correlation function up to the highest PbO content ( $x_M = 0.75$ ), suggesting significant numbers of superstructural units. In addition, the fact that  $x_4$  is non-zero at  $x_M = 0.75$  (Fig. 2) means that, at this composition, there must be  $\text{BO}_4$  tetrahedra present with non-bridging oxygen atoms and that the simple ionic modifier model of Section 5.2 does not apply.

## 7. $\text{M}_2\text{O}_3\text{--B}_2\text{O}_3$ , $\text{B}_2\text{O}_3\text{--MO}_2$ AND $\text{B}_2\text{O}_3\text{--M}_2\text{O}_5$ SYSTEMS

With the exception of the  $\text{Bi}_2\text{O}_3\text{--B}_2\text{O}_3$  system, there are very few binary crystalline polymorphs for the systems comprising  $\text{B}_2\text{O}_3$  and another glass-former, or that involving the conditional glass-former  $\text{TeO}_2$  {Fig. 1(C)}, and it is particularly interesting to note that none occur in the technologically important  $\text{B}_2\text{O}_3\text{--SiO}_2$  system or its  $\text{GeO}_2$  analogue. Crystal structures have been determined for 3 of the 5 binary  $\text{Bi}_2\text{O}_3\text{--B}_2\text{O}_3$  polymorphs in Fig. 1(C). The structure of Bi·3B has layers of alternating  $\text{B}\phi_4^-$  and  $\text{B}\phi_2\text{O}^-$  units (cf. glass model of Section 5 at  $x_M = 0.5$ ), while 3Bi·5B contains  $\text{B}_5\phi_6\text{O}_5^{7-}$  anions (di-pentaborate groups with all terminal oxygen atoms non-bridging) and 2Bi·B has isolated  $\text{BO}_3^{3-}$  units.

The compound  $\text{BPO}_4$  is a III-V analogue of  $\text{SiO}_2$ , having crystalline polymorphs with both quartz and cristobalite structures, but, as discussed elsewhere [39], the requirement of a network with only even membered rings of alternating  $\text{BO}_4$  and  $\text{PO}_4$  tetrahedra means that the region of configuration space available for glass formation at this composition is very small and experimentally inaccessible by conventional melt quenching techniques. The compound  $\text{BAsO}_4$  ( $\text{B}_2\text{O}_3\text{--As}_2\text{O}_5$  system), which also has both quartz and cristobalite polymorphs, does however form a glass, as does  $\text{BVO}_4$  ( $\text{B}_2\text{O}_3\text{--V}_2\text{O}_5$  system), but in both cases the boron atoms are present as  $\text{BO}_3$  triangles [40] and hence the network is not restricted to even membered rings.

## 8. CONCLUSIONS

From the preceding sections, it is apparent that a study of the appropriate crystal structures can yield considerable insight into the structures of borate glasses, provided suitable allowance is made for the extra degrees of network freedom necessary for glass formation. However, the information which can be inferred is limited by the fact that many crystalline borate polymorphs



either have unknown structures or have merely been established to be isostructural with another compound, without detailed structural parameters such as bond lengths and angles being determined. Hence there is a great need for further crystallographic studies of borate systems.

A number of criteria have been discussed relevant to the formation of vitreous borates containing superstructural units and used to further refine a structural model proposed by Bray [8]. As in the case of Zachariasen's criteria for glass formation, these criteria should not be taken as hard and fast rules, but rather as general guidelines. The fact that a given feature does not occur in the crystalline state should not be taken to infer that it does not occur in the glass, but that it is energetically unfavourable and hence will be likely to occur with a low probability. As with crystalline defects, a small concentration of an unfavourable configuration may be desirable for entropic reasons.

#### Acknowledgement

The authors would like to thank R.L. Snyder for his help in searching various crystallographic databases and G.D. Chryssikos for helpful discussions concerning the structures of the crystalline diborates.

#### REFERENCES

- [1] *Borate Glasses, Crystals and Melts*, Eds A.C. Wright, S.A. Feller and A.C. Hannon (Soc. Glass Technol., Sheffield, 1997), in press.
- [2] W.H. Zachariasen, *J. Amer. Chem. Soc.* **54** (1932), 3841.
- [3] H. Rawson, *Inorganic glass-forming systems* (Academic Press, London, 1967).
- [4] O.V. Mazurin, M.V. Streltsina and T.P. Shvaiko-Shvaikovskaya, *Svoistva Steklo i Stekloobrazuyushchikh Rasplavov (The properties of Glasses and Glass-Forming Systems)*, Vol. 2 (Nauka, Leningrad, 1975) and Vol. 4, Part 1 (1980).
- [5] A.C. Wright, N.M. Vedishcheva and B.A. Shakhmatkin, in: *Borate Glasses, Crystals and Melts*, Eds A.C. Wright, S.A. Feller and A.C. Hannon (Soc. Glass Technol., Sheffield, 1997), in press.
- [6] G. Heller, *Gmelin Handbuch der Anorganischen Chemie*, Vol. 28, *Borverbindungen Part 7* (Springer-Verlag, Berlin, 1975).
- [7] J.E. Shelby, *J. Non-Cryst. Solids* **49** (1982), 287.
- [8] P.J. Bray, *J. Non-Cryst. Solids* **75** (1985), 29.
- [9] J. Krogh-Moe, *Phys. Chem. Glasses* **3** (1962), 1.
- [10] J. Krogh-Moe, *Acta Crystallogr.* **B30** (1974), 578.
- [11] G.E. Jellison Jr., S.A. Feller and P.J. Bray, *Phys. Chem. Glasses* **19** (1978), 52.
- [12] N.M. Vedishcheva, B.A. Shakhmatkin, A.C. Wright, D.I. Grimley, G. Etherington and R.N. Sinclair, in: *Fundamentals of Glass Science and Technology* (ESG, Venice, 1993) p. 459.
- [13] P.J. Bray, M. Leventhal and H.O. Hooper, *Phys. Chem. Glasses* **4** (1963), 47.
- [14] N.M. Vedishcheva, B.A. Shakhmatkin, A.C. Wright, R.N. Sinclair and D.I. Grimley, *Bol. Soc. Esp. Ceram. Vid.* **31-C**, **3** (1992), 41.
- [15] G. Hägg, *J. Chem. Phys.* **3** (1935), 42.
- [16] J. Krogh-Moe, *Phys. Chem. Glasses* **6** (1965), 46.
- [17] G.E. Jellison Jr. and P.J. Bray, *J. Non-Cryst. Solids* **29** (1978), 187.
- [18] S.A. Feller, W.J. Dell and P.J. Bray, *J. Non-Cryst. Solids* **51** (1982), 21.
- [19] B.N. Meera and J. Ramakrishna, *J. Non-Cryst. Solids* **159** (1993), 1.

- [20] R.N. Sinclair, A.C. Wright, A.J. Wanless, A.C. Hannon, S.A. Feller, M.T. Mayhew, B.M. Meyer, M.L. Royle, D.L. Wilkerson, R.B. Willaims and B.C. Johanson, in: *Borate Glasses, Crystals and Melts*, Eds A.C. Wright, S.A. Feller and A.C. Hannon (Soc. Glass Technol., Sheffield, 1997), in press.
- [21] G.E. Walrafen, S.R. Samanta and P.N. Krishnan, *J. Chem. Phys.* **72** (1980), 113.
- [22] L.C. Snyder, *Bull. Amer. Ceram. Soc.* **57** (1978), 825.
- [23] M.P. Teter, in: *Borate Glasses, Crystals and Melts*, Eds A.C. Wright, S.A. Feller and A.C. Hannon (Soc. Glass Technol., Sheffield, 1997), in press.
- [24] P.A.V. Johnson, A.C. Wright and R.N. Sinclair, *J. Non-Cryst. Solids* **50** (1982), 281.
- [25] A.C. Hannon, D.I. Grimley, R.A. Hulme, A.C. Wright and R.N. Sinclair, *J. Non-Cryst. Solids* **177** (1994), 299.
- [26] E. Chason and F. Spaepen, *J. Appl. Phys.* **64** (1988), 4435.
- [27] J. Swenson and L. Börjesson, in: *Borate Glasses, Crystals and Melts*, Eds A.C. Wright, S.A. Feller and A.C. Hannon (Soc. Glass Technol., Sheffield, 1997), in press.
- [28] G.E. Gurr, P.W. Montgomery, C.D. Knutson and B.T. Gorres, *Acta Crystallogr.* **B26** (1970), 906.
- [29] F.C. Kracek, G.W. Morey and H.E. Merwin, *Amer. J. Sci.* **35A** (1938), 143.
- [30] G.E. Jellison Jr., L.W. Panek, P.J. Bray and G.B. Rouse Jr., *J. Chem. Phys.* **66** (1977), 802.
- [31] A.C. Wright, N.M. Vedishcheva and B.A. Shakhmatkin, *J. Non-Cryst. Solids* **192&193** (1995), 92.
- [32] J. Krogh-Moe, *Acta Crystallogr.* **B30** (1974), 747.
- [33] J. Krogh-Moe, *Acta Crystallogr.* **18** (1965), 77.
- [34] J. Krogh-Moe, *Acta Crystallogr.* **B30** (1974), 1827.
- [35] J. Zhong and P.J. Bray, *J. Non-Cryst. Solids* **111** (1989), 67.
- [36] M.M. Shultz, N.M. Vedishcheva and B.A. Shakhmatkin, in: *Fizika i Khimiya Silicatos (Physics and Chemistry of Silicates)*, Eds M.M. Shultz and R.G. Grebenshchikov (Nauka, Leningrad, 1987) p. 5.
- [37] J. Krogh-Moe, *Acta Crystallogr.* **B28** (1972), 168.
- [38] J. Krogh-Moe and P.S. Wold-Hansen, *Acta Crystallogr.* **B29** (1973), 2242.
- [39] A.C. Wright and J.A.E. Desa, *Phys. Chem. Glasses* **19** (1978), 140.
- [40] P. Beekenkamp and J.M. Stevels, *Phys. Chem. Glasses* **4** (1963), 229.

## GLASS FORMATION AND LOCAL TOPOLOGICAL INSTABILITY OF ATOMIC STRUCTURE

T. EGAMI

Department of Materials Science and Engineering, University of Pennsylvania, Philadelphia, PA  
19104-6272

### ABSTRACT

A direct connection between the local topology of the atomic structure of liquids and glasses and thermodynamic quantities through the atomic level stresses is suggested for metallic alloys. In particular the role of local topological instability in the phase transformations involving liquid and glass will be discussed. It is pointed out that a single local geometrical criterion can explain various phase transformations, such as melting, glass transition, and glass formation by solid state reaction and liquid quenching.

### 1. INTRODUCTION

One of the main difficulties in formulating theories of a glassy and liquid state is that it is not easy to describe the atomic structures of glasses and liquids with sufficient accuracy. In particular in order to elucidate subtle phenomena such as glass transition and structural relaxation one has to know the temperature dependence of the structure of the glass and liquid state, while even the proper choice of an order parameter is unclear. The purpose of this paper is to advance the view that the topological description of local atomic structure can be used as a basis for a statistical theory of metallic glasses and liquids, when it is used in conjunction with the idea of atomic level stresses.

Topological description of local atomic structure has been widely used in characterizing both the continuous random network (CRN) structure and the dense random packed (DRP) structure [1]. However it is usually not possible to find direct links between the topological parameters and thermodynamic quantities. On the other hand in metallic glasses such a link may be established by deploying the concept of atomic level stresses [2,3]. In this paper we review this connection, and discuss how it will lead to the local topological instability criterion recently proposed as a universal criterion for metallic glass formation that semi-quantitatively explains melting of crystalline metals, glass transition, solid state amorphization as well as glass formation by liquid quenching from an atomistic point of view [4,5].

### 2. DESCRIPTION OF THE LOCAL STRUCTURE

The basis for a topological description of the atomic structure is the definition of the atomic connectivity network. This can be done readily for covalently bonded solids such as oxide glasses, while for metallic solids the definition is less clear. However, the presence of a well defined first peak in the pair-density function (PDF) with a deep minimum before the second

peak is sufficient to define the atomic connectivity by metallic bonding. Once the topology of the structure is established local geometry has to be introduced in order to make a connection to the energy, since even for the same topology the energy is dependent on the local distortion of the structure. However, it is not easy to determine the local strain, since in order to define the strain a reference structure has to be defined. For crystalline structure the reference structure is of course the ideal perfectly periodic structure, while in glasses such a reference structure cannot be uniquely defined.

For this purpose we introduced the concept of the atomic level stress [2] which can be uniquely defined by,

$$\sigma^{\alpha,\beta}(i) = \frac{1}{\Omega_i} \sum_j f_{ij}^{\alpha} r_{ij}^{\beta} \quad (1)$$

where the  $j$ -th atom is a nearest neighbor of the  $i$ -th atom,  $f_{ij}^{\alpha}$  is the  $\alpha$  component of the two-body force, and  $r_{ij}^{\beta}$  is the  $\beta$ -component of the separation, between the  $i$ -th and  $j$ -th atoms, and  $\Omega_i$  is the local (Voronoi) volume of the  $i$ -th atom. Since the pair-wise force is roughly proportional to the deviation in the bond length from the ideal value, the local stress quite effectively and meaningfully describes the local distortion of the structure. Local strains at each atom can then be defined using elastic constants. There are six independent components of the stress tensor, namely a hydrostatic stress (pressure),  $p$ , and five shear stresses represented by the average (von Mises) stress,  $\tau$ . In terms of the spherical harmonics equivalents [3] they correspond to the  $\ell = 0$  (pressure) term and the  $\ell = 2$  (shear) terms. The potential energy due to local distortion can be expressed in the mean-field approximation in terms of the self-energy of these stress components as [3,6]

$$E = \frac{\Omega}{2B} \sum_i p_i^2 + \frac{5\Omega}{4G} \sum_i \tau_i^2 \quad (2)$$

where  $B$  is the bulk modulus,  $G$  is the shear modulus,  $\Omega$  is the local volume, and the local variation in  $B$ ,  $G$  and  $\Omega$  has been neglected. In the liquid state the thermal average of this potential energy is equal to  $(3/2)kT$  owing to the virial theorem. Thus each of the six components of the stress tensor obtains  $(1/4)kT$ ;

$$\frac{\Omega}{2B} \langle p_L^2 \rangle = \frac{\Omega}{4G} \langle \tau_L^2 \rangle = \frac{kT}{4} \quad (3)$$

This result has been checked by molecular dynamics simulation for a model iron and was shown to be surprisingly accurate for a high temperature liquid, in spite of numerous approximations involved in deriving it [6]. At low temperatures departures from this relationship is observed due to glass transition.

It has been shown that the pressure is related to the coordination number,  $N_c$  [3,7]. This is quite reasonable, since a small coordination number defines a small hole for an atom to fit in, then the atom to be fitted will be under compression. It can be shown that if an atom  $A$  with the

radius  $r_A$  is placed in the DRP structure of element B with the radius  $r_B$  the average coordination of A in equilibrium is given by [7,8]

$$N_c(A) = \frac{4\pi[1 - \sqrt{3}/2]}{1 - \sqrt{r_A(r_A + 2r_B)/(r_A + r_B)}} = \frac{4\pi[1 - \sqrt{3}/2]}{1 - \sqrt{x(x+2)/(x+1)}} \quad (4)$$

where  $x = r_A/r_B$ . This curve is given in Fig. 1. Here the metallic nature of the bond that allows the DRP structure is important. In covalent solids the value of  $N_c$  is chemically constrained, so that such a relation does not hold.

Now let us now try to place a B atom in a hole to which an A atom fits nicely. First the B atom has to be deformed to the size of an A atom. This is done by changing the B-B bond length,  $2r_B$ , to the A-B bond length,  $r_A + r_B$ . Then the volume strain is given by,

$$\epsilon^T = \left( \frac{r_A + r_B}{2r_B} \right)^3 - 1 \quad (5)$$

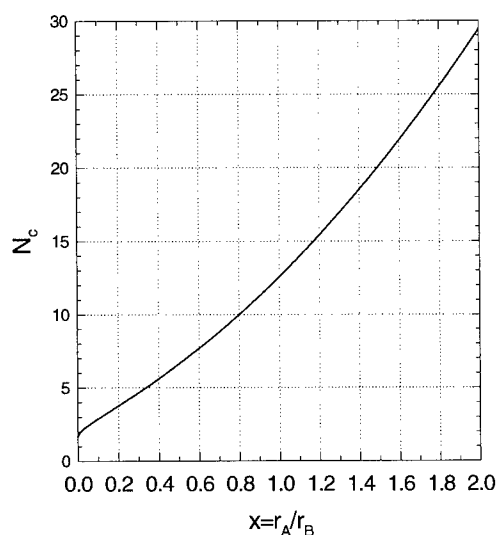


Fig. 1 Coordination number  $N_c$  of an A atom with the radius  $r_A$  embedded in the DRP structure of B with the radius  $r_B$  as a function of  $x = r_A/r_B$ .

In the case of a solid (glass) this local strain is relaxed by the B matrix being elastically deformed to accommodate the inserted atom. This is very much like the situation of an elastic body inserted in an elastic medium studied by Eshelby using continuum mechanics [9]. Using his result the local pressure is given by

$$p_s = \frac{2(1-2\nu)}{3(1-\nu)} B\epsilon^T \quad (6)$$

where  $\nu$  is the Poisson's ratio ( $=1/4$  for central force systems). However, in the high temperature liquid the atomic structure is rapidly changing with time, and the local stresses are quickly dissipated in time. Thus the matrix has no time to relax, so that the transient pressure at that moment is given by

$$p_L = B\epsilon^T \quad (7)$$

The difference between  $p_S$  (relaxed) and  $p_L$  (unrelaxed) has a major implication for the glass transition phenomenon as we discuss below.

By combining equations (4) through (7) the local pressure can be related to the local coordination number. By linearizing them with respect to  $\delta = r_A/r_B - 1$  and assuming  $v = 1/4$ , we obtain,

$$N_c = 4\pi \left[ 1 + \frac{2\sqrt{3}+3}{6} \delta + \dots \right] \quad (8)$$

$$\left( \frac{N_c}{4\pi} - 1 \right) = \frac{2\sqrt{3}+3}{9} \frac{p_L}{B} \quad (9)$$

Thus we can deduce the temperature dependence of the fluctuation in the coordination number in the liquid state;

$$\left\langle \left( \frac{N_c}{4\pi} - 1 \right)^2 \right\rangle = \left( \frac{2\sqrt{3}+3}{9} \right)^2 \frac{kT}{2\Omega B} \quad (10)$$

that shows that the thermal average of the square of the local deviations in the coordination number is proportional to temperature, scaled by a bulk modulus, which certainly is an intuitively reasonable result.

### 3. STABILITY OF LOCAL TOPOLOGY AND MELTING

Let us now imagine a gedanken experiment, or computer experiment, in which the value of  $r_A$  is continuously changed. The relation between the atomic size and the coordination described by eq. (4) (Fig. 1) suggests that as  $r_A$  is changed  $N_c$  must change, but since  $N_c$  is an integer the change has to be locally *discontinuous*. For instance, if we start with the value of  $r_A$  corresponding to  $N_c = 12$ ,  $r_A(N_c=12)$ , by the time  $r_A$  is increased to a value corresponding to  $N_c = 13$ ,  $r_A(N_c=13)$ , the local structure would be completely unstable, and if the supplies of thermal energy and other atoms are readily available, the local coordination will change from 12 to 13 by taking on another atom. Actually the crossover should occur earlier, with the change in  $r_A$  corresponding to the change in  $N_c$  by about  $1/2$ . This corresponds to the change in the value of  $x$  by

$$|\delta x_{crit}| = \frac{1}{2} \frac{\partial x}{\partial N_c} \Big|_{x=1} = 0.037 \quad (11)$$

that correspond to the volume strain of

$$|\epsilon_v| = \frac{3}{2} \delta x_{crit} = 0.0554 \quad (12)$$

This suggests that the structure should become unstable when the volume changes this much. Indeed most of the elemental metals melt at the volume expansion of about 6 - 8 % as shown in Fig. 2. This is a strong evidence that the critical condition (12) is approximately valid. In fact the condition (12) is probably an underestimate. The corresponding value of  $N_c$  should change by a little more than  $\frac{1}{2}$  for the structural change to occur, because such a transition is of the first order. For a more accurate estimate the presence of a surface and the need of nucleation have to be taken into account. At this moment we are making a very rough estimate.

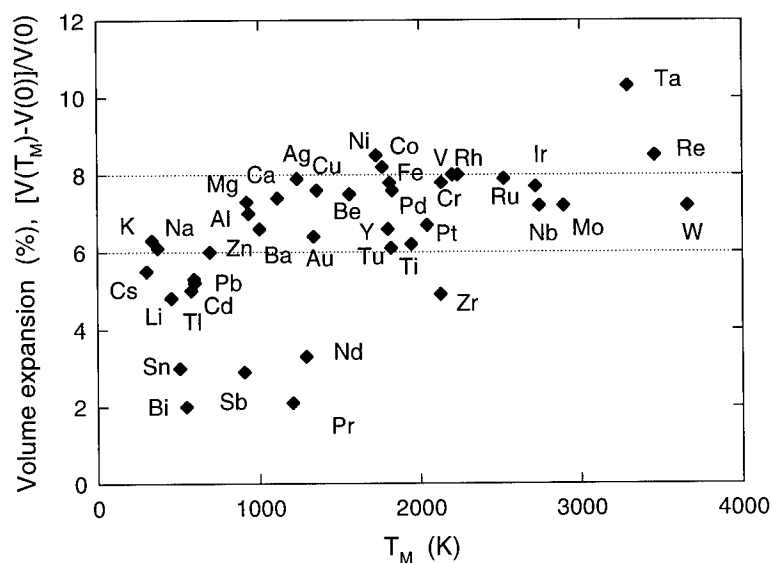


Fig. 2 Volume expansion at the melting temperature  $T_M$  for various metallic elements. Except for elements such as Bi, Sn, Sb, Pr and Nd for which electronic excitations are expected to alter the effective atomic size, thermal expansion at  $T_M$  is surprisingly constant at 6 - 8 % [5].

#### 4. GLASS TRANSITION

The condition of criticality  $\delta N_c = \pm 0.5$ , combined with the equation (9) suggests that if the local pressure exceeds the value,

$$|p_L| \geq \frac{9}{8\pi} \left( \frac{2}{3} \sqrt{3} - 1 \right) B = 0.0554 B \quad (13)$$

then that atomic site is topologically unstable. This result is in agreement with (12), and identifies the free-volume elements in glasses. If the density of the atoms exceeding this condition is high enough the system will be a liquid, while their density reaching the percolation concentration should mark the glass transition. For the 3-d closed packed structure the percolation concentration is about 15 % [1]. This happens to be equal to the portion beyond  $\sigma$  in the gaussian distribution. Thus at the glass transition temperature  $T_g$ ,

$$\frac{\langle p^2 \rangle^{1/2}}{B} = 0.0554 \quad (14)$$

or,

$$\frac{\langle p^2 \rangle}{B^2} = \frac{kT_g}{2\Omega B} = 3.069 \times 10^{-3} \quad (15)$$

The value of  $T_g$  thus calculated agrees well with the computer simulation [6], and experiments [5,10]. For the Lennard-Jones glass this result predicts  $kT_g = 0.245 \epsilon$ , while the computer simulation shows  $kT_g \sim 0.27 \epsilon$  [11], again in excellent agreement. To our knowledge this is the first time that the value of  $T_g$  was calculated from the potential parameters.

Even in the liquid state, however, some atomic clusters may have a longer life-time, for instance when they have an icosahedral topology [12]. In this case the atomic strain relaxes to the neighbors creating long range stress field, *a la* Eshelby. The pressure at the central atom is given by (6), about a half of that in the liquid state. Once this happens the atomic level pressure of the atom in such a cluster is likely below the critical value (13), and thus the life-time of the cluster becomes even longer. This feed-back mechanism must be the one that leads to the bifurcation of liquid-like and solid-like clusters as envisioned by Cohen and Grest [13].

## 5. GLASS FORMATION

### A. Solid state amorphization

As has been suggested by Okamoto *et al.* solid state amorphization by alloying is just a melting phenomenon brought about by the chemical pressure of alloying [14,15]. If an A atom is dissolved in the B matrix, the A atom experiences a pressure due to the size difference,

$$p_A = B_A \frac{2(1-2\nu)}{3(1-\nu)} \epsilon_v^r \quad (16)$$

$$\epsilon_v^r = \left[ \left( \frac{2(c_A x + 1 - c_A)}{(1 + c_A)x + 1 - c_A} \right)^3 - 1 \right]$$



where  $c_A$  is the concentration of A,  $B_A$  is its bulk modulus. Since the pressure of A is related to that of the matrix B by,

$$c_A \Omega_A p_A + (1 - c_A) \Omega_B p_B = 0, \quad (17)$$

$$p_B = -\frac{c_A}{1 - c_A} \frac{\Omega_A}{\Omega_B} p_A$$

Expanding by  $\delta$ , the volume strain on B is,

$$\epsilon_B = \frac{p_B}{B_B} \approx -\frac{2c_A}{9} \frac{B_A}{B_B} \frac{\Omega_B - \Omega_A}{\Omega_B} \quad (18)$$

Neglecting the difference between  $B_A$  and  $B_B$  the critical concentration of A to become amorphized is given by,

$$c_A^{crit} \frac{|\Delta\Omega|}{\Omega_B} = \frac{9}{2} \epsilon_v^{crit} = 0.25 \quad (19)$$

The critical concentration given by (19) corresponds to the concentration at which the value of  $T_0$  [16] becomes zero. Adjusting for the finite temperature this gives the glass forming composition range of 19 atomic % Zr to 39 atomic % Ni for the Zr-Ni system at 300°C. This estimate agrees well with observation [5].

#### B. Glass formation by rapid quenching.

This in fact is the first case the topological instability condition was applied to obtain the critical concentration [17]. At that time, however, we did not recognize the broad implication of this criterion. Applying the same criticality condition for crystalline nuclei formed during the cooling of a liquid, one obtains the condition for the critical concentration,

$$c_A^{crit} \frac{|\Delta\Omega|}{\Omega_B} = 2\epsilon_v^{crit} = 0.1 \quad (20)$$

which has been successfully tested [17,18].

## 6. CONCLUSION

One of the major difficulties in constructing a theory of glasses and liquids is that it is not easy to describe the structure of glasses and liquids with accuracy sufficient to relate to thermodynamical properties. Our proposal is to utilize the concept of the atomic level stresses. In the systems with metallic bonding they are closely related to the topology of the structure, and their magnitude can be calculated as a function of temperature in the mean-field approximation. Furthermore by introducing the criterion of local topological instability, melting of crystals, glass transition, solid state amorphization and glass formation by quenching can all be quantitatively

explained. Thus at least for metallic elements and alloys basic elements for the quantitative theory of glasses and liquids appear to be almost at hand.

#### ACKNOWLEDGMENT

This work has been supported by the National Science Foundation through DMR96-28134.

#### References:

1. *e.g.*, R. Zallen, *The Physics of Amorphous Solids* (John Wiley & Sons, New York, 1983).
2. T. Egami, K. Maeda and V. Vitek, *Phil. Mag. A* **41**, 993 (1980).
3. T. Egami and D. Srolovitz, *J. Phys. F*, **12**, 2141 (1982).
4. T. Egami, in *Science and Technology of Rapid Solidification and Processing*, ed. M. A. Otonari (Kluwer Academic, Netherlands, 1995) p. 291.
5. T. Egami, *Mater. Sci. Eng.*, in press.
6. S.-P. Chen, T. Egami and V. Vitek, *Phys. Rev. B* **37**, 2440 (1988).
7. T. Egami and V. Vitek, in *Amorphous Materials: Modeling of Structure and Properties*, ed. V. Vitek (TMS-AIME, Warrendale, Pa, 1983) p. 127.
8. T. Egami and S. Aur, *J. Non-Cryst. Solids*, **89**, 60 (1987).
9. J. D. Eshelby, *Proc. Roy. Soc. A* **241**, 376 (1957).
10. T. Egami, *Rep. Prog. Phys.* **47**, 1601 (1984).
11. J. R. Fox and H. C. Andersen, *Ann. N. Y. Acad. Sci.* **371**, 123 (1981).
12. T. Tomida and T. Egami, *Phys. Rev. B* **52**, 3290 (1995).
13. M. H. Cohen and G. Grest, *Phys. Rev. B*, **20**, 1077 (1979).
14. M. J. Sabochick and N. Q. Lam, *Phys. Rev. B*, **43**, 5243 (1991).
15. R. Devanathan, N. Q. Lam, P. R. Okamoto and M. Meshii, *Phys. Rev. B*, **48**, 42 (1993).
16. T. B. Massalski, in *Proc. 4<sup>th</sup> Int. Conf. Rapidly Quenched Metals*, (The Japan Inst. Metals, Sendai, 1982) p. 203.
17. T. Egami and Y. Waseda, *J. Non-Cryst. Solids*, **64**, 113 (1984).
18. S. H. Liou and C. L. Chien, *Phys. Rev. B* **35**, 2443 (1987).

## INTERMEDIATE RANGE ORDER IN SODIUM TELLURITE GLASSES

J. W. Zwanziger, J. C. McLaughlin, S. L. Tagg

Department of Chemistry, Indiana University, Bloomington, IN 47405, jzwanzig@indiana.edu

### ABSTRACT

Information about the spatial distribution of sodium cations in sodium tellurite glasses is obtained from the decay rate of sodium spin echoes. The spin echoes decay due to the magnetic dipole coupling between sodium nuclei, with each pair contributing to the rate in proportion to  $1/r^6$ , where  $r$  is the distance between the pair. The experiment is used to probe the sodium distributions in sodium tellurite glasses as a function of sodium oxide content, and the resulting distance distributions are interpreted by comparison with model distributions. At low sodium contents the distribution is similar to that of a random model in which the sodium ions are constrained to be no closer than a minimum cut-off distance. At higher contents the distributions deviate significantly from the random model, suggesting the onset of medium range order in the distribution of sodium ions. This order is most pronounced at 20% sodium oxide content, the composition at which this glass has been claimed to have maximum stability against devitrification.

### INTRODUCTION

Whereas tellurite ( $\text{TeO}_2$ ) is only a conditional glass former, requiring fast quenching from the melt to obtain glasses, alkali tellurites  $((\text{M}_2\text{O})_x(\text{TeO}_2)_{1-x})$ ,  $\text{M} = \text{Li}, \text{Na}, \text{K}, \text{Rb}$  have composition ranges of good glass formation that require only modest cooling rates. These glass families exhibit stability maxima, in that the difference between the crystallization temperature observed upon heating the glass and the glass transition temperature itself reaches a maximum as a function of composition [1]. In this sense certain compositions are most stable against devitrification. This behavior is shown for  $(\text{Na}_2\text{O})_x(\text{TeO}_2)_{1-x}$  glasses in Figure 1. The stability maximum is achieved at about 20 mol-% added  $\text{Na}_2\text{O}$ . Interestingly this system also displays a crystalline phase at this composition [2].

The relationship between the glass structure at the atomic level, and bulk properties, such as the stability against devitrification, is undoubtedly complex. In the case of  $(\text{Na}_2\text{O})_x(\text{TeO}_2)_{1-x}$  glasses the atomic structure undergoes substantial changes as a function of composition, beginning at about the 20 mol-% composition. At this composition the coordination number of oxygen around the sodium cations begins to decrease, from nearly six at compositions less than 20 mol-%, to about five at the 35 mol-% composition [3]. Moreover, the typical sodium environment at the 20 mol-% composition differs substantially between the glass and the crystal, with the glass showing the *more* symmetric local environment. These findings indicate that, while the coordination of the sodium itself does not deviate markedly from typical behavior in solid oxides [3, 4], the glass structure as a function of composition begins to change substantially at the 20 mol-% composition.

Changes in the glass structure have been suggested also in Raman [5, 6] and diffraction [7] studies, which have focussed on the tellurite network. As sodium oxide (or any modifier) is added, the network is cleaved, eventually resulting in  $\text{TeO}_3^{2-}$  ions at high modification levels. This process, as quantified by the appearance of non-bridging oxygen, has been inferred from vibrational spectroscopy and neutron diffraction experiments. No dramatic changes near the 20 mol-% composition were suggested, however.

In the present contribution we report experiments that measure the distribution of distances between pairs of sodium cations in  $(\text{Na}_2\text{O})_x(\text{TeO}_2)_{1-x}$  glasses. These measurements show evidence of substantial intermediate range ordering in the sodium distribution at the 20 mol-% composition. Compositions on both sides of this value show less ordering. The stability of the glass at this composition may well depend on the excess ordering observed. In the following sections we describe the experiments performed, followed by the results. We then provide discussion and interpretation, and finally conclusions of the study and directions for future research.

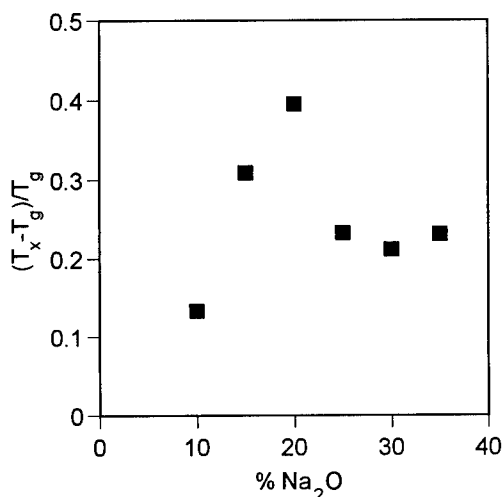


Figure 1: Difference between crystallization temperature,  $T_X$ , and glass transition temperature,  $T_g$ , scaled to  $T_g$ , for sodium tellurite glasses as a function of  $\text{Na}_2\text{O}$  content. After ref. 1.

## EXPERIMENT

$(\text{Na}_2\text{O})_x(\text{TeO}_2)_{1-x}$  glasses were made by combining  $\text{TeO}_2$  with  $\text{Na}_2\text{CO}_3$ , and heating to  $800^\circ\text{C}$  for 15 minutes. By this time gas evolution had ceased. The liquids were quenched by pouring onto stainless steel. Electron microprobe analyses indicate that the final compositions are accurate to within two percentage points. The sodium-containing crystals studied were purchased and used as received.

The NMR experiment employed was a spin echo with variable dephasing time. The pulse sequence is  $\pi/2_x - \tau - \pi_y$  - acquire, that is, a preparation pulse, followed by a dephasing time  $\tau$ , followed by a refocussing pulse. The resulting echo forms at time  $\tau$  after the refocussing pulse. As discussed in more detail below, the echo amplitude decreases with increasing  $\tau$ , due to magnetic dipole interactions that are not refocussed by this pulse sequence.

The experiments were carried out on a home-built NMR spectrometer and an 8.46 T magnet, resulting in a  $^{23}\text{Na}$  Larmor frequency of 95.2 MHz. Moderate pulse powers were used, such that the  $\pi/2$  pulse time was typically 5–7  $\mu\text{sec}$ . This condition (discussed below) resulted in full excitation of the  $^{23}\text{Na}$  central transition, with minimal coherence in the satellite transitions [8, 9]. A particularly important experimental detail was the use of small samples, typically 25% of the volume of the radiofrequency coil, and centered in the coil [8]. This geometry minimizes inhomogeneity effects at the ends of the coil, and was essential to the success of the experiments.

## RESULTS

Figure 2 shows data from the spin echo experiment, for one glass composition. The experiment was performed on  $(\text{Na}_2\text{O})_x(\text{TeO}_2)_{1-x}$  glasses of composition  $x = 0.10$ – $0.30$ . Data on selected compositions were also acquired at  $-110^\circ\text{C}$ . This data was indistinguishable from that at ambient temperature, indicating that ion mobility in  $(\text{Na}_2\text{O})_x(\text{TeO}_2)_{1-x}$  was negli-

gible in its effect on the echo amplitudes. The same experiment was performed on a variety of sodium-containing crystalline salts, to use as checks of the accuracy and precision of the data.

## DISCUSSION

The experiment is well-known in studies of spin-1/2 nuclei like phosphorus-31 and carbon-13; its use for quadrupolar nuclei (spin  $I > 1/2$ ) has been developed and exploited by Haase and Oldfield [8] and Gee and Eckert [9]. The echo intensity decays with lengthening refocussing times due to the magnetic dipolar interactions between sodium nuclei. The dipole-dipole Hamiltonian is truncated by the dominant Zeeman Hamiltonian, and takes the form

$$H_D^0 = \frac{1}{4} \gamma^2 \hbar^2 \sum_{j,k} \frac{1 - 3 \cos^2 \theta_{jk}}{r_{jk}^3} (3I_{jz}I_{kz} - \mathbf{I}_j \cdot \mathbf{I}_k). \quad (1)$$

Here  $\gamma$  is the gyromagnetic ratio of  $^{23}\text{Na}$ ,  $j$  and  $k$  label different sodium nuclei, with spin  $\mathbf{I}_j$  and  $\mathbf{I}_k$  respectively, and separated by distance  $r_{jk}$ .  $\theta_{jk}$  is the angle between the internuclear vector and the applied magnetic field, taken to be in the  $z$  direction. Because the dipole interaction is bilinear in the spin operators, it is not refocussed by the pulse sequence. This happens essentially because *both* spin operators are flipped, leading to no change. In contrast, other interactions that are linear in  $\mathbf{I}_j$ , including chemical shift, heteronuclear dipole interactions, and the central transition of the second order quadrupole effect, are refocussed and thus can be ignored in their effect on the echo amplitude.

The echo decay describes the resonance linewidth due solely to  $H_D^0$ , and can be simply expressed as the second moment of the resonance line. For short refocussing times ( $\tau \lesssim 200 \mu\text{sec}$ ) the echo amplitude  $I(2\tau)$  decays as a Gaussian, and can be expressed as

$$\frac{I(2\tau)}{I(0)} = \exp[-M_2(2\tau)^2/2]. \quad (2)$$

The second moment,  $M_2$ , follows from a second-order perturbation theory treatment of the evolution due to  $H_D^0$ ; here we merely quote the result, after averaging over all angles  $\theta_{jk}$ , and using constants appropriate to  $^{23}\text{Na}$ , as [8, 9]

$$M_2 = 2.66 \times 10^9 \sum_{j,k} \frac{1}{r_{jk}^6} \text{rad}^2/\text{sec}^2. \quad (3)$$

Thus from the slopes of graphs of  $\ln I(2\tau)/I(0)$  plotted as a function of  $(2\tau)^2$ , we extract  $M_2$  and hence information about the distances between sodium nuclei in the glass. These  $M_2$  values for  $(\text{Na}_2\text{O})_x(\text{TeO}_2)_{1-x}$  glasses are shown in Figure 3(a).

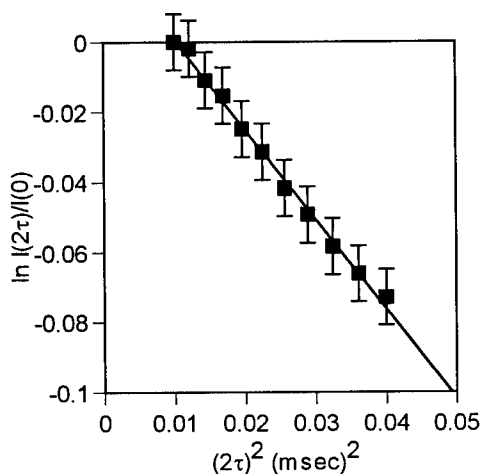


Figure 2: Logarithmic decay of echo intensities, plotted versus the square of the dephasing time, for one sodium tellurite glass. The slope of this plot gives  $M_2/2$ .

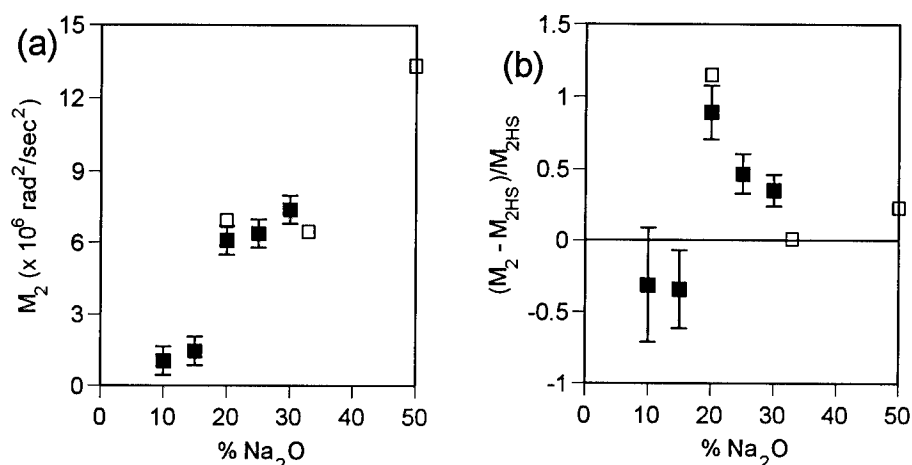


Figure 3: (a)  $M_2$  for sodium in  $(\text{Na}_2\text{O})_x(\text{TeO}_2)_{1-x}$  glasses and crystals as a function of composition. (b) Difference between the second moment,  $M_2$ , and the hard sphere value,  $M_{2HS}$ , scaled to the latter, as a function of sodium content. For both plots, ■ represents glass samples (experimental  $M_2$ 's), and □ represents crystals ( $M_2$  calculated from crystal structure).

The information on inter-sodium distances contained in  $M_2$  is not simple to interpret. While the form of Equation 3 is explicit, it is only useful for crystals, for which all  $r_{jk}$  are known. For glasses it is convenient to rewrite Equation 3 in terms of the sodium-sodium pair distribution function  $g(r)$ . This is done by replacing the sum in Equation 3 with an integral, and realizing that the weight contributed at each distance  $r$  is given by the value of the radial distribution function at that distance. Thus we have

$$M_2 \propto \sum_{j,k} \frac{1}{r_{jk}^6} \rightarrow \int_{\text{sample}} \frac{4\pi r^2 \rho_0 g(r)}{r^6} dr, \quad (4)$$

where  $\rho_0$  is the bulk number density of sodium. From Equation 4 it is clear that  $M_2$  yields  $\langle r^{-6} \rangle$ , where the averaging is carried out with respect to the sodium radial distribution function. Thus  $M_2$  strongly emphasizes the correlations in the first few shells of atoms, with neighbors farther away contributing little. Quantitatively, this experiment yields information on correlations out to about 10 Å, in that by this distance  $M_2$  as reached more than 95% of its final value.

Our measurements of  $M_2$  show two gross qualitative features: a monotonic increase with increasing sodium content, and a sharp rise near the 20 mol-% composition. The overall increase with sodium content is trivial, in that as sodium is added, the average distances are decreased, leading to larger  $M_2$ 's. To interpret the data more fully, we compare the measurements to  $M_2$ 's extracted from several models. One class of model we examined is based on crystal structures of sodium tellurites. For example, we calculated  $M_2$  for the Na<sub>7</sub>Te<sub>4</sub>O<sub>9</sub> crystal structure, and also the  $M_2$ 's for the same structure isotropically dilated or compressed to yield the correct number density of each glass. The agreement with the

data for models of this type was poor, in large part because such models predict a quadratic increase in  $M_2$  with sodium density. The increase seen in Figure 3(a) is more nearly linear.

The qualitative behavior of  $M_2$  was captured better by a more random model, which we constructed by considering the radial distribution function of a hard sphere liquid at the same number density of each glass. Note that we do not mean to suggest that the sodium ions in tellurite glasses behave dynamically like a hard sphere liquid, but rather that as a first approximation their distribution in space can be mimicked by the atomic distribution of a hard sphere liquid. For each glass composition we constructed a hard sphere liquid of the same number density as the sodium in that glass, using 3.2 Å as the closest approach distance. This value was chosen based on the known sodium tellurite crystal structures ( $\text{Na}_2\text{Te}_4\text{O}_9$  [2],  $\text{Na}_2\text{Te}_2\text{O}_5$  [10],  $\text{Na}_2\text{TeO}_3$  [11]) for which the sodium ions never approach closer than this value. This is much larger than the ionic radius of sodium, of course, because the sodium cations are coordinated by oxygen and thus are always separated by at least one oxygen coordination shell, leading to the larger minimum distance. The resulting packing fractions for the hard sphere liquids were of order 0.1–0.2, far below the packing fraction at which a hard sphere liquid crystallizes [12]. From the  $g(r)$  for each model  $M_2$  was calculated, using Equation 4. These  $M_2$  increase essentially linearly with sodium density over the range studied, much more like the glass data.

To make a detailed comparison between the data and the hard sphere model, we subtract the hard sphere  $M_2$  from the experimental  $M_2$ , and scale by the model value. This plot is shown in Figure 3(b). In this figure we see that at low sodium content the sodium ions are perhaps slightly anti-correlated in position with respect to the hard sphere model, though given the error bars this difference may be insignificant. The differences at 20 mol-% and above are significant, however, and show that the ions are more correlated in their positions than in the hard sphere model. Taking the hard sphere model as the randomly packed reference system, we interpret this difference as a decrease in randomness, in other words the growth of order, at these compositions. The 20 mol-% composition shows the greatest degree of ordering in this sense.

We estimate the length-scale of ordering in comparison to the hard sphere reference model, by stretching the hard sphere  $g(r)$ , starting at the 3.2 Å cut-off. We then calculate  $M_2$  for the stretched  $g(r)$ , while renormalizing the amplitude to keep the effective sodium density fixed. This procedure has the effect of extending correlations in the hard sphere  $g(r)$ , mimicking the effect of intermediate range order within the context of the hard sphere reference system. For the 20 mol-% composition, where the experimental  $M_2$  exceeds the hard sphere  $M_2$  by some 90%, this analysis indicates that the ordering length scale *exceeds* the 10 Å range over which this experiment is sensitive.

## CONCLUSIONS

The present experiment probes the spatial distribution of sodium in  $(\text{Na}_2\text{O})_x(\text{TeO}_2)_{1-x}$  glasses, as a function of composition. The basic quantity extracted is a moment of the sodium radial distribution function, specifically  $\langle r^{-6} \rangle$ . To interpret this in terms of distributions we compare to model systems, finding that a hard sphere distribution of sodium atoms with closest approach distance of 3.2 Å (as found in crystalline  $(\text{Na}_2\text{O})_x(\text{TeO}_2)_{1-x}$  phases) captures the simplest aspects of the data. However, there appears to be excess ordering of the sodium cations near the 20 mol-% composition, with length scale exceeding the 10 Å distances over which this experiment is sensitive.

This ordering is not immediately apparent in the structure factors obtained from neutron

diffraction, because the Na-Na contribution is small [13]. For example, the first sharp diffraction peak does not scale in amplitude or location with sodium content. We are analyzing our neutron diffraction data more fully, to combine information on the tellurite network with the present results, and explain the strong composition dependence of the glass stability.

#### ACKNOWLEDGMENTS

This research was supported by the National Science Foundation, grant number DMR-9508625.

#### REFERENCES

- [1] J. Heo, D. Lam, G. H. Sigel, Jr., E. A. Mendoza, and D. A. Hensley, *J. Am. Ceram. Soc.* **75**, 277 (1992).
- [2] S. L. Tagg, J. C. Huffman, and J. W. Zwanziger, *Chem. Mater.* **6**, 1884 (1994).
- [3] S. L. Tagg, R. E. Youngman, and J. W. Zwanziger, *J. Phys. Chem.* **99**, 5111 (1995).
- [4] J. W. Zwanziger, S. L. Tagg, and J. C. Huffman, *Science* **268**, 1510 (1995).
- [5] T. Sekiya, N. Mochida, A. Ohtsuka, and M. Tonokawa, *J. Non-Crystalline Solids* **144**, 128 (1992).
- [6] M. Tatsumisago, T. Minami, Y. Kowada, and H. Adachi, *Phys. Chem. Glasses* **35**, 89 (1994).
- [7] S. Neov, V. Kozhukharov, I. Gerasimova, K. Krezhov, and B. Sidzhimov, *J. Phys. C* **12**, 2475 (1979).
- [8] J. Haase and E. Oldfield, *J. Magn. Reson. A* **101**, 30 (1993).
- [9] B. Gee and H. Eckert, *Solid State NMR* **5**, 113 (1995).
- [10] S. L. Tagg, J. C. Huffman, and J. W. Zwanziger, Sodium ditellurite  $\text{Na}_4\text{Te}_4\text{O}_{10}$  crystal structure, in press at *Acta Chem. Scand.*, 1996.
- [11] R. Masse, J. C. Guitel, and I. Tordjman, *Mat. Res. Bull.* **15**, 431 (1980).
- [12] P. M. Chaiken and T. C. Lubensky, *Principles of condensed matter physics*, Cambridge University Press, Cambridge, 1995.
- [13] S. L. Tagg and J. W. Zwanziger, Neutron diffraction studies of sodium tellurite glasses, unpublished data.



## TWO SPECIES/NONIDEAL SOLUTION MODEL FOR AMORPHOUS/AMORPHOUS PHASE TRANSITIONS

CORNELIUS T. MOYNIHAN

Materials Science and Engineering Department

Rensselaer Polytechnic Institute, Troy, NY 12180-3590, moynic@rpi.edu

### ABSTRACT

A simple macroscopic thermodynamic model for first order transitions between two amorphous phases in a one component liquid is reviewed, augmented and evaluated. The model presumes the existence in the liquid of two species, whose concentrations are temperature and pressure dependent and which form a solution with large, positive deviations from ideality. Application of the model to recent data indicates that water can undergo an amorphous/amorphous phase transition below a critical temperature  $T_c$  of 217K and above a critical pressure  $P_c$  of 380 atm.

### INTRODUCTION

The plausibility of first order thermodynamic transitions between two equilibrium liquid phases appears to be well established conceptually and theoretically (see [1-4] and references cited therein). More convincingly, such amorphous/amorphous (a/a) transitions have been observed visually in the liquid for three substances -  $H_2O$  [5],  $Al_2O_3$ - $Y_2O_3$  melts [6,7] and triphenylphosphite [8]. In the present paper we discuss and enlarge upon a simple thermodynamic model for a/a phase transitions in one component liquids and apply the model to data relevant to the a/a transition in water.

### TWO SPECIES/NONIDEAL SOLUTION MODEL

#### Background

The model considered here, in its simplest form, has been termed variously the "two species model" [9], "two state model" [10,11], "two level model" [12,13], "mixture model" [14] and "bond-lattice model" [15,16]. One assumes in a one component condensed phase (crystal or liquid) the existence of two "species", A and B, which can be interconverted via a physicochemical process or "chemical reaction" of the form:



The equilibrium concentrations of species A and B are dependent on temperature  $T$  and pressure  $P$ , so that the "chemical reaction" contributes to the  $T$  and  $P$  dependence of the thermodynamic properties. A simple crystal state example of such a process is vacancy formation in a metal. Of importance for the present discussion is the fact that processes of this sort are manifested in all liquids and are commonly referred to as "structural relaxation", whose kinetically induced disequilibrium at low temperatures is responsible for the glass transition [13,15-18].

In the simplest versions of this model the two species, A and B, are assumed to form an ideal solution. This assumption leads to a continuous, monotonic variation in the concentrations of the two species as a function of  $T$  and  $P$ . If, however, the two species are

assumed to form a nonideal solution, then, under certain circumstances, the concentrations of A and B may exhibit a discontinuous change as  $T$  or  $P$  are varied, i.e., a first order phase transition. This was first explicated in detail by Aptekar and Ponyatovskii [12], who used this treatment to model an unusual fcc→fcc phase transition in crystalline Ce metal, where the two species were taken to be  $\text{Ce}^{+4}$  and  $\text{Ce}^{+3}$  ions. This approach, which we will henceforth term the "two species/nonideal solution model", was also developed by Rapoport [9] to account for maxima in the melting point vs.  $P$  curves of metals. Although Rapoport mentioned that the model could lead to "separation (of a melt) into two phases", he did not explore this aspect in detail, and one cannot discern from his papers whether he thought formation of the second liquid phase was a true first order phase transition or was similar to liquid-liquid immiscibility in a two component melt.

#### Thermodynamics of the Two Species/Nonideal Solution Model

At a given  $T$  and  $P$  the Gibbs free energy per mole of species for a one component liquid or crystal consisting of interconvertible species A and B is given by

$$G = (1 - X)G_A + XG_B \quad (2)$$

where  $X$  is the mole fraction of species B, and  $G_A$  and  $G_B$  are the molar free energies or chemical potentials of A and B. If we assume that A and B form a regular solution with interaction energy parameter  $W$ , then  $G_A$  and  $G_B$  can be expressed as [19]:

$$G_A = G_A^\circ + V_A^\circ(P - P^\circ) + RT \ln(1 - X) + WX^2 \quad (3a)$$

$$G_B = G_B^\circ + V_B^\circ(P - P^\circ) + RT \ln X + W(1 - X)^2 \quad (3b)$$

where  $R$  is the ideal gas constant,  $G_A^\circ$  and  $G_B^\circ$  are respectively the standard molar free energies of A and B at temperature  $T$  (pure A and B at standard pressure  $P^\circ = 1$  atm), and similarly for the standard molar volumes  $V_A^\circ$  and  $V_B^\circ$ . If we take pure A at pressure  $P$  and temperature  $T$  as our reference state, then via Eqs. (2) and (3) the relative molar free energy  $\Delta G$  at that  $T$  and  $P$  is given by:

$$\begin{aligned} \Delta G &\equiv G - G_A^\circ - V_A^\circ(P - P^\circ) \\ &= -XRT \ln K + X\Delta V^\circ(P - P^\circ) + (1 - X)RT \ln(1 - X) + XRT \ln X + WX(1 - X) \end{aligned} \quad (4)$$

where  $K$  is the equilibrium constant for reaction (1):

$$\ln K = -\Delta G^\circ/RT = -\Delta H^\circ/RT + \Delta S^\circ/R \quad (5)$$

$\Delta G^\circ (\equiv G_B^\circ - G_A^\circ)$  is the standard Gibbs free energy change for reaction (1) at a given  $T$ , and similarly for the standard enthalpy, entropy and volume changes,  $\Delta H^\circ$ ,  $\Delta S^\circ$  and  $\Delta V^\circ$ . In what follows we shall assume that  $\Delta H^\circ$ ,  $\Delta S^\circ$  and  $\Delta V^\circ$  are constant and independent of  $T$ . We shall also presume that we have written the A→B reaction in the endothermic direction ( $\Delta H^\circ > 0$ ), so that B is the species that predominates at high temperature.

The predictions of Eq. (4) for the two species, one component system are most readily illustrated using isothermal, isobaric plots of  $\Delta G/RT$  vs. mole fraction  $X$  of species B. To this end, it is convenient to define a reduced temperature  $T_r$  given by

$$T_r = T/T_c \quad (6)$$

where  $T_c$  in turn is a critical temperature related to the regular solution interaction energy parameter  $W$  by

$$W = 2RT_c \quad (7)$$

Equations (4) and (5) may then be rewritten in the form

$$\frac{\Delta G}{RT} = -X \ln K + X \left( \frac{\Delta V^\circ}{RT_c} \right) \left( \frac{P - P^\circ}{T_r} \right) + (1 - X) \ln(1 - X) + X \ln X + \frac{2X(1 - X)}{T_r} \quad (8)$$

and

$$\ln K = - \frac{(\Delta H^\circ/RT_c)}{T_r} + \frac{\Delta S^\circ}{R} \quad (9)$$

Shown in Fig. 1 are a series of  $\Delta G/RT$  vs.  $X$  isotherms at constant  $P$  ( $= 1$  atm) calculated from Eqs. (8) and (9) using the following set of reduced parameters:

$$\Delta S^\circ/R = 3.00, \quad \Delta H^\circ/RT_c = 2.40, \quad \Delta V^\circ/RT_c = 8.1 \times 10^{-5} \text{ atm}^{-1} \quad (10)$$

The equilibrium(e) state of the system at a given reduced temperature  $T_r$  corresponds to the composition  $X_e$  (denoted by o's in Fig. 1) at the deepest minimum in the  $\Delta G/RT$  vs.  $X$  plot. At the lowest reduced temperature in Fig. 1 ( $T_r = 0.69$ ) there is only one minimum, corresponding to an equilibrium composition  $X_e$  rich in species A ( $X_e < 0.5$ ). As  $T_r$  is increased, a second minimum begins to develop on the B-rich side and at  $T_r = 0.80$  in Fig. 1 becomes equal in depth to the minimum on the A-rich side. Hence at  $T_r = 0.80$  in Fig. 1 one can have two phases present at equilibrium, one rich in species A ( $X_e < 0.5$ ) and one rich in species B ( $X_e > 0.5$ ). With further increase in the reduced temperature the minimum on the B-rich side drops below that on the A-rich side, so that there is again only one equilibrium composition, now rich in species B ( $X_e > 0.5$ ). Consequently, at temperature  $T_r = 0.80$  in Fig. 1 a first order phase transition has taken place, during which the system changes discontinuously during heating at constant  $P$  from a crystal or liquid rich in species A to one rich in species B. For a liquid system we will designate this first order amorphous/amorphous transition temperature  $T_{aa}$ .

$T_{aa}$  is pressure dependent. Shown in Fig. 2 are several isothermal, isobaric  $\Delta G/RT$  vs.  $X$  plots calculated using the parameters in Eq. (10) for different pressures and temperatures along the  $P/T_r$  line which (at low  $T_r$  values) gives rise to double  $\Delta G/RT$  minima of equal depth and the a/a transition. As  $T_r$  increases the double minima become shallower and move closer together along the composition axis, so that at and above the critical temperature  $T_c$  ( $T_r = 1$ ) (or at and beyond a corresponding critical pressure  $P_c$  ( $= 7390$  atm in Fig. 2)) the double  $\Delta G/RT$  minima are no longer present and the a/a phase transition can no longer take place.

The thermodynamics of the two species/nonideal solution model are specified in terms of four parameters -  $\Delta H^\circ$ ,  $\Delta S^\circ$ ,  $\Delta V^\circ$  and  $W$  (or  $T_c = W/2R$ ). At any given  $T$  and  $P$  the equilibrium(e) state, i.e., composition  $X_e$ , corresponds to the deepest minimum and hence to a point of zero slope on the  $\Delta G$  or  $\Delta G/RT$  vs.  $X$  plot. Differentiating Eq. (4) and using Eq. (5), one gets:

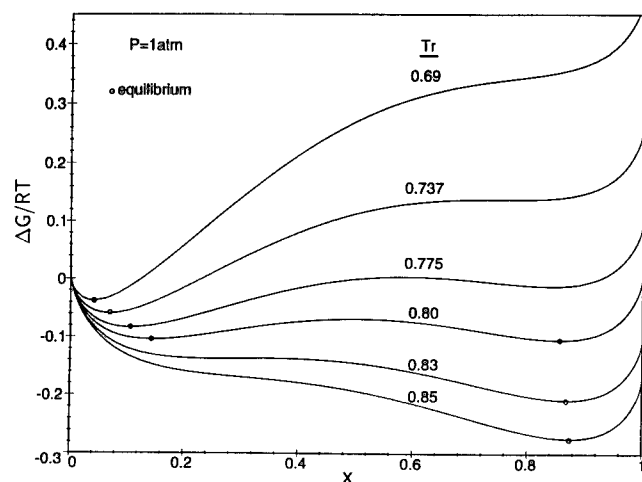


**Figure 1.** Isothermal plots of  $\Delta G/RT$  vs. mole fraction  $X$  of species B at constant  $P$  ( $=1$  atm) calculated using the parameters in Eq. (10). ( $\circ$ ) equilibrium compositions  $X_e$  at the various reduced temperatures  $T_r$ .

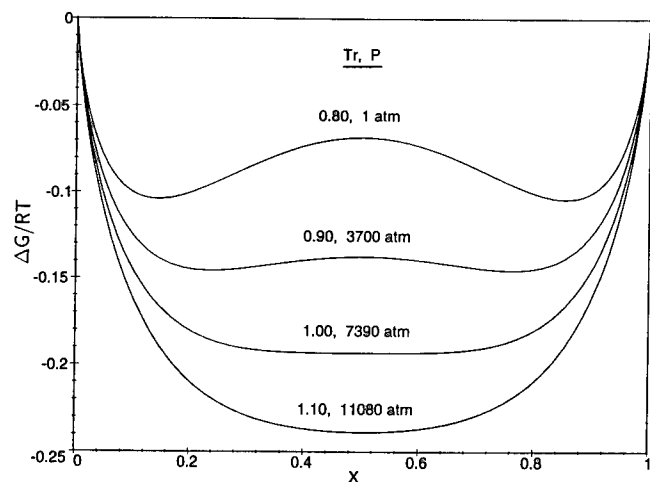


**Figure 2.** Isothermal, isobaric  $\Delta G/RT$  vs.  $X$  plots calculated using the parameters in Eq. (10) for  $P$ 's and  $T_r$ 's along the  $P/T_r$  line for the a/a transition. The critical point corresponds to  $T_r = 1$ .

$$\left(\frac{\partial \Delta G}{\partial X}\right)_e = \Delta H^\circ - T\Delta S^\circ + \Delta V^\circ(P - P^\circ) + RT \ln\left(\frac{X_e}{1 - X_e}\right) + W(1 - 2X_e) = 0 \quad (11)$$

$X_e$  may be obtained by solving Eq. (11) numerically. In some cases, such as the  $\Delta G/RT$  plots in Fig. 1 for  $0.737 \leq T_r \leq 0.83$ , there are two or three solutions to Eq. (11), and the value of  $X_e$  is the solution that yields the lowest value of  $\Delta G$  or  $\Delta G/RT$ .

The conditions for the a/a phase transition in a liquid are easily intuited from Eq. (4). At a given  $T$  and  $P$  the sum of the first two terms on the right side of Eq. (4) is linear in composition  $X$ , while the sum of the last three terms is identical to the Gibbs free energy of mixing of a two component regular solution and is symmetric about the composition  $X = 0.5$  [19]. Hence to produce double  $\Delta G/RT$  minima of equal depth (cf. Figs. 1 and 2), the sum of these first two terms must vanish, leading to the following condition at the a/a transition temperature  $T_{aa}$  and pressure  $P_{aa}$ :

$$-RT_{aa} \ln K + \Delta V^\circ(P_{aa} - P^\circ) = \Delta H^\circ - T_{aa}\Delta S^\circ + \Delta V^\circ(P_{aa} - P^\circ) = 0 \quad (12)$$

Differentiation of this expression yields the Clayperon equation for the temperature dependence of the pressure at the a/a transition:

$$dP_{aa}/dT_{aa} = \Delta S^\circ/\Delta V^\circ \quad (13)$$

In addition, to produce double minima of equal depth in the  $\Delta G/RT$  vs.  $X$  plot at the a/a transition we must require that the plot exhibit a maximum at the midpoint composition  $X = 0.5$  (again cf. Figs. 1 and 2), so that

$$(\partial^2 \Delta G / \partial X^2) |_{X=0.5} < 0 \quad (14)$$

Applying this condition to Eq. (4) yields

$$W > 2RT_{aa} \quad (15)$$

Since  $T_{aa}$  (in kelvins) must be positive, only two species liquids with positive values of the regular solution interaction energy parameter,  $W > 0$ , can exhibit an a/a phase transition. The temperature corresponding to an equality in Eq. (15) is the critical temperature  $T_c$  (cf. Eq. (7)).

Combination of Eqs. (7), (12) and (15) leads to a final, overall constraint for liquids which can exhibit an a/a phase transition in the context of the present model, namely, that Eq. (12) must be satisfied at a temperature  $T_{aa} < W/2R = T_c$ . Mathematically, this constraint, which was not pointed out in earlier papers [9,12], may be stated as:

$$\frac{W}{2R} > \frac{\Delta H^\circ + \Delta V^\circ(P - P^\circ)}{\Delta S^\circ} > 0 \quad (16)$$

The  $T$  and  $P$  dependences of the equilibrium species concentration  $X_e$  make contributions to the equilibrium thermodynamic properties heat capacity  $C_P$ , thermal expansion coefficient  $\alpha$  and isothermal compressibility  $\kappa$ , over and above the "background" contributions from the ordinary vibrational and rotational degrees of freedom of the individual A and B species. Two species/nonideal solution model expressions for these

excess contributions, which we will designate  $\Delta C_P$ ,  $\Delta\alpha$  and  $\Delta\kappa$ , may be obtained in a straightforward fashion from Eqs. (4), (5) and (11):

$$\Delta C_P = -T \left( \frac{\partial^2 \Delta G}{\partial T^2} \right)_e = \frac{[\Delta H^\circ + \Delta V^\circ(P - P^\circ) + W(1 - 2X_e)][\Delta S^\circ - R \ln(\frac{X_e}{1-X_e})]}{[RT/X_e(1 - X_e)] - 2W} \quad (17)$$

$$V\Delta\alpha = \left( \frac{\partial^2 \Delta G}{\partial T \partial P} \right)_e = \frac{\Delta V^\circ[\Delta S^\circ - R \ln(\frac{X_e}{1-X_e})]}{[RT/X_e(1 - X_e)] - 2W} \quad (18)$$

$$V\Delta\kappa = - \left( \frac{\partial^2 \Delta G}{\partial P^2} \right)_e = \frac{(\Delta V^\circ)^2}{[RT/X_e(1 - X_e)] - 2W} \quad (19)$$

where  $V$  is the molar volume. Note that to calculate values of  $\Delta C_P$ ,  $V\Delta\alpha$  and  $V\Delta\kappa$  at a given  $T$  and  $P$ , one must first obtain the value of  $X_e$  by solving Eq. (11).

## AMORPHOUS/AMORPHOUS PHASE TRANSITION IN WATER

### Background

Experimental studies at low temperatures (77-150K) on amorphous water produced by vapor deposition or by pressurization of ice Ic have shown that it can exist in two polymorphic forms - low density amorphous (LDA)  $H_2O$ , which appears to be rather like a disordered form of ice I, and high density amorphous (HDA)  $H_2O$ , which appears to be similar to ordinary liquid water (see [5,20] and references cited therein). At higher temperatures the equilibrium thermodynamic properties, such as  $C_P$ ,  $\alpha$  and  $\kappa$ , of supercooled liquid water immediately below the equilibrium freezing point exhibit anomalous behavior, increasing rapidly in magnitude with decreasing  $T$  and (at 1 atm) appearing to be headed toward a divergence at about 228K [21,22]. In the temperature region (roughly 150 to 236K) between those covered by the above studies there is a lack of experimental data due to the instability of amorphous or liquid  $H_2O$  against crystallization. Recently, very convincing attempts to reconcile the observed polymorphism of water at very low temperatures and the anomalous behavior in the supercooled region near the freezing point have been made using molecular dynamics (MD) simulations ([2,23] and references cited therein) and a modified Van der Waals equation of state [24]. In addition, Ponyatovskii and coworkers [25] used the two species/nonideal solution model to characterize the a/a transition in water. The results of their analysis were almost totally conditioned by a need to estimate the critical temperature  $T_c$  ( $\approx 228K$ ) for the a/a transition from the extrapolated temperature of divergence of the thermodynamic properties of supercooled  $H_2O$ . In what follows the two species/nonideal solution model is used to characterize the a/a transition in water via analysis of more recent data, which analysis precludes the need to estimate  $T_c$  in this manner.

### Analysis Assuming $H_2O$ as the Interconvertible Species Formula

Shown schematically in Fig. 3 are recent results of Mishima [20] in the form of a specific volume  $v$  vs.  $P$  plot for the interconversion of LDA and HDA water due to pressure changes in a narrow temperature range ( $135 \pm 5K$ ). On compression LDA  $H_2O$  transforms quite sharply into HDA  $H_2O$  at 3200 atm. On subsequent decompression the HDA  $H_2O$

transforms equally sharply back into LDA H<sub>2</sub>O at 500 atm. These two transformation pressures are quite reproducible [20,26]. Moreover, since the extrapolated glass transition temperature  $T_g$  of H<sub>2</sub>O is 138K [21], the results of Fig. 3 are for H<sub>2</sub>O in (or very nearly in) the equilibrium liquid states.

In analyzing the data of Fig. 3 we shall make the assumption that the two transformation pressures, 500 and 3200 atm, are those at which the HDA H<sub>2</sub>O and LDA H<sub>2</sub>O phases respectively lose their metastability at 135K. That is, (135K, 500 atm) and (135K, 3200 atm) are points on the two spinodal lines of the LDA/HDA H<sub>2</sub>O thermodynamic stability diagram. In terms of the two species/nonideal solution model, such spinodal points appear on  $\Delta G/RT$  vs.  $X$  plots for  $T$ 's and  $P$ 's where at some composition the plot goes "flat" ( $\partial(\Delta G/RT)/\partial X = 0$  and  $\partial^2(\Delta G/RT)/\partial X^2 = 0$ ), e.g., the plots in Fig. 1 for  $T_r$  values of 0.737 and 0.83. It is easily shown from Eq. (4) that the pressure  $P_{aa}$  for the a/a transition at a given  $T$  is the mean of the two spinodal pressures, as illustrated in Fig. 4 (discussed below). Hence at temperature  $T_{aa} = 135K$  the equilibrium LDA H<sub>2</sub>O  $\rightarrow$  HDA H<sub>2</sub>O a/a transition pressure is given by:

$$P_{aa} = \frac{500 \text{ atm} + 3200 \text{ atm}}{2} = 1850 \text{ atm} \quad (20)$$

If, in addition, we know the standard molar volume change  $\Delta V^\circ$ , then via Eq. (12) the logarithm of the equilibrium constant,  $\ln K$ , at  $T_{aa} = 135K$  can be calculated. For this temperature the only remaining unknown in Eq. (4) or Eq. (8) is the interaction energy parameter  $W$  or critical temperature  $T_c (=W/2R)$ , and this may be evaluated by determining the value of  $W$  which gives rise to  $\Delta G/RT$  vs.  $X$  isobars at 135K that exhibit spinodal points at pressures of 500 and 3200 atm.

In our initial analysis of the data in Fig. 3 we assumed that the interconvertible species were individual H<sub>2</sub>O molecules, e.g., in the terminology of Ref. [24] "strongly H-bonded" molecules which predominate in the LDA polyamorph and "weakly H-bonded" molecules which predominate in the HDA polyamorph. In what follows we will let  $X$  stand for the mole fraction of the HDA H<sub>2</sub>O species. The standard molar volume change  $\Delta V^\circ$  (for the pure LDA H<sub>2</sub>O  $\rightarrow$  pure HDA H<sub>2</sub>O interconversion) is related to the specific volume change  $\Delta v$  ( $= -0.22 \text{ cm}^3/\text{g}$ ) at 135K and 1850 atm in Fig. 3 by the following expression:

$$M\Delta v = (X_e'' - X_e')\Delta V^\circ \quad (21)$$

where  $X_e'$  and  $X_e''$  are the HDA H<sub>2</sub>O species mole fractions in the two phases at the a/a transition point (cf. Fig. 4) and  $M$  is the species molecular weight (18.0 g/mol H<sub>2</sub>O for individual H<sub>2</sub>O molecules). An initial estimate of  $\Delta V^\circ$  was made by setting  $X_e' = 0$  and  $X_e'' = 1$  in Eq. (21). An initial estimate of  $\ln K$  at 135K was then made using Eq. (12), after which an initial estimate of  $W$  was obtained (by trial and error) by requiring spinodal points on the 135K  $\Delta G/RT$  vs.  $X$  plots calculated for 500 and 3200 atm, as illustrated in Fig. 4. Calculation of the  $\Delta G/RT$  vs.  $X$  plot at the a/a transition pressure of 1850 atm using these initial values of  $\Delta V^\circ$ ,  $\ln K$  and  $W$  then yields the values of the equilibrium species mole fractions  $X_e'$  and  $X_e''$ , so that an improved estimate of  $\Delta V^\circ$  may be obtained from Eq. (21). Repetition of the above procedure converges after a few iterations on the following values for the interspecies conversion LDA H<sub>2</sub>O  $\rightarrow$  HDA H<sub>2</sub>O, assuming H<sub>2</sub>O as the species formula:

$$\Delta V^\circ = -4.5 \text{ cm}^3/\text{mol H}_2\text{O} \quad (22a)$$

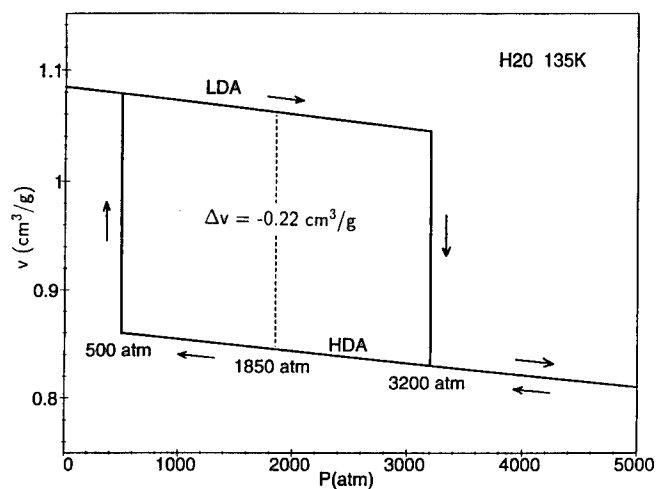


**Figure 3.** Schematic plot of experimental specific volume  $v$  vs.  $P$  data reported in Ref. [20] showing the interconversion of LDA  $\text{H}_2\text{O}$  and HDA  $\text{H}_2\text{O}$  in response to  $P$  changes at  $135 \pm 5\text{K}$ .

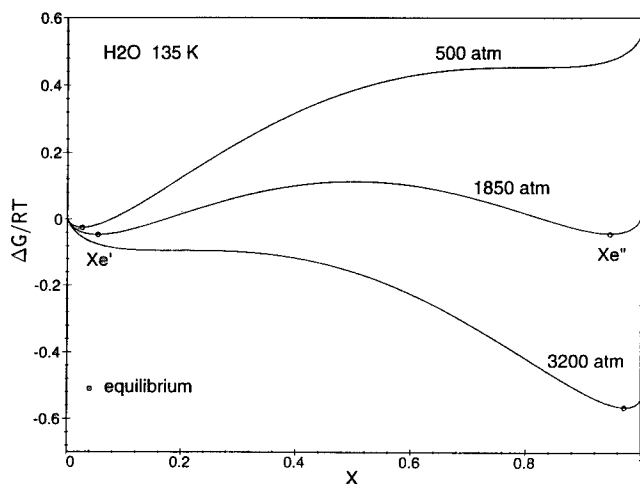


**Figure 4.**  $\Delta G/RT$  vs.  $X$  isobars for water at 135K calculated using the  $\Delta V^\circ$ ,  $\ln K$  and  $W$  values in Eqs. (22). The plots for 500 and 3200 atm exhibit spinodal points. The 1850 atm plot indicates an a/a transition at this  $P$ .  $X_e'$  and  $X_e''$  are the mole fractions of the HDA  $\text{H}_2\text{O}$  species in the two phases in equilibrium at 135K and 1850 atm.



$$\ln K = -0.75 \text{ at } 135K \quad (22b)$$

$$W = 3610 \pm 170 \text{ J/mol } H_2O, \quad T_c = W/2R = 217 \pm 10K \quad (22c)$$

The  $\Delta G/RT$  vs.  $X$  plots in Fig. 4 were calculated using the above parameters. The uncertainties in  $W$  and  $T_c$  were calculated assuming an uncertainty of  $\pm 5K$  in the a/a transition temperature plus uncertainties of  $\pm 10\%$  in the transition pressures (500 and 3200 atm) in Fig. 3. Insertion of the value of  $\ln K$  at 135K into Eq. (5) gives a relation between the  $\Delta H^\circ$  and  $\Delta S^\circ$  values:

$$\frac{\Delta H^\circ}{R} = 135\left(\frac{\Delta S^\circ}{R}\right) + 101 \quad (23)$$

Analysis of Mishima's data in Fig. 3 effectively yields three of the four parameters needed to characterize the  $H_2O$  species interconversion and the a/a transition in water -  $\Delta V^\circ$ ,  $W$  (or  $T_c$ ) and a relation between  $\Delta H^\circ$  and  $\Delta S^\circ$ . The fourth parameter may be obtained by fits using Eqs. (17)-(19) to the excess thermodynamic properties  $\Delta C_P$ ,  $V\Delta\alpha$  and  $V\Delta\kappa$  in the supercooled regime. There is a problem in this undertaking, namely, dissection of the experimental  $C_P$ ,  $V\alpha$  and  $V\kappa$  data into the excess parts arising from the  $T$  and  $P$  dependence of the species concentrations and the "background" contributions [14,21,27,28]. To avoid introducing additional adjustable parameters, we made the approximation that the "background" contributions are temperature independent in the region covered by the data from 277K (the  $T$  of maximum density at 1 atm) down to 236K. Using  $C_P$  and  $V\alpha$  as examples, we are thus assuming that in this  $T$  range

$$\Delta C_P(T) - \Delta C_P(277K) \approx C_P(T) - C_P(277K) \quad (24a)$$

$$V\Delta\alpha(T) - V\Delta\alpha(277K) \approx V\alpha(T) - V\alpha(277K) \quad (24b)$$

and will fit the data in this form. Judging from experimental estimations of the "background" contributions for  $H_2O$  by Angell and coworkers [21,27,28], this approximation is not likely to inject serious errors into the data analysis.

Shown in Fig. 5 are plots vs.  $T$  of the heat capacity data of Angell et al. [29] for supercooled water at 1 atm displayed in the form of Eq. (24a). Also shown are three  $[\Delta C_P(T) - \Delta C_P(277K)]$  vs.  $T$  curves calculated from Eq. (17) using the parameters in Eqs. (22a,c) and (23) for different values of  $\Delta S^\circ/R$ . The best fit to the data in Fig. 5 corresponds to  $\Delta S^\circ/R = 0.98$ , and curves calculated using the other two  $\Delta S^\circ/R$  values, which differ by only  $\pm 10\%$  from the best fit value, are clearly incompatible with the data. In Fig. 6 is shown a similar plot for the thermal expansion coefficient data for supercooled  $H_2O$  at 1 atm obtained from the specific volumes reported in Ref. [14], along with the best fit curve calculated from Eq. (18) and the parameters in Eqs. (22a,c) and (23). The best fit  $\Delta S^\circ/R$  value ( $= 0.98$ ) for the  $V\alpha$  data is the same as that for the  $C_P$  data. Fits similar to those in Figs. 5 and 6 were also carried out using Eq. (19) for the temperature dependence of the isothermal compressibility  $V\kappa$  data [27] of supercooled water at three different pressures - 10, 50 and 100 MPa. The corresponding best fit  $\Delta S^\circ/R$  values were 1.13, 0.98 and 0.82, which on the average are equal to and individually deviate no more than 16% from the best fit  $\Delta S^\circ/R$  value for the  $C_P$  and  $V\alpha$  data.

In view of the degree of approximation introduced into these analyses by our assumption of  $T$  independent "background" contributions, it appears that the

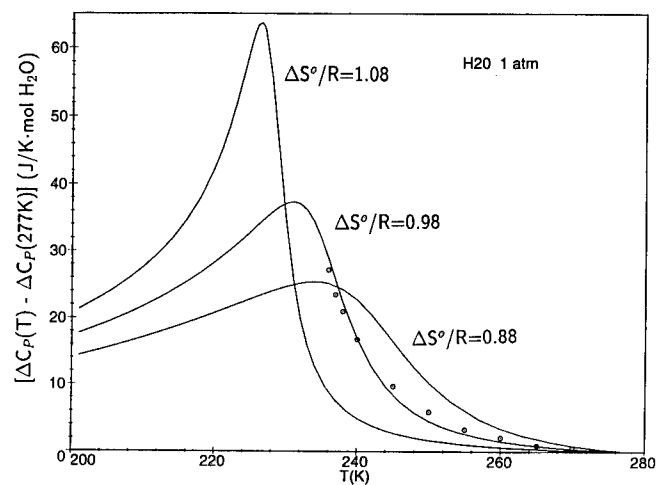


**Figure 5.** Heat capacity of supercooled water at 1 atm plotted in the form of Eq. (24a) vs.  $T$ . Points (o) are experimental data from Ref. [29]. Curves were calculated using Eq. (17) and the parameters in Eqs. (22a,c) and (23) for three  $\Delta S^\circ/R$  values.

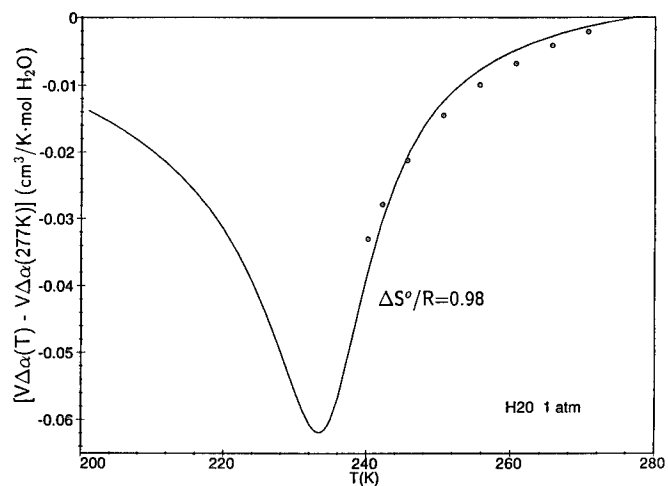


**Figure 6.** Product of molar volume  $V$  times thermal expansion coefficient  $\alpha$  of supercooled water at 1 atm plotted in the form of Eq. (24b) vs.  $T$ . Points (o) were obtained from experimental data in Ref. [14]. Curve is best fit of data to Eq. (18) using the parameters in Eqs. (22a,c) and (23).

thermodynamic data for supercooled water as well as the a/a transformation data in Fig. 3 are well described by the two species/nonideal solution model (assuming H<sub>2</sub>O as the species formula) using the  $\Delta V^\circ$  and  $W$  or  $T_c$  values in Eqs. (22a,c) along with values of

$$\Delta S^\circ = 0.98R = 8.1 \text{ J/mol H}_2\text{O} \cdot \text{K} \quad (25)$$

and, via Eq. (23),

$$\Delta H^\circ = 1940 \text{ J/mol H}_2\text{O} \quad (26)$$

Given the previously mentioned similarity of LDA H<sub>2</sub>O to ice I and of HDA H<sub>2</sub>O to ordinary liquid water, one might expect these  $\Delta S^\circ$  and  $\Delta H^\circ$  values to be smaller than but of the same order of magnitude as the entropy of fusion (= 22.0 J/mol H<sub>2</sub>O·K) and the enthalpy of fusion (= 6010 J/mol H<sub>2</sub>O) of ice I to form liquid H<sub>2</sub>O at 273K. This is indeed the case.

Using the value of  $P_{aa} = 1850 \text{ atm}$  at  $T_{aa} = 135\text{K}$  from Fig. 3, the critical pressure  $P_c$  at temperature  $T_c = 217\text{K}$  may be calculated from Eq. (13):

$$P_c = 380 \text{ atm} \quad (27)$$

Shown in Fig. 7 is a  $T$  vs. specific volume equilibrium phase diagram calculated using the parameters in Eqs. (22a,c), (25) and (26) for the a/a transition in water. Corresponding a/a transition pressures are also shown at several  $T$ 's along the coexistence line. The starting points for the calculation were the experimental LDA and HDA  $v$  values in Fig. 3 at 135K and 1850 atm. In addition, "background" values of the thermal expansion coefficient  $\alpha_{bkg} (= 0.46 \times 10^{-3} \text{K}^{-1})$  and isothermal compressibility  $\kappa_{bkg} (= 1.62 \times 10^{-5} \text{atm}^{-1})$ , estimated from data in Refs. [27,28] and assumed to be  $T$  and  $P$  independent and the same for both the LDA and HDA species, were used in the calculation. The  $T_c$  and  $v_c$  values - 217K and 1.01 cm<sup>3</sup>/g - at the critical point (the maximum) in Fig. 7 are in rather good agreement with the values - 235K and 1.02 cm<sup>3</sup>/g - estimated from MD calculations in Ref. [23], but not so for the  $P_c$  values - 380 atm vs. 1970 atm.

#### Analysis Assuming Other Formulae for the Species in Water

We discuss here an important feature of the present model which seems to have been overlooked in earlier papers [9,12,25], namely, that in analysis of actual experimental data one must make an assumption about the formula of the species and that the results of the analysis, such as the value calculated for  $T_c$ , are strongly conditioned by this assumption. Equation (4) is an expression for the relative free energy  $\Delta G$  of one mole total of interconvertible species (A plus B), not one mole of molecular formula units of the substance. Suppose, for example, we had assumed above that the formula of the species in water was (H<sub>2</sub>O)<sub>2</sub> instead of H<sub>2</sub>O, e.g., that the LDA and HDA species were respectively fully associated and partially associated pairs of H<sub>2</sub>O molecules. This assumption would double the species molecular weight  $M$  (36.0 g/mol (H<sub>2</sub>O)<sub>2</sub> instead of 18.0 g/mol H<sub>2</sub>O), which via Eqs. (21) and (12) would in turn double the initial estimates of  $\Delta V^\circ$  and  $\ln K$  to be used in Eq. (4). The entropy of mixing terms -  $(1 - X)RT \ln(1 - X)$  and  $XRT \ln X$  - in Eq. (4), however, are for mixing of one mole total of the two species and are not changed. The net result is that the value of  $W$  obtained via subsequent calculations using Eq. (4) (as in Fig. 4) assuming (H<sub>2</sub>O)<sub>2</sub> as the species formula differs from (and is not simply twice) the

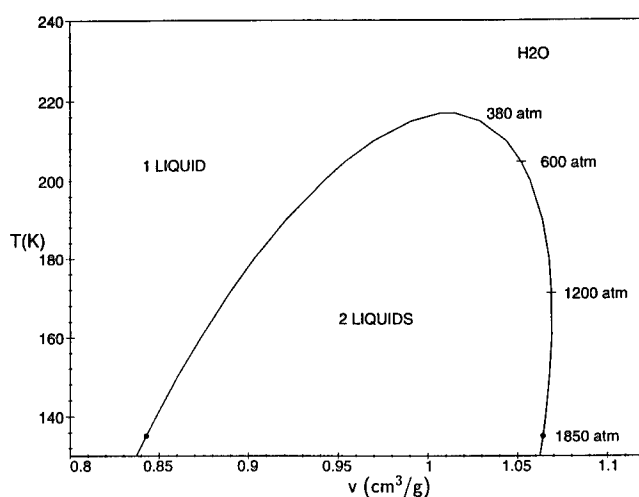


**Figure 7.** Temperature vs. specific volume equilibrium phase diagram calculated for the a/a transition in water. Points (o) are experimental values from Fig. 3.  $P_{aa}$  values are shown at several  $T$ 's along the coexistence line.

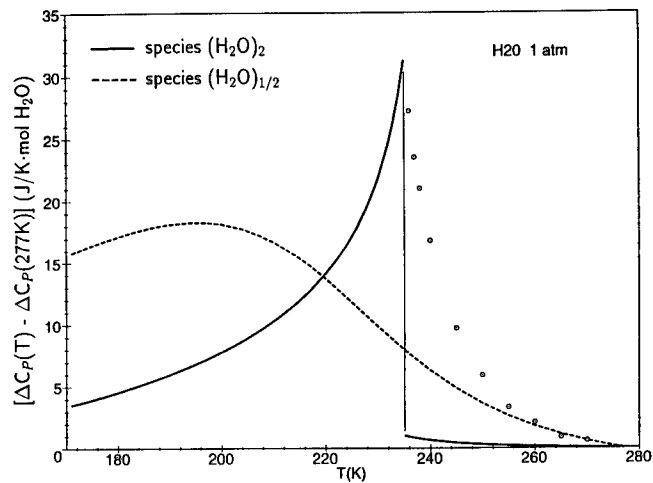


**Figure 8.** Best fits to  $C_p$  vs.  $T$  data (o) for supercooled water at 1 atm attainable assuming  $(H_2O)_2$  (—) and  $(H_2O)_{1/2}$  (---) as species formulae. Best fit curve for  $(H_2O)_2$  formula displays an a/a transition just below 236K.

$W$  value obtained assuming  $H_2O$  as the species formula. The value of  $T_c$  obtained from Eq. (7), where the units of  $W$  must be taken as "J/mol species", is consequently also changed.

To illustrate this, the data for water in Fig. 3 were analyzed as in the previous section assuming a variety of other species formulae -  $(H_2O)_{1/2}$ ,  $(H_2O)_2$  and  $(H_2O)_5$ . The  $(H_2O)_{1/2}$  formula would be appropriate if one identified the LDA and HDA species with strong and weak forms of the O-H-O linkages between neighboring water molecules, since there are two moles of such linkages per mole of  $H_2O$  molecules. The  $(H_2O)_5$  formula might be appropriate if one assumed, as has been suggested [14], that the difference between LDA  $H_2O$  and HDA  $H_2O$  is due to structure differences involving O...O second nearest neighbors. The  $T_c$  values obtained from these analyses are listed below.

$(H_2O)_{1/2}$ species	$T_c = 190K$	
$(H_2O)_2$ species	$T_c = 265K$	(28)
$(H_2O)_5$ species	$T_c = 390K$	

However, if one now proceeds to fit the excess thermodynamic properties of supercooled water assuming these alternative species formulae, it is found that acceptable agreement with the data cannot be achieved. This is illustrated in Fig. 8, which shows the best fits to the  $C_P$  data obtainable for the formulae  $(H_2O)_{1/2}$  and  $(H_2O)_2$ . Note that the high  $T_c$  values produced by assuming the  $(H_2O)_2$  and  $(H_2O)_5$  formulae pose special problems, since these  $T_c$  values fall within the temperature range of experimental data for liquid water, and in this range no a/a transitions have been observed at positive pressures up to 1900 atm [21,27]. The only solution to this dilemma is to assume that the corresponding critical pressures  $P_c$  are highly negative, so that via Eq. (13) and the negative values of  $\Delta V^\circ$  the a/a transition pressure becomes positive only below the lowest temperature at which experimental data have been measured, e.g., below 236K for the  $C_P$  data. As a consequence, the best fit curve for the  $C_P$  data in Fig. 8 for formula  $(H_2O)_2$  exhibits an a/a transition and a discontinuity in  $C_P$  just below 236K.

It thus appears that  $H_2O$  is the only species formula capable of describing the data for water using the two species/nonideal solution model. Taken in a positive sense, this may mean the model can provide some information on the structures of the polyamorphs involved in an a/a transition, in much the same way that the magnitude of the freezing point depression observed for a dilute solution of a solute in water allows one to determine whether or not the solute is highly dissociated in aqueous solution. For the case of water, the present results suggest that structural differences between the LDA and HDA forms are at the level of individual  $H_2O$  molecules, which counters to a degree criticism levelled in Ref. [14] against MD simulations [2,23] for liquid water. In a possibly more realistic sense, however, our finding that the predictions of the model depend on the formula assumed for the species may simply mean that the model contains five, not four, adjustable parameters.

## DISCUSSION AND CONCLUSIONS

The two species/nonideal solution model for liquids, as presented here, can be expected to give at best a semiquantitative account of actual data. This is evident, first, if one compares our present analysis of the data for water with that carried out using a "mixture model" by Vedamuthu et al. [14]. These investigators found that four adjustable parameters characterizing changes in the species concentrations were needed to describe

within experimental error the variation in one equilibrium property, volume  $V$ , over a modest  $T$  range (239 to 313K) at a single pressure (1 atm). Here we have used a model with four analogous adjustable parameters to describe the variation in two properties of water,  $V$  and  $H$ , over a much larger  $T$  range (135 to 277K) and a large  $P$  range (1 to 1850 atm). Second, the simple regular solution expression for mixing of components in a binary solution is an approximation and is expected to work well only at high  $T$ 's ( $T/T_c \geq 2$ ) [19]. Here we have used simple regular solution thermodynamics at much lower  $T$ 's ( $0.6 \leq T/T_c \leq 1.3$ ) in analyzing the  $H_2O$  data. Third, the two species/nonideal solution model contains only one internal or order parameter, the species mole fraction  $X$  associated with reaction (1). All known experimental values of the Prigogine-Defay ratio for liquids indicate that two or more internal parameters are needed to account for their excess thermodynamic properties [17].

Keeping the above comments in mind, the two species/nonideal solution model nonetheless provides an excellent, lowest-order-of-approximation equation of state (Eq.(4)) for interpreting and gaining insight into experimental data relevant to the a/a transition in liquids. For example, all liquids exhibit the structural relaxation process and hence conform to the presumption of the model of the existence of interconvertible species. However, Eq. (16) imposes a rather severe thermodynamic constraint on the occurrence of an a/a transition. Hence one might expect that the species interconversion and mixing thermodynamics will satisfy Eq. (16) and that an a/a phase transition can take place only for a subset - possibly a small minority - of liquids. Note further that, presuming  $W > 0$ , the likelihood of satisfying Eq. (16) is enhanced at positive  $P$ 's if the value of  $\Delta V^\circ$  for the conversion of the low  $T$  species to the high  $T$  species is negative. It is possibly no accident that most of the liquids or amorphous solids for which an a/a transition has either been observed or is strongly indicated, e.g.,  $H_2O$ ,  $SiO_2$ ,  $Si$  and  $Al_2O_3$ - $Y_2O_3$  [2], meet this  $\Delta V^\circ < 0$  condition.

Finally, it is worth noting that the two species/nonideal solution model need not be viewed as an exotic treatment put forward only to explain a/a transitions or unusual crystal/crystal transitions. As should be immediately apparent from Eqs. (12) and (13), Eq. (4) is a robust equation of state capable of describing any first order transition between one component condensed phases, where the assumption of constant  $\Delta H^\circ$ ,  $\Delta S^\circ$  and  $\Delta V^\circ$  values is a reasonable approximation. Ordinary crystal/crystal and crystal/liquid transitions, which exhibit no signs of critical point behavior, may be thought of as limiting cases of this model for which  $T \ll T_c$  in the experimental data range. Note from Fig. 7 that indications of critical point behavior - marked bending of the two coexistence lines toward one another to merge at the critical point - appear in the phase diagram only at  $T$ 's near  $T_c$ . In this perspective, observation of ordinary crystal/crystal phase transitions is presumably truncated by the intervention of melting and subsequent observation of crystal/liquid phase transitions truncated in turn by sublimation/vaporization at  $T$ 's well below the relevant  $T_c$ 's. That the critical temperatures for these ordinary condensed phase/condensed phase transitions should be extraordinarily high is also not surprising in the context of the model, given the result exemplified by Eq. (28) that a high value of  $T_c$  is expected for interconvertible species which contain many atoms or molecules. Literal application of the model to an fcc  $\rightarrow$  hcp transition in crystalline metal  $M$  would, for example, require the presumption of species formulae no smaller than  $M_{13}$ .

## ACKNOWLEDGMENTS

The author wishes to thank C. A. Angell, T. Grande, P. F. McMillan, P. H. Poole and H. E. Stanley for extremely helpful discussions and correspondence on this topic.

## REFERENCES

1. C. A. Angell, *Science* **267**, 1924 (1995).
2. P. H. Poole, T. Grande, F. Sciortino, H. E. Stanley and C. A. Angell, *Comput. Mater. Sci.* **4**, 373 (1995).
3. P. K. Gupta, *J. Non-Cryst. Solids* **195**, 158 (1996).
4. P. H. Poole, T. Grande, C. A. Angell and P. F. McMillan, *Science* **275**, 322 (1997).
5. O. Mishima, K. Takemura and K. Aoki, *Science* **254**, 406 (1991).
6. S. Aasland and P. F. McMillan, *Nature* **369**, 633 (1994).
7. P. F. McMillan, C. Ho, S. Aasland, A. Yeganeh-Haeri and R. Weber, this volume.
8. I. Cohen, A. Ha, X. Zhao, M. Lee, T. Fischer, M. J. Strouse and D. Kivelson, *J. Phys. Chem.* **100**, 8518 (1996).
9. E. Rapoport, *J. Chem. Phys.* **46**, 2891 (1967); **48**, 1433 (1968).
10. C. M. Davis, Jr., and T. A. Litovitz, *J. Chem. Phys.* **42**, 2563 (1965).
11. P. B. Macedo, W. Capps and T. A. Litovitz, *J. Chem. Phys.* **44**, 3357 (1966).
12. I. L. Aptekar and E. G. Ponyatovskii, *Fiz. Metal. Metalloved.* **25**, 777 (1968); **25**, 1049 (1968).
13. O. V. Mazurin and V. K. Leko, *Sov. J. Glass Phys. Chem.* **9**, 113 (1983).
14. M. Vadamuthu, S. Singh and G. W. Robinson, *J. Phys. Chem.* **98**, 2222 (1994).
15. K. J. Rao and C. A. Angell, in *Amorphous Materials*, edited by R. W. Douglas (Wiley-Interscience, New York, 1972), pp. 171-181.
16. C. A. Angell and K. J. Rao, *J. Chem. Phys.* **57**, 470 (1972).
17. P. K. Gupta and C. T. Moynihan, *J. Chem. Phys.* **65**, 4136 (1976); C. T. Moynihan and P. K. Gupta, *J. Non-Cryst. Solids* **29**, 143 (1978).
18. C. T. Moynihan, in *Reviews in Mineralogy*, Vol. **32**, edited by J. F. Stebbins, P. F. McMillan and D. B. Dingwell (Mineralogical Soc. of America, Washington, DC, 1995), pp. 1-19.
19. See any text on chemical or materials thermodynamics.
20. O. Mishima, *J. Chem. Phys.* **100**, 5910 (1994).
21. C. A. Angell, in *Water-A Comprehensive Treatise*, Vol. **7**, edited by F. Franks (Plenum, New York, 1982), pp. 1-81.
22. C. A. Angell, *Ann. Rev. Phys. Chem.* **34**, 593 (1983).
23. F. Sciortino, P. H. Poole, U. Essmann and H. E. Stanley, *Phys. Rev. E* **55**, 727 (1997).
24. P. H. Poole, F. Sciortino, T. Grande, H. E. Stanley and C. A. Angell, *Phys. Rev. Lett.* **73**, 1632 (1994).
25. E. G. Ponyatovskii, V. V. Sinand and T. A. Pozdnyakova, *JETP Lett.* **60**, 360 (1994).
26. H. E. Stanley, private communication following a visit by him to Mishima's laboratory.
27. H. Kanno and C. A. Angell, *J. Chem. Phys.* **70**, 4008 (1979).
28. R. J. Speedy and C. A. Angell, *J. Chem. Phys.* **65**, 851 (1976).
29. C. A. Angell, M. Oguni and W. J. Sichina, *J. Phys. Chem.* **86**, 998 (1982).

**Part VI**

**Structure and Dynamics of Glasses  
and Glass Formers**



## DEVELOPMENT OF THE GLASSY STATE OF BENZOPHENONE AND EFFECT OF HEATING RATE FROM THE GLASSY STATE ON SOLIDIFICATION

Paul E. Thoma and John J. Boehm  
Johnson Controls, Inc., Central Research, P.O. Box 591, Milwaukee, WI 53201-0591 USA

### ABSTRACT

Benzophenone supercools to a glass when cooled to  $-100^{\circ}\text{C}$ . In fact, it is difficult to freeze benzophenone on cooling. In this investigation, the effect of cooling rate and the minimum cooling rate to obtain benzophenone as a glass is determined. From the glassy state, the influence of heating rate on the solidification temperature of benzophenone is determined. When heated at  $3^{\circ}\text{C}/\text{min}$ , solidification starts at about  $-29^{\circ}\text{C}$ . Upon additional heating, melting usually starts at about  $+24^{\circ}\text{C}$ , which is  $23^{\circ}\text{C}$  lower than the solid equilibrium structure melting temperature of  $47^{\circ}\text{C}$ . Occasionally the solid that forms at about  $-29^{\circ}\text{C}$  undergoes a solid state phase transformation at about  $+22^{\circ}\text{C}$ , when heated at  $3^{\circ}\text{C}/\text{min}$ . If this solid state phase transformation occurs, then the solid benzophenone starts to melt at  $47^{\circ}\text{C}$ . When solid benzophenone with the equilibrium structure is cooled to  $-100^{\circ}\text{C}$ , no solid state phase transformation occurs. It appears that the structure that solidifies at  $-29^{\circ}\text{C}$  is metastable.

### INTRODUCTION

Many polymers, such as polyethylene terephthalate (PET), have a solidification temperature that is dependent on cooling rate. As the cooling rate increases, the solidification temperature of PET decreases. At a cooling rate greater than about  $50^{\circ}\text{C}/\text{min}$ , homopolymer PET does not crystallize, but instead becomes a glass at low temperatures. When heated from the glassy state, spontaneous solidification (crystallization) occurs. Solidification starts around  $140^{\circ}\text{C}$  when the heating rate is  $30^{\circ}\text{C}/\text{min}$ .

Most simple organic compounds, when cooled, do not supercool very much before solidification occurs. However, Thoma [1] shows that a class of simple organic compounds having a three-dimensional partially charged pocket and a partially charged projection of opposite charge do supercool significantly. When in the liquid state, the attraction between neighboring molecules is significant and the probable reason for supercooling. The partially charged projection of one molecule is attracted to the oppositely charged pocket of another molecule and forms an ordered structure that hinders solidification. When the structure of a molecule promotes a strong attractive interaction between neighboring molecules, the amount of supercooling is so great that a glass forms when the liquid is cooled. Thoma [1] shows that 4-methylbenzophenone supercools and forms a glass at low temperatures ( $-56^{\circ}\text{C}$ ).

Benzophenone also supercools and forms a glass at low temperatures. The purpose of this investigation is to determine the influence of cooling rate on the ability of benzophenone to form a glass. It is also a purpose of this investigation to determine the effect of heating rate from the glassy state on the solidification of benzophenone and the subsequent melting of the solid phase.

### MATERIAL AND TEST METHODS

The experimental material used in this investigation is benzophenone having a purity of 99.9% (GLC) and is obtained from Aldrich Chemical Company, Inc. The structure of benzophenone is shown in Figure 1.

Differential scanning calorimetry (DSC) [2] is used to determine the transformation temperatures of benzophenone. TA Instruments DSC test equipment and 0.25 inch x 0.25 inch x 0.004 inch glass slides (reference and sample pans) are used. A DSC sample having a weight of  $2.0 \pm 0.5$  mg is used. When determining the effect of cooling rate on the development of the glassy state, the DSC sample is heated from room temperature to  $65^{\circ}\text{C}$  (sample melts) and then cooled to  $<-100^{\circ}\text{C}$ . The heating rate during sample melting and the cooling rate during the cooling portion of

the test are controlled and the same. The rate values used are 0.3, 1, and 30°C/min. When determining the effect of heating rate from the glassy state on the solidification of benzophenone, the DSC sample is heated from room temperature to 65°C (sample melts), cooled to <-100°C at the rate of 30°C/min., and then heated to 65°C. The controlled heating rates used during the heating portions of the test are 0.3, 1, 3, 10, and 30°C/min.

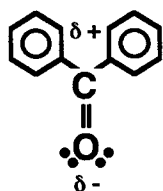


Figure 1. Structure of benzophenone.

## RESULTS AND DISCUSSION

When solid benzophenone is heated, melting starts between 46.7°C and 47.9°C, and is not dependent on heating rate (Table I).

Table I - Effect of Heating Rate on the Melting of Benzophenone

Heating Rate, °C/minute	Start of Melting, °C			Number of Samples
	Average	High	Low	
0.3	47.3	47.6	47.0	14
1	47.3	47.8	47.1	15
3	47.3	47.6	47.1	8
10	46.7	47.1	46.2	14
30	47.9	48.5	47.6	8

When benzophenone is cooled from the liquid state, it is difficult to solidify benzophenone. Thoma [1] shows that benzophenone does not solidify when cooled to -100°C at the rate of 2°C/min. The supercooling of benzophenone is attributed to its molecular characteristics. Benzophenone (Figure 1) consists of two phenyl groups joined to a carbon atom by single bonds and an oxygen atom joined to the carbon atom by a double bond. The phenyl groups are free to rotate and form a permanent three-dimensional pocket with the carbon atom. The oxygen atom is at a fixed position in relation to the phenyl groups. A bond angle of about 120° exists between the two phenyl groups and the carbon atom, and between a phenyl group, the carbon atom, and the oxygen atom. A charge gradient exists across the molecule with the oxygen atom acting as a partially charged projection from the benzophenone molecule. The permanent three-dimensional pocket formed by the rotating phenyl groups is also partially charged, but of opposite sign. The partially charged oxygen atom is attracted to the oppositely charged pocket of another molecule. The attraction between neighboring molecules and fit of the oxygen atom in the pocket are probably responsible for the supercooling of benzophenone.

In this study, liquid benzophenone is cooled at rates of 0.3, 1, and 30°C/min. to a temperature of <-100°C. Solidification does not occur at cooling rates of 1 and 30°C/min. This is in agreement with the findings of Thoma [1] at a cooling rate of 2°C/min. However, at a cooling rate of 0.3°C/min., 3 of 7 samples solidify with an average start of solidification of -30.5°C (Table II), which is about 78°C below its melting temperature. These results show that it is difficult to solidify benzophenone on cooling and that its solidification is cooling rate dependent. When solidification does not occur during cooling to <-100°C, benzophenone becomes a glass.

Figures 2 and 3 are heating portions of DSC plots at heating rates of 1 and 10°C/min. Heating starts from a temperature of <-100°C, after being rapidly cooled (30°C/min.) to <-100°C as a liquid. At approximately -60°C, a glass transition is observed (Figure 3). The presence of a glass transition indicates that benzophenone forms a glass when cooled to -100°C.

Table II - Effect of Cooling Rate on the Solidification of Benzophenone

Cooling Rate, °C/minute	Start of Solidification, °C			Number of Samples
	Average	High	Low	
0.3	-30.5	-28.2	-32.8	3 of 7 samples solidified
1	No samples solidified			0 of 7 samples solidified
30	No samples solidified			0 of 8 samples solidified

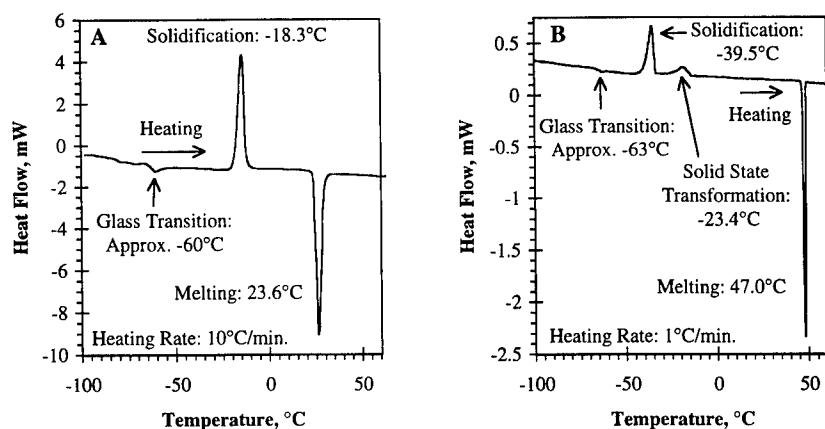


Figure 2. Heating portion of DSC plots of benzophenone.

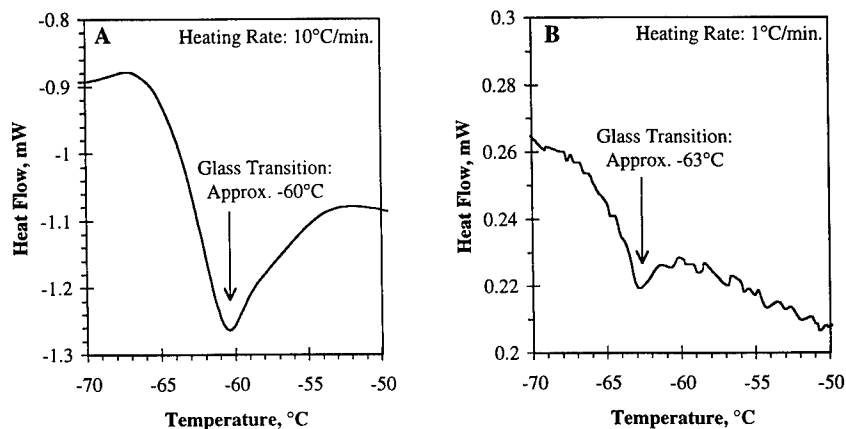


Figure 3. Heating portion of DSC plots of benzophenone showing glass transition.

When heated from the glassy state at heating rates of 0.3, 1, 3, and 10°C/min., solidification occurs at a temperature that is dependent on the heating rate (Figure 4). The slower the heating rate; the lower the solidification temperature. The graph in Figure 4 shows that a near linear relationship exists between solidification temperature and heating rate on a log scale. There is also a trend that a greater percentage of samples solidify as the heating rate decreases. At a heating rate of 0.3°C/min., all of the samples solidify, and at a heating rate of 10°C/min, 50% of the samples solidify. No samples solidify at a heating rate of 30°C/min.

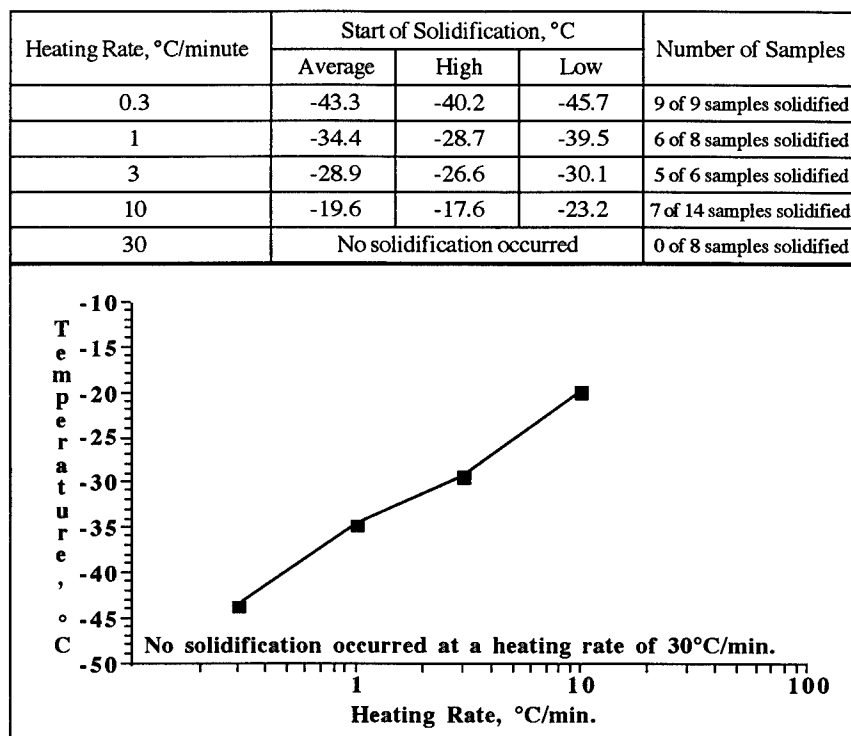


Figure 4. Effect of heating rate from the glassy state on the solidification of benzophenone.

When solidified benzophenone is heated to higher temperatures, melting eventually occurs (Table III). At the lowest heating rate of 0.3°C/min., all of the samples start melting at about 47°C. However, at a heating rate of 1°C/minute, 50% of the samples start melting at about 47°C (Figure 2B) and 50% of the samples start melting at 24.7°C. When the heating rate is 3°C/min., 20% of the samples start melting at about 47°C and 80% of the samples start melting at 24.2°C. All of the samples start melting at about 23.7°C when the heating rate is 10°C/min. (see Figure 2A). Since no samples solidify at a heating rate of 30°C/min., no samples melt. These results show that benzophenone can melt at two different temperatures, and that the temperature at which benzophenone melts is dependent on the heating rate. Benzophenone melts at a higher temperature (about 47°C) when it solidifies and melts at lower heating rates (0.3°C/min.). Benzophenone melts at a lower temperature (about 24°C) when it solidifies and melts at higher heating rates (10°C/min.) (Figure 2A). However, all of the solid as-purchased benzophenone melts at about 47°C regardless of heating rate (see Table I).

Examination of the DSC plot of benzophenone at a heating rate of 1°C/min. (Figures 2B and 5)

shows that after solidification occurs a second exothermic peak occurs that starts at  $-23.4^{\circ}\text{C}$ . This peak is attributed to a solid state phase transformation in which the structure that forms during solidification transforms to another structure that melts at  $47^{\circ}\text{C}$ . When the structure that forms during solidification does not transform in the solid state (Figure 2A), then melting occurs at about  $24^{\circ}\text{C}$ . The solid state phase transformation is also dependent on heating rate (Table IV). At a heating rate of  $10^{\circ}\text{C}/\text{min.}$ , the solid state transformation does not occur. At a heating rate of  $3^{\circ}\text{C}/\text{min.}$ , the solid state transformation starts at  $22^{\circ}\text{C}$ , which is slightly lower than the start of melting of benzophenone if the solid state transformation does not occur. As the heating rate decreases, the solid state transformation temperature also decreases. At heating rates of 0.3 and  $1^{\circ}\text{C}/\text{min.}$ , the average start of the solid state transformation is  $-21.5^{\circ}\text{C}$ .

Is the structure that solidifies when benzophenone is heated from the glassy state a metastable structure or a low temperature equilibrium structure? To resolve this question, solid as-purchased benzophenone is slowly cooled at the rate of  $0.3^{\circ}\text{C}/\text{min.}$  to  $-100^{\circ}\text{C}$ . The DSC plots show no solid

Table III - Effect of Heating Rate from the Glassy State on the Melting of Benzophenone

Heating Rate, $^{\circ}\text{C}/\text{minute}$	Start of Melting, $^{\circ}\text{C}$			Number of Samples
	Average	High	Low	
0.3	47.1	47.4	47.0	3 of 3 samples melted
1	47.0	47.0	46.9	3 of 3 samples melted
	24.7	24.7	24.6	3 of 3 samples melted
3	46.8	46.8	46.8	1 of 1 sample melted
	24.2	24.6	24.0	4 of 4 samples melted
10	23.7	24.0	23.6	7 of 7 samples melted
30	No solidification occurred, therefore, no melting occurred			None

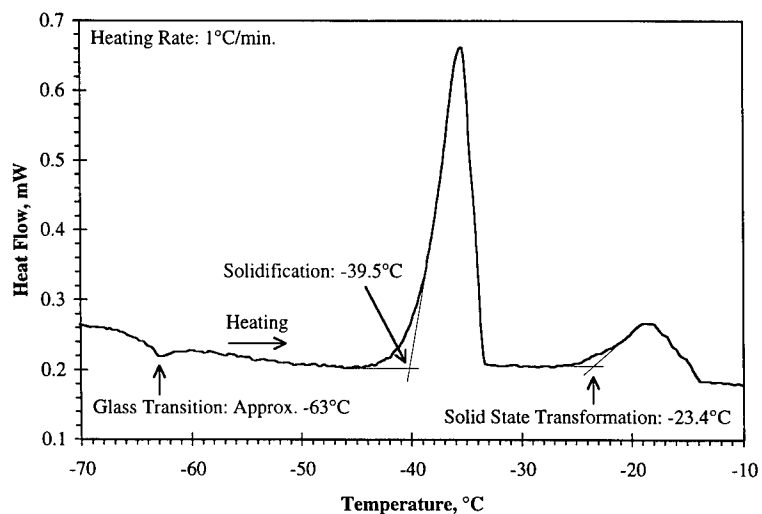


Figure 5. Heating portion of DSC plot of benzophenone showing transformations

Table IV - Effect of Heating Rate from the Glassy State on a Solid State Phase Transformation

Heating Rate, °C/minute	Start of Solid State Transformation, °C			Number of Samples
	Average	High	Low	
0.3	-21.4	-5.3	-29.3	4 of 4 samples transformed
1	-21.5	-19.8	-23.4	3 of 6 samples transformed
3	+22.0	+22.0	+22.0	1 of 5 samples transformed
10	None			0 of 7 samples transformed
30	No solidification occurred, therefore, no solid state transformation occurred			None

state phase transformation during the slow cooling run, which suggests that the solid that forms when benzophenone is heated from the glassy state is a metastable structure. This apparent metastable structure transforms to an equilibrium structure if slowly heated.

It is important to comment on the melting characteristics of the solid that forms during slow cooling of the liquid. Liquid benzophenone supercools and occasionally solidifies at about -30°C when cooled at the rate of 0.3°C/min. (Table II). When rapidly heated (30°C/min.), the solid either melts near 24°C or undergoes a solid state phase transformation and melts near 47°C. These results indicate that the apparent metastable solid forms from the liquid upon slow cooling and when benzophenone is heated from the glassy state.

## CONCLUSIONS

Results obtained in this investigation indicate that benzophenone has the following properties:

- Benzophenone is difficult to solidify on cooling and its solidification is cooling rate dependent;
- If benzophenone does not solidify on cooling, it becomes a glass;
- When heated from the glassy state, the solidification of benzophenone is heating rate dependent;
- The solid that forms, when benzophenone is heated from the glassy state, appears to be a metastable structure that melts at a lower temperature than the equilibrium solid;
- The solid that forms, when benzophenone is cooled and supercools, appears to be a metastable structure;
- The apparent metastable solid transforms in the solid state to an equilibrium solid, and the solid state transformation temperature is heating rate dependent.

## REFERENCES

1. P.E. Thoma, "A Mechanism for Supercooling in Organic Liquids", Thermodynamics and Kinetics of Phase Transformations, Materials Research Society Symposium in Boston, MA (Nov. 27 - Dec. 1, 1995), J.S. Im, B. Park, A.L. Greer and G.B. Stephenson Eds. (Materials Research Society, Pittsburgh, PA, USA, Vol. 398, 1996) pp. 87-92.
2. T. Hatakeyama and F.X. Quinn, Thermal Analysis - Fundamentals and Applications to Polymer Science, John Wiley & Sons, Chichester, England, 1994, pp. 5-17.

## STRUCTURAL STUDIES OF RARE-EARTH DOPED PHOSPHATE GLASSES

A. Matic \*, L. Börjesson\*, A. Wannberg \*\*, R. L. McGreevy \*\*

\*Dept. of Applied Physics, Chalmers University of Technology, S-412 96 Göteborg, Sweden, matic@fy.chalmers.se

\*\* Studsvik Neutron Research Laboratory, S-611 82 Nyköping, Sweden

### ABSTRACT

We have performed neutron scattering experiments on rare-earth (La, Pr, Ho) doped phosphate glasses around the metaphosphate composition  $R(PO_3)_3$ . Combining the diffraction experiment with Reverse Monte Carlo simulations we obtain a 3-D model of the structure. Our models propose a rare-earth ion environment primarily consisting of oxygens with the average rare earth-oxygen distances; 2.56, 2.51 and 2.40 Å for the La, Pr and Ho samples respectively. We also observe that the rare earth ions are not uniformly distributed. The first R-R shell is on average about 3.3 Å to be compared with a value of 7 Å for a uniform distribution of R ions in the structure. From the models we also conclude that a chain like structure of the phosphate network is in agreement with the experiment.

### INTRODUCTION

Phosphate glasses display features that make them attractive to use in various applications. In general the glasses have low losses from the UV to IR region, they can be chemically modified in several ways and preparation is usually easy due to moderate melting temperatures and the ease of glass formation. With rare-earth ion doping the phosphate glasses will also display interesting luminescent and magnetic properties. The materials are then of potential for applications in opto-electronics and laser technology. The rare-earth doped phosphates have also been used as model systems to study low frequency dynamics in the glassy state [1].

Vitreous  $P_2O_5$  is a classical network glass (together with  $SiO_2$ ,  $B_2O_3$  and  $GeO_2$  glasses). The structure is a 3-dimensional network of interconnected  $-PO_4-$  tetrahedra. In a pure phosphate glass the tetrahedra are linked through three of the oxygens while the fourth oxygen is doubly bonded to the phosphorus atom and does not participate in the network formation [2].  $v-P_2O_5$  is a very unstable and volatile glass and applications are limited, if any. When a modifier oxide is added, e. g. a rare-earth oxide ( $R_2O_3$ ), the network breaks up creating non bridging oxygens in the structure which coordinate the metal ions of the modifier oxide. With increasing amount of modifier oxide the number of non-bridging oxygens, per  $PO_4$  unit, will go from zero, for the unmodified glass, up to three for orthophosphates. The compound formed when a modifier oxide is added will usually be more stable than the pure phosphate glass; the metaphosphate composition,  $R(PO_3)_x$ , is especially stable and hence suitable for applications. At this composition the host structure consists principally of chains of corner linked  $PO_4$  tetrahedra with 2 non-bridging oxygens per tetrahedron. The metal ions of the modifier oxide will not participate in the network but will associate to the non-bridging oxygens.

Previous structural studies of rare-earth phosphate glasses report inter atomic distances and coordination numbers for the rare-earth ions [3], [4]. The results show that the oxygen-rare earth distances shorten with atomic number, in agreement with the lanthanide radius contraction. The average coordination numbers are reported to be between 5 and 9, assuming oxygen as the only nearest neighbours. There have also been some indications that even though glasses are at the metaphosphate composition the structure is more three dimensional than chain like as in e. g. silver-metaphosphate glasses. The reason for this is suggested to be that the high valence of the rare-earth ions,  $R^{3+}$ , causes a increased branching of the chains and cross linking.

In this work we have investigated the structure of rare-earth doped metaphosphate glasses,  $R(PO_3)_3$  with  $R=La, Pr, Ho$ , using neutron diffraction and reverse Monte Carlo (RMC) simulations. From RMC simulations we obtain 3-D structural models from which partial correlations, coordination numbers and inter atomic distances can be determined. The aim is to gain further insight in the glass structure, in particular the structure around the rare-earth ions, in order to contribute to the understanding of the relationships between structural modifications, induced by the rare-earth additives, and the luminescent and magnetic properties.

## EXPERIMENT

The samples used in this work were made by standard melt quenching methods and the procedure is described elsewhere [5]. In the experiment the La- and Ho-sample were in powder form while the Pr sample was in the shape of a glass rod.

The neutron diffraction experiments were performed at the Liquid and Amorphous materials Diffractometer (SLAD) at the Studsvik Neutron Research Laboratory, Sweden. The incident neutrons had a wavelength of 1.1 Å and were detected at 2θ angles between 3° and 135° (corresponding to  $0.3 \text{ Å}^{-1} < Q < 10.5 \text{ Å}^{-1}$  in momentum transfer) with a resolution of  $\Delta 2\theta = 0.6^\circ$  at  $2\theta = 56^\circ$ . The data were corrected for absorption, multiple scattering, container and background effects using the program package CORRECT, resulting in the total differential scattering cross section  $I(Q)$ . Due to the rare-earth ions,  $I(Q)$  will contain both structural and paramagnetic contributions (except for La). The magnetic and the structural contributions are additive and before any structural analysis takes place the magnetic part has to be subtracted. The analysis of the magnetic scattering follows the one in [7] and we have estimated the magnetic form factor using parameters from Lisher et al [8]. No parameters were reported for  $Ho^{3+}$  ions and instead a linear interpolation of magnetic scattering from  $Er^{3+}$  and  $Dy^{3+}$  has been used. The magnetic scattering will mainly contribute to the low  $Q$  part and decreases monotonically to zero at high  $Q$  values. After subtraction of the magnetic scattering and the incoherent structural part only the coherent structural scattering is left which is proportional to the static structure factor  $S(Q)$ , related to the atomic pair correlation function,  $G(r)$ , via a direct Fourier transform:

$$G(r) = \frac{1}{2\pi\rho_0} \int_0^\infty Q(S(Q) - 1) \sin(Qr) dq + 1 \quad (1)$$

where  $\rho_0$  is the average number density. In an experiment the  $Q$ -range is limited and this will affect the real space resolution in  $G(r)$ .

Structural models of the glasses were produced using the Reverse Monte Carlo (RMC) simulation method [6]. In the RMC calculation the experimental static structure factor,  $S_{exp}(Q)$ , is fitted with a calculated structure factor,  $S_{RMC}(Q)$ , from a computer configuration. The result of a RMC simulation is a 3-dimensional structural model, in agreement with the experimental structure factor, from which the partial structure factors,  $S_{ij}(Q)$ , and the partial pair correlation functions,  $G_{ij}(r)$ , can be calculated. Inter atomic distances and coordination numbers can be determined directly from the configuration. Periodic boundary conditions are applied to the model and the macroscopic density, closest approach distances and chemical knowledge are used to obtain physically sensible models. Our models consisted of 6500 atoms in a cubic box with the number of the different atoms corresponding to the metaphosphate composition,  $R(PO_3)_3$ . The phosphorous atoms were constrained to a 4 fold coordination with respect to oxygen, to account for the fact that the structure is built up of  $PO_4$  tetrahedra. The closest approach distances for the different pairs of atoms were estimated from results of EXAFS studies on rare-earth phosphates [3] and from studies of other phosphate glasses [9], see table I.



Table I Closest approach distances used as constraints in the RMC models.

Sample	P-P (Å)	P-O (Å)	O-O (Å)	P-R (Å)	O-R (Å)	R-R (Å)
La(PO <sub>3</sub> ) <sub>3</sub>	2.10	1.4	2.15	2.10	2.00	2.9
Pr(PO <sub>3</sub> ) <sub>3</sub>	2.10	1.35	2.10	2.3	2.00	2.9
Ho(PO <sub>3</sub> ) <sub>3</sub>	2.10	1.4	2.10	2.10	2.00	2.9

The initial models were built following the method described in [9] and hard sphere Monte Carlo (HSMC) were used to obtain models with PO<sub>4</sub> chains at the appropriate density. The rare-earth atoms were then added randomly to the structure and HSMC was run until all closest approach constraints were fulfilled. This starting configuration was then used for the RMC simulation.

## RESULTS

The static structure factors with the magnetic contributions added are displayed in fig. 1. The La-glass has no magnetic contribution and the scattering intensity hence tends to the compressibility limit in the low Q part. For the Pr and especially the Ho sample there is considerable intensity at small Q values due to the paramagnetic scattering. Subtracting the magnetic contribution, the structure factors for the three samples will look similar. This indicates that there are no larger structural differences between the three glasses.

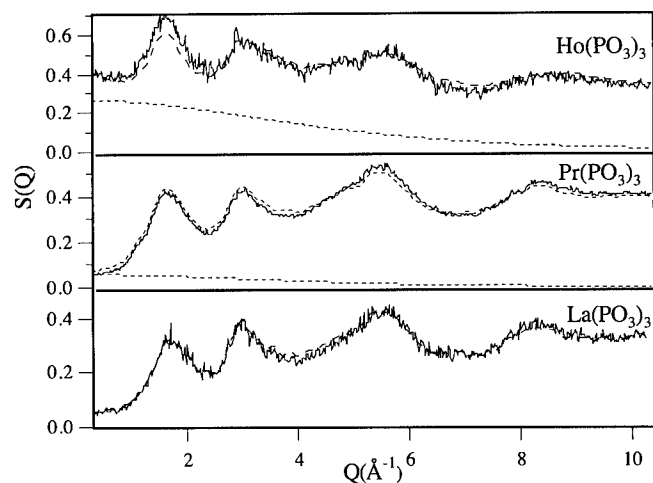


Fig. 1 The structure factors for the three samples. The magnetic contribution has been added to the Pr and Ho sample. The broken lines are the structure factors calculated from the RMC-models. The dotted lines in the Ho and Pr graphs are the magnetic contributions.

The RMC simulations, using the previously described constraints, could reproduce the structure factors for the three samples well, see fig. 1. The discrepancy is a bit larger for the Ho-sample, probably due to the small amount of sample available introducing somewhat larger errors in the corrections of the neutron scattering data. Furthermore the correction for the paramagnetic contribution is largest and least well determined for the Ho sample.

In fig. 2 the partial rare-earth pair correlation functions, from RMC, are displayed;  $G_{P-R}$ ,  $G_{O-R}$  and  $G_{R-R}$ . From these functions average inter atomic distances and coordination numbers can be determined.

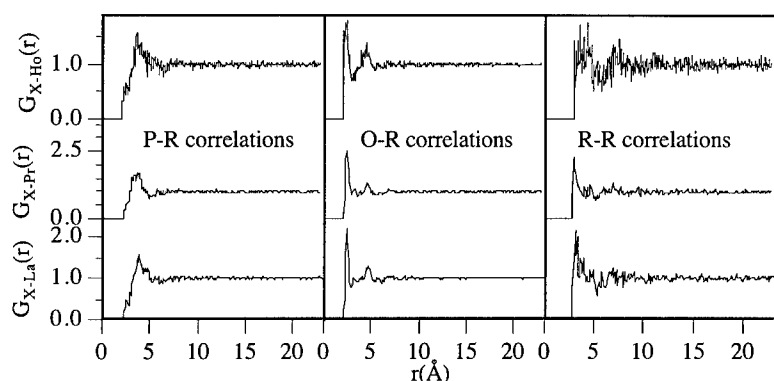


Fig. 2 Partial pair correlation functions correlation functions for the rare earth ions.

In  $G_{O-R}(r)$  two peaks are observed, around 2.5 and 4.5 Å, indicating two characteristic oxygen-rare earth distances. The average rare earth-phosphorus distance is about 3.8 Å and the closest approach distance between two rare earth ions is between 3.3-4 Å. At about 7 Å a weak peak in  $G_{R-R}$  indicates a second characteristic rare earth-rare earth correlation. Average inter atomic distances and coordination number obtained from the RMC models are summarised in table II.

Table II Average inter atomic distances and coordination numbers for the rare earth pair correlations.

Sample	Pair correlation	Distance (Å)	Coordination number
La(PO <sub>3</sub> ) <sub>3</sub>	La-O	2.53	4.3
	La-2ndO	4.7	22.1
	La-P	3.9	9.59
	La-La	3.4	2.9
Pr(PO <sub>3</sub> ) <sub>3</sub>	Pr-O	2.50	4.98
	Pr-2ndO	4.6	26.2
	Pr-P	3.72	7.97
	Pr-Pr	3.0	2.7
Ho(PO <sub>3</sub> ) <sub>3</sub>	Ho-O	2.40	4.52
	Ho-2ndO	4.5	25.14
	Ho-P	3.8	9.38
	Ho-Ho	3.9	2.05

Since the RMC simulation produces a 3-D configuration it is also possible to study the environment of each rare-earth ion. Coordination numbers have been determined individually for each ion for a distance corresponding to the minimum after the first peak in  $G_{O-R}(r)$ . The histograms in fig. 3 show the percentage of ions having a certain coordination number. The

distribution peaks for a coordination between 4-7 oxygens, but a relatively large spread is observed, indicating a variation of the rare-earth environment.

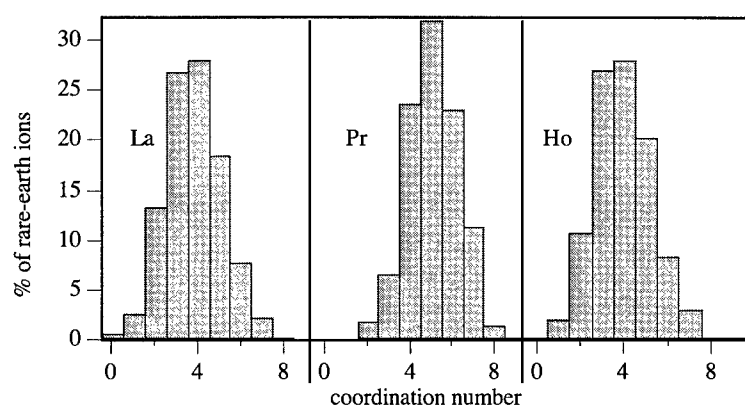


Fig. 3 Histogram of the number of rare-earth ions having a certain coordination number at a distance corresponding to the minima after the first peak in  $G_{O-R}(r)$ .

## DISCUSSION

The neutron scattering experiment together with the RMC simulations shows that the general model of phosphate glasses consisting of corner linked  $PO_4$  tetrahedra is appropriate. The initial RMC models were built as a chain like host structure with the rare-earth atoms randomly distributed. The final fitted models shows no larger deviation from the chain structure. The ratio of bridging to non-bridging oxygens is around 1:1.2, for all three samples, and hence branching and cross linking is not that frequent. We also observe that the rare earth ions enter in-between the neighbouring phosphate chains and primarily coordinate to the oxygens. From the partial pair correlation functions of the RMC models it can be observed that the rare-earth oxygen distance is around 2.5 Å and decreases with the increase in atomic number. This is in agreement with the lanthanide contraction and is in agreement with previously reported results from EXAFS and X-ray measurements [2], [3]. As expected the lanthanide ions coordinate many oxygens, on average about 4-5 for all three samples. This result is similar to what has been reported from the mentioned X-ray studies [3] but somewhat lower than what was determined by EXAFS [2]. There seems, however, not to be a unique environment around the rare earth ions. The histogram in fig. 3 shows a substantial spread in the coordination number indicating that different environments are present. The second rare earth-oxygen correlation, observed around 4.6 Å, is probably associated with oxygens in tetrahedra for which another oxygen directly coordinates the rare earth ion, hence the large coordination number for this correlation. The same should be the case for the phosphorous correlation around 3.8 Å which has somewhat larger coordination number than the first oxygen correlation.

From the partial R-R pair correlation function, in fig. 2, we determine a closest approach distance between rare earth ions just above 3 Å, though it is not well defined and there is a large variation from ion to ion. This distance is much shorter than what would be expected from an even uniform distribution of the ions which would be around 7 Å. In the Ho-sample such a correlation is also weakly present. The short closest approach distance suggests a tendency for clustering of the rare-earth ions.

In a recent study, involving measurements of the elastic modulus, of the rare-earth doped phosphate glasses [3] there were indications that the fractal dimensionality of the host network should be around 3, indicating a 3-D host structure rather than the normally found chain like structure for the meta-phosphate glasses. Our models did not show such a 3-D structure. Instead they agree very well with the general model of 1-D phosphate chains with the cations coordinating to the non-bridging oxygens along the chain. The high valency of the rare-earth ions will however cause them to coordinate to oxygens belonging to different chains. This will probably cause a strong cross linking of the chains, resulting in a more rigid structure which is 3-D like.

## CONCLUSIONS

The present neutron diffraction experiment combined with Reverse Monte Carlo simulations produces structural models that indicate that phosphorous and oxygens form a  $\text{PO}_4$  chain structure with little branching. The rare earth ions are surrounded by a relatively large number of oxygens,  $\approx 4.5$ , as expected. However a relatively large variation is observed for individual rare-earth ions. The models also indicate that the rare-earth ions are not uniformly distributed but tend to form local clusters. To further investigate the local environment around the rare-earth ions a combination of neutron scattering and X-ray scattering would be helpful. In the RMC method both experiments can be fitted simultaneously and hence the obtained models would be even more consistent.

## REFERENCES

1. A. Brodin, A. Fontana, L. Börjesson, L. M. Torell and G. Carini, *Phys. Rev. Lett* 73, 2067, (1994)
2. S. W. Martin, *Eur. J. Solid State Inorg. Chem.*, t. 28, 163-205, (1991)
3. D. T Bowron, G. A. Saunders, R. J. Newport, B. D. Rainford and H. B. Senin, *Phys. Rev. B*, 53, 9, 5268-75, (1996)
4. D. T Bowron, G. Bushnell-Wye, R. J. Newport, B. D. Rainford and G. A. Saunders, *J. Phys. Cond. Matter*, 8, 3337-46, (1996)
5. A. Mierzejewski, G. A. Saunders, H. A. A. Sidek and B. Bridge, *J. Non-Cryst. Solids* 104, 323, (1988)
6. R.L. McGreevy and L. Pusztai *Mol. Simulat.* 1 (1988) 359
7. D. A Keen and R. L. McGreevy, *J. Phys.: Condens. Matter* 3, 7383-94, (1991)
8. E. J. Lisher and J. B. Forsyth, *Acta Cryst. A* 27, 545-549, (1971)
9. J. D. Wicks, L. Börjesson, G. Bushnell-Wye, W.S Howells and R. L. McGreevy, *Physica Scripta*, vol. T57, 127-132, (1995)

## 2D LATTICES ON SUBSTRATES WITH RANDOMLY DISTRIBUTED PINNING CENTERS: A POSSIBLE SCALING LAW FOR DOMAIN SIZES

Surajit Sen \*, Zhi-Xiong Cai \*\* and David J. Schummer\*

\*Physics Department, State University of New York - Buffalo, Buffalo, N.Y. 14260-1500

\*\*Materials Science Division, Brookhaven National Laboratory, Upton, N.Y. 11973

### ABSTRACT

We consider 2D lattices which are disordered by an external field, in this case by a dense, random distribution of attractive pinning centers of an underlying substrate. The preferred configuration of the 2D system with screened-Coulomb two-body interactions and a fixed number of particles is a triangular lattice configuration. The pinning centers strongly affect the triangular lattice configuration. By keeping the location and the density of the pinning centers fixed, we study the effects of pinning strength on the structural properties of the lattice. We find that the strongly disordered lattice prefers to form irregular domains of size  $s$  which are composed entirely of topological defects. The distribution of sizes of these domains,  $D(s)$  suggest that  $s^{-\tau}$  for sufficiently large  $s$ . Our results are consistent with  $\tau \geq 2$  in the solid phase and  $\tau < 2$  in the liquid phase. We present a general argument in support of our findings and suggest that the physics which dictates the structure of 2D lattices on substrates with randomly distributed pinning centers is the same as that for a broad range of problems in which an external field strongly influences the behavior of an interacting physical system.

### INTRODUCTION

2D lattices on randomly distributed pinning potentials are realized in a variety of circumstances [1-2]. The most common examples in physical systems include solid films with quenched impurities and/or on rough substrates and flux-line lattices in layered type-II superconductive films [1-2]. At present, however, very little appears to be known about the structural properties of two-dimensional lattices in random potentials. In the present study, we address the problem of determining the structural properties of 2D lattices in the presence of long-ranged repulsive inter-particle interactions with fixed total number of particles in the system and in the presence of a large number of randomly distributed attractive pinning sites.

In a set of previous studies we have studied the structural properties of a repulsive screened-Coulomb system in the presence of a substrate described by a strong but uniform corrugation potential [3-6]. These studies were formulated in the context of the structure of Rb ions on the graphitic substrates found in alkali-metal graphite intercalation compounds. It is well known that in the absence of a substrate corrugation potential, a 2D lattice prefers to form a triangular lattice (see for instance in Ref. [7]). The corrugation can affect the triangular lattice structure significantly. In the case of  $RbC_{24.57}$ , where 24.57 reflects a "magic density" of the system, the Rb ions make nanodomains of 17 ions surrounded by thick domain walls. At slightly different stoichiometries, the structure can be viewed as essentially the same as that in the "magic" stoichiometry with regions in which the domains are smaller or larger and there are associated distortions in the domain walls [3-5].

Building on these earlier studies we now show that in the presence of randomly distributed attractive pinning centers, the same 2D interacting system prefers to form domains made of clusters of topological defects (i.e., dipoles with sites having 5-fold and 7-fold coordination) against a triangular lattice background. The cluster sizes do not appear to possess a characteristic length scale at a given temperature but instead seem to appear in all length scales. Our simulations suggest that at temperatures  $T < T_c$ , where  $T_c$  is the melting temperature of the system, the distribution of cluster sizes possibly decay more rapidly than the decay that is found when  $T > T_c$ . We present a general theoretical argument that supports our findings [8].

## THE MODEL

To systematically study the domain structure of the 2D lattices in random pinning potentials, we consider a simple model which contains the interaction between the particles and that between the particle and the randomly distributed pinning centers [1]. We reduce the number of parameters in the problem and consider tuning only the pinning strength of the individual pinning sites while keeping the density and the distribution of pinning sites fixed [1]. We also keep the particle density fixed. Using such a model we can quantitatively study the effects of pinning strength in determining the amount of disorder in the pinned lattice.

The interaction energy of the  $N$  particle system with  $N_p$  randomly distributed pinning sites is defined as

$$V = \sum_{i,j=1(i \neq j)}^N V_2(|\vec{r}_i - \vec{r}_j|) + \sum_{i=1}^N \sum_{p=1}^{N_p} V_p(|\vec{r}_i - \vec{r}_p|), \quad (1)$$

which consists of both one and two-body interactions. The two-body interaction potential between the particles is chosen to be similar to that between the alkali metal ions in graphite intercalation compounds (see for example Refs. [3-5,9-10] where some details concerning this potential are given). Any two particles which are mutually separated by a distance  $r_{ij} \equiv |\vec{r}_i - \vec{r}_j|$ , interact with an energy given by

$$V_2(r_{ij}) = \frac{q^2}{r_{ij}} \exp\{-r_{ij}/\lambda\}, \quad (2)$$

where  $q^2 = 4.8028 \times 10^{-10}$  esu, and  $\lambda = 2.1$  Å is the screening length. Our model for  $V_2$  is taken from the one for  $Rb$  ions against a jellium background (which is used to maintain overall charge neutrality in alkali-metal graphite intercalation compounds [3-5,9-10]). Therefore, although  $q$  appears in Eq.(2) above, for all practical purposes our system can be regarded as charge neutral. The one-body pinning potential is assumed to consist of a random distribution of attractive Gaussian potential wells, whose functional form  $V_p$  is given by,

$$V_p = -\frac{A_p}{2\pi} \exp(-(|\vec{r}_i - \vec{r}_p|)^2 / R_p^2), \quad (3)$$

where  $A_p$  represents the strength of the pinning center,  $R_p$  represents the width of the pins and is chosen to be in the units of length  $a_0$  which was kept as 2.46 Å (for purposes of comparison with previous works in [3-6]), and  $\vec{r}_p$  is the location of the center of the  $p^{th}$  pin.

The pinning centers are distributed randomly within the simulation cell. The magnitudes of  $A_p$  that we consider in this study range between 5 and 10 in the chosen energy unit ( $300k_B$ ,  $k_B$ =Boltzmann constant). This implies that the pins exert a significant attractive force on the particles in our system.

Periodic boundary conditions are utilized in all of the simulations. The presence of pinning centers have a considerable effect on the structure and dynamics of our system as shown previously [1-2]. We have fixed the area of the supercell in our model system, thus by varying the number of pins  $N_p$  we can vary the density of the pins. The structure of the lattice is very sensitive to the pinning strength  $A_p$ . As  $A_p$  increases, the lattice breaks into domains of varying size in order to minimize the pinning energy. In the limit of large  $A_p$ , the system resembles an amorphous solid or "glass-like" phase below the melting temperature [1]. In this report we assume that  $N_p = N$ . We also use the same random configuration of pinning centers in all of our simulations presented here so that the only variable in this study is controlled by  $A_p$ . At such a high density of pinning centers, the effects of pinning become obvious in the relatively small systems that we can simulate using Molecular Dynamics simulations. In what follows, we report on the effect of  $A_p$  on the structure of the glass-like phase in this strong pinning regime.

## THE METHOD AND THE CALCULATIONS

The Molecular Dynamics simulations were performed using the microcanonical ( $E$ ,  $V$ ,  $N$ ,  $\mathbf{P}$ ) ensemble, where  $\mathbf{P}$  is the total linear momentum of the system [3-6]. The Newtonian equations of motion for the system were integrated forward in time using a fifth-order Gear predictor-corrector algorithm and the center of mass of the system was zeroed in every integration step [11]. The mass unit was set as 1 amu and the particles were assumed to have the mass of Rb ions which meant that our natural time unit was approximately 1 picosecond. The runs for which the results are reported here had  $N = 1024$  distributed in a  $72a_0 \times 72a_0$  rhombic supercell which is commensurate with the triangular lattice for the particle density we studied. We considered cases with  $N_p$  equalling 1024 per supercell. The time step used in the simulation was 0.006ps. Based upon our experience with previous studies [4-6], we believe that this was a sufficiently fine integration time step for reliable calculation of the structure and dynamics of the present system. Starting from randomly distributed particles and pinning sites, the system was first heated up to about  $T = 300\text{K}$  ( $T$  being the system temperature) and equilibrated. This temperature is well above the melting temperature  $T_m \sim 200\text{K}$  [1]. The temperature was then reduced in steps of 20K down to  $T = 50\text{K}$  by carefully scaling down the velocities and by equilibrating the systems for  $\sim 300\text{ps}$ . Thus, for each temperature, 50,000 time steps/particle were used to equilibrate the system before calculating the thermal averages of various quantities by using the data from the next 100,000 time steps.

Let us first note [1] that the presence of  $N_p$  pins where  $N_p$  is sufficiently large with strong enough  $A_p$  ( $A_p$  between 5 and 10) causes a significant number of topological defects  $\delta$  (a topological defect being a pair of particles, one with 5 and the other with 7 nearest neighbors in an otherwise 6-fold coordinated background) in the system. For  $1/2 < N_p/N < 1$  and  $A_p = 10$ , we find that the  $\delta \sim T^0$ , i.e., approximately a constant regardless of whether the 2D lattice behaves as a solid or a liquid. If  $N_p \approx N$  with  $5 \leq A_p \leq 10$ , however, we find that  $\delta$  begins to become strongly dependent upon  $T$ . This is clearly visible by

observing Fig.1(a-d), where we present the lattice pictures for  $A_p = 5$ ,  $T = 50K$  (Fig.1(a))

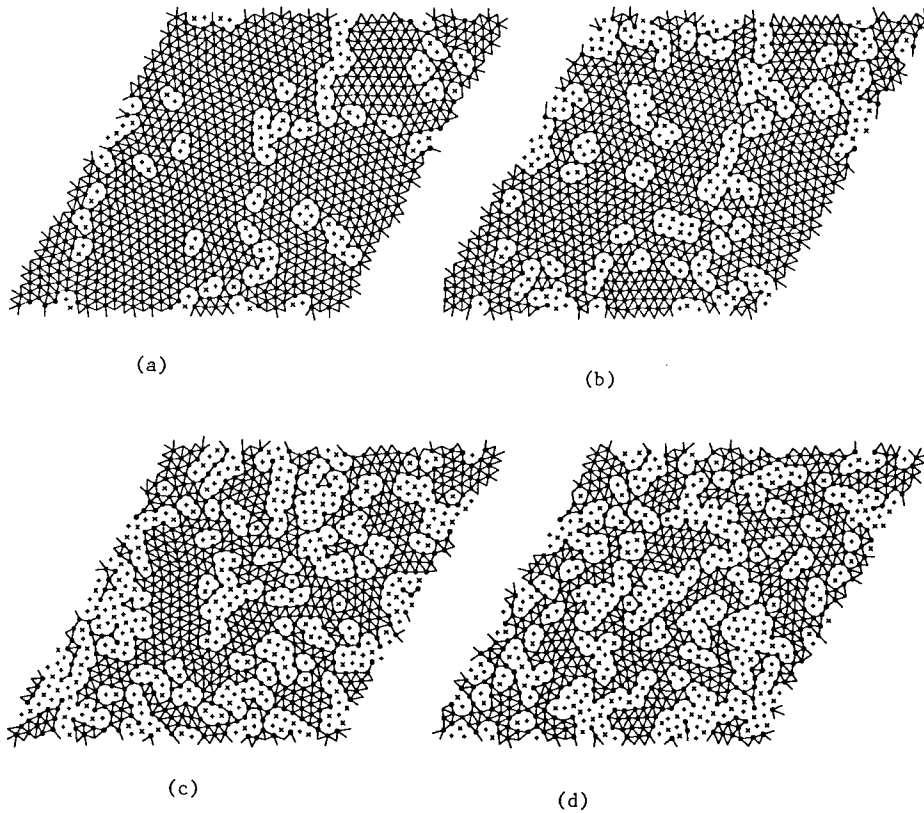


Figure 1: Lattice configuration for  $N = N_p = 1024$  and (a)  $A_p = 5$ ,  $T = 50K$ ; (b)  $A_p = 5$ ,  $T = 200K$ ; (c)  $A_p = 10$ ,  $T = 50K$ ; (d)  $A_p = 10$ ,  $T = 200K$ . The solid line links the sites with 6-fold coordinates. The “x” and “+” indicate the 5 and 7 fold coordinates, respectively.

and  $T = 200K$  (Fig.1(b)) and  $A_p = 10$ ,  $T = 100K$  (Fig.1(c)) and  $T = 200K$  (Fig.1(d)).

To quantify our observations, we measure the areas occupied by the regions that contain the clustered 5-7 pairs in Fig.1(a-d). We denote the area of an island of 5-7 pairs to be  $s$  and probe the behavior of the number of islands  $D(s)$  of size  $s$  at a given temperature. The plots of  $D(s)$  versus  $s$  at  $T = 100K$  when the system is in a solid phase and at  $T = 200K$  when the system is in the liquid phase are shown in Fig.2. The data at each  $T$  represent the aggregate of the values for  $D(s)$  collected for  $A_p$  of 5,6,7,8,9 and 10. This has been done to reduce the noise in the data for each  $A_p$ , and after having confirmed that at individual  $A_p$ 's, one finds the same behavior of  $D(s)$  as in any other. Thus, we contend that the actual magnitude of  $A_p$  is not very important provided it is sufficiently large with respect to the



inter-particle interaction and given that  $N_p$  is sufficiently large compared to  $N$ . Accurate Molecular Dynamics calculations for systems with long-ranged and competing interactions are a challenge to carry out for systems with more than  $10^4$  particles. Thus, the data on the structural properties contain a significant amount of scatter. We show plots of  $\log D(s)$  versus  $\log s$  in Fig.2. The slopes are calculated via regression analyses and the errors are given in Fig.2. Our results are *consistent* with the hypothesis that  $D(s) \sim s^{-\tau}$ , where  $\tau \geq 2$  for  $T < T_c$  and  $\tau < 2$  for  $T > T_c$ . Thus, more large islands of 5-7 pairs form above  $T_c$  than at  $T < T_c$ . Given the higher thermal energies at  $T > T_c$ , this is a reasonable result. We believe that this simple behavior that is apparent in the structural features of our disordered 2D solid emerges from the competition between an external field and the internal interactions. At  $T < T_c$ , when the system is in the non-diffusive or solid phase, there is an upper limit in the number of island sizes that can form due to the external field and thermal effects. This is responsible for  $\tau \geq 2$  as we argue below. However, when the system becomes diffusive at  $T > T_c$ , this upper limit disappears and the external field can exert a stronger influence in forming larger islands of 5-7 pairs. This results in  $\tau < 2$ .

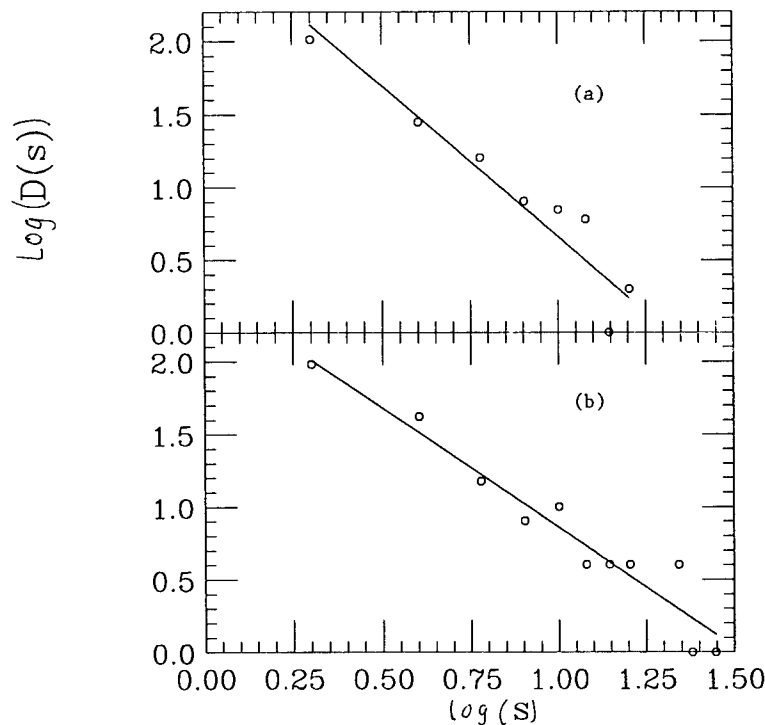


Figure 2: Plots of  $D(s)$  vs  $s$  for a  $N = N_p = 1024$  system using log-log scale. (a) At  $T = 100\text{K}$  regression analysis yields a slope of  $\tau = 2.1 \pm 0.2$  (similar numbers are found for all  $T < T_c \approx 200\text{K}$ ) and (b) at  $T = 200\text{K}$  solid line yields a  $\tau = 1.6 \pm 0.1$  (similar numbers are found for all  $T > T_c$ ).

## THEORETICAL ARGUMENTS

It is instructive to do some simple minded analysis to understand the crossover behavior in  $\tau$  as the system undergoes a transition from the solid to the liquid phase [8]. Let us consider a system which can form more 5-7 pairs upon the slightest increase in temperature. Let  $L$  be the linear dimension of the system and  $D(s, L)$  be the probability that any increase in temperature causes islands of size  $s_m$  where  $s_m$  can be  $\sim L$ . Then the first moment  $A \equiv \sum_{s=0}^L s D(s, L) \geq kL$ , where  $k > 0$ . If we let  $L \rightarrow \infty$ , then  $A \rightarrow \infty$ . If we suppose that  $D(s, \infty)$  in this disordered system has an algebraic tail, i.e.,  $D(s, \infty) \rightarrow 1/s^{1+a}$  for large  $s$ , then  $a < 1$  for  $A \rightarrow \infty$ . Thus, islands of size  $s \rightarrow \infty$  are possible at this critical state. However, if  $A < \infty$ , then  $a \geq 1$ , i.e.,  $D(s) \sim 1/s^\tau$  with  $\tau \geq 2$ . This is the scenario we realize when  $T < T_c$ . Because  $A < \infty$ , this case implicitly requires that there be a cut-off in the size of the largest islands that can form in this system.

## ACKNOWLEDGEMENT

SS was partly supported by the Multidisciplinary Pilot Project Program at SUNY-Buffalo. ZXC was supported by the DOE under contract number DE-AC0276CH00016.

## REFERENCES

1. Z.-X. Cai, S. Sen and D.O. Welch, Phys. Rev. B **51**, 15873 (1995)
2. A.C. Shi and A.J. Berlinsky, Phys. Rev. B **47**, 652 (1993).
3. H. Seong, S. Sen, T. Cagin and S.D. Mahanti, Phys. Rev. B **45**, R8841 (1992); Phys. Rev. B **46**, 8748 (1992).
4. S. Sen, H. Seong, T. Cagin and S.D. Mahanti, in *Computer Simulation Studies in Condensed Matter IV*, Eds. D.P. Landau *et al.* (Springer, Berlin, 1993).
5. T. Cagin, S. Sen, H. Seong and S.D. Mahanti, Mol. Simulat. **10**, 43 (1993).
6. J.D. Fan, Z.-X. Cai, G. Reiter, and S.C. Moss, Phys. Rev. B **48**, 1853 (1993).
7. B.I. Halperin and D.R. Nelson, Phys. Rev. B **19**, 2457 (1979).
8. S. Sen and S. Pal, Physica A **233**, 77 (1996); D. Dhar, *ibid* A **186**, 82 (1992); G.H. Huber, M.H. Jensen and K. Sneppen, Phys. Rev. E **50**, R2133 (1995).
9. M. Plischke and W.D. Leckie, Can. J. Phys. **60**, 1139 (1982).
10. J.D. Fan, G. Reiter and S.C. Moss, Phys. Rev. Lett. **64**, 188 (1990).
11. M.P. Allen and D.J. Tildesley, *Computer Simulation of Liquids* (Clarendon, Oxford, 1987), Appendix E.

## EFFECT OF SIZE DISPERSITY ON THE MELTING TRANSITION

M.R. SADR-LAHJANY<sup>1</sup>, P. RAY<sup>2</sup>, S. T. HARRINGTON<sup>1</sup> AND H.E. STANLEY<sup>1</sup>

<sup>1</sup> Center for Polymer Studies and Department of Physics, Boston University, Boston, MA 02215, USA <sup>2</sup>The Institute of Mathematical Sciences, CIT Campus, Madras - 600 113, India

### ABSTRACT

We present a molecular dynamics simulation study of the liquid-solid transition in a two dimensional system consisting of particles of two different sizes interacting via a truncated Lennard-Jones potential. We work with equal number of particles of each kind and the dispersity  $\Delta$  in the sizes of the particles is varied by changing the ratio of the particle sizes only. For the monodisperse case ( $\Delta = 0$ ) and for small values of  $\Delta$ , we find a first order liquid-solid transition on increasing the volume fraction  $\rho$  of the particles. As we increase  $\Delta$ , the first-order transition coexistence region weakens gradually and completely disappears at high dispersities around  $\Delta = 0.10$ . At these values of dispersity the high density phase lacks long range translational order but possesses orientational order with a large but finite correlation length. The consequences of this effect of dispersity on the glass transition and on the melting transition in general are discussed.

### INTRODUCTION

The liquid-solid transition in a system of densely-packed interacting particles has attracted considerable attention in recent years[1]. Such a system undergoes a transition from a disordered liquid phase to an ordered solid phase on increasing the volume fraction of the particles. It was further observed that polydispersity in the sizes of the particles has a profound effect on the transition. With increasing dispersion, the solid structure becomes unstable and above a certain degree of dispersity the solid cannot form at all[2]. The consequence of this should be very important from the experimental point of view since colloidal suspensions in general do have particles of various sizes and show the liquid-solid transition [3] and in the simulations of glass transition, particles of different sizes are always considered [4]. Still, the effect of size dispersity on the liquid-solid transition has not received sufficient attention. In this paper, we study the effect of size-dispersity on the liquid-solid transition for interacting particles in two dimensions.

The instability of the solid phase with increasing size dispersity is not striking, as one would intuitively expect that a high dispersity naturally destroys the crystal order needed to form a solid. But molecular dynamics (MD) simulation studies in three dimensions [2], and similar recent studies in two dimensions [5], consistently show the gradual weakening of the first order transition with increasing dispersity  $\Delta$  and find the existence of a critical value  $\Delta_c$  where the line of first-order transitions ends. At  $\Delta_c$ , one does not see the first order transition. This prediction also arises from a study employing the density functional theory[6] and simpler models of crystals[7]. The phase diagram is remarkably similar to the first order transitions ending in a critical point that one observes in the temperature driven liquid-gas transition. We study the transition at and around  $\Delta_c$  by carefully examining the nature of the phases obtained at different densities and dispersities.

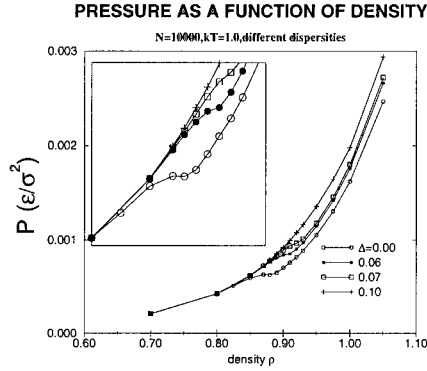


Figure 1: Pressure versus density plots for different dispersities. The small dispersity curves show the first order phase transition from the low density liquid phase to the high density 2d-solid phase with the intermediate flat coexistence region. The inset is a blow up of the coexistence regions at different dispersities.

## MODEL AND SIMULATION

We report a molecular dynamics simulation study of a 50 – 50 mixture of Lennard-Jones (LJ) particles of two different sizes. The particles are contained in a two dimensional box of linear size  $L$  with periodic boundary condition used on all walls. We have performed our simulations for  $N = 400, 2500$  and  $10000$  particles. To each particle we assign a radius proportional to its LJ diameter and define the density  $\rho$  as the ratio of the total area occupied by the particles to the total area of the box.

The degree  $\Delta$  of size dispersity is quantified by the relative width of the bimodal particle size distribution function. Here we present results for dispersities  $\Delta = 0, 0.06, 0.07$  and  $0.10$ . All physical quantities are measured in reduced units in which the average LJ diameter  $\sigma$ , LJ energy scale  $\epsilon$  and the mass of each particle are one. Our results are all collected from the isothermal hyper-surface of the phase space with  $kT = 1.0$ , where  $k$  is the Boltzmann constant. Pressure  $P$  is computed using the virial relation[8].

## RESULTS

Fig. 1 shows the  $P - \rho$  diagrams for different dispersities  $\Delta$ . For small  $\Delta$ , we observe the flat coexistence region which is a characteristic feature of first order phase transition. This region shrinks as  $\Delta$  increases and near  $\Delta = 0.1$  disappears completely.

Fig. 2 shows the mean square displacement (MSD) of the particles at different phases for  $\Delta = 0$  and  $0.1$ . The plots for  $\Delta = 0$  essentially have three features: (i) a late time diffusive regime for low densities (ii) a frozen regime where the diffusion is very small for high densities (iii) a sudden change in the MSD behavior between the two regimes on varying the density. This jump is one of the characteristic features of a first-order phase transition. We observe these features for other  $\Delta$  values but with increasing  $\Delta$ , the magnitude of the jump in the MSD plot decreases and the system goes from liquid to solid regime rather

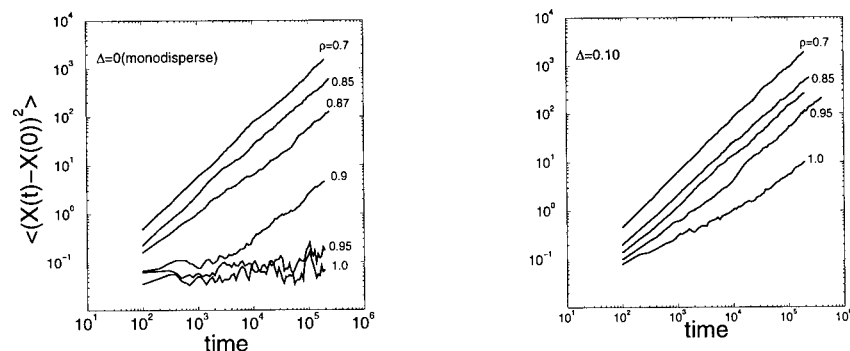


Figure 2: Mean square displacement of the particles versus time at different densities  $\rho$  (denoted at the end of the curve) for  $\Delta = 0$  and  $\Delta = 0.10$ .

continuously. On the other hand the MSD plot for  $\Delta = 0.10$  shows that at high dispersity, the system does not become solid even at  $\rho = 1.0$ .

In order to study the translational symmetry at different phases, we measure the total pair distribution function  $g(r)$  (Fig. 3). The form of  $g(r)$  for the low density phase has a liquid-like structure. On the other hand for  $\Delta = 0$ , the solid phase at high densities shows a clear 2d solid-like structure with pronounced peaks, and deep dips which persist up to long distances, with the amplitude of the peaks decreasing slowly. This quasi-long-range translational symmetry is expected for solids in two dimensions [9]. For large values of dispersity around  $\Delta = 0.10$  and high density the system does not show the solid structure mentioned above and lacks translational order.

Next, we study the orientational order of the phases by measuring the hexagonal order parameter  $\psi_6$  [10] which characterizes the local bond orientational order around particles. The absolute value of  $\psi_6$  increases from a small positive value to one as the structure changes from disorder to an ordered triangular lattice. We have plotted the distribution of  $|\psi_6|$  for all particles (see Fig. 4). The liquid phase has a flat distribution, thus not showing any local orientational order [10]. The solid phase shows a high degree of local orientational order, since it forms a nearly perfect triangular lattice. On the other hand for  $\Delta = 0.10$  the  $\rho = 1.0$  system shows a hump near unity but also a big tail extending down to zero. The hump confirms the existence of local hexagonal order which has also been observed in experiments on bidisperse hard spheres [11]. The presence of the long tail indicates that there are many orientational defects in the system, as a result of size dispersity. These defects are disclinations and appear as distorted hexagonal or pentagonal and heptagonal neighboring particle arrangements around the particles.

## CONCLUSION

We find that a geometrical factor like the dispersity  $\Delta$  in the particle sizes has a similar effect on the liquid-solid transition as the temperature (thermal energy) has on the liquid-

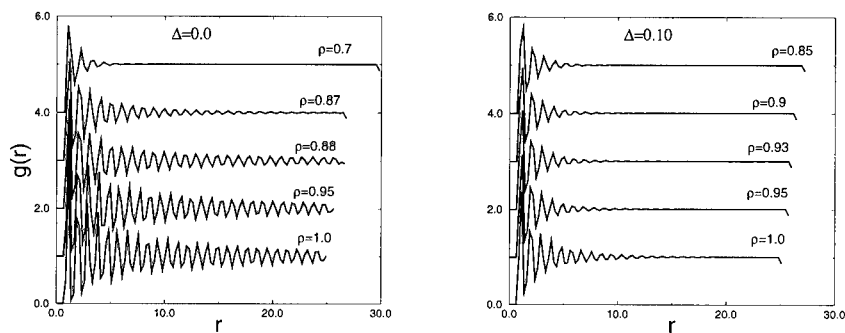


Figure 3: Total pair distribution function for two different dispersities, all graphs are centered around  $g(r) = 1.0$  but are shifted to make comparison easier; In monodisperse systems, the low density plots show the characteristics of liquid and the high density ones that of solid. For  $\Delta = 0.10$  systems, even the highest density studied,  $\rho = 1.0$  does not show the quasi-long-range order which is characteristic of a  $2d$  solid.

gas transition.  $\Delta$  weakens the first order transition from the liquid state to the solid state driven by the volume fraction  $\rho$  of the particles. This observation supports the earlier similar observations in different systems like in elastic disk systems[5] and in colloidal systems [2] with polydispersity in the sizes of the particles. We further observe that at high values of  $\Delta$ , the system always remains at the fluid phase. This is the region where one can observe glass transition. Our study provides a quantitative measure of the size dispersity  $\Delta$ , which would be needed to observe the glass transition. It further indicates that there may not be any true phase transition (in the thermodynamic sense) in the process of glass transition. We will provide detailed evidence for this conclusion elsewhere[12] ( see also [13]). However, much detailed study, specially on the effect of temperature is needed to say anything conclusively.

#### ACKNOWLEDGMENTS

We wish to thank L. Amaral, B. Kutnjak-Urbanc and W. Kob for useful discussions and remarks. The Center for Polymer studies is supported by NSF.

#### REFERENCES

- [1] M. A. Glaser and N. A. Clark , Adv. Chem. Phys. **83**, 543 (1993)
- [2] E. Dickinson and R. Parker, Chem. Phys. Lett. **79**, 3 (1981); E. Dickinson, R. Parker and M. Lal, *ibid*, 578
- [3] In Proceedings of the Winter Workshop on Colloidal Crystals, eds. P. Pierański and F. Rothan, J. Physique Colloq. C **3**, 46 (1985)

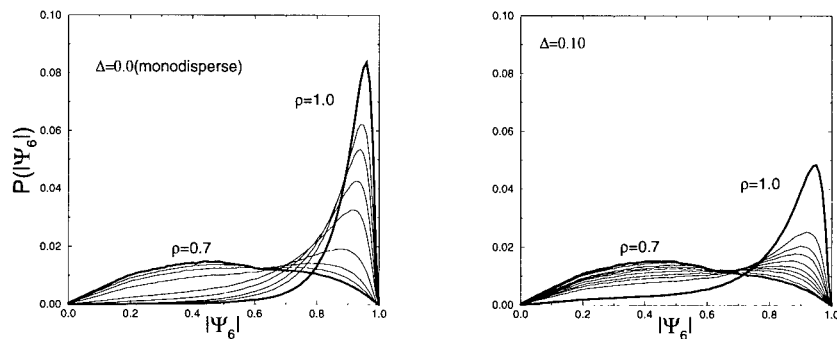


Figure 4:  $|\psi_6|$  distribution for two different dispersities; For monodisperse systems,  $\rho = 0.7$  plot belonging to the liquid phase shows no orientational order,  $\rho = 0.875$  plot has a developing hump along with a very fat tail indicating the coexistence of the solid and liquid phases,  $\rho = 0.9$  to  $\rho = 1.0$  on the other hand have pronounced peak near one and diminishing tails, indicating a triangular lattice arrangement of the particles. On the other hand, for  $\Delta = 0.1$ , even at  $\rho = 1.0$ , we find a long tail in the distribution indicating the presence of many defects in the form of dislocations and disclinations and absence of true long range orientational order.

- [4] W. Kob and H. C. Andersen, Phys. Rev. **52**, 4134 (1995)
- [5] W. Vermöhlen and N. Ito, Phys. Rev. E **51**, 4325 (1995)
- [6] J. L. Barrat and J. P. Hansen, J. Physique **47**, 1547 (1986)
- [7] P. N. Pusey, J. Physique **48**, 7.9 (1987)
- [8] M.P. Allen, D.J. Tildesley *Computer Simulation of Liquids*, (Oxford University Press, New York, 1989)
- [9] K. Strandburg, Rev. of Mod. Phys. **60**, 161 (1988)
- [10] M. A. Glaser and N. A. Clark, in *Geometry and Thermodynamics*, eds. J. C. Tolédano, p. 193 (Plenum Press, New York, 1990); M. A. Glaser, N. A. Clark, A.J. Armstrong and P.D. Beale, in *Springer Proceedings in Physics*, Vol. 52: *Dynamics and Patterns in Complex Fluids*, eds. A. Onuki, K. Kawasaki, p. 141 (Springer-Verlag Berlin, Heidelberg 1990)
- [11] D. R. Nelson, M. Rubinstein and F. Spaepen, Phil. Mag. A **46**, 105 (1982)
- [12] M. R. Sadr-Lahijany, P. Ray and H. E. Stanley, unpublished
- [13] C. Dasgupta, A. V. Indrani, S. Ramaswamy and M. K. Phani, Europhys. Lett. **15** (3), 307 (1991)

size  $\xi$ . In organic structural glasses estimates for  $\xi$  based on various measurements have been in the range 2-3 nm at  $T_g$  [6]. These cooperative units may be viewed for illustrative purposes as *droplets* [7] of typical volume  $\xi^3$  and dipole moment  $p_d \sim (\xi/a)^{3/2} p_0$ , where  $a$  is the typical spacing between elementary dipoles which have typical moment  $p_0$ . Assuming droplets re-orient independently in an applied field, the number of droplets in a sample of volume  $\Omega$  which contribute in  $\Delta\omega$  is given by:

$$N(\Delta\omega) \sim \frac{\Omega \epsilon''(\omega, T)}{\xi^3 \epsilon''(\omega, T)} \quad (1)$$

We note that in any more complex model in which the droplets are not independent [8,9],  $N(\Delta\omega)$  would be effectively reduced. When  $N(\Delta\omega)$  is quite small, approximately 3 [10,8], tell-tale deviations from bulk-like behavior would be expected. Namely fluctuations in  $\epsilon''(\omega, T)$  or noise as a function of frequency, time, sample, or thermal cycle would be observed.  $\epsilon'(\omega, T)$  may also exhibit fluctuations which would be smaller by approximately  $\epsilon''(\omega, T) / \epsilon'(\omega, T)$ . Thus the sample volume required can be conservatively estimated:

$$\Omega \sim \frac{3\xi^3 \epsilon''(\omega, T)}{\epsilon''(\omega, T)} \quad (2)$$

For glycerol at  $T=193K$ , where  $\epsilon'' \sim 0.1$  at 1 kHz, we find a  $\Omega \sim 1 \times 10^{-16} \text{ cm}^3$ , e.g. a cube of about 50 nm on a side. At lower temperatures or higher frequencies the volume needed increases, but the dielectric constant decreases as does signal. In polymers such as PVAc the sample volume needed would be even larger. The effective volume probed by our technique turns out to be of this order, see discussion below.

## EXPERIMENT

Since the invention of the atomic force microscope (AFM) 1986 [11], the number of applications is growing rapidly. We employ a non contact capacitance measurement scheme [12] as well as force modulation techniques [13]. In non contact mode, the cantilever is vibrated at its resonance frequency close to the sample surface. When a voltage is applied between tip and the sample, the resonance frequency  $\omega$  of the cantilever will change with distance according to:

$$\omega^2 - \omega_0^2 = -\frac{1}{2m} V^2 \frac{\partial^2 C}{\partial z^2} \quad (3)$$

where  $\omega_0$  is the resonance frequency far away,  $m$  the mass of the cantilever,  $V$  the applied voltage and  $C$  the capacitance [12]. If the absolute distance  $z$  is known, the capacitance and hence the dielectric constant can be calculated. Fluctuations in the dielectric constant can be directly related to fluctuations in the resonance frequency. The effective volume sampled is of order of the tip radius cubed, see Fig. 1.



With force modulation techniques viscoelastic properties of the sample can be studied [13]. The cantilever is in contact with the sample thus exerting a static force. With a piezo this force can be modulated by actuating either the sample or the cantilever in a sinusoidal manner. The in-phase and out-of-phase response of the sample correspond to the elastic and dissipative response respectively.

For our mesoscopic studies, we have constructed our own variable temperature AFM utilizing ultra-high sensitivity piezoresistive cantilevers [14] from Park Scientific. The deflection of these cantilevers is simply measured by means of their resistance change, which is typically about 3 Ohm/ $\mu\text{m}$ . The micro machined structure is a single crystal Si beam, 2 $\mu\text{m}$  thick, 50 $\mu\text{m}$  wide and 150 $\mu\text{m}$  long. At the end a 3 $\mu\text{m}$  high conical tip with radius of curvature of about 50nm extends up. These levers have a spring constant of typically 1 N/m, resonance frequencies of 50-100 kHz and quality factor  $Q > 10^4$  in high vacuum. The deflection of the cantilever can be sensed to better than 0.1 Å resolution. A piezo, integrated in the holder, allows us to drive the cantilever.

Thermal expansion and drift are major problems in variable temperature SPM designs. To minimize these effects, we kept the symmetry of our design strictly cylindrical and chose molybdenum for its low thermal expansion coefficient as the main material. But in addition we can adjust the thermal compensation in the z direction. The sample stage and the lever support consist of two cylindrical Mo parts, separated by three Mo rods. The cantilever holder, which has a negative thermal expansion coefficient of about -500 Å/K, is mounted on a nickel rod in the center of the lever support, see Fig. 2. Nickel's coefficient of thermal expansion is about a factor of two bigger than molybdenum. By adjusting the effective length of the Ni and Mo rods with removable micrometers, the thermal compensation in z direction can be tuned with an ultimate resolution of 0.5 nm/K (at a specified temperature).

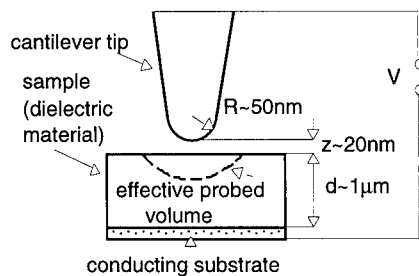


Figure 1. Capacitance measurement setup. Cantilever vibrates at its resonance frequency  $f_R$ . Fluctuations in  $f_R$  can be related to fluctuations in the dielectric constant of the sample. The probed volume is of the order of  $R^3$ .

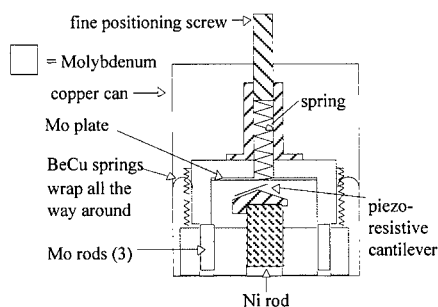


Figure 2. The cross section of the AFM is shown. The molybdenum rods and the Ni rod in the center can be moved with micrometers (not shown for clarity). The sample is deposited onto the Mo plate. Fine positioning is achieved by a differential spring system.

The micrometer for the Ni rod is also used for coarse positioning of the cantilever. Fine adjustment of the sample tip distance is provided by means of a differential spring system. A 100 turn/in. screw compresses a spring, which in turn deforms a Mo plate (Fig. 2) where the sample is mounted. The resolution of this mechanism is 5 Å/deg.

The AFM sits inside a copper can, which is weakly thermally linked to a copper tank. This tank can be cooled with LN<sub>2</sub> or chilled water depending on the desired base temperature (total operating range 80K-400K). The can sits in a small UHV chamber, mounted on a vibration-isolation air table. An ion pump provides vibration-less vacuum.

## RESULTS

The thermal stability of our design was tested by recording the change in resonance frequency of the cantilever for a certain temperature change. The local slope of the resonance frequency versus distance curve has to be known. The resonance frequency is not only a function of distance, but depends also on the temperature. But this effect is linear and small ( $\sim 1\text{Hz/K}$ ) and can be subtracted. The current setup shows a thermal drift of about 200 Å/K at room temperature. Even better values will be achieved by iteratively moving the Mo and Ni rods with micrometers in or out.

Fig. 3 shows the resonance frequency as a function of distance for a 2 Volt bias between tip and Mo plate (no sample was mounted). In order to derive the capacitance, the absolute sample-tip distance has to be known. Distance changes are known from the calibration of the differential spring system. One way of measuring the absolute distance is to measure the vibration amplitude of the cantilever while increasing the driving amplitude. When the cantilever starts to tap the surface, the vibration amplitude stays constant. The distance can be derived from this amplitude. At three points the absolute distance was measured and used to scale the curve (see Fig. 3). From this curve the capacitance can be derived according to equation 3, see inset Fig. 3.

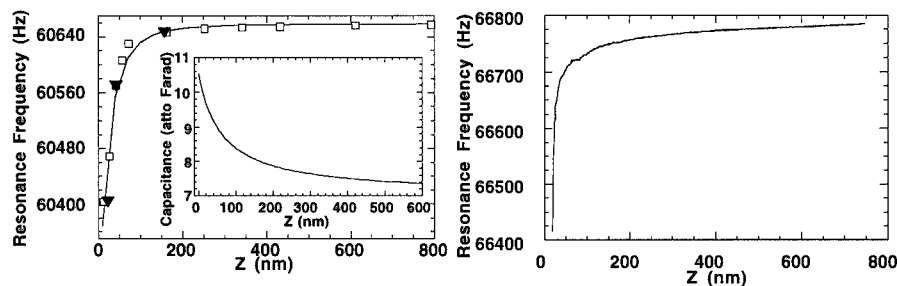


Figure 3. Open squares: measured resonance frequency of the cantilever with 2 V bias as function of height above a Mo surface. Solid line: Fit with sphere/plane surface model. Solid triangles: measured distance at three frequencies. Inset: capacitance vs. z.

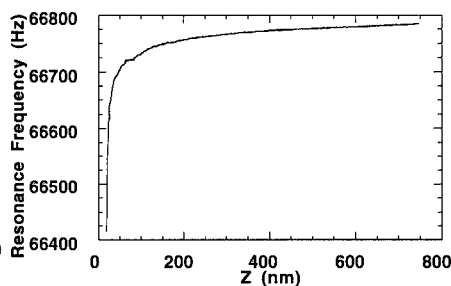


Figure 4. Cantilever resonance frequency as a function of distance from a PVAc surface with a 2 Volt bias.

At a typical distance of 200 Å the capacitance is of order of  $10^{-17}$  F. The resolution is in the  $10^{-21}$  F range, in agreement with [12]. Fig. 4 shows the same measurement with a PVAc film, note the different curvature.

We have carried out force-modulation studies on hard (Mo) and soft (PMMA and PVAc, spun on the Mo plate in a dilute solution) materials as a function of frequency and sample height. The in-phase and out-of-phase response of the cantilever is analyzed as a function of modulation frequency using a lockin amplifier. The results for Mo and PMMA are relatively uninteresting, but do reveal the background noise and phase shifts produced by the cantilever electrical circuit system itself. The results for PVAc, which has a glass transition near 40 C, deserve further discussion.

Fig. 5 shows the out-of-phase amplitude vs. frequency for PVAc at several temperatures in the vicinity of the glass transition. The static cantilever deflection produced a static loading force corresponding to an applied stress of about  $10^6$  N/m<sup>2</sup> in this instance, which is added to the force modulation. A clear peak is observed which moves to higher frequencies with increasing temperature. This loss peak marks the glass transition and the temperature dependence of the peak frequency is very consistent with bulk measurements [15]. Thus this mesoscopic method can be used to identify the glass transition temperature and study dynamics. Note that since the strain field produced by this applied stress will be significant to a depth of order the tip radius (50nm), we are probing bulk properties more than surface properties, albeit in mesoscopic volumes.

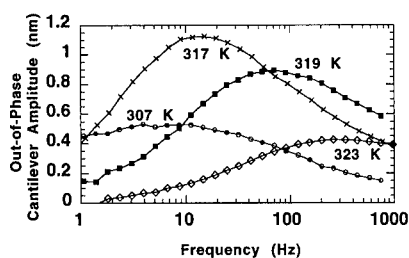


Figure 5. Out-of-phase response of PVAc to an applied sinusoidal stress vs. frequency for different temperatures.

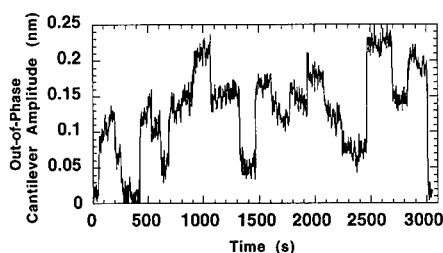


Figure 6. Out-of-phase response of PVAc vs. time. Applied stress is increasing in 10nm steps.

Figure 6 shows the out-of-phase amplitudes of the cantilever at 500 Hz for PVAc at 303K as a function of time while increasing the static loading force. This is achieved by moving the sample position toward the cantilever in 10nm steps. Notice that the loss (out-of-phase amplitude) makes sharp jumps up or down. In some instances slow relaxation is observed. In other cases sharp changes are observed with no change in loading force. These effects are only observed in a narrow range of temperature below the glass transition. A similar experiment done on the Mo surface showed only small changes in the response which are consistent with background noise. These observations are preliminary and will require further experiments and analysis to fully understand them. But they are strongly suggestive that just below its glass transition, PVAc

fluctuates between a solid-like and a viscous liquid-like response. In this instance the fluctuations are occurring as a function of applied stress. We have also observed such fluctuations after bringing the tip out of contact and back in at the same loading force. Some of the observations indicate large discrete relaxations of the compliance, suggestive of highly cooperative relaxation processes, possibly involving clusters.

## CONCLUSION

We have shown that our AFM is capable of measuring dielectric as well as viscoelastic properties of glassy samples to high precision on a mesoscopic length scale. At the same time we are able to operate over a wide range of temperature with minimal drift and in high vacuum. First intriguing results on PVAc include the observation of large fluctuations of the viscoelastic properties as a function of applied stress below the glass transition. Further measurements and analysis are needed to understand these effects. Dielectric fluctuation studies are in progress and will compliment the viscoelastic studies.

## ACKNOWLEDGMENTS

We thank M. Tortonese and Park Scientific for the piezolevers. This work is supported by the National Science Foundation DMR 9458008.

## REFERENCES

1. See review by C. A. Angell, *Science* **267**, 1224 (1995) and following articles in the same issue.
2. Richard M. Ernst, Sidney R. Nagel and Gary S. Grest, *Phys. Rev. B* **43**, 8070 (1991).
3. Narayanan Menon and Sydney R. Nagel, *Phys. Rev. Lett.* **74**, 1230 (1995).
4. Andrew I. Mel'cuk, Raphael A. Ramos, Harvey Gould, W. Klein, and Raymond D. Mountain, *Phys. Rev. Lett.* **75**, 2522 (1995).
5. N. E. Israeloff, *Phys. Rev.* **B53** (Rapid Comm.), R11913 (1996).
6. J. Schuller, Yu.B. Mel'nichenko, R. Richert and E.W. Fischer, *Phys. Rev. Lett.* **73**, 2224 (1994).
7. D. S. Fisher and D. A. Huse, *Phys. Rev. Lett.* **56**, 2401 (1986).
8. K.S. Ralls and R. A. Buhrman, *Phys. Rev. Lett.* **60**, 2434 (1988); G. A. Garfunkel, G. B. Alers, M. B. Weissman, and N. E. Israeloff, *Phys. Rev.* **B40** (RC), 8049 (1989).
9. N. E. Israeloff, M. B. Weissman, G. J. Nieuwenhuys, and J. Kosiorowska, *Phys. Rev. Lett.* **63**, 794 (1989); N. E. Israeloff, G. B. Alers, and M. B. Weissman, *Phys. Rev.* **B 44** (Rapid Comm.), 12613 (1991).
10. M. B. Weissman, *Rev. Mod. Phys.* **60**, 537 (1988).
11. G. Binnig, C. Quate and Ch. Gerber, *Phys. Rev. Lett.* **56**, 930 (1986).
12. Y. Martin, D.W. Abraham and H.K. Wickramasinghe, *Appl. Phys. Lett.* **52**, 1103 (1988).
13. M. Radmacher, R. W. Tillmann, and H. E. Gaub, *Biophys. J.* **64**, 735 (1993).
14. M. Tortonese, Ph.D. Thesis, Stanford University, 1993.
15. J. E. Mckinney, H. V. Belcher, *J. Res. Nat. Bur. Stds.* **67A**, 43 (1963).

## LIQUID-LIQUID PHASE SEPARATION OF MELTS AND GLASSES IN FERRIC FERROUS OXIDE-SILICA SYSTEM

A. YASUMORI\*, A. KOIKE\*, Y. KAMESHIMA\*, K. OKADA\*, T. YANO\*,  
M. YAMANE\*, and S. INOUE\*\*

\*Dept. of Inorganic Mater., Tokyo Institute of Technology, Meguro-ku, Tokyo 152 JAPAN

\*\*National Institute for Research in Inorganic Materials, Namiki, Tsukuba 305 JAPAN

### ABSTRACT

The existence of liquid-liquid miscibility gap in ferric ferrous oxide-silica system has been reported, however, the phase separation phenomena and the derived morphology of the phase separated glasses are uncertain. In this study, the melt-quenched samples of 5 Fe<sub>3</sub>O<sub>4</sub>-95 SiO<sub>2</sub> and 15 Fe<sub>3</sub>O<sub>4</sub>-85 SiO<sub>2</sub> (mol%) were prepared by melting at 2300°C or 2200°C (expected to be above miscibility gap), and subsequently at 1800°C or 1750°C (in immiscible region) by use of infrared image furnace and quenching at the rate of  $\approx 10^2$  K/sec. The glassy materials exhibited phase separation having discrete spherical particles or interconnected structure due to the composition, melting temperature and time. Also, the segregation of Fe component occurred during melting, which was caused by the difference of specific gravity of components in the melt.

### INTRODUCTION

Phase separation is a widespread phenomenon in glassy materials and porous glasses prepared by such phenomenon and subsequent acid leaching have been applied in various fields of engineering as filters, supports, etc.. [1, 2, 3] Considering applications of phase separated glasses from other points of view, the glasses containing fine particles derived by phase separation are expected to show high functional properties which are applicable to non-linear optical devices and advanced magnetic materials having single domain. Especially, when phase separated glasses are prepared from liquid-liquid immiscible melts under micro gravity condition and by subsequent operations such as elongation or compression, the glassy materials containing genuine spherical particles or regularly deformed ones will be obtained without segregation of component due to the difference of specific gravity. The former material will become a micro cavity laser device and the later one will appear anisotropic properties. [4, 5]

There are many binary silicate systems having liquid-liquid miscibility gap such as alkaline earth-silica and zinc oxide-silica systems. Ferric ferrous oxide-silica system also has widespread liquid-liquid miscibility gap as shown in Fig. 1. [6, 7, 8] In high silica composition of this system, FeO-Fe<sub>2</sub>O<sub>3</sub>-rich particles will be there in SiO<sub>2</sub>-rich glass matrix and this phase separated materials are hopeful as the base of the new functional materials showing highly optical, magnetic, and magneto-optical properties. However, its miscibility gap and the tie line in high temperature region, and the morphology of the glassy materials has not been investigated yet. Furthermore, Fe-rich phase may segregate from SiO<sub>2</sub>-rich matrix during melting under terrestrial gravity due to the difference of their specific gravity.

In this study, the melts and their quenched glassy materials of ferric ferrous oxide-silica system in miscibility gap were prepared. The morphology of phase separated structure and fluctuations of the compositions were investigated in order to obtain the behavior of phase separation in this system for further experiment under micro gravity.

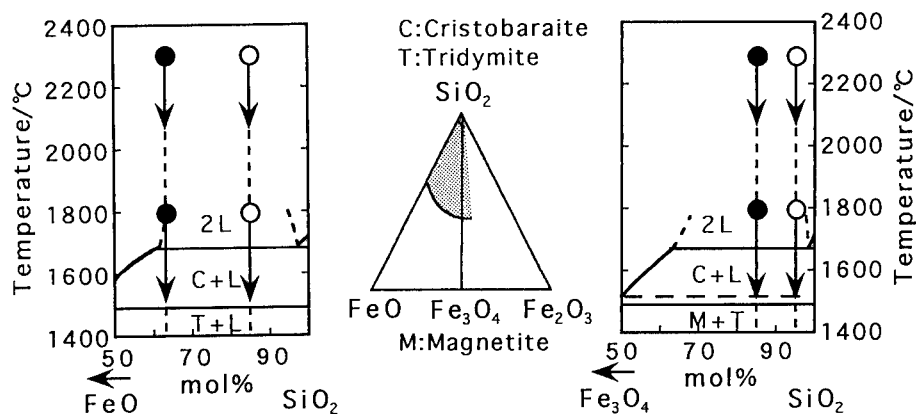


Figure 1 Phase Diagram of Ferric Ferrous Oxide-Silica System. [1,2,3]

## EXPERIMENT

Reagent grade  $\alpha$ -quartz ( $\text{SiO}_2$ ) and magnetite ( $\text{Fe}_3\text{O}_4$ ) fine powder in the composition of 5  $\text{Fe}_3\text{O}_4$ -95  $\text{SiO}_2$  and 15  $\text{Fe}_3\text{O}_4$ -85  $\text{SiO}_2$  (mol%) were mixed and calcined at  $1350^\circ\text{C}$  for 24 h in vacuo ( $\approx 10^{-2}$  torr). Calcined powder was molded into rod shape by use of a cold isostatic press (98 MPa). The rod samples were sintered at  $1350^\circ\text{C}$  for 24 h in vacuo. The sintered rods were melted at  $2300^\circ\text{C}$  or  $2200^\circ\text{C}$  under Ar gas atmosphere by use of an infrared image furnace with 5.4 kW Xe lamp (Nichiden Machinery, FQ-50XS) in order to obtain a homogeneous single liquid phase. Subsequently, the melts were cooled to  $1800^\circ\text{C}$  or  $1750^\circ\text{C}$  and were held there for promoting phase separation. Finally, the melts were quenched by moving them from the focal point of the image furnace. The temperature of the melting drop was measured by use of the radiation pyrometer with  $5\text{ }\mu\text{m}$  infrared ray (Japan Sensor, TSS-15G) from the bottom of the melting drop as shown in Fig. 2.

The sintered rods melted with a little sublimation of silica component, especially, at higher temperature range. The temperature of the melting drop changed from  $2300^\circ\text{C}$  to  $1800^\circ\text{C}$  within few seconds by reducing the power of Xe lamp. The cooling rate of the samples from  $1800^\circ\text{C}$  to  $1000^\circ\text{C}$  was  $\approx 10^2$  K/sec. The quenched drops were cut vertically and polished. The surfaces of cross section of the samples were etched with aqueous  $\text{HF}+\text{H}_2\text{SO}_4$  solution (0.05 mass%). Their

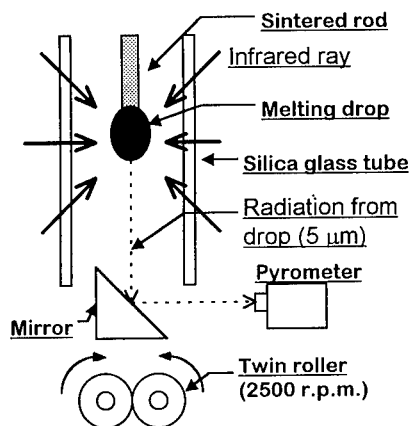


Figure 2 Schematic Illustration of Infrared Image Furnace.

morphology was observed by scanning electron microscope (SEM; JEOL, JSM-T200) and the fluctuation of composition in the sample was analyzed by EDX system (SEIKO EG & G, SED-8600). Also, XRD patterns of the sintered rods and the melt-quenched samples were measured by use of X-ray diffraction meter (Cu-K $\alpha$  radiation, Rigaku Geigerflex system).

## RESULTS

### XRD measurements

The XRD patterns of the sintered rods and the quenched samples are shown in Fig. 3 (a) and (b). Crystalline phases in the sintered rods were tridymite (SiO<sub>2</sub>), fayalite (Fe<sub>2</sub>SiO<sub>4</sub>) and a trace of diffraction peaks of magnetite (Fe<sub>3</sub>O<sub>4</sub>). The quenched sample in the composition of 5 Fe<sub>3</sub>O<sub>4</sub>-95 SiO<sub>2</sub> (mol%) showed a halo pattern with very little and broad peaks of fayalite and iscorite (Fe<sub>7</sub>SiO<sub>10</sub>). On the contrary, all the quenched samples in the composition of 15 Fe<sub>3</sub>O<sub>4</sub>-85 SiO<sub>2</sub> (mol%) showed obvious diffraction peaks of fayalite with a halo.

### EDX analysis

The fluctuations of composition in the quenched samples (5 Fe<sub>3</sub>O<sub>4</sub>-95 SiO<sub>2</sub>) melted at 2300°C for 4 and 6 min were shown in Fig. 4 (a) and (b), respectively. The concentration of Fe (atom%) obtained by the EDX measurement was converted into Fe<sub>3</sub>O<sub>4</sub> mol% in Fe<sub>3</sub>O<sub>4</sub>-SiO<sub>2</sub> binary system. The concentration of Fe in the sample melted for 4 min was constant and as same as the starting composition. However, in the sample melted for 6 min, Fe component concentrated at the bottom of the drop. There was no fluctuation of composition in the quenched sample further held at 1800°C for 4 min. On the other hand, all the samples (15 Fe<sub>3</sub>O<sub>4</sub>-85 SiO<sub>2</sub>) showed no fluctuation of composition and the converted value was as same as starting composition, either.

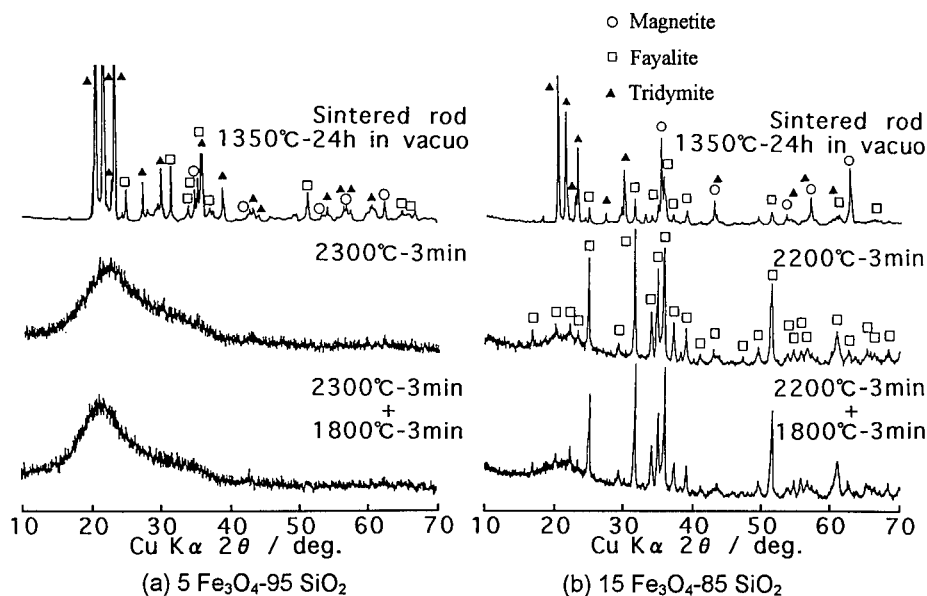


Figure 3 XRD Patterns of Melt-Quenched Samples.

### SEM observation

The SEM micrographs of the etched surface of the cross section in the sample ( $5 \text{ Fe}_3\text{O}_4\text{-}95 \text{ SiO}_2$ ) melted at  $2300^\circ\text{C}$  are shown in Fig. 5. In the sample held for 4 min, there were no etch pits of phase separated particles except for scratches caused by polishing. On the contrary, the sample held at 6 min had different morphology, that is, the bottom region of

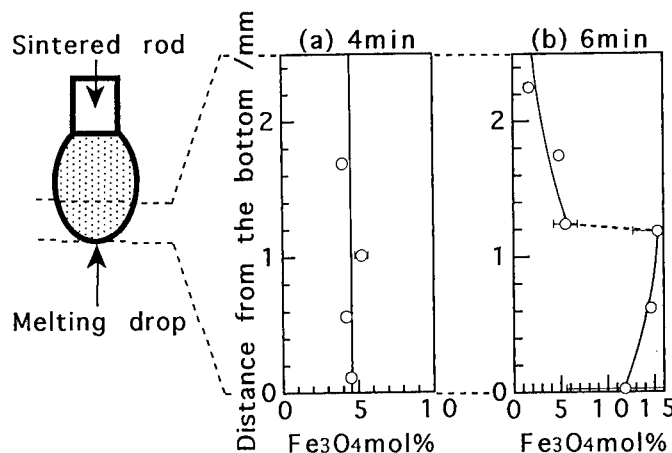


Figure 4 Fluctuation of the Composition in the Samples Melted at  $2300^\circ\text{C}$ .

drop, in which Fe component concentrated, exhibited interconnected structure. The micrographs of the samples subsequently held at  $1800^\circ\text{C}$  for 3 min are shown in Fig. 6 (a). The samples exhibited pronounced and discrete etch pits of submicron-order.

On the other hand, all the samples in  $15 \text{ Fe}_3\text{O}_4\text{-}85 \text{ SiO}_2$  (mol%) had the interconnected structure as shown in Fig. 6 (b). This structure was similar to that observed at the bottom region of the sample ( $5 \text{ Fe}_3\text{O}_4\text{-}95 \text{ SiO}_2$ ) held at  $2300^\circ\text{C}$  for 6 min of which converted composition was almost 15 mol% of  $\text{Fe}_3\text{O}_4$ .

### DISCUSSION

The valence of Fe ions in the quenched glassy sample ( $5 \text{ Fe}_3\text{O}_4\text{-}95 \text{ SiO}_2$ ) maintained that in the sintered rod or, at least, the sample did not oxidized further to consider that the diffraction angles of the halo and its shoulder were very close to those of fayalite and iscorite, which arose under low oxygen pressure at higher temperature [9], though the stable phases are hematite ( $\alpha\text{-Fe}_2\text{O}_3$ ) and tridymite in normal

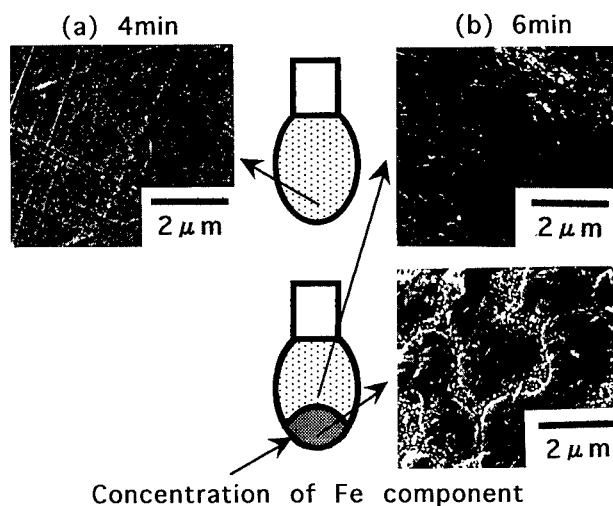


Figure 5 SEM Photographs of the Samples Melted at  $2300^\circ\text{C}$  for 4 min or 6 min.



atmospheric condition. In this composition, the melting at 2300°C was enough to obtain a homogeneous melt, that is, 2300°C was above miscibility gap. The discrete etch pits on the cross section of the sample held at 1800°C represented that FeO-Fe<sub>2</sub>O<sub>3</sub>-rich discrete particles were embedded in a continuous SiO<sub>2</sub>-rich matrix according to the nucleation and growth mechanism. The volume fraction of FeO-Fe<sub>2</sub>O<sub>3</sub>-rich phase in this sample was estimated from the volume change of etch pits depending on the etching time and was about 2%. This result is consistent with that the composition of the melt stood just inside of tie line in SiO<sub>2</sub>-rich side in Fe<sub>3</sub>O<sub>4</sub>-SiO<sub>2</sub> binary system, estimating the volume fraction of such phase from the lever rule.

Also the melting at the higher temperature for a long time resulted in the segregation of the composition by not only the phase separation phenomenon but also the difference of specific gravity of the components in the melt. The interconnected structure existed at the bottom of droplet was caused by spinodal decomposition, because the composition of Fe component at that region changed to that near the center of expected miscibility region in Fe<sub>3</sub>O<sub>4</sub>-SiO<sub>2</sub> system.

All the quenched samples (15 Fe<sub>3</sub>O<sub>4</sub>-85 SiO<sub>2</sub>) were partially crystallized and exhibited the interconnected structure. This structure suggested that spinodal decomposition also occurred during melting or quenching because this composition locates near the center of miscibility gap in Fe<sub>3</sub>O<sub>4</sub>-SiO<sub>2</sub> system. It was still unclear whether the melting temperature, 2300°C or 2200°C, was higher than consolute temperature of this system or not, because the quenching rate was not so fast due to the limitation of experimental conditions. The partial crystallization of quenched sample also derived from both slow quenching rate and decrement of the viscosity owing to its FeO-Fe<sub>2</sub>O<sub>3</sub> rich composition. In fact, the sample which was rapidly quenched by use of twin roller system (rotation speed; 2000 r.p.m.) exhibited no diffraction peak except halo on its XRD pattern, though the melting temperature of the drop was uncertain in the range between 2300°C and 1900°C because the sample drop moved out from the focal isothermal zone by the operation of falling the melting drop in present experimental condition.

The found crystalline phase in the sample (15 Fe<sub>3</sub>O<sub>4</sub>-85 SiO<sub>2</sub>) was only fayalite. This suggests that the reduced condition was also maintained during melting and quenching. On the photographs in Fig. 6 (b), FeO-Fe<sub>2</sub>O<sub>3</sub>-rich phase consisted of small fine particles which were probably fayalite crystallites and the volume fractions of such phase were 45, 38 and 40 % in the

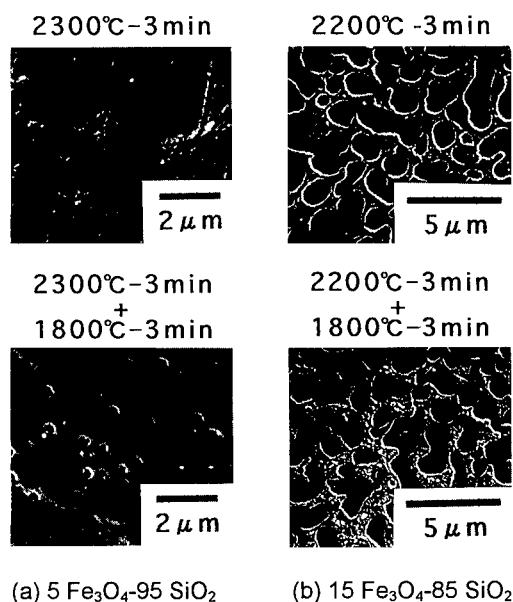


Figure 6 SEM Photographs of the Samples Melted at 2300°C or 2200°C and subsequently at 1800°C.

samples melted at 2300°C, 2200°C and 1800°C, respectively. From the phase diagrams as shown in Fig. 1, the position of starting composition in the miscibility gap shifted to the Fe-rich side with the change of Fe ions from trivalent to divalent condition. Therefore, from the lever rule, the volume fraction of Fe-rich phase increased with the higher melting temperature, because the higher temperature promotes the change of valence to the reduction state.

## CONCLUSIONS

The glassy materials in ferric-ferrous-silica system showed phase separated structure consisting of discrete spherical particles, or interconnected structure owing to the composition of the melt. Moreover, not only the composition but also the melting temperature affected the valence condition of Fe ions, that is, the morphology and mechanism of phase separation. Therefore, the valence condition of Fe ions in the samples are necessary to be measured in any event in order to infer the phase separation phenomenon in this system for future experiments under micro gravity.

Also, the segregation of Fe component was found to occur during melting, which was caused by the difference of specific gravity of components in the melt. This fact suggested that micro gravity condition is essential for the preparation of high functional materials utilizing phase separation, especially the materials containing heavier ions.

## ACKNOWLEDGMENT

This study was carried out as a part of "Space Utilization Frontiers Joint Research Projects" promoted by NASDA and Japan Space Utilization Promotion Center. Also, a part of this study was supported by a Grant-in-Aid for Scientific Research from the Ministry of Education, Science, Sports and Culture, Japan, No. 08650778.

## REFERENCES

1. T. H. Elmer, Am. Ceram. Soc. Bull., **57**, 1051 (1978)
2. S. Hirai, A. Morikawa, Y. Ishinaga, K. Okuta and Y. Wada, Bull. Chem. Soc. Jpn, **50**, 3411 (1977)
3. M. Umino, T. Yano, A. Yasumori, S. Shibata and M. Yamane, in Ceramic Transaction vol. 31 edited by K. Ishizaki, L. Sheppard, S. Okada, T. Hamasaki, and B. Huybrechts (the American Ceramic Society, Ohio, 1993) p. 191; T. Yazawa and H. Tanaka, ibid., p. 213
4. H. Taniguchi, T. Fujiwara, H. Yamada, S. Tanosaki and M. Baba, Appl. Phys. Lett., **62**, 2155 (1993)
5. T. Takamori and M. Tomozawa, J. Am. Ceram. Soc., **59**, 377 (1976)
6. N. L. Bowen and J. F. Schairer, Am. J. Sci., 5<sup>th</sup> Ser., **24**, 200 (1932)
7. B. Phillips and A. Muan, J. Am. Ceram. Soc., **42**(9), 415 (1959)
8. E. F. Osborn and A. Muan, revised and redrawn Phase Equilibrium Diagrams of Oxide Systems, Plate 6 (the American Ceramic Society and the Edward Orton, Jr., Ceramic Foundation, 1960)
9. D. R. Wones and M. C. Gilbert, Am. J. Sci., **267-A**, 480 (1969)

## THE EFFECT OF IRON AND OXYGEN ADDITIONS ON THE PROPERTIES OF Zr-Al-Cu-Ni BULK METALLIC GLASS FORMING ALLOYS

J. ECKERT, N. MATTERN, M. SEIDEL AND L. SCHULTZ

Institut für Festkörper- und Werkstofforschung Dresden, D-01171 Dresden, Germany

### ABSTRACT

The effect of iron and oxygen additions on the thermal stability of rapidly quenched amorphous  $\text{Zr}_{65}\text{Al}_{17.5}\text{Cu}_{17.5}\text{Ni}_{10}$  was studied by x-ray diffraction and differential scanning calorimetry. With increasing Fe content the glass transition temperature  $T_g$  and the crystallization temperature  $T_x$  shift to higher temperatures. The increase is more significant for  $T_g$  than for  $T_x$ , resulting in a decrease of the supercooled liquid region with increasing Fe content. For oxygen additions  $T_x$  decreases with increasing oxygen content whereas  $T_g$  increases slightly, causing a decrease of the supercooled liquid region with increasing oxygen content. The results reveal that even minor iron or oxygen contaminations lead to drastic changes in the glass transition behavior and the crystallization mode. Large iron or oxygen contents lead to the formation of nanocrystalline microstructures instead of coarse-grained material.

### INTRODUCTION

The new class of multicomponent metallic glasses with excellent glass forming ability and wide supercooled liquid region has attracted a lot of interest recently [1-3]. These alloys can be prepared as bulk samples even at low cooling rates of 10 K/s or less and have considerable potential as advanced engineering materials due to their excellent processing capabilities of the supercooled liquid, low coefficient of friction, high wear resistance as well as high strength and good corrosion resistance [4].

These alloys contain highly reactive elements and oxygen or metallic contaminations are frequently present already in the starting constituents, *e.g.* transition metal or rare earth elements. Furthermore, contaminations might also be introduced during alloy preparation by quenching or solid state processing. For example, mechanically alloyed powders typically contain some iron impurities due to the wear debris of the steel milling tools [5, 6]. In the past evidence has built up that for instance already a small amount of oxygen significantly affects the glass transition and crystallization behavior of metallic glasses [7, 8]. However, no detailed understanding of the role of contaminations on the properties of bulk metallic glass forming alloys exists up to now. The aim of this paper is to study the influence of iron and oxygen additions on the glass transition and crystallization behavior of the bulk metallic glass forming  $\text{Zr}_{65}\text{Al}_{17.5}\text{Cu}_{17.5}\text{Ni}_{10}$  alloy in some detail for different iron and oxygen contents.

### EXPERIMENTAL METHODS

Prealloyed ingots were molten from pure elements (purity 99.9%) in an arc furnace under a Ti-gettered argon atmosphere. Amorphous ribbons 10 mm in width were quenched by single-roller melt-spinning in a Bühler melt-spinning device under argon. The oxygen containing alloys were prepared by adjusting the oxygen partial pressure upon arc-melting and melt-spinning.

Thermal analysis was performed in a Netzsch DSC 404 differential scanning calorimeter at a heating rate of 20 K/min in purified argon. X-ray diffraction patterns were measured with a Philips PW3020 Bragg-Brentano diffractometer equipped with a secondary graphite monochromator using CuK $\alpha$  radiation. Chemical analysis was done by electron microprobe analysis, atomic absorption spectroscopy, hot extraction and optical emission spectroscopy.

## RESULTS AND DISCUSSION

Figure 1 shows x-ray diffraction patterns for as-quenched  $\text{Zr}_{65}\text{Al}_{7.5}\text{Cu}_{17.5}\text{Ni}_{10}$  ribbons with different iron or oxygen content. All diffraction patterns exhibit only the typical broad diffuse maxima characteristic of an amorphous phase. No indication for crystalline phases is evident in the x-ray patterns, even for large iron contents. The scattering vector  $Q_p$  related to the position of the first diffuse maximum between  $30^\circ < 2\theta < 50^\circ$  and defined as  $Q_p = 4\pi\sin\Theta_{\text{max}}/\lambda$ , shifts to larger values with increasing Fe content (Fig. 2). A linear extrapolation to 100% Fe gives  $Q_p = 31 \text{ nm}^{-1}$  which is similar to the value for amorphous iron or iron-based alloys. In contrast,  $Q_p$  slightly decreases with increasing oxygen content. The continuous change of  $Q_p$  with iron and oxygen additions indicates that both elements are probably truly alloyed in a homogeneous amorphous phase. No clustering or iron-rich amorphous second phase occurs, even for large iron contents of up to 20 at.%. The increase of  $Q_p$  with iron addition points to substitution of Zr and the other elements by iron with shorter interatomic distances Fe-Zr and Fe-Fe. The measured interference function  $I_s(Q)$  representing the weighted sum of the partial interference functions ( $I_s(Q) = \sum \sum w_i I_{ij}$ ) shifts with iron addition especially due to the increasing contribution of  $I_{\text{Fe-Zr}}$ . The decrease of  $Q_p$  with the small amount of oxygen points to a possible increase of Zr-Zr distances by interstitial oxygen. For clarification, more detailed investigations are necessary.

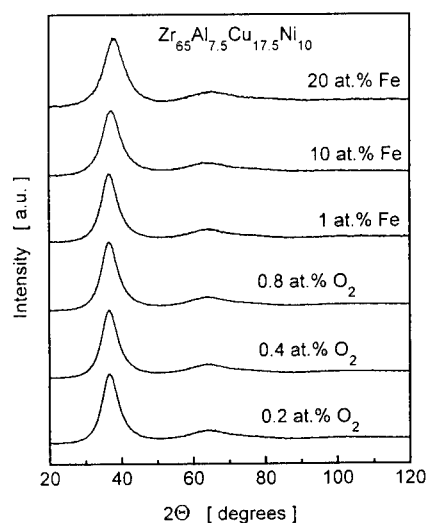


Figure 1: X-ray diffraction patterns for  $\text{Zr}_{65}\text{Al}_{7.5}\text{Cu}_{17.5}\text{Ni}_{10}$ -based ribbons with different iron or oxygen content.

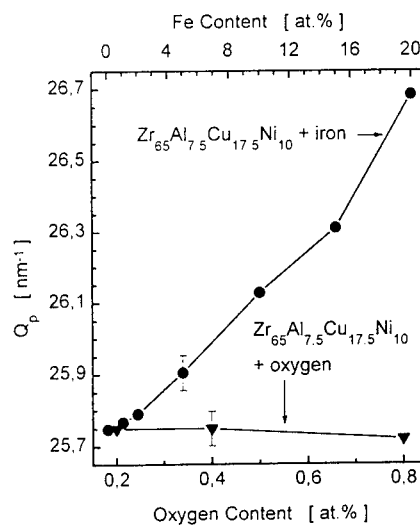


Figure 2: Scattering vector  $Q_p$  for  $\text{Zr}_{65}\text{Al}_{7.5}\text{Cu}_{17.5}\text{Ni}_{10}$ -based ribbons with different iron or oxygen content.

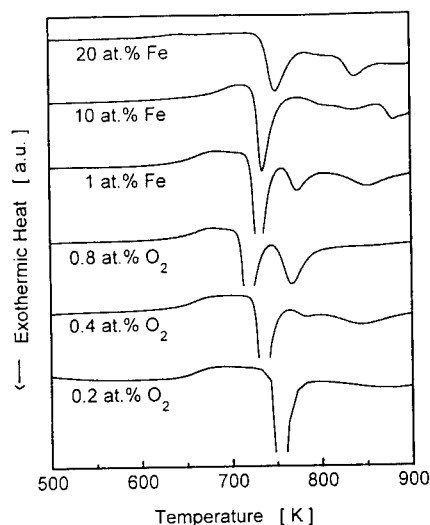


Figure 3: DSC scans (heating rate 20 K/min) for  $\text{Zr}_{65}\text{Al}_{7.5}\text{Cu}_{17.5}\text{Ni}_{10}$ -based ribbons with different iron or oxygen content.

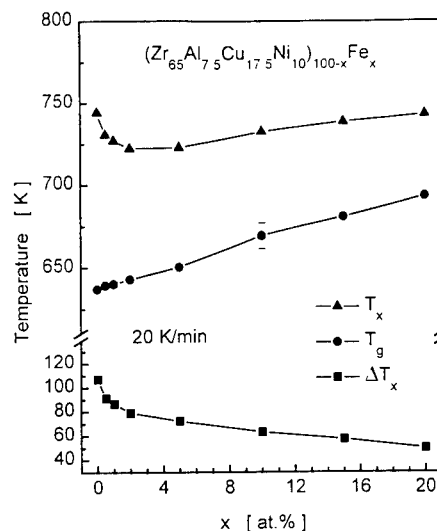


Figure 4: Variation of  $T_g$ ,  $T_x$ , and  $\Delta T_x$  for  $\text{Zr}_{65}\text{Al}_{7.5}\text{Cu}_{17.5}\text{Ni}_{10}$ -based ribbons versus iron content.

Iron and oxygen additions lead to significant changes in the DSC traces (Fig. 3). Most prominent is the change from one sharp crystallization event to two or three peaks. The thermal stability data as a function of Fe content are summarized in Fig. 4 (the glass transition temperature  $T_g$  and the crystallization temperature  $T_x$  are defined as the onset temperatures of the glass transition or the first crystallization peak, respectively).  $T_g$  increases continuously with increasing Fe content.  $T_x$  decreases for small Fe additions and, after passing through a minimum for 2 at.% Fe, increases slower with increasing Fe content than  $T_g$ . Hence, the supercooled liquid region  $\Delta T_x = T_x - T_g$  decreases with increasing Fe content. This is similar as for  $\text{Zr}_{65}\text{Cu}_{35-x}\text{Al}_x$  glasses, exhibiting a decrease in thermal stability upon replacement of Al by Fe [9].

An increase in oxygen content slightly increases  $T_g$  and decreases  $T_x$ , thus reducing  $\Delta T_x$  from 107 K to 67 K for oxygen contents of 0.2 and 0.8 at.%, respectively (Fig. 5). Extrapolating our data to zero oxygen content gives  $\Delta T_x = 120$  K, which is comparable to the value for cast bulk  $\text{Zr}_{65}\text{Al}_{7.5}\text{Cu}_{17.5}\text{Ni}_{10}$  [10]. The results indicate that oxygen has a stronger effect on thermal stability than iron. Only 0.8 at.% oxygen reduce  $\Delta T_x$  to 67 K, but 5–10 at.% Fe are necessary to obtain a similar value (Figs. 4 and 5). This agrees well with very recent reports for slowly cooled bulk samples, also showing the important role of oxygen with respect to restricting bulk glass formation at low cooling rates [11, 12]. However, the reason for the decrease in  $T_x$  with oxygen is still under debate. Besides possible surface crystallization or heterogeneous crystallization due to oxide formation [7] the most likely explanation is related to oxygen-induced phase separation in the supercooled liquid state, which results in a large number of nucleation sites for crystallization of an oxygen-stabilized metastable phase [8].

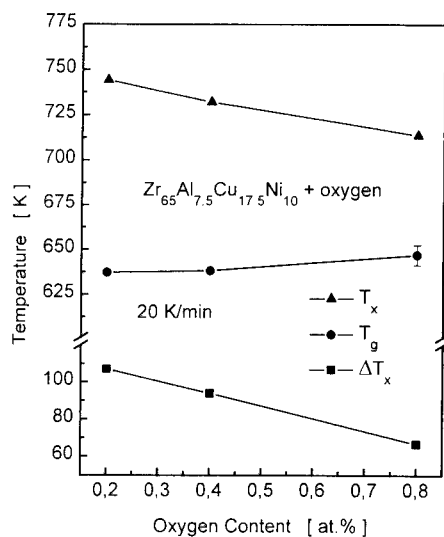


Figure 5: Variation of  $T_g$ ,  $T_x$ , and  $\Delta T_x$  for  $Zr_{65}Al_{7.5}Cu_{17.5}Ni_{10}$ -based ribbons versus oxygen content.

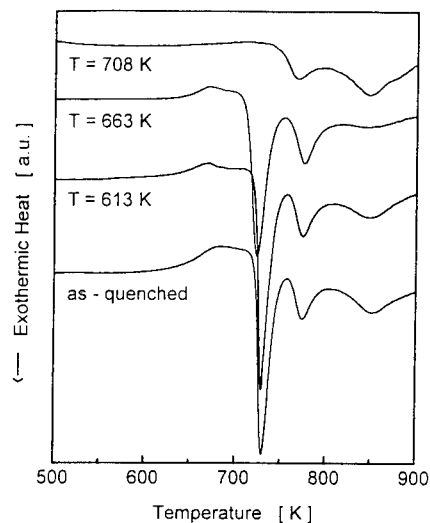


Figure 6: DSC scans (heating rate 20 K/min) for  $(Zr_{65}Al_{7.5}Cu_{17.5}Ni_{10})_{99}Fe_1$  in the as-quenched condition and after annealing for 30 min at different temperatures.

Fig. 6 shows the DSC scans of amorphous as-quenched  $(Zr_{65}Al_{7.5}Cu_{17.5}Ni_{10})_{99}Fe_1$  and after annealing for 30 min at different temperatures.  $T_g$  is not influenced by annealing but only the specific heat difference between the amorphous state and the supercooled liquid state decreases upon preannealing. This is due to relaxation of the sample during annealing below as well as above  $T_g$ . Annealing at 613 K retains the amorphous structure without indications for crystallization. Annealing at 663 K reduces  $T_x$  from 727 K for the as-quenched sample to 708 K after annealing, resulting in a smaller supercooled liquid region. The drop of  $T_x$  points to an incubation behavior of crystallization. During preannealing atomic rearrangements occur via formation of critical nuclei. The sample annealed at 708 K is partially crystallized which is correlated with the disappearance of the first crystallization peak. Annealing at 873 K for 30 min leads to complete crystallization. Similar results were observed for the other samples with different iron or oxygen content. Preannealing at temperatures around  $T_g$  leads to relaxation and reduces the specific heat difference between the amorphous and the supercooled liquid state. Annealing at higher temperatures in the supercooled liquid region triggers crystallization and, therefore, reduces  $\Delta T_x$ . These findings are very similar to pure  $Zr_{65}Al_{7.5}Cu_{17.5}Ni_{10}$  [13].

X-ray patterns for iron-containing samples after isothermal annealing for 30 min at different temperatures are shown in Figs. 7 and 8. Isothermal annealing clearly exhibits incubation behavior of crystallization. Crystallization is observed for  $(Zr_{65}Al_{7.5}Cu_{17.5}Ni_{10})_{99}Fe_1$  after 30 min at 708 K (Fig. 7) or after 30 min at 783 K for  $(Zr_{65}Al_{7.5}Cu_{17.5}Ni_{10})_{80}Fe_{20}$  (Fig. 8) in agreement with the DSC results. The crystallization behavior is strongly affected by the iron content. Pure amorphous  $Zr_{65}Al_{7.5}Cu_{17.5}Ni_{10}$  crystallizes by simultaneous formation of tetragonal  $CuZr_2$  and

other unknown phases [13]. Depending on the heat treatment a metastable cubic fcc phase of the  $\text{NiZr}_2$ -type with lattice parameter  $a = 1.22 \text{ nm}$  as an intermediate phase is observed during the first stage of crystallization. For the iron-containing alloys the phase sequence is altered with increasing iron content  $x$ . For  $x \geq 1$  the  $\text{NiZr}_2$ -type phase forms as the first step of crystallization. This phase represents the main fraction of the  $(\text{Zr}_{65}\text{Al}_{17.5}\text{Cu}_{17.5}\text{Ni}_{10})_{99}\text{Fe}_1$  alloy annealed at 708 K (Fig. 7). As illustrated for  $(\text{Zr}_{65}\text{Al}_{17.5}\text{Cu}_{17.5}\text{Ni}_{10})_{80}\text{Fe}_{20}$ , the structure of the alloys with  $1 \leq x \leq 20$  consists of  $\text{NiZr}_2$ -type phase and amorphous phase after the first step of crystallization (Fig. 8). The grain size of the fcc phase decreases with increasing Fe content, as indicated by the significantly broader diffraction peaks for  $(\text{Zr}_{65}\text{Al}_{17.5}\text{Cu}_{17.5}\text{Ni}_{10})_{80}\text{Fe}_{20}$  annealed at 783 K compared to the narrower peaks observed for  $(\text{Zr}_{65}\text{Al}_{17.5}\text{Cu}_{17.5}\text{Ni}_{10})_{99}\text{Fe}_1$  annealed at 708 K (Figs. 7 and 8). Using the well-known Scherrer equation gives an estimate of the grain size of about 5 nm for  $(\text{Zr}_{65}\text{Al}_{17.5}\text{Cu}_{17.5}\text{Ni}_{10})_{80}\text{Fe}_{20}$  and of 25 nm for  $(\text{Zr}_{65}\text{Al}_{17.5}\text{Cu}_{17.5}\text{Ni}_{10})_{99}\text{Fe}_1$ . At higher temperatures the  $\text{NiZr}_2$ -type phase transforms to stable crystalline phases. For  $0 \leq x \leq 5$  identical x-ray diffraction patterns were observed after annealing at 873 K. For  $x \geq 10$  different (unknown) phases are found after complete crystallization (Fig. 8). The addition of oxygen affects the crystallization behavior of amorphous  $\text{Zr}_{65}\text{Al}_{17.5}\text{Cu}_{17.5}\text{Ni}_{10}$  in a similar way concerning the metastable  $\text{NiZr}_2$ -type phase. For 0.4 at.% oxygen the fcc phase forms together with tetragonal  $\text{CuZr}_2$  after annealing at 708 K. The sample with 0.8 at.% oxygen crystallizes via formation of the fcc phase in the first stage.

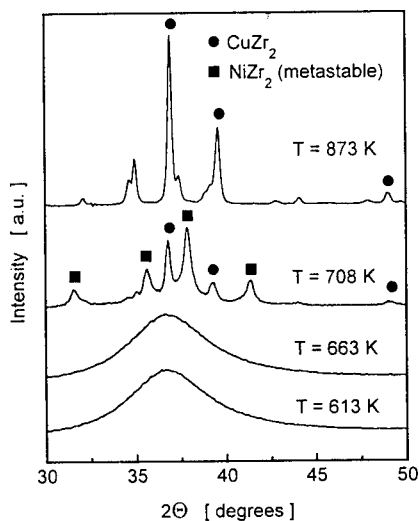


Figure 7: X-ray diffraction patterns for  $(\text{Zr}_{65}\text{Al}_{17.5}\text{Cu}_{17.5}\text{Ni}_{10})_{99}\text{Fe}_1$  in the as-quenched condition and after annealing for 30 min at different temperatures.

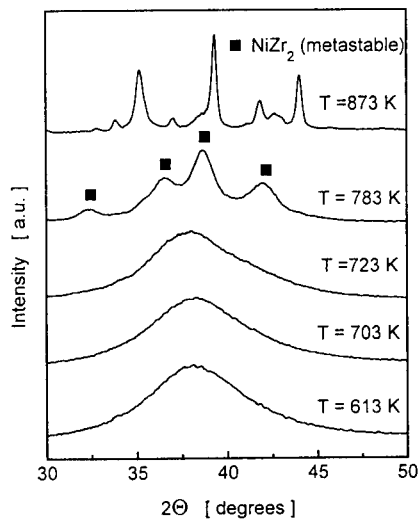


Figure 8: X-ray diffraction patterns for  $(\text{Zr}_{65}\text{Al}_{17.5}\text{Cu}_{17.5}\text{Ni}_{10})_{80}\text{Fe}_{20}$  in the as-quenched condition and after annealing for 30 min at different temperatures.

## CONCLUSIONS

The thermal stability of rapidly quenched amorphous  $Zr_{65}Al_{7.5}Cu_{17.5}Ni_{10}$  is strongly affected by iron or oxygen additions. The glass transition and crystallization temperature as well as the extension of the supercooled liquid region depend on the actual composition of the alloy. Together with the composition dependence of the position of the amorphous maximum this indicates that iron and oxygen are truly alloyed in the amorphous phase. Structural relaxation of the as-quenched state is observed for temperatures below and above  $T_g$ . In contrast to the pure metallic glass, a metastable cubic  $NiZr_2$  phase forms at the early stages of crystallization. Large iron or oxygen contents reduce the grain size of this phase to the nanometer range, indicating that both elements lead to drastic changes in the crystallization mode and kinetics, i.e. the formation of nanocrystals instead of large grains. Further work including microstructure investigations has to be done to fully characterize the development of the microstructure, the nucleation behavior with respect to impurity-driven phase separation in the supercooled liquid state, and the time-temperature dependence of crystallization of these new metallic glasses.

## ACKNOWLEDGMENTS

The authors would like to thank W. Gude, U. Kühn, H. Schulze and K. Stange for technical assistance, I. Bäcker, A. Kersebrock and W. Michel for chemical analysis, and I. Börner, A. Gebert, A. Kübler and N. Schlorke for stimulating discussions and effective cooperation. Financial support by the German Science Foundation under grant DFG Ec 111/7-1 is gratefully acknowledged.

## REFERENCES

1. A. Inoue, M. Kohinata, K. Ohtera, A.P. Tsai and T. Masumoto, *Mater. Trans. JIM* **30**, 378 (1989).
2. A. Inoue, T. Zhang and T. Masumoto, *J. Non-Cryst. Solids* **156-158**, 473 (1993).
3. A. Peker and W.L. Johnson, *Appl. Phys. Lett.* **63**, 2342 (1993).
4. W.L. Johnson, *Mater. Sci. Forum* **225-227**, 35 (1996).
5. M. Seidel, J. Eckert and L. Schultz, *J. Appl. Phys.* **77**, 5446 (1995).
6. M. Seidel, J. Eckert and L. Schultz, *Proc. ISMANAM-96*, Rome, May 1996; *Mater. Sci. Forum* (in print).
7. D.E. Polk, C.E. Dube and B.V. Giessen, in *Rapidly Quenched Metals III*, edited by B. Cantor (Metals Society, London, 1978) p. 220.
8. U. Köster, J. Meinhardt, S. Roos and A. Rüdiger, *Mater. Sci. Forum* **225-227**, 311 (1996).
9. A.P. Tsai, D. Kawase, A. Inoue and T. Masumoto, *Scr. Metall. Mater.* **29**, 657 (1993).
10. T. Zhang, A. Inoue and T. Masumoto, *Mater. Trans. JIM* **32**, 1005 (1991).
11. A. Inoue, Y. Shinohara, Y. Yokoyama and T. Masumoto, *Mater. Trans. JIM* **36**, 1276 (1995).
12. W.L. Johnson (private communication).
13. N. Mattern, J. Eckert, M. Seidel, U. Kühn, S. Doyle and I. Bäcker, *Proc. RQ-9*, Bratislava, August 1996; *Mater. Sci. Eng. A* (in print).



## SPECTRAL CHARACTERIZATION AND EXCITED-STATE INTERACTIONS BETWEEN RARE EARTH IONS DOPED IN BOROSILICATE AND SOL-GEL GLASSES: ENERGY TRANSFER UP-CONVERSION IN THE Pr-Sm SYSTEM

Z. Assefa\*, R. G. Haire\*, and N. A. Stump\*

\*Oak Ridge National Laboratory, CASD, P. O. Box 2008, Oak Ridge, TN 37831-6375.

\*Winston-Salem State University, Dept of Physical Sciences, Winston-Salem, NC 27110.

### ABSTRACT

Spectroscopic properties of selected 4f-elements in a sol-gel and two high temperature silicate based glasses are reported. In particular, the spectral properties of the  $\text{Eu}^{3+}$  ion have been used to probe the local coordination environment of the f-elements in these glass matrices. Luminescence studies of the high temperature glasses indicated that the electric dipole allowed f-f transitions dominate the spectra which suggests that the local symmetry around the 4f-ions is low. Temperature-dependent spectroscopic studies of the sol-gel glasses indicated that the f-elements retain a "solution-like" environment prior to thermal processing. After heat treatment, an increase in the emission intensities of the electric-dipole transitions is accompanied by a concomitant decrease in the magnetic-dipole allowed transitions. Moreover, excited state interactions has also been observed in the high temperature glasses that contain certain multiple f-elements. In Pr-Sm systems, exclusive excitation of the  $\text{Sm}^{3+}$  ion with a 514 nm argon ion laser line provides a higher-energy emission band (ca. 490 nm) from the  $\text{Pr}^{3+}$  ion ( $^3\text{P}_0 \rightarrow ^3\text{H}_4$ ) transition. This energy up-conversion is attributed to energy transfer from the  $^6\text{H}_{13/2}$  level of the  $\text{Sm}^{3+}$  ion to the  $^3\text{H}_6$  state of the  $\text{Pr}^{3+}$  ion. Following a second photon absorption, the  $\text{Pr}^{3+}$  ion is excited to the emitting  $^3\text{P}_0$  level.

### INTRODUCTION

Luminescence studies of f-elements in glassy matrices has attracted a considerable interest, due to the possible implication in solid-state laser and related optical applications [1, 2]. Understanding the local environment around the optically active ion is crucial for materials engineering, since the performance of such optical devices largely depends on the nature of the bonding interaction between the f-ions and the glass matrices [3]. In this regard, the  $\text{Eu}^{3+}$  ion is an ideal optical probe. One feature is that the  $^5\text{D}_0 \rightarrow ^7\text{F}_0$  emission band is non-degenerate and splitting or broadening reflects a dissimilar bonding environment. Another luminescence feature that provides information on the local environment is the "hypersensitive"  $^5\text{D}_0 \rightarrow ^7\text{F}_2$  transition. In the  $\text{Eu}^{3+}$  ion, an increase in the relative intensity of this electric-dipole allowed ( $^5\text{D}_0 \rightarrow ^7\text{F}_2$ ) transition is linked to deviations from an inversion symmetry. We have taken advantage of these spectroscopic features to monitor the "structural" variations in the local bonding environments in both high temperature borosilicate and sol-gel derived glasses.

In addition, the  $\text{Pr}^{3+}$  ion energy-level scheme is especially useful for applications involving fluorescence arising from two-step photo-excitation and energy up-conversion [4]. Laser and energy up-conversion properties have been documented in praseodymium(III) doped crystals and glasses. Examples include  $\text{Pr}^{3+}$  ion doped in  $\text{LaCl}_3$  glasses that showed "up-converted" emission at  $20930 \text{ cm}^{-1}$  following excitation at  $17050 \text{ cm}^{-1}$  [5]. Two- and three-ion cooperative up-conversion has also been noted for the  $\text{Pr}^{3+}$  ion in  $\text{LaF}_3$ , where emission from the  $^1\text{S}_0$  high-energy excited level has been observed when a radiative energy capable of exiting to the much lower,  $^3\text{P}_0$ ,

level is used [6].

In this paper, we present spectroscopic studies involving the  $\text{Eu}^{3+}$  ion as a probe to the local coordination environment of f-elements doped in high temperature borosilicate glasses and a sol-gel matrix. In addition, we present spectroscopic investigations on the excited-state interactions between multiple f-ions in the high temperature glasses. In particular, we report the nature of the energy transfer up-conversion that has been observed in the Pr-Sm system.

## EXPERIMENTAL

Two high temperature glasses were studied in this work. The 850 °C melting glass had a composition of :  $\text{SiO}_2$  (50 %);  $\text{B}_2\text{O}_3$  (18%);  $\text{Na}_2\text{O}$  (24%); Ca (3%). The higher melting (1400 °C) "lead borosilicate" glass had the following nominal weight percentages:  $\text{SiO}_2$  (30 %);  $\text{B}_2\text{O}_3$  (6 %);  $\text{Al}_2\text{O}_3$  (13%);  $\text{PbO}$ (3%) and  $\text{La}_2\text{O}_3$  (10 - 15 %). Both glasses were prepared by dissolving the f-element oxide in the molten glasses. Platinum containers were used for the dissolution procedure.

The sol-gel samples were prepared via acid-hydrolysis (0.1 N  $\text{HNO}_3$ ) and condensation of tetramethoxysilane (TMOS). The lanthanide was introduced in the initial stage of the process by dissolving the nitrate salt in water. The top of the glass cylinder containing the mixture was partly covered to reduce volatilization during the condensation process. Densification provided a clear glass after several days.

The spectroscopic investigations were conducted using Argon-ion laser ( Coherent Models 90 and 306 ) as the excitation source. The luminescence spectra were recorded with a double, 2 m spectrophotometer ( Raman Model HG.2S, Jobin-Yvon/Instrument SA ), having a resolution of  $0.5 \text{ cm}^{-1}$  at 514.5 nm. Emission from the sample was detected by a photon counting system, which employed a photomultiplier tube ( Hamamatsu R636 ) and a multichannel analyzer ( Nicolet 1170) interfaced with a personal computer. Data analysis was conducted with a "SpectraCalc" software (Galactic Industries )

## RESULTS

The emission spectra of the  $\text{Eu}^{3+}$  ion doped in the high temperature ( 1400 °C ) glass and sol-gel matrices are shown in Figure 1. In the high temperature glass photo-excitation with 514 nm radiation provides emission (figure 1a ) originating from the  $^5\text{D}_0$  excited state to the various  $^7\text{F}_j$  ground manifolds. The  $^5\text{D}_0 \rightarrow ^7\text{F}_0$  transition is observed at 578.5 nm. Three weak, but well resolved bands are also evident for the magnetic-dipole  $^5\text{D}_0 \rightarrow ^7\text{F}_1$  transitions at 586, 591, and 596 nm. The most intense band in this spectrum corresponds to the electric-dipole allowed  $^5\text{D}_0 \rightarrow ^5\text{F}_2$  transition. The dominance of the  $^5\text{D}_0 \rightarrow ^7\text{F}_2$  transition, indicates a lack of an inversion center for the local symmetry of the  $\text{Eu}^{3+}$  ion. Similar results were obtained for the  $\text{Eu}^{3+}$  ion doped in the lower temperature (850 °C) glass.

Spectroscopic studies have also been conducted in sol-gel matrix in order to compare the  $\text{Eu}^{3+}$  ion bonding interactions with those in the melt-derived silicate glasses. In Figures 1b, c & d are shown the temperature-dependent emission spectra of a 10 %  $\text{Eu}^{3+}$  ( g Eu/g  $\text{SiO}_2$  ) doped in a sol-gel glass. The spectral profile and relative intensities of the various transitions show a dependence on the heating temperature, which provides insight into the bonding environment of the  $\text{Eu}^{3+}$  ion brought about by heating.

At room temperature the  $^5\text{D}_0 \rightarrow ^7\text{F}_0$  transition shows a single sharp band at 578.6 nm (figure 1b). The overall spectral profile of this spectrum, as well as the ratio of the  $^5\text{D}_0 \rightarrow ^7\text{F}_1$  to the  $^5\text{D}_0 \rightarrow ^7\text{F}_2$

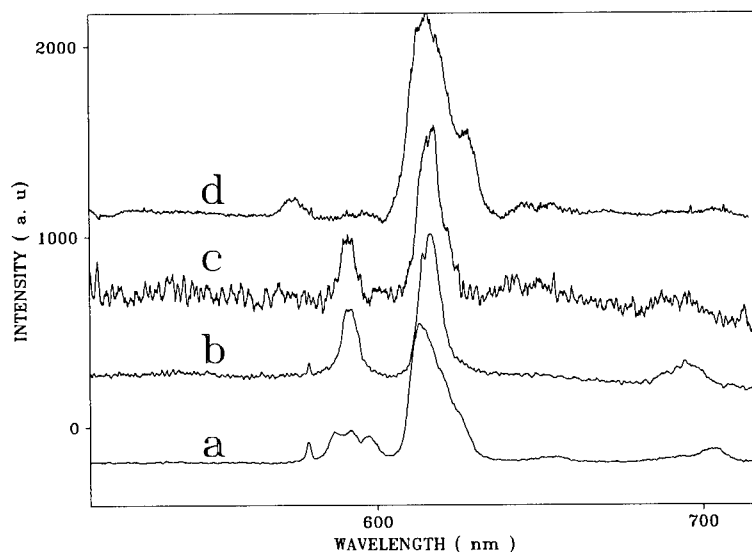


**Figure 1.** Emission Spectra of  $\text{Eu}^{3+}$  doped in: a) HT borosilicate glass; Sol-gel, (b) at room temperature; (c) heated at 400 °C; (d) heated at 800 °C

transition, is very similar to the emission spectrum of  $\text{Eu}(\text{NO}_3)_3$  in aqueous solution [7]. The strong similarity between the spectroscopic properties of  $\text{Eu}(\text{NO}_3)_3$  in the sol-gel and in aqueous solution suggests that no major coordination changes have taken place around the lanthanide ion. The sol-gel matrix provides a local “aqueous micro-environment” for the encapsulated  $\text{Eu}(\text{NO}_3)_3$  in the silanol network [8]. Significant spectral changes take place upon heating the sol-gel sample. All of the luminescence bands show broadening upon increasing the heating temperature. The intensity of the “environmentally sensitive”,  $^5\text{D}_0 \rightarrow ^7\text{F}_2$  transition increases with a concomitant decrease of the magnetic-dipole  $^5\text{D}_0 \rightarrow ^7\text{F}_1$  transition with heat treatment at higher temperatures. The spectral broadening noted following heat treatment clearly indicates that a change in the local environment of the lanthanide ion takes place at these higher temperatures. The data provide evidence for the start of some bonding interaction between the rare earth ion and the silanol groups of the matrix. From the spectroscopic results we infer that the lanthanide-silanol interaction becomes dominant only after the removal of the counter ion (nitrate) and volatile components from the matrix through heat treatment and the process continues up to a temperature of ca. 800 °C.

Nevertheless, significant spectral differences between the melt-derived silicate glasses and the sol-gel matrices remain even after heating the latter to 800 °C; one being that the spectral broadening is more intense in the sol-gel glasses after heat treatment. As discussed above, the  $^5\text{D}_0 \rightarrow ^7\text{F}_0$  transition in the high temperature glasses (figure 1a) is sharper as compared to the heat treated sol-gel products (figure 1c). The data suggest that a more uniform local environment for the f-element is attained in the high temperature melt-derived glasses than the heat treated sol-gel matrix.

In the sol-gel glasses, the lanthanide ion is uniformly distributed at the initial stage of the process, as indicated from the sharpness of the  $^5\text{D}_0 \rightarrow ^7\text{F}_0$  transition (figure 1b). This suggests that

the lanthanide is encapsulated within the silicate matrix, which behaves primarily as a non-interacting solvent. However, the removal of the counter anion and volatile components initiate bonding interactions between the lanthanide ion and the sol-gel matrix. The spectroscopic data clearly indicate that  $\text{Eu}^{3+}$  ions in the sol-gel matrix encounter minor differences in their surroundings when they interact with the silanol groups. As a consequence, spectral broadening and lack of splitting in the emission bands that originate from closely spaced multiple sites is observed. Thus, the lanthanide ions occupy several site symmetries when bonding interactions occur between the encapsulated f-ions and the sol-gel matrix at higher temperatures. The cause for the differences in site occupation is unclear at the moment even though similar broadening have been observed in the spectral profile of some actinide ions encapsulated in sol-gel matrices [9].

#### Excited-State Interaction

The high temperature (1400 °C) glasses doped with certain combinations of f-elements show special excited-state interactions. Among the lanthanide combinations that we have studied, the Pr-Sm interaction is particularly interesting as it leads to the observation of energy up-conversion. When a  $\text{Sm}^{3+}$  doped high temperature glass is excited with a 514 nm laser line, all of the characteristic f - f transitions for the ion are observed. Three sharp, strong bands are observed at 17740, 16640, and 15425  $\text{cm}^{-1}$  which correspond to the  $^4\text{G}_{5/2} \rightarrow ^6\text{H}_{5/2}$ ,  $^6\text{H}_{7/2}$ , and  $^6\text{H}_{9/2}$  transitions, respectively. Weak shoulders are observed at 17536, 16466 and 15260  $\text{cm}^{-1}$  as stark components of these transitions. Emission is not observed when the 514 nm laser line is used to excite the  $\text{Pr}^{3+}$  ion doped high temperature glass. The reason is that the  $\text{Pr}^{3+}$  ion does not have an excited level that matches (or nearly matches) the 514 nm excitation energy.

The situation changes when glasses containing both the  $\text{Sm}^{3+}$  and  $\text{Pr}^{3+}$  ions are excited with the 514 nm radiation. In Figure 2 are shown the emission spectra of the mixed Pr-Sm sample. Excitation with the 514 nm laser line provides all of the characteristics f - f transitions corresponding to the  $\text{Sm}^{3+}$  ion emission ( figure 2a). Interestingly, a higher-energy emission corresponding to the  $\text{Pr}^{3+}$  ion  $^3\text{P}_0 \rightarrow ^3\text{H}_4$  transition is also evident at the blue side of the excitation wavelength ( figure 2b).

Several mechanisms have been considered to understand this phenomenon. A conventional two-photon absorption ( by the  $\text{Pr}^{3+}$  ion ) is unlikely, as an energy level lying approximately twice the laser photon-energy above the ground state is not present [7]. A two-step, sequential excitation process has also been ruled out due to the lack of up-conversion emission in samples prepared from the  $\text{Pr}^{3+}$  ion alone. Since the up-conversion emission has been observed only in samples containing both the  $\text{Pr}^{3+}$  and  $\text{Sm}^{3+}$  ions, it indicates that excited-state interactions between the two f-ions is important in the overall process.

Shown in Figure 3 is the dependence of the "up-converted" emission intensity on the flux of the exciting laser radiation; which depends quadratically on the flux. This quadratic dependence of the laser-induced fluorescence, at 490 nm, indicates the importance of energy transfer from an excited  $\text{Sm}^{3+}$  ion to the  $\text{Pr}^{3+}$  ion in observing the "up-converted" emission band [4]. We attribute the phenomenon to energy transfer from the  $^6\text{H}_{13/2}$  level of the  $\text{Sm}^{3+}$  ion to the  $^3\text{H}_6$  state of the  $\text{Pr}^{3+}$  ion. Following a second photon absorption, the  $\text{Pr}^{3+}$  ion is then excited to the emitting  $^3\text{P}_0$  level. these lower excited levels. Experimental evidence exists which support the idea that the energy transfer process takes place at these lower excited levels. For example, excitation of the Pr-Sm sample with 350 nm radiation provides emission corresponding only to the  $\text{Sm}^{3+}$  ion f - f transition; emission is not evident from the  $\text{Pr}^{3+}$  ion ( figure 2c). In a situation where an excited-state interaction takes place at higher emitting levels, the sensitized emission should be

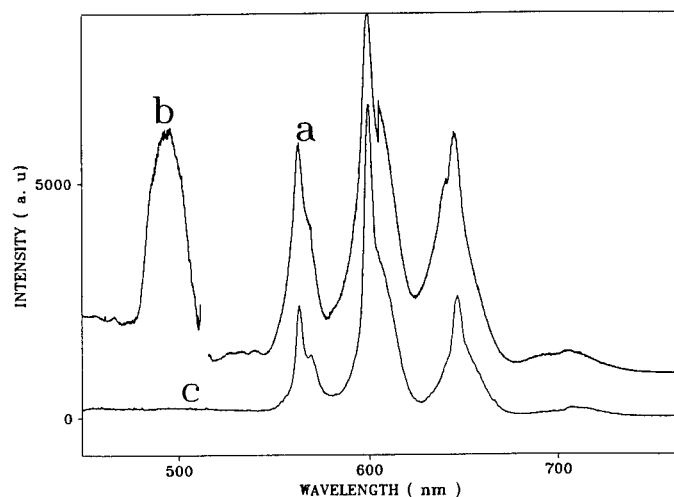


**Figure 2.** Emission spectra of the Pr-Sm co-doped high temperature 1400 °C glass: (a) Emission bands corresponding to the  $\text{Sm}^{3+}$  ion f-f transitions. The 514 nm line was used for sample excitation; (b) Up-conversion emission corresponding to the  $\text{Pr}^{3+}$  ion  $^3\text{P}_0 \rightarrow ^3\text{H}_4$  transition. Note that the band is situated at the “blue” side of the excitation wavelength (514 nm); (c) Spectrum recorded after exciting with a 360 nm laser line. Emission bands corresponding to the  $\text{Pr}^{3+}$  ion f-f transitions are absent with this excitation.

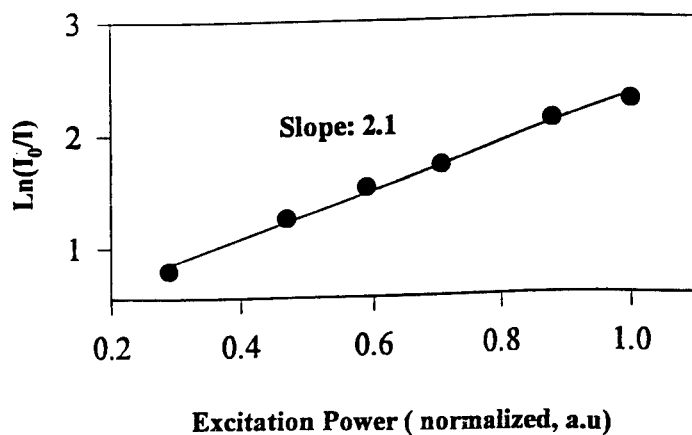


**Figure 3.** Up-conversion emission intensity of the Pr-Sm system showing a quadratic dependence on the excitation flux.

independent of the excitation wavelength. However, the dependence of the sensitized emission upon the excitation wavelength ( in the Pr-Sm system ) suggests the  $\text{Pr}^{3+}$  ion is excited by a photon absorption following energy transfer from an excited  $\text{Sm}^{3+}$  ion. This implies that the overall process leading to the up-conversion emission involves a two-photon absorption. We suggest that the process progresses as follows. In the first step, the  $\text{Sm}^{3+}$  ion is excited to the  $^4\text{F}_{3/2}$  level by 514 nm photon absorption. Following relaxation to the emitting  $^4\text{G}_{5/2}$  level, the excited ion falls radiatively to the  $^6\text{H}_{13/2}$  level. This level (  $^6\text{H}_{13/2}$  ) is nearly in resonant with the  $^3\text{H}_6$  level of the  $\text{Pr}^{3+}$  ion. Excitation of the  $\text{Pr}^{3+}$  ions to the  $^3\text{H}_6$  level may occur through a non-radiative energy transfer mechanism. A second 514 nm photon absorption by the excited  $\text{Pr}^{3+}$  ion raises it to the emitting  $^3\text{P}_0$  level, where the up-conversion emission originates. Efforts to fully understand the mechanism of the excited-state interaction and the efficiency of the energy transfer process in this high-phonon silicate matrix is under way in our laboratory.

## CONCLUSIONS

The spectral properties of the  $\text{Eu}^{3+}$  ion have been used to probe the local coordination environment of the f-elements in two high temperature borosilicate and a sol gel matrices. In the high temperature glasses electric dipole allowed f - f transitions dominate the spectra, suggesting the local symmetry around the 4f-ions is low. Studies on the sol-gel glasses as a function of thermal treatments indicate that f-ions retain a solution-like environment prior to heating. An increase in the emission intensities of the electric-dipole allowed transitions is accompanied by a concomitant decrease in the magnetic dipole-allowed transitions after heating. Moreover, excited state interaction has been observed in the high temperature glasses containing multiple f-elements. In the Pr-Sm system, exclusively exciting the  $\text{Sm}^{3+}$  ion with a 514 nm argon ion laser provides a higher-energy emission band ( ca. 490 nm ) from the  $\text{Pr}^{3+}$  ion (  $^3\text{P}_0 \rightarrow ^3\text{H}_4$  ) transition. The interaction involves an overall two photon absorption that leads to energy transfer up-conversion.

## ACKNOWLEDGMENT

This research is sponsored by the Division of Chemical Sciences, Office of Basic Energy Sciences, US Department of Energy, under contract DE-AC05-96OR22464 with Oak Ridge National Laboratory, managed by Lockheed Martin Energy Research Corp.

## REFERENCES

1. B. Viana, N. Koslova, P. Aschehoug, C. Sanchez, J. Mater. Chem. **5**, 719 (1995).
2. I. M. Thomas, S. A. Payne and G. D. Wilke, J. Non-Cryst. Solids **151**, 183 (1992).
3. L. L. Hench and J. K. West, Eds., Chemical Processing of Advanced Materials (Wiley, New York, 1992 ) p. 823.
4. R. Reisfeld and C. K. Jorgensen, Lasers and Excited States of Rare Earths (Springer-Verlag, Berlin, Heidelberg, New York, 1977) p. 35.
5. D. J. Zalucha, J.C. Wright, F. K. Fong, J. Chem. Phys. **59**, 997 (1973).
6. L. S. Lee, S. C. Rand, A. L. Schawlow, Phys. Rev. B, **29**, (12) 6901 (1984).
7. M. J. Lochhead, K. L. Bray, J. Non-Crystalline Solids, **170**, 143 (1994).
8. G. W. Scherer, J. Non-Crystalline Solids, **100**, 77 (1988).
9. N. A. Stump, R. G. Haire, S. Dai. (MRS Symposium II28.11, Boston, MA 1996).

## SPECTROSCOPIC INVESTIGATIONS OF THE NETWORK STRUCTURE IN BOROVANADATE GLASSES

O. ATTOS, M. MASSOT, H.S. MAVI and C. JULIEN

Laboratoire de Physique des Solides, Université Pierre et Marie Curie, associé au CNRS (ERS 113), 4 place Jussieu, 75252 Paris cedex 05, France

### ABSTRACT

Borovanadate glasses with mixed conductivity, i.e., simultaneous ionic and electronic carriers have been obtained in the system  $(100-x)[B_2O_3-Li_2O]-xV_2O_5$  ( $0 \leq x \leq 30$  mole%). To understand the origin of the conductivity in these glasses, the compositional dependence of the network structure has been studied by Raman and infrared spectroscopy.

### INTRODUCTION

In recent years, fast ionic conducting glasses and cathodic materials based on semi-conducting oxide glasses have entered the field of interest as promising candidates in the development of high energy storage systems. According to previous works, lithium borate glasses exhibit a high ionic conductivity which depends on the lithium content and on the nature of the negative sites [1]. Glasses with vanadium are known to have semi-conducting properties due to the presence of vanadium in two valence states,  $V^{4+}$  and  $V^{5+}$ . The hopping of the unpaired  $3d^1$  electrons from  $V^{4+}$  to  $V^{5+}$  site is responsible of the electrical transport [2]. Also, mixed conductivity, i.e. simultaneous ionic and electronic conductivity, was observed in borovanadate glasses [3] and had revealed the possibility of using them as cathode in battery applications [4].

The objective of the present work is to study by Raman scattering and infrared spectroscopy, the compositional dependence of the network structure in borovanadate glasses near the metaborate composition in a wide range of  $V_2O_5$  composition (0 - 30 mole%).

### EXPERIMENTS

Glasses of chemical formulae  $(100-x)[B_2O_3-Li_2O]-xV_2O_5$  ( $0 \leq x \leq 30$  mole%) have been prepared by the process described in ref. 3. For optical experiments, the samples were cut in parallelepipeds with polished faces ( $4 \times 4 \times 2 \text{ mm}^3$ ).

Raman scattering spectra were recorded between 4 and  $1800 \text{ cm}^{-1}$  using a Jobin-Yvon U 1000 spectrometer. The excitation source was the 514.5 nm line of an argon-ion laser operating at a power of 100 mW. The scattered light was detected by a cooled photomultiplier ITT FW 130 coupled with a computerised photon-counting system. To get a high signal-noise ratio, each spectrum is the result of the average of 10 successive scans with a spectral resolution of  $2 \text{ cm}^{-1}$ . The Raman spectra in the spectral range 600 to  $1200 \text{ cm}^{-1}$  have been fitted by using the GRAM/386 software from Galactic Industries Co. The curve fitting is based on the original algorithm of non-linear peak fitting described by Marquardt and known as the Levenberg-Marquardt method [5].

Infrared spectra were obtained with the use of a Fourier transform Bruker IFS 113 vacuum interferometer. The reflected interferograms were detected by a nitrogen cooled MCT 18-21 detector. Each spectrum is the average of 100 scans with recorded with a resolution of  $2 \text{ cm}^{-1}$  in the frequency range from 500 to  $4000 \text{ cm}^{-1}$ .

## RESULTS AND DISCUSSION

Unpolarised Raman spectra of the borovanadate glasses are presented in Fig. 1. Spectra obtained for other intermediate concentrations are shown in Fig. 2 in the range 600 to 1200  $\text{cm}^{-1}$ . In the pure metaborate glass, the Raman spectrum is composed by four broad bands observed at about 500, 760, 960, and between 1220 and 1450  $\text{cm}^{-1}$ . They correspond to vibrations of typical structural units within the B—O network. Those at ca. 760  $\text{cm}^{-1}$  are the typical signature of large borate rings containing four-co-ordinated boron atoms, essentially diborate groups obtained by the transformation of  $\text{B}_{\text{III}}$  atoms into  $\text{B}_{\text{IV}}$  one [6]. These groups with  $\text{B}_{\text{IV}}$  atoms are linked by small chains of planar  $\text{BO}_3$  triangles. The shoulder at 700  $\text{cm}^{-1}$  comes from vibrations of  $\text{BO}_3$  triangles with three bridging-oxygen atoms while the band at 960  $\text{cm}^{-1}$  is attributed to vibrations of  $\text{BO}_3$  triangles with one non-bridging oxygen atom (NBO).

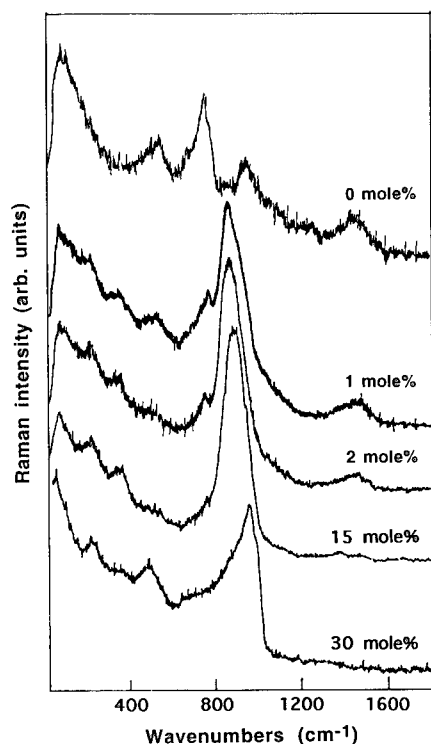


Fig. 1. Raman spectra of the glass system  $(100-x)[\text{B}_2\text{O}_3\text{-Li}_2\text{O}]\text{-}x\text{V}_2\text{O}_5$  as a function of the  $\text{V}_2\text{O}_5$  content.

Upon the  $\text{V}_2\text{O}_5$  addition, at very low concentration ( $x < 1$  mole%), a new band appears at a frequency near 890  $\text{cm}^{-1}$ . It becomes very broad and intense and its intensity increases up to a maximum for  $x \approx 15$  mole%, while its frequency shifts from 890 to 930  $\text{cm}^{-1}$ . Then, its intensity decreases in the  $\text{V}_2\text{O}_5$  concentration range from 15 to 30 mole%.



The comparison with Raman spectra of crystalline vanadates such as  $\text{Cu}_2\text{V}_4\text{O}_7$ , which have two polymorphic forms, has permitted us to propose a structural model in which the vanadium atoms can be found in two different oxygen surroundings: the  $\alpha$ -phase composed of  $\text{VO}_4$  tetrahedra shared by corner, and the  $\beta$ -phase in which each vanadium atom is surrounded by five oxygen atoms to form distorted trigonal bipyramids connected by edges (fig 2-f) [7].

From these assumptions, a fitting have been done assuming: (i) a linear combination of the two Raman spectra shown in Fig. 2-f for the band at  $900\text{ cm}^{-1}$ , (ii) a linear baseline for the spectra, and (iii) a mixed Gauss-Lorentz line shape for each of the bands used in the fit [8]. The Raman bands are centred at  $895\text{ cm}^{-1}$  for  $\text{VO}_4$  tetrahedra and at  $850, 910$  and  $950\text{ cm}^{-1}$  for  $\text{VO}_5$  trigonal bipyramids [20]. To take account of the B-O network vibrations, two other peaks are introduced in the fit at about  $690\text{ cm}^{-1}$  and  $760\text{ cm}^{-1}$  [6]. The shape and the frequency of this band are functions of the relative concentration between  $\text{VO}_4$  tetrahedra and  $\text{VO}_5$  bipyramids.

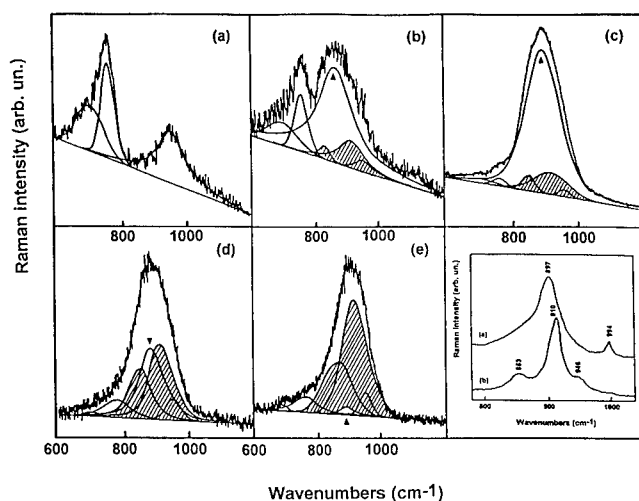


Fig. 2. Raman spectra and calculated curves of  $(100-x)[\text{B}_2\text{O}_3\text{-Li}_2\text{O}]\text{-}x\text{V}_2\text{O}_5$  glasses in the spectral range  $600\text{-}1200\text{ cm}^{-1}$ . The peak labelled with arrow is attributed to tetrahedral  $\text{VO}_4$  while those with atched area correspond to  $\text{VO}_5$  trigonal bipyramid: a)  $x=0$  mole%; b)  $x=0.5$  mole%; c)  $x=5$  mole%; d)  $x=10$  mole%; e)  $x=20$  mole%; f) Raman spectra of  $\alpha\text{-Cu}_2\text{V}_4\text{O}_7$  (a) and  $\beta\text{-Cu}_2\text{V}_4\text{O}_7$  (b).

Fig. 2 shows different fits in the  $600$  to  $1200\text{ cm}^{-1}$  spectral range obtained with the previous assumptions. In the spectrum of lithium metaborate, three bands corresponding to the set of vibrations describes previously are found at  $690, 760$  and  $960\text{ cm}^{-1}$  (Fig. 2-a). When  $\text{V}_2\text{O}_5$  is added in small quantity ( $x=0.5$  mole%), the Raman spectrum shows that the vanadium belongs to  $\text{VO}_4$  tetrahedra (Fig. 2-b) and that it induced an increase in the number of  $\text{B}_{\text{IV}}$  atoms in the network at the expense of the  $\text{BO}_3$  triangles with NBO. This is deduced from the decrease of the intensity of the band at  $960\text{ cm}^{-1}$ , in spite of the fact that the latter contained also a small contribution from  $\text{VO}_5$  pyramids. At about  $x=5$  mole%, the number of  $\text{VO}_4$  units seems to be maximun (fig 2-c). Between  $x=5$  and  $x=10$  mole%, the tetrahedral  $\text{VO}_4$  are transformed into distorted  $\text{VO}_5$  trigonal bipyramids (fig. 2-d). At the end,  $x \geq 20$  mole%, the  $\text{VO}_5$  units are the

main part of the V—O network (Fig 2-e). The similarity of the fitted components with the spectra described for each pyrovanadate form is evident and shows the existence of an intermediate range order on the scale of two corner-shared  $\text{VO}_4$  tetrahedra or four edge-shared  $\text{VO}_5$  bipyramids (Fig. 3). Recently Hayakawa et al. [9] have obtained similar results in NMR and IR studies of lead vanadate glasses.



Fig. 3. Basic structural units building up the V—O part of the glass network.  
(a) tetrahedral  $\text{VO}_4$  and (b) trigonal bipyramids  $\text{VO}_5$ .

With the increase of the vanadium oxide, the bands corresponding to V—O and V—O—V vibrations are observed at 230 and at 350  $\text{cm}^{-1}$  [10]. The vibration of the  $\text{V}=\text{O}$  bond is located at 970  $\text{cm}^{-1}$  in the glass with  $x=30$  mole%. Observed at 995  $\text{cm}^{-1}$  in pure  $\text{V}_2\text{O}_5$  with tetragonal  $\text{VO}_5$  pyramids in the V—O network [10], its frequency is lowered to 970  $\text{cm}^{-1}$  by the attractive interaction between the  $\text{Li}^+$  cations and the  $\text{V}=\text{O}$  bonds which converts tetragonal pyramids into trigonal bipyramids.

The infrared spectra of the borovanadate glasses are shown in Fig. 4 up to 15 mole of  $\text{V}_2\text{O}_5$ . For the pure metaborate glass,  $\text{B}_2\text{O}_3\text{-Li}_2\text{O}$ , the infrared spectrum exhibits four bands at 700, 950-1000, 1250 and 1330-1400  $\text{cm}^{-1}$ . The first one corresponds to the bending vibration of B—O—B bridges while the three others are attributed to the stretching vibrations in  $\text{BO}_4$  tetrahedra included in diborate groups, planar  $\text{BO}_3$  triangles with non-bridging oxygen atom (NBO) and planar  $\text{BO}_3$  triangles in which all the oxygen atoms are bridging [12].

It is interesting to remark the very high sensitivity of the infrared spectra to the vanadium oxide addition. The presence of an extremely small quantity of  $\text{V}_2\text{O}_5$  ( $x=0.25$  mole%) into the B—O network is responsible of the disappearance of the band at 1250  $\text{cm}^{-1}$ . Simultaneously, the spectrum shows an important increase in the intensity of the band at 950-1000  $\text{cm}^{-1}$ . Though this frequency range corresponds to V—O vibrations ( $\text{VO}_4$  tetrahedra at 840  $\text{cm}^{-1}$  and  $\text{V}=\text{O}$  at 930  $\text{cm}^{-1}$ ) [11], but because the very small amount of  $\text{V}_2\text{O}_5$  in the glass, the enhancement of the strength of those bands is attributed to the formation of  $\text{BO}_4$  tetrahedra at the expense of  $\text{BO}_3$  triangles with NBO. NMR measurements done by Zhonghong et al. [13] also report that the number of  $\text{B}_{\text{IV}}$  atoms increases with the addition of  $\text{V}_2\text{O}_5$  in the concentration range  $0 \leq x \leq 10$  mole%.

By transforming  $\text{B}_{\text{III}}$  atoms into  $\text{B}_{\text{IV}}$  one, vanadium oxide acts as a "network modifier". The increase of the number of  $\text{BO}_4$  results in an increase of the connectivity of the covalent network.

It gets a three-dimensional character which appears in the increase of the glass-transition temperature,  $T_g$ , in the  $V_2O_5$  concentration range  $0 \leq x \leq 10$  mole%, for example[14].

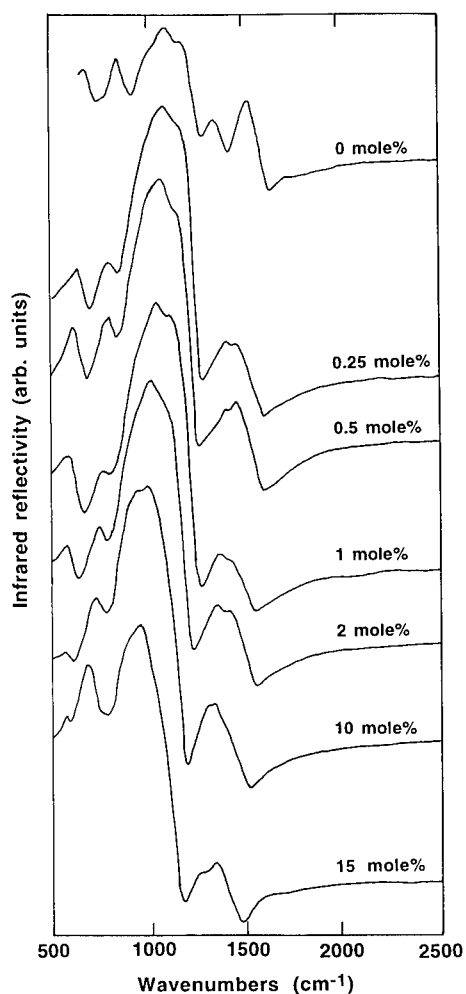


Fig. 4. Infrared spectra of the glass system  $(100-x)[B_2O_3-Li_2O]-xV_2O_5$  with  $0 \leq x \leq 20$  mole%.

With the increase of the vanadium oxide content, the maximum of this band shifts toward lower frequency and reaches  $930\text{ cm}^{-1}$  for  $x=15$  mole%. As it was said before, two contributions must be now considered to understand the shape and the frequency dependence of this band: the stretching vibration of the  $BO_4$  tetrahedra (right side of the band), and the vibration of  $VO_4$  tetrahedra and of the  $V=O$  in trigonal bipyramids (left side of the band). As the addition of

V<sub>2</sub>O<sub>5</sub> in higher quantity ( $10 \leq x \leq 15$  mole%) is responsible of a decrease of the number of BO<sub>4</sub> tetrahedra.[15], the intensity of the high frequency side of the band decreases while the low frequency part of the band is enhanced by the increase of the vibrational contribution of the covalent V—O network which becomes to replace the B—O matrix in the glass.

In this compositional range, V<sub>2</sub>O<sub>5</sub> acts as a glass former. Because the tendency of vanadium oxides to form layered structures, the 3-D character of the glassy matrix disappears and one of its manifestation is a decrease of the number of four-co-ordinated boron atoms. This was also shown by the decrease of T<sub>g</sub> under the V<sub>2</sub>O<sub>5</sub> addition in the concentration range  $15 \leq x \leq 30$  mole% [16].

## CONCLUSION

Raman and infrared spectroscopy have been used as complementary techniques to study the change in the structural properties of the covalent network with the vanadium pentoxide addition in the concentration range  $0 \leq x \leq 30$  mole% in lithium metaborovanadate glasses.

Raman scattering spectra have shown that VO<sub>4</sub> tetrahedra are present in the network at low V<sub>2</sub>O<sub>5</sub> content. They are transformed into VO<sub>5</sub> trigonal bipyramids with the increase of the V<sub>2</sub>O<sub>5</sub> concentration. Infrared spectra have revealed that V<sub>2</sub>O<sub>5</sub>, at low concentration acts as a glass modifier by increasing the number of tetrahedral BO<sub>4</sub> units. In this case, it was accommodated into the B—O network in VO<sub>4</sub> tetrahedra. It behaves like a glass former with the increase of its concentration and the V—O part of the network is formed by VO<sub>5</sub> trigonal bipyramids.

This duality in the V<sub>2</sub>O<sub>5</sub> behaviour is of great importance for the electrical conductivity of lithium borovanadate glasses [3]. When V<sub>2</sub>O<sub>5</sub> is added as modifier, the glass is an ionic conductors and the ionic conductivity is due to the hopping of the Li<sup>+</sup> cations from one BO<sub>4</sub><sup>-</sup> tetrahedra to an other one. Then, they can be mixed conductors when V<sub>2</sub>O<sub>5</sub> contributes to the network as a glass former. In this case, the vanadium-oxygen part of the network is composed of trigonal bipyramids VO<sub>5</sub> with the possibility to found the vanadium in different valence states. The electronic conductivity becomes possible by electron hopping from V<sub>4</sub><sup>+</sup> to V<sub>5</sub><sup>+</sup> sites.

## REFERENCES

- [1] H.L. Tuller, D.P. Button and D.R. Uhlmann, J. Non-Cryst. Solids **40**, 93 (1980).
- [2] M. Sayer and A. Mansingh, J. Non-Cryst. Solids **58**, 91 (1983).
- [3] O Attos, Étude des phénomènes de transport dans les borovanadates, Thèse de l'Université P. et M. Curie, Paris, 1995 (unpublished).
- [4] C Julien and G.A. Nazri, Solid State Batteries: Material Design and Optimisation, Kluwer Academic Publ., Boston, (1994).
- [5] D.W Marquardt, J. Soc. Ind. Appl. Math. **11**, 431, (1963).
- [6] M. Massot, M. Balkanski, A. Levasseur, Microionics - Solid State Integrable Batteries, edited by M. Balkanski (Elsevier Sciences Publishers B. V., 1991), p. 139.
- [7] W de Waal and C. Hutter, Mat Res. Bull. **29**, 843 (1994).
- [8] W. Soppe, J. Kleerebezem and H.W. den Hartog, J. Non-Cryst. Solids **93**, 142 (1987).
- [9] S. Hayakawa, T. Yoko and S. Sakka, J. Non-Cryst. Solids **183**, 73 (1995).
- [10] C. Sanchez, J. Livage and G. Lucazeau, J. Raman Spect. **12**, 68 (1982).
- [11] Y. Dimitiev, V. Dimitov, M. Arnaudov and D. Topalov, J. Non-Cryst. Solids **57**, 147 (1983).
- [12] M. Massot, C. Julien and M. Balkanski, Infrared Physics **29**, 775 (1989).
- [13] J. Zhonghong and T. Yongxing, J. Non-Cryst. Solids **146**, 57 (1992).
- [14] O. Attos, M. Massot, M. Balkanski, E. Haro-Poniatowski and M. Asomoza, J. Non-Cryst. Solids (to be published).

# Optical Spectroscopy of Pentavalent Chromium Ions in Glass

Huabiao Yuan<sup>a</sup>, Weiyi Jia<sup>b</sup>, D. Cohen<sup>a</sup>, W.M. Yen<sup>a</sup> and B.G. Aitken<sup>c</sup>

a: Department of Physics & Astronomy, University of Georgia, Athens, GA 30602

b: Department of Physics, University of Puerto Rico, Mayaguez, PR 00680

c: Technology Group, Corning Inc., Sullivan Park, Corning, NY 14831

In this work, we report the first spectroscopic observation of octahedrally coordinated pentavalent chromium ions in BaCaMg aluminate glasses. A broad band emission peaking at 780 nm with band width of  $3000\text{ cm}^{-1}$  has been observed at 12K. The measurements of fluorescence decay, time-resolved emission and excitation spectra reveal that the emission band is an overlapped luminescence originating from both the  ${}^2\text{E}$  to  ${}^2\text{T}_2$  transition of octahedrally coordinated  $\text{Cr}^{5+}$  and a charge transfer transition of  $\text{Cr}^{6+}\text{O}_4$  groups.

## INTRODUCTION

Chromium ions have been playing an important role in spectroscopy and laser physics since 1960. It is well known that the first laser in history was made of ruby, of which the lasing ion is  $\text{Cr}^{3+}$  [1]. The first solid state tunable ionic laser, the Alexandrite laser, is also activated with  $\text{Cr}^{3+}$  [2]. Not long ago, it was found that  $\text{Cr}^{4+}$  is an excellent lasing ion in the near infrared [3]. Various types of  $\text{Cr}^{4+}$  lasers have been developed [4]. More recently,  $\text{Cr}^{2+}$  was found to lase when doped into CdSe crystals [5]. It is therefore of great interest to search for materials to host  $\text{Cr}^{5+}$  and to study their optical properties.

$\text{Cr}^{5+}$  has a  $3d^1$  electron configuration, which makes it attractive.  $\text{Ti}^{3+}$  ( $3d^1$ ) sapphire lasers have shown outstanding performance with wide tunability, high output and ultra short pulses. This achievement has stimulated the spectroscopic investigation of various  $3d^1$  ions. In addition, the  $3d^1$  ion  $\text{V}^{4+}$  has also shown broad band emission up to room temperature in  $\text{Al}_2\text{O}_3$  and  $\text{YAlO}_3$ .

Compared with  $\text{Ti}^{3+}$  and  $\text{V}^{4+}$ ,  $\text{Cr}^{5+}$  emission has hardly been observed. Although it was studied with EPR as early as 1956 [6], no luminescence from  $\text{Cr}^{5+}$  was reported in the following 40 years. Only recently, near-infrared (NIR) emission from  $\text{Cr}^{5+}$  in tetrahedral coordination was observed by Hanzenkamp et al. [7].

In this paper, we report the first observation of luminescence from octahedrally coordinated  $\text{Cr}^{5+}$  in glass. The emission was found to be overlapped with the emission of a charge transfer transition of  $\text{Cr}^{6+}\text{O}_4$  groups.

## EXPERIMENT

The glass sample was provided by Corning Inc. It was made from a mixture containing (in mol%) 55%  $\text{AlO}_{1.5}$ , 30%  $\text{CaCO}_3$ , 7.5%  $\text{Ba}(\text{NO}_3)_2$ , 7.5%  $\text{MgO}$  and 0.025%  $\text{CrO}_3$ . The mixture was melted in a platinum crucible at  $1650^\circ\text{C}$  for 3 hours. The glass was annealed at  $725^\circ\text{C}$  to release thermal strain.

EPR analysis at 9.7GHz was carried out at Corning Inc. It was found that 48.8% of Cr ions are in the pentavalent state. No  $\text{Cr}^{3+}$  was detected. The remaining Cr ions exist as  $\text{Cr}^{4+}$  and  $\text{Cr}^{6+}$ .

For photoluminescence measurement, the sample was mounted onto the cold finger of a closed-cycle cryo-refrigerator and pumped by emissions of a Spectra-Physics model-2040E cw Argon laser. For time-resolved fluorescence and decay process measurements, a home-made dye laser pumped by a Quanta-Ray DCR 210 Nd:YAG pulse laser was used. A Spex 1401 double spectrometer equipped with R943 PMT was employed to detect emission. The cw signal was analyzed through a photon counter SRS-400. The decay process was recorded by a SRS-430 multichannel scaler. For time-resolved fluorescence measurements, a SRS-250 boxcar averager was used for the fast-decay component, while a gated photon counter was used for the slow-decay component. All the spectra have been corrected by the spectral response of the system.

## EXPERIMENTAL RESULTS

As mentioned before, the glass sample contains  $\text{Cr}^{4+}$ ,  $\text{Cr}^{5+}$  and  $\text{Cr}^{6+}$ . The absorption from 520 nm to the near infrared and the fluorescence in the infrared range originating from  $\text{Cr}^{4+}$  have been well studied in a similar glass sample [8] from Corning and will not be discussed in this letter. The absorption spectrum of this sample has an intense band peaked at 370 nm with a long shoulder extending to 500 nm. The source of the absorption is still uncertain, but absorption maxima at this wavelength in Cr-doped alkali silicate glasses have been attributed to  $\text{Cr}^{6+}$  [9].

Fig. 1 shows a broad band luminescence centered at approximately 780 nm under cw pumping of an Ar laser. The spectrum spans over  $5000\text{ cm}^{-1}$  with a full width at half maximum (FWHM) of  $3500\text{ cm}^{-1}$ . It can be seen that the luminescence is shifted to the red on increasing the pumping wavelength from 458 nm through 476, 502 nm to 529 nm. The spectral shifts indicate either a large inhomogeneous Cr site distribution or the existence of multiple optical centers. In addition, a weak emission peak at 550 nm was also observed, the intensity of which increases when the pumping wavelength is longer.

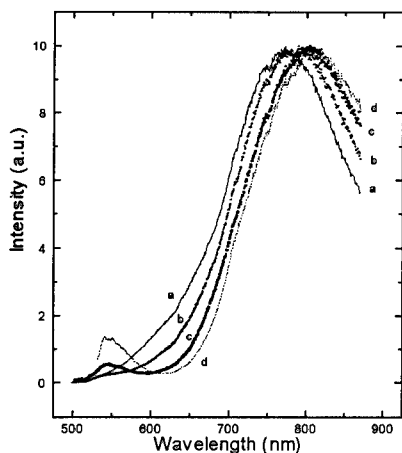


Figure 1. CW luminescence spectra at 12K pumped by different Ar laser lines: (a) 458nm, (b) 476nm, (c) 502nm and (d) 529nm.

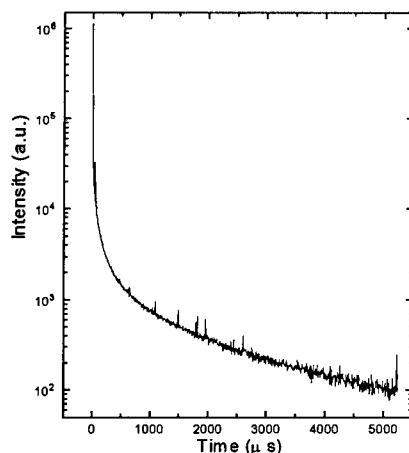


Figure 2. Luminescence decay curve at 12K, excited at 449nm, monitored at 714nm.

The decay of the luminescence was measured at 714 nm and is shown in Fig. 2. The decay curve is not of a single exponential function. It consists of two major components: a fast one and a slow one. The fast component has a large initial intensity and a typical decaytime of 1.1  $\mu$ s. The slow component has a typical decaytime of 1.3 ms. A difference of three orders in the lifetimes indicate that two active centers in the glass are involved in the broad band emission.

In order to separate the luminescence band from each optical center, time-resolved luminescence was measured, and the results are shown in Fig. 3. The pumping dye laser was set at 443 nm with a pulse width of 10 ns. For the fast-decay component, the sampling gate with a fixed delay of 1  $\mu$ s was set at a width of 1.5  $\mu$ s. For the measurement of the slow-decay component, the gate was delayed by 1 ms and with a width of 4 ms. The fast-decay fluorescence peaks at 745 nm with a bandwidth of 2800  $\text{cm}^{-1}$ . It is tentatively assigned to the electronic energy transition of  $\text{Cr}^{5+}$ . The slow-decay fluorescence peaks at 800 nm with a similar bandwidth and is assigned to the charge transfer transition of  $\text{Cr}^{6+}\text{O}_4$  groups.

To extract the absorption information of each individual ion, time-resolved excitation experiments were performed. The emission was monitored at 714 nm. The spectra are shown in Fig. 4. For excitation of  $\text{Cr}^{5+}$ , the sampling gate with a fixed delay of 1  $\mu$ s was set at a width of 1.5  $\mu$ s. For  $\text{Cr}^{6+}$ , the gate was delayed by 1 ms with a width of 4 ms. The excitation spectrum of  $\text{Cr}^{5+}$  shows two peaks at 445 and 485 nm, while the excitation spectrum of  $\text{Cr}^{6+}\text{O}_4$  has a single peak at 445 nm. These peaks can barely be seen on the shoulder of the absorption spectrum.

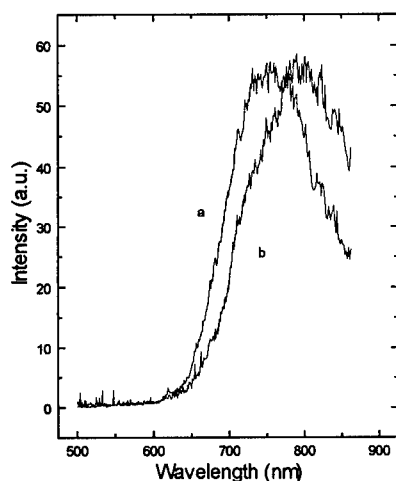


Figure 3. Time-resolved luminescence spectra at 12K pumped by 443nm. (a) fast-decay component, (b) slow-decay component.

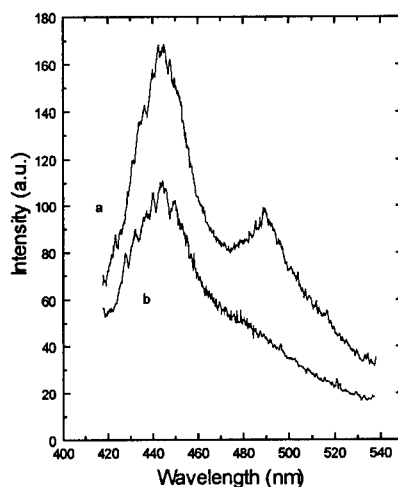


Figure 4. Time-resolved excitation spectra at 12K. Luminescence monitored at 714nm. (a) fast-decay component, (b) slow-decay component.

Due to the limitation of our home made dye laser, the excitation spectrum measurement could not be extended to the UV range. In order to identify the source of the intense absorption peak at 370 nm, the sample was pumped by the third harmonic of a Nd:YAG laser, 355 nm. It was found that the excitation at this wavelength has little contribution to the luminescence. The intensity of luminescence is only 1% of that when pumped at 450 nm with the same power. As 355 nm is close to the peak of the absorption band, the absorbance at 355 nm is 5 times as large as that at 450 nm. If the absorption were from the emitting center, the luminescence should have been 500 times stronger. Therefore the weak luminescence by pumping at 355 nm indicates that the 370 nm absorption peak may not be related with either  $\text{Cr}^{5+}$  or  $\text{Cr}^{6+}$ .

The temperature dependence of the lifetimes of the luminescence was measured at 700 nm. The lifetime of the fast component remains at the 1  $\mu\text{s}$  level from 12K to 70K, then reduces to 0.2  $\mu\text{s}$  at room temperature. The lifetime of the slow component decreases from 1.37 to 1.14 ms as temperature increases from 12K to room temperature.

The lifetime of the 550 nm emission shown in Fig. 1 is on the order of 100  $\mu\text{s}$ . Apparently the emission is from some other unknown impurity and is neither related with  $\text{Cr}^{5+}$  nor  $\text{Cr}^{6+}$ .

## DISCUSSION

The luminescence reported here is certainly not from  $\text{Cr}^{4+}$ , which has emission in the infrared from 1.2 to 1.6  $\mu\text{m}$  in aluminate glasses [8]. Although the spectral range is similar to that of  $\text{Cr}^{3+}$  emission in glass, this possibility is ruled out since EPR signals and absorption features from  $\text{Cr}^{3+}$  have not been observed in this glass sample. We tentatively ascribe the cw fluorescence band to both  $\text{Cr}^{5+}$  and  $\text{Cr}^{6+}\text{O}_4$  emissions.

In an octahedral crystal field, the energy level of a  $3d^1$  ion,  ${}^2D$ , splits into two energy levels: the ground state  ${}^2T_2$  and the excited state  ${}^2E$ . In a distorted octahedral crystal field, both  ${}^2T_2$  and  ${}^2E$  states may further split due to a low symmetry crystal field or the Jahn-Teller effect. In the case of  $\text{Ti}^{3+} : \text{Al}_2\text{O}_3$  [10,11,12], the  ${}^2E$  state splits because of the static Jahn-Teller effect, with two components at 20,400 and 18,200  $\text{cm}^{-1}$ , separated by 2,200  $\text{cm}^{-1}$ . The ground state  ${}^2T_2$  experiences smaller splitting on the order of 100  $\text{cm}^{-1}$  due to spin-orbit coupling and the dynamic Jahn-Teller effect. The emission is in the spectral range from 600 to 1100 nm, peaking at 700 nm. The lifetime is 3.9  $\mu\text{s}$  at low temperatures.

As an isoelectronic  $3d^1$  ion,  $\text{Cr}^{5+}$  in this glass has shown spectroscopic properties similar to those of  $\text{Ti}^{3+}$ . The emission band (745 nm) of  $\text{Cr}^{5+}$  is broader due to inhomogeneity in the glass sample. The short-lived component in the decay curve is from  $\text{Cr}^{5+}$  with a lifetime of 1.1  $\mu\text{s}$ . The two peaks at 445 and 490 nm in the excitation spectrum are the crystal field-split components of the  ${}^2E$  state.

In addition, it can be concluded from the spectroscopic results that  $\text{Cr}^{5+}$  in aluminate glass is not tetrahedrally, but octahedrally coordinated. In a tetrahedral crystal field, the energy order of the  ${}^2E$  and  ${}^2T_2$  states is reversed and  ${}^2E$  serves as the ground state. Since the crystal field strength,  $10Dq$ , is four-ninths that of an octahedral field, the energy separation between the  ${}^2T_2$  and  ${}^2E$  states are smaller. Thus the emission is expected to be at longer wavelength, further in the infrared range. Hanzenkamp reported the emission from tetrahedral  $\text{Cr}^{5+}$  in  $\text{LiPO}_3$  crystal to be at 9000  $\text{cm}^{-1}$  [7].

In table I are listed some spectroscopic results of various  $3d^1$  ions. By comparison, it can be seen that our spectroscopic observation is consistent with the assignment of octahedral coordination to  $\text{Cr}^{5+}$ .



Table I. Spectroscopic data of  $3d^1$  ions at low temperature ( $\sim 10K$ ).

Ion	Coordination	Emission max.	FWHM	Lifetime	Reference
Ti <sup>3+</sup>	Octahedral	700nm	1800cm <sup>-1</sup>	3.9 $\mu$ s	[10,11,12]
V <sup>4+</sup>	Octahedral	635nm	3100cm <sup>-1</sup>	1.27 $\mu$ s	[13]
Cr <sup>5+</sup>	(Octahedral)	745nm	2800cm <sup>-1</sup>	1.1 $\mu$ s	(this paper)
Cr <sup>5+</sup>	Tetrahedral	1.1 $\mu$ m	1900cm <sup>-1</sup>	100ns	[7]
Mn <sup>6+</sup>	Tetrahedral	1.1 $\mu$ m	1800cm <sup>-1</sup>	2 $\mu$ s	[14]

#### Charge transfer transition of Cr<sup>6+</sup>O<sub>4</sub>

Cr<sup>6+</sup> may exist in this glass as Cr<sup>6+</sup>O<sub>4</sub> "molecules". Since the 2p electrons form a closed shell, the ground state of the group is an orbital and spin singlet, <sup>1</sup>A<sub>1</sub>. A charge transfer state will have an electronic configuration Cr<sup>5+</sup>O<sup>-</sup> (3d<sup>1</sup>2p<sup>5</sup>). This configuration corresponds to two different states with 7-fold orbital degeneracy, a spin triplet and a spin singlet. In a tetrahedral crystal field, the orbital degeneracy is lifted which results in two sets of energy levels: triplets <sup>3</sup>A<sub>1</sub>, <sup>3</sup>T<sub>1</sub> and <sup>3</sup>T<sub>2</sub>, and singlets <sup>1</sup>A<sub>1</sub>, <sup>1</sup>T<sub>1</sub> and <sup>1</sup>T<sub>2</sub>. The lowest charge transfer state is a spin triplet. Due to the spin forbidden nature of the transition to the ground state, the lifetime of the luminescence is expected to be quite long. The slow-decay luminescence with a lifetime of 1 ms observed in this glass is therefore ascribed to the charge transfer transition of Cr<sup>6+</sup>O<sub>4</sub>. The excitation band of the slow-decay luminescence is broad and peaked at 445 nm. A similar charge transfer transition has been reported in KBr/K<sub>2</sub>CrO<sub>4</sub> [15].

#### CONCLUSIONS

The luminescence of octahedrally coordinated Cr<sup>5+</sup> in aluminate glass has been observed for the first time. The spectrum is overlapped with the emission of a charge transfer transition of Cr<sup>6+</sup>O<sub>4</sub>. Time-resolved emission and excitation experiments were performed to reveal the spectroscopic properties of the Cr<sup>5+</sup> ions. The results are consistent with the assignment to the octahedrally coordinated 3d<sup>1</sup> configuration.

#### ACKNOWLEDGMENTS

Authors appreciate the help from Dr. W.M.Dennis in setting up the dye laser. This work is supported in part by the National Science Foundation. One of the authors (WJ) is grateful for the support by NASA under grant MURC-NCCW-0088, ARO under grant DAAH04-96-10416, and NSF under grant EHR-9108775.

## REFERENCES

- [1] T.H. Maiman, *Nature*, **187**, 493 (1960).
- [2] J.C. Walling, O.G. Peterson, H.P. Jenssen, R.C. Morris and E.W. O'Dell, *IEEE J. Quant. Electron.*, **16**, 1302 (1980).
- [3] V. Petricevic, S.K. Gayen and R.R. Alfano, *Appl. Phys. Lett.*, **53**, 2590 (1988).
- [4] H.Eilers, W.M. Dennis, W.M. Yen, S. Kück, K. Peterman, G. Huber and W.Jia, *IEEE J. Quant. Electron.*, **29**, 2508 (1993).
- [5] L.D. DeLoach, R.H. Page, G.D. Wilke, S.A. Payne, and W.F. Krupe, *OSA Proceedings on Advanced Solid-State Lasers*, **24**, 127 (1995).
- [6] A. Carrington, D.J.E. Ingram, D. Schonlond and M.C.R. Symons, *J. Chem. Soc.*, **12**, 4710 (1956).
- [7] M.F. Hazenkamp and H.U. Güdel, *Chem. Phys. Lett.*, **251**, 301 (1996).
- [8] X. Wu, S. Huang, U. Hömmerich, W.M. Yen, B.G. Aitken, and M. Newhouse, *Chem. Phys. Lett.*, **233**, 28 (1995).
- [9] P. Nath, A. Paul and R.W. Douglas, *Phys. Chem. Glasses*, **6** (6), 203 (1965).
- [10] B.F. Gächter, and J.A. Koningstein, *J. Chem. Phys.*, **60**, 2003 (1974).
- [11] P.F. Moulton, *J. Opt. Soc. Am. B*, **3** (1), 125 (1986).
- [12] P. Albers, E. Stark and G. Huber, *J. Opt. Soc. Am. B*, **3** (1), 134 (1986).
- [13] J.-P. Meyn, T. Danger, K. Petermann and G. Huber, *J. Lumin.*, **55**, 55 (1993).
- [14] T.C. Brunold, M.F. Hazenkamp and H.U. Güdel, *J. Am. Chem. Soc.*, **117**, 5598 (1995).
- [15] G.A.M. Dalhoeven, G. Blasse, *Chem. Phys. Lett.*, **76**, (1), 27 (1980).

## NEW Fe-Ni BASED METAL-METALLOID GLASSY ALLOYS PREPARED BY MECHANICAL ALLOYING AND RAPID SOLIDIFICATION

J.J. SUÑOL\*, M.T. CLAVAGUERA-MORA\*\*, N. CLAVAGUERA\*\*\*, T. PRADELL\*\*\*\*

\*Grup de Recerca en Materials, Universitat de Girona, Santaló s/n. 17071-Girona, Spain.

\*\*Grup de Física de Materials I, Dept de Física, Universitat Autònoma de Barcelona, 08193-Bellaterra, Spain.

\*\*\*Grup de Física de l'Estat Sòlid, Dept ECM, Facultat de Física, Universitat de Barcelona, Diagonal 647, 08028-Barcelona, Spain.

\*\*\*\*Dept Física, ESAB ads. Universitat Politècnica de Catalunya, Urgell 187, 08036-Barcelona, Spain.

### ABSTRACT

Mechanical alloying and rapid solidification are two important routes to obtain glassy alloys. New Fe-Ni based metal-metalloid (P-Si) alloys prepared by these two different processing routes were studied by differential scanning calorimetry and transmission Mössbauer spectroscopy. Mechanical alloyed samples were prepared with elemental precursors, and different nominal compositions. Rapidly solidified alloys were obtained by melt-spinning. The structural analyses show that, independent of the composition, the materials obtained by mechanical alloying are not completely disordered whereas fully amorphous alloys were obtained by rapid solidification. Consequently, the thermal stability of mechanically alloyed samples is lower than that of the analogous material prepared by rapid solidification. The P/Si ratio controls the magnetic interaction of the glassy ribbons obtained by rapid solidification. The experimental results are discussed in terms of the degree of amorphization and crystallization versus processing route and P/Si ratio content.

### INTRODUCTION

Fe-based alloys prepared by rapid solidification (RS) have excellent magnetic properties. These alloys were widely investigated during the last two decades [1]. Nevertheless, they did not attain an important level of applicability in the industrial processes, as could be expected from their good magnetic properties. The possible cause is that these materials were usually obtained only by RS in ribbon form and this limits its technological use.

In recent years, the mechanical alloying technique (MA) was introduced to produce Fe-Based amorphous alloys [2-3]. Using MA at ambient temperature amorphous powders have been obtained in great quantity and a very large composition range.

This work deals with analysis and comparison of powders obtained by MA in a planetary mill and by melt spinning under controlled atmosphere.

### EXPERIMENTAL

The powdered materials were synthesized by milling mixtures of elemental powders (particle size up to 25  $\mu\text{m}$ ) in containers closed under an Ar atmosphere. Elemental Fe, Ni, P and Si were used to prepare alloy powders with the following nominal compositions:  $\text{Fe}_{40}\text{Ni}_{40}\text{P}_{20-x}\text{Si}_x$  with  $x = 6, 10$  or  $14$ . These samples were labeled as MA(A), MA(B) and MA(C), respectively. The

powders were milled in a Frisch Pulverisette 7 planetary ball mill, using hardened steel containers and balls. The ball-to-powder weight ratio was 5:1 and the milling intensity was held at an intensity setting of 7.

The melt-spun ribbons were produced by quenching the molten alloy on the surface of a rapidly spinning (about  $30 \text{ ms}^{-1}$ ) Cu wheel, under an Ar atmosphere. To prevent P sublimation, the  $\text{Fe}_3\text{P}$  compound was used along with elemental Fe, Ni and Si to prepare ribbons with the same nominal compositions as the powders. These samples were labeled as RS(A), RS(B) and RS(C) when  $x = 6, 10$  or  $14$ , respectively.

Differential scanning calorimetry (DSC) was carried out in a DSC-7 Perkin-Elmer calorimeter heating the samples at different rates:  $\beta = 2.5\text{-}5\text{-}10\text{-}20\text{-}40 \text{ K/min}$  in an inert atmosphere.

Structural analysis were performed by x-ray diffraction (XRD) analysis and transmission Mössbauer spectroscopy (TMS) measurements at room temperature using a  $^{57}\text{Co}$  in Rh source and calibrated with an  $\alpha\text{-Fe}$  foil. The spectra were fitted with the program of Brand [4] by using an histogram magnetic hyperfine-field distribution and the Hesse-Rübartsch method [5], and including a linear correlation between the isomer shift and the magnetic field to take into account at least partially the asymmetries typical of Fe-P based amorphous alloys [6]. The spectra of the crystallized samples have been fitted by Lorentzian lines corresponding to the different crystalline Fe sites neighborhoods. Previous studies on powders have already reported on the evolution of the degree of amorphization achieved by mechanical alloying as a function of the milling time [7-8].

## RESULTS

### As-prepared powders and ribbons

XRD patterns in RS alloys show the typical halos of an amorphous structure [9]. MA alloys after 32 milling show some remains of crystalline  $\alpha\text{-Fe}$  and Ni elemental precursors.

TMS analyses show that, independent of the composition, the materials obtained by RS are fully amorphous. After milling MA(A) and MA(C) for 32h, less than 5% of the Fe remains unreacted. For samples MA(B) the amount of unreacted Fe decreases from 10% to 5% if we increase the milling time from 32h to 64h. Figures 1 and 2 show the respective Mössbauer spectra of amorphous samples MA(C) obtained after 32h milling and RS(A) as well as after crystallization. Figure 3 shows the hyperfine magnetic field (HF) distribution of amorphous and crystallized MA(C) (32h). The HF distribution of the amorphous phase shows the typical shape of amorphous P-bearing phases. Similar shapes of the HF distribution are obtained for MA and RS samples, although the presence of unreacted iron is clearly detected in the spectra of MA samples.

Regarding the influence of the nominal composition of the alloys in the amorphous phase, Mössbauer analysis show that the P/Si ratio controls the magnetic interaction of the amorphous phase: The lower the value of this ratio the higher is the average hyperfine magnetic field (AHF) for a given Fe, Ni content. Figure 4 shows the evolution of the values of both AHF and the standard deviation (std) as a function of the Si content for the RS samples. The values of the isomer shift (IS) and the quadrupole splitting (QS) for these samples are reported in Figure 5 for the RS samples. There is a small reduction in the value of IS with the increase of Si content. That means, there are slight changes of the short-range-order (SRO) in the amorphous state.

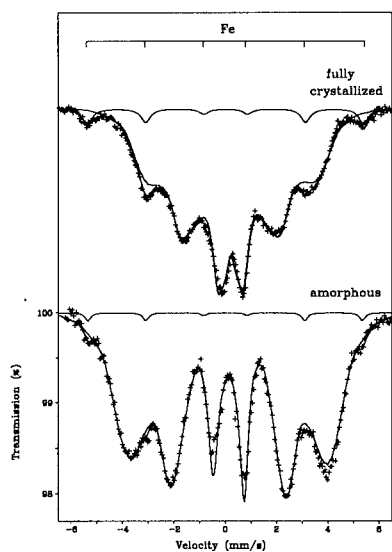


Fig. 1.- Mössbauer spectra of as-prepared (bottom) and crystallized (top) samples MA(C).

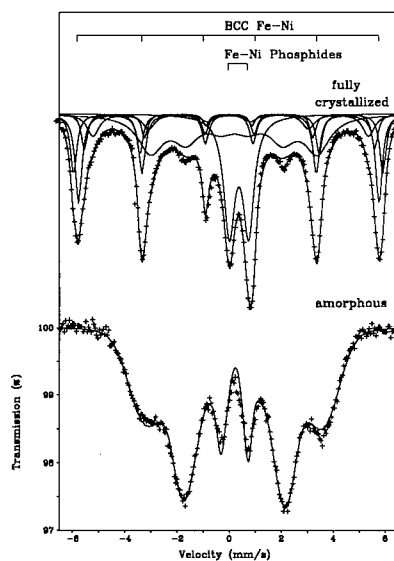


Fig. 2.- Mössbauer spectra of as-prepared (bottom) and crystallized (top) samples RS(A).

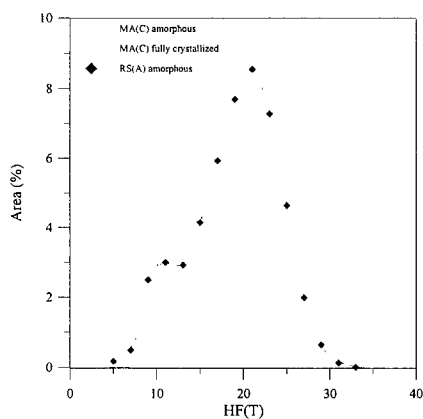


Fig. 3.- Magnetic hyperfine field distribution of the spectra of figure 1.

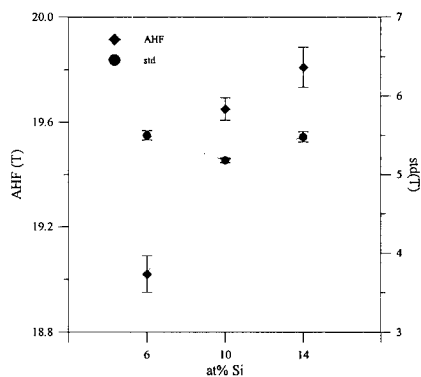


Fig. 4.- Average magnetic Hyperfine field (AHF) and standard deviation (std) as a function of the Si content for the RS samples.

The same trend can be deduced for the MA samples. However, the results are less evident for these samples, since a change of the P/Si content results in a different degree of amorphization when applying the same milling time. In fact, in the mechanical alloyed powders, the P/Si ratio controls the amorphization rate. We found that the lowest amorphization rate is obtained for a ratio  $P/Si = 1$ .

#### Crystallized samples

DSC measurements performed on the different powders and ribbons support the existence of an amorphous phase deduced from X-Ray diffraction (XRD) [9]. Figure 6 shows DSC scans performed at a heating rate of 20 K/min, for Fe-based milled and quenched samples, respectively. In all heating experiments several exothermic processes were detected that are related to the crystallization of the amorphous-like alloy. There are at least three processes for samples MA. The first one is shallow and broad. It is typical for a relaxation process and starts at about 300°C. A main crystallization peak starts at about 360°C and in samples MA(A) and MA(B) it overlaps with the third crystallization peak. Result from samples MA(B) include 32h and 64h milling. As established by TMS, the degree of amorphization of samples MA(B) milled 64h is comparable to the one obtained in samples MA(A) and MA(C) by 32h milling duration. In agreement with this result, the onset of the main crystallization peak shifts to higher temperature on increasing milling time in samples MA(B). That means, samples with a ratio  $P/Si = 1$  are the most difficult to amorphize by MA. In addition, comparison of the thermal stability versus P/Si ratio indicates that the crystallization temperature decreases when the glass forming ability increases. The crystallization process in the rapidly solidified samples produces a very sharp main exothermic peak and at least one flat high temperature second peak. Both, the onset temperature of the main peak and the crystallization enthalpy are comparatively higher for rapidly solidified samples than for sample MA, as expected since the last ones are powders with some remains of crystallinity. Coupled TMS and DSC analysis of the broad exothermic effect starting at temperatures below the main crystallization peak in the MA samples suggests that it corresponds to diffusion controlled grain growth of preexisting crystallites [10].

The apparent activation energy,  $E$ , of the crystallization processes was calculated from the continuous heating data. In particular, we use the Ozawa method [11]. The values obtained are between 2.4 and 3.9 eV in mechanically alloyed samples and between 3.1 and 6.9 in rapidly quenched samples. Similar results have been obtained in other Fe-Ni based metal-metalloid alloys [12].

XRD patterns of crystallized alloys indicate that the crystallization products are bcc(Fe,Ni), fcc(Ni,Fe), and (Fe,Ni)-phosphides and -silicides. TMS spectra show that in both, MA and RS alloys, Fe is mostly alloyed to the main crystalline phase [(Fe,Ni) alloy]. The TMS spectra of the crystallized RS alloys (see figure 2) show the simultaneous presence of both ferromagnetic (Fe,Ni) alloy phases (bcc and fcc). In addition, with some phases related with (Fe,Ni)-phosphides and a magnetic phase, probably related with a not completed crystallization process, are obtained.

TMS spectra of crystallized samples of comparatively well amorphized MA alloys correspond to the typical INVAR magnetic collapse of fcc binary Fe-Ni alloys at 30-40 at % Ni [13], as shown in Fig 1. The characteristic collapse of the magnetic hyperfine field is clearly seen in the corresponding hyperfine magnetic field distribution, shown in figure 4 for sample RS(C).

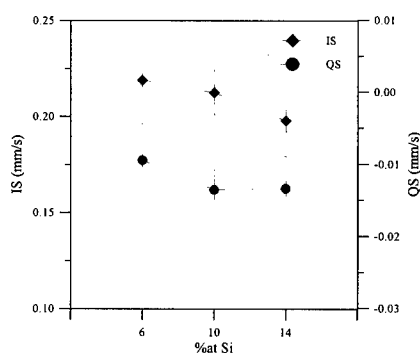


Fig. 5.- IS and QS as a function of the Si content for the RS samples.

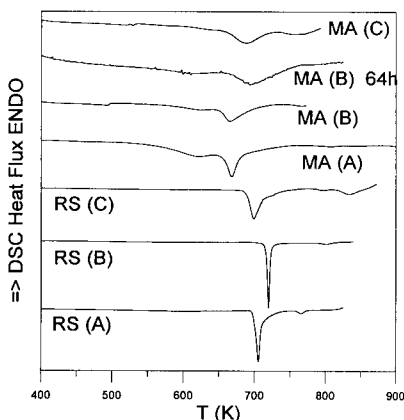


Fig. 6.- DSC continuous heating curves for the MA samples (milling time 32h), MA(B) with milling time 64h and RS samples.

The INVAR behaviour is not obtained for the RS samples, but similar Fe-Ni bearing phase are expected for TMS. It is well known that the stability of bcc and fcc phases in the INVAR composition range phases may be obtained by different preparation routes [14].

## CONCLUSIONS

The nominal composition of the alloys influences the stability of the amorphous phase. The P/Si ratio controls the magnetic interaction. The lower the value of this ratio the higher is the average hyperfine magnetic field for a given Fe,Ni content. Changing the P/Si content results in a different degree of amorphization when applying the same milling time and also in slight changes of the SRO.

Samples with a ratio P/Si = 1 are the most difficult to amorphize by MA. The degree of amorphization of samples MA(B) milled 64h is comparable to the one obtained in samples MA(A) and MA(C) by 32h milling duration. In these samples the amount of bcc-Fe unreacted is always less than 5%.

Both the onset temperature of the main peak and the crystallization enthalpy are comparatively higher for samples RS than for sample MA. The value of the apparent activation energy,  $E_a$  of the main crystallization process is between 2.4 and 3.9 eV in MA samples and between 3.1 and 6.9 in RS samples.

The crystallization products of the RS alloys are both (bcc and fcc) ferromagnetic (Fe,Ni) alloy phases, and some minor phases related to (Fe,Ni)-phosphides, (Fe,Ni)-silicides and a magnetic phase, probably related with a not completed crystallization process. TMS spectra of crystallized samples of comparatively well amorphized MA alloys correspond to the typical INVAR magnetic collapse of fcc binary Fe-Ni alloys at 30-40 at % Ni.

## ACKNOWLEDGMENTS

The Laboratori de Física Atòmica i Nuclear of the University of Barcelona is acknowledged for the TMS facilities. Financial support from CIRIT (project N° 1995SGR-514), from CICYT (projects N° MAT96-692 and MAT96-769) and from CEE (project N° C11\*-CT94-0029) is acknowledged.

## REFERENCES

1. H.-J. Güntherodt and H. Beck, editors, Glassy Metals I, Springer Verlag, Berlin, 1982; H. Beck and H.-J. Güntherodt, editors, Glassy Metals II, Springer Verlag, Berlin, 1983.
2. H.R. Pak, J. Chu, R.J. Angelis and K. Okazaki, *Mater Sci Eng*, **A118**, p. 147 (1989).
3. H. Miura, S. Isa, K. Omuro, *J. Non-Cryst. Solids*, **117-118**, p. 741 (1990).
4. R.A. Brand, NORMOS programs, version 1990.
5. J. Nesse and A. Rübartsch, *J. Phys. E: Sci. Instrum.* **7**, p. 526 (1974).
6. R.E. Vanderberghe, D. Gryffroy and E. De Grave, *Nuc.Inst & Methods in Phys Res.*, **B26**, p. 603 (1987).
7. M.T. Clavaguera-Mora, J.J. Suñol and N. Clavaguera in Nanostructured and Non-Crystalline Materials, edited by M. Vázquez and A. Hernando, (World Scientific, Singapore, 1995), p. 44-48.
8. T. Pradell, N. Clavaguera, J.J. Suñol and M.T. Clavaguera-Mora, in Proc. Int. Conf. on the Applications of Mössbauer Effect ICAME95, edited by I. Ortali (Società Italiana di Fisica, Bologna 1996), pp. 433-436.
9. J.J. Suñol, PhD thesis, Universitat Autònoma de Barcelona, 1996.
10. T. Pradell, J.J. Suñol, M.T. Clavaguera-Mora and N. Clavaguera, *Materials Science Forum*, **235-238**, p. 169 (1997).
11. T. Ozawa, *Bull. Chem. Soc. Japan* **38**, p. 1181 (1965).
12. S. Suriñach, J.J. Suñol and M.D. Baró, *Mater Sci Eng*, **A181/A182**, p. 1285 (1994).
13. S.M. Mahmood, K.H. Rousan, A.F. Lehlooh and S. Mahmoud, *Solid State Communications* **95**, p. 879 (1995).
14. K. Sumiyana, *Phys. Stat. Sol.* **126**, p. 291 (1991).



## SYNTHESIS AND PROPERTIES OF BULK METALLIC GLASSES IN Pd-Ni-P AND Pd-Cu-P ALLOYS

Y. HE and R. B. SCHWARZ

Center for Materials Science, MS K-765, Los Alamos National Laboratory, Los Alamos, NM 87545, U. S. A.

### ABSTRACT

Bulk amorphous Pd-Ni-P and Pd-Cu-P alloy rods with diameters ranging from 7 to 25 mm have been synthesized over a wide composition range using a fluxing technique. For most bulk amorphous Pd-Ni-P alloys, the difference  $\Delta T = T_x - T_g$  between the crystallization temperature  $T_x$  and the glass transition temperature  $T_g$  is larger than 90 K, while for bulk amorphous Pd-Cu-P alloys,  $\Delta T$  varies from 27 to 73 K. Pd<sub>40</sub>Ni<sub>40</sub>P<sub>20</sub> has the highest glass formability, and 300-gram bulk amorphous cylinders, 25 mm in diameter and 50 mm in length, can be easily produced. This size, however, is not an upper limit. The paper presents the glass formation ranges for both ternary alloy systems and data on the thermal stability of the amorphous alloys, as well as their specific heat, density, and elastic properties.

### INTRODUCTION

Bulk glass formation in metallic systems is usually difficult. Unlike traditional oxide glasses which can be easily formed using low cooling rates, metallic glasses can, in general, only be formed using high cooling rates. This is because undercooled metallic melts have high atomic mobility and thus cooling rates on the order of  $10^6$  K/sec are needed to prevent the melt from crystallizing while it is cooled from its melting temperature,  $T_m$ , to the glass transition temperature,  $T_g$ . Recently, a number of multicomponent metallic alloy systems have been found to have extraordinary glass forming ability. These alloy systems include La-Al-(Ni,Cu) [1], Mg-(Cu,Ni)-Y [2], Zr-Al-(Cu,Ni,Co) [3,4], Zr-Ti-Cu-Ni-Be [5], Nd-Al-(Cu,Ni,Co,Fe) [6], and Ti-Zr-Ni-Cu [7]. Most of these alloys can be quenched from the melt into a bulk amorphous state at a relative cooling rate of 1–100 K/sec. By bulk we mean a sample with minimum dimensions of about 1 mm. Because bulk amorphous alloys have large technological potential, understanding their synthesis and finding new compositions are topics of great scientific interest.

Pd<sub>40</sub>Ni<sub>40</sub>P<sub>20</sub> was one of the first bulk amorphous alloys discovered. By quenching the melt in water, Chen produced amorphous Pd<sub>40</sub>Ni<sub>40</sub>P<sub>20</sub> alloy rods with diameters of 1–3 mm [8]. Using surface etching and thermal cycling to eliminate the surface impurities, Drehman *et al.* [9] successfully produced amorphous Pd<sub>40</sub>Ni<sub>40</sub>P<sub>20</sub> solids with minor diameters up to 5.3 mm; and by fluxing molten Pd<sub>40</sub>Ni<sub>40</sub>P<sub>20</sub> with dehydrated B<sub>2</sub>O<sub>3</sub>, Kui *et al.* [10] were able to prepare amorphous Pd<sub>40</sub>Ni<sub>40</sub>P<sub>20</sub> buttons with the minimum dimension of about 10 mm. These previous studies have concentrated on the particular composition of Pd<sub>40</sub>Ni<sub>40</sub>P<sub>20</sub>. In recent publications, we reported the homogeneity range for bulk glass formation in the Pd-Ni-P system [11,12]. In this paper we report a new ternary bulk glass forming system, Pd-Cu-P. The properties of bulk Pd-Cu-P and Pd-Ni-P glasses are compared and discussed.

## SYNTHESIS OF BULK AMORPHOUS ALLOYS

The synthesis of bulk amorphous Pd-Ni-P and Pd-Cu-P alloys was based on an improved fluxing technique [11,12], which was pioneered by Turnbull and his colleagues [9,10]. The alloy synthesis starts by mechanically alloying mixtures of elemental powders [13]. The alloyed powders are then purified in molten  $B_2O_3$  which dissolves oxide impurities which would otherwise act as heterogeneous nucleation centers in the undercooled molten alloy. The bulk amorphous alloy was formed by quenching the molten alloy in water. The cooling rates are estimated at no more than 100 K/s. The structure and properties of the amorphous alloys was investigated by X-ray diffraction, optical microscopy, scanning electron microscopy, scanning differential calorimetry (DSC), and resonant ultrasound spectroscopy (RUS).

### BULK GLASS FORMATION RANGE

#### Pd-Ni-P System

Using the fluxing technique, bulk amorphous Pd-Ni-P alloy rods with a critical diameter of 10 mm can be formed over a wide range of metal compositions, as indicated in Fig. 1. For bulk glass formation, however, the phosphorus concentration must be maintained close to 20 at.%. Previous research has shown that the glass forming ability correlates with the difference  $\Delta T = T_x - T_g$ . For the Pd-Ni-P system,  $\Delta T$  is largest for  $Pd_{40}Ni_{40}P_{20}$  and we have found that amorphous  $Pd_{40}Ni_{40}P_{20}$  cylinders, 25 mm in diameter and 300 g in weight, can be easily produced [11]. Clearly, this size is not the upper limit for bulk glass formation in  $Pd_{40}Ni_{40}P_{20}$ .

Drehman and Greer [14] studied the kinetics of crystal nucleation and growth in  $Pd_{40}Ni_{40}P_{20}$  glass. They determined that for this alloy the steady-state homogeneous nucleation rate is as low as  $10^6 \text{ m}^{-3} \text{ s}^{-1}$ , which is the lowest value reported in any metallic glass. The crystal

growth rate at 590 K is estimated to be less than  $10^{-10} \text{ m/s}$ . Based on these data, and provided heterogeneous nucleation has been effectively suppressed, the critical cooling rate for glass formation in  $Pd_{40}Ni_{40}P_{20}$  is estimated to be as low as  $10^{-3} \text{ K/s}$ . Experimentally, we have found that mm-size  $Pd_{40}Ni_{40}P_{20}$  liquid can be vitrified without crystallization at a cooling rate of 0.34 K/s [15], while an upper bound of the critical cooling rate of 0.17 K/s has also been reported for  $Pd_{40}Ni_{40}P_{20}$  [16]. With such a low critical cooling rate, it should be possible to prepare much larger bulk glasses in this alloy system.

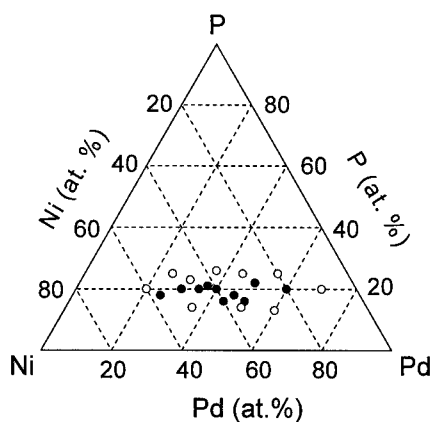


Figure 1. Bulk glass formation range in Pd-Ni-P system. Filled circles denote the formation of glassy rods with diameters of at least 10 mm. For the open circles, the 10-mm diameter rods were crystalline.

### Pd-Cu-P System

The bulk glass forming range for 7-mm diameter amorphous Pd-Cu-P rods is shown in Fig. 2. Similar to Pd-Ni-P system, the glass formation range is restricted to near 20 at.% phosphorus. However, the palladium content for bulk glass formation is limited to 40-60 at.%, which is narrower than that for Pd-Ni-P alloys. Clearly, the glass forming ability for the Pd-Cu-P system is not as good as that of the Pd-Ni-P system.

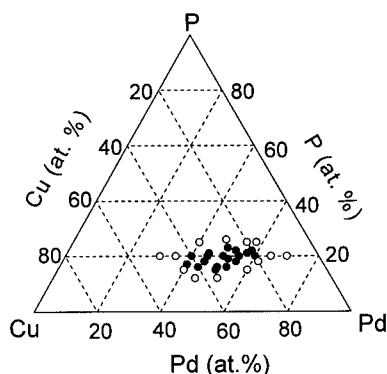


Figure 2. Bulk glass formation range in the Pd-Cu-P system. Filled circles denote the formation of glassy rods with diameters of at least 7 mm.

### Pd-Cu-Ni-P

The bulk glass-forming ability of the Pd-Ni-P and Pd-Cu-P ternary alloys can be substantially enhanced by going to the quaternary Pd-Ni-Cu-P system. Indeed, it has been reported recently that a 40-mm diameter glassy rod of  $\text{Pd}_{40}\text{Cu}_{30}\text{Ni}_{10}\text{P}_{20}$  can be prepared by water quenching [17]. We have found that using the  $\text{B}_2\text{O}_3$  flux, a 16-mm diameter amorphous rod can be prepared by cooling the same melt in air. The composition range for bulk glass formation in the Pd-Cu-Ni-P system is being investigated.

### THERMAL STABILITY

When the temperature is increased to above  $T_g$ , the amorphous solid becomes an undercooled liquid and its viscosity decreases drastically. Since crystallization does not occur until the temperature is further increased to approach  $T_x$ , the temperature interval  $\Delta T = T_x - T_g$  is a measure of the thermal stability of the undercooled liquid. The values of  $\Delta T$  must be associated with a given heating rate, which here is 20 K/min. Fig. 3 shows the DSC traces for several bulk glassy Pd-Cu-P, Pd-Ni-P, and Pd-Cu-Ni-P alloys. These bulk glass formers are characterized by large values of  $\Delta T$ . For all the 10-mm diam. glassy Pd-Ni-P rods we prepared,  $\Delta T > 60$  K, with the alloys near the  $\text{Pd}_{40}\text{Ni}_{40}\text{P}_{20}$  composition reaching  $\Delta T > 100$  K [11]. For the glassy Pd-Cu-P alloys,  $\Delta T$  ranges from 27 K to 73 K.

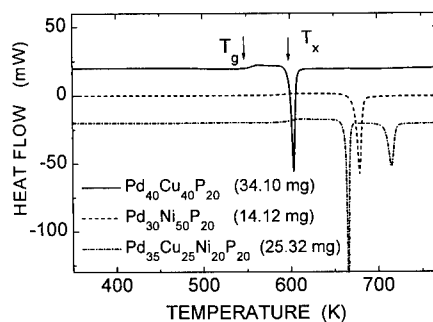


Figure 3. DSC traces for three bulk glassy Pd-(Cu,Ni)-P alloys, scanned at 20 K/min.

The formation of amorphous alloys via the undercooling of melts requires we prevent the melt from crystallizing while its temperature is reduced from the liquidus temperature  $T_l$  to  $T_g$ . The reduced glass transition temperature  $T_{rg} = T_g / T_l$ , has been shown to be a measure of the

alloy's glass forming ability [18,19]. The values of  $T_g$ ,  $T_x$ ,  $T_l$ ,  $T_{rg}$ , and the enthalpy of crystallization  $\Delta H_x$  are listed in Table 1 for a selected number of glassy alloys. In this table, the  $T_{rg}$  value for  $\text{Pd}_{40}\text{Ni}_{40}\text{P}_{20}$  was calculated using the (upper) liquidus temperature,  $T_l = 991$  K. If we use the solidus temperature for this alloy,  $T_s = 875$  K, then  $T_{rg}$  is 0.66, as often quoted in the literature [19].

Table 1  $T_g$ ,  $T_x$ ,  $\Delta T$ ,  $T_l$ ,  $T_{rg}$ , and  $\Delta H_x$  for bulk amorphous Pd-Ni-P and Pd-Cu-P alloys determined by DSC at a scanning rate of 20 K/min.

Composition	$T_g$ (K)	$T_x$ (K)	$\Delta T$ (K)	$T_l$ (K)	$T_{rg}$	$\Delta H_x$ (kJ/mole)
$\text{Pd}_{30}\text{Ni}_{50}\text{P}_{20}$	583	673	90	1010	0.58	5.94
$\text{Pd}_{40}\text{Ni}_{40}\text{P}_{20}$	576	678	102	991	0.58	7.37
$\text{Pd}_{50}\text{Ni}_{28}\text{P}_{22}$	584	676	92	972	0.60	6.06
$\text{Pd}_{40}\text{Cu}_{40}\text{P}_{20}$	548	599	51	843	0.65	2.66
$\text{Pd}_{50}\text{Cu}_{30}\text{P}_{20}$	562	619	57	863	0.65	3.92
$\text{Pd}_{60}\text{Cu}_{20}\text{P}_{20}$	596	660	64	916	0.65	4.04

## SPECIFIC HEAT

The specific heat,  $C_p$ , of the Pd-Ni-P and Pd-Cu-P glassy alloys near  $T_g$  was measured by DSC at a heating rate of 20 K/min. A sapphire single crystal was used as reference material. All the specimens used in these measurements were cut from 7-mm diameter amorphous rods. Fig. 4 shows the results for  $\text{Pd}_{40}\text{Cu}_{40}\text{P}_{20}$ . The open circles show  $C_p$  of the as-prepared glass whereas the open triangles are measurements for the same glass after heating it to 563 K and immediately cooling it to room temperature. The difference between these two curves between 475 and 560 K is due to an irreversible structural relaxation in the as-prepared glass. The solid symbols show  $C_p$  for the crystallized glass (after annealing it at 673 K for 30 min.).

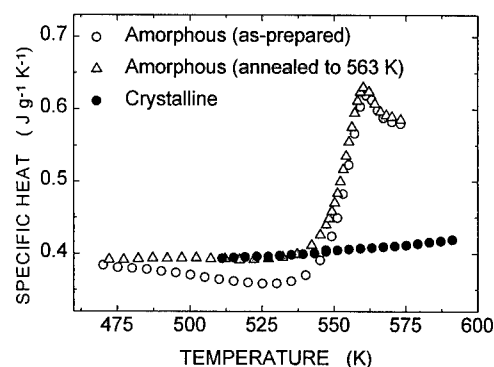


Fig. 4. Specific heat of glassy and crystallized  $\text{Pd}_{40}\text{Cu}_{40}\text{P}_{20}$ .

565 K in the  $C_p$  curves of the glass in the both the as-prepared and relaxed states is due to the reversible glass transition. The two open-symbol curves show that the as-prepared glass, obtained by water-quenching a 7-mm diameter rod, contains a significant amount of excess free volume, which relaxes upon annealing. Similar  $C_p$  measurements for glassy Pd-Ni-P alloys suggest that in this system, the as-prepared glasses contain smaller amounts of excess free volume. Nevertheless, the difference in free volume between the as-prepared and

annealed Pd<sub>40</sub>Ni<sub>40</sub>P<sub>20</sub> glasses has been detected by positron annihilation measurements [20].

## ELASTIC PROPERTIES

Understanding the elastic properties of a material is essential for engineering applications. The elastic properties of several bulk amorphous Pd-Ni-P and Pd-Cu-P alloys were determined by resonant ultrasound spectroscopy (RUS). In this technique, the spectrum of the mechanical resonance of a parallelepiped sample is measured and compared with a theoretical spectrum calculated for a given set of elastic constants. The true set of elastic stiffness constants is calculated by a recursive regression method that optimizes a match between the two spectra. Further details of this technique have been described elsewhere [21,22]. An isotropic amorphous alloy has only two independent second order elastic stiffness constants. The room-temperature elastic moduli for a number of bulk amorphous alloys are listed in Table 2. Table 2 also lists the density  $\rho$  of these bulk glasses, which was measured using the Archimedes' method with pure ethanol as immersion fluid. The last column in the table lists the Debye temperature of the alloys, deduced from the measured room temperature elastic constants and density. For the same Pd and P content, Ni-containing glasses have slightly higher Debye temperatures than the corresponding Cu-containing glasses. The general trend in the Debye temperature data agrees with the fact that the Debye temperature of the metallic elements decreases in the order of Ni to Cu to Pd.

Table 2 Room-temperature elastic constants, Young's modulus  $E$ , bulk modulus  $B$ , shear modulus  $G$ , Poisson's ratio  $\nu$ , density  $\rho$ , and the Debye temperature  $\Theta_D$  of a number of selected Pd-Ni-P and Pd-Cu-P bulk amorphous alloys. The elastic moduli are in units of GPa and  $\rho$  is in units of g/cm<sup>3</sup>.

Sample	$C_{11}$	$C_{12}$	$C_{44}$	$E$	$B$	$G$	$\nu$	$\rho$	$\Theta_D$ (K)
Pd <sub>25</sub> Ni <sub>57</sub> P <sub>18</sub>	232	152	40.0	112	179	40.0	0.396	8.97	311
Pd <sub>40</sub> Ni <sub>40</sub> P <sub>20</sub>	229	156	36.6	103	180	36.6	0.405	9.36	286
Pd <sub>50</sub> Ni <sub>34</sub> P <sub>16</sub>	230	152	39.2	110	178	39.2	0.397	9.84	285
Pd <sub>40</sub> Cu <sub>40</sub> P <sub>20</sub>	202	136	33.2	93	158	33.2	0.402	9.30	269
Pd <sub>50</sub> Cu <sub>30</sub> P <sub>20</sub>	205	139	32.7	92	161	32.7	0.405	9.46	262
Pd <sub>60</sub> Cu <sub>20</sub> P <sub>20</sub>	210	145	32.3	91	167	32.3	0.409	9.78	254

## CONCLUSIONS

Our research reveals that bulk glass formation in the Pd-Ni-P and Pd-Cu-P alloys requires removing or neutralizing all heterogeneous nucleation centers in the undercooled liquid. Heterogeneous nucleation can be avoided by fluxing the melt in molten B<sub>2</sub>O<sub>3</sub>, which reduces and/or dissolves the oxide inclusions that may act as heterogeneous nucleation centers in the undercooled melt. When this is done, bulk amorphous Pd-Ni-P and Pd-Cu-P rods can be produced. The Pd-Ni-P system has a wide bulk glass formation range, and 10-mm diameter

amorphous rods can be formed in alloys containing between 25 to 60 at.% Pd. Bulk glass formation in Pd-Cu-P system, which is reported here for the first time, has a relatively narrower glass-forming range. Preliminary results show that the glass forming ability of the quaternary Pd-Ni-Cu-P system is higher than that of either the Pd-Ni-P or the Pd-Cu-P systems. All the ternary bulk glasses are characterized by large values of  $\Delta T = T_x - T_g$ . The bulk Pd-Cu-P glasses, obtained at estimated cooling rates of 100 K/s, have appreciable excess free volume which give clear signatures in the specific heat measurements.

#### ACKNOWLEDGMENTS

The authors thank A. Migliori for facilitating his ultrasonic spectroscopy apparatus for the elastic constant measurements. This work was supported by the U.S. Department of Energy, Office of Basic Energy Science, Division of Materials Sciences.

#### REFERENCES

1. A. Inoue, T. Zhang, and T. Masumoto, *Mater. Trans. JIM*, **31**, 425 (1990).
2. A. Inoue, A. Kato, T. Zhang, S. G. Kim, and T. Masumoto, *Mater. Trans. JIM*, **32**, 609 (1991).
3. T. Zhang, A. Inoue and T. Masumoto, *Mater. Trans. JIM*, **32**, 1005 (1991).
4. A. Inoue, T. Zhang, N. Nishiyama, K. Ohba and Y. Masumoto, *Mater. Trans. JIM*, **34**, 1234 (1993).
5. A. Peker and W. L. Johnson, *Appl. Phys. Lett.* **63**, 2342 (1993).
6. Y. He, C. E. Price, S. J. Poon and G. J. Shiflet, *Phil. Mag. Lett.* **70**, 371 (1994).
7. X. H. Lin and W. L. Johnson, *J. Appl. Phys.* **78**, 6514 (1995).
8. H. S. Chen, *Acta Metall.* **22**, 1505 (1974).
9. A. J. Drehman, A. L. Greer, and D. Turnbull, *Appl. Phys. Lett.*, **41**, 716 (1982).
10. H. W. Kui, A. L. Greer, and D. Turnbull, *Appl. Phys. Lett.*, **45**, 615 (1984).
11. Y. He, R. B. Schwarz, and J. I. Archuleta, *Appl. Phys. Lett.*, **69**, 1861 (1996).
12. R. B. Schwarz and Y. He, *International Symposium on Metastable. Mechanically Alloyed and Nanocrystalline Materials (JSMNAN-96)*, Rome, Italy, 20-24 May, 1996, in press.
13. Y. He and R. B. Schwarz, preprint, Los Alamos National Laboratory, 1996.
14. A. J. Drehman and A. L. Greer, *Acta Metall.*, **32**, 323 (1984).
15. Y. He and R. B. Schwarz, unpublished results, Los Alamos National Laboratory, 1996.
16. R. Willnecker, K. Wittmann and G. P. Görlner, *J. Non-Cryst. Solids*, **156-158**, 450 (1993).
17. A. Inoue, N. Nishiyama, and T. Matsuda, *Mater. Trans. JIM*, **37**, 181 (1996).
18. D. Turnbull, *Contemp. Phys.*, **10**, 473 (1969).
19. H. A. Davies, in *Amorphous Metallic Alloys*, edited by F. E. Luborsky (Butterworths, Boston, 1983), pp. 8-25.
20. B. Somieski, L. Hulet, Y. He, and R. B. Schwarz, unpublished results, Oak Ridge and Los Alamos National Labs, 1996.
21. A. Migliori, J. L. Sarrao, W. M. Visscher, T. M. Bell, M. Lei, Z. Fisk, and R. G. Leisure, *Physica B* **183**, 1 (1993).
22. V. -T. Kuokkala and R. B. Schwarz, *Rev. Sci. Instrum.* **63**, 3136 (1992).

## NITRIDATION OF BIORESORBABLE PHOSPHATE GLASS

H. JIANG, W.C. LACOURSE

New York State College of Ceramics, Alfred University, Alfred, NY 14802

### ABSTRACT

The bioresorbable  $10\text{CaO} \cdot 35\text{Na}_2\text{O} \cdot 55\text{P}_2\text{O}_5$  glass was nitrified by melting the glass under anhydrous ammonia. The nitrified glasses were fiberized at about  $720^\circ\text{C}$  in air. The dynamic and the equilibrium pH value of the glass increases with the increase of nitrogen content. The incorporation of nitrogen not only increases the glass transition temperature, but also improves the chemical durability and makes it easier to fiberize. Further more, the nitrified glass is more resistant to devitrification.

### INTRODUCTION

Many phosphate materials such as hydroxyapatites, tricalcium phosphate have been studied extensively for their potential application as bioresorbable materials. but these materials are difficult to fiberize [1]. To satisfy this, researchers paid a lot of interest to the  $\text{Na}_2\text{O}-\text{CaO}-\text{P}_2\text{O}_5$  system glass because it is biocompatible and amenable to fiberization. However, this composition lacks mechanical strength and proper dissolution rate for body implant application.

The nitridation of phosphate glass was done first to develop its application in low temperature soldering [2-6]. Phosphate glasses have high thermal expansion and low melting temperature, this makes it well suited for sealing for high expansion, low melting aluminum alloys, but poor chemical durability limits their practical use. Nitridation with ammonia can decrease the rate of dissolution in water by several orders without any large increasing in melting temperature or large reduction in the thermal expansion.

In this work, nitridation of the  $35\text{Na}_2\text{O} \cdot 10\text{CaO} \cdot 55\text{P}_2\text{O}_5$  glass was carried out to improve its chemical durability. The nitrified glass was remelted in air and  $\text{N}_2$  to study the stability of nitrogen. The dynamic pH values of the glasses and fibers were measured to study the dissolution process in water.

### EXPERIMENTAL

#### Glass Preparation

The phosphate glass with a composition of  $35\text{Na}_2\text{O} \cdot 10\text{CaO} \cdot 55\text{P}_2\text{O}_5$  was prepared from reagent-grade  $\text{NaH}_2\text{PO}_4 \cdot \text{H}_2\text{O}$ ,  $\text{CaCO}_3$ , and  $\text{NH}_4\text{H}_2\text{PO}_4$ . The powdered batch was melted in alumina crucible under air at  $750^\circ\text{C}$  for 1 hr. The glass melt was quenched into a clean high-purity graphite boat which was transferred into the tube furnace shown in Fig. 1. Then the glass was remelted at  $900^\circ\text{C}$  under dry nitrogen for 1 hr. Previous work had shown that this treatment was sufficient to remove most chemically dissolved water [7]. Afterwards, the atmosphere inside the silica glass tube was changed to anhydrous ammonia, and the glass was reacted at different temperatures for different times. After nitridation, the graphite boat was removed from the furnace and the

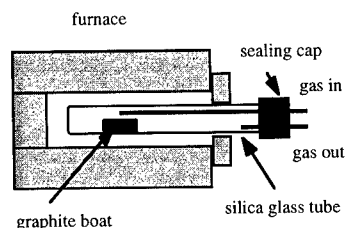


Fig. 1. The tube furnace for nitridation.

glass was quenched into a metal mold and annealed at about 320 °C for 1 hour in air.

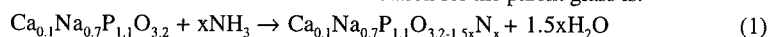
#### Characterization of the Glass and Glass Fiber

About 0.5 g glass powder of CNP-N1 was remelted at 700 °C in air. Glass fibers were drawn from glasses CNP-N1 and CNP-N5 at about 700 °C to 740 °C in a platinum bushing under air. The glass transition temperatures were measured by DSC with heating rate of 10 °C/min using the intercept method for the onset of the transition. 1 g powder sample of the bulk glass and glass fiber was dissolved in 100 ml distilled or de-ionized water at room temperature. The dynamic pH values of the solutions were measured. The equilibrium pH values were measured after 5 months. By using DSC, the peak crystallization temperatures were measured with different temperature increasing rates.

### RESULTS AND DISCUSSION

#### The Nitrogen Content and Glass Transition Temperature

The nitrogen content was calculated by assuming that every two nitrogen atoms replace three oxygen atoms. The chemical reaction of the nitridation for the parent glass is:



The nitrogen contents were calculated from the original weight of the glass and the weight after

Table I. Nitrogen content and glass transition temperature.

Glass	Nitriding Temp., °C	Nitriding Time, hr	N Content (wt%)	T <sub>g</sub> , °C	T <sub>c</sub> , °C
CNP			0	260	356
CNP-N1	750	4	4.95	342	none
CNP-N2	735	4	3.10	307	none
CNP-N3	720	8	2.30	308	436
CNP-N5	750	6	6.24	355	none
CNP-N1 Fiber				343	none
CNP-N5 Fiber				356	none

nitridation and are shown in Table I. As indicated before [2], the nitrogen content increases with increasing the nitriding time or temperature. Table I also shows that the glass transition temperature increases when the nitrogen content increases, since nitrogen increases the cross linking of the glass network.

#### Nitrogen Stability and Fiberization

As stated before, fiberization is very important for bioresorbable materials. But for nitrided phosphate glass, it is unknown if nitrogen is retained during fiberization, especially when the fiber is drawn in air. It is shown in Fig.2 that nitrogen is stable during remelting in air for up to 2 hours because the glass transition temperature does not change after remelting. This makes it possible to draw the glass fiber in air. Table I shows that the glass fibers drawn in air at about 700 °C to 740 °C have the same glass transition temperatures as the parent glass. This is different from the previous investigation when melts were held at a higher temperature[8]. It was also found in this study that the oxynitride glass is very easy to be fiberized according to its viscosity change with temperature change.



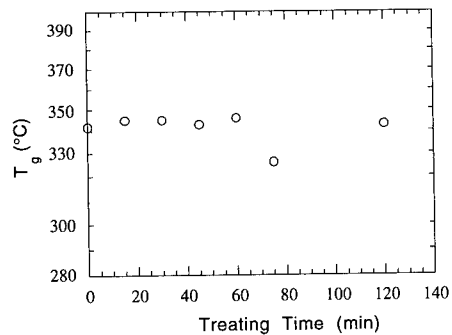


Fig.2. Glass transition temperature of the remelted CNP-N1 glasses.

#### Dissolution in Water and Dynamic pH Values

The Dynamic pH values of the nitrated glasses and glass fibers are shown in Fig.3 to Fig.6. It is evident that the dynamic and equilibrium pH value of the glass or glass fiber increases with increasing its nitrogen content. The nitrogen containing glass has a much lower dissolution rate

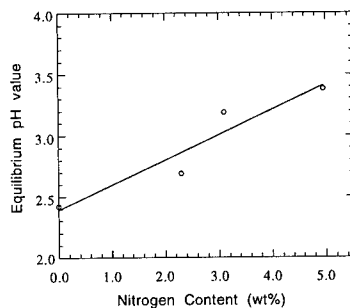
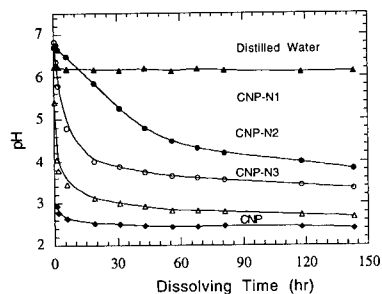


Fig.3. Dynamic pH values of the glass solutions. Fig.4. The equilibrium pH values of glasses.

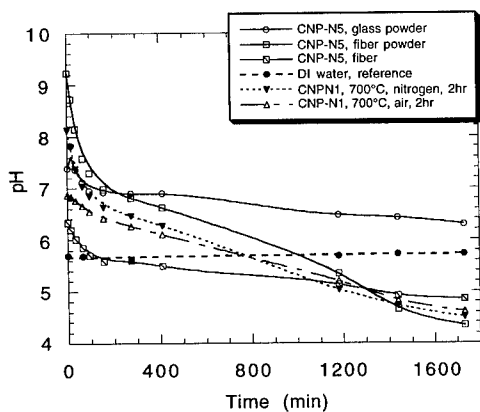


Fig.5. Dynamic pH values of the nitrated glasses and glass fiber in DI water.

than the unnitrided glass. This can be explained by considering the structure change of the glass structure and thus the changes in the hydrolysis and hydration reaction mechanics caused by

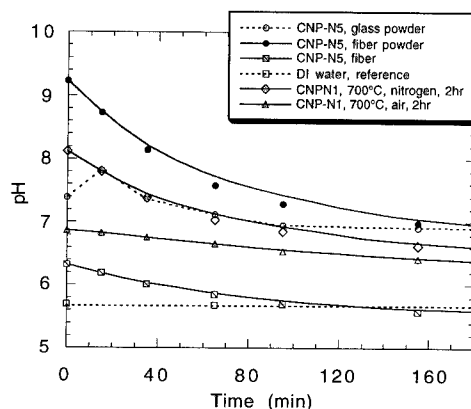
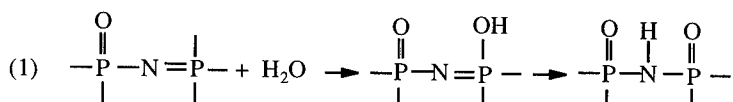


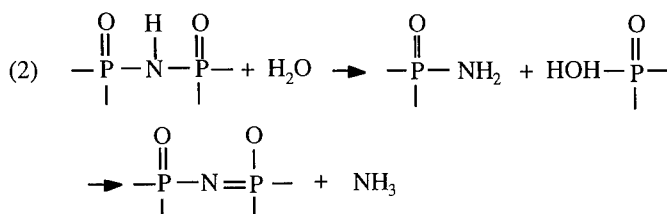
Fig.6. The pH values in the initial dissolving stage.

nitrogen incorporation. The structure units of phosphate glasses are the  $[\text{PO}_4]$  tetrahedra that have a double  $\text{P}=\text{O}$  bond. The  $[\text{PO}_4]$  tetrahedra form the glass network, sharing from a maximum of three oxygens in  $\text{P}_2\text{O}_5$  glass, to a minimum of two or less in the chains that make up the structure of glasses with 50 mol% or less  $\text{P}_2\text{O}_5$ . In the phosphate glasses, the hydrolysis reactions take place first by the destruction of the polymeric structure. This is caused by the breaking of ionic bonds between the chains and the formation of hydroxyl groups, thus resulting in the intact chains. The final stage of the dissolution is the hydrolysis of the  $\text{P}-\text{O}$  chains by breaking the  $\text{P}-\text{O}$  bonds inside the chains, until the formation of orthophosphates. For the unnitrided CNP glass, the pH value decreases as more and more glass is dissolved. Fig.3 shows that the unnitrided glass has the lowest pH value, and it arrives at the equilibrium pH value most quickly.

As shown previously [2,4], nitrogen atoms enter the phosphate glass network by partially replacing both the bridging and non-bridging oxygens, forming both  $=\text{N}-$  and  $>\text{N}-$  bonded with P. Three oxygens are replaced by every two nitrogens incorporated. The  $=\text{N}-$  nitrogen creates a branching point where a non-bridging oxygen existed in the tetrahedra and the  $>\text{N}-$  nitrogen creates a branching point in the chain where a bridging oxygen existed. The cross-linking is increased by this reaction. Moreover, because of their covalent nature, the  $\text{P}-\text{N}$  or  $\text{P}=\text{N}$  bonds are more resistant to hydrolysis than the  $\text{P}-\text{O}$  or  $\text{P}=\text{O}$  bonds. It has been proposed that the hydrolysis of the nitrided phosphate glasses takes place by the following reactions [3]:

The same reactions occur for the non-bridging N atoms. During the hydrolysis, the release of  $\text{Na}^+$  and  $\text{Ca}^{2+}$  and the formation of ammonia will increase the pH value of the solution, but the hydrolysis of  $\text{P}-\text{O}-\text{P}$  chains will decrease the pH value. The  $\text{NH}_3$  compensation gives rise to the higher pH value of the nitrided glass than the unnitrided glass, and the higher the nitrogen content, the higher pH value. The higher pH value and lower dissolution rate are desired for the application as bioresorbable material. The pH value change is also a confirmation of reactions (1) and (2). The higher initial pH values are due to the dissolved ammonia and the release of  $\text{Na}^+$  and  $\text{Ca}^{2+}$ . It could be desirable to have the pH remain constant at about 7.4. Miskey [8] has shown that this is possible for some nitrided compositions.





### Crystallization

The peak crystallization temperatures of CNP and CNP-N1 glasses measured by DSC under different temperature increasing rates are shown in Fig. 7. According to JMV theory [9], the relationship between the peak temperature of crystallization and the temperature increasing rate is as following equation:

$$\ln\left(\frac{T_p^2}{\alpha}\right) = \ln\left(\frac{E}{R}\right) - \ln(v) + \frac{E}{RT_p} \quad (2)$$

Where  $T_p$  is the peak crystallization temperature,  $\alpha$  is the temperature increasing rate,  $E$  is the activation energy of crystallization,  $v$  is the jump frequency of the atoms,  $R$  is the gas constant. Fig.8 shows the JMV results for the nitrated CNP-N3 and unnitrated CNP glasses. From Fig.8, the activation energy for CNP glass was calculated to be  $E_{\text{CNP}}=116 \text{ kJ/mol}$ ,  $v_{\text{CNP}}=1.5 \times 10^8 \text{ s}^{-1}$ ; For CNP-N3 glass, the activation energy is  $E_{\text{CNP-N3}}=163 \text{ kJ/mol}$ ,  $v_{\text{CNP-N3}}=2.5 \times 10^{10} \text{ s}^{-1}$ . CNP-N3 glass

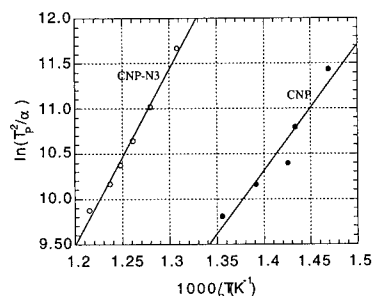


Fig.7. The peak temperatures of crystallization.

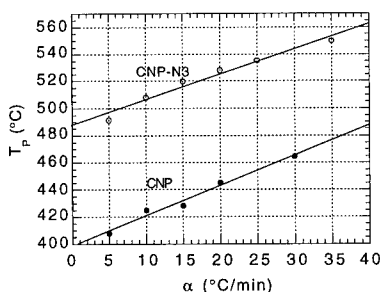


Fig.8. The JMV crystallization kinetics

has a higher activation energy and higher crystallization temperature than CNP glass. The higher the nitrogen content, the more difficult for the devitrification. CNP-N3 has the lowest nitrogen content and is the only nitrated glass having crystallization peak in DSC curve (see Table I). For the high nitrogen containing glass such as CNP-N5, devitrification did not occur even after treating the glass at temperature between  $T_g$  and the melting temperature for several hours. In the DSC curves, the crystallization peak of CNP glass is much sharper than that of CNP-N3 glass. It has been reported that a Li-P-O-N glass containing 6.5 wt% nitrogen was annealed at  $500^\circ\text{C}$  in nitrogen for 8 days with no detectable crystallinity (by XRD) [10].

As indicated before, nitrogen dissolution into the phosphate glass increased the cross-linking of the glass network, thus increasing the viscosity compared to the unnitrated glass at the same temperature. This has been confirmed by the previous measurement of the viscosity of the nitrated

alkali metaphosphate glasses [2]. The crystallization is highly affected by the viscosity of the melt. The higher the viscosity, the slower the crystallization process, because the high viscosity increases the potential barrier or activation energy for the crystallization, preventing the diffusion of the atoms. Furthermore, the covalent nature of the N-P bond increases the mixed bonding fraction, making it more to be devitrified.

## CONCLUSIONS

10CaO·35Na<sub>2</sub>O·55P<sub>2</sub>O<sub>5</sub> system bioresorbable glass was nitrided by melting the glass under anhydrous ammonia at 720 to 750 °C. Increasing nitrogen content is accompanied by increases in the glass transition temperature and chemical durability, as measured by dynamic and equilibrium pH values in water. These changes in the properties are caused by the structure change after nitridation, i.e., the increasing in the cross-linking of the glass network. The nitrided glasses were remelted and fiberized in air at 700 to 740 °C. There is no change in the glass transition temperature after remelting or fiberization. This indicates that the nitrogen dissolved in the glass is stable during remelting in air. The fiberizability, higher pH value, and the lower dissolution rate in water are beneficial for the orthopedic application.

It has been shown by DSC study that the nitrided glass is more difficult to be devitrified probably due to the increase in viscosity.

## REFERENCES

1. B. Kumar, and S. Lin, *Bioceramics*, vol. 3, Proceedings of the 3rd International Symposium on ceramics in Medicine, Terre Haute, Indiana, USA, 1990, pp.271-278.
2. M.R. Reidmeyer, and D.E. Day, *J. Non-Crystalline Solids* **181**, p.201-214(1995).
3. L. Pascual, and A. Durán, *Glastech. Ber.* **64**, p.43-48(1991).
4. M. Rajaram, and D.E. Day, *J. Am. Ceram. Soc.* **70**, p.203-207(1987).
5. Y.B. Peng, and D.E. Day, *Glass Technol.* **36**, p.206-212(1995).
6. L. Pascual, and A. Durán, *Mater. Res. Bull.* **31**, p.77-95(1996).
7. J.A. Raguso, Master Thesis, Alfred University, 1989.
8. D.M. Miskey, Master Thesis, Alfred University, 1992.
9. N.P. Bansal, and R.H. Doremus, *J. Thermal Anal.* **29**, p.115-119(1984).
10. R.W. Larson, and D.E. Day, *J. Non-Crystalline Solids* **88**, p.97-113(1986).

## FORMATION AND PROPERTIES OF AMORPHOUS AND NANOCRYSTALLINE PHASES IN MECHANICALLY ALLOYED FE-BASED MULTICOMPONENT ALLOYS

N. SCHLORKE, J. ECKERT AND L. SCHULTZ

Institut für Festkörper- und Werkstofforschung Dresden, D-01171 Dresden, Germany

### ABSTRACT

Multicomponent Fe-Al-P-C-B alloys have been prepared by mechanical alloying of elemental powder mixtures. X-ray diffraction data were recorded to monitor the structural development of the powders. Coexistent amorphous and nanoscale crystalline phases are found for a variety of alloys. Some alloys exhibit an extended supercooled liquid region before crystallization. The compositional dependence of glass formation and the thermal stability of the resulting phases were investigated by constant-rate heating differential scanning calorimetry (DSC), isothermal annealing experiments, and thermomechanical analysis (TMA). The results are compared with data for melt-spun ribbons.

### INTRODUCTION

Recently, new amorphous alloys with excellent glass forming ability and a wide supercooled liquid region before crystallization have been found in Zr-, La-, and Mg-based alloys [1, 2]. More recently, Inoue *et al.* have also succeeded in finding ferromagnetic Fe-based glassy alloys exhibiting a supercooled liquid region [3, 4] and demonstrated that bulk glassy alloys with diameters up to 1.5 mm can be produced by casting into copper molds [5]. However, the preparation of bulk amorphous samples is limited by the appropriate composition of the material [5, 6] because changes in composition strongly affect the required cooling rates for obtaining bulk samples. In contrast, it is well known that mechanical alloying as a special form of solid state reaction can also lead to amorphization in a wide composition range without any restriction of the sample size and geometry [7]. This enables the production of bulk amorphous samples through the powder metallurgy route and subsequent warm consolidation in the supercooled liquid region with low viscosity. This paper describes the successful use of mechanical alloying to produce multicomponent Fe-based powders exhibiting a significant supercooled liquid region, similar as it has been found for rapidly quenched ribbons [3, 4]. Furthermore, first results for the substitution of Fe by Co or Ni are reported.

### EXPERIMENTAL METHODS

To receive the desired composition of the alloys, elemental powders (purity 99.9%) with a particle size of less than 150  $\mu\text{m}$  were mixed and sealed in a hardened steel vial under a purified argon atmosphere. Mechanical alloying was performed in a Retsch PM 4000 planetary mill using hardened steel balls with a ball-to-powder weight ratio of 15:1. To reveal information about the structure of the samples, x-ray diffraction patterns were recorded with  $\text{CoK}\alpha$ -radiation in a Philips PW 1050 diffractometer. The grain size of the nanocrystalline phases was

determined using the well-known Scherrer formula. Due to wear debris of the milling tools, chemical analysis of the milled powders revealed a slight increase of the Fe content ( $< 0.8$  at.% Fe) compared to the nominal composition of the alloys. Thermal analysis was done in a Perkin-Elmer DSC 7 and TMA 7 at heating rates of 10 and 40 K/min.

## RESULTS AND DISCUSSION

Figure 1 shows x-ray diffraction patterns for  $\text{Fe}_{72}(\text{Al}_5\text{P}_{11}\text{C}_6\text{B}_4)_{1+2/26}$  after different milling times as a typical example. With increasing processing time a decrease of the crystalline Fe and Al diffraction peaks and the formation of a broad diffuse diffraction intensity corresponding to an amorphous phase can be seen. In addition, a broadening of the bcc Fe lines due to a decreasing grain size and an increase in atomic-level strain is observed. In contrast to single-phase amorphous ribbons produced by rapid quenching [3, 4], mechanical alloying of elemental powders reveals an additional nanoscale bcc Fe-rich phase after 130 h of milling. For the initially quaternary  $\text{Fe}_{79}\text{P}_{11}\text{C}_6\text{B}_4$  alloy and a substitution of Fe by 5 at.% Al ( $\text{Fe}_{74}\text{Al}_5\text{P}_{11}\text{C}_6\text{B}_4$ ) and 2 at.% Ga ( $\text{Fe}_{72}\text{Al}_5\text{P}_{11}\text{C}_6\text{B}_4\text{Ga}_2$ ) the formation of an amorphous/nanocrystalline phase mixture is obtained (Fig. 2). Figure 3 shows x-ray diffraction patterns for  $\text{Fe}_{74-x}(\text{Al}_5\text{P}_{11}\text{C}_6\text{B}_4)_{1+x/26}$  with different composition. This change in composition was chosen to maintain a fixed  $\text{Al}_5\text{P}_{11}\text{C}_6\text{B}_4$ -ratio. Starting with  $\text{Fe}_{74}\text{Al}_5\text{P}_{11}\text{C}_6\text{B}_4$  a change of the Fe content in  $\text{Fe}_{74-x}(\text{Al}_5\text{P}_{11}\text{C}_6\text{B}_4)_{1+x/26}$  ( $x = 2, 4, 5, 6$ ) also leads to an amorphous/nanocrystalline phase mixture after a milling time of 130 h for all compositions. Using the well-known Scherrer formula, the average grain size was estimated from the full-width at half maximum (FWHM) of the Fe reflections after correction for instrumental broadening. For all samples investigated a grain size of  $10 \pm 2$  nm was found.

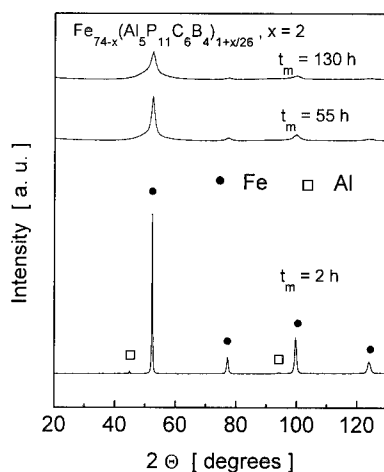


Figure 1: X-ray diffraction patterns for  $\text{Fe}_{72}(\text{Al}_5\text{P}_{11}\text{C}_6\text{B}_4)_{1+2/26}$  after different milling times.

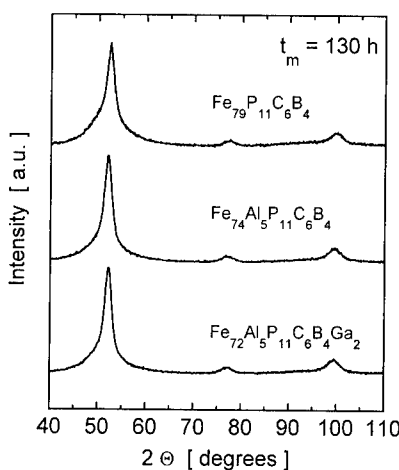


Figure 2: X-ray diffraction patterns for  $\text{Fe}_{79}\text{P}_{11}\text{C}_6\text{B}_4$ ,  $\text{Fe}_{74}\text{Al}_5\text{P}_{11}\text{C}_6\text{B}_4$  and  $\text{Fe}_{72}\text{Al}_5\text{P}_{11}\text{C}_6\text{B}_4\text{Ga}_2$  after 130 h of milling.

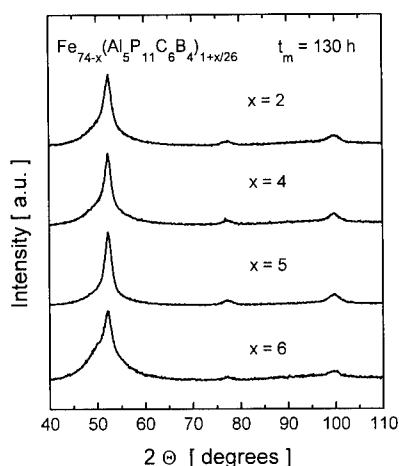


Figure 3: X-ray diffraction patterns for  $\text{Fe}_{74-x}(\text{Al}_5\text{P}_{11}\text{C}_6\text{B}_4)_{1+x/26}$  after 130 h of milling.

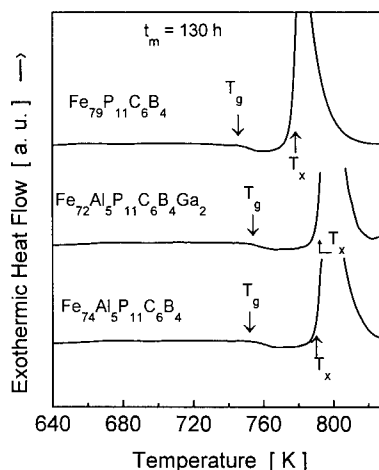


Figure 4: DSC scans (heating rate 40 K/min) for  $\text{Fe}_{79}\text{P}_{11}\text{C}_6\text{B}_4$ ,  $\text{Fe}_{72}\text{Al}_5\text{P}_{11}\text{C}_6\text{B}_4\text{Ga}_2$  and  $\text{Fe}_{74}\text{Al}_5\text{P}_{11}\text{C}_6\text{B}_4$  after 130 h of milling.

The thermal stability of the milled powders was investigated by DSC. All samples exhibit an endothermic event reflecting the heat capacity anomaly characteristic of the glass transition and a sharp exothermic reaction at higher temperatures corresponding to the crystallization of the samples (Figs. 4 and 5). The alloys remain in the supercooled liquid state over an extended temperature range  $\Delta T_x = T_x - T_g$  ( $T_g$ : glass transition temperature,  $T_x$ : crystallization temperature). The substitution of Fe in  $\text{Fe}_{79}\text{P}_{11}\text{C}_6\text{B}_4$  by 5 at.% Al and 2 at.% Ga leads to an extension of the supercooled liquid region from 30 to 40 and 42 K, respectively (Fig. 4). This influence of Al and Ga on the extension of the supercooled liquid region was also found for rapidly quenched ribbons [3, 4]. The DSC scans for  $\text{Fe}_{74-x}(\text{Al}_5\text{P}_{11}\text{C}_6\text{B}_4)_{1+x/26}$  samples with fixed  $\text{Al}_5\text{P}_{11}\text{C}_6\text{B}_4$ -ratio also reveal extended supercooled liquid regions of 40 to 50 K (Fig. 5). It is interesting to note that the largest  $\Delta T_x$ -value of 50 K was found for the powder with the lowest Fe content ( $x = 6$ ). To further prove the amorphicity of the alloys, we performed isothermal annealing experiments. For all samples the shape of the isothermal heat flow signal is characteristic for the formation and growth of nuclei [8]. The measured heat release of 1.85 kJ/mol for  $\text{Fe}_{74}\text{Al}_5\text{P}_{11}\text{C}_6\text{B}_4$  as a typical example is nearly identical to the crystallization enthalpy  $\Delta H = 1.88$  kJ/mol found in the constat-rate heating DSC scan. This confirms that the exothermic event is related to the crystallization of the amorphous phase and not to grain growth of the nanocrystalline bcc Fe phase.

Figure 6 shows the x-ray diffraction patterns for 130 h milled samples where Fe in the  $\text{Fe}_{74}\text{Al}_5\text{P}_{11}\text{C}_6\text{B}_4\text{Ga}_2$  alloy was replaced by Co or Ni. The Co- and Ni-based alloys exhibit only a small amount of remaining crystalline hcp or fcc phases besides the amorphous phase, indicating that amorphization is more pronounced than for the Fe-based alloys. Both the Co- and Ni-based alloys exhibit broad exothermic DSC maxima between about 550 – 660 K, followed by a sequence of exothermic events occurring in the temperature range of 720 – 820 K, which is comparable to the crystallization temperatures of the Fe-based alloys (Fig. 7). Obviously, the

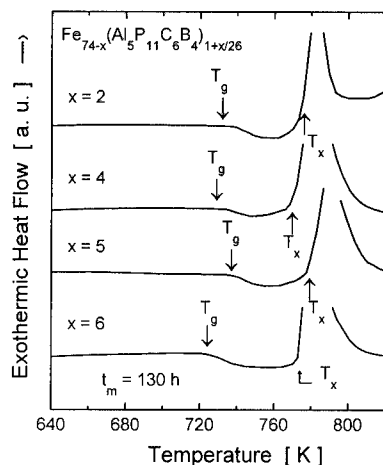


Figure 5: DSC scans (heating rate 40 K/min) for  $\text{Fe}_{74-x}(\text{Al}_5\text{P}_{11}\text{C}_6\text{B}_4)_{1+x/26}$  after 130 h of milling.

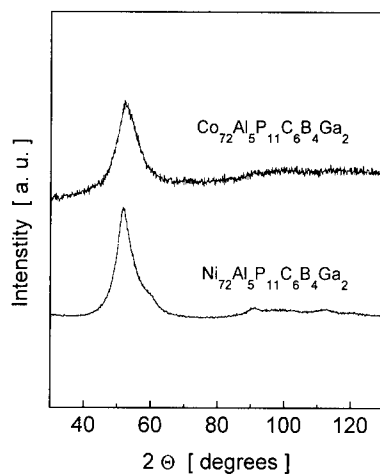


Figure 6: X-ray diffraction patterns for  $\text{Co}_{72}\text{Al}_5\text{P}_{11}\text{C}_6\text{B}_4\text{Ga}_2$  and  $\text{Ni}_{72}\text{Al}_5\text{P}_{11}\text{C}_6\text{B}_4\text{Ga}_2$  after 130 h of milling.

substitution of Fe by Co or Ni changes the crystallization behavior. No supercooled liquid regions were found for these powders. This is in contrast to rapidly quenched samples of comparable composition with additional 3 at.% Cr or V exhibiting  $\Delta T_x$ -values above 45 K [9]. Thus Cr or V additions seem to be essential for the achievement of a supercooled liquid region.

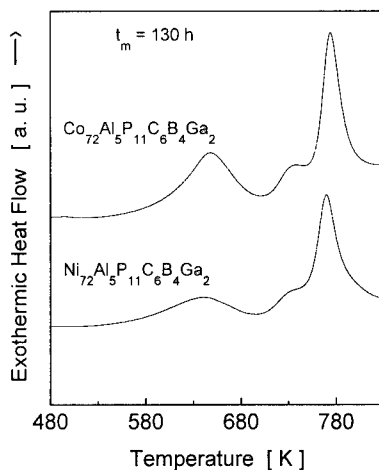


Figure 7: DSC scans (heating rate 40 K/min) for  $\text{Co}_{72}\text{Al}_5\text{P}_{11}\text{C}_6\text{B}_4\text{Ga}_2$  and  $\text{Ni}_{72}\text{Al}_5\text{P}_{11}\text{C}_6\text{B}_4\text{Ga}_2$  after 130 h of milling.

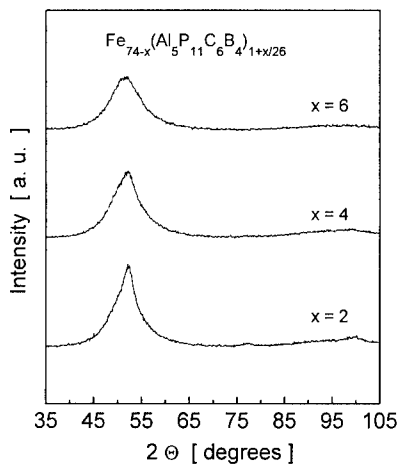


Figure 8: X-ray diffraction patterns for  $\text{Fe}_{74-x}(\text{Al}_5\text{P}_{11}\text{C}_6\text{B}_4)_{1+x/26}$  after 450 h of milling.



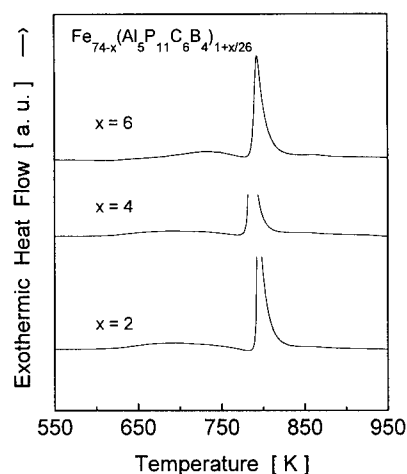


Figure 9 : DSC scans (heating rate 40 K/min) for  $\text{Fe}_{74-x}(\text{Al}_5\text{P}_{11}\text{C}_6\text{B}_4)_{1+x/26}$  after 450 h of milling.

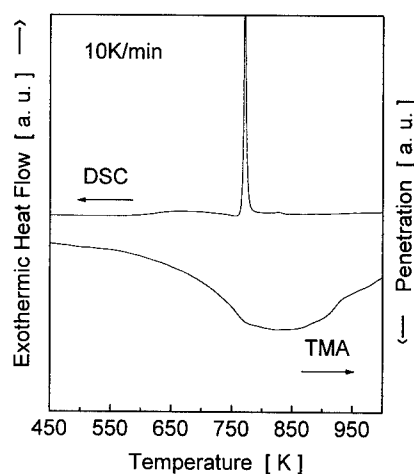


Figure 10: DSC and TMA scans (heating rate 10 K/min) for  $\text{Fe}_{72}(\text{Al}_5\text{P}_{11}\text{C}_6\text{B}_4)_{1+2/26}$  after 450 h of milling.

To gain fully amorphous phases for the Fe-based alloys, we increased the milling time to 450 h. Figure 8 shows the x-ray diffraction patterns for  $\text{Fe}_{74-x}(\text{Al}_5\text{P}_{11}\text{C}_6\text{B}_4)_{1+x/26}$  alloys ( $x = 2, 4, 6$ ) revealing that extended processing produces fully amorphous material for  $x = 6$  and only a very small amount of residual bcc phase for  $x = 4$ . The corresponding DSC scans are shown in Fig. 9. In the temperature range from 650 to 760 K a broad and relatively weak exothermic event can be seen, followed by an endothermic event and the sharp exothermic crystallization peak. For  $x = 2$ , the amount of amorphous material also increased compared to 130 h of milling. However, no full amorphization was achieved even after 450 h of milling; the residual crystalline bcc phase is clearly visible. To further investigate the transformation behaviour of the samples, we performed additional TMA investigations. Figure 10 shows the TMA and DSC scans for  $\text{Fe}_{72}(\text{Al}_5\text{P}_{11}\text{C}_6\text{B}_4)_{1+2/26}$  after 450 h of milling as a typical example. At a temperature of about 650 K a strong decrease in the sample length can be seen in the TMA scan. This sample contraction is believed to be caused by the decrease in viscosity of the sample during the transition from the amorphous state to the supercooled liquid state above  $T_g$ . The combination of DSC and TMA experiments proves that milling for 450 h leads to amorphous material exhibiting a glass transition. However, the nature of the broad low-temperature exothermic DSC event is still unclear. Most likely same part of this reaction is due to structural relaxation. In addition, it cannot be ruled out that also some grain growth of nanoscale bcc crystallites or precipitation of other nanoscale phases might occur in this temperature regime. For clarification, further experiments are under way.

## CONCLUSIONS

Mechanical alloying of  $\text{Fe}_{74-x}(\text{Al}_5\text{P}_{11}\text{C}_6\text{B}_4)_{1+x/26}$  powders ( $2 \leq x \leq 6$ ) leads to amorphous/nanocrystalline phase mixtures after milling for 130 h. With increasing  $x$  the amount of residual bcc phase increases. Despite the existence of the nanoscale bcc phase besides the amorphous phase an extended supercooled liquid region before crystallization was found after 130 h of milling. Extended milling for 450 h leads to more pronounced amorphization and almost fully amorphous powder was obtained for  $x = 6$ . However, the glass transition is not as clearly visible as for the 130 h milled samples. Changes in composition of the amorphous phase upon extended milling due to wear debris from the milling tools and perhaps some oxygen uptake due to not perfectly sealed vials are likely to be the reason for the change of the thermal stability of the material. The substitution of Fe by Co or Ni leads to a larger amount of amorphous material for the same milling time. No distinct glass transition and supercooled liquid region was found for these alloys. In addition, the crystallization behavior changed from one sharp peak for the Fe-based alloys to two exothermic events for the Co- and Ni-based powders. This indicates a change in the crystallization mode from the simultaneous formation of several crystalline phases for the Fe-based alloys to a two-step crystallization process for the Co- and Ni-based powders. To obtain a better understanding of the glass formation and crystallization processes of these mechanically alloyed powders further work including microstructure investigations is necessary to characterize the influence of milling conditions and impurities on the phase formation and the thermal stability of these new multicomponent metallic glasses.

## ACKNOWLEDGMENTS

The authors would like to thank W. Gude and H. Schulze for technical assistance, and M. Seidel and A. Kübler for stimulating discussions and effective cooperation. N. Schlorke gratefully acknowledges financial support from the German Science Foundation (Graduiertenkolleg „Struktur- und Korrelationseffekte in Festkörpern“).

## REFERENCES

1. A. Inoue, T. Zhang and T. Masumoto, *J. Non-Cryst. Solids* **156-158**, 473 (1993).
2. T. Masumoto, *Mater. Sci. Eng.* **A179/A180**, 8 (1994).
3. A. Inoue and J. S. Gook, *Mater. Trans. JIM* **36**, 1180 (1995).
4. A. Inoue and J. S. Gook, *Mater. Trans. JIM* **36**, 1282 (1995).
5. A. Inoue, Y. Shinohara and J.S. Gook, *Mater. Trans. JIM* **36**, 1427 (1995).
6. A. Inoue, T. Zhang and T. Masumoto, *Mater. Trans. JIM* **32**, 1005 (1991).
7. L. Schultz, *Mater. Sci. Eng.* **87**, 15 (1988).
8. L.C. Chen and F. Spaepen, *Nature* **336**, 366 (1988).
9. A. Inoue and A. Katsuya, *Mater. Trans. JIM* **37**, 1332 (1996).

## AUTHOR INDEX

- Aasland, Siv, 377  
 Aitken, B.G., 483  
 Aliev, F.M., 273  
 Ambroise, J.P., 151  
 Arbe, A., 3, 17  
 Assefa, Z., 471  
 Attos, O., 477  
  
 Bagliesi, M.G., 157  
 Bakke, Eric, 369  
 Beaufls, S., 151  
 Boehm, John J., 429  
 Böhmer, R., 47, 117  
 Börjesson, L., 435  
 Bouchaud, J.P., 203  
 Brodin, A., 35  
 Busch, Ralf, 369  
  
 Cai, Zhi-Xiong, 441  
 Castro, J., 247  
 Chakraborty, Bulbul, 229  
 Chamberlin, R.V., 117  
 Chen, Sow-Hsin, 235  
 Cianflone, F., 157  
 Clavaguera, N., 489  
 Clavaguera-Mora, M.T., 489  
 Coddens, G., 151  
 Cohen, D., 483  
 Colmenero, J., 3, 17  
 Colucci, Dina M., 171  
 Coniglio, A., 223  
 Cormack, Alastair N., 241, 259  
  
 Doyama, M., 279  
 Dressel, M., 47  
  
 Eckert, J., 465, 507  
 Ecolivet, C., 151  
 Egami, T., 397  
 Etrillard, J., 151  
  
 Fecht, H-J., 307  
 Frauenfelder, Hans, 343  
 Fujisaki, M., 163, 285  
 Funke, K., 319  
  
 Gallier, J., 151  
 Gallo, Paola, 235  
 Geyer, U., 295, 301  
 Gibson, J. Murray, 349  
 Glotzer, S.C., 223  
 Gorshunov, B., 47  
 Gu, Lei, 229  
 Guéguen, E., 151  
  
 Habasaki, J., 91  
 Haire, R.G., 471  
 Harrington, S.T., 447  
  
 He, Y., 495  
 Heuer, A., 105  
 Higuchi, M., 163  
 Hiwatari, Y., 91  
 Ho, Chung, 377  
  
 Inoue, S., 459  
 Israeloff, N.E., 253, 453  
  
 Jan, N., 223  
 Jia, Weiyl, 483  
 Jiang, H., 501  
 Johnson, William L., 295, 301, 369  
 Julien, C., 477  
  
 Kalia, Rajiv K., 267  
 Kameshima, Y., 495  
 Kieffer, John, 331  
 Kob, Walter, 59  
 Kogure, Y., 279  
 Koike, A., 459  
 Kuebler, S.C., 105  
  
 LaCourse, W.C., 501  
 Leporini, D., 157  
 Loidl, A., 47  
 Loretto, D., 349  
 Lunkenheimer, P., 47  
  
 Mabuchi, T., 357  
 Macht, M-P., 301  
 Marchand, R., 151  
 Massot, M., 477  
 Masuhr, Andreas, 369  
 Matic, A., 435  
 Matsui, J., 163, 285  
 Matsumoto, H., 357  
 Mattern, N., 465  
 Mavi, H.S., 477  
 McGreevy, R.L., 435  
 McKenna, Gregory B., 171  
 McLaughlin, J.C., 405  
 McMahon, B.H., 337  
 McMillan, Paul F., 377  
 Mezard, M., 203  
 Mijangos, C., 17  
 Mijovic, Jovan, 195  
 Moynihan, Cornelius T., 133, 411  
 Müller, J.D., 337  
  
 Nagasawa, H., 357  
 Nauroth, Markus, 59  
 Ngai, K.L., 81, 141, 147  
 Nienhaus, G.U., 337  
  
 Odagaki, T., 163, 285  
 Okada, I., 91  
 Okada, K., 459

Okun, K., 105  
Omel'tchenko, Andrey, 267

Pakula, T., 211  
Park, Byeongwon, 259  
Piché, L., 183  
Pimenov, A., 47  
Poole, P.H., 223  
Pradell, T., 489

Qiu, Y., 301

Ray, P., 447  
Reinecke, H., 17  
Richert, R., 127  
Richter, D., 3  
Rizos, A.K., 141, 147  
Roland, C.M., 81  
Rufflé, B., 151

Sadr-Lahijany, M.R., 447  
Sahnoune, A., 183  
Schienner, B., 47, 117  
Schlorke, N., 507  
Schneider, S., 295, 301  
Schneider, U., 47  
Schultz, L., 465, 507  
Schummer, David J., 441  
Schwarz, R.B., 495  
Sciortino, Francesco, 235  
Seidel, M., 465  
Sen, Surajit, 441  
Shakhmatkin, Boris A., 381  
Sidebottom, D.L., 189  
Simon, Sinee L., 177  
Sinha, G.P., 273  
Sokolov, A.P., 69  
Sorensen, C.M., 189

Spiess, H.W., 105  
Stanley, H.E., 447  
Stump, N.A., 471  
Suñol, J.J., 489

Tagg, S.L., 405  
Tartaglia, Piero, 235  
Teichmann, J., 211  
Thiyagarajan, P., 295  
Thoma, Paul E., 429  
Tombrello, T.A., 301  
Torell, L.M., 35  
Toudic, B., 151  
Tracht, U., 105  
Treacy, M.M.J., 349

Vashishta, Priya, 267  
Vedishcheva, Natalia M., 381

Walther, L.E., 453  
Wang, Jinghan, 267  
Wang, W., 253  
Wannberg, A., 435  
Weber, Richard, 377  
Whang, J-H., 133  
Wright, C.A., 337  
Wright, Adrian C., 381

Yamane, M., 459  
Yano, T., 459  
Yasui, Itaru, 357  
Yasumori, A., 459  
Yeganeh-Haeri, Amir, 377  
Yen, W.M., 483  
Yuan, Huabiao, 483  
Yuan, Xianglong, 241

Zwanziger, J.W., 405

## SUBJECT INDEX

- 2E to 2T<sub>2</sub> transition, 489
- $\alpha$  process, 3
- Adam-Gibbs parameter, 163
- AFM, 453
- alkali
  - metasilicate glasses, 91
  - silicates, 331
- alloying, 489
- amorphous(-), 507
  - amorphous phase transition, 411
  - phase, 295
  - semiconductor, 349
- annealing, 349
- atomic level stresses, 397
- B<sub>2</sub>O<sub>3</sub> glass, 133
- Be diffusivity, 301
- benzophenone, 429
- binary soft-sphere, 285
- bioresorbable, 501
- borate
  - glass, 259
  - glasses, 381
- borovanadate, 477
- Boson Peak, 69, 81, 151
- $\beta_{\text{slow}}$  process, 151
- bulk metallic glass(es), 301, 307, 495
  - formers, 369
  - forming alloys, 465
- cathodic materials, 477
- cation diffusion, 331
- chemical
  - durability, 501
  - structure, 171
- coherent neutron scattering, 151
- composition effect, 489
- computer simulation, 59
- conductivity spectra, 319
- conformational substates (CS), 337
- cooperative
  - jump motion, 91
  - length scale, 147
- cooperativity, 211
- coordination number, 241
- correlation functions, 349
- coupling model, 81, 247
- critical amplitudes, 59
- crystalline, 319
  - polymorphs, 381
- crystallization, 465, 489
- Debye-Stokes-Einstein law, 157
- decomposition, 295
- defect model, 35
- depolarized light scattering, 151
- dielectric
  - relaxation, 127
  - spectra, 3
  - spectroscopy, 47
- differential scanning calorimetry (DSC), 177
- diffraction, 357
- diffusion mechanism, 301
- disordered systems, 203
- dispersity, 447
- domains, 441
- dynamic(s), 229
  - heterogeneity, 127
  - of
    - liquids, 211
    - polymers, 211
    - proteins, 343
- pH, 501
- effect of dispersity on glass transition, 447
- elastic properties, 495
- electrical relaxation, 133
- Electron Spin Resonance spectroscopy, 157
- electron transfer, 337
- embedded atom method, 279
- energy
  - landscape, 337, 343
  - transfer, 471
- ensemble averaged dynamic light
  - scattering, 189
- enthalpy recovery, 177
- entropic instability, 307
- ergodicity breaking, 189
- fast
  - dynamics, 17, 81
    - in glass, 69
  - processes, 47, 223
- ferric ferrous oxide-silica, 459
- fiberization, 501
- first-order phase transition, 377
- fluxing techniques, 495
- 4-fold co-ordinated boron atoms, 381
- fracture, 267
- fragility, 171, 183
- frustrated spin model, 229
- generalized
  - capacity, 285
  - susceptibility, 285
- glass(-), 377, 429, 483
  - formation range, 495
  - forming
    - ability, 369
    - regions, 381
    - systems, 17

like behavior, 273  
 structure, 405  
 transition, 17, 69, 105, 127, 133, 147, 183, 189, 229, 253, 279, 397, 453, 465  
     dynamics, 163  
     temperature, 301  
 glasses, 471  
 glassy, 229, 319  
     dynamics, 229  
 glycerol, 47, 253  
  
 heat capacity, 171  
 heterogeneous relaxation, 105  
  
 infrared, 477  
     image furnace, 459  
 inhomogeneous optical linewidth, 127  
 intermediate scattering function, 59  
 intermolecular cooperativity, 195  
 ionically conducting glasses, 133  
 iron and oxygen additions, 465  
 Ising spin glass, 223  
  
 jump relaxation model, 319  
  
 Kohlrausch function, 331  
  
 lattice model, 211  
 length scale of cooperative motion, 141  
 Lévy flight, 91  
 light scattering, 133  
 liquid(-)  
     crystals, 273  
     dispersed in nanoporous media, 273  
     solid transition, 447  
 local jump, 3  
 luminescence, 471  
  
 magnetic relaxation, 247  
 MD simulated, 241  
 mechanical, 307  
     alloying, 489  
     relaxation, 279  
 mechanically alloyed FE-based, 507  
 medium-range order, 349, 405  
 melt spinning, 489  
 mesoscopic, 453  
 metallic glasses and liquids, 397  
 metastable, 429  
     glassy, 307  
 mixed  
     alkali, 91  
     conductivity, 477  
 Mode-Coupling  
     equations, 59  
     Theory (MCT), 35, 47, 59, 151, 189, 203, 235  
 modeling DSC, 177  
 modification, 141  
  
 molecular  
     dynamics, 357  
         simulation(s) (MD), 91, 259, 267, 285, 331  
     motions, 3  
 molten electrolytes, 319  
 Monte Carlo simulations, 223  
 morphology, 459  
 Mössbauer spectroscopy, 489  
 multicomponent alloys, 507  
 multi-time correlation functions, 105  
  
 nanocrystalline, 507  
     microstructures, 465  
 nanometer size pores, 147  
 network  
     forming glasses, 35  
     structures, 357  
 neutron scattering, 17, 435  
 nitridation, 501  
 nonergodicity parameters, 59  
 nonexponential time dependencies, 343  
 nonfragile glass-forming liquid, 151  
 non-Gaussianity, 163  
 nonresonant spectral hole burning, 117  
 nontrapped jump motion, 163  
  
 octahedrally coordinated, 489  
 1/f dielectric fluctuations, 253  
 ortho terphenyl, 189  
 oxide glasses, 357  
  
 pentavalent chromium, 483  
 phase separation, 459  
 phosphate, 501  
     glasses, 435  
 photon correlation spectroscopy, 141  
 physical aging, 177  
 pinning, 441  
 polyamorphism, 377  
 polymeric glasses, 177  
 polymorphic crystallization, 295  
 potentials, 357  
 properties, 307  
 propylene-carbonate, 47  
 protein(s), 343  
     dynamics, 337  
     function, 337  
 PVAc, 453  
 PVC, 3, 253  
  
 quasielastic  
     contribution, 69, 81  
     neutron scattering, 3  
     scattering, 35  
  
 Raman, 477  
     scattering, 35  
 rapidly quenched amorphous  
      $\text{Zr}_{65}\text{Al}_{17.5}\text{Cu}_{17.5}\text{Ni}_{10}$ , 465

rare-earth, 435  
 rate memory, 105  
 reactive systems, 195  
 reduced dimension, 147  
 relaxation, 211  
   phenomena, 343  
   processes, 91  
   response, 171  
   time, 183  
 reorientational dynamics, 195  
 Reverse Monte Carlo, 435  
 rotational  
   correlation functions, 235  
   dynamics, 157  
  
 Salol, 47  
 scaling law, 441  
 silica, 267  
 simulation(s), 211, 235  
 sizes, 447  
*slip* boundary conditions, 157  
 slow  
   dielectric relaxation, 117  
   dynamics, 235, 273  
 small(-)  
   angle neutron, 295  
   particles, 247  
 soda-lime-silicate glass, 241  
 sodium  
   distributions, 405  
   tellurite glasses, 405  
 soft  
   magnetic amorphous alloys, 489  
   potential model, 35  
 sol-gel, 471  
 solidification temperature, 429  
 solid-state phase transformation, 429  
 solvation dynamics, 127  
 solvent dynamics, 141  
 spatial and dynamic heterogeneities, 223  
 specific heat, 495  
 speckle, 349  
 spectroscopy, 483  
 spin  
   echoes, 405  
   glass(es)  
     mean-field theories, 203  
     without disorder, 203  
  
 Spin Glass Theory, 203  
 spinodal decomposition, 295  
*stick* boundary conditions, 157  
 Stokes-Einstein, 301  
 stretched exponential, 343  
 stretching exponent, 369  
 strong liquids, 369  
 structural  
   glasses, 229  
   recovery, 177  
   relaxation, 133  
 supercooled  
   liquid(s), 117, 295, 301  
     region, 465  
   water, 235  
 supercools, 429  
 superstructural units, 381  
  
 TEM, 349  
 thermal  
   activation, 211  
   expansion, 171  
   gradients, 177  
   stability, 465  
 thermodynamic properties, 307  
 thin films, 147  
 topological description, 397  
 2D lattices on substrates, 441  
 two species/nonideal solution model, 411  
  
 ultrasonic relaxation, 183  
 undercooled liquid states, 307  
 up-conversion, 471  
  
 variable coherence microscopy, 349  
 vibrational, 81  
 viscosities, 369  
 Vogel-Fulcher-Tammann temperature  
   dependence, 319  
  
 waiting time distribution, 163  
 water, 411  
  
 Y<sub>2</sub>O<sub>3</sub>-Al<sub>2</sub>O<sub>3</sub> liquids, 377